

POLITECNICO DI TORINO
Repository ISTITUZIONALE

Aeronautics and Astronautics, AIDAA XXVII International Congress

Original

Aeronautics and Astronautics, AIDAA XXVII International Congress / De Rosa, S.; Petrolo, M.; Zaccariotto, M.. - (2023).

Availability:

This version is available at: 11583/2983591 since: 2023-11-04T12:45:18Z

Publisher:

Materials Research Forum LLC

Published

DOI:

Terms of use:

This article is made available under terms and conditions as specified in the corresponding bibliographic description in the repository

Publisher copyright

(Article begins on next page)

Aeronautics and Astronautics

AIDAA XXVII

International Congress



Edited by
Sergio De Rosa, Marco Petrolo,
Mirco Zaccariotto

MIRF

Aeronautics and Astronautics

AIDAA XXVII International Congress

AIDAA XXVII International Congress, 4th-7th September 2023,
Padova, Italy

Editors

Sergio De Rosa¹, Marco Petrolo², Mirco Zaccariotto³

¹Università di Napoli Federico II, Italy

²Politecnico di Torino, Italy

³Università di Padova, Italy

Peer review statement

All papers published in this volume of “Materials Research Proceedings” have been peer reviewed. The process of peer review was initiated and overseen by the above proceedings editors. All reviews were conducted by expert referees in accordance to Materials Research Forum LLC high standards.

Copyright © 2023 by authors



Content from this work may be used under the terms of the Creative Commons Attribution 3.0 license. Any further distribution of this work must maintain attribution to the author(s) and the title of the work, journal citation and DOI.

Published under License by **Materials Research Forum LLC**
Millersville, PA 17551, USA

Published as part of the proceedings series

Materials Research Proceedings

Volume 37 (2023)

ISSN 2474-3941 (Print)

ISSN 2474-395X (Online)

ISBN 978-1-64490-280-6 (Print)

ISBN 978-1-64490-281-3 (eBook)

This book contains information obtained from authentic and highly regarded sources. Reasonable efforts have been made to publish reliable data and information, but the author and publisher cannot assume responsibility for the validity of all materials or the consequences of their use. The authors and publishers have attempted to trace the copyright holders of all material reproduced in this publication and apologize to copyright holders if permission to publish in this form has not been obtained. If any copyright material has not been acknowledged please write and let us know so we may rectify in any future reprint.

Distributed worldwide by

Materials Research Forum LLC

105 Springdale Lane

Millersville, PA 17551

USA

<https://www.mrforum.com>

Manufactured in the United State of America

10 9 8 7 6 5 4 3 2 1

Table of Contents

Preface

Scientific Committee

Aeroacoustics

Aeroacoustic assessment of blended wing body configuration with low noise technologies

Francesco P. Adamo, Mattia Barbarino et al..... 2

Leonardo I4N research program – design of novel acoustic liners for aero engine nacelles

Giuseppe Dilillo, Paul Murray, Nicola Gravagnone, Massimiliano Di Giulio 6

Aeroacoustics computation based on harmonic balance solution

Luca Abergo, Alberto Guardone 10

Experimental investigation of the noise emitted by two different propellers ingesting a planar boundary layer

Michele Falsi, Ismaeel Zaman, Matteo Mancinelli, Stefano Meloni, Roberto Camussi, Bin Zang, Mahdi Azarpeyvand 17

Predicting noise spectrum of a small drone rotor in a confined environment: a lattice Boltzmann Vles analysis

Riccardo Colombo, Lorenzo Maria Pii, Gianluca Romani, Maurizio Boffadossi 21

Aeroelasticity

On the influence of airframe flexibility on rotorcraft pilot couplings

Carmen Talamo, Andrea Zanoni, Davide Marchesoli, Pierangelo Masarati 26

Tiltrotor whirl-flutter stability analysis using the maximum Lyapunov characteristic exponent estimated from time series

Gianni Cassoni, Alessandro Cocco, Aykut Tamer, Andrea Zanoni, Pierangelo Masarati..... 30

Wind tunnel flutter tests of a strut-braced high aspect ratio wing

Luca Marchetti, Stephan Adden, Michael Meheut, Sergio Ricci..... 34

New insights on limit cycle oscillations due to control surface freeplay

Nicola Fonzi, Sergio Ricci, Eli Livne 38

Aeroelastic design and optimization of strut-braced high aspect ratio wings

Toffol Francesco, Sergio Ricci..... 42

Ten years of aero-servo-elastic tests at large POLIMI's wind tunnel for active flutter control and loads alleviation

Sergio Ricci 48

Aeronautical Propulsion

Studies in hydrogen micromix combustor technologies for aircraft applications

Ainslie D. French, Giuseppe Mingione, Antonio Schettino, Luigi Cutrone, Pietro Roncioni 53

Performance assessment of low-by-pass turbofan engines for low-boom civil supersonic aircraft	
Francesco Piccionello, Grazia Piccirillo , Nicole Viola	57
Numerical and experimental studies on BLI propulsor architectures	
A. Battiston, A. Magrini, R. Ponza, E. Benini, J. Alderman	61

Aeronautical Systems

Neural networks for the identification of degraded components of aircraft fuel quantity system	
Rosario Arcuri, Roberta Masciullo, Roberto Bertola	66
Hardware-in-the-loop validation of a sense and avoid system leveraging data fusion between radar and optical sensors for a mini UAV	
Marco Fiorio, Roberto Galatolo, Gianpietro Di Rito	70
A parametric model for thermal management system for more electric and hybrid aircraft	
Sofia Caggese, Marco Fioriti, Flavio Di Fedè	76
Preliminary design of an electromechanical actuator for eVTOL aircrafts in an urban air mobility context	
Roberto Guida, Antonio Carlo Bertolino, Andrea De Martin, Giovanni Jacazio, Massimo Sorli	80
Landing gear shock absorbers guidelines	
Guida Michele, Marulo Giovanni, Marulo Francesco	84
Experiments and simulations for the development of a dual-stator PMSM for lightweight fixed-wing UAV propulsion	
Aleksander Suti, Gianpietro Di Rito, Roberto Galatolo, Luca Sani, Giuseppe Mattei	89
Target localization with a distributed Kalman filter over a network of UAVs	
Salvatore Bassolillo, Egidio D'Amato, Massimiliano Mattei, Immacolata Notaro	94

Air Traffic Control, Aircraft Operations and Navigation

Integration in controlled airspace: definition and validation of link loss contingency procedures for RPAS in terminal manoeuvring areas	
G. D'Angelo, G. Pompei, A. Manzo, G. Riccardi, U. Ciniglio	99
Hybrid graph-clothoid based path planning for a fixed wing aircraft	
Luciano Blasi, Egidio D'Amato, Immacolata Notaro, Gennaro Raspaolo	104
Navigation services from large constellations in low earth orbit	
Giovanni B. Palmerini, Prakriti Kapilavai	108

Aircraft Design and Aeronautical Flight Mechanics

A tool for risk assessment after a catastrophic event during suborbital flight operations	
Giulio Avanzini, Giovanni Curiazio, Lorenzo Vampo	114

Cruising by air and sea: brief history, status and outlook for a submersible aircraft	
Sergio De Rosa, Marco Cinque, Giuseppe Petrone, Leonardo Lecce.....	118
Low-boom supersonic business jet: aerodynamic analysis and mission simulation towards a CO2 emission standard	
Giacomo Richiardi, Samuele Graziani, Oscar Gori, Nicole Viola.....	122
Effects of different drag laws on ice crystals impingement on probes mounted on a fuselage	
A. Carozza, P.L. Vitagliano, G. Mingione	127
Morphing technology for gust alleviation: an UAS application	
Fernando Montano, Vincenzo Gulizzi, Ivano Benedetti	133
Multidisciplinary design, analysis and optimization of fixed-wing airborne wind energy systems	
Filippo Trevisi, Alessandro Croce, Carlo Emanuele Dionigi Riboldi	137

Artificial Intelligence Application

Refinement of structural theories for composite shells through convolutional neural networks	
Marco Petrolo, Pierluigi Iannotti, Mattia Trombini, Mattia Melis.....	141
Decision trees-based methods for the identification of damages in strongly damped plates for aerospace applications	
Alessandro Casaburo, Cyril Zwick, Pascal Fossat, Mohsen Ardabilian, Olivier Bareille, Franck Sosson.....	146
SHM implementation on a RPV airplane model based on machine learning for impact detection	
G. Scarselli, F. Dipietrangelo, F. Nicassio	150

Fluid-Dynamics

Assessment and optimization of dynamic stall semi-empirical model for pitching aerofoils	
Enrico Galli, Gregorio Frassoldati, Davide Prederi, Giuseppe Quaranta.....	156
Pattern recognition of the flow around a pitching NACA 0012 airfoil in dynamic stall conditions	
Giacomo Baldan, Alberto Guardone	161
RANS transition model predictions on hypersonic three-dimensional forebody configuration	
Luigi Cutrone, Antonio Schettino	166
A finite-volume hybrid WENO/central-difference shock capturing approach with detailed state-to-state kinetics for high-enthalpy flows	
Francesco Bonelli, Davide Ninni, Gianpiero Colonna, Giuseppe Pascazio.....	170
Quantum computing CFD simulations: state of the art	
Giulio Malinverno, Javier Blasco Alberto, Jon Lecumberri SanMartin	174

Analysis of plasma formation during hypersonic flight in the earth atmosphere Salvatore Esposito, Domenic D' Ambrosio	179
Multi-step ice accretion on complex three-dimensional geometries Alessandro Donizetti, Tommaso Bellosta, Mariachiara Gallia, Andrea Rausa, Alberto Guardone	184
Large Eddy simulations and Reynolds-averaged Navier-Stokes simulations of separation-induced transition using an unstructured finite volume solver Manuel Carreño Ruiz, Domenic D' Ambrosio	189
High-fidelity simulation of the interaction between the wake of a descent capsule and a supersonic parachute Luca Placco, Giulio Soldati, Alessio Aboudan, Francesca Ferri, Matteo Bernardini, Federico Dalla Barba, Francesco Picano.....	193
Impact of a wedge in water: assessment of the modeling keyword, presence of cavitation and choice of the filter most suitable for the case study D. Guagliardo, E. Cestino, G. Nicolosi, E. Guarino, A. Virdis, A. Alfero, D. Pittalis, M.L. Sabella	197
Thermal fluid-structure interaction by discontinuous Galerkin methods Vincenzo Gulizzi	202
Conjugate heat transfer applied to transitory analysis for rocket engine cooling systems design Vincenzo Barbato, Matteo Fiore, Francesco Nasuti.....	206
Assessment of aerodynamics of low Martian atmosphere within the CIRA program TEDS Francesco Antonio D' Aniello, Pietro Catalano, Nunzia Favaloro	211
A combustion-driven facility to study phenomenologies related to hypersonic sustained flight Antonio Esposito	218
Development of a DNS solver for compressible flows in generalized curvilinear coordinates Giulio Soldati, Alessandro Ceci, Sergio Pirozzoli	222
Numerical tank self-pressurization analyses in reduced gravity conditions Francesca Rossetti, Marco Pizzarelli, Rocco Pellegrini, Enrico Cavallini, Matteo Bernardini.....	226
Aerodynamic analysis of a high-speed aircraft from hypersonic down to subsonic speeds Giuseppe Pezzella, Antonio Viviani	230

General Session

Virtual testing application to ESA micro vibrations measurement system Lorenzo Dozio, Leonardo Peri, Michele Pagano, Pietro Nali.....	235
---	-----

Nonlinear transient analyses of composite and sandwich structures via high-fidelity beam models	
Matteo Filippi, Rodolfo Azzara, Erasmo Carrera	239
BEA: Overview of a multi-unmanned vehicle system for diver assistance	
Leonardo Barilaro, Jason Gauci, Marlon Galea, Andrea Filippozzi, David Vella, Robert Camilleri	243
Requirements definition in support of digital twin platform development	
Castrese Di Marino, Valeria Vercella, Rocco Gentile, Giacomo Nasi, Stefano Centomo	249
Coupling effect of acoustic resonators for low-frequency sound suppression	
G. Catapane, L.M. Cardone, G. Petrone, O. Robin, F. Franco.....	254
New UAV ice tunnel characterization	
Arrigo Avi, Giuseppe Quaranta, Riccardo Parin.....	258
Remote sensing validation with in-situ measurements for efficient crop irrigation management	
I. Terlizzi, F. Morbidini, C. Maucieri, C. Bettanini, G. Colombatti, S. Chiodini, F. Toson, M. Borin	262
DUST mitigation technology for lunar exploration and colonization: existing and future perspectives	
Guido Saccone, Nunzia Favaloro	266
A static, refractive and monolithic Fourier spectrometer for an HEMERA balloon flight	
Fabio Frassetto, Lorenzo Cocolab, Paola Zuppella, Vania Da Deppo, Riccardo Claudi, Luca Poletto.....	270
Ascent trajectory of sounding balloons: dynamical models and mission data reconstruction	
C. Bettanini, M. Bartolomei, A. Aboudan, L. Olivieri.....	274
Italian space agency space transportation activities and programs	
Marta Albano, Rocco Carmine Pellegrini, Roberto Bertacin, Simone Ciabuschi, Simone Illiano, Rocco Maria Grillo, Enrico Cavallini.....	280

Materials and Aerospace Structures

Nonlinear mechanical analysis of aerospace shell structures through the discontinuous Galerkin method	
Giuliano Guarino, Alberto Milazzo.....	287
Exploring aerospace advancements and global collaborations: a comprehensive analysis of MCAST's aerospace program in Malta	
Leonardo Barilaro, Lorenzo Olivieri, Mark Wylie, Joseph Borg.....	291
Comparison of lattice core topologies in sandwich structures	
G. Mantegna, C.R. Vindigni, D. Tumino, C. Orlando, A. Alaimo	296
Thermal buckling analysis and optimization of VAT structures via layer-wise models	
A. Pagani, E. Zappino, R. Masia, F. Bracaglia, E. Carrera	300

Surface node method for the peridynamic simulation of elastodynamic problems with Neumann boundary conditions	
Francesco Scabbia, Mirco Zaccariotto, Ugo Galvanetto	304
Crack localization on a statically deflected beam by high-resolution photos	
Andrea Vincenzo De Nunzio, Giada Faraco	308
Adaptive finite elements based on Carrera unified formulation for meshes with arbitrary polygons	
Maria Cinefra, Andrea Rubino	313
Analysis of the manufacturing signature on AFP-manufactures variable stiffness composite panels	
Alfonso Pagani, Alberto Racionero Sánchez-Majano	317
An analytical tool for studying the impact of process parameters on the mechanical response of composites	
E. Zappino, M. Petrolo, R. Masia, M. Santori, N. Zobeiry	321
Acoustic characteristics evaluation of an innovative metamaterial obtained through 3D printing technique	
L.M. Cardone, S. De Rosa, G. Petrone, G. Catapane, A. Squillace, L. Landolfi, A.L.H.S. Detry	325
Hygrothermal effects in aeronautical composite materials subjected to freeze-thaw cycling	
Christian Bianchi, Pietro Aceti, Giuseppe Sala	329
Polymer matrices for composite materials: monitoring of manufacturing process, mechanical properties and ageing using fiber-optic sensors	
Davide Airolidi, Pietro Aceti, Giuseppe Sala	333
An energy-based design approach in the aero-structural optimization of a morphing aileron	
Alessandro De Gaspari, Vittorio Cavalieri, Nicola Fonzi	337
A boundary element method for thermo-elastic homogenization of polycrystals	
Dario Campagna, Vincenzo Gulizzi, Alberto Milazzo, Ivano Benedetti	341
Flutter instability in elastic structures	
Davide Bigoni, Francesco Dal Corso, Andrea Piccolroaz, Diego Misseroni, Giovanni Noselli	345
Can we use buckling to design adaptive composite wings?	
Chiara Bisagni	349
Immersed boundary-conformal coupling of cylindrical IGA patches	
Giuliano Guarino, Pablo Antolin, Alberto Milazzo, Annalisa Buffa	353
Folding simulation of TRAC longerons via unified one-dimensional finite elements	
Riccardo Augello, Erasmo Carrera, Alfonso Pagani, Sergio Pellegrino	357
Numerical-analytical evaluation about the impact in water of an elastic wedge using the SPH method	
D. Guagliardo, E. Cestino, G. Nicolosi	363

Data-driven deep neural network for structural damage detection in composite solar arrays on flexible spacecraft	
Federica Angeletti, Paolo Gasbarri, Marco Sabatini	368
A numerical parametric study on delamination influence on the fatigue behaviour of stiffened composite components	
Angela Russo, Andrea Sellitto, Concetta Palumbo, Rossana Castaldo, Aniello Riccio	373
On the use of double-double design philosophy in the redesign of composite fuselage barrel components	
Antonio Garofano, Andrea Sellitto, Aniello Riccio	377
Multifunctional composites as Solid-Polymer-Electrolytes (SPE) for Lithium Ion Battery (LIB)	
Salvatore Mallardo, Gennaro di Mauro, Michele Guida, Pietro Russo, Gabriella Santagata, Rosa Turco	381
Virtual element method for damage modelling of two-dimensional metallic lattice materials	
Marco Lo Cascio, Ivano Benedetti, Alberto Milazzo.....	386
A meso-scale model of progressive damage and failure in LSI-produced ceramic matrix composites for aerospace applications	
A. Airoidi, M. Riva, E. Novembre, A.M. Caporale, G. Sala, M. De Stefano Fumo, L. Cavalli	390
A peridynamics elastoplastic model with isotropic and kinematic hardening for static problems	
Mirco Zaccariotto, Atefeh Pirzadeh, Federico Dalla Barba, Lorenzo Sanavia, Florin Bobaru, Ugo Galvanetto.....	394
Structural batteries challenges for emerging technologies in aviation	
Gennaro Di Mauro, Michele Guida, Gerardo Olivares, Luis Manuel Gomez	399
Dynamic buckling structural test of a CFRP passenger floor stanchion	
Gennaro Di Mauro, Michele Guida, Fabrizio Ricci, Leandro Maio	404
Deep learning algorithms for delamination identification on composites panels by wave propagation signals analysis	
Ernesto Monaco, Fabrizio Ricci	409
Deployment of a CubeSat radiative surface through an autonomous torsional SMA actuator	
Filippo Carnier, Alberto Riccardo Donati, Elena Villa, Daniela Rigamonti, Paolo Bettini.....	413
Development of an FBG-based hinge moment measuring system for wind tunnel testing	
A. Taraborrelli, A. Gurioli, P. De Fidelibus, E. Casciaro, M. Boffadossi, P. Bettini	417
Buckling and post-buckling response of curved, composite, stiffened panels under combined loads including pressurization	
Luisa Boni, Daniele Fanteria, Tommaso Lucchesi	421

MOST Project

Insights on state of the art and perspectives of XR for human machine interfaces in advanced air mobility and urban air mobility

Sandhya Santhosh, Francesca DeCrescenzo, Millene Gomes Araujo, Marzia Corsi, Sara Bagassi, Fabrizio Lamberti, Filippo Gabriele Praticò, Domenico Accardo, Claudia Conte, Francesco De Nola, Marco Bazzani, Joyce Adriano Losi 426

Electric conversion of a general aviation aircraft: a case study

Sergio Bagarello, Ivano Benedetti..... 431

Aerodynamic design of advanced rear end for large passenger aircraft

Salvatore Corcione, Vincenzo Cusati, Fabrizio Nicolosi 435

Towards multidisciplinary design optimization of next-generation green aircraft

Luca Pustina, Matteo Blandino, Pietro Paolo Ciottoli, Franco Mastroddi 440

Improvements in on-board systems design for advanced sustainable air mobility

Claudia Conte, Domenico Accardo 444

Recent developments about hybrid propelled aircraft: a short review

L.M. Cardone, S. De Rosa, G. Petrone, F. Franco, C.S. Greco 448

Refined structural theories for dynamic and fatigue analyses of structure subjected to random excitations

Matteo Filippi, Elisa Tortorelli, Marco Petrolo, Erasmo Carrera..... 453

Satellite and Space Systems

Facility for validating technologies for the autonomous space rendezvous and docking to uncooperative targets

M. Sabatini, G.B. Palmerini, P. Gasbarri, F. Angeletti 458

Simulation of in-space fragmentation events

Lorenzo Olivieri, Cinzia Giacomuzzo, Stefano Lopresti, Alessandro Francesconi 465

Scientific activity of Sapienza University of Rome aerospace systems laboratory on the study of lunar regolith simulants, focusing on their effect on the microwave fields propagation

Andrea Delfini, Roberto Pastore, Fabio Santoni, Michele Lustrino, Mario Marchetti 469

The new transmitting antenna for BIRALES

G. Bianchi, S. Mariotti, M.F. Montaruli, P. Di Lizia, M. Massari, M.A. De Luca, R. Demuru, G. Sangaletti, L. Mesiano, I. Boreanaz 474

Continuous empowering with laser power transmission technologies for ISRU moon assets: CIRA approach

Maria Chiara Noviello, Nunzia Favaloro 478

Preliminary design of a CubeSat in loose formation with ICEYE-X16 for plastic litter detection

Francesca Pelliccia, Raffaele Minichini, Maria Salvato, Salvatore Barone, Salvatore Dario dell'Aquila, Vincenzo Esposito, Marco Madonna, Andrea Mazzeo, Ilaria Salerno, Antimo Verde, Marco Grasso, Antonio Gigantino, Alfredo Renga 483

A revisited and general Kane's formulation applied to very flexible multibody spacecraft	
D.P. Madonna, P. Gasbarri, M. Pontani, F. Gennari, L. Scialanga, A. Marchetti	487
Concept and feasibility analysis of the Alba CubeSat mission	
M. Mozzato, S. Enzo, R. Lazzaro, M. Minato, G. Bemporad, D. Visentin, F. Filippini, A. Dalla Via, A. Farina, E. Pilone, F. Basana, L. Olivieri, G. Colombatti, A. Francesconi	495
Space object identification and correlation through AI-aided light curve feature extraction	
Chiara Bertolini, Riccardo Cipollone, Andrea De Vittori, Pierluigi Di Lizia, Mauro Massari.....	499
Development of a smart docking system for small satellites	
Alex Caon, Luca Lion, Lorenzo Olivieri, Francesco Branz, Alessandro Francesconi	504
AUTOMA project: technologies for autonomous in orbit assembly operations	
Alex Caon, Martina Imperatrice, Mattia Peruffo, Francesco Branz, Alessandro Francesconi ...	508
Overview of spacecraft fragmentation testing	
Stefano Lopresti, Federico Basana, Lorenzo Olivieri, Cinzia Giacomuzzo, Alessandro Francesconi.....	513
Feasibility analysis of a CubeSat mission for space rider observation and docking	
Chilin Laura, Bedendo Martina, Banzi Davide, Casara Riccardo, Costa Giovanni, Dolejsi Elisabetta, Quitadamo Vincenzo, Trabacchin Nicolò, Visconi Delia, Visentin Alessia, Basana Federico, Olivieri Lorenzo, Colombatti Giacomo, Francesconi Alessandro.....	518
Analysis of small spacecraft Mars aerocapture through a single-event drag modulation	
Tobia Armando La Marca, Giorgio Isoletta, Michele Grassi.....	522
Onboard autonomous conjunction analysis with optical sensor	
Luca Capocchiano, Michele Maestrini, Mauro Massari, Pierluigi Di Lizia	526
Mini-IRENE, a successful re-entry flight of a deployable heatshield capsule	
Stefano Mungiguerra, Raffaele Savino, Paolo Vernillo, Luca Ferracina, Francesco Punzo, Roberto Gardi, Maurizio Ruggiero, Renato Aurigemma, Pasquale Dell'Aversana, Luciano Gramiccia, Samantha Ianelli, Giovanni D'Aniello, Marta Albano	530
Electro-thermal dynamic simulations and results of a deorbiting tethered system	
G. Anese, G. Colombatti, A. Brunello, A. Valmorbida, G. Polato, S. Chiodini, E.C. Lorenzini	534
Mechanical and pneumatic design and testing of a floating module for zero-gravity motion simulation	
Simone Galleani, Thomas Berthod, Alex Caon, Luca Lion, Federico Basana, Lorenzo Olivieri, Francesco Branz, Alessandro Francesconi	538
Simulations for in-flight stellar calibration aimed at monitoring space instruments optical performance	
Casini Chiara, P. Chioetto, A. Comisso, A. Corso, F. Frassetto, P. Zuppella, V. Da Deppo	542
Reduced-order modelling of the deployment of a modified flasher origami for aerospace applications	
A. Troise, P. Celli, M. Cinefra, V. Netti, A. Buscicchio.....	547

Deployment profile analysis for tethered deorbiting technologies	
G. Polato, A. Valmorbida, A. Brunello, G. Anese, S. Chiodini, G. Colombatti, E.C. Lorenzini	553
The Janus COM mechanism onboard the JUICE probe to the Jovian system	
G. Colombatti, A. Aboudan, M. Bartolomei, S. Chiodini, A. Dattolo, G. Noci, F. Sarti, T.Bilotta, A.Colosimo	558
Comparison of LARES 1 and LARES 2 missions - one year after the launch	
Ignazio Ciufolini, Antonio Paolozzi, Emiliano Ortore, Claudio Paris, Erricos C. Pavlis, John C. Ries, Richard Matzner.....	563
Tracking particles ejected from active asteroid Bennu with event-based vision	
Loïc James Azzalini, Dario Izzo	567
Totimorphic structures for space application	
Amy Thomas, Jai Grover, Dario Izzo, Dominik Dold	572
Pushing the limits of re-entry technology: an overview of the Efesto-2 project and the advancements in inflatable heat shields	
Giuseppe Guidotti, Giuseppe Governale, Nicole Viola, Ingrid Dietleinc, Steffen Callsen, Kevin Bergmann, Junnai Zhai, Roberto Gardi, Barbara Tiseo, Ysolde Prevereaud, Yann Dauvois, Giovanni Gambacciani, Giada Dammacco	576
The ATEMO device: a compact solution for earth monitoring	
Federico Toson, Alessio Aboudan, Carlo Bettanini, Giacomo Colombatti, Irene Terlizzi, Sebastiano Chiodini, Lorenzo Olivieri	581
The Hera Milani mission	
M. Cardi, M. Pavoni, D.Calvi, F. Perez, P. Martino, I. Carnelli, Milani consortium members	585
Small celestial body exploration with CubeSat Swarms	
Emmanuel Blazquez, Dario Izzo, Francesco Biscani, Roger Walker, Franco Perez-Lissi	590

Space Flight Mechanics

Low-energy earth-moon mission analysis using low-thrust optimal and feedback control	
A. Almonte, I. Ziccardi, A. Adriani, A. Marchetti, M. Pontani	596
The application of modal effective mass for PCB friction lock compliance against spacecraft launch random vibration spectrum	
Mark Wylie, Leonardo Barilaro	601
Near-optimal feedback guidance for low-thrust earth orbit transfers	
D. Atmaca, M. Pontani	606
Reduced-attitude stabilization for spacecraft boresight pointing using magnetorquers	
Fabio Celani	611
Trajectory optimization and multiple-sliding-surface terminal guidance in the lifting atmospheric reentry	
Edoardo Maria Leonardi, Mauro Pontani.....	615

Analytic formulation for J2 perturbed orbits	
Silvano Sgubini, Giovanni B. Palmerini	621
Low-thrust maneuver anomaly detection of a cooperative asset using publicly available orbital data	
Riccardo Cipollone, Pierluigi di Lizia.....	625
Efficient models for low thrust collision avoidance in space	
Juan Luis Gonzalo, Camilla Colombo, Pierluigi Di Lizia, Andrea De Vittori, Michele Maestrini, Pau Gago Padreny, Marc Torras Ribell, Diego Escobar Antón.....	630
An overview of the ArgoMoon and LICIAcube flight dynamics operations	
Marco Lombardo, Luis Gomez Casajus, Marco Zannoni, Igor Gai, Edoardo Gramigna, Paolo Tortora, Elisabetta Dotto, Marilena Amoroso, Simone Pirrotta, Valerio Di Tana, Biagio Cotugno, Silvio Patruno, Francesco Cavallo, the LICIAcube Team..	634
Re-entry predictions of space objects and impact on air traffic	
Franco Bernelli-Zazzera, Camilla Colombo, Mattia Recchia	639

Space Propulsion

Update on green chemical propulsion activities and achievements by the University of Padua and its spin-off T4I	
F. Barato, A. Ruffin, M. Santi, M. Fagherazzi, N. Bellomo, D. Pavarin	645
1D numerical simulations aimed to reproduce the operative conditions of a LOx/LCH4 engine demonstrator	
Angelo Romano, Daniele Ricci, Francesco Battista	654
Fast reconfiguration maneuvers of a micro-satellite constellation based on a hybrid rocket engine	
Antonio Sannino, Stefano Mungiguerra, Sergio Cassese, Raffaele Savino, Alberto Fedele, Silvia Natalucci	660
Tests and simulations on 200N paraffin-oxygen hybrid rocket engines with different fuel grain lengths	
Stefano Mungiguerra, Daniele Cardillo, Giuseppe Gallo, Raffaele Savino, Francesco Battista.....	664
Thermite-for-demise (T4D): thermite characteristics heuristic optimization on object- and spacecraft-oriented re-entry models	
Alessandro Finazzi, Filippo Maggi, Tobias Lips	668
Numerical and experimental assessment of a linear aerospike	
Emanuele Resta, Gaetano Maria Di Cicca, Michele Ferlauto, Roberto Marsilio	675
Numerical suite for the design, simulation and optimization of cathode-less plasma thrusters	
Nabil Souhair, Mirko Magarotto, Raoul Andriulli, Fabrizio Ponti	679
Particle migration modeling in solid propellants	
Raoul Andriulli, Nabil Souhair, Luca Fadigati, Mattia Magnani, Fabrizio Ponti	690
Validation of a numerical strategy to simulate the expansion around a plug nozzle	
Marco Daniel Gagliardi, Luca Fadigati, Nabil Souhair, Fabrizio Ponti.....	695

Special Session in Memory of Professor Debei

Solar simulator facility for the verification of space hardware performance C. Bettanini, M. Bartolomei, S. Chiodini, L. Tasinato, P. Ramous, F. Dona, S. Debei.....	700
Trajectory reconstruction by means of an event-camera-based visual odometry method and machine learned features S. Chiodini, G. Trevisanuto, C. Bettanini, G. Colombatti, M. Pertile.....	705
The wide angle camera of rosetta Giampiero Naletto	709
Development of a modular central electronic unit (CEU) for data handling and management in Martian atmosphere investigations L. Marrocchi, M. Marchetti, F. Costa, S. Debei.....	713
SIMBIO-SYS, the remote sensing instruments on board the BepiColombo mission G. Cremonese, C. Re, the SIMBIO-SYS team.....	717
The ESA PANGAEA programme: training astronauts in field science Matteo Massironi, Francesco Sauro, Samuel J. Payler, Riccardo Pozzobon, Harald Hiesinger, Nicolas Mangold, Charles S. Cockell, Jesus Martínez Frias, Kåre Kullerud, Leonardo Turchi, Igor Drozdovskiy, Loredana Bessone	721
Front cover for space optical telescopes. a legacy from ROSETTA to JUICE G. Parzianello, M. Bartolomei, S. Chiodini, M. Zaccariotto, G. Colombatti, A. Aboudan, C. Bettanini, S. Debei.....	725

Vibroacoustics

In-vacuo structured fabrics for vibration control Paolo Gardonio, Sofia Baldini, Emiliano Rustighi, Ciro Malacarne, Matteo Perini.....	731
Experimental application of pseudo-equivalent deterministic excitation method for the reproduction of a structural response to a turbulent boundary layer excitation Giulia Mazzeo, Mohamed Ichchou, Giuseppe Petrone, Olivier Bareille, Francesco Franco, Sergio De Rosa.....	736
Labyrinth quarter-wavelength tubes array for the reduction of machinery noise G. Catapane, G. Petrone, O. Robin, J.-C. Gauthier-Marquis, S. De Rosa	740
Comparative study of shock response synthesis techniques for aerospace applications Ada Ranieri, Simone De Carolis, Giuseppe Carbone, Michele Dassisti, Andrea De Cesaris, Leonardo Soria	744
Vibro-acoustic analysis of additively manufactured acoustic metamaterial via CUF adaptive finite elements M. Rossi, M.C. Moruzzi, S. Bagassi, M. Corsi, M. Cinefra	748

XR and Human Factors for Future Air Mobility

A brief review of pilots' workload assessment using flight simulators: subjective and objective metrics Giuseppe Iacolino, Antonio Esposito, Calogero Orlando, Andrea Alaimo	754
--	-----

Applying an interior VR co-design approach for the medical deployment vehicle of the future	
J. Herzig, F. Reimer, M. Lindlar, P. Weiland, J. Biedermann, F. Meller, B. Nagel	758
Innovative ideas for the use of augmented reality devices in aerodrome control towers	
Jürgen Teutsch.....	763
ADS-B driven implementation of an augmented reality airport control tower platform	
Tommaso Fadda, Sara Bagassi, Marzia Corsi.....	767
Maturity-based taxonomy of extended reality technologies in aircraft lifecycle	
Sara Bagassi, Marzia Corsi, Francesca De Crescenzo, Martino Carlo Moruzzi, Sandhya Santhosh.....	771

Keyword index

Preface

AIDAA (www.aidaa.it), founded in 1920, was one of the first Aerospace Associations worldwide and aims to promote the development and diffusion of aeronautical and space science. AIDAA organizes an international congress every other year, sharing the most recent progress in Aerospace Science and Technology.

AIDAA is the hosting society of three world congresses in 2024: the International Astronautical Congress (IAC 2024, Milano); the Congress of the International Council of Aeronautical Sciences (ICAS, Firenze); the AIAA/CEAS Aeroacoustics Congress (Roma). For the first time, these congresses are hosted by the same country just a few weeks apart. To pave the way to 2024, AIDAA launched the Aerospace Italy 2024 Initiative, www.aidaa.it/aerospaceitaly2024/, to promote and support the organization of events in Italy and define the Road to 2024.

The 27th AIDAA Congress (<https://www.aidaa.it/aidaa2023/>) was held in the Beato Pellegrino Complex of the University of Padua from the 4th to the 7th of September 2023. About 176 papers were presented in all scientific and aerospace engineering fields, including aerodynamics and fluid dynamics, propulsion, materials and structures, aerospace systems, flight mechanics and control, space systems, and missions. Two hundred fifteen attendees participated, and eight plenary talks were delivered: the Vice-President of the Azerbaijan Space Agency, Azercosmos, Dunay Badirkhanov; Professor Gianluca Iaccarino from Stanford; Franco Malerba, the first Italian astronaut; Professors Giorgio Guglieri and Erasmo Carrera from the Politecnico di Torino; Dr Ian Carnelli of the European Space Agency; the director of the ZAL Centre for Applied Aeronautical Research, Roland Gerhards; and Professor Daniele Ragni from the Delft University of Technology.

Scientific Committee

Sergio De Rosa, Università di Napoli Federico II
Marco Petrolo, Politecnico di Torino
Mirco Zaccariotto, Università di Padova
Sara Bagassi, Università di Bologna
Carlo Bettanini, Università di Padova
Damiano Casalino, TU Delft
Camilla Colombo, Politecnico di Milano
Paolo Gasbarri, Università di Roma La Sapienza
Dario Izzo, ESA
Alberto Milazzo, Università di Palermo
Alfonso Pagani, Politecnico di Torino
Giuseppe Pascazio, Politecnico di Bari
Marilena D. Pavel, TU Delft
Raffaele Savino, Università di Napoli Federico II
Zdravko Terze, University of Zagreb
Francesco Topputo, Politecnico di Milano
Michele Guida, Università di Napoli Federico II
Andrea Alaimo, Università di Enna Kore
Tommaso Andreussi, Scuola Superiore Sant'Anna
Roberto Camussi, Università di Roma 3
Margherita Capriotti, San diego State University
Rauno Cavallaro, Universidad Carlos III Madrid
Domenic D'Ambrosio, Politecnico di Torino
Luciano Demasi, San Diego State University
Gianpietro Di Rito, Università di Pisa
Dominik Dold, ESA
Roberto Galatolo, Università di Pisa
Tomatz Goetzendorf-Grabowski, Warsaw University of Technology
Gianluca Iaccarino, Stanford University
Mohamed Ichchou, Ecole Centrale Lyon
Łukasz Kiskowiak, Military University of Technology
Michelle Lavagna, Politecnico di Milano
Enrico Lorenzini, Università di Padova
Salvo Marcuccio, Università di Pisa
Roberto Marsilio, Politecnico di Torino
Francesco Marulo, Università di Napoli Federico II
Pierangelo Masarati, Politecnico di Milano

Marco Montemurro, École Nationale Supérieure d'Arts et Métiers
Fabio Olivetti, Università di Bologna
Fabrizio Oliviero, TU Delft
Francesco Picano, Università di Padova
Sergio Ricci, Politecnico di Milano
Lorenzo Trainelli, Politecnico di Milano
Mauro Valorani, Università di Roma La Sapienza
Wenbin Yu, Purdue University
Navid Zobeiry, University of Washington
Erasmo Carrera, Politecnico di Torino
Fausto Cereti
Harijono Djojodihardjo, Putra University
Amalia Ercoli Finzi, Politecnico di Milano
Aldo Frediani, Università di Pisa
Paolo Gaudenzi, Università di Roma La Sapienza
Vittorio Giavotto, Politecnico di Milano
Gary H. Koopmann, Pennsylvania State University
Leonardo Lecce, Università di Napoli Federico II
Luigi Morino, Università degli Studi Roma Tre
Olivier Pironneau, Sorbonne-Université
Egbert Torenbeek, TU Delft
Ernesto Vallerani, International Space Pioneers

Aeroacoustics

Aeroacoustic assessment of blended wing body configuration with low noise technologies

Francesco P. Adamo^{a,*}, Mattia Barbarino^{2,b} et al.

¹CIRA, Italian Aerospace Centre, Capua (Italy)

² CIRA, Italian Aerospace Centre, Capua (Italy)

^af.adamo@cira.it, ^bm.barbarino@cira.it

Keywords: Aeroacoustics, Low Noise Technologies, BWB, Distributed Electric Propulsion, Regional Aircraft, Shielding effect, Airport Noise, Footprint

Abstract. An aeroacoustic assessment of promising novel aircraft concepts (BOLT and REBEL, two Blended wing bodies respectively with conventional and hybrid engines) devoted to fly in 2035-2050 scenario coupled with Low Noise Technologies (LNT) developed inside the framework of ARTEM project (H2020)[1] has shown. The noise assessment of each noise source of the AAC (Advanced Air Concepts) has been provided including the attenuation due to the masking effects due to the fuselage. The results are then used for the noise impact on the ground, through a ray-tracing method and taking into account the installative effects, with a comparison with standard/similar aircraft. Finally, the noise assessment of a AAC&Standard fleet on a reference airport has been provided.

Introduction

The main noise sources of novel BWB configuration BOLT and REBEL have been analyzed though some of the most used semi-empirical or numerical models well known in literature, then noise predictions have been coupled with Low Noise Technologies in order to satisfy the community requests. The effects of the installation of these LNTs, together with the shielding effect due to the particular shape of the Blended-Wing-Body, have been analyzed, following the most common noise metrics, in terms of single aircraft and fleet simulation on a reference airport.

Aeroacoustic Approach

The methodology proposed for the aeroacoustic analysis of the noise impact of BOLT and REBEL follows four steps: i) Aerodynamic modelling, focused on REBEL and the effects of a set of DEP; ii) Aeroacoustic modelling for each noise sources, generating noise hemispheres; iii) Scattering modeling where the fuselage effects of the BWB have been evaluated; iv) Ground propagation modelling where the noise assessment at ground level for a single fly-over event and then a fleet simulation at two certification points have been performed.

Validation of noise models

Reference data for an aircraft with similar characteristic to one of two disruptive concepts analyzed – BOLT – have been collected in order to compare them with the results predicted with the noise source models.

The comparison has been made using the NPD (Noise Power Design) curves provided by ANP database[1] for a range of altitudes that varies from 630 to 12000 ft and the airspace has been defined to correctly predict the SEL (*Sound Exposure Level*) as a time integrated noise index derived from the SPL (*Sound Pressure Level*) as shown, for several thrusts, in *Figure 1*. The results show good agreement between experimental data and theoretical prediction.



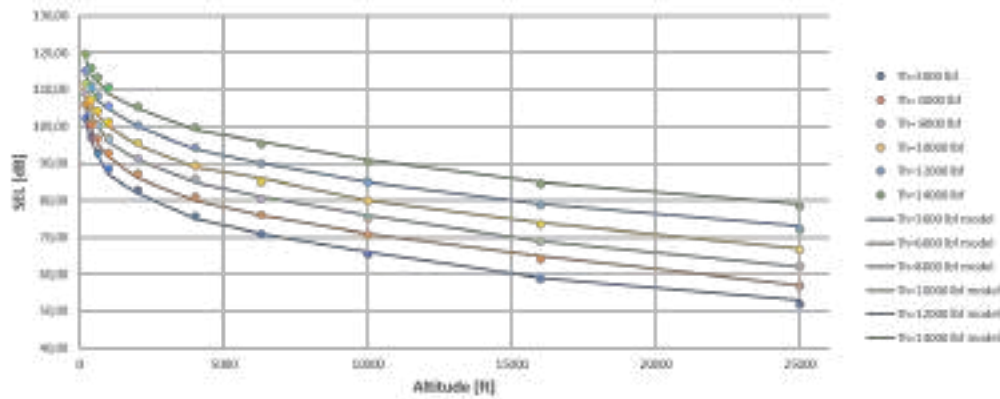


Figure 1: SEL comparison calculated for a reference aircraft similar to BOLT, for different thrusts. Circles represent exp data (SEL, ANP); Lines represent model (SEL predicted).

Fuselage shielding

The shielding effects by the BWB fuselage have been evaluated on hemispheres surrounding the aircraft, with a radius of 50m and with a twofold approach assuming the absence of mean flow: the first one is based on discontinuous Galerkin method developed by ACTRAN[2] while the second one is based on the fast shielding approach (method of Maekawa[3]), more suitable for medium-high frequencies. The results show a good agreement among two approaches and in particular show that, for the first two blade passing frequencies (the most annoying part of the overall noise), the attenuation due to the configuration can reach 20 dB (in front of the aircraft): the fuselage shielding plays a crucial role for the noise reduction of such aircrafts (Figure 2).

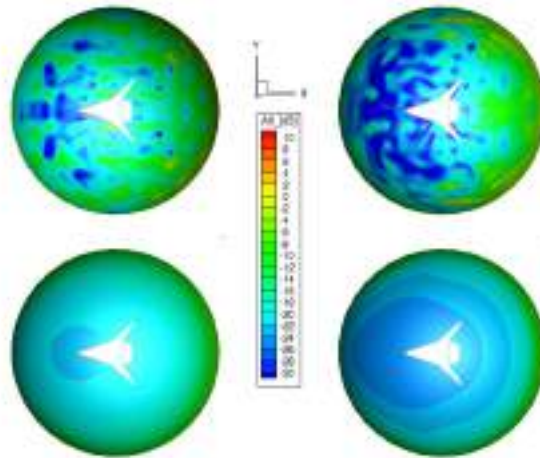


Figure 2: Attenuation effects at the BPF and comparison between DGM Method (on the top) and fast shielding approach (bottom figure). On the left 1st BPF, on the right 2nd.

BOLT and REBEL assessment

The attention is then focused on the noise analysis of BOLT and REBEL with and w/o low noise technologies (LNT) developed inside the framework of ARTEM project. Their coupling was done taking in account the feasibility of the single LNT analyzed, the degree of risk and the scaling to BOLT and REBEL. The main LNT analyzed and the related noise source involved can be summarized in the following list: i) Innovative liners on slanted septum core (fan noise); ii) High Lift Devices; iii) Flap porous treatments for Jet Interactions; iv) Jet Installation Effects; v) Landing Gear Effects. The contribution of each LNT has been considered in terms of Insertion Loss (IL). The noise predictions have been done considering firstly the noise results got with the noise models for each noise source of the aircraft, then applying the LNT related to each noise source and finally summing energetically the new noise results and projecting them on takeoff/flyover and landing

dedicated trajectories. The final assessment of this procedure is shown, only for BOLT, into *Figure 3*:

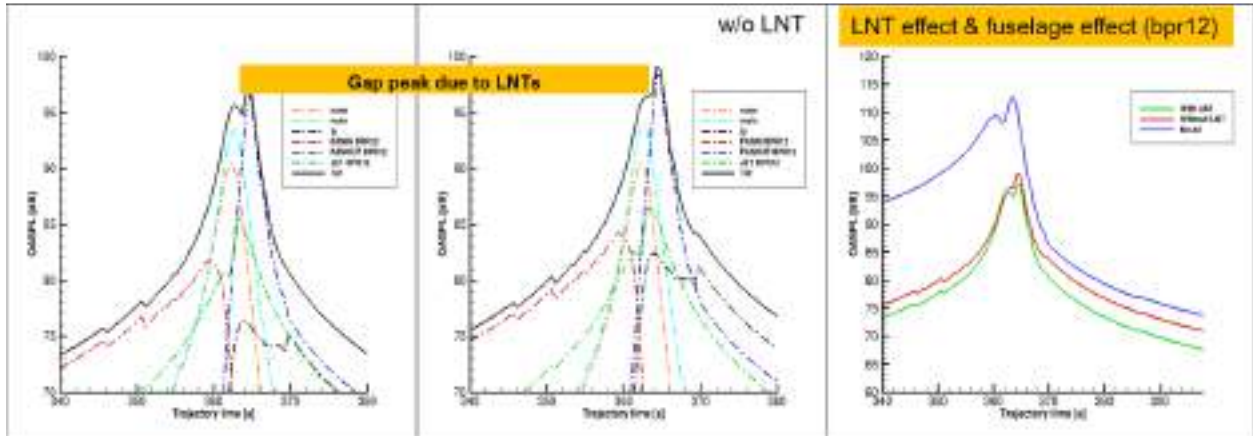


Figure 3: Each noise source is shown (fan, jet, main and nose landing gear, trailing edge, total). First two pictures on the left shows the gap due to LNTs; third on right the gap due to the fuselage effect. BOLT, takeoff, mic at $x=2300$ m.

Then BOLT and REBEL SELs are predicted for each noise sources as shown in figure below:

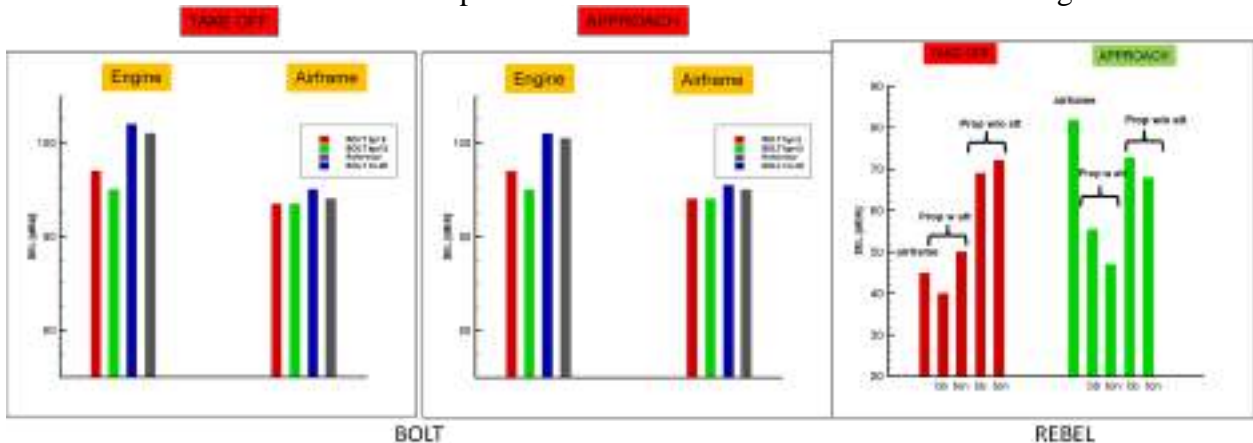


Figure 4: first two figures on the left: SEL of each noise source in BOLT; third figure on the right: REBEL SELs of each noise source (propeller noise, tonal and broadband component).

Acoustic impact on a reference airport

The acoustic impact on a selected airport (Naples, Italy) of BOLT and REBEL has been simulated. *Figure 5* shows the results derived from comparing BOLT with a reference aircraft. The results clearly show a noise reduction due to BOLT configuration. Same conclusions arise simulating a fleet simulation of AACs and comparing with standard aircraft. (*Table 1*).

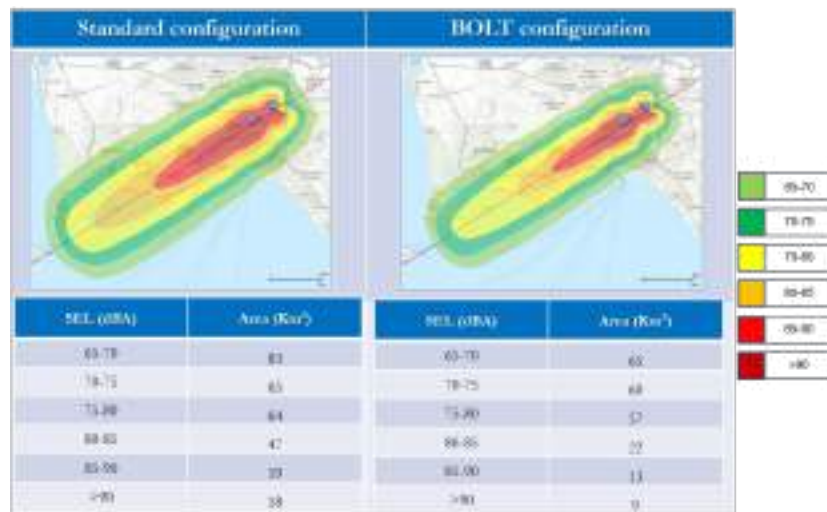


Figure 5: Acoustic impact comparison: Single event contours (take off).

L_{DEN} [dBA]	Area (standard – novel) [Km ²]
60-65	-3
65-70	-1
70-75	-1
75-80	0
80-85	0
>85	-0,3

Table 1: Equal loudness LDEN contours: standard scenario - 2050 scenario.

Conclusions

AAC as BOLT and REBEL satisfy the community requests of noise reduction. This is mainly due to the fuselage shielding effect of BWB configuration and secondary to the application of Low Noise Technologies. Further investigations will have to pursue this twice way in order to reach the main target of the noise reduction.

References

- [1] <https://cordis.europa.eu/project/id/769350>
- [2] <https://doi.org/https://www.acare4europe.org/>
- [3] Chevaugnon N. et al., Efficient discontinuous Galerkin methods for solving Aeroacoustics problems, 11th AIAA/CEAS Aeroacoustic Conference, 23-25 May 2005, Monterey, California.
- [4] Maekawa Z., Noise Reduction by Screens. Applied Acoustics. 1968. 1,157-173.
[https://doi.org/10.1016/0003-682X\(68\)90020-0](https://doi.org/10.1016/0003-682X(68)90020-0)

Leonardo I4N research program – design of novel acoustic liners for aero engine nacelles

Giuseppe Dilillo^{1,a}, Paul Murray^{1,b}, Nicola Gravagnone^{2,c} and Massimiliano Di Giulio^{2,d}

¹Leonardo S.p.A., Aircraft Division, Venegono Superiore, 21040, Italy

²Leonardo S.p.A., Aircraft Division, Pomigliano d'Arco, 80038, Italy

^agiuseppe.dilillo@leonardo.com, ^bpaul.murray.ext@leonardo.com,

^cnicola.gravagnone@leonardo.com, ^dmassimiliano.digiulio@leonardo.com

Keywords: Novel, Aero Engine, Inlet, Acoustic, Liner, Broadband, Attenuation

Abstract. The minimisation of aircraft noise remains a major challenge for the aerospace industry. Noise certification limits continue to be driven lower over time to counter the impact of the steadily increasing number of noise events in the vicinity of airports, along with an increased sensitivity of the public to aircraft noise. This, in turn, ensures that considerable engineering time and effort is used to target all of the major contributors to aircraft noise. Aircraft noise sources include engine fan inlet, fan bypass, jet, and airframe noise, among others. Fan inlet, bypass, and core, ducts are typically lined with absorbing acoustic panels in order to minimise radiated fan noise. This paper is focussed on the latter, describing work to address the design and optimisation of novel acoustic liners.

Introduction

In recent years, the design and manufacture of more efficient aero engine duct acoustic panels has been receiving increased attention. However, the design process cannot be performed in isolation, as the requirement for ever lower aircraft noise levels may be impeded somewhat by the drive to reduce Specific Fuel Consumption (SFC). In particular, modern aero engine ducts have progressively larger fan diameters, and higher bypass ratios. They also have reduced duct lengths in order to minimise weight. While both of these modifications help to reduce fuel consumption, from a noise perspective the ensuing reduction in duct lined length-to-height ratio reduces the attenuation for a given liner design. Hence, for a fixed source level, liner efficiency must be improved just to maintain the status quo. Further challenges are also introduced as modern engine fans generally rotate less quickly, and have fewer blades, than their predecessors. This leads to a tonal content shifted towards lower frequencies, while higher frequencies remain important for broadband noise sources, thus broadening the target frequency range for the acoustic linings. This scenario is particularly challenging for traditional liner designs, as their maximum efficiency is realized over a relatively narrow bandwidth. Hence, if possible, novel designs must be introduced with larger attenuation bandwidths adapted to the source of modern engines.

The Leonardo Innovation for Nacelles (I4N) programme has a work stream dedicated to the design of novel aero engine duct liners. This paper summarises the progress realised to date in liner design. The studies have led to the development of a number of low weight novel liner configurations of varying complexity which are predicted to show improved broadband attenuation when compared to that realised for traditional designs. Work has included the development and validation of acoustic liner impedance models [1], liners with porous cell walls and cells which are considerably wider than traditional designs [2], and the design and manufacture of novel liners with complex cavities (replacing traditional straight cavities) [3,4]. The attenuation potential of the novel designs is improved further by increasing the integrity of duct liner attenuation modelling



significantly, in particular by using a more representative source content and by including the influence of boundary layer refraction at the duct walls [5]. Each of the above subjects are now addressed.

Development and validation of a single degree of freedom perforate impedance model under high SPL and grazing flow

Normal incidence impedance, grazing flow in-situ impedance, and insertion loss testing of a range of Single Degree-Of-Freedom (SDOF) perforates was performed, along with insertion loss tests on a complex cavity panel with varying cell widths and path lengths [1]. Grazing flow measurements, performed in the Santa Catarina grazing flow facility in Brazil, acquired liner impedance and attenuation data at Mach numbers up to 0.6, and at SPLs up to 155dB. The semi-empirical impedance models developed were validated by employing them in calculations of lined duct insertion loss (Figure 1). The studies also confirmed the potential for complex cavity designs to provide improved broadband attenuation (Figure 1).

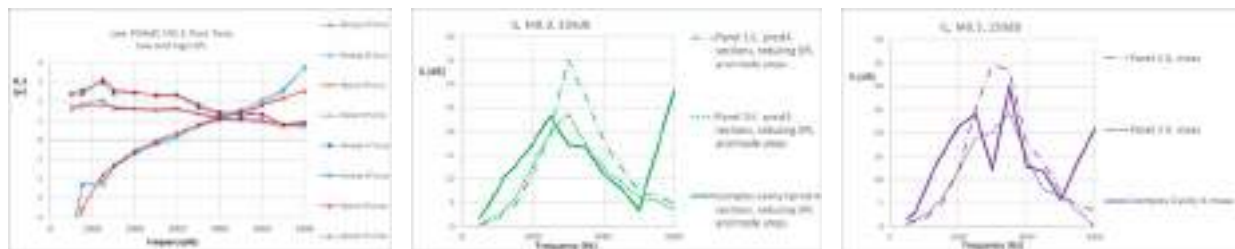


Figure 1. SDOF Perforate Impedance Prediction vs Measurement (left), plus predicted (centre) and measured (right) insertion loss showing bandwidth benefits of complex cavities

Optimisation of non-locally reacting liners for improved duct attenuation

Traditional aero engine liner configurations have narrow cells (approx. 10mm wide) which allow only a plane wave to propagate within them at the frequencies of interest for community noise. The liner response is then independent of the angle of incidence of the impinging sound, and it is considered “locally reacting”. As such, the acoustic response may be characterized uniquely by an impedance, defined as the complex ratio of the acoustic pressure and velocity at the liner surface. Should the cell width increase, additional modes may propagate within the cells, and the liner response becomes a function of the incident mode content.

It is well known that non-locally reacting porous materials show good broadband behaviour. However, they may not be used in aero engines given their propensity to retain fluids. In this work [2], a set of parametric studies were also performed to look at the acoustic attenuation of non-locally reacting liners which are also suitable to fly within aero engine ducts.

The COMSOL Multiphysics® simulation software was used to model the lined propagation for a number of designs under uniform flow. The FEM model was validated initially against insertion loss measurements performed for traditional liners in the NLR rectangular Flow Duct Facility (FDF) in Holland. Thereafter, a parametric study was performed to look at the impact of adjusting these designs to incorporate varying cell widths and varying cell wall resistances. The study demonstrated potential gains in insertion loss for the non-locally reacting designs over that predicted for traditional designs (Figure 2).

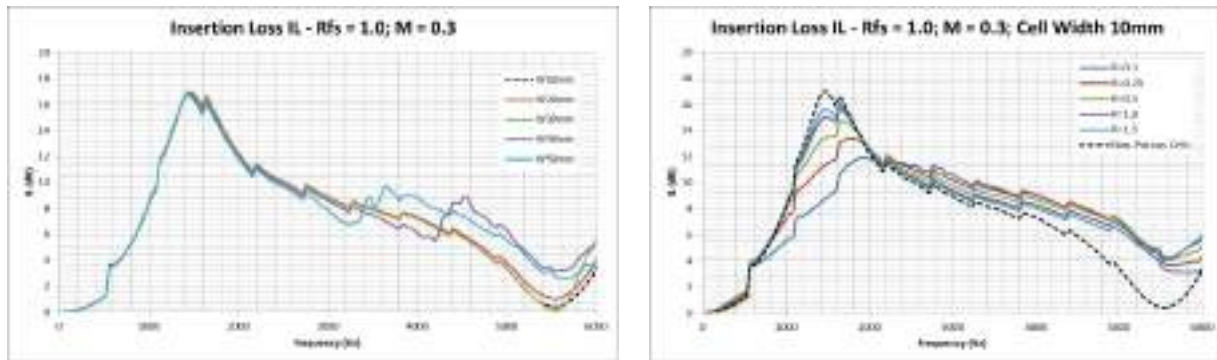


Figure 2. Downstream propagation at Mach 0.3 – Wide cell performance (left) and porous cell wall performance (right)

Improved aero engine inlet attenuation from novel broadband liners

The work presented in [4] continues the research activity initiated in [3], where a novel broadband liner, which uses a core of complex cavities, was designed and optimised to maximise the normal incidence sound absorption over a wide frequency range, including low frequencies. In [4], the novel broadband liner concept was optimised to improve the AneCom inlet attenuation over a wide bandwidth. The liner optimisation incorporated the measured AneCom fan noise circumferential modal content and it also included the impact of wall boundary layer refraction. The geometry of the broadband liner was optimised for two different overall panel depths, 24mm and 40mm, with the deeper panel allowing lower frequencies to be targeted via the inclusion of longer folded cavities. The predicted performance (Figure 3) of the two broadband liner geometries was compared with that predicted for the traditional liners tested by Leonardo previously at AneCom, along with their re-optimised designs, which also account for the impact of the measured source and the wall boundary layer refraction. The novel designs were able to provide significant improvements in attenuation across the frequency range where the AneCom source was loudest in the far-field.

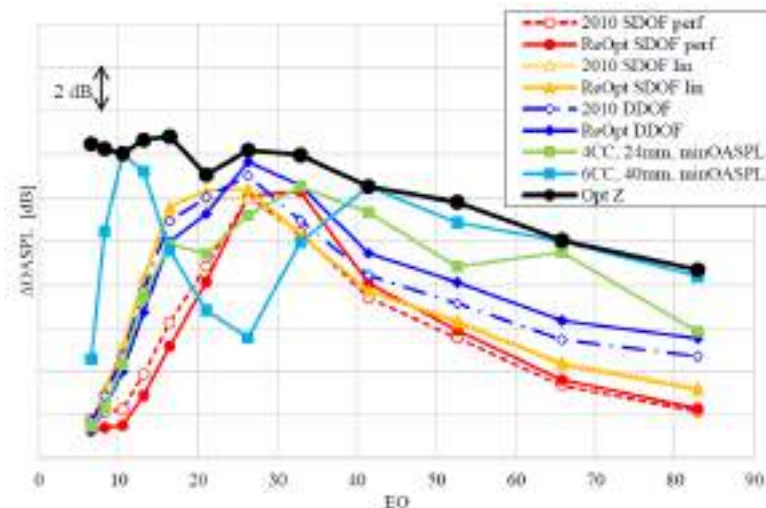


Figure 3. Predicted far-field attenuation at 18.5m from the AneCom inlet, between 40° and 90°, using the measured fan noise source and assuming shear flow in the inlet duct.

Impact of the engine fan source and wall boundary layer on inlet liner design

This work [5] sought to validate far-field predictions of engine liner attenuation. An improved version of the Leonardo cylindrical duct propagation and radiation code (NextGen Liner Multiphysics Code, NLMC) was developed to allow the inclusion of the measured modal source content along with the impact of refraction when sound propagates through the shear layer at the

inlet wall. These aspects are generally not included by the industry. Application of the NLMC code was shown to provide excellent agreement with in-duct and far-field measurements, providing confidence in the acceptability of the assumed simplifications in the modelling. The predictions for an equal energy per mode source and no boundary layer were also found to be significantly different from those using a more representative source (measured circumferential amplitudes and equal energy per associated radial modes) and including boundary layer refraction (Figure 4).

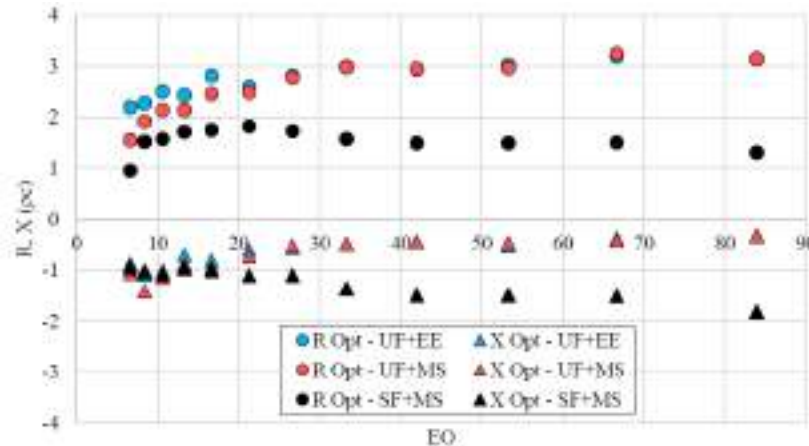


Figure 4. Impact of modelling integrity on the engine inlet optimum resistance (R) and reactance (X) at Approach. Uniform flow with equal energy per mode (NoBL+EE) or measured source (NoBL+MS), and shear flow measured source (BL+MS)

Conclusion

This paper has provided a brief overview of the aero engine acoustic design studies performed by Leonardo under the auspices of the I4N research programme. A series of coordinated activities has led to a significantly improved understanding and capability in the design of advanced aero engine nacelle liners. The novel designs can provide improved attenuation levels, accompanied by an increased bandwidth of attenuation, when compared to that of traditional designs currently flying. The design activity has led to the manufacture of four novel inlet liners which were tested successfully in the AneCom facility in May 2023.

References

- [1] P. B. Murray and M. Di Giulio, "Development and validation of a single degree-of-freedom perforate impedance model under high SPL and grazing flow", *AIAA 2022-2929*, Southampton, UK, 2022. <https://doi.org/10.2514/6.2022-2929>
- [2] N. Gravagnone, P. Murray and M. Di Giulio, "Optimisation of non locally reacting liners for improved duct attenuation", *AIAA 2022-2931*, Southampton, UK, 2022. <https://doi.org/10.2514/6.2022-2931>
- [3] G. Dilillo, Design and Optimisation of Acoustic Liners with Complex Cavities for Improved Broadband Noise Absorption, Politecnico di Milano, Tesi di Laurea Magistrale in Ingegneria Aeronautica, 2020.
- [4] G. Dilillo, P. Murray and M. Di Giulio, "Improved aero engine inlet attenuation from novel broadband liners", *AIAA 2022-2965*, Southampton, UK, 2022. <https://doi.org/10.2514/6.2022-2965>
- [5] G. Dilillo, P. Murray and M. Di Giulio, "Impact of the engine fan source and wall boundary layer on inlet liner design", *AIAA 2022-2964*, Southampton, UK, 2022. <https://doi.org/10.2514/6.2022-2964>

Aeroacoustics computation based on harmonic balance solution

Luca Abergo^{1,a*} and Alberto Guardone^{1,b}

¹Department of Aerospace Science and Technology, Politecnico di Milano, Building B12, Via La Masa 34, Milano, MI 20156, Italy

^aluca.abergo@polimi.it, ^balberto.guardone@polimi.it

Keywords: Aeroacoustics, Harmonic Balance, ROM, FWH

Abstract. This paper presents a new open-source framework to compute the noise emitted by aerodynamic bodies whose motion is dominated by a specific frequency. This flow behavior is typical of propellers, pitching blades and wind turbines. The reduced order model called harmonic balance is used to compute the unsteady flow solution reducing the computational cost. K frequencies are solved by obtaining the conservative variables at N -time instances inside one period, where $N = 2k+1$. The time history of the surface flow solution is reconstructed with a Fourier integration. The Kirchhoff Ffowcs Williams Hawkings integral formulation, implemented in SU2, is used to compute the sound pressure level perceived by farfield observers. The integral formulation propagates the acoustic solution with a computational cost independent of observer distance. The noise emittance of a pitching wing is computed with the proposed framework and compared with a fully time accurate solution showing a very good agreement.

Introduction

Noise emittance due to the airframe is gaining importance in many aeronautical areas, in particular concerning wind turbines, pitching blades and propellers for urban air mobility. Both need to interact with residential neighbors and comply with strict regulations and noise certification requirements. It is necessary to develop reliable and verified noise emission models that can be integrated in design processes. Obtaining an accurate prediction of the noise emittance is challenging and computationally expensive due to its unsteadiness and turbulent nature. An accurate time-resolved flow solution is required. In a modular style, a CFD-CAA aeroacoustic solver had been implemented in the open-source high fidelity software SU2 [1]. Although high-fidelity models are essential, approaches with a modest level of computational complexity are required to include noise into a design environment. The Kirchhoff Ffowcs Williams Hawkings integral formulation (FWH), implemented in SU2 in the Di Francescantonio version [2], is used to compute the sound pressure level (SPL) perceived by farfield observers. The integral formulation propagates the acoustic solution with a computational cost independent of observer distance. In this work, only the solid surface version is used therefore the surface flow unsteady solution is needed as sound source.

Typically, a fully Unsteady Reynolds Averaged Navier Stokes (URANS) is solved with a dual time stepping method and the flow solution at every time step is stored. The novelty of this work is the introduction of a reduced order model to compute the flow solution and use it as noise sources, reducing the computational effort needed. Quasi-periodic flows, like wind turbines or propellers, which are dominated by a set of frequencies can be efficiently solved with a harmonic balance method. It avoids the time-consuming transient calculation that is typical in time accurate CFD. With respect to other frequency methods, the harmonic balance is a time-spectral method where the k frequencies solved are not necessarily integral multiples of one another. Moreover, it is highly parallelized. The harmonic balance method [3] can well capture the time history of the aerodynamic coefficient with a relatively low number of frequencies solved. The HB matrix and the N -instance, where $N = 2k + 1$ conservative variable vector are combined to generate a matrix-



vector product corresponding to the time derivative of the state variables. To sum up, the problem is formulated and solved as N steady-state problems, advancing in parallel in the pseudo-time and linked by a low order representation of the time derivative. Once N time solutions are obtained a more time accurate flow history inside a single period is reconstructed through a Fourier interpolation. Since for the tonal acoustic only the variables on the solid surface are needed, the interpolation is limited to this portion of the CFD domain.

This paper is structured as follows. In Sections 2 and 3, we present the aeroacoustics framework and the numerical tools employed. In Section 4, the results obtained on a pitching wing are presented and the difference between the fully time accurate and the solution obtained with the reduced order method are analyzed. In the end, in Section 5 we summarize the findings and comment on future perspectives.

Harmonic Balance

This section introduces the governing flow equations and the reduced order model used to solve them. After temporal discretization and spatial integration across a control volume, the unsteady compressible Navier-Stokes equations are provided using the finite volume approach and are written as:

$$D_t U |\Omega| + R(U) = 0 \quad (1)$$

Where Ω is the control volume and U the conservative variables. The residual $R(U)$ contains the convective and viscous fluxes integrated over the control volume's interfaces. D_t is the derivative operator with respect to the control volume and to time. A dual time-stepping integration method is used in SU2, at each physical time instance a steady-state problem is solved in the pseudo-time τ :

$$|\Omega| \frac{\partial U_n}{\partial \tau} + D_t |\Omega| U_n + R(U_n) = 0 \quad (2)$$

When dealing with high computational demanding time accurate method, it becomes interesting to introduce reduced-order models and study the range of applicability. Harmonic balance (HB) can be used to solve quasi-periodic flows, dominated by a set of frequencies that are not necessarily integral multiples of one another. The theory about HB, here briefly presented, was implemented in SU2 software by [3]. The harmonic balance time operator \mathcal{D}_t must be introduced.

Given $\bar{\omega}$ the vector of K frequency to be solved, the N flow solution U will be obtained at the t_n time instance in the period T , where $N = 2K + 1$ and $t_n = (n - 1) T/N$. Being E the Discrete Fourier Transform (DFT) matrix, defined as:

$$E_{k,n} = \frac{1}{N} e^{-i\omega_k t_n} \quad (3)$$

The spectral operator matrix H is found to be:

$$H = E^{-1} D E \text{ where } D = \text{diag}(\bar{\omega}) \quad (4)$$

Defined \bar{U} as the vector containing the conservative variables for all the N time instance, the harmonic balance operator is given by:

$$\mathcal{D}_t(\bar{U}) = H \bar{U} \quad (5)$$

Replacing the harmonic balance operator in equation (2) and defining q as the pseudo time step it is obtained that each time instance is solved in a steady-state manner, with all the time instances marching with the corresponding local pseudo-time step:

$$|\Omega| \frac{\partial U_n}{\partial \tau} + |\Omega| H \bar{U} + R(U_n^{q+1}) = 0 \quad (6)$$

In conclusion with harmonic balance, we obtain a discrete flow solution in a flow period with a time step $\Delta t = T/(N - 1)$ without computing the typical transitory of the unsteady flows. However, concerning acoustic propagation a more time accurate surface flow solution is needed. To obtain it, a Fourier interpolation is performed for each conservative variable ϕ at each surface node of the grid. An arbitrary time resolution Δt^* related to a larger number of time instances inside N^* the period can be selected and the relative ϕ^* are obtained with:

$$\phi^* = E^{*-1}(E\phi) \quad (7)$$

where E^{*-1} is the bigger IDFT rectangular matrix of dimension $N^* \times N$.

Acoustic Formulation

The Ffowcs Williams-Hawkings (FW-H) equation is solved in this work to transmit pressure changes on the emission surface to observers in the farfield. The so-called "wind tunnel configuration" is taken into consideration, in which the source and observer move simultaneously while maintaining a constant distance between them. In a modular style, the FWH formulation implemented in C++ [4] takes as input the interpolated flow solution obtained with HB. Concerning SU2, the version of the integral formulation proposed by Di Francescantonio is implemented, which is an extension of the Farassat work [5] to general moving surfaces in which combines the positive aspect of the Kirchhoff and FWH equations:

$$4\pi p' = \int_S \left[\frac{\rho_0 (\dot{U}_i n_i + U_i \dot{n}_i)}{r|1 - M_r|^2} \right]_{ret} dS + \int_S \left[\frac{\rho_0 U_i n_i K}{r^2|1 - M_r|^3} \right]_{ret} dS + \frac{1}{c} \int_S \left[\frac{\dot{F}_i \hat{r}_i}{r|1 - M_r|^2} \right]_{ret} dS + \int_S \left[\frac{F_i \hat{r}_i - F_i M_i}{r^2|1 - M_r|^2} \right]_{ret} dS + \frac{1}{c} \int_S \left[\frac{F_i \hat{r}_i K}{r^2|1 - M_r|^3} \right]_{ret} dS$$

where

$$K = \dot{M}_i \hat{r}_i r + M_r c - M^2 c, \\ U_i = u_i + [(\rho/\rho_0) - 1] (u_i - v_i), \\ \hat{r}_i = r_i/r,$$

M stands for the Mach number, r for Euclidean observer distance from the source node, u is the flow velocity, v represents the grid velocity and P_{ij} stands for the perturbation stress tensor. The derivatives are calculated in the time that the observer hears the noise signal, which is known as the retarded time. This formulation can handle both permeable and solid surfaces; a solid surface is one that prevents mass transit through it, such as the aerodynamic body itself. The loading noise contribution is connected to the final three components, whereas the first two terms are related to thickness noise contribution.

Numerical Simulation

To validate the capability of the proposed framework to predict tonal noise emitted by quasi period flow a pitching straight wing has been simulated. The wing has a chord of 1m and a span of 3m, the section is a NACA6410 airfoil. In standard conditions of pressure and temperature, the freestream Mach number is $M = 0.796$, resulting in a Reynold number of $12.56 \text{ E}6$. Jameson-Schmidt-Turkel convective scheme is used with the 2th order artificial dissipation term set at 0.02 and the 4th = 0.02. SA one equation turbulence model is applied. A hybrid grid of around 1 million elements is generated with Pointwise, with a first cell high low enough to obtain $y^+ < 1$ on the entire surface. The rigid motion is imposed by a prescribed time-varying angle of attack, calculated with:

$$\alpha(t) = 1.06 \sin(\omega t) + \alpha_0$$

where $\alpha_0 = 0^\circ$ and $\omega = 109.339$.

The test case is simulated both with a standard fully time accurate URANS with 100 time steps per period and with the Harmonic Balance method. Concerning HB, the solution is obtained both for 3- and 5-time instances corresponding to a frequency vector of $\bar{\omega} = [0; \pm\omega_1]$ in the first case and $\bar{\omega} = [0; \pm\omega_1; \pm\omega_2]$ in the second one, with $\omega_1 = \omega = 109.339$ and $\omega_2 = 2\omega_1$. After, with the Fourier interpolation the surface flow time solution with the same Δt of the URANS is obtained. For every time instance in the HB simulation, the residual density must be reduced by eight orders of magnitude.

The next figures show the comparison of the lift and drag coefficient. Concerning the C_l a very good matching is obtained already with only three frequencies, instead for the C_d it is necessary to increase the length of $\bar{\omega}$ to reduce the relative error.

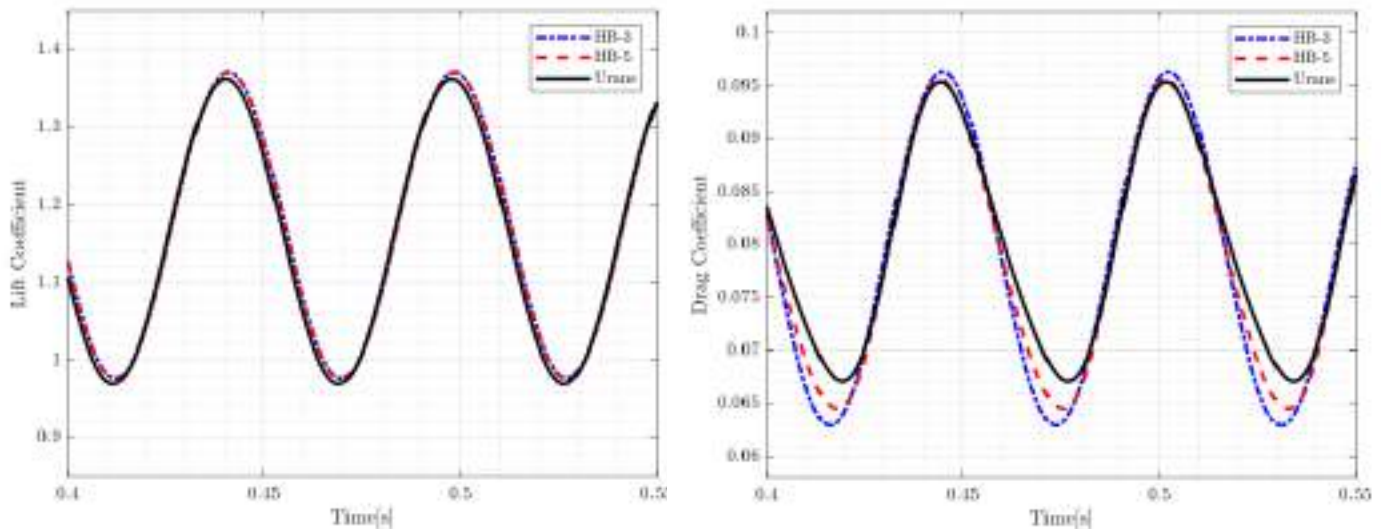


Figure 2 Lift (left) and drag (right) coefficient comparison between HB and Urans for one period of oscillation.

The sound pressure level (SPL) in dB perceived by 17 microphones is computed with the FWH module. The observers are equally distributed on an arch with radius 10m, centered in the middle of the span and the chord, on a plane perpendicular to the wing.

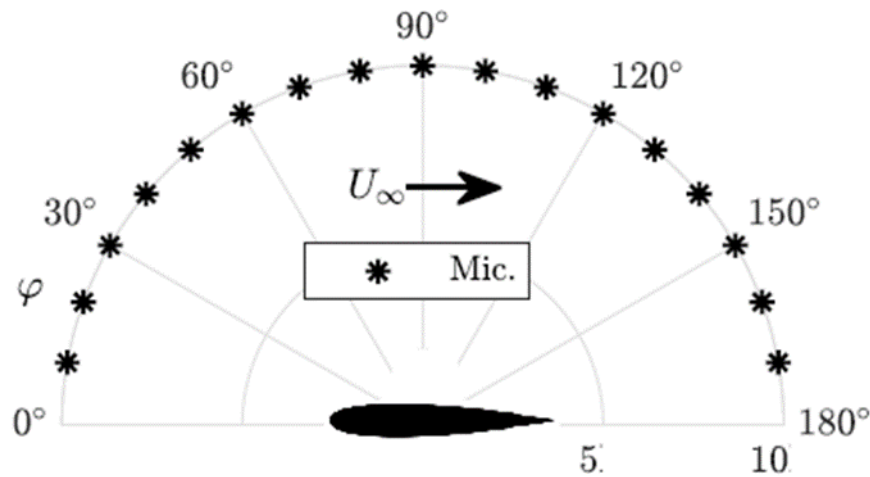


Figure 3 Farfield observer position and reference of system.

First it is reported the pressure perturbation perceived by two observers. The harmonic balance reported is the one obtained with 5 frequencies. It can be observed that there is perfect matching for the microphone positioned at $\varphi = 90^\circ$ instead a higher relative error is found in the downstream direction $\varphi = 170^\circ$, Fig(4). The same trend is reflected for the SPL computed for the entire arch, Fig(5). The relative error is everywhere lower than 1%, which is a remarkable result, Fig(5). There is not only a good matching in the integral value, but also the spectrum directivity plots obtained with the two solutions show are almost identical, see Fig(6).

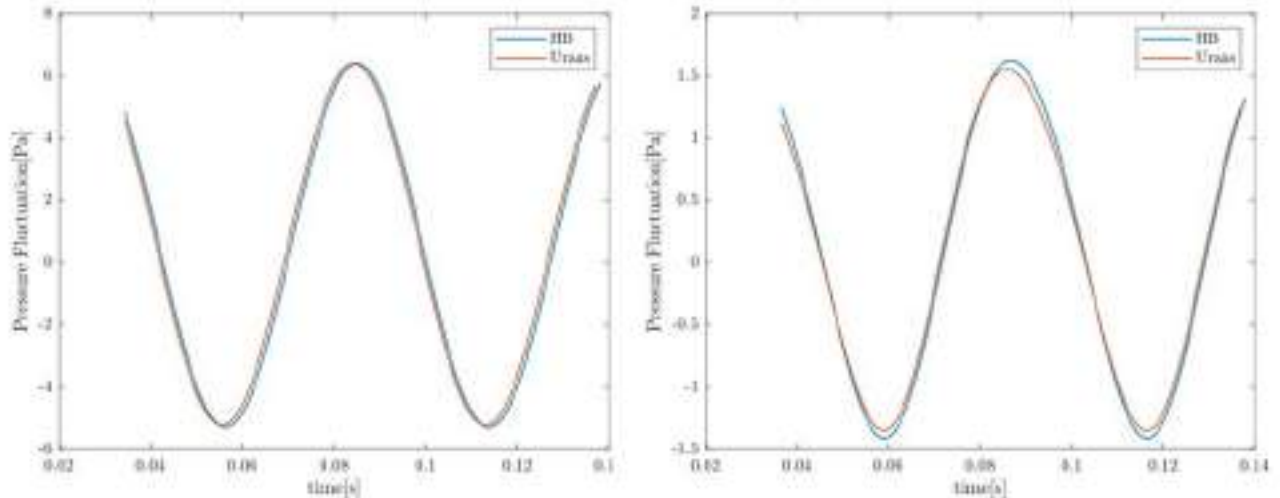


Figure 4 Pressure perturbation perceived by the microphone at $\varphi = 90^\circ$ (left) and $\varphi = 170^\circ$ (right).

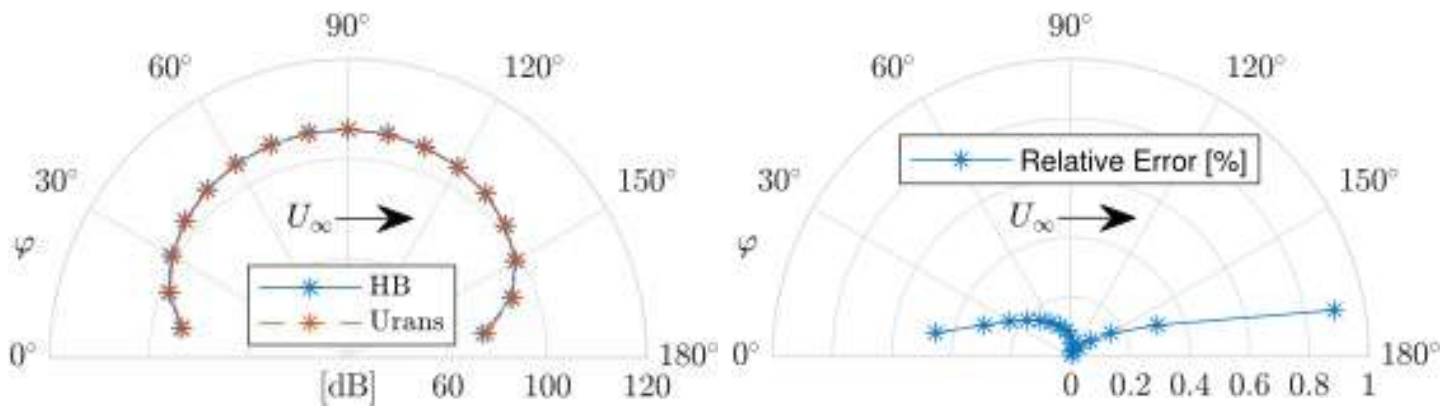


Figure 5 SPL perceived by 17 microphones (left) and relative error between the HB and Urans solution (right)

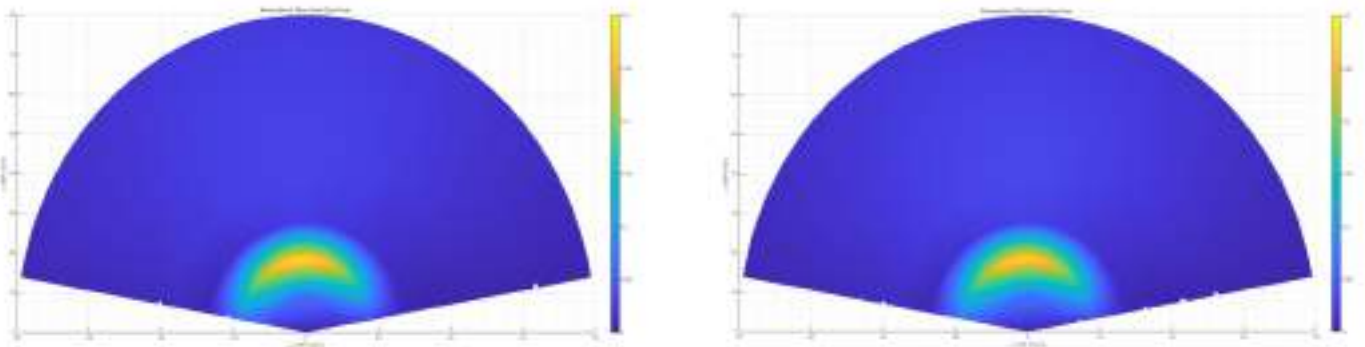


Figure 6 Directivity spectrum obtained with HB solution(left) and Urans solution (right).

Conclusions

In this work, a new open-source framework for computing the sound pressure level perceived by farfield observers is presented. The framework is specific for quasi-periodic flows. The reduced order model Harmonic Balance method is used to compute the flow solution. With this time-spectral method it is not necessary to simulate the transient period typical of an unsteady CFD but the converged solution is directly obtained advancing in the pseudo time. Following, a more time accurate solution is obtained with a Fourier interpolation only for the surface nodes. The acoustic module, where the integral FWH formulation is implemented, takes the interpolated solution as noise sources, and propagates to farfield observers. The proposed framework has been tested on a pitching wing and the results compared with fully time accurate solution obtained with a standard Urans. Five frequencies are sufficient to obtain a good approximation of the integral aerodynamic coefficients. Concerning the acoustics, a good matching is found between the two solutions not only in terms of SPL but also comparing the directivity spectrum. The promising results obtained suggest the application of the proposed framework to more complex cases like propellers or helicopter blades.

References

- [1] T. D. Economon, F. Palacios, S. R. Copeland, T. W. Lukaczyk and J. J. Alonso, "SU2 An open-source suite for multiphysics simulation and design," *Aiaa Journal*, vol. 54, no. 3, pp. 828-846, 2016. <https://doi.org/10.2514/1.J053813>
- [2] P. Di Francesantonio, "A new boundary integral formulation for the prediction of sound radiation," *Journal of Sound and Vibration*, vol. 202, no. 4, pp. 491-509, 1997. <https://doi.org/10.1006/jsvi.1996.0843>
- [3] A. Rubino, M. Pini, P. Colonna, T. Albring, S. Nimmagadda, T. Economon and J. Alonso, "Adjoint-based fluid dynamic design optimization in quasi-periodic unsteady flow problems using a harmonic balance method," *Journal of Computational Physics*, vol. 372, pp. 220-235, 2018. <https://doi.org/10.1016/j.jcp.2018.06.023>
- [4] L. Abergo, M. Morelli, S. F. Pullin, B. Y. Zhou and A. Guardone, "Adjoint-Based Aeroacoustic Optimization of Propeller Blades in Rotating Reference Frame," in *AIAA Aviation*, San Diego, 2023. <https://doi.org/10.2514/6.2023-3836>
- [5] F. Farassat, "Linear Acoustic Formulas for Calculation of Rotating Blade Noise," *AIAA journal*, vol. 19, no. 9, pp. 1122-1130, 1981. <https://doi.org/10.2514/3.60051>
- [6] P. Spalart and S. Allmaras, "A one-equation turbulence model for aerodynamic flows," in *30th aerospace sciences meeting and exhibit*, 1992. <https://doi.org/10.2514/6.1992-439>

Experimental investigation of the noise emitted by two different propellers ingesting a planar boundary layer

Michele Falsi^{1,a,*}, Ismaeel Zaman^{2,b}, Matteo Mancinelli^{1,c}, Stefano Meloni^{3,d},
Roberto Camussi^{1,e}, Bin Zang^{2,f} and Mahdi Azarpeyvand^{2,g}

¹Department of Civil, Computer Science and Aeronautical Technologies Engineering, Roma Tre University, Via Vito Volterra, 62, 00146 Roma RM (IT)

²Faculty of Engineering, University of Bristol, Bristol, BS8 1TR (UK)

³Department of Economics, Engineering, Society and Business, Organization, University of Tuscia, 01100 Viterbo (IT)

^amichele.falsi@uniroma3.it, ^bi.zaman@bristol.ac.uk, ^cmatteo.mancinelli@uniroma3.it,
^dstefano.meloni@unitus.it, ^eroberto.camussi@uniroma3.it, ^fnick.zang@bristol.ac.uk,
^gm.azarpeyvand@bristol.ac.uk

Keywords: Aeroacoustics, Rotor Noise, Boundary Layer Ingestion

Abstract. Novel-aircraft concepts consider the possibility of placing the propulsor very close to the fuselage to ingest the incoming airframe boundary layer. In this configuration, the engine takes in flow at a reduced velocity, thus consuming less fuel in the combustion process. However, this induces a series of noise consequences that alter the noise perceived by an observer. The present work reports an experimental investigation to compare the far-field noise directivity emitted by two different propellers ingesting a boundary layer at two different states. The experiments have been performed in the anechoic wind tunnel at the University of Bristol. The experimental setup consists of a propeller placed in the proximity of a tangential flat plate, which represents a simplified model of a fuselage. Two tripping devices placed 1 m (6.5 rotor radii) upstream of the propeller have been used to generate distinct boundary layer thicknesses. Results from two distinct propellers with three and five blades have been compared, varying the advance ratio J from 0.56 to 0.98. Far-field noise has been acquired using a microphone array positioned in the plate plane. The data have been analysed in the frequency domain, providing an extensive characterization of the far-field directivity. Results show a general increase in noise when the propeller ingests a thicker boundary layer. Furthermore, a change in directivity pattern is observed varying the advance ratio, suggesting a variation of the underlying physics. Finally, considering different J , the overall noise emission appears to be dependent on the number of blades.

Introduction

In the pursuit of more sustainable and efficient air transportation, researchers and engineers are continuously seeking innovative solutions to enhance aircraft performance. An approach that has garnered considerable attention is the concept of Boundary Layer Ingestion (BLI), which involves the ingestion of the slow-moving boundary layer air into the propulsion system of an aircraft. In fact, the boundary layer experiences lower velocities compared to the free stream airflow. This low-velocity air has significant kinetic energy remaining, which can potentially be harnessed to improve the overall aerodynamic efficiency of the aircraft. BLI aims to capture this underutilized energy by ingesting the boundary layer air into the propulsion system, thereby reducing drag. As a consequence, it has the potential to increase the propulsive efficiency of an aircraft by capitalizing on the kinetic energy in the boundary layer air [1]. By ingesting and re-energizing this slower-moving air, the propulsion system can produce more thrust for the same amount of fuel,



resulting in improved fuel economy and reduced emissions [2,3]. However, one of the potential disadvantages of BLI is the increase in the aircraft noise emitted in the far-field [4,5].

Experimental setup

The experiments herein presented were carried out at the University of Bristol's Lawson anechoic wind tunnel. This facility is a closed-circuit, temperature-controlled wind tunnel that is 16.6 m long, 6.8 m wide, and 4.6 m high. The wind tunnel uses a nozzle with a contraction ratio of 8.4 and exit dimensions of 775 mm in height and 500 mm in width, which can achieve freestream velocities of up to 40 m/s and has a high flow uniformity across its exit plane. The anechoic chamber is acoustically lined with acoustic foam wedges and it allows for anechoic measurements down to 160 Hz, according to the ISO 3745 standardized testing procedure [6].

A general overview of the experimental setup is shown in Fig. 1 in which an array of 21 GRAS 40 PL microphones with a radius of 1.75 m (11.5 rotor radii) was positioned parallel to the plate. The array covers angles from $\theta = 35^\circ$ to $\theta = 135^\circ$ from upstream to downstream with $\Delta\theta = 5^\circ$ between every microphone. Two propellers, one with three blades and the other with five blades, both featuring a common radius of $R = 0.152$ m, are mounted on a steel rig positioned 1 m (6.5 rotor radii) downstream of the wind tunnel contraction.

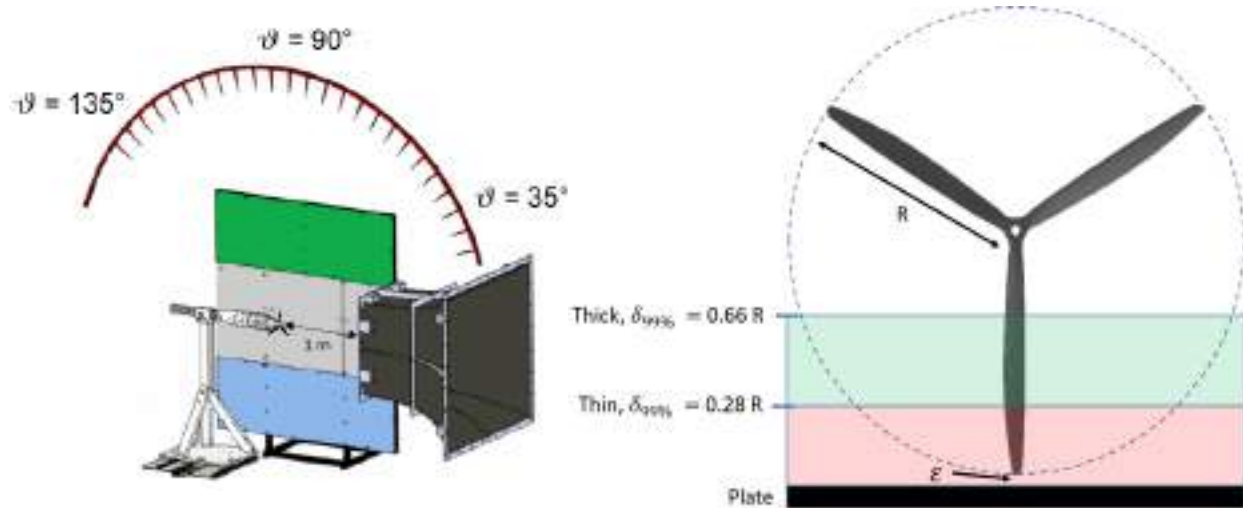


Fig. 1: Experimental setup.

Fig. 2: Boundary layer thicknesses at the propeller location.

Both propellers share the same airfoil shape and geometry, ensuring consistent baseline characteristics for comparison (see [4]). The wind tunnel velocity is fixed at $U_\infty = 20$ m/s, while the propeller RPMs are varied to achieve a range of advance ratios spanning from $J = [0.56, 0.98]$. Two Aluminium metal foam porous material tripping devices, referred to as 'Thick' and 'Thin', were strategically placed after the contraction exit to manipulate the boundary layer thickness at the propeller location. The Thick tripping device had a thickness of 10 mm, while the Thin tripping device had a thickness of 5 mm. Prior to the experimental measurements, a preliminary hot-wire test campaign was conducted to assess the boundary layer thickness and the turbulence intensity (TI) at the propeller position. The results showed that the boundary layer thickness was $\delta = 0.66 R$ with $TI = 7.76\%$ for the Thick trip and $\delta = 0.28 R$ with $TI = 3.89\%$ for the Thin trip, as shown in Fig. 2. These measurements were obtained without the propeller installed and served as an estimation of the boundary layer ingested by the propeller during subsequent experiments. In all presented results, a tip gap of $\epsilon = 5$ mm ($\epsilon/R = 0.03$) was maintained between the propeller tip and the plate.

Results

Four representative advance ratios were chosen to compare the three and five-bladed propellers: $J = 0.56$, $J = 0.65$, $J = 0.75$, $J = 0.98$, where $J = U_\infty/nD$, with $n = RPM/60$ and $D = 2R$. For each microphone the Overall Sound Pressure Level (OASPL) was calculated as:

$$OASPL = 10 \log_{10} \int_{f_1}^{f_2} \frac{PSD}{P_{ref}^2} df, [dB]$$

where $f_1 = 160 \text{ Hz}$ which is the wind tunnel cut - off frequency, $f_2 = 10000 \text{ Hz}$, $P_{ref} = 20 \cdot 10^{-6} \text{ Pa}$ and PSD indicates the Power Spectral Density of the signal evaluated with the Welch's method. Fig. 3 displays the OASPL results as a function of polar angles for both the three-bladed and five-bladed configurations, considering various values of J . The figure distinguishes between the thicker boundary layer cases, represented by dashed lines with cross markers, and the thinner boundary layer cases, represented by solid lines with dots.

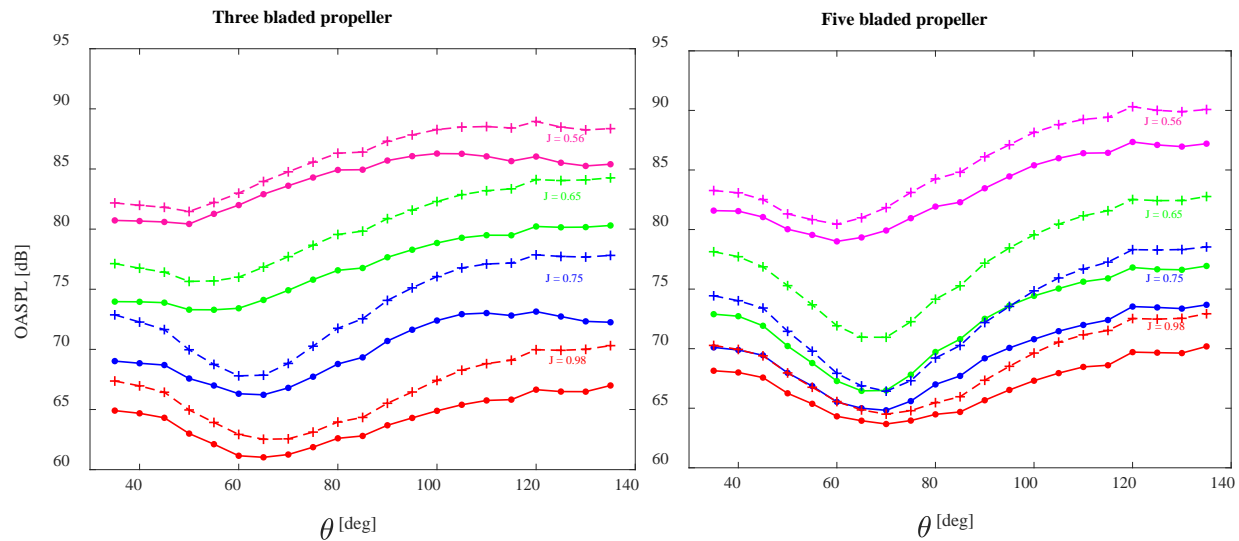


Fig. 3: OASPL for three-bladed propeller (left) and five-bladed propeller (right). Dashed lines with cross markers refer to the thicker boundary layer (Thick) whereas solid lines with dots refer to the thinner boundary layer (Thin).

In both configurations, the ingestion of a thicker boundary layer by the propeller leads to an amplified level of noise across all polar angles. This increase in noise is attributed to heightened pressure fluctuations on the propeller blades, induced by turbulence within the thicker boundary layer. The effect is particularly pronounced at higher polar angles (wake side), specifically for J values of 0.65 and 0.75. Additionally, a noticeable change in noise emission directivity is observed at high J , characterized by a distinct dip around $\theta = 70^\circ$. This change is more pronounced in the five-bladed configuration. As a result, comparing the two plots in Fig. 3, a general trend of increased noise is evident in the three-bladed case compared to the five-bladed case, considering equal J values.

Conclusions

This study aimed to investigate the far-field noise characteristics of propellers operating in close proximity to a flat plate, ingesting a boundary layer with two different thicknesses. We compared the experimental results obtained from two propellers with three and five blades, with the advance ratio varying from $J = 0.56$ to $J = 0.98$. Far-field noise data were acquired using a microphone

array positioned in the plate plane. The results of the study revealed a general increase in noise levels when the propeller ingested a thicker boundary layer. This observation underscores the influence of boundary layer thickness and turbulence intensity on noise generation. Additionally, variations in the advance ratio led to changes in the noise directivity pattern, suggesting alterations in the underlying physics of noise emission. Finally, considering different advance ratios, the overall noise emission appeared to exhibit a trend based on the number of propeller blades with a general increase considering the three-bladed case. In a potential future development, varying the thickness of two boundary layers while maintaining the same turbulence intensity could help differentiate their individual impacts on far-field noise.

Acknowledgments

This work has been supported by the European Union's Horizon 2020 research and innovation program under project ENODISE (Enabling optimized disruptive airframe-propulsion integration concepts) grant agreement No. 860103.

References

- [1] Smith L, 1993, Wake Ingestion Propulsion Benefit, Journal of Propulsion and Power 9 74–82. <https://doi.org/10.2514/3.11487>
- [2] Ahuja J and Mavris D, 2021, A Method for Modeling the Aero-Propulsive Coupling Characteristics of BLI Aircraft in Conceptual Design, AIAA Scitech Forum 2021. <https://doi.org/10.2514/6.2021-0112>
- [3] Yildirim A, Gray J, Mader C and Martins J, 2021, Performance Analysis of Optimized STARC-ABL Designs Across the Entire Mission Profile, AIAA Scitech Forum 2021. <https://doi.org/10.2514/6.2021-0891>
- [4] Zaman I, Falsi M, Zang B, Azarpeyvand M and Camussi R, 2023, Experimental Parametric Investigation of the Haystacking Phenomenon for Propeller Boundary Layer Ingestion, AIAA AVIATION 2023 Forum. <https://doi.org/10.2514/6.2023-4054>
- [5] Zaman I, Falsi M, Zang B, Azarpeyvand M and Camussi R, 2023, Effect of Tip Gap on Nearfield and Farfield Acoustics of Propeller Boundary Layer Ingestion, AIAA AVIATION 2023 Forum. <https://doi.org/10.2514/6.2023-4055>
- [6] Mayer Y, Kamliya Jawahar H, Szoke M, Showkat Ali S and Azarpeyvand M, 2019, Design and Performance of an Aeroacoustic Wind Tunnel Facility at the University of Bristol, Applied Acoustics 155 358–370. <https://doi.org/10.1016/j.apacoust.2019.06.005>

Predicting noise spectrum of a small drone rotor in a confined environment: a lattice Boltzmann Vles analysis

Riccardo Colombo^{1,a}, Lorenzo Maria Pii^{2,b}, Gianluca Romani^{2,c},
Maurizio Boffadossi^{1,d}

¹Dipartimento di Scienze e Tecnologie Aerospaziali - Politecnico di Milano, Via La Masa, 34 -
20156 Milano - Italy

²Dassault Systèmes Italia Srl, Viale dell'Innovazione, 3 - 20125, Milano Italy

^ariccardo15.colombo@mail.polimi.it, ^blorenzomaria.pii@3ds.com,
^cgianluca.romani@3ds.com, ^dmaurizio.boffadossi@polimi.it

Keywords: Propeller Aerodynamics, Laminar Separation Bubble, Aerodynamic Noise, Lattice-Boltzmann Method, Very-Large-Eddy-Simulation, Confined Aeroacoustics

Abstract. The objective of this paper is to study the predictive capabilities of a Very-Large-Eddy-Simulation CFD solver for the simulation of the flow past a small drone propeller blade. The solver is based on a Lattice-Boltzmann Method coupled with an FW-H acoustic analogy to compute the far field noise. The method is able to cope with the anechoic test chamber to predict the complex flow-field and the characteristic boundary layer phenomena (such as laminar separation, transition and reattachment). The acoustic hybrid formulation provides tonal and broadband noise radiation in agreement with the experimental data. Frequency spectrum prediction exhibited a strong low-frequency tonal contribution at multiples of the blade passing frequency related to the interaction with coherent vortical structures in hover, and a high-frequency broadband hump due to the laminar separation bubble at high advance ratio.

Introduction

The design of small rotors, aerodynamically and aeroacoustically efficient, is a research field of great interest. According to a recent experiment of propeller at low Reynolds number ($Re < 70000$) Grande et al. [5] at TU Delft have observed a very complex flow, involving laminar separation, transition, and reattachment, where the size and the position of the Laminar Separation Bubble (LSB) greatly affect the propeller broadband noise spectrum.

The prediction of such non-linear phenomena can be extremely challenging even for high-fidelity (Computational Fluid Dynamics) CFD solvers. Typically, CFD solvers are based on a hybrid turbulence model and use an artificial trip to enforce boundary-layer transition. Previous studies performed by Casalino et al. [2, 3] have been focused on predicting far field noise using Dassault Systèmes PowerFLOW® software, which is based on Lattice Boltzmann Method (LBM) and Very Large Eddy Simulation (VLES). The Lattice-Boltzmann method [3] is based on statistical advection and collision of fluid particles by a number of distribution functions aligned with pre-defined discrete lattice velocity directions. Flow variables such as density and velocity are computed by taking the appropriate moments of the distribution function. The relaxation time and other parameters of the distribution function are computed by considering the turbulent motion computed using a two-equation transport model based on the $k-\epsilon$ re-normalization group theory. Conversely to RANS models, Reynolds stresses are not explicitly added to the flow governing equations but are a consequence of an alternation of the gas relaxation properties that lead the flow towards a state of dynamic equilibrium. LBM/VLES model can be interpreted as an extension of the kinetic theory from a gas of particles to a gas of eddies [4]. It can be demonstrated that the effective Reynolds stresses have a nonlinear structure and are better suited to represent turbulence



in a state far from equilibrium, such as in the presence of shear and rotation. Being the LBM low dissipative, compressible, and intrinsically unsteady, it constitutes a well-suited model for aeroacoustics simulations.

In this work, the aerodynamic noise generated by the propeller is evaluated by means of an hybrid FW-H calculation [1] based on a time-advanced solution of Farassat's formulation of the Ffowcs Williams & Hawkings' (FW-H) equation applied to the propeller blades, hub and nacelle surface pressure LBM solution. Although a favorable agreement with experiments was obtained by Casalino et al. in previous studies [2, 3], some inconsistencies were found and possibly attributed to the absence of the experimental test section in the simulation [5] and grid resolution. Therefore, the aim of the present study is to further validate the aeroacoustics and aerodynamic predictive capabilities of the LBM/VLES approach, including the simulation of the actual anechoic test section by means of an Acoustic Porous Medium. Moreover, no artificial trip is used to trigger transition, and the effect of grid resolution refinement on the prediction of Laminar Separation Bubble (LSB) and related phenomena is further assessed.

Computational setup

The propeller geometry considered in TU-Delft experiments [5] is based on 2-bladed APC 9x6 propeller, with 0.30 m of diameter. The angular velocity considered is 4000 RPM, corresponding a Blade Passing Frequency (BPF) of 133.3 Hz; the blade-tip Mach number is 0.19. Two different advance ratios were considered: $J = V_\infty / nD = 0.0$ and 0.6.

The unconfined computational fluid domain is a spherical volume with a radius of 80m, centered around the propeller hub. The mesh (Fig. 1) increases the resolution as the distance from the propeller decreases, using different volumes for each resolution level. The overall mesh size is of 3.8 million voxels. The anechoic TU-Delft A-Tunnel is modelled by means of an Acoustic Porous Medium, using an equivalent acoustic porosity and tortuosity. The geometry of the inner volume of the test section, as well as the nozzle's geometry were simulated with the actual dimensions of the chamber (6.4m×6.4m×3.2m for the test section, with a 1m wide opening on the ceiling and a 1.4m walls thickness).

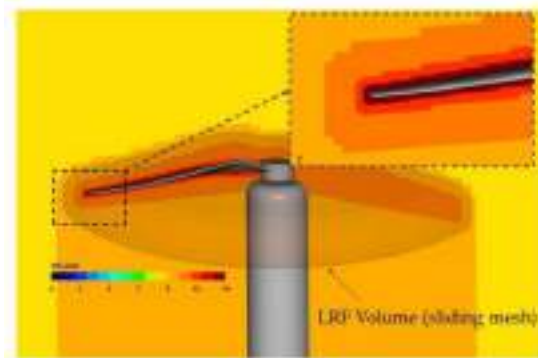


Fig. 1 Mesh with different VR level near the blades

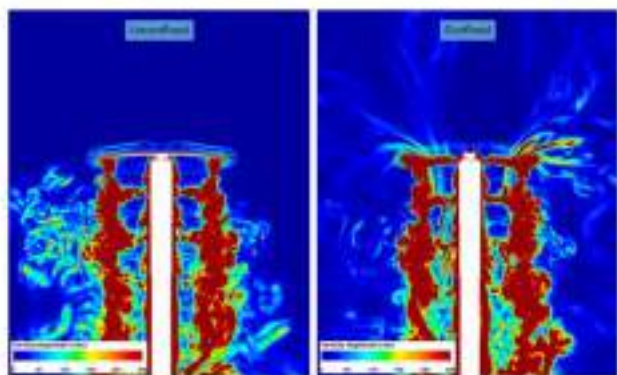


Fig. 2 Instantaneous vorticity field for the unconfined (left) and confined (right) simulation

Results

The results firstly presented are relative to the hover case in which confinement effects are more significant. To investigate the impact of confinement effects on the turbulence ingested and generated by the propeller, an instantaneous vorticity snapshot can be considered as shown in Fig.2. The confined case shows the expected presence of large vortical structures that are stretched along the flux tube streamlines and ingested by the rotor.

For the aeroacoustics analysis in Fig.3 the comparison between numerical and experimental far field noise for both unconfined and confined simulations is shown. The noise spectra are reported in terms of Power Spectral Density (PSD) versus the frequency normalized by the Blade Passing Frequency (BPF). The unloaded electric motor noise and wind tunnel background noise are included in the plots. It is worth noting that the primary sources of experimental uncertainty are: (i) the background noise, which is responsible for high levels of broadband noise at low frequency; (ii) the loaded electric motor noise and non-perfect balance of blade loading, leading to low-frequency tone increases at harmonics of the shaft frequency (BPF-0.5, 1, 1.5, etc.); and (iii) the unloaded electric motor noise, adding mid-frequency tonal contributions approximately between BPF-5 and BPF-25 and between BPF-50 and BPF-70. It can be observed that BPF-1 is accurately predicted by the numerical simulations for both cases. In the hovering confined case, all tonal peaks from BPF-1 to BPF-10 exhibit an additional tonal contribution resulting from unsteady loading compared due to the ingestion of recirculating vortical structures.

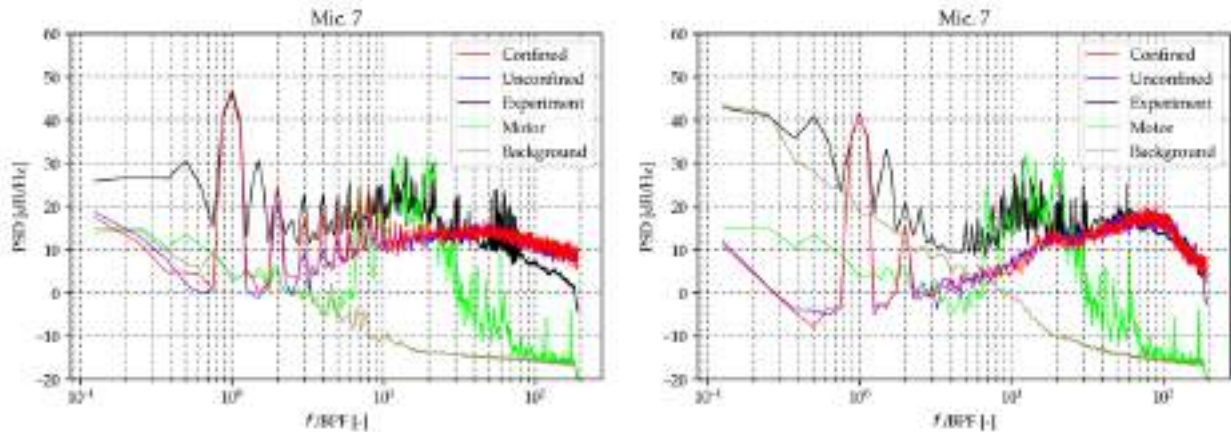


Fig. 3 Far field noise prediction for $J=0$ (left) and $J=0.6$ (right)

With regards to the broadband noise component, while the case $J=0.6$ excellently matches experimental results, there appears to be an overestimation of noise levels above BPF-50 in hover for both the confined and unconfined simulations.

Aiming to address the discrepancies of the broadband noise between simulations and experiments and to obtain a better simulation of LSB, additional simulations were considered for the hover case. The mesh resolution was increased with an additional refinement (one level higher than previous simulations, with voxel size half of the previous one). An improvement of the broadband contribution at frequencies above BPF-50 can be observed in Fig. 4. The enhanced prediction can be attributed to a better simulation of reattachment points of the LSB. Time-averaged surface streamlines of Fig. 4 clearly show the presence of the Laminar Separation Bubble. The most significant improvement can be observed in the last 25% of the blade span, close to the blades tip where the reattachment point is better aligned with the experiments.

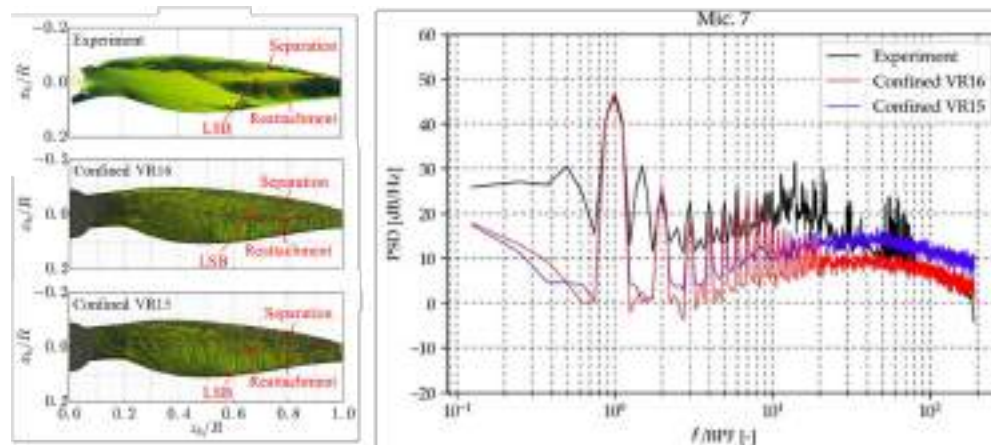


Fig. 4 Comparison of averaged streamlines for the refined simulation along with experimental oil-flow viz (left) and far field noise prediction (right).

Conclusion

This study focused on predicting far field noise spectrum, aerodynamic characteristics and boundary layer evolution (laminar separation, transition and reattachment) for a small drone rotor. Numerical simulations are performed, in both free-field and confined environments, for two different advance ratios by means of the industrial LBM-based CFD solver PowerFLOW®. The simulation aims to replicate experimental studies conducted in TU-Delft. Flow confinement simulation have a significant impact on recirculating turbulence ingested by the propeller, resulting in enhanced tonal noise prediction during hovering. An analysis of the LSB indicates that the observed broadband misprediction in hover was likely caused by an incorrect prediction of the reattachment point of LSB, resulting in an overestimation of the broadband noise. Extra simulations, performed for the hovering case with increased resolution mesh in the proximity of the expected LSB give a better accuracy in predicting trailing-edge noise, with agreement between the simulated broadband component and experimental data. Confined simulations also reveal an enhancement in the mid frequency spectrum due to turbulence impingement noise. This study demonstrates the capabilities of the industrial LBM/VLES software PowerFLOW® in accurately predicting complex flow-field, noise levels and natural boundary layer transition phenomena without the use of artificial triggering systems.

References

- [1] D. Casalino; An advanced time approach for acoustic analogy predictions. Journal of Sound and Vibration, Vol. 261, n. 4, 583-612, 2003. [https://doi.org/10.1016/S0022-460X\(02\)00986-0](https://doi.org/10.1016/S0022-460X(02)00986-0)
- [2] D. Casalino, G. Romani, E. Grande, D. Ragni, and F. Avallone; Definition of a benchmark for low reynolds number propeller aeroacoustics. Aerospace Science and Technology, 2020. <https://doi.org/10.1016/j.ast.2021.106707>
- [3] D. Casalino, G. Romani, R. Zhang, and H Chen; Lattice-boltzmann calculations of rotor aeroacoustics in transitional boundary layer regime. AIAA 2022-2862, 2022. <https://doi.org/10.2514/6.2022-2862>
- [4] Hudong Chen, Steven A Orszag, Ilya Staroselsky, and Sauro Succi; Expanded analogy between Boltzmann kinetic theory of fluids and turbulence. Journal of Fluid Mechanics, 519:301–314, 2004. <https://doi.org/10.1017/S0022112004001211>
- [5] E. Grande, G. Romani, D. Ragni, F. Avallone, and D. Casalino; Aeroacoustic investigation of a propeller operating at low Reynolds numbers. AIAA Journal, Vol. 60, No. 2, 2022. <https://doi.org/10.2514/1.J060611>

Aeroelasticity

On the influence of airframe flexibility on rotorcraft pilot couplings

Carmen Talamo^{1,a,*}, Andrea Zanoni^{1,b}, Davide Marchesoli^{1,c},
Pierangelo Masarati^{1,d}

¹Politecnico di Milano, Dipartimento di Scienze e Tecnologie Aerospaziali, Campus Bovisa, Via
La Masa 34, 20156 Milano, Italy

^acarmen.talamo@polimi.it, ^bandrea.zanoni@polimi.it,
^cdavide.marchesoli@polimi.it, ^dpierangelo.masarati@polimi.it

Keywords: Rotorcraft-Pilot Coupling, Multibody Modelling, Biodynamic Feedthrough

Abstract. A set of numerical simulations of the interactional dynamics of the pilot-rotorcraft system is performed. The aim of the numerical analysis is to evaluate the stability of the closed-loop system in hovering conditions, focusing on the influence of the first airframe flexible mode, the one with the most participation in relative motion between the main rotor and the pilot's seat and closest in frequency to pilot-vehicle interaction. Two approaches are employed. First, a linear analysis, in which the modal representation of the airframe flexible mode is added to a linearized model of the helicopter vertical motion and the helicopter dynamics is coupled with a single degree of freedom linearized model of the pilot biomechanics. Subsequently, a multibody model of the helicopter is coupled with the same linear model of the pilot, trimmed in hover and perturbed by a vertical gust. A sensitivity analysis shows that such mode has a significant influence on the stability of the closed loop system, especially if its frequency is close to the natural frequency of the pilot's biomechanics, as one might expect.

Introduction

The interaction between pilot and vehicle dynamics represents a challenging issue for rotorcraft. Rotorcraft-Pilot-Couplings (RPC) can be at the root of different kinds of unwanted, adverse feedback loops: PIO (Pilot-Induced Oscillations) and PAO (Pilot-Assisted Oscillations). The latter, the object of this research, are characterized by the involuntary participation of the pilot. Human-machine coupling can be described by a feedback loop that connects the rotorcraft and the pilot. While aeroelastic effects on PAOs due to structural flexibility have been the subject of previous research [1], also addressing tiltrotor aeroelasticity [2], no extensive sensitivity analysis has been performed so far. This work aims at filling this gap through a numerical investigation.

Problem description

The goal of this work is to perform a closed loop stability analysis for the coupled rotorcraft-pilot system. For both parts of this work the pilot is described by a state space representation of the BDFT (Biodynamic feedthrough). The BDFT is defined as the transfer function between the control inceptor rotation and the airframe acceleration input. The pilot model is coupled with another state space system that describes the helicopter dynamics. The vertical acceleration of the airframe is fed through the pilot biomechanics to the collective control deflection, which in turn produces a vertical acceleration of the airframe.

Methods

The work has been divided into two parts. In the first part, the analysis is performed using Linear Time Invariant (LTI) models. To represent the selected rotorcraft, a simple analytical model consisting of the helicopter heave motion and the main rotor coning motion as proposed in [3] has been used, considering data representative of a light helicopter of the class of the BO105. Modal data available from previous work supports the modal representation of an analytical model



including the dynamics of the airframe. A sensitivity analysis has been performed, changing the frequency of the first airframe flexible mode, the one closest to the frequency of the pilot's biomechanics and the most involved in the relative vertical motion between the main rotor mast and the pilot's seat, to understand how this parameter can affect the stability of the closed loop system composed by helicopter and pilot. In the second part of this work the rotorcraft is represented through a flexible multibody model, implemented in the free, general-purpose multibody solver MBDyn. The results are used to investigate how well such a simple analytical model can predict the results obtained from a full flexible multibody model.

Analytical model

Elastic airframe addition

The analytical airframe representation proposed in [3] has been enhanced by adding airframe flexibility, described using a modal model obtained from a finite element analysis. The first four mode frequencies are listed in Table 1.

Table 1: Airframe modes

Mode	1	2	3	4
Frequency [Hz]	5.8	7.7	11.4	12.6

The first and the third modes present the most participation of hub and pilot seat vertical relative displacement. It is worth noticing that the third mode is outside the frequency range typical of PAO events (3-7 Hz): *therefore, only the effect of the first mode is analyzed in detail.*

Closed loop sensitivity analysis

The loop transfer function of the pilot-vehicle system can be written as:

$$H_{LTF}(s) = -G H_{BDFT}(s) H_{HELI}(s)$$

Equation 1

where G is the gear ratio between the collective inceptor deflection and blade pitch, $H_{HELI}(s)$ is the transfer function between the collective pitch and the pilot seat vertical acceleration.

Figure 1 shows how the 1st airframe mode (at 5.8 Hz) affects the loop transfer function.

After adding the airframe elasticity, a sensitivity analysis has been performed moving the 1st mode frequency in the range $[f \pm 40\%]$. The gain and phase margins on the system's closed-loop transfer function have been chosen as indices to evaluate the system's stability.

The sensitivity analysis results are presented in Figure 2. The mode frequency increases from red to blue. The gain margin rises when the mode frequency increases. When the frequency is set to the lower end the gain margin is negative, therefore the system is unstable. Moving towards the upper bound the gain margin increase shows a non-linear trend. The most significant improvements are visible up to 5.5 Hz; the value tends to settle for higher frequencies. The explanation behind this behavior is related to that of the pilot. The typical frequencies that describe the human response in these conditions are in the range [1.5 Hz–4.5 Hz]; departing from this range the mode frequency has less influence on the system's stability.

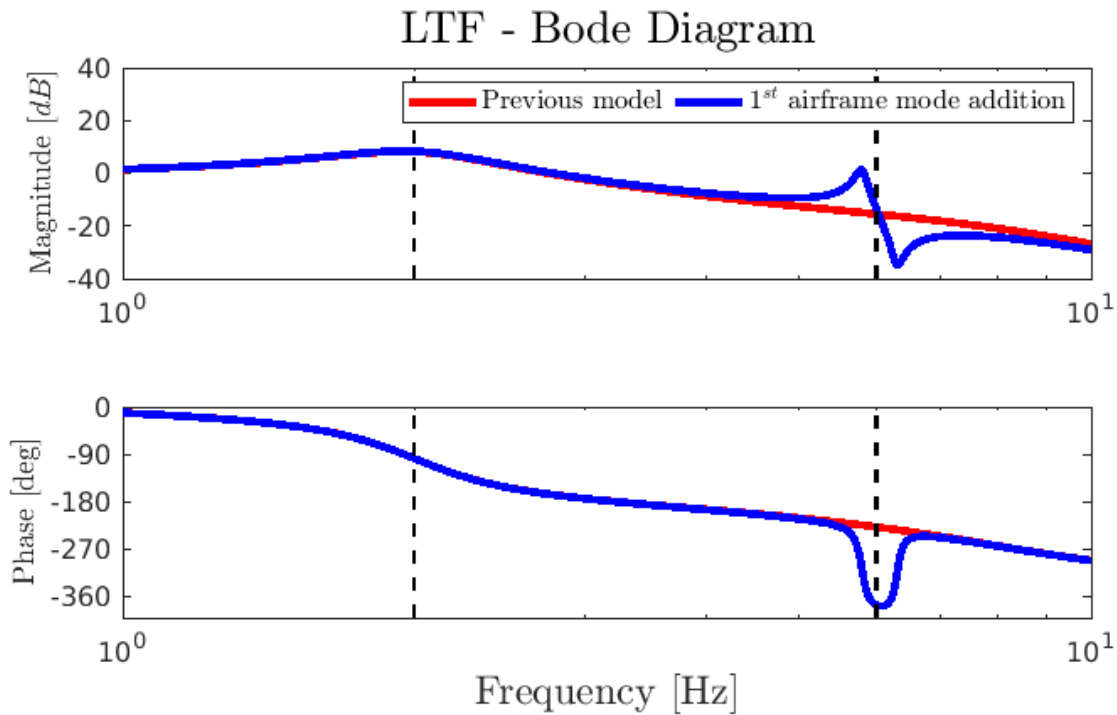


Figure 1: Loop transfer function, with and without 1st airframe mode

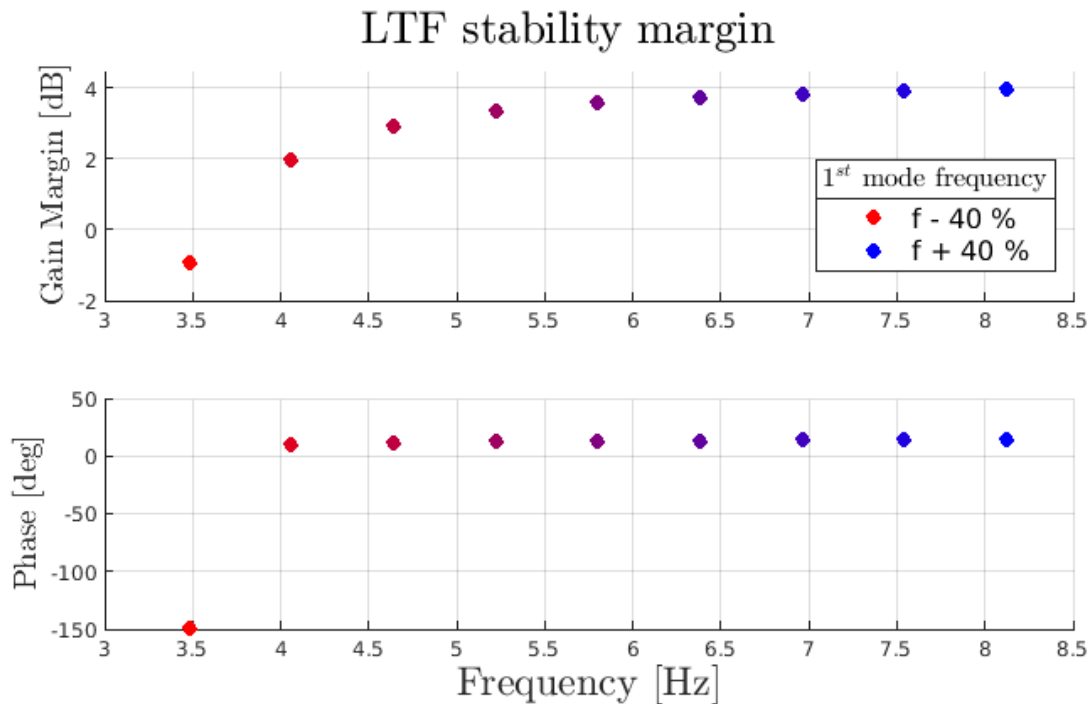


Figure 2: LTF stability margin changing 1st mode airframe frequency

Multibody model

After studying the collective bounce using a simple analytical model, a more detailed, fully flexible multibody model has been used to describe the dynamics of the helicopter.

For fairness of comparison the same pilot model is used and, as in the analytical study, only the first airframe mode has been enabled for the airframe dynamics.

The 1st airframe frequency has been moved to the value corresponding to zero gain margin. The model had been trimmed in hover, after which a perturbation in the form of a gust in the vertical direction has been introduced, after 5 seconds of simulation time, and the system's response has been evaluated. (Figure 3)

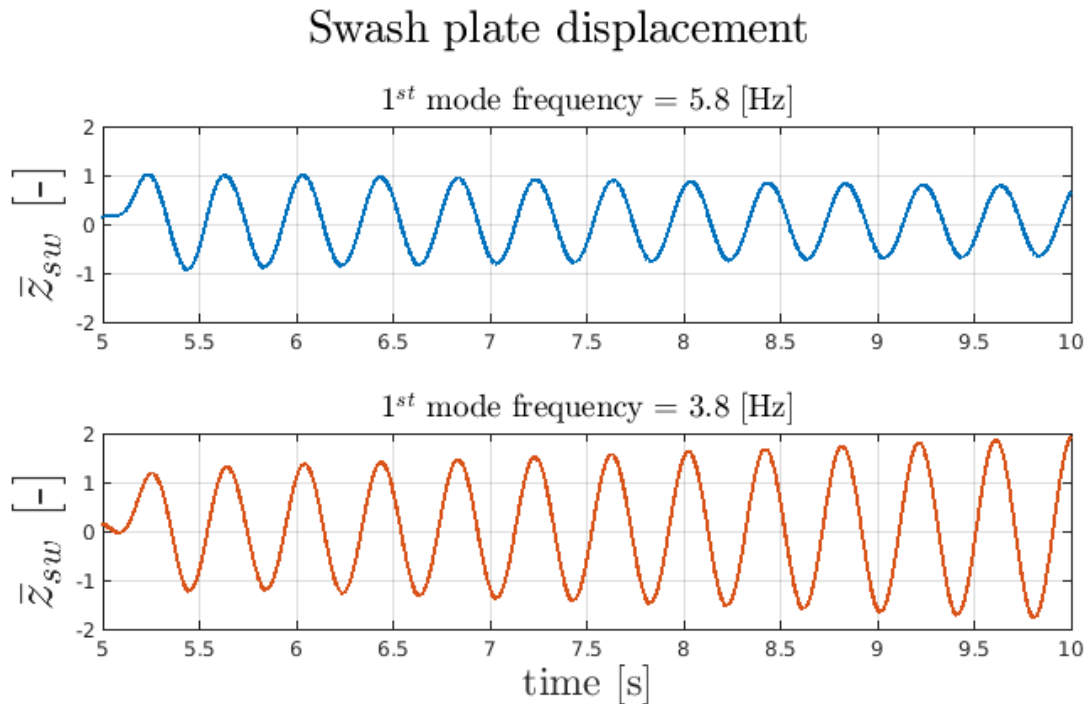


Figure 3: Closed-loop system vertical gust response

In Figure 3, \bar{z}_{sw} (the normalized swashplate displacement with respect to its value at 5 s) is shown. After 5 seconds, the perturbation starts. When the 1st frequency is set to the nominal value listed in Table 1, the amplitude of the oscillations slowly decreases (damping $\xi = 0.005$). If the 1st airframe frequency is reduced to 3.8 Hz, i.e., the value corresponding to marginal stability in the LTI system, the system is not able to absorb the disturbance and the oscillations increase: the system is unstable (damping $\xi = -0.007$). It is worth stressing that the results in Figure 3 have been obtained increasing the pilot gain transfer function by 35%. The increased stability margin is probably due to increased damping introduced by the flexible dynamics of the system and by the nonlinearities included in the multibody simulations.

Conclusions

This work analyzes how the airframe mode can play a key role in rotor pilot coupling. It shows that the reduction of stability margins, and the possible development of instability, is also related to the airframe elasticity. More analyses and investigations are nonetheless needed to enhance the comprehension of the phenomenon.

References

- [1] Dieterich O., et al. "Adverse rotorcraft-pilot coupling: Recent research activities in Europe," 34th European Rotorcraft Forum 2008
- [2] Muscarello V., et al. 2019, "Aeroelastic rotorcraft-pilot couplings in tiltrotor aircraft," Journal of Guidance, Control, and Dynamics. <https://doi.org/10.2514/1.G003922>
- [3] Muscarello V., et al. "The Role of Rotor Coning in Helicopter Proneness to Collective Bounce," Aerospace Science and Technology

Tiltrotor whirl-flutter stability analysis using the maximum Lyapunov characteristic exponent estimated from time series

Gianni Cassoni^{1,a,*}, Alessandro Cocco^{1,2,b}, Aykut Tamer^{3,c},
Andrea Zanoni^{1,d}, Pierangelo Masarati^{1,e}

¹ Politecnico di Milano, Milano - Italy

² University of Maryland, College Park, MD - USA

³ University of Bath, Bath - UK

^agianni.cassoni@polimi.it, ^bacocco1@umd.edu, ^cat2849@bath.ac.uk, ^dandrea.zanoni@polimi.it,
^epierangelo.masarati@polimi.it

Keywords: Lyapunov Characteristic Exponents, Whirl-Flutter, Stability, Multibody Dynamics, Jacobian-Less Methods

Abstract. Stability analysis and assessment are fundamental in the analysis and design of dynamical systems. Particularly in rotorcraft dynamics, problems often exhibit time-periodic behavior, and modern designs consider nonlinearities to achieve a more accurate representation of the system dynamics. Nonlinearities in rotorcraft may arise from factors such as nonlinear damper constitutive laws or the influence of fluid-structure interaction, among others. Regardless of their origin, quantifying the stability of nonlinear systems typically relies on calculating their Jacobian matrix. However, accessing the Jacobian matrix of a system is often challenging or impractical, calling for the use of data-driven methods. This introduces additional complexity in capturing the characteristic dynamics of the system. Hence, a data-driven approach is proposed that utilizes the Largest Lyapunov Characteristic Exponent, obtained by analyzing the system's time series.

Introduction

When faced with a nonlinear problem in its general form,

$$\dot{x} = f(x, t)$$

stability is a local property of a specific solution, $x(t)$, resulting from a corresponding set of initial conditions, $x(t_0) = x_0$, i.e., of a Cauchy problem. One commonly encountered instance is the Linear, Time-Invariant (LTI) scenario. In this context, Lyapunov Characteristic Exponents (LCEs) quantify the growth or decay rate of disturbances from a typical solution in the nonlinear differential problem across distinct directions within the state space, providing insight into the stability of the reference solution in relation to these directions. Consider a solution $x(t)$ for $t \geq t_0$ (some call it the ‘fiducial trajectory’), and a solution ${}_i x(t)$ of the problem.

$${}_i \dot{x} = f_{/x}|_{x(t),t} {}_i x, \quad {}_i x(t_0) = {}_i x_0$$

for a perturbation ${}_i x_0$ of arbitrary magnitude and direction. LCEs are defined as

$$\lambda_i = \lim_{t \rightarrow \infty} \frac{1}{t} \ln \| {}_i x(t) \|$$

When all the Lyapunov Characteristic Exponents (LCEs) are negative, the solution exhibits exponential stability. Conversely, if at least one LCE is positive, the reference solution is unstable



or may lead to a chaotic attractor. When the largest LCE – or LCEs – are zero, a limit cycle oscillation (LCO) can be expected. This means that in the state space there exists one or multiple independent directions along which the solution neither expands nor contracts, converging instead to a self-sustained periodic motion. When multiple largest LCEs are equal to zero, a higher-order periodic or quasi-periodic attractor arises, such as a multi-dimensional torus. It is important to exercise caution when interpreting the LCEs as eigenvalues of Linear, Time-Invariant (LTI) problems, as demonstrated in [5], as they are not always equivalent.

Jacobian-Less Methods: Max LCE from Time Series

The MLCE is the LCE associated with the least damped principal direction of the problem, which represents the most critical stability indicator. Among the algorithms proposed in the literature, the one proposed by Rosenstein et al. [1] is used in this work. It is defined by the following steps. By utilizing the trajectory matrix, $\mathbf{X} \in \mathbb{R}^{M \times m}$, the full phase-space can be reconstructed using the time delay method, if needed, along with estimating the embedding dimension, m (estimated following Takens' theorem), and the reconstruction delay, J , where $M = N - (m - 1)J$ and N is the length of the time series. In this context, each column of matrix \mathbf{X} is a phase-space vector.

$$\mathbf{X} = [\mathbf{X}_1 \mathbf{X}_2 \dots \mathbf{X}_m]$$

After constructing the trajectory matrix, the algorithm locates the nearest neighbor, \mathbf{X}_j , of each point on the trajectory, which is found by searching the point that minimizes the distance from each reference point, \mathbf{X}_j . The distance is expressed as

$$d_j(0) = \min_{\mathbf{X}_j} \|\mathbf{X}_j - \mathbf{X}_j\|$$

where $d_j(0)$ is the initial distance from the j th point to its nearest neighbor, and $\|\cdot\|$ denotes the Euclidean norm. Nearest neighbors must have a temporal separation greater than the mean period (\bar{T} , the reciprocal of the mean frequency of the power spectrum, although it can be expected that any comparable estimate, e.g., using the median frequency of the magnitude spectrum, yields equivalent results) of the time series, $|j - \hat{j}| > \bar{T}$. The largest Lyapunov exponent is then estimated as the mean rate of separation of the nearest neighbors. The j th pair of nearest neighbors diverge approximately at a rate given by the largest Lyapunov exponent:

$$d_j(l) \approx C_j e^{\lambda_1(l \Delta t)}$$

where C_j is the initial separation. By taking the logarithm of both sides which represents a set of approximately parallel lines, for $j = 1, \dots, M$, each with a slope roughly proportional to λ_1 . The largest Lyapunov exponent is calculated using a least-squares fit to the “average” line defined by

$$y(l) = \frac{1}{\Delta t} \langle \log d_j(l) \rangle$$

where $\langle \cdot \rangle$ denotes the average over all values of j .

XV-15 Model Whirl Flutter

Building upon the previous research conducted in [2], the aeroelastic simulation of the XV-15 tiltrotor is now considered. For this analysis, an aeroservoelastic model is employed, encompassing all significant structural components. The airframe model comprises various elements, such as the flexible wing, rigid fuselage, empennages, control surfaces (elevator, rudder, flaps, and flaperons), and nacelle tilt mechanisms. Additionally, the model, originally developed in [4], incorporates crucial cockpit elements (a seat and control inceptors - collective and cyclic) to explore rotorcraft-pilot couplings. To develop this model, the MBDyn multibody solver (<https://mbdyn.org/>) is utilized, to represent the fundamental frequencies and mode shapes of the complete aircraft, with specific emphasis on the wing-nacelle section. The proprotor, featuring a three-bladed stiff-in-plane rotor with a gimballed hub, comprises the blades, flexible yoke, and pitch control chain. The flexibility of the wing, rotor blades, and yokes of the two rotors is modeled using an original

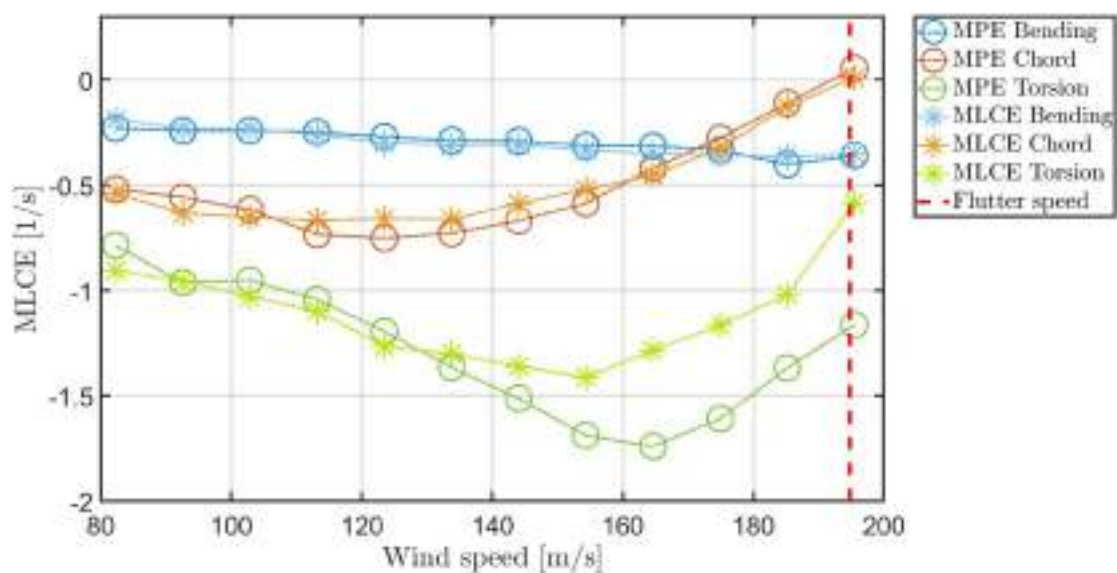


Figure 1: MLCE of the XV-15 in the standard operating condition for the airplane mode.

geometrically exact composite-ready beam finite element model known as “finite volume” [3], which is well-suited for multibody dynamics. The Whirl-Flutter phenomenon was observed through a two-phase approach involving excitation with a sinusoidal input through the swashplate, after reaching the desired trim configuration, followed by a free response phase. By linear interpolation, the instability region under the standard operating condition for the airplane mode was estimated to be $U_{\infty} = 195.5$ m/s (indicated by the dotted red line in Fig. 1). Notably, the proposed method successfully recovered the accurate estimation of the Whirl-Flutter instability previously documented in [4], validating its reliability. However, it is important to note that time series analysis methods are sensitive to changes in the observation window. Due to the system's rapid convergence compared to other directions, evaluating it accurately poses challenges, particularly in the case of torsion. To verify the obtained results, a comparison was made with those obtained using the Matrix Pencil Estimation method (MPE). In the chord direction (with a configuration in airplane mode and idle engines), a time series depicting a slow limit cycle was obtained at $U_{\infty} = 185.2$ m/s (Fig. 2). Interestingly, when solely considering the linear component, the system appears to exhibit growth. However, the system converges to a limit cycle. The

amplitude, A , in Fig. 2 used to compare the solution obtained by the MPE method is determined by selecting the maximum value present in the time series.

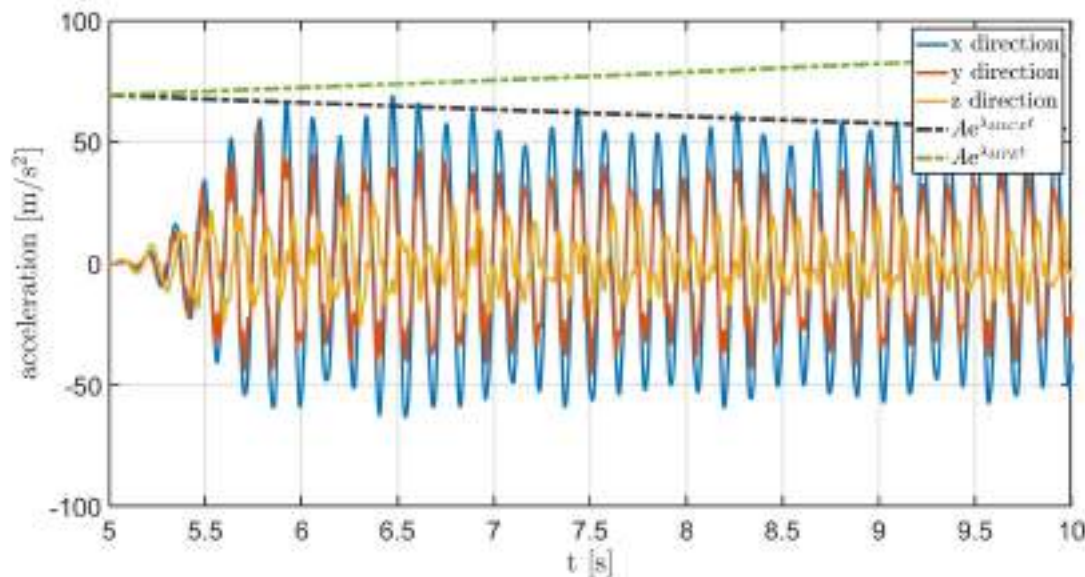


Figure 2: Time history with an input perturbation in the chord, at the hub location.

Conclusion

The presented approach is employed for investigating the whirl flutter instability of a tiltrotor. By extensively exploring its nonlinear dynamics, it becomes feasible to expand the understanding of various instabilities, particularly in cases where linear methods fall short in capturing the entirety of the response domain. Future advancements will involve coupling the method with the vortex particle solver DUST (<https://www.dust-project.org/>) to have a more detailed account for the aerodynamic interactions.

References

- [1] M.T. Rosenstein, J.J. Collins, C.J. De Luca. A practical method for calculating largest Lyapunov exponents from small data sets. *Physica D: Nonlinear Phenomena*, 65(1–2):117–134, May 1993. [https://doi.org/10.1016/0167-2789\(93\)90009-P](https://doi.org/10.1016/0167-2789(93)90009-P)
- [2] A. Cocco, A. Savino, P. Masarati. Flexible multibody model of a complete tiltrotor for aeroservoelastic analysis. 18th International Conference on Multibody Systems, Nonlinear Dynamics, and Control (MSNDC) of ASME IDETC/CIE Conference, 08 2022. V009T09A026. <https://doi.org/10.1115/DETC2022-89734>
- [3] G.L. Ghiringhelli, P. Masarati, P. Mantegazza. A multi-body implementation of finite volume C^0 beams. *AIAA-Journal*, 38(1):131–138, January 2000. <https://doi.org/10.2514/2.933>
- [4] A. Cocco, A. Savino, A. Zanoni, P. Masarati. Comprehensive simulation of a complete tiltrotor with pilot-in-the-loop for whirl-flutter stability analysis. In 48th European Rotorcraft Forum, Winterthur, Switzerland, September 6–8 2022. <https://hdl.handle.net/11311/1220824>
- [5] G.A. Leonov, N.V. Kuznetsov. Time-varying linearization and the perron effects. *International Journal of Bifurcation and Chaos*, Vol. 17, No. 04, pp. 1079-1107 (2007). <https://doi.org/10.1142/S0218127407017732>

Wind tunnel flutter tests of a strut-braced high aspect ratio wing

Luca Marchetti^{1,a,*}, Stephan Adden^{2,b}, Michael Meheut^{3,c}, and Sergio Ricci^{1,d}

¹ Politecnico di Milano, Department of Aerospace Science and Technology, via La Masa 34, 20156, Milano, Italy

² IBK Innovation GmbH & Co. KG, 21129 Hamburg, Germany

³ The French Aerospace Lab ONERA, Location Palaiseau, France

^aluca.marchetti@polimi.it, ^bstephan.adden@ibk-innovation.de, ^cmichael.meheut@onera.fr, ^dsergio.ricci@polimi.it

Keywords: Strut-Braced Wing, High Aspect Ratio Wing, Nonlinear Aeroelasticity, Flutter

Abstract. Increasing the wing aspect ratio is one way to improve aircraft aerodynamic efficiency. This reduces the induced drag term but, at the same time, produces an increment of the wing loads, hence an increase of the structural weight. One design solution to reduce the wing root bending moment, which is the main driver of the weight of the wing, is the addition of a strut. This work deals with the experimental identification of the flutter behavior of an ultra-high aspect ratio (19) strut-braced wing in a wind tunnel. The inherent non-linear behavior of such a structure that has two different effects on the wing when loaded in compression and in tension is coupled with large deformations due to its extreme flexibility. From here derives the extreme importance of experimental tests to understand how different parameters of such a design can impact its aeroelastic behavior.

Introduction

New aircraft configurations such as the strut-braced wing require experimental studies, as results coming from simulations are less trustworthy than those regarding traditional and well-tested configurations. Data should be collected to assess both static and dynamic aeroelastic behavior, with the ultimate goal of validating numerical models and techniques. After a scaling process of a typical strut-braced wing reference aircraft provided by ONERA, a 1:10 scale model for wind tunnel testing is designed by Polimi and IBK allowing for some variations in the geometry and kinematics of the strut. A pneumatic system is designed for the excitation of the model inside the wind tunnel when turbulence is not enough. The dynamic response is measured both in terms of accelerations and displacements, using accelerometers and an optical system to track the motion of some markers on the model.

Reference aircraft

Reference aircraft is an Onera concept [1,2]. Typical mission and fuselage use an Airbus A321 as a baseline. It's a strut-braced configuration with an aspect ratio of 19. This results in a 55 m wingspan. Two engines are mounted on the rear of the cabin, the empennage layout is a T-tail. The connection between the strut and the main wing is not straight, but the strut is bent in a way that allows it to enter the wing perpendicularly, improving its aerodynamic behavior at transonic speeds.

Description of the model

The test model consists of a scaled left-wing clamped at the root and mounted in a vertical position. A constant Froude scaling approach was adopted with a geometric scale factor of 1:10.





Figure 1 Wind tunnel model

The design of the structure is decoupled from the aerodynamics. For the main wing, a single glass fiber spar is used. It is obtained by milling a thick glass fiber plate with full rectangular cross-sections defined at 9 spanwise locations to correctly match out-of-plane and in-plane bending stiffnesses. The resulting torsional stiffness is representative of the correct one. The aerodynamic shape is obtained with 8 3D printed sectors attached to the spar at just one point spanwise so that they can transfer the aerodynamic loads to the structure without contributing to the overall stiffness.

For the strut, two options were designed: one stiffer than the reference with a full rectangular section aluminum spar and 3D printed aerodynamic sectors; and a second one with the correct stiffness obtained with a steel wire, but no aerodynamics attached. From here on we will refer to these two configurations as the “Aero” configuration and the “Wire” configuration. Both struts are hinged to the ground, the axis of rotation being parallel to the fuselage direction. A parallel hinge is also used to connect the strut to the wing. A rail on the floor and a plate at the connection with the wing allow 4 different chordwise positions for both strut configurations. This is done with the goal to obtain a sensitivity regarding this design parameter.

Description of measurement system

Two quantities are measured during the tests: accelerations and positions: 17 accelerometers are installed inside the main wing, all reading accelerations in the out-of-plane direction. 2 accelerometers are installed on the strut in the Aero configuration. All the wires pass inside the model and through a hole in the floor of the test chamber, where signals are acquired by a SCADAS acquisition system. Acquisitions and postprocessing are performed using Simcenter Testlab. As a main source of excitation for the structure, the turbulence inside the wind tunnel is used, which is near to a white noise excitation. In addition, a compressed air pulse is also available to get an impact-like effect. The high-pressure line of the wind tunnel (8 bar) is linked to a small tube passing inside the model to reach the 7th aerodynamic sector (near the tip of the wing). A hole in the lower skin allows the air pulse to act perpendicular to the chord exciting the out-of-plane bending of the wing. Since the hole is positioned towards the trailing edge, a partial excitation of the torsion is obtained, too. A button in the control room opens a valve allowing for remote control of the pulse excitation. This system is used both to excite the structure in the no-wind conditions and to tune the optical system. This consists of 6 infrared cameras which track the position of 53 optical markers placed on the model (only 32 in the wire configuration).

Testing procedure

Wind tunnel tests were carried out at the large wind tunnel facility at Politecnico di Milano (GVPM). The test section is a 4 m by 4 m square, top speed is 54 m/s (near the scaled cruise dynamic pressure).

Static aeroelastic assessment was performed changing the angle of attack and measuring the deformed shape with the optical system. This was done at low speeds (10 m/s and 20 m/s) with angles ranging from -3° to $+5^\circ$ with 1° increments.

Dynamic characteristics of the structure were assessed with modal analysis at different airspeeds. Operational Modal Analysis was used to identify frequency, damping and shape of the normal modes of the structure for wind speeds between 10 m/s and 54 m/s (maximum speed of the wind tunnel) with 5 m/s increments. Air pulse was used to identify normal modes at 0 m/s.

The first test consisted in changing the angle of attack to evaluate the influence of the prestress in the strut on the aeroelastic response. Three angles were tested: 0° , 1° and 2° . The chordwise

position of the strut was fixed, and its configuration was too (aero). The second test consisted in changing the chordwise position of the strut and its configuration. 8 tests were performed at a fixed angle of attack (1°) to investigate all available options (4 chordwise positions and 2 strut configurations). As a third and last test, the aero configuration was modified to block the hinge connecting the strut and the wing. Data were collected for just one chordwise position at the usual angle of attack (1°) to be able to compare the aeroelastic response in three different conditions for the strut.

Results: Static Aeroelasticity

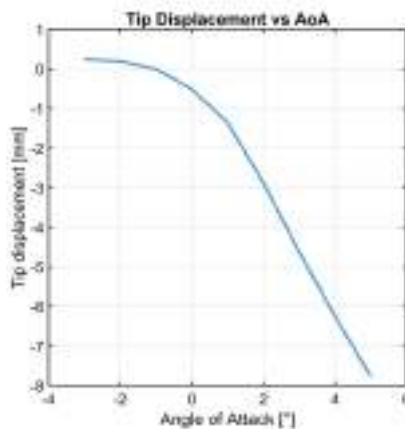


Figure 2 Tip displacement VS AoA

The measured displacement of the tip of the wing is reported in Fig.2

This is obtained at a fixed airspeed of 20 m/s and a range of angles of attack from -3° and $+5^\circ$. The behavior is linear just in a small range of angles of attack. When the strut is compressed, the nonlinear trend is evident, but also at the upper bound of the tested range, the concavity of the curve starts to change.

Results: Dynamics and Flutter

As a first way to interpret the results, all chordwise positions for the same strut configuration are plotted overlapped, just to see the general trend of the curves and the dispersion of the data. In both the strut configurations, we can see a convergence of the frequency of the 3rd bending mode and the first torsional mode. The damping of the bending mode changes concavity and tends to the zero-damping axis. We can't conclude that this will result in a flutter condition, but this behavior is typical of a pre-flutter condition. Results from the wire configuration are less scattered than those coming from the aero configuration, both for the absence of the aerodynamics on the strut and for the absence of hybrid modes coming from the coupling between the wing and strut bending with different phases. Lower frequency modes are far less consistent, especially around 30 m/s where results become very scattered. At some speeds, modes

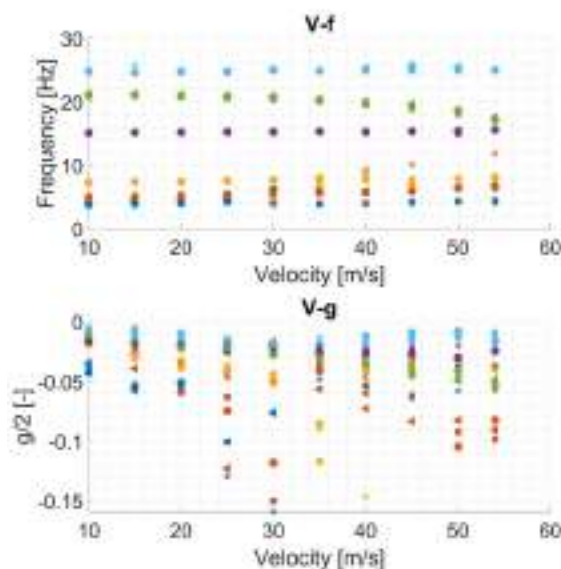


Figure 3 Wire configuration V-f-Vg

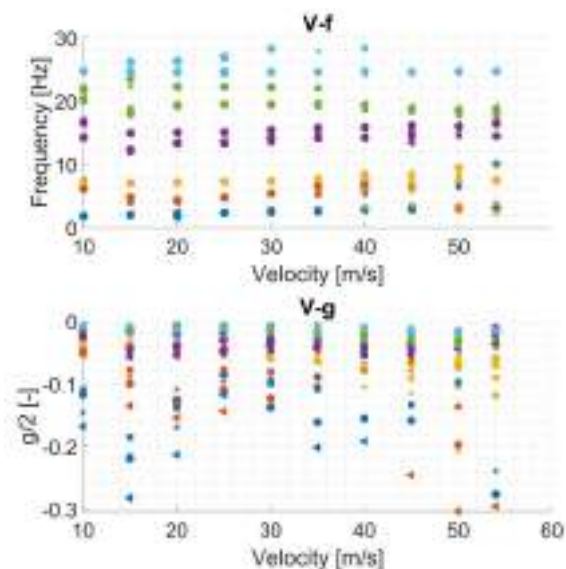


Figure 4 Aero configuration V-f-Vg

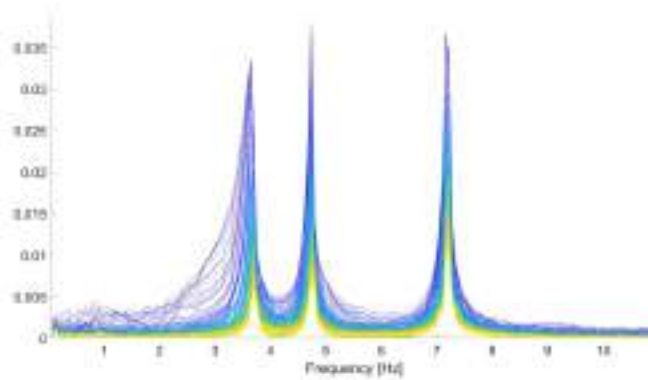


Figure 5 Zeroed Early-Time Fast Fourier Transform

with the same shape as the second bending mode appear both at their expected frequency and at the frequency of the first bending mode. This is a behavior found in nonlinear modes, where frequency and damping depend on vibration amplitude and modal shapes are not unique anymore. A test is performed to check if the modes of this kind of structure can be nonlinear. It is the Zeroed Early-Time Fast Fourier Transform [3]. At least the first mode appears to be nonlinear.

Conclusions

Data was collected for different configurations of the strut at different airspeeds. Initial analyses of the static deformations show a clear nonlinear behavior. Flutter analyses show a potential flutter condition inside the flight envelope of the reference aircraft. A nonlinearity of the normal modes was detected.

Summary

A clamped wing in a strut-braced configuration was tested at Politecnico di Milano in its large wind tunnel facility to gain insights into its static and dynamic aeroelastic behavior. This was achieved using accelerometers for the dynamics and an optical system for the statics. Both static and dynamic characteristics appear to be nonlinear.

Acknowledgement

This project U-HARWARD has received funding from the Clean Sky 2 Joint Undertaking (JU) under grant agreement No 886552. The JU receives support from the European Union's Horizon 2020 research and innovation programme and the Clean Sky 2 JU members other than the Union.

References

- [1] CARRIER, Gerald G., et al. Multidisciplinary analysis and design of strut-braced wing concept for medium range aircraft. In: *AIAA SCITECH 2022 Forum*. 2022. p. 0726. <https://doi.org/10.2514/6.2022-0726>
- [2] Delavenne, M., et al. "Multi-fidelity weight analyses for high aspect ratio strut-braced wings preliminary design." *IOP Conference Series: Materials Science and Engineering*. Vol. 1226. No. 1. IOP Publishing, 2022. <https://doi.org/10.1088/1757-899X/1226/1/012009>
- [3] ALLEN, Matthew S.; MAYES, Randall L. Estimating the degree of nonlinearity in transient responses with zeroed early-time fast Fourier transforms. *Mechanical Systems and Signal Processing*, 2010, 24.7: 2049-2064. <https://doi.org/10.1016/j.ymssp.2010.02.012>

New insights on limit cycle oscillations due to control surface freeplay

Nicola Fonzi^{1,a*}, Sergio Ricci^{1,b} and Eli Livne^{3,c}

¹Politecnico di Milano, Milano, Italy

²University of Washington, Department of Aeronautics and Astronautics, Seattle, USA

^anicola.fonzi@polimi.it, ^bsergio.ricci@polimi.it, ^celi@aa.washington.edu

Keywords: Aeroelasticity, Flutter, Limit Cycle Oscillation

Abstract. A new experimental wind tunnel test-bed has been developed for the study of limit cycle oscillations induced by control surface freeplay. Studies of the effects of a single nonlinearity, made possible by the new horizontal tail plane, are described here. Several effects are considered, starting from a reference configuration: the effect of changes in inertia and stiffness, a time-varying gap size, and an aerodynamic preload due to an angle of attack. Both time marching simulations and describing functions analytical methods have been used to understand the experimental measurements and study the capability of the methods to capture the physical behavior. Good agreement was found in all cases and physical insights are gained from the mathematical models. Limitations of the analytical tools are also addressed, focusing on the important difference between the self-excited dynamics of the nonlinear system and its forced response to external excitations.

Introduction

Research on limit cycle oscillations (LCO) and other nonlinear aeroelastic mechanisms due to control surface hinge nonlinearities has gained significant traction since the 1990's. The drivers include the prevalence of the problem in many aeroelastic flight vehicle systems, the growing number of large dynamically actuated control surfaces where keeping tight tolerances on the freeplay over time can be demanding, the growing power of simulation capabilities (in computing hardware and the theory involved), and major developments over the last forty years or so in the area of nonlinear dynamic systems. The challenge has been known and tackled for years in analysis, simulation, as well as wind tunnel and flight tests. Recent reviews include [1], [2] and the technically thorough [3]. Those three sources cite many, if not most, of the works on control surface freeplay and on aeroelastic nonlinear behavior in the years prior to their publication, providing a state of the art view of the field.

An examination of the work done in this area so far reveals needs for more work in a few particular areas. First, the effects of time-dependent freeplay gap variation, the effects of interacting multiple local nonlinearities, and the effects of control / actuator freeplay on the active control of aeroelastic systems, including gust load alleviation and flutter suppression. Some research on interacting multiple structural nonlinearities has been reported over the years (see [4]–[9]). This area, however, still lacks sufficient experimental work.

Very little work has been reported on the time varying freeplay gap problem, and never in the context of an actuation failure [10].

Driven to cover by analytical and experimental work areas in which not enough research has been done to date, a new project was launched by the Politecnico di Milano (POLIMI) and the University of Washington (UW) to study realistic aeroelastic systems, representing real aircraft, and investigate the effects of multiple control surface hinge nonlinearities, time-varying freeplay gaps, a wide range of freeplay gaps from the very small to the large, and the effects of control surface freeplay on active flutter suppression.



A series of studies, using systems of increasing complexity, tackled first a system with a single nonlinearity and a constant gap size [11], then a system where the gap size was dynamically changing with time [12], and finally the same system subject to preload. Meanwhile, the development of a wind tunnel model of a full aircraft configuration, designed to have multiple nonlinearities, was carried out, and wind tunnel tests were performed in February of 2023. The work with the full-configuration wind tunnel model will be described in future papers. In the present paper, a review of the results obtained with the single nonlinearity system is presented. Building on the results previously presented previously by the authors, the effect of aerodynamic and mechanical preload on the LCO is investigated. Recent advances in the Describing Function (DF) technique are used to shed light on the phenomena observed in the simulations and in the test. The effect of gravity is discussed as a source of natural quenching of the nonlinear phenomena. Finally, the sensitivity of different systems to perturbations is established by studying the effects of different angles of attack of the lifting surface.

The results presented here for the case of single nonlinearity will be the base for the upcoming analysis and test results considering multiple nonlinearities.



Figure 1: Photo of the test model, installed in the wind tunnel

Test models

The test model is the right horizontal tail of the modified X-DIA, with a nonlinearity in the elevator's hinge attachment rotation. The test model is shown above. At the root of the model a hinge nonlinearity-generating mechanism can be seen. A close up view of this mechanism is also presented. The model was designed to create an accurate freeplay gap, taking into account production and mounting tolerances, which can also be dynamically or statically varied. The gap-generating mechanism also allows for the accurate measurement of the hinge movement itself. The entire mechanism is held by two structural ribs, 18 millimetres apart. Both ribs host a radial bearing, which sustains the same shaft, glued to the elevator aerodynamic surface.

Selected results

As mentioned in the introduction, several studies have been performed to understand the effect of different parameters on the LCO. These include the effect of different gap sizes, different inertial and elastic configurations, time varying gap sizes, and different preloads. Here, as an example, the experimental measurements related to the effect of the angle of attack are reported. In figure below,

the experimental LCO amplitude, computed as the RMS rotation, normalized by the gap size, is reported for various gap sizes and for two angles of attack (0.5° and 1.0°).

The angle of attack has the immediate effect of quenching the LCO in some conditions. By looking at the freeplay values for which LCO is completely quenched, it can be noticed that in a practical application, with a realistic gap size, the control surfaces that are usually at some angle of attack will often show no LCO due to this quenching effect. However, during maneuvers when the aerodynamic moment (and thus aerodynamic preload) disappears, LCO reappears, leading to vibrations that can range from the uncomfortable to dangerous.

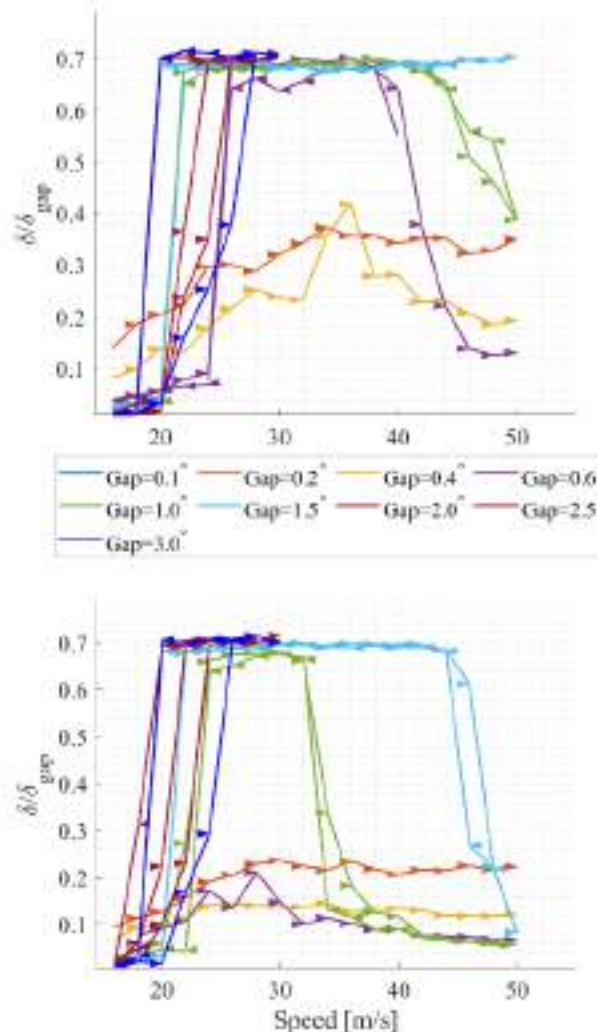


Figure 2: Effect of angle of attack on the LCO amplitude

With an angle of attack as small as half of a degree, LCO due to freeplay is quenched for freeplay gaps smaller than 0.4° , thus well within the limits imposed by regulatory agencies. In the middle of the plot it can be seen how the green and red curves are not overlapping with the others and are placed at a significantly smaller amplitude. This is signifying the disappearance of LCO and the start of a forced response movement of smaller amplitude due to external excitation.

An angle of attack of a degree quenches LCOs with a gap smaller than 0.6° and significantly limits the range of speed for which some larger gaps are creating the limit cycle oscillations. This is an important consideration for practical applications, but it must be approached with care. As previously mentioned, LCO can indeed develop with small gaps, including those within the regulations, if no angle of attack is present.

Relatively large gap values were also tested, up to a value of 3.0° . Due to the important vibrations transmitted to the main structure in those cases, the wind speed was limited to preserve the model integrity.

Summary

In this presentation, a comprehensive overview of the physics of limit cycle oscillations is provided. Several effects affecting the LCO amplitude and frequency are explored. The obtained conclusions will serve as a foundation for further work, exploiting a more complex system, with multiple nonlinearities.

Acknowledgements

Support by the Federal Aviation Administration as well as contributions by Wael Nour and Sohrob Mottaghi from the FAA are gratefully appreciated.

References

- [1] J. Panchal and H. Benaroya, "Review of control surface freeplay," *Prog. Aerosp. Sci.*, vol. 127, p. 100729, Nov. 2021. <https://doi.org/10.1016/j.paerosci.2021.100729>
- [2] D. D. Bueno, L. D. Wayhs-Lopes, and E. H. Dowell, "Control-surface structural nonlinearities in aeroelasticity: A state of the art review," *Aiaa J.*, vol. 60, no. 6, pp. 3364–3376, 2022. <https://doi.org/10.2514/1.J060714>
- [3] G. Dimitriadis, *Introduction to Nonlinear Aeroelasticity*. Chichester, UK: John Wiley & Sons, Ltd, 2017. doi: 10.1002/9781118756478
- [4] E. J. Breitbach, "Flutter Analysis of an Airplane With Multiple Structural Nonlinearities in the Control System," NASA Technical Paper 1620, 1980.
- [5] R. M. Laurenson and R. M. Trn, "Flutter Analysis of Missile Control Surfaces Containing Structural Nonlinearities," *AIAA J.*, vol. 18, no. 10, pp. 1245–1251, 1980. <https://doi.org/10.2514/3.50876>
- [6] C. L. Lee, "An Iterative Procedure for Nonlinear Flutter Analysis," *AIAA J.*, p. 8, 1986. <https://doi.org/10.2514/3.9352>
- [7] B. H. K. Lee and A. Tron, "Effects of structural nonlinearities on flutter characteristics of the CF-18 aircraft," *J. Aircr.*, vol. 26, no. 8, Art. no. 8, Aug. 1989. <https://doi.org/10.2514/3.45839>
- [8] M. Manetti, G. Quaranta, and P. Mantegazza, "Numerical Evaluation of Limit Cycles of Aeroelastic Systems," *J. Aircr.*, vol. 46, no. 5, Art. no. 5, Sep. 2009. <https://doi.org/10.2514/1.42928>
- [9] Y.-J. Seo, S.-J. Lee, J.-S. Bae, and I. Lee, "Effects of multiple structural nonlinearities on limit cycle oscillation of missile control fin," *J. Fluids Struct.*, vol. 27, no. 4, Art. no. 4, May 2011. <https://doi.org/10.1016/j.jfluidstructs.2011.02.009>
- [10] M. A. Padmanabhan, "Sliding wear and freeplay growth due to control surface limit cycle oscillations," *J. Aircr.*, vol. 56, no. 5, Art. no. 5, 2019. <https://doi.org/10.2514/1.C035438>
- [11] N. Fonzi, H. Curasi, S. Ricci, and E. Livne, "Experimental Studies on Dynamic Freeplay Nonlinearity," in *19th International Forum on Aeroelasticity and Structural Dynamics (IFASD 2022)*, 2022, pp. 1–20.
- [12] N. Fonzi, S. Ricci, and E. Livne, "Numerical and experimental investigations of freeplay-based LCO phenomena on a T-Tail model," in *AIAA Scitech 2022 Forum*, San Diego, CA, U.S.A., May 2022. <https://doi.org/10.2514/6.2022-1346>

Aeroelastic design and optimization of strut-braced high aspect ratio wings

Francesco Toffol^{1,a*}, Sergio Ricci^{1,b}

¹ Department of Aerospace Science and Technology, Politecnico di Milano, via la Masa 34, 20126, Milano, Italy

^afrancesco.toffol@polimi.it, ^bsergio.ricci@polimi.it

Keywords: Strut-Braced Wing, High Aspect Ratio Wing, Conceptual Design

Abstract. To improve aircraft aerodynamic efficiency, a possible solution is to increase the wing aspect ratio to reduce the induced drag term. As a drawback, the span increase introduces an increment of the wing loads, specially of the wing root bending moment that drives the sizing of the wing. Structural mass must be added to withstand higher loads, reducing the aerodynamic advantage from a fuel consumption point of view, as it can be instinctively seen in the Breguet's range equation. To limit the load increment due to the increased span, a possible solution is the usage of a strut: this kind of structure modifies the load path spanwise, diminishing the wing internal forces and reducing the wing penalty mass. In this framework, a lot of research is done studying Ultra-High Aspect Ratio Strut-Braced Wing, where the aspect ratio of such configuration is exasperated above 15, and the resulting wing is extremely flexible and may experience large deformation under loading. Moreover, the over determined structure realized by the fuselage-wing-strut connections deserves particular attention to fully characterize the aeroelastic interaction among the structural elements. For this reason, a two-step design approach that exploits NeoCASS (GUESS + NeOPT) is used to provide a sizing of the wing and of the strut considering several structural and aeroelastic constraints (e.g. flutter and ailerons effectiveness).

Introduction

In the framework of the Clean Aviation program, the HERWINGT project studies new wing configurations for a future regional aircraft carrying 80 passengers. In the project, alongside with innovative powertrain solutions, Ultra High Aspect Ratio Wings (UHARWs) are studied to improve the aerodynamic performance thanks to the reduction of the induced drag. As a drawback, the increase of the aspect ratio introduces higher bending moment for the wing sizing, that starts a snowball effect on the structural mass needed to withstand the loads. Therefore, the design becomes multidisciplinary and it's a trade-off between the aerodynamic performance advantages and the structural mass penalty. A possible solution to limit the structural mass is the Strut-Braced Wing (SBW) configuration, that redistributes the loads between the wing and the strut. This solution is becoming popular in the aviation industry, and it is proved by many project and programs focused on such configuration, for example [1]-[5]. This new configuration introduces new challenges since the conceptual design phases, where statistical approaches like [6][7] are no more valid for the wing structural mass estimation due to the lack of statistical sample for such configuration. Moreover, to fully exploit the benefits of using composite materials and their higher strength to weight ratio, novel physical based approaches must be adopted since the early design phases.

For this reason, in the WP1 of the HERWINGT project, Polimi is involved in the identification of the best wing configuration to be developed in the following of the project, using its in-house developed code NeoCASS [8][11] and its optimization module NeOPT [13][14] (Figure 1).



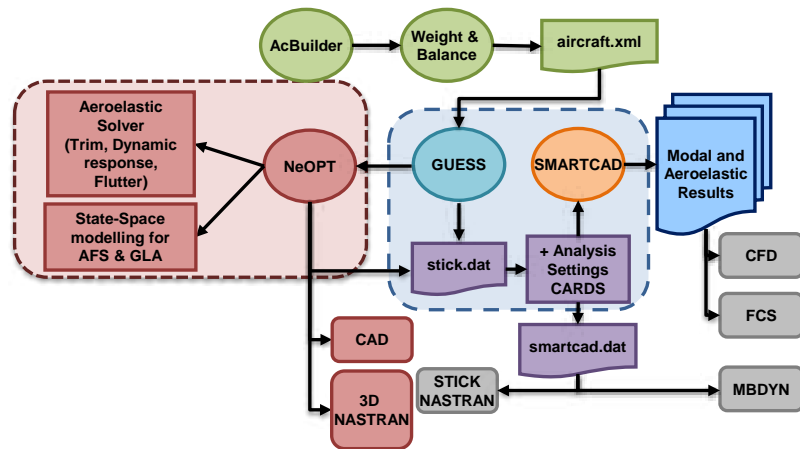


Figure 1: NeoCASS environment from [15]

When dealing with UHARWs, classical fully-stressed approaches may miss some important aeroelastic aspect of such configurations, for example the wing deformation, the divergence and control surfaces effectiveness. For this reason, an approach like the one adopted by NeOPT is convenient: in addition to classical stress and buckling criteria, whichever aeroelastic response can be accounted during the optimization, e.g. flutter or control surface efficiency.

Wing conceptual design in the HERWING project

In the framework of the HERWING project, a reference aircraft carrying 80 passengers is studied. The wing is high-mounted and equipped with two propellers. An initial wing layout was used as starting point for the study of the most promising solution, and its main characteristics are reported in Table 1. It is a trapezoidal wing that is rectangular up to the kink, then a constant tapering is applied. The wing is completely flat, i.e. no dihedral is present. From the material point of view, the wing is required to be in composite material with a symmetric and balanced layup, with at least 10% of ply oriented in the three main directions (0°-45°-90°).

Table 1: Reference wing geometry

Area [m ²]	Span [m]	Root Chord [m]	Tip Chord [m]	Aspect Ratio [-]	Engine Span [m]	Kink [m]	Outboard Sweep [°]
73.3	29.65	2.92	1.48	12	5.555	5.555	2.62

Starting from this configuration, the wing was stretched increasing the aspect ratio and keeping the same wing surface, to have the same wetted area, associate to the viscous drag, but increasing the aspect ratio so reducing the induced drag term. The constraints accounted in the wing stretching are: the maximum span achievable remaining in the same Aerodrome Reference Code (ARC= C), that is 36m; the wing tip minimum chord that must be guaranteed to fit the actuation systems, that is 1.4m; the kink position is kept fixed as well as the LE sweep angle.

This approach resulted in a reduction of the root and tip chords, while the LE position was kept constant.

Performing a full geometry optimization would take too much time in this design phases, where it is way more important to understand the sensitivity of the design to the macro parameters rather than finding the optimal solution. For this reason, a parametric study increasing the aspect ratio was performed, considering AR=12,13,15,17. The wings considered for the analysis are illustrated in Figure 2. Despite the maximum span allowed is 36m, the wing is stretched to a maximum of 35m to leave 0.5m for each side to eventually install wing tip device like winglets.

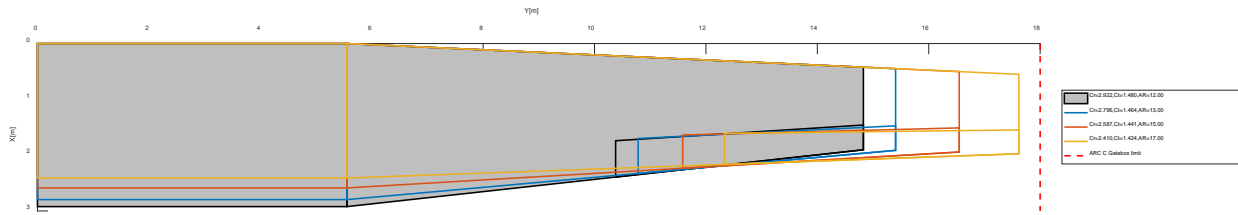


Figure 2: Wing layout selected for the conceptual parametric study.

The design strategy adopted was to perform an initial screening of the solution with the GUESS module, the module of NeoCASS dedicated to the quick and simplified structural sizing, and then to perform a refined optimization of some configuration with NeOPT able to consider a 3D wingbox and different aeroelastic constraints.

Initially, the wing was studied for all the aspect ratio in both cantilevered (CNT) and strut braced (SBW) configurations. The SBW with AR17 immediately showed a considerable weight reduction w.r.t. the CNT wing, for this reason only the AR17 was considered for the SBW configuration.

All the wings were designed with a maneuver envelope compliant with EASA CS25 regulations [16], that results in 45 maneuvers (pull-up, push-down, high lift, roll, sideslip, etc,...), in different flight points (VA, VS, VMO, VD,...). The structural masses of the wingbox and strut-wingbox (spar, stringers, caps, skins) are reported in Table 2 and plotted in Figure 3. Wing group it is intended as the sum of the wing and the strut items.

Table 2: GUESS sizing results for the considered configuration, wing and strut structural masses

Item	CNT AR=12	CNT AR=13	CNT AR=15	CNT AR=17	SBW AR=17
Wing [kg]	1145	1255	1516	1821	828
Strut [kg]	0	0	0	0	615
Wing + Strut [kg]	1145	1255	1516	1821	1211

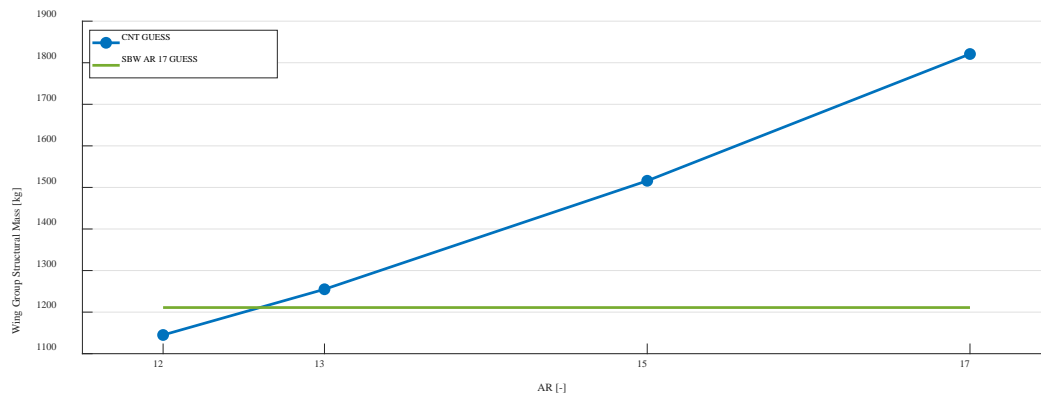


Figure 3: Wing group structural mass evolution with AR

The results obtained show that the SBW wing group with AR=17 has the same weight of the CNT with AR = 12.5. Despite CNT AR = 12 is lighter than the SBW AR=17 solution, the induced drag is term is around 40% higher for the CNT solution. For this reason, the focus is moved on the SBW configuration only, which design was refined with NeOPT considering different structural layout.

The refinement performed with NeOPT considered the same load conditions (45 maneuvers). In addition to the structural constraints, a minimum aileron efficiency must be guaranteed to

preserve the aircraft handling qualities. The aileron efficiency is expressed as the ration between the flexible and rigid roll moment derivative w.r.t. the aileron deflection $C_{L,\delta}$ (Eq.(1)).

$$\frac{C_{L,\delta \text{ flexible}}}{C_{L,\delta \text{ rigid}}} > 0.5 \quad (1)$$

The internal structure layouts considered are listed in Table 3.

Table 3: Structural configuration considered for the NeOPT refinement.

SBW ID	η , Wing Strut Connection [Span %]	Rib Pitch [m]	Stringer Pitch [m]	Spar Number
1	50	0.5	0.16	2
2	50	0.5	0.16	3
3	50	1.0	0.16	3
4	50	0.5	No stringer	3
5	50	1.0	0.16	4
6	66	0.5	0.16	2
7	31	0.5	0.16	2

The results of the sizing are reported in Table 4

*Table 4: NeOPT Sizing results. * Not converged*

SBW ID	1	2	3	4	5	6	7
Wing Mass [kg]	1108	1181	3686*	1700	3355	992	1499
Strut Mass [kg]	383	383	383	383	383	536	386
Wing Group Mass [kg]	1491	1564	4069	2083	3738	1528	1885

From the optimization results, the most convenient layout is a conventional 2 spar with 0.5m rib pitch. Three and four spar configurations were considered to increase the rib pitch, but this solution was not effective for the SBW configuration. Indeed, the strut introduces relevant compression load on the inboard portion of the wing and the increased rib pitch makes the buckling of the stiffened panels critical.

The sensitivity w.r.t. the connection point between the wing and the strut is studied for the two-spar configuration in three different section spanwise, which are 31% 50% and 66%. The first value is studied to evaluate a possible configuration where the engine and the strut are connected to the wing in the same span location, having a single reinforced wing rib for both the items. The second point is exactly the mid wing, while the last one is the optimal point found in previous studies [17]. The obtained data were fitted with a 2nd order polynomial function and a minimum in the structural mass was found for an $\eta=0.56$, as shown in Figure 4.

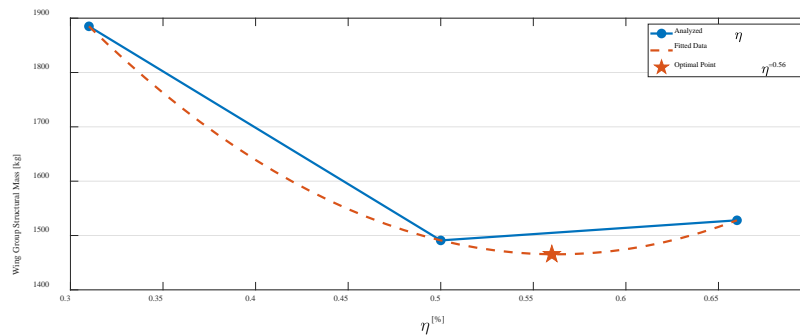


Figure 4: Wing group structural mass evolution w.r.t. the strut-wing connection point.

Conclusion

In the HERWINGT project different SBW configuration were sized, investigating the different structural layout options and connection point for the strut. The most promising solution in terms of wing structural mass was not directly considered, but it was identified with a parametric study: it is a 2 spar layout with 0.5m rib pitch and a connection between the wing and the strut placed at 56% of the span.

Acknowledgements

This project has received funding from the Clean Aviation Joint Undertaking under grant agreement No. 101102010. The granting authority receives support from the European Union's Horizon Europe research and innovation programme and the Clean Aviation Joint Undertaking members other than the Union.



Disclaimer

Funded by the European Union. Views and opinions expressed are however those of the author(s) only and do not necessarily reflect those of the European Union or Clean Aviation Joint Undertaking. Neither the European Union nor the granting authority can be held responsible for them.

References

- [1] Gur, O.; Bhatia, M.; Schetz, J.A.; Mason, W.H.; Kapania, R.K.; Mavris, D.N. Design Optimization of a Truss-Braced-Wing Transonic Transport Aircraft. *J. Aircr.* 2010, 47, 1907–1917. <https://doi.org/10.2514/1.47546>
- [2] Bradley, M.K.; Droney, C.K.; Allen, T.J. Subsonic Ultra-Green Aircraft Research (No. NF1676L-19776). Available online: <http://web.archive.org/web/20220303155711/https://ntrs.nasa.gov/api/citations/20120009038/downloads/20120009038.pdf> (accessed on 19 January 2023).
- [3] Hosseini, S.; Ali Vaziri-Zanjani, M.; Reza Ovesy, H. Conceptual Design and Analysis of an Affordable Truss-Braced Wing Regional Jet Aircraft. *Proc. Inst. Mech. Eng. Part G: J. Aerosp. Eng.* 2020. <https://doi.org/10.1177/0954410020923060>
- [4] Harrison, N.A.; Gatlin, G.M.; Viken, S.A.; Beyar, M.; Dickey, E.D.; Hoffman, K.; Reichenbach, E.Y. Development of an Efficient $m = 0.80$ Transonic Truss-Braced Wing Aircraft. In *Proceedings of the AIAA Scitech 2020 Forum*, Orlando, FL, USA, 6 January–10 January 2020. <https://doi.org/10.2514/6.2020-0011>

- [5] Ricci, S., Paletta, N., Defoort, S., Benard, E., Cooper, J. E., & Barabinot, P. (2022). U-HARWARD: a CS2 EU funded project aiming at the Design of Ultra High Aspect Ratio Wings Aircraft. In AIAA Scitech 2022 Forum (p. 0168). <https://doi.org/10.2514/6.2022-0168>
- [6] D. Raymer, Aircraft design: a conceptual approach. American Institute of Aeronautics and Astronautics, Inc., 2012. <https://doi.org/10.2514/4.869112>
- [7] E. Torenbeek, Synthesis of subsonic airplane design: an introduction to the preliminary design of subsonic general aviation and transport aircraft, with emphasis on layout, aerodynamic design, propulsion and performance. Springer Science & Business Media, 2013.
- [8] L. Cavagna, S. Ricci, and L. Travaglini, "Neocass: an integrated tool for structural sizing, aeroelastic analysis and mdo at conceptual design level," Progress in Aerospace Sciences, vol. 47, no. 8, pp. 621–635, 2011. <https://doi.org/10.1016/j.paerosci.2011.08.006>
- [9] L. Cavagna, S. Ricci, and L. Travaglini, "Structural sizing and aeroelastic optimization in aircraft conceptual design using neocass suite," in 13th AIAA/ISSMO Multidisciplinary Analysis Optimization Conference, p. 9076, 2010. <https://doi.org/10.2514/6.2010-9076>
- [10] L. Cavagna, S. Ricci, and L. Riccobene, "A fast tool for structural sizing, aeroelastic analysis and optimization in aircraft conceptual design," in 50th AIAA/ASME/ASCE/AHS/ASC Structures, Structural Dynamics, and Materials Conference 17th AIAA/ASME/AHS Adaptive Structures Conference 11th AIAA No, p. 2571, 2009. <https://doi.org/10.2514/6.2009-2571>
- [11] L. Cavagna, S. Ricci, and L. Riccobene, "Structural sizing, aeroelastic analysis, and optimization in aircraft conceptual design," Journal of Aircraft, vol. 48, no. 6, pp. 1840–1855, 2011. <https://doi.org/10.2514/1.C031072>
- [12] Fonte, F., & Ricci, S. (2019). Recent developments of NeoCASS the open source suite for structural sizing and aeroelastic analysis. In 18th International Forum on Aeroelasticity and Structural Dynamics (IFASD 2019) (pp. 1-22)
- [13] Toffol, F., & Ricci, S. (2023). A Meta-Model for composite wingbox sizing in aircraft conceptual design. Composite Structures, 306, 116557. <https://doi.org/10.1016/j.compstruct.2022.116557>
- [14] Toffol, F., & Ricci, S. (2023). Preliminary Aero-Elastic Optimization of a Twin-Aisle Long-Haul Aircraft with Increased Aspect Ratio. Aerospace, 10(4), 374. <https://doi.org/10.3390/aerospace10040374>
- [15] Toffol, F. (2021). Aero-servo-elastic optimization in conceptual and preliminary design.
- [16] EASA Easy Access Rules for Large Aeroplanes. Available online: <http://web.archive.org/web/20230119132207/https://www.easa.europa.eu/en/downloads/136694/en>. (accessed on 19 January 2023).
- [17] Carrier, G. G., Arnoult, G., Fabbiane, N., Schotte, J. S., David, C., Defoort, S., ... & Delavenne, M. (2022). Multidisciplinary analysis and design of strut-braced wing concept for medium range aircraft. In AIAA SCITECH 2022 Forum (p. 0726). <https://doi.org/10.2514/6.2022-0726>

Ten years of aero-servo-elastic tests at large POLIMI's wind tunnel for active flutter control and loads alleviation

Sergio Ricci

Politecnico di Milano, Department of Aerospace Science and Engineering, Via La Masa 34,
Milano, Italy

sergio.ricci@polimi.it

Keywords: Aeroelastic Wind Tunnel Testing, Gust Loads Alleviation, Flutter Suppression

Abstract. Born in the autumn of 2001, but fully operational since 2023, the large wind tunnel of Politecnico di Milano turns 20 this year and today it is one of the 4 large research infrastructures of the University. Designed, from the point of view of fluid dynamics, entirely within Politecnico, it is a close circuit wind tunnel characterized by a particular design that includes two test sections. The boundary layer section (14m x 4m x 38m), located in the return circuit, is particularly suitable for testing objects subjected to the action of the wind such as bridges, skyscrapers, stadiums and large roofing systems; this section is widely used for research in the wind energy sector. The low turbulence section (4m x 4m x 6m), located as usual between the convergent and divergent parts of the tunnel, is mainly used for aeronautical tests, such as airplanes and helicopters, but not only. Suffice it to recall the numerous tests carried out in the field of sport aerodynamics, because the dimensions allow the equipment to be tested directly with the athletes. The paper briefly describes the most relevant aero-servo-elastic tests carried out during the last 10 years of activity.

Introduction

In the late 1990s Politecnico di Milano decided to organize itself over a network of different campus, two in Milano, and other outside Milano in other cities such as Lecco, Como, Mantova and Piacenza. The new Bovisa campus, north side of the city, allowed to create large new laboratories for the Departments that decided to move there, at first Aerospace Department, followed by Mechanical and Energy. The design of the new spaces and new buildings has made it possible to create the large new wind tunnel, I would say unique in the university context.

The new wind tunnel, designed by taking advantage of the internal competences, is a traditional close circuit plant, but with unusual space organization. Indeed, the return circuit is used as a large chamber for wind engineering applications, with a maximum speed of 16 m/s, while two interchangeable test rooms of 4x4x6 m and a maximum speed of 55 m/s are used for typical aeronautical applications. Two characteristics make this wind tunnel especially useful for aeroelastic testing. At first, the large test rooms allow for testing large scale models, in some cases components at full scale. Second, the flow generation system based on 14 fans for a total of 1.5 MW power is fully protected by a steel grid, so that it cannot be damaged by possible brake of aeroelastic models. During years of activity the wind tunnel has been equipped with dedicated equipment for aeroelastic tests that will be presented in the following. Due to the limited space, mainly two kinds of aeroelastic tests will be briefly described: gust loads alleviation, and active flutter suppression tests.



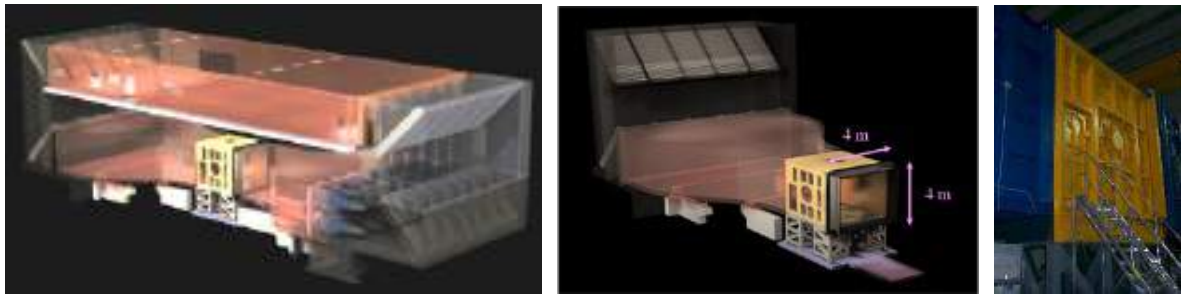


Figure 1: The POLIMI's large wind tunnel

Gust Load Alleviation Tests

During recent years a lot of studies have been dedicated to the implementation of maneuver and gust load alleviation techniques (MLA and GLA), as part of a more general strategy to decrease the environmental impact of future transport aircraft. Indeed, these techniques are believed capable for a further structural weight reduction of about 20%. Two are typically the challenges in testing in wind tunnel GLA control systems. The biggest part of the gust response is due to rigid body motion, so at least plunge and pitch motions must be reproduced. Second, due to the scale factor the bandwidth of actuators requested demands for sufficient space to install inside the model the actuators. These challenges have been addressed at POLIMI by means of the following strategies.

At first, a half model is usually adopted, and due to installation and accessibility problem, the half model is vertically mounted, the connection between the half fuselage and the wind tunnel floor is realized with a pivot, that preserves the pitch free body motion, mounted on a sledge that preserves the plunge free body motion. Since the gravity acts perpendicularly to the lift, a dedicated Weight Augmentation System (WAS) is used to artificially generate the weight force. The WAS consists in a linear electric actuator that acts on the moving sledge in correspondence of the center of gravity of the aircraft, reproducing the weight force indeed. An important ratio which cannot be preserved is the one between the inertial and gravity forces, represented by the Froude number. Thanks to the WAS, it is possible to impose the force that counteracts the lift force, and in the case of unit load factor $n=1$ it is the weight force. In this way the Froude scaling is preserved only for the plunge motion. For what concerns the model scaling, an iso-frequency approach is adopted, so that the control system designed for the full-scale aircraft can be plugged and played for the wind tunnel test. The different control surfaces are driven by Harmonic drive electric motors that guarantee large bandwidth, typically 15 Hz, and zero free play due to a patented gear box. A dedicated six vanes gust generator has been designed and manufactured able to produce typical 1-cos discrete gust as well as continuous gust excitation with prescribed PSD.

The equipment described above has been successfully tested during different European projects, such as GLAMOUR "*Gust Load Alleviation techniques assessment on wind tUnnel Model of advanced Regional aircraft*" (JTI-CS-2013-1-GRA-02-022), as well as the Clean Sky 2 AIRGREEN2 project. Figure 2, left shows the WTT3 1:8 scaled aeroelastic model representative of the future twin prop regional aircraft designed, manufactured, and tested by POLIMI in AIRGREEN project while in the same figure, on the right, a summary of results comparing the root bending moment reduction capabilities for different flight envelope velocities as well different control laws.

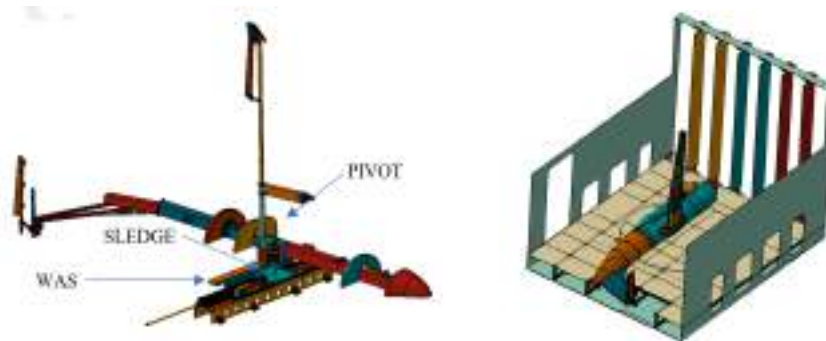


Figure 2: Photo of the aeroelastic half model installed on the WAS system (left) and the gust generator (right)

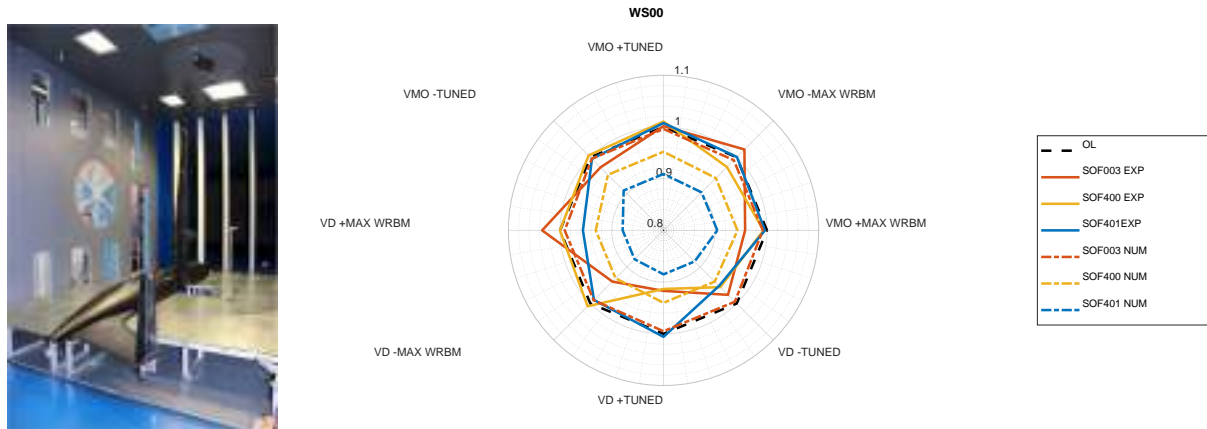


Figure 3: The WTT3 model (left) and the typical test results (right)

Active Flutter Suppression Tests

During the last 10 years POLIMI also acquired a deep knowledge in the design and manufacturing of aeroelastic scaled wind tunnel models used for validation of new active control strategies. One of them is for sure the so-called X-DIA model, three surfaces fully dynamically aircraft 1:10 scaled with respect the reference aircraft developed originally in the 3AS EU project and since then used for many wind tunnel test campaigns for multi surface aeroelastic control. The model has been updated in 2017 to a new, conventional configuration in the framework of the Active Flutter Suppression project in cooperation with the University of Washington in Seattle, USA, and FAA to investigate the robustness of active flutter suppression technologies. Different control laws have been developed and successfully tested, from the simple ones such as Static Output Feedback and ILAF, up to the more sophisticated and robust, such as H infinity. The ailerons, driven by Harmonic drive motors have been used for control. Dedicated safety devices installed on the tip based on a small moving mass from the rear to the forward position were adopted to stop the flutter in an automatic way in case of failure of the control system. The tests have been conducted with the model installed in the testing room by means of cable so to simulate the free-free conditions. During this study, more than 50 flutter conditions have been tested without any damage to the model, showing a very high reliability for the entire system.

During last two year the project focused on the effect of LCOs due to the free play in the control surfaces. Special devices have been designed and manufactured so to be able to apply accurate and small enough gaps to the elevators of X-DIA model. They have been tested separately and last February 2023 the new tailplanes have been installed on the X-DIA model to repeat the active flutter suppression tests in presence of LCOs. Due to the need to accurately set the angle of attack and side du to their strong effect on the preload in presence of gap on control surfaces, the model

has been installed on a pylon, equipped with accurate alfa and beta positioning system. Due to the presence of the flexible pylon, the model shows now two flutter mechanisms: the original one, i.e. a symmetric bending torsion at 41.5 m/s, and a new one, an antisymmetric bending torsion at 47.5 m/s. This situation creates a challenging goal since, to identify the second flutter, it is necessary to control the first one. This has been done successfully, then also the second flutter has been actively controlled.



Figure 4: The XDIA model in free-free condition (left) and installed on the pylon (right)

Summary

In this paper a summary of the aeroelastic wind tunnel testing performed at POLIMI's large wind tunnel has been reported.

Acknowledgement

The large set of aeroelastic activities in the framework of different international projects has been possible thanks to the passion, dedication, and competence of many colleagues and students at different level involved. I would like to thank first Prof. Paolo Mantegazza that about 35 years ago founded the aeroelasticity branch at DAER-POLIMI. Then, the contribution of L. Riccobene, A. De Gaspari, F. Fonte, F. Toffol, L. Marchetti, N. Fonzi, V. Cavalieri and G. Bindolino is kindly acknowledged.

References

- [1] Ricci, S., Toffol, F., De Gaspari, A., Marchetti, L., Fonte, F., Riccobene, L., Mantegazza, P., Berg, J., Livne, E., Morgansen, K., Wind Tunnel System for Active Flutter Suppression Research: Overview and Insights, AIAA Journal, Vol. 60, N. 12, 2022, p. 6692-6714. <https://doi.org/10.2514/1.J061985>
- [2] N. Fonzi, S. Ricci, and E. Livne, "Numerical and experimental investigations of freeplay-based LCO phenomena on a T-Tail model," in AIAA Scitech 2022 Forum, San Diego, CA, U.S.A. May 2022. <https://doi.org/10.2514/6.2022-1346>
- [3] Ricci, S., De Gaspari, A., Fonte, F., Riccobene, L., Toffol, F., Mantegazza, P., Karpel, M., Roizner, F., Wiberman, R., Weiss, M., Cooper, J.E., Howcroft, C., Calderon, D., Adden, S., Design and Wind Tunnel Test Validation of Gust Load Alleviation Systems, 58th AIAA/ASCE/AHS/ASC Structures, Structural Dynamics, and Materials Conference AIAA SciTech 2017, ISBN: 9781624104534, p. 1-12, Grapevine, TX, USA, 9-13 Jan. 2017. <https://doi.org/10.2514/6.2017-1818>
- [4] Toffol, F., Marchetti, L., Ricci, S., Fonte, F., Capello, E., Malisani, S., Gust and Manoeuvre Loads Alleviation Technologies: Overview, Results and Lesson Learned in the Framework of the Cs2 Airgreen2 Project, 19th International Forum on Aeroelasticity and Structural Dynamics (IFASD 2022), 2023, ISSN: p. 1-24, Madrid, Spain, 13-17 June 2022.

Aeronautical Propulsion

Studies in hydrogen micromix combustor technologies for aircraft applications

Ainslie D. French^{1,a*}, Giuseppe Mingione^{1,b}, Antonio Schettino^{1,c},
Luigi Cutrone^{1,d}, Pietro Roncioni^{1,e}

¹CIRA (Italian Aerospace Research Centre), Aerothermodynamics & Fluid Mechanics Dept., Via
Maiorise, 81043 Capua (CE), Italy

^aa.french@cira.it, ^bg.mingione@cira.it, ^ca.schettino@cira.it, ^dl.cutrone@cira.it, ^ep.roncioni@cira.it

Keywords: Hydrogen, Micromix Combustion, Flamelets

Abstract. Within the context of future aircraft turbine engine development technology, hydrogen has fast become one of the most favored candidates as an alternative fuel due to the possibility of producing extremely low levels of pollutants in particular NO_x. The principal component of such an engine technology is the hydrogen micro-mix combustor which provides a solution to safe hydrogen combustion avoiding auto-ignition and flashbacks by addressing novel methods of hydrogen-air mixing. The current design concepts include a typical injection manifold composed of multiple concentric arrays of micro-mix combustors which produce hundreds of miniature low temperature diffusion flames having very low NO_x levels.

Introduction

Air transport requires much energy and therefore it is necessary to have a fuel with a high energy density. Conventionally, jet kerosene produced from fossil fuels has been the main propellant used in aviation. The main problem with using kerosene as an aviation fuel is the environmental impact due to the production of the greenhouse gas, CO₂, which accounts for about 2,5% of global emissions as well as CO, SO_x.

A switch to hydrogen propelled aircraft would produce zero CO₂, CO, SO_x emissions and, when combined with a suitable technology may substantially reduce the levels of NO_x emitted into the atmosphere and potentially eliminate other pollutants. Additionally, hydrogen has an energy density almost three times that of kerosene but requires heavier storage facilities to kerosene. The main disadvantage of hydrogen is that it requires about five times the volume of conventional fuel to carry the same amount of energy and consequently new concepts for aircraft design need to be addressed to enable safe, light storage of liquid hydrogen.

Currently two lines of research are being pursued towards the application of combusted hydrogen as a propellant both of which aim to reduce the levels of NO_x produced: Lean Direct Injection (LDI), which tends to limit the levels of NO_x emissions to those of current kerosene fuelled engines and the Micromix combustor technology which aims to lower the levels of NO_x produced compared to kerosene. This latter technology is investigated in this paper.

Preliminary investigations and experiments using hydrogen were first conducted by Funke-et-al [1] using a hydrogen air mixture using an experimental test rig constructed for the GTCP 36-300 APU which was modified to incorporate a hydrogen combustor mechanism consisting of concentric arrays of numerous miniature micro-mix combustors as shown in Fig. 1.



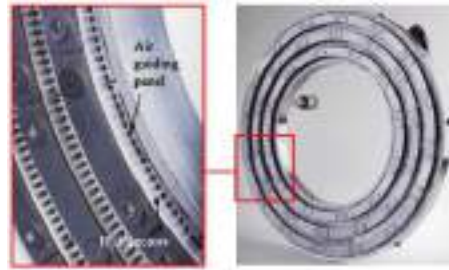


*Fig. 1 Prototype micro-mix combustor for gas turbine
Honeywell/Garrett APU GTCP 36-300 [2]*

Numerical method

The commercial program ANSYS-FLUENT [3] was used as the main software used to obtain flow solutions for all test cases. Calculations using the FGM method with partially premixed combustion were conducted and compared with results from simulations using the eddy dissipation method also performed for a baseline test case hypothetical APU micromixer design at a relatively low pressure described by Ghali [4]. The chemical kinetic mechanism for the first series of FGM simulations used the Naik model [5] consisting of 9 species and 21 reactions. Turbulence was modelled using the $k-\omega$ SST turbulence model by Menter [6].

This turbulence model is particularly suited to these kinds of simulations where the recirculation and mixing of hydrogen is of primary importance. The model is capable of accurately capturing the detail of the turbulent flow both through the viscous sublayer down to the solid wall as well the large-scale eddies in the recirculation region and the small-scale eddies in the vicinity of the hydrogen jet.

To calculate the concentration of NO in ANSYS-FLUENT the extended Zeldovich chemical kinetic scheme was used, the details of which are given in [3] and where the calculation is restricted to thermal NO_x formation.

Computational domain and numerical results

A structured grid having almost 580,000 cells was created using the ANSYS-ICEMCFD grid generator which satisfied the grid quality requirements where the air inlet is over the left vertical face and the hydrogen inlet is the cylindrical vertical tube shown in Fig. 2.

Mass flow rate boundary conditions are set with an air inlet temperature of 422K at a pressure of 2.5 atm., a hydrogen inlet temperature of 300K and the mass flow rates listed in Table 1 at a pressure of 1 atm. and pressure outlet boundary conditions of 2.4 atm. Adiabatic no slip boundary conditions were applied at the walls.

Table 1: Equivalence ratios and hydrogen mass flow rates for combustor

Equivalence ratio ϕ	H ₂ mass flow rate (kg·s ⁻¹)
0.3	4.335 x 10 ⁻⁶
0.4	5.75 x 10 ⁻⁶
0.5	7.225 x 10 ⁻⁶
0.6	8.67 x 10 ⁻⁶

The results are presented from Fig. 3 to Fig. 9. Fig. 3 shows the flame anchored between two relatively large recirculation regions on the symmetry plane, the upper region being slightly larger than the lower one. The upper inner vortex originates from the main air jet whilst the lower vortex originates from the recirculated combusted gas downstream of the hydrogen jet. The velocity at the air channel exit is approximately 100 m·s⁻¹ which is also consistent with that associated with

the low pressure drop of a typical combustor. The velocity at the downstream edge of the H_2 channel at the entrance to the chamber is about $250 \text{ m}\cdot\text{s}^{-1}$.



Fig. 2: Computational domain used in calculations

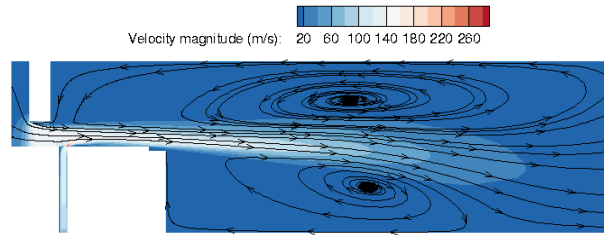


Fig. 3: Calculated flow field and stabilising vortices with EDM model for $\phi = 0.4$

Fig. 4 and Fig. 5 show the temperature and NO distributions for different equivalence ratios on the symmetry plane obtained with the EDM model. The temperatures are consistent with those in [4], where a maximum flame temperature of about 2600 K is predicted for the highest equivalence ratio of $\phi = 0.6$ associated with a larger more extended flame.

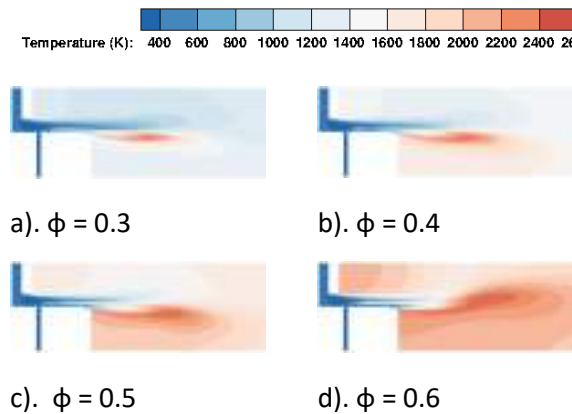


Fig. 4: Flame temperature for different equivalence ratios with EDM

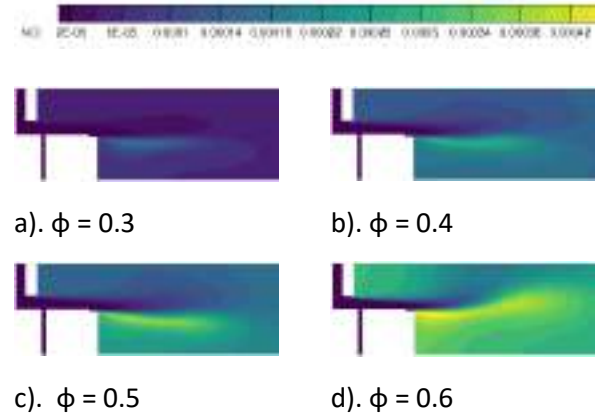


Fig. 5: Mass fraction of pollutant for different equivalence ratios with EDM

Similar distributions using the FGM method are shown in Fig. 6 and Fig. 7.

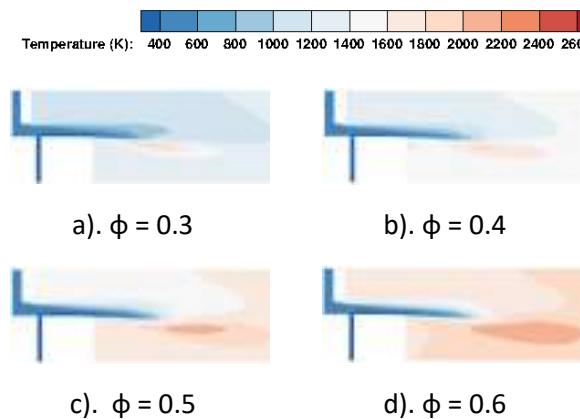


Fig. 6: Flame temperature for different equivalence ratios with FGM - Naik

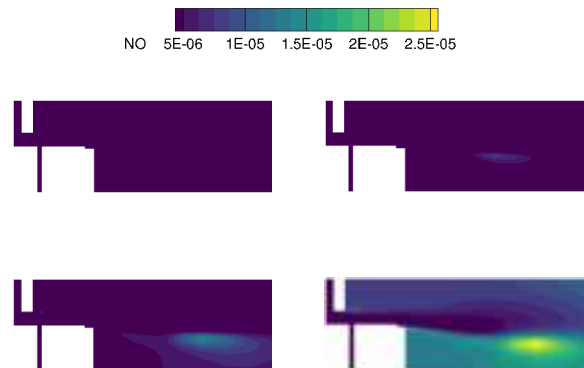


Fig. 7: Mass fraction of pollutant for different equivalence ratios with FGM - Naik

The flame temperature is about 200K lower than with the EDM due to the energy consumed in the chemical reactions in the FGM model compared to the single step reaction in EDM calculation with a corresponding reduction in NO concentrations.

The results for mass-averaged temperature and NO emissions corrected to 15% O₂ are shown in Fig. 8 and Fig. 9. The flame temperature and NO emissions are a direct consequence of equivalence ratio, the lower the equivalence ratio, the shorter and cooler the flames with the associated reductions in NO emissions.

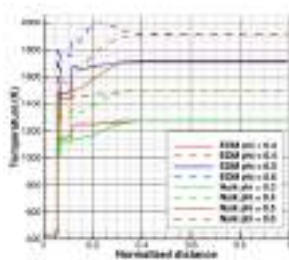


Fig. 8: Mass weighted average temperature along combustor length for EDM and FGM -Naik for different equivalence ratios

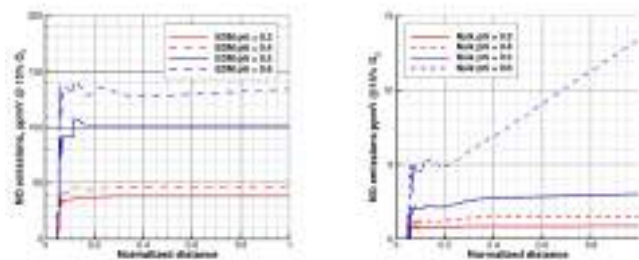


Fig. 9: NO distributions along combustor length for EDM and FGM-Naik models for different equivalence ratios

Summary

Comparison of results between the EDM and the FGM-Naik model demonstrated that the temperature distributions were in good agreement but much lower NO levels, of about three orders of magnitude were obtained with the latter model. Qualitative comparison of the temperature and NO emission levels indicated satisfactory agreement with the trends expected in the physics where higher temperatures and higher NO concentrations were obtained for increasing equivalence ratios which were also in broad agreement with similar results available in the literature [4].

References

- [1] Funke, H. H.-W., Boerner, S., Keinz, J., Kusterer, K., Kroniger, D., Kitajima, J., Kazari, M., Horikawa, A., "Numerical and Experimental Characterization of Low NOX Micromix Combustion Principle for Industrial Gas Turbine Applications", GT2012-69421, Proceedings of ASME Turbo Expo 2012, June 11-15, 2012. <https://doi.org/10.1115/GT2012-69421>
- [2] Haj Ayed, A., Kusterer, K., Funke, H.H.-W., Keinz, J., Striegan, C., Bohn, D., "Experimental and numerical investigations of the dry-low. NOx hydrogen micromix combustion chamber of an industrial gas turbine", Propulsion and Power Research 2015; 4(3):123-131. <https://doi.org/10.1016/j.jprr.2015.07.005>
- [3] ANSYS, ANSYS Fluent Theory Guide Release 15.0, ANSYS Inc., 2013.
- [4] Ghali, P.F., Khandelwal, B., "Design and Simulation of a Hydrogen Micromix Combustor", AIAA Sci-Tech Forum, 19-21 January 2021., M. Rodriguez, J.A. Voigt and C.S. Ashley, U.S. Patent 6,231,666. (2001).
- [5] Reaction Design: San Diego, 2015. Ansys Chemkin Theory Manual 17.0 (15151).
- [6] Menter, F.R., "Two-equation eddy-viscosity turbulence models for engineering applications", AIAA Journal, Vol. 32, No. 8, 1994, pp. 1598-1605. <https://doi.org/10.2514/3.12149>

Performance assessment of low-by-pass turbofan engines for low-boom civil supersonic aircraft

Francesco Piccionello^{1,a*}, Grazia Piccirillo^{1,b} and Nicole Viola^{1,c}

¹Politecnico di Torino, Department of Mechanical and Aerospace Engineering, Corso Duca degli Abruzzi 24, 10129, Torino, Italy

^as301549@studenti.polito.it, ^bgrazia.piccirillo@polito.it, ^cnicole.viola@polito.it

Keywords: Low-By-Pass Turbofan, Supersonic Aircraft, Conceptual Design, MORE&LESS

Abstract. This paper presents an approach to evaluate the performance of low-bypass turbofan engines without afterburner for a low-boom supersonic aircraft operating at Mach 1.5. The proposed method focuses on optimizing the propulsive performance by minimizing fuel consumption while meeting mission profile requirements. The study contributes to the MORE&LESS project, providing methods for rapidly designing novel supersonic propulsion concepts with improved environmental performance. The research conducts a thermodynamic analysis for on-design engine conditions based on the Modified Specific Heat (MSH) gas model. Specific non-installed thrust and fuel consumption are estimated for cruise phase. Then, the engine cycle analysis is also performed to study off-design performance, including simplified models to account for engine drag and calculate installed thrust and fuel consumption. MATLAB simulations are employed to determine thrust and consumption based on the specific mission profile of the Mach 1.5 case-study, allowing for comparison of different engine types. Ongoing work involves the optimization of engine parameters such as compression ratio, bypass ratio, and turbine inlet temperature, targeting further fuel consumption reduction and pollutant emission estimations.

Introduction

The next generation of supersonic aircraft is shifting towards low-boom configurations with slender structures and cruising Mach numbers of about 1.5. Extensive research is underway to identify the most suitable propulsion system that can effectively fulfil the specific mission requirements of these aircraft. Low-bypass turbofan engines are currently considered the most promising solution. Therefore, this paper aims at analysing the use of low-by-pass turbofan for low-boom civil supersonic aircraft cruising at Mach 1.5. The proposed approach relies on a series of previous studies. In [1] the performances of the engine were computed performing on-design and off-design analyses. Similar considerations could be done for [2], which focused on the cycle and engine layout of similar boom jet. The aim of this paper is to develop the approach proposed in [4] and [6], in which the engine is designed considering some mission phases estimating fuel consumption and expanding off-design analysis to the entire mission profile.

The initial analysis focuses on the engine's parametric cycle, or on-design cycle, considering the aircraft high-level requirements related to the propulsion system, such as the desired cruise thrust, and geometrical constraints. Subsequently, the sea-level thrust is calculated solving the off-design equations using the Newton-Rapson algorithm. During this phase, limitations to the operation of the afterburner are also considered, in order to minimize the acoustic impact of the engine. Once the engine meets all the requirements and constraints, the main parameters are fixed. The final analysis involves evaluating the Thrust-Specific Fuel Consumption (TSFC) during each phase of ASTOS (Aerospace Trajectory Optimization Software) mission profile. Multiple iterations can be performed to assess the mission average TSFC reduction, which serves as figure of merit for performance comparison. The analyses were conducted using MATLAB routines,



which were developed to contribute to the EU-funded MORE&LESS project, providing methods for rapidly designing novel supersonic propulsion concepts with better environmental performance. The high-level requirements of the considered aircraft are in Table 1.

Table 1. Low-boom supersonic jet high-level requirements

Low-boom supersonic jet high-level requirements	
Cruise Mach Number	1.5
Cruise altitude	16 km
Payload	8-12 passengers
Range	6500 km
Propellant	biofuel

The Methodology section specifies how these requirements were used as inputs to develop an *ad hoc* propulsive system. Outputs in terms of fuel consumption and fuel mass flow rate for different turbofan engine designs are presented in the Results section. Considerations and final remarks are drawn in the Conclusion section.

Methodology

The workflow adopted is depicted in Fig. 1, while the inputs required to start the analysis are listed in Table 2.

Table 2. Inputs: Engine requirements

Cruise Thrust	30 kN
SL Thrust	143.1 kN
Inlet Diameter	1.10 m
Number of Engines	2

First, the required thrust during cruise and geometrical constraints (inlet and nacelle size) are considered. On-design analysis is carried out, using altitude and flight Mach number as main inputs. According to [7], two turbofan mixed flows engines are the appropriate propulsion systems configuration for this type of jet. It is also possible to consider separated flow turbofans [2], however the increase of fan diameter lead by by-pass must be taken in consideration due to aerodynamics implications. Then, sea-level thrust is computed setting Mach number and altitude equal to zero (sea level static thrust). The mission duration is around 16000 seconds, divided into 486 points, so each step is around 32 seconds. At each step time, a flight Mach number, altitude and required thrust is given, it is possible to calculate the engine thrust from off-design tuning the throttle, to reach required thrust with a residual less 10 N. The inlet temperature is chosen as throttle parameters, varying it until convergence with a step of 2 Kelvin. Additionally, Fig.1 reports the output of engine/mission analysis. It is also possible to consider the installation losses due to nacelles.

However simplified model in this paper is adopted for the inlet (Eq. 1) and an average value of 0.03 of uninstalled thrust for the nozzle.

$$T = F - \phi_{inlet} \cdot F - \phi_{nozzle} \cdot F \approx 0.95 \cdot F \quad (1)$$

It is possible to summarize the uninstalled thrust calculations using off-design relationship, reported in the following equation (Eq.2):

$$F = F(M_0(t_k), Alt(t_k), \tau(t_k)) \quad (2)$$

Known the installed thrust, it is possible to calculate the installed thrust fuel consumption directly, using Eq. 3:

$$TSFC = \frac{\dot{m}_f}{T} \quad (3)$$

Mass fuel rate \dot{m}_f is computed from off-design algorithm using Newton-Raphson method to solve non-linear system of equations. TSFC varies during the mission and the thrust fuel consumption during mission profile is known at each point, so it is possible to optimize the engine achieving the fuel consumed reduction, changing the on-design engine parameters such as by-pass (BPR), overall pressure ratio (OPR) and fan pressure ratio (FPR). For on-design inlet turbine temperature, it is possible to consider the level of technology of the evaluated engine, assign the desired value.

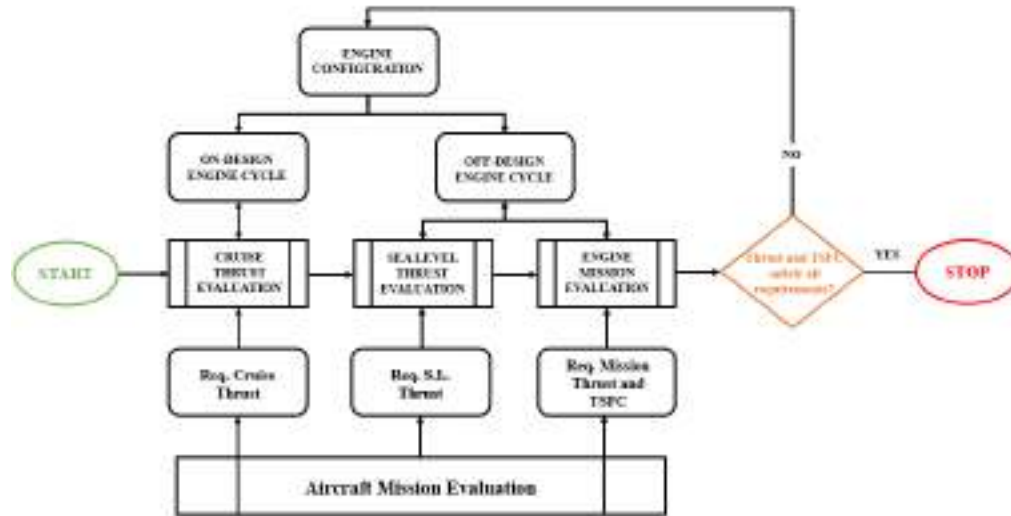


Figure 1. Methodology workflow

Results

The methodology previously described has been used to optimize a turbofan engine for supersonic low-boom jet. Letter B indicates the by-pass ratio and letter O the engine OPR. The compression ratio of the fan is calculated so that the ratio of total pressures inside the mixer is equal to 1 [4]. It is assumed that the power and flow rate spills to the engine to be zero according to a technological level equal to 4 [6] as the efficiencies of the various components that make it up. The starting engine has a bypass ratio of 0.20, and an OPR of 20 (TURB MIX B020-O20). The engine delivers sufficient thrust throughout the mission while consuming about 11121.40 kg of fuel. An attempt can be made to increase the bypass ratio in order to reduce fuel consumption. It is observed that excessive increase in the bypass ratio (0.600) results in insufficient thrust output from the engine. Consequently, the bypass ratio is adjusted to 0.400, and the process is iterated. As can be seen in Table 3, there is a reduction in engine consumption. Another way to reduce the TSFC of the engine is to increase the total compression ratio of the engine, up to a limit value equal to 30.

Table 3. Engine fuel used.

	Single Engine	Two Engine	[%] of fuel saved
TURB MIX B020-O20	11121.40 kg	22242.79 kg	0%
TURB MIX B040-O20	8919.91 kg	17839.81 kg	-20%
TURB MIX B040-O24	9036.41 kg	18072.83 kg	-19%
TURB MIX B040-O26	8625.68 kg	17251.36 kg	-22%

Keeping the engine by-pass constant, we can reach up to 26. Note that the TURB configuration MIX B040 O24 has higher fuel consumption than TURB MIX B040 O24. The explanation for

these counterintuitive results lies in the numerical error related to the throttle setting during the mission. Fig. 2 and 3 show the fuel flow rate and TSFC values of the four engines.

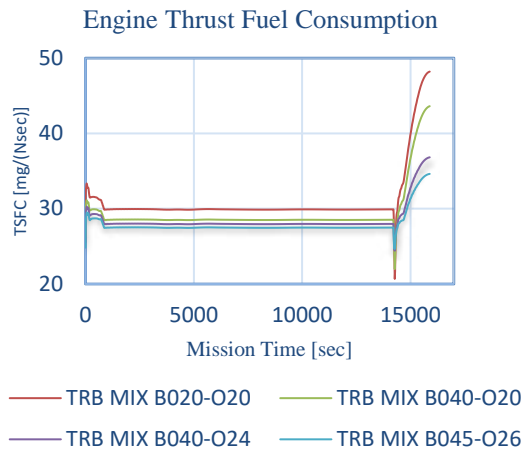


Figure 2: Engine TSFC

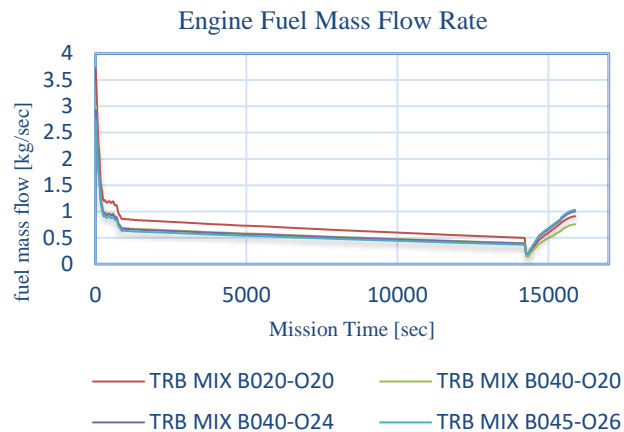


Figure 3: Fuel Mass Flow Rate

Conclusions

The method presented here calculates the performance of a mixed flow turbofan engine for a Mach 1.5 low boom supersonic aircraft, supporting the activities of the MORE&LESS project. Simple equations implemented in MATLAB were used for on-design and off-design thermodynamic cycle calculations. It was found that the model has limitations in throttle adjustment but can still yield results in agreement with literature using minimal input. The method is suitable for preliminary sizing in early project phases, with potential for further improvement in component mapping, throttle adjustment, and emissions modeling.

References

- [1] Aria Tahmasebi, Linköping. (n.d.). *Turbofan Engine Modeling - For the The fighter Aircraft of The Future*. Aeronautical Engineering Spring 2022.
- [2] Debiassi, M. (2003). Conceptual Development of Quiet Turbofan Engines for Supersonic Aircraft. *Journal of Propulsion and Power*.
- [3] Fronseca, V. F., & Lacava, R. F. (2018). Turbofan engine performance optimization on aircraft cruise thrust level. *Journal of the brazilian Society of Mechanical Sciences and Engineering*.
- [4] J. Mattingly and W. Heiser United States Air Force Academy, Colaro Springs. (1986). Performance Estimation of the Mixed Flow, Afterburning, Cooled, Two-spool Turbofan Engine with Bleed and Power Extraction, 1986. AIAA. <https://doi.org/10.2514/6.1986-1757>
- [5] Mattingly, J. D., & Jr., J. D. (1996). *Elements of Turbine Propulsion*. McGraw-Hill Series in Aeronautical and Aerospace Engineering.
- [6] Mattingly, J. D., Heiser, W. H., & Pratt, D. T. (2002). *Aircraft Engine Design Second Edition*. AIAA Education Series. <https://doi.org/10.2514/4.861444>
- [7] Melker Nordqvist, J. k. (2017). Conceptual Design of a Turbofan Engine for Supersonic Business Jet (ISABE-2021-22635).

Numerical and experimental studies on BLI propulsor architectures

A. Battiston^{1*}, A. Magrini^{1,2}, R. Ponza¹, E. Benini², J. Alderman³

¹HIT09 S.r.l., Padova (Italy)

²University of Padova, Padova (Italy)

³Aircraft Research Association ARA, Bedford (United Kingdom)

Keywords: Boundary Layer Ingestion, Jet Propulsion, Aerodynamics, Optimization, Computational Fluid Dynamics

Abstract. An increasing awareness about the impact of civil air transportation emissions is currently driving a low-carbon technology transition, towards more sustainable propulsion strategies. Boundary layer ingesting systems are one of the most promising solutions, as a closer integration between fuselage and propulsors is considered a key in the achievement of more sustainable architectures. Such architecture is characterized by a high level of integration between the airframe and propulsors, making the design process become a major challenge. The present work deals with a complete CFD based design and optimization of a propulsive fuselage concept, both in terms of airframe shape and fan design.

Introduction

The present work deals with the activities carried out in the Clean Sky 2 project SUBLIME. The aim of this project was to advance the state of art in BLI studies by means of wind tunnel activities supported by high fidelity CFD simulations to consistently predict the behavior of BLI architectures that minimize inlet flow distortion and maximize the power saving. The design activity has been separately carried out for the wind tunnel test model (WTT) – subjected to geometrical constraints – and an unconstrained full scale (FS) model, using for both cases a momentum-based approach for the definition of a proper performance metric, a surrogate of the propulsive power defined starting from the aircraft net assembly force (NAF): starting from the Net Assembly Force, a surrogate of the net propulsive thrust is introduced by subtracting to the NAF a reference airframe drag:

$$\Delta\text{NAF} = \text{NAF} - D_{\text{ref}} \quad (1)$$

ΔNAF takes into account the installation effects of the BLI nacelle and the variations in the fuselage shape with reference to a non-BLI configuration. The surrogate of the propulsive efficiency is then defined as:

$$\eta_{\Delta\text{NAF}} = \frac{-\Delta\text{NAF} V_{\infty}}{W_{\text{fan}}} \quad (2)$$

This performance metric has been used during the CFD-based design optimization of the propulsors. For both the WTT and the FS cases, a sequential approach has been followed : (a) geometric parametrization of the propulsor and its connection to the airframe ; (b) design space investigation aimed at determining the most influential design variables and the research space ; (c) shape optimization carried out using GeDEA-II[2-8], a proprietary genetic algorithm. A CFD approach has been considered at each step for the BLI propulsor performance evaluation.

BLI360 Design Optimization

The BLI360 design has been carried out for both the WTT and FS cases. In particular, the WTT configuration was subject to a high degree of geometrical constraints, thus reducing the design variables space and therefore limiting the optimization process. As stated in the previous section,

the design process followed a similar approach for each case, starting with a 2D axisymmetric design space investigation. The results of the WTT design space investigation suggested that geometries with low hub radii and short nacelles feature higher values of the ΔNAF efficiency. Furthermore, this metric has a maximum for a certain range of fan pressure ratio, between 1.3 and 1.5, as seen in Fig. 1. The FS Design of Experiments led to an analogue result.

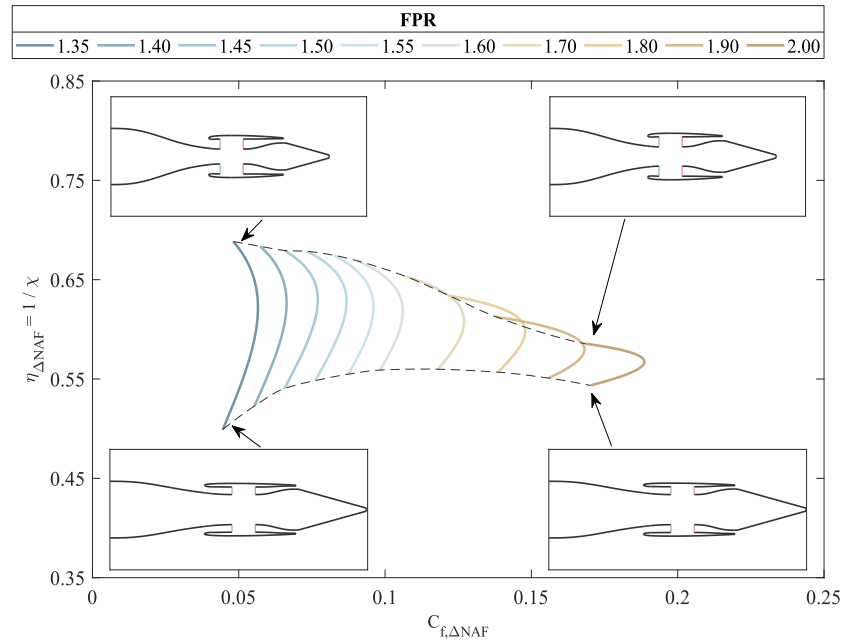


Figure 1: WTT design space investigation results.

A 2D optimization has been conducted to obtain a starting geometry for the 3D design. The objective was the maximization of the ΔNAF efficiency for an arbitrary set of NAF values. The three-dimensional design has therefore been set up by considering three different azimuth profiles of the propulsor: such profiles have been parametrized in terms of highlight height and axial displacement of the cowl maximum radius point (points “A”). Furthermore, interpolation laws between the highlight points and the points “A” of each profile have been defined. Given the high set of constraints of the WTT model, a design space investigation between the design variables defining the interpolation laws and profiles shapes has been conducted, leading to a population of individual with slight variations in terms of performance. Being the FS model geometrically unconstrained, an optimization has been produced. Fig. 2 shows the optimization results in the objectives space. The lack of a Pareto front has been justified by having fixed the fan pressure ratio and the nozzle contraction ratio to the 2D optimum values. The previous design space investigations suggested that these parameters were the main performance drivers. Therefore, any increase in the efficiency is due to a decrease in the drag-components of the axial force.

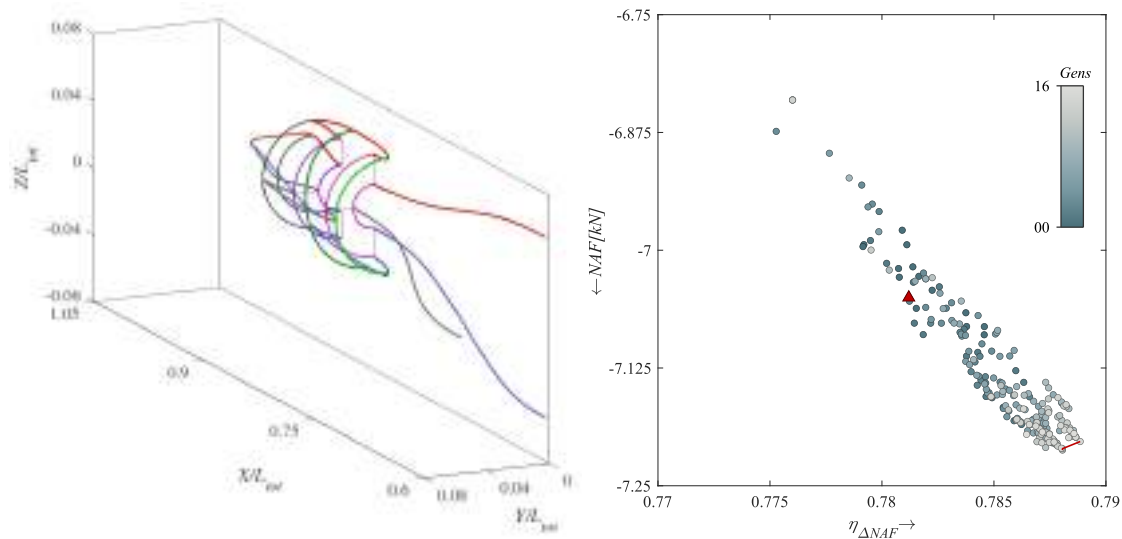


Figure 2: BLI360 FS Model Parametrization and Optimization Results.

SUBLIME Experimental campaigns

The SUBLIME project involved two wind tunnel test campaigns. The first was un-powered where three main configurations were tested which included a reference (without a propulsor), BLI360 and BLI180 boundary layer ingesting propulsor configurations which included exhaust plug changes for intake mass flow variation. The second test campaign concerned only the BLI360 configuration but the nacelle pressurized with an ejector system to simulate the exhaust flow. The test campaigns were carried out in the 9'x8' ARA Transonic wind tunnel at Mach = 0.2 to 0.8 with variation in α and β . Figure 3 shows the model in the wind tunnel & with center cover removed showing the high pressure air manifold for the ejector.

The model instrumentation included a rear fuselage balance, fuselage static pressures and provision for boundary layer rakes. The configurations with propulsors were equipped with AIP rakes for assessment of intake mass flow & distortion characteristics. The wake of the model was measured via a motorized traversing rake system mounted between the support booms to provide high-resolution wake plane data for all configurations.



Figure 3: SUBLIME BLI360 configuration in wind tunnel

Acknowledgments

This study is financed by the Clean Sky 2 project SUBLIME (Supporting Understanding of Boundary Layer Ingestion Model Experiment). The project has received funding from the

European Union's Horizon 2020 research and innovation program under grant agreement number 864803.

References

- [1] Lee, D., Fahey, D., Skowron, A., Allen, M., Burkhardt, U., Chen, Q., Doherty, S., Freeman, S., Forster, P., Fuglestedt, J., Gettelman, A., De León, R., Lim, L., Lund, M., Millar, R., Owen, B., Penner, J., Pitari, G., Prather, M., Sausen, R., and Wilcox, L., "The contribution of global aviation to anthropogenic climate forcing for 2000 to 2018," *Atmospheric Environment*, Vol. 244, 2021, p. 117834. <https://doi.org/10.1016/j.atmosenv.2020.117834>
- [2] Toffolo, A., and Benini, E., "Genetic Diversity as an Objective in Multi-Objective Evolutionary Algorithms," *Evol. Comput.*, Vol. 11, No. 2, 2003, p. 151–167. <https://doi.org/10.1162/106365603766646816>
- [3] Ronco, C., and Benini, E., "GeDEA-II: A Simplex Crossover Based Evolutionary Algorithm Including the Genetic Diversity as Objective," *Applied Soft Computing*, Vol. 13, 2013, pp. 2104–2123. <https://doi.org/10.1016/j.asoc.2012.11.003>
- [4] Toffolo, A., and Benini, E., "A new pareto-like evaluation method for finding multiple global optima in evolutionary algorithms," *Late Breaking Papers at the 2000 Genetic and Evolutionary Computation Conference*, 2000, pp. 405–410.
- [5] Comis Da Ronco, C., Ponza, R., and Benini, E., "Aerodynamic shape optimization of aircraft components using an advanced multi-objective evolutionary approach," *Computer Methods in Applied Mechanics and Engineering*, Vol. 285, 2015, pp. 255–290. <https://doi.org/10.1016/j.cma.2014.10.024>
- [6] Benini, E., Ronco, C., and Ponza, R., "Aerodynamic Shape Optimization in Aeronautics: A Fast and Effective Multi-Objective Approach," *Archives of Computational Methods in Engineering*, Vol. 21, 2014, pp. 189–271. <https://doi.org/10.1007/s11831-014-9123-y>
- [7] Massaro, A., and Benini, E., "A Surrogate-Assisted Evolutionary Algorithm Based on the Genetic Diversity Objective," *Applied Soft Computing*, Vol. 36, 2015, pp. 87–100. <https://doi.org/10.1016/j.asoc.2015.06.026>
- [8] Benini, E., Venturelli, G., and Łaniewski, W., "Comparison between pure and surrogate assisted evolutionary algorithms for multiobjective optimization," *Front. Artif. Intell. Appl.*, Vol. 281, 2016, pp. 229–242.

Aeronautical Systems

Neural networks for the identification of degraded components of aircraft fuel quantity system

Rosario Arcuri^{1,a *}, Roberta Masciullo^{2,b} and Roberto Bertola^{3,c}

¹Aircraft Technologies and Systems, AT&S Virtual Engineering, Leonardo Aircraft Division, Corso Francia 426, 10146, Turin (TO), Italy

²Aircraft Systems, Hydraulic & Fuel System, Leonardo Aircraft Division, Corso Francia 426, 10146, Turin (TO), Italy

³Aircraft Systems, Eurofighter Project Integrator, Leonardo Aircraft Division, Corso Francia 426, 10146, Turin (TO), Italy

^arosario.arcuri@leonardo.com, ^broberta.masciullo@leonardo.com,
^croberto.bertola@leonardo.com

Keywords: Aircraft Systems, Fuel system, Fuel Gauging System, Machine Learning

Abstract. The physical and software architecture design of the fuel system of high-performance aircrafts is very complex and represents a challenging topic for aeronautic engineers. Among the main functionalities, there is the calculation of the on board fuel quantity, consisting in data computed by the fuel gauging sub-system, shown to the pilot on the cockpit display and used by the flight control system for aircraft controllability. Due to the large number of sensors and to a strongly ramified calculation code, faults and performance degradation of components, are difficult to be detected/isolated, since the operation would require an invasive investigation on the aircraft. To reduce the impact of the fault detection and isolation process in terms of time and costs, a digital twin of the fuel system has been developed and coupled with a condition-monitoring algorithm based on machine-learning methods. It is thus possible to quickly replicate the mission profiles during which the faults can occur, to calculate the residual fuel mass in parallel with the fuel computer and to precisely identify which component caused the system failure. A neural network, trained on experimental flight data, has been developed to provide reliable data. Once validated, the neural network is coupled with a 0D model that simulates the movement of the fuel inside the tank. In this way, it is possible to obtain the mass of fuel, simulating any flight mission profile. This approach optimizes the analysis of system malfunctions in terms of time and costs, highlighting unexpected mass values, otherwise undetectable. The reliability of the neural network can clearly be increased by training the algorithm with additional flight data, which can be derived from experimental or virtual flights simulated using the 0D model. The versatility of this process makes it applicable for different aircrafts as well as for further developments.

Introduction

During last years, more and more studies and applications are focusing on Artificial Intelligence (AI). AI allows to solve complex problems by processing large amounts of data. In industrial context, investing in the development of new products that use artificial intelligence recommends optimizing time/costs thanks to its versatility and taking advantage of predictive analysis with autonomous machine learning [1,2].

In particular, in the aeronautical industry, AI, supported by digital models, can be a valid support in predicting behavior problems from complex aircraft systems which are constituted of different subsystems with dedicated functionality. With data acquired during the operational life of the aircraft, it is possible to train a machine learning algorithm for debugging failures that have occurred on one or more functionalities, or for predicting new ones. In this context, the digital twin

of the aircraft can be a valid support for testing the system recursively, avoiding experimental tests. The knowledge enhanced with this type of activity would allow the deploy of more accurate future system already in the design phase.

This paper presents the application of machine learning, supported by a digital twin, for the identification of the degradation of the fuel gauging system components. For this purpose, two models have been developed that can run alone or interact with each other:

1. Behavioral System Model: tank volume discretization in AMESsim starting from 3D CAD data. The model describes the whole tank geometry and connect each tank compartment domain with the respective rib and spar holes. Imposing the motion due to the aircraft manoeuvre, it is possible to simulate the fuel dynamics inside the tank. Furthermore, the engine feeding, refueling, defueling and venting subsystem has been modelled.
2. Neural Network (NN) for Fuel Gauging: Machine-learning based model developed in Matlab/Simulink environment, which, starting from probes and load factors data, determines the total quantity of fuel. This model exploits the Neural Networks capability to interpolate and extrapolate complex multi-dimension data with very high accuracy without the use of fuel gauging design algorithm.

Fuel Gauging System

The main function of fuel management and gauging subsystem is to provide an accurate measure of on-board fuel quantity [3]. The probes and compensators of gauging system relate to fuel computer, that elaborate the signals derived by gauging component and calculate total fuel mass and aircraft lateral and longitudinal CG position. The fuel tanks quantity data are displayed on cockpit to be available for pilot during flight and are used by the flight control system for aircraft controllability.

Fuel System Behavioral Model

This kind of model is necessary to be used to train a neural network by replacing data retrieved from experimental flights, allowing save time/cost to run tests on the system that would otherwise not be possible in terms of number and variety.

The model has been developed in two phases: the first is the extraction of geometry from CAD data of fuel tank in Catia V5 and then 1D sketching in Simcenter AMESim 2021.1. The CAD contains details (presence of flanges or grooves) and elements (presence of rivets, gaskets) which are not of interest for this application. For this reason, each compartment within the tank has been approximated as a closed cuboid following ribs, spars, top surface and bottom surface of the tank. The tank compartments geometry has been discretized through Amesim Aircraft Fuel System library, and then the whole tank reconstructed with holes, pumps and probes using Amesim 1D sketching (Fig. 1). The model has been validated by matching flight tests: probe signals and fuel mass outputs by Amesim model has been correlated with the same data available from flight recorder, refining the simplifications made on tank geometry. This model can be considered the digital twin of fuel system: it makes possible to simulate the behavior of the fuel inside the tank and thus the center of gravity displacement used by the flight control system for aircraft controllability. In particular, it is possible to have as output the wetted height of fuel probes starting from aircraft load factors and initial fuel quantity. These data can be used to monitor life cycle of the probes and their eventual degradation comparing simulation and real flights data.

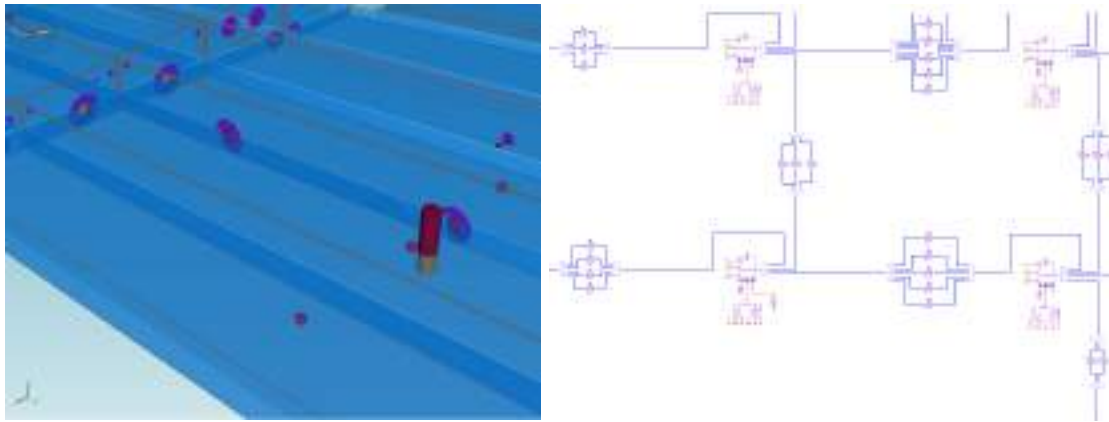


Fig. 1 – AMESim model

NN for Fuel Gauging

For the development of the NN it is necessary to have a training dataset correlating NN inputs with NN outputs that must be as large as possible. This approach is useful when one or more output variables depend on several input variables: in this case it is not always easy or possible to find an analytical correlation using more traditional methods. The resulting model will be a black box with the possibility of being stimulated in different ways.

In this application the main goal of the model is to correlate the signals of the fuel probes and aircraft load factors with the quantity of fuel inside the tank. This correlation can derive either from experimental flights or from virtual flights simulated using the digital twin model, either way the reliability of the neural network increases automatically by increasing the number of flight data provided to the algorithm. Different NN configurations have been studied: the most performant NN as trade-off between accuracy and training time required, resulted in a two-layer feedforward network with sigmoid hidden neurons and linear output neuron exploited with Bayesian regularization training algorithm.

The main application of this NN is the investigation of degraded component of fuel system: a test has been reported in Fig. 2 and Fig. 3. The signal supplied by a specific probe during the test flight is taken, and in one case it is fictitiously amplified (Test #1) and in the other fictitiously reduced (Test #2) for a limited amount of time, as shown in Fig. 2. This determines an altered trend of the computed mass of fuel contained in the tank, clearly departing from the actual trend. In particular, in Fig. 3 it is possible to observe that an amplification on the signal of this specific probe determines a reduction (almost a rigid translation) of fuel; opposite effect on the total mass for a reduction of the signal. This is an expected trend: indeed, the relationship between probe output signal and fuel mass is not univocal, each probe concurs with different weight to fuel quantity computation. Using the described NN algorithm, it is possible to identify which probe is degraded comparing NN fuel mass data with flight fuel quantity.

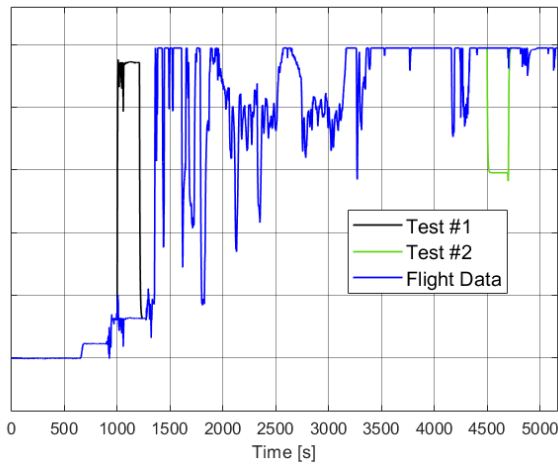


Fig. 2 - Probe Signal Output

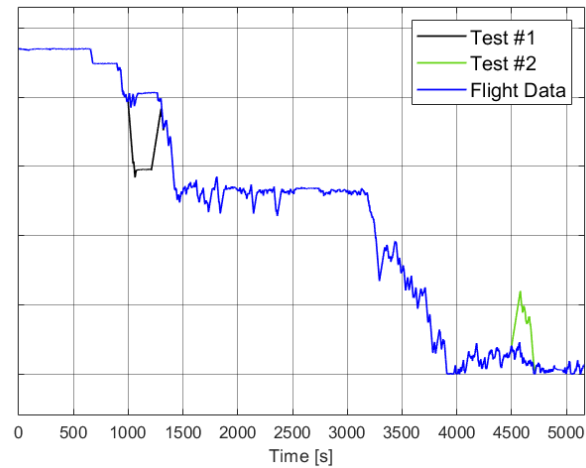


Fig. 3 - Total Fuel Mass

Conclusion

The paper presents the modelling activity carried out for on-service aircraft fuel system: a digital twin has been developed coupled with a machine learning algorithm. The results provide high accuracy with respect to flight test data, by permitting to predict faults and performance degradations of fuel system components with a robust approach as well as by avoiding invasive investigation of the aircraft. Therefore, this approach, highlighting unexpected mass values, optimizes in terms of time and costs the analysis of system component malfunction cases which would otherwise be more time demanding and invasive. The generality of this process makes it applicable for different on-service aircraft as well as for further developments.

References

- [1] G. Silvestri, F. Bini Verona, M. Innocenti, M. Napolitano, Fault detection using neural networks, IEEE World Congress on Computational Intelligence, 1994.
<https://doi.org/10.1109/ICNN.1994.374815>
- [2] M. T. Hagan, H. B. Demuth, M. Hudson Beale, O. De Jesus, Neuron Model and Networks Architectures, in "Neural Network Design", 2nd Edition.
- [3] R. Langton, C. Clark, M. Hewitt, L. Richards, Aircraft Fuel Systems, United Kingdom, 2009.
<https://doi.org/10.2514/4.479632>

Hardware-in-the-loop validation of a sense and avoid system leveraging data fusion between radar and optical sensors for a mini UAV

Marco Fiorio^{1,a *}, Roberto Galatolo^{1,b} and Gianpietro Di Rito^{1,c}

¹Largo Lucio Lazzarino 2, 56122, Pisa, Italy

^amarco.fiorio@dici.unipi.it, ^broberto.galatolo@unipi.it, ^cgianpietro.di.rito@unipi.it

Keywords: Sense And Avoid, Unmanned Aerial Vehicles, Hardware in the Loop, Data Fusion

Abstract. The present work illustrates the results obtained at the conclusion of the three-year project TERSA (Tecnologie Elettriche e Radar per Sapr Autonomi), involving the aerospace section of the Dept. of Civil and Industrial Engineering (DICI) of the University of Pisa and its industrial partners. The project aimed at the design and development of a fully autonomous Sense and Avoid (SAA) prototype system, based on data fusion between optical and radar sensors data, for a tactical lightweight surveillance UAV (MTOW<25Kg). The problem of non-cooperative collision avoidance is well known in literature and is currently a central theme of investigation within the aeronautical industry, considering the growing UAV traffic and the consequent need to employ autonomous self-separation technologies in the market. Several past works have investigated the most varied solutions for the Sense problem utilizing optical, acoustic, electro-magnetic signals or a combination of the previous. Likewise, the Avoidance problem has been successfully tackled in literature by means of a wide variety of different approaches ranging from rule-based methods, strategies based on game theory, force field methods, optimization frameworks leveraging genetic algorithms and nonlinear programming techniques and geometric methods. Yet, to the knowledge of the authors, no previous work found in literature has successfully demonstrated and validated the real-time simultaneous interaction of both sense and avoid functionalities within a highly integrated simulation environment. The present work describes the implementation of a complex, nonlinear, simulation environment conceived in order to perform real-time, Hardware-in-the-Loop (HIL), testing of the effective cooperation between sense and the avoid algorithms constituting the core of the SAA system developed within the context of the project. The system effectiveness has been validated by means of complex dynamic simulations, comprising an accurate, fully nonlinear, flight mechanic model of the aircraft, a graphic rendering engine of the scene, proper video capture and transmission pipelines, computer vision algorithms and collision avoidance logics running on the target hardware (Nvidia Jetson Nano) and tailored noise resilient data fusion algorithms. Results show the effectiveness of the system in detecting impending collisions and performing last-resort resolution manoeuvres with high computational efficiency and update frequencies compatible with real world applications in Unmanned Aircraft Systems (UAS).

Introduction

Unmanned aircraft systems (UAS) undoubtedly represent the future of the aeronautic world. The growth in popularity of these highly autonomous aircraft system is driven by the numerous potential applications, their inherent flexibility, lower maintenance cost w.r.t to manned aircraft and the current general willingness to achieve a greener and more sustainable aviation industry. UAS, due to their inherent lower weights, represent indeed the ideal field of application to test innovative electric propulsion systems, characterized by lower emissions. Furthermore, the



disruptive military potential of UAS proved itself beyond any doubts in the ongoing Ukrainian conflict, where, for the first time in history, UAS and small drones have been massively used in order to carry out hundreds of thousands of sorties on both sides since the start of the hostilities. For civil applications however, the non-trivial problem of integrating autonomous aircraft systems into non segregated airspace still presents to date a combination of technical and regulatory challenges to solve. Under the general and widely accepted principles that a UAS shall comply with existing regulations and procedures, its operations shall not increase the risk to other users and its integration shall not force other users to carry additional equipment, the development of a suitable Sense and Avoid (SAA) is considered a fundamental milestone towards the future integration of UAS into non segregated airspaces. Said system, should allow the UAS to perceive and avoid obstacles as a human pilot does, effectively empowering the aircraft with separation provision and collision avoidance capabilities. When it comes to the physical implementation of a SAA system, taking into account the dimensional and ponderal constraints of mini-UAVs which often hinder the applicability of more conventional systems (such as ADB-S or TCAS), multisensory architectures seem to be the most prominent solution widely investigated in literature. In particular, SAA system based on data fusion between RADAR and optical sensors have been the subject of several studies [1, 2, 3] which have outlined the benefits of a solution that allows to compensate for the shortcomings of each sensor type, reducing noise and increasing at the same time system robustness and accuracy. During the design phase of such a complex system, simulation models are helpful to validate system requirements and predict system response before actual flight tests can take place. Unfortunately, the simulation of the interaction between the avoidance and the sensing algorithms of a multisensory SAA system is no simple matter. The nontrivial dependency between the source data fed as input to the sensing algorithms (optical data from the camera and range information from the radar) and the attitude and position states of the aircraft (which in turn depend on the output of the avoidance algorithms) give rise to an interconnected problem, to address which, a dedicated HIL simulation environment was developed in the laboratories of the aerospace section of the Dept. of Civil and Industrial Engineering of the University of Pisa. The present work shortly describes the architecture of the SAA system developed within the context of TERSA project and focuses on the description of the nonlinear, HIL, simulation framework specifically created to test the effectiveness of the system utilizing an accurate dynamic model of the aircraft, with aerodynamic data provided by courtesy of Sky-Eye-Systems (SES). The last section briefly describes the simulation conducted and comments on the results.

System Overview

The SAA system has been developed following a multisensory architecture approach that leverages data fusion between a radar, which provides target distance and velocity reading, and Electro Optical (EO) sensor which allows for an accurate angular reconstruction of the target within the field of view of the camera [4, 5]. An High level diagram of the system architecture is presented in Fig. 1; Fig. 2 shows the prototype of the system built by the aerospace section of DICI, in partnership with Echoes [6] within the scope of TERSA project, that was successfully tested at the airfield of Tassignano (Lucca) using a Rapier X-25 aircraft as a moving target [7].

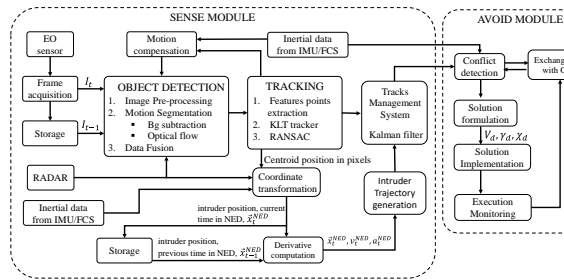


Fig. 1: SAA system architecture

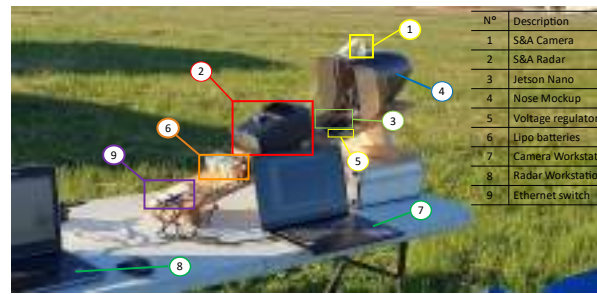


Fig. 2: SAA prototype

In a nutshell, both radar and the optical sensor, continuously scan the air space in front of the aircraft in search of a potential non cooperative intruder. The detection algorithm for the optical sensor is based on an implementation of Single Gaussian Models (SGM) background subtraction algorithm. Motion compensation schemes are employed in order to greatly reduce the noise caused by the ego motion of the camera. Specifically, at each iteration step, the background model is continuously warped (updated) according to an homography matrix which is iteratively obtained via a RANSAC procedure, where matching points between current frame and background model are fed as input. Such correspondences between points are computed by an efficient matching algorithm (i.e. pyramidal implementation of the KLT tracker), while feature points are extracted by means notorious Harris Corner algorithm. Various blobs obtained from the detection stage are then collapsed into single tracks using an implementation of Connected Component Analysis (CCA). Validation based on statistical criteria are then applied to the track readings, in order to make sure that such tracks exhibit a certain regularity in terms of position within the field of view (FOV) and dimension of the visual track itself to further suppress background noise. Once tracks are validated, the pixel position of the intruder aircraft centroid within the FOV is transformed into elevation and azimuth angles in a body fixed reference frame using geometric relationships involving intrinsic parameters of the camera. Such angles, together with the distance reading provided by the radar and the attitude, position/velocity states of the UAV are fed as input to an Extended Kalman Filter (EKF) which performs data fusion and outputs the position and velocity states of the target aircraft in an inertial reference system. These states in turn, constitutes the input to the avoidance routines which continuously check for impending violations of the self-separation condition. When a collision is predicted (meaning that at a certain future time the relative distance between UAV and intruder aircraft will be less than a certain safety threshold), a geometric conflict resolution approach based on the strategies discussed in [8, 9], transforms the dynamic problem into a relative static kinematic problem and computes the tangency solution (i.e. a trajectory which results in the UAV being tangent to the safety bubble at the point of closes approach). The system has been extensively tested in a simulation campaign detailed in the following sections.

Simulation Framework

Initially, a simplified simulation model was devised in order to test avoidance algorithms independently from computer vision part. A Simulink model has been created featuring a realistic 6 DOF, nonlinear, data base driven model of the reference UAV, where the aerodynamic database and the FCS laws has been provided by courtesy of SES. The model features an automatic trim routine leveraging gradient descent optimization, that computes the initial inputs in terms of control surface deflections and engine settings in order to trim the aircraft at various conditions. Avoidance algorithms have been implemented by means of tailored “m-functions”, together with the EKF and a waypoint follower block for the trajectory recovery after the end of the avoidance manoeuvre. The position states of the intruder aircraft are considered known in advance, albeit injected with gaussian noise in order to simulate sensor noise. System effectiveness has been tested for a variety of initial conditions in terms of relative position w.r.t to the intruder aircraft ($\Psi_0 =$

$0^\circ \div 45^\circ$) and intruder speed ($V_0^{Intr} = 22 \div 42 \text{ m/s}$), which is assumed to be constant during the simulation, see Fig. 3; the initial heading angle of the intruder aircraft Ψ_{Intr} is precomputed taking into account each aircraft relative initial position and speed magnitude to ensure that a collision will always take place. The avoidance manoeuvre is accomplished by means of a coordinated turn in the horizontal plane. The effectiveness of the manoeuvre is evaluated according to a series of performance metrics (Fig. 4) together with the respect of safe envelope boundaries in terms of load factor limits, maximum bank angle and control saturations.

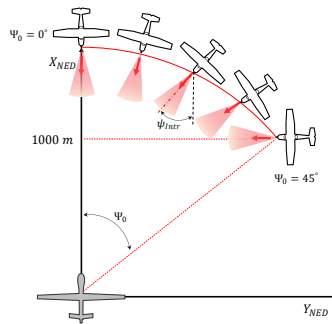


Fig. 3: Simulation initial conditions

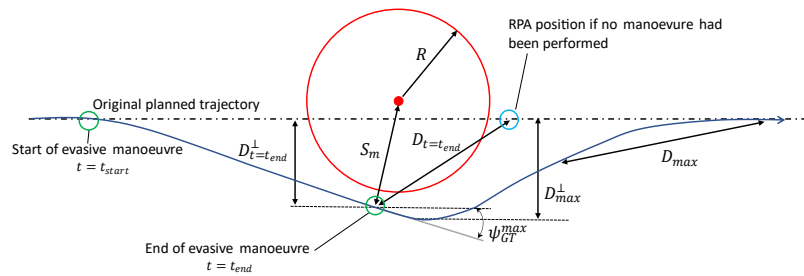


Fig. 4: Evaluation metrics

After the verification of the correct behaviour of the avoidance algorithms and the correct operation of the EKF, more complex simulations have been conducted inserting computer vision algorithms in the close loop, with the aim of validating the simultaneous interaction between sense and avoid modules. This time, intruder aircraft states are no longer assumed known beforehand but only the relative distance is known in a body fixed reference frame. Once again, this measure is injected with gaussian noise. Position states are reconstructed in real time based on the output of the computer vision algorithms that process a realistic rendering of the scene produced by the Open-source flight simulator *Flight Gear* (FG).

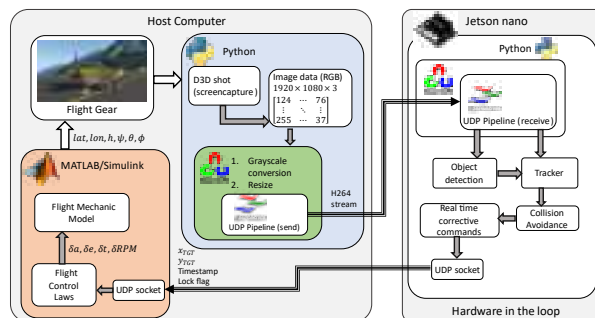


Fig. 5: Scheme of the HIL simulation framework



N°	Description
1	Workstation
2	Jetson nano
3	Ethernet switch
4	KVM switch
5	Jetson Display
6	Workstation 2 nd Display.

Fig. 6: HIL Simulation setup of the SAA system

Basically, as shown in Fig. 5, the Simulink model outlined above, drives an instance of the FG software, running on the workstation which in turn generates a realistic 3D scene comprising accurate weather, lightning conditions, background settings etc. Being an open-source software, tailored modifications have been implemented in order to setup a camera view positioned in front of the aircraft (as to replicate the real EO sensor of the SAA system). Likewise, FG is also configured to display an intruder aircraft model, following a pre-cooked trajectory. Proper synchronization functions make sure that both the Simulink model, the intruder aircraft and FG rendering output are in sync. The workstation screen where FG is opened is captured at a high rate by a dedicated Python module; the obtained frames are then packed into a video stream leveraging the Gstreamer framework and sent to the Video Processing Unit (VPU), Jetson Nano embedded

platform, where, thanks to extensive optimisation efforts in the design of the algorithms, object detection and tracking algorithms run in real time ($\sim 25\text{Hz}$) together with avoidance routines. When a collision is predicted and a real time corrective manoeuvre is computed, the prescribed heading angle is fed back in real time to the UAV's FCS in the Simulink model via a dedicated UDP port. This allows for the generation of a realistic synthetic imagery representative of the scene, which evolves according to the dynamic manoeuvre of the aircraft. The simulation setup implemented at the laboratories of the DICl is shown in Fig. 6.

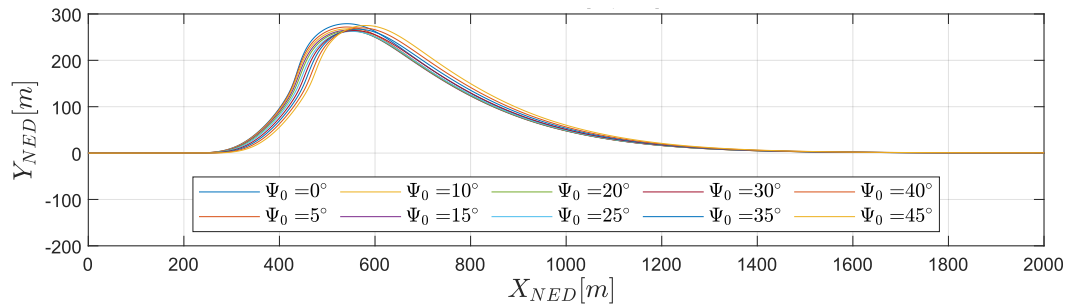


Fig. 7: Avoidance trajectory at various initial intruder positions

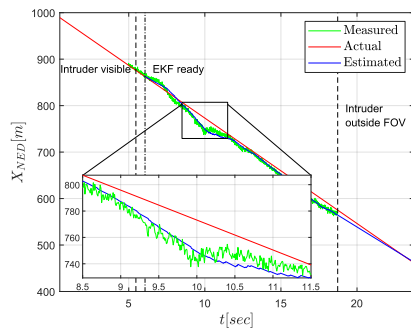


Fig. 8: Intruder position state X

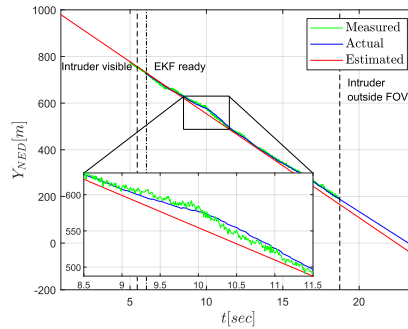


Fig. 9: Intruder position state Y

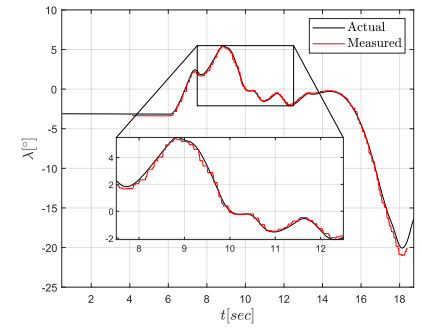


Fig. 10: Intruder elevation angle



Fig. 11: Rendering # 1



Fig. 12: Rendering # 2



Fig. 13: Rendering # 3

Simulation Results

Fig. 7 shows the evasive manoeuvre (seen from above) for various values of Ψ_0 for the highest intruder speed ($V_0^{Intr} = 42 \text{ m/s}$) obtained with the simplified simulation model. Fig. 8-9 instead show the position state X, Y of the intruder aircraft (Cessna 172p), reconstructed by the EKF in the complete simulation with the Jetson Nano as hardware in the loop (intruder approaching from port side, @ 52 m/s). Fig. 10 shows the intruder elevation angle reconstructed by the computer vision algorithms plotted against the actual one, while Fig. 11-13 depicts the actual rendering of the scene generated by FG. Plots of the performance parameters of the evasive manoeuvre are omitted for brevity. However, simulation have shown that the system satisfies the requirements for all the tested initial conditions, without invalidating the safe boundary limits. Minimum distance to the intruder is never violated and the evasive manoeuvre is conducted correctly.

Conclusions

The present work has illustrated the complex simulation environment implemented at the Fly-by-wire laboratories of the DICI of the University of Pisa, within the context of the TERSA project which has proved a crucial and invaluable tool for the preliminary validation of a multisensorial Sense and Avoid system. The framework has allowed the verification of the correct simultaneous interaction between avoid and sense algorithms as well as the verification of the requirements of the chosen hardware in terms of available computational power.

Funding & Acknowledgements

This research was co-funded by the Italian Government (Ministero delle Imprese e del Made in Italy, MIMIT) and by the Tuscany Regional Government, in the context of the R&D project “Tecnologie Elettriche e Radar per SAPR Autonomi (TERSA)”, Grant number: F/130088/01-05/X38.

The authors wish to thank Sky Eye Systems (Italy) for the support to the research activity and for providing the UAV aero-mechanical data and FCS laws that allowed the creation of an accurate dynamic simulation model.

References

- [1] G. Fasano, D. Accardo and A. Moccia, "Sense and Avoid for Unmanned Aircraft Systems," *IEEE A&E SYSTEM MAGAZINE*, pp. 82-110, November 2016.
<https://doi.org/10.1109/MAES.2016.160116>
- [2] G. Fasano, D. Accardo, A. E. Tirri and A. Moccia, "Radar/electro-optical data fusion for non-cooperative UAS sense and avoid," *Aerospace Science and Technology*, vol. 46, pp. 436-450, 2015. <https://doi.org/10.1016/j.ast.2015.08.010>
- [3] S. Ramasmy and R. sabatini, "A Unified Approach to Cooperative and Non-Cooperative Sense-and-Avoid," in *International Conference on Intelligent robots and Systems (IROS)*, Vancouver, BC, Canada, 2017., 2017.
- [4] M. Fiorio, R. Galatolo and G. D. Rito, "Sense and Avoid system for a mini UAV based on data fusion between electro-optical and radar sensors," in *AIDAA XVI International Congress*, Pisa, 2021.
- [5] M. Fiorio, R. Galatolo and G. D. Rito, "Object Detection and Tracking Algorithms Based on KLT Feature Tracker for a Sense and Avoid System," in *AIDAA XXVI International Congress*, Pisa, 2021.
- [6] "Echoes Tech," 2022. [Online]. Available: <https://www.echoes-tech.it/>
- [7] "Sky Eye Systems," [Online]. Available: <https://www.skyeyesystems.it/>
- [8] C. Carbone, U. Ciniglio, F. Corrado and S. Luongo, "A Novel 3D Geometric Algorithm for Aircraft Autonomous Collision Avoidance," in *Proceedings of the 45th IEEE Conference on Decision and Control*, San Diego, CA, USA, 2006.
<https://doi.org/10.1109/CDC.2006.376742>
- [9] K. D. Bilimora, "A GEometric Optimization Approach to Aircraft Conflict Resolution," in *AIAA Guidance, Navigation, and Control Conference and Exhibit*, Denver, CO, USA, 2000.

A parametric model for thermal management system for more electric and hybrid aircraft

Sofia Caggese^{1,a*}, Marco Fioriti^{1,b} and Flavio Di Fede^{2,c}

¹Department of Mechanical and Aerospace Engineering, Politecnico di Torino, C.so Duca degli Abruzzi n.24, Turin, Italy

²Leonardo Labs, Future Aircraft Technologies, Leonardo S.p.A., c.so Castelfidardo 22, 10138 Turin, Italy

^asofia.caggese@polito.it, ^bmarco.fioriti@polito.it, ^cflavio.difede.ext@leonardo.com

Keywords: Thermal Management System, Hybrid Aircraft, Liquid-to-Liquid Heat Exchanger, Nanofluid

Abstract. In the last decade, the hybrid and electric propulsive systems have been gaining increasing interest to cut down greenhouse gas emissions and thus reduce the environment impact of the aerospace sector. The paper reports the development of a parametric model to design and simulate the Thermal Management System (TMS) of an hybrid electric regional aircraft. Considering the need for a compact design and avoiding the generation of additional drag, a liquid-to-liquid offset strip fin surface heat exchanger is selected. Analysis and modelling of the system are performed for both traditional and innovative coolant, namely, as nanofluids. Five different thermal load conditions are analyzed, which correspond to five different levels of hybridization defined in terms of reduction of CO₂ emission. The most demanding one entails a reduction up to 50% of CO₂ and a thermal load of 67.2 kW to be dissipated. The paper also aims to investigate the most challenging conditions for TMS design and whether the suitability of nanofluids as superior heat carriers. In fact, using nanofluids it is possible to reduce the size of heat exchanger, thanks to the higher thermal conductivity compared to conventional coolant.

Introduction

The primary concerns for climate change are emission of CO₂, NO_x and non-volatile particulate matter (nvPM). In 1983 ICAO Council established the Committee on Aviation Environmental Protection (CAEP), as technical assistant to formulate new strategies and to adopt new Standards and Recommended Practices (SARPs) related to international civil aviation noise and emissions [1]. In 2019, the European Parliament declared a climate emergency and established the European Green Deal. The main goals are to reduce emissions by 55% by 2030 and to achieve net carbon neutrality in Europe by 2050, in order to limit global warming below the 1,5 °C rise [2]. The aviation target is to halve emissions from 2005 levels by 2050. To reach this task new technologies and policies are improved. Electrified systems, biofuels, synfuels, hydrogen, fuel cells, electric motors and batteries are potential sustainable solutions[1]. One of the main challenges is the thermal power control and dissipation of new adopted propulsive system. The Thermal Management System (TMS) is the appropriate system to accomplish these tasks. The TMS acquires, through heat acquisition techniques, the generated thermal power from the heat sources and transfers it, through heat rejection mechanisms, to the terminal heat sinks. The new components needed to implement the electrified propulsion systems, such as the electric motor, the PEM fuel cell, and the battery, are sources of “low grade” heat [2]. For the traditional thermal engine, the heat load is higher than the new heat sources, due to the lower efficiency, but it is directly dissipated from combustion gases. Consequently, for traditional aircraft, little attention is paid to the TMS design. Therefore, the waste heat temperature of low-grade heat source is lower than traditional propulsive system. The absence of exhaust gases is a limitation for the new adopted



heat sources and the thermal load to dissipate could exceed one megawatt. Traditionally, aircraft TMS adopts ram air cooling system or liquid cooling system using water, oil or fuel. Heat exchanger is the major implemented device in both conventional and innovative propulsive system. Especially compact heat exchangers are used into aerospace applications [4]. The reference aircraft is a regional aircraft with parallel hybrid propulsion system [5].

Architecture and design

The devised concept features a liquid cooling system involving a coolant, such as water-ethylene glycol mixture, in the main loop, and fuel as the working fluid in the second loop. The main loop transfers the thermal load from the heat source to the liquid-to-liquid heat exchanger, while the second loop transfer it from the heat exchanger to the heat sink. Using fuel as the working fluid, wing fuel tanks are used as terminal heat sinks. The fuel is taken from the hub of the wing tanks and, after the heat exchange with the coolant, it is then returned to the tip of the wing tanks. A schema of TMS concept is reported in Fig. 1.

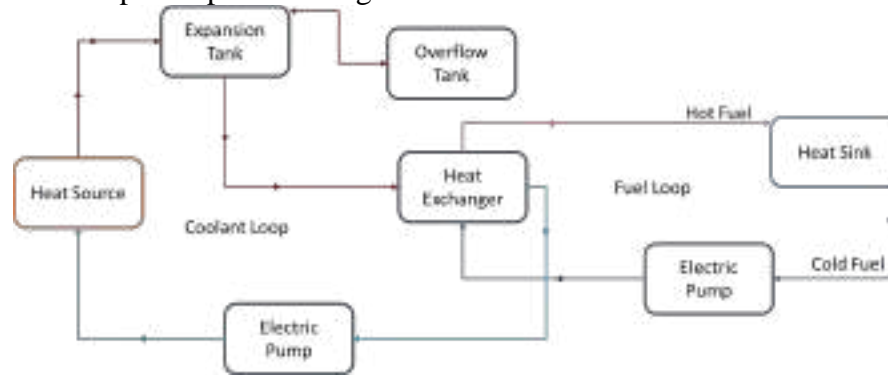


Fig. 1 – Simplified schema for architecture of liquid cooling system

The work aims to design a parametric model of a liquid-to-liquid heat exchanger and to integrate it into the TMS. The heat exchanger is a device that allow heat exchange between two fluids operating at different temperatures. The design differs according to the field of application. In the aerospace domain, the use of compact heat exchangers, characterized by small volumes due to lamellar surfaces that expand the heat exchange surface area, is favoured. The developed device is an offset strip fin surface heat exchanger, considering their typical compactness, with unmixed crossflow arrangement. Sizing is implemented through an iterative python code. At each iteration, the heat exchanger grows in the three dimensions to reach the size to satisfy the design temperature convergence. Type of internal geometry, types of fluids involved in, inlet temperature of both fluids and relative mass flow rates are input required by the parametric model. As output, the python script provides the spatial dimensions, effectiveness, volume and mass of the heat exchanger, core pressure drop, outlet temperature and regimes established of the two fluids involved, and also addresses the system electric consumption, distribution pipe's characteristics and overall TMS mass. The effectiveness-NTU method is used as design approach for heat exchanger. The model is based on the formulation presented by [4]. Effectiveness, ε , is defined as

$$\varepsilon = \frac{\dot{Q}}{\dot{Q}_{max}} = \frac{C_h(T_{h,i} - T_{h,o})}{C_{min}(T_{h,i} - T_{c,i})} = \frac{C_c(T_{c,o} - T_{c,i})}{C_{min}(T_{h,i} - T_{c,i})}, \quad (1)$$

where C_c and C_h are respectively the cold and hot stream heat capacity rates, $T_{h,i}$ and $T_{h,o}$ indicate inlet and outlet hot stream temperatures, $T_{c,i}$ and $T_{c,o}$ indicate inlet and outlet cold stream temperatures. Defining NTU, the number of thermal units, ε -NTU relationship (Eq. 2) can be used.

$$\varepsilon = f(NTU, C^*) = f\left(\frac{UA}{C_{min}}, \frac{C_{min}}{C_{max}}\right). \quad (2)$$

ε -NTU relationship differs for each configuration, for crossflow arrangement configuration is:

$$\varepsilon = 1 - \exp \left\{ \frac{NTU^{-0.22}}{C^*} [\exp(-C^*NTU^{0.78}) - 1] \right\}. \quad (3)$$

Test case

Analysis and modelling of the system are performed for the electric motor and the inverter as heat sources. The selected heat source sets the design temperature for coolant convergence loop. The outlet coolant temperature from the heat source is 90 °C and the inlet coolant temperature in the heat source is expected to reach 65 °C. The analyses are performed in hot day condition for both ground and ceiling conditions (FL250), considering both traditional and innovative coolant, respectively 40% water-ethylenic glycol mixture and nanofluids. Both heat source and heat exchanger are located into the engine nacelle, and the heat sinks are represented by wing tanks, so 80% of wingspan is considered as distance to be covered by fuel. The five test cases represent the requirements for five different levels of hybridization, corresponding to a progressive reduction in carbon dioxide emissions due to the increased propulsive power generated from electric motor at the expense of conventional propulsion. They are proposed to evaluate the operation of liquid cooling system with several levels of thermal load, as indicated by Table 1.

Table 1 – Test Case Input

Test case	ΔCO_2	Thermal power EM+PE [kW]		TMS coolant mass flow [kg/s]	
		Take Off	Ceiling	Take Off	Ceiling
Test case 1	-10%	14.3	14.3	0.136	0.136
Test case 2	-20%	28.3	28.3	0.270	0.270
Test case 3	-30%	41.2	41.2	0.393	0.393
Test case 4	-40%	54.2	54.2	0.517	0.517
Test case 5	-50%	67.2	67.2	0.641	0.641

Fig. 2 reports the sizing script outputs: ground condition in blue line, ceiling condition in green line. Each dot depicts a test case. The dimensioning condition is identified in Test case 5, -50% CO2 emission, in the ground condition.

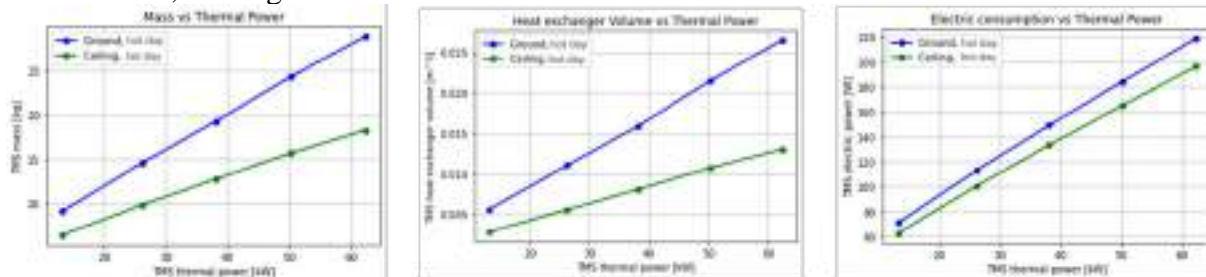


Fig. 2 – Test Case Output

The mass of heat exchanger is 6.6 kg, that is 22.7% of overall TMS weight, 28.9 kg and its volume is 0.026 m³. The electric consumption amounts to 219 W, distributed in 135 W required by coolant loop dedicated electric pump and 84 W required by fuel loop dedicated electric pump. Table 2 reports significant output of heat exchanger model for test case 5 at ground level.

Table 2 - Test Case 5 output: ground condition

Output Test Case 5 - ground					
Efficiency	[-]	0.450	Volume	[m³]	0.026
Pressure Drop - coolant	[Pa]	244.307	Length side 1	[m]	0.325
Pressure Drop - fuel	[Pa]	311.548	Length side 1	[m]	0.325
Weight	[kg]	6.56	Height	[m]	0.251

A sensitivity analysis is performed for three values of fuel mass flow rate, a design parameter. The increase in fuel flow rate achieves a reduction on heat exchanger mass of 15.8% and a 15.5% reduction on volume, but with an 11.4% increase on electric consumption. Despite the lower weight of the heat exchanger, due to the other components of the TMS, the TMS overall mass does not achieve the same benefit.

Nanofluids

Nanofluids are a new class of nanotechnology. Escalating interest of the last decade is based on the higher thermal conductivity compared to conventional coolant. They are engineered by suspending nanoparticles (1-100 nm) in a base fluid, such as water, oil, mixture of water and ethylenic glycol or traditional heat transfer fluids. The goal is to reach a significant improvement in thermal properties by a uniform and stable suspension of nanoparticles, thanks to a small concentration, less than 1% by volume. A lot of experiments are reported in the state of the art [5] of nanofluids coolant, with ceramic oxides nanoparticles, metallic carbides, metals, carbon nanotubes and others and for each of them experimental equations are presented. In this work, theoretical thermophysical equations are adopted, as defined in Chapter 5 of [5]. Thanks to 0.502% of Al_2O_3 , TMS obtains a mass reduction of 10% and a smaller heat exchanger. Different types of nanoparticles at different concentrations are tested. The best case resulted in a 12% overall weight loss and 15% heat exchanger volume reduction.

Conclusion

The developed parametric model provides the design of a liquid-to-liquid heat exchanger integrated into TMS concept. For the most demanding test case, over 67 kW to be dissipated, the overall TMS weight is 29 kg and the heat exchanger volume is 0.026 m^3 . The sensitivity analysis reports, by increasing the fuel flow rate, an increase in the electrical power required by the electric pumps, a marked reduction in the heat exchanger dimensions and a slight reduction of TMS mass. If the purpose of design is volume optimization, the increasing fuel flow rate is promising, without achieving significant mass benefits. The use of nanofluids offers a good potential, but presently, not so great as promise in state of the art. Further investigation is needed to better understand the interactions between nanoparticles and base fluids and to predict the actual behavior.

References

- [1] ICAO, 2019 Environmental Report, Aviation and Environment, [https://www.icao.int/environmental-protection/Documents/ICAO-ENV-Report2019-F1-WEB%20\(1\).pdf](https://www.icao.int/environmental-protection/Documents/ICAO-ENV-Report2019-F1-WEB%20(1).pdf)
- [2] <https://eur-lex.europa.eu/legal-content/EN/TXT/HTML/?uri=CELEX:52019DC0640>
- [3] A.S.J. van Heerden, D.M. Judt, S. Jafari, C.P. Lawson, T. Nikolaidis, D. Bosak, Aircraft thermal management: Practices, technology, system architectures, future challenges, and opportunities, (2021). <https://doi.org/10.1016/j.paerosci.2021.100767>
- [4] J. E. Hesselgreaves, R. Law, D. Reay, Compact Heat Exchangers. Selection, Design and Operation, 2nd ed., Elsevier Ltd, 2017. <https://doi.org/10.1016/B978-0-08-100305-3.00002-1>
- [5] <https://www.clean-aviation.eu/about-us/who-we-are>
- [6] S. K. Das, S. U. S. Choi, W. Yu, T. Pradeep, NANOFLUIDS, Science and technology, Wiley, 2008. <https://doi.org/10.1002/9780470180693>

Preliminary design of an electromechanical actuator for eVTOL aircrafts in an urban air mobility context

Roberto Guida^{1,a,*}, Antonio Carlo Bertolino^{1,b}, Andrea De Martin^{1,c},
Giovanni Jacazio^{1,d} and Massimo Sorli^{1,e}

¹Department of Mechanical and Aerospace Engineering, Politecnico di Torino, Corso Duca degli Abruzzi, 24, Torino, 10129, Piemonte, Italy

^aroberto.guida@polito.it, ^bantonio.bertolino@polito.it, ^candrea.demartin@polito.it,
^dgiovanni.jacazio@polito.it, ^emassimo.sorli@polito.it

Keywords: Preliminary Design, Preliminary Sizing, EMA, e VTOL, Urban Air Mobility

Abstract. Urban areas face issues like traffic congestion, noise, and pollution. In this context Urban Air Mobility (UAM) offers a solution by utilizing the urban airspace for transportation, in particular, the exploiting of Electric Vertical Take-Off and Landing (eVTOL) vehicles is promising in terms of noise and environmental pollution, despite challenges like safety issues and financial constraints. To overcome these issues, Prognostic and Health Management (PHM) plays a vital role in ensuring safety and reliability. The proposed case study focuses on a compact Electro-Mechanical Actuator (cEMA) for flap control surface. A preliminary design is proposed with the aim of reducing dimensions and weight while maintaining performance and reliability. This work represents one of the first steps in the creation of a digital twin for the design, sizing, and application of PHM logics.

Introduction

The issue of overcrowding in cities and the resulting environmental and noise pollution, has spurred the search for alternative mobility solutions. One potential solution is Urban Air Mobility (UAM), which aims to establish a safe, and sustainable air transportation system within cities [1]. UAM should be exploited for various purposes, including passenger transport, package delivery, and emergency services [2]. It is part of the broader concept of Advanced Air Mobility (AAM) [3], which encompasses emerging aviation markets. UAM primarily utilizes electrically powered Vertical Take-Off and Landing (VTOL) aircrafts. The development of all-electric aircraft with compact Electro-Mechanical Actuators (cEMAs) has been driven by the need to reduce environmental pollution in cities [4]. However, progress in UAM has been hindered by a few fatal accidents, noise restrictions, and financial challenges [5]. In this context, safety, airworthiness, propulsion efficiency, and performance are crucial aspects in UAM research [6]. A way to improve the safety and the reliability of these systems is the application of Prognostic and Health Management (PHM) techniques. About that the development of High-fidelity (HF) model allows the study of performance variations and the identification of potential defects to obtain the definition of a Digital Twin (DT) to be used as a virtual test bench of the real system.

Requirements of the cEMA

The first step in the cEMA design and sizing is the definition of the control surface chosen as case study and then the related specific requirements. Despite variations in configuration [7], eVTOL aircrafts share similar actuation systems. The case study chosen is the flap actuator responsible for the thrust vectoring in a tiltrotor aircraft.

Performance requirements. The steady-state performance requirements involve accuracy, resolution, and hysteresis. The first one must be achievable under all operating conditions including actuator faults that do not result in the complete system failure. In the present work, a



minimal accuracy equal to 0.3° is considered [8]. The resolution is due to the sensors system and must be smaller than the required accuracy to properly control the surface. The hysteresis represents the difference between the input command required for the two different directions moving of the surface to achieve the same angle movement. At a first approximation this requirement can be negligible and calculated after the overall EMA sizing. The dynamic performance requirements address the analysis of the actuator response to commands and disturbances in both time and frequency domains, and it aims at studying the stability, the tracking, the impedance, and the damping characteristics of the system. These requirements are mostly linked to the definition of the control algorithm and parameters. Another technical requirements regard the maximum load the servo actuator must bear: it depends on factors such as overall inertia, maximum external load, and friction losses. Finally, the maximum and effective strokes as well as the rated speed of the actuator need to be determined. For this application a minimum stroke of 90° is needed, in addition a minimum-security margin of about 20% in both directions is considered and the total operational actuator stroke shall be from -20° to 110° . The rated speed is defined for assuring that the actuator, without external load and with the power supply at the minimum guaranteed level, reaches its maximum stroke within a specified time. For this application a minimum speed has been set to $360^\circ/\text{s}$ [9,10].

Safety and reliability requirements. To define safety and reliability requirements, it is essential to determine the expected operational lifespan of the system. During this time the system should ensure the requirements without the need for structural component replacement. The flap actuator system reliability is commonly associated with the failure rate, which represents the frequency of failure occurring within a specific period of time. The loss of control, due to a single failure or combination of failures, shall be less than 1×10^{-6} per flight hour [11,12].

Proposed architecture design

To meet the demanding requirements of UAM EMAs in terms of compactness, simplex solutions often fall short of airworthiness standards. Previous literature has presented various fault-tolerant architectures based on redundancy for EMAs [13]. The conventional EMA architecture for flight control actuators is typically composed of an electric motor, power electronics and control electronics (including sensors), mechanical transmission (with gearboxes, reducers or ball screws), and fail-safe devices (e.g., clutches, brakes) [14].

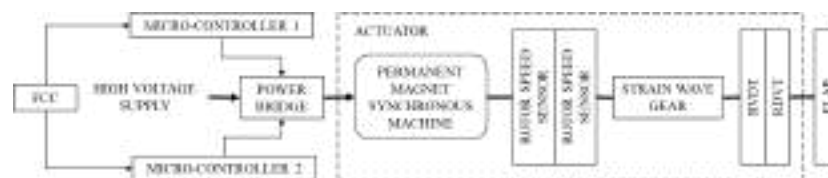


Figure 2. Proposed architecture.

In the case study, a compact rotary-output actuator architecture is chosen to fulfill the size and weight requirements for UAM applications. This architecture comprises a six-phase permanent magnet synchronous machine, fault-tolerant control electronics, a strain wave gear, and several sensors (Fig. 2).

Electric motor. In the aerospace industry, various types of electric motors have been considered for converting electrical energy into mechanical energy. The selection process involves evaluating factors such as losses, cooling, weight, volume, and other distinctive features, advantages, and disadvantages [11]. For aviation purposes, the chosen electric motor must exhibit thermal robustness and high efficiency to minimize power losses and associated cooling requirements. Four types of electric motors are considered: Permanent Magnet Synchronous Machine (PMSM), Electrically excited Synchronous Machine (ESM), Switched Reluctance Machine (SRM), and Induction Machine (IM). Among these options, the PMSM is identified as the most suitable for

Control electronics. The Electronic Control Unit (ECU) typically manages the position and speed control loops, while the current control is handled by the Motor Drive Electronics (MDE). To achieve the reliability requirements, a fault-tolerant architecture with two control channels is implemented. The architecture utilizes a dual-control/single-drive setup, and each control channel communicates with the Flight Control Computer (FCC) via separate lines.

The Preliminary System Safety Assessment (PSSA) is a top-down process that assigns reliability and safety requirements from systems to components. In Fig. 3 a preliminary example of a qualitative FTA for this specific case study is proposed [11,16,17].



Figure 3. Preliminary FTA of an EMA for eVTOL flap surface in an UAM context.

UAM offers a solution to novelty urban transport challenges and eVTOL vehicles show promise in reducing noise and environmental pollution. The presented case study focuses on a cEMA for flap surface. A preliminary design sizing approach is proposed to reduce dimensions and weight while maintaining performance and efficiency. This work represents a first step in the development of a digital twin, enabling design, sizing, and application of PHM for the cEMA.

This study was carried out within the MOST – Sustainable Mobility National Research Center and received funding from the European Union Next-GenerationEU (PIANO NAZIONALE DI RIPRESA E RESILIENZA (PNRR) – MISSIONE 4 COMPONENTE 2, INVESTIMENTO 1.4 – D.D. 1033 17/06/2022, CN00000023). This manuscript reflects only the authors' views and opinions, neither the European Union nor the European Commission can be considered responsible for them.

[1] “What is UAM.” <https://www.easa.europa.eu/en/what-is-uam>.

- [2] R. Goyal and A. Cohen, “Advanced Air Mobility: Opportunities and Challenges Deploying eVTOLs for Air Ambulance Service,” *Applied Sciences (Switzerland)*, vol. 12, no. 3, Feb. 2022. <https://doi.org/10.3390/app12031183>
- [3] R. Goyal, C. Reiche, C. Fernando, and A. Cohen, “Advanced air mobility: Demand analysis and market potential of the airport shuttle and air taxi markets,” *Sustainability (Switzerland)*, vol. 13, no. 13, Jul. 2021. <https://doi.org/10.3390/su13137421>
- [4] D. P. Rubertus, L. D. Hunter, and G. J. Cecere, “Electromechanical Actuation Technology for the All-Electric Aircraft,” *IEEE Trans Aerosp Electron Syst*, vol. AES-20, no. 3, pp. 243–249, 1984. <https://doi.org/10.1109/TAES.1984.310506>
- [5] A. P. Cohen, S. A. Shaheen, and E. M. Farrar, “Urban Air Mobility: History, Ecosystem, Market Potential, and Challenges,” *IEEE Transactions on Intelligent Transportation Systems*, vol. 22, no. 9, pp. 6074–6087, Sep. 2021. <https://doi.org/10.1109/TITS.2021.3082767>
- [6] W. Johnson, C. Silva, and E. Solis, “Concept Vehicles for VTOL Air Taxi Operations.”
- [7] A. Bacchini and E. Cestino, “Electric VTOL configurations comparison,” *Aerospace*, vol. 6, no. 3, Mar. 2019. <https://doi.org/10.3390/aerospace6030026>
- [8] S. E. Lyshevski, “Electromechanical Flight Actuators for Advanced Flight Vehicles.”
- [9] I. Chakraborty, D. N. Mavris, M. Emeneth, and A. Schneegans, “A methodology for vehicle and mission level comparison of More Electric Aircraft subsystem solutions: Application to the flight control actuation system,” *Proc Inst Mech Eng G J Aerosp Eng*, vol. 229, no. 6, pp. 1088–1102, May 2015. <https://doi.org/10.1177/0954410014544303>
- [10] J. W. Bennett, B. C. Mecrow, A. G. Jack, and D. J. Atkinson, “A prototype electrical actuator for aircraft flaps,” in *IEEE Transactions on Industry Applications*, May 2010, pp. 915–921. doi: 10.1109/TIA.2010.2046278
- [11] M. Mazzoleni, · G. Di Rito, and F. Previdi, “Electro-Mechanical Actuators for the More Electric Aircraft.” [Online]. Available: <https://www.springer.com/gp/authors-editors/journal-author/journal-author-helpdesk/>
- [12] J. D. Booker, C. Patel, and P. Mellor, “Modelling green vtol concept designs for reliability and efficiency,” *Designs (Basel)*, vol. 5, no. 4, Dec. 2021. <https://doi.org/10.3390/designs5040068>
- [13] M. A. A. Ismail, S. Wiedemann, C. Bosch, and C. Stuckmann, “Design and evaluation of fault-tolerant electro-mechanical actuators for flight controls of unmanned aerial vehicles,” *Actuators*, vol. 10, no. 8, Aug. 2021. <https://doi.org/10.3390/act10080175>
- [14] M. Budinger, A. Reyssset, E. Halabi, C. Vasiliu, and J.-C. Maré, “Optimal preliminary design of electromechanical actuators, Electro-Mechanical Actuators for the More Electric Aircraft,” *Proceedings of the Institution of Mechanical Engineers*, vol. 228, no. 9, 2013. <https://doi.org/10.1177/0954410013497171i>
- [15] I. Schäfer, “Improving the Reliability of EMA by using Harmonic Drive Gears.”
- [16] Y. Cao, J. Wang, X. Rong, and X. Wang, “Fault Tree Analysis of Electro-mechanical Actuators.”
- [17] A. Raviola, A. De Martin, R. Guida, G. Jacazio, S. Mauro, and M. Sorli, *Harmonic Drive Gear Failures in Industrial Robots Applications: An Overview*.

Landing gear shock absorbers guidelines

Michele Guida^{1,a}, Giovanni Marulo^{1,b} and Francesco Marulo^{1,c*}

¹Department of Industrial Engineering, Via Claudio, 21 – 80125 Napoli – Italy

^amichele.guida@unina.it , ^bnanni.marulo@hotmail.it , ^cfrancesco.marulo@unina.it

Keywords: Aeronautical History, Landing Gear, Shock Absorber, Numerical-Experimental Correlation

Abstract. This paper is based on an old paper presented by Eng. Ermanno Bazzocchi almost seventy years ago [1] and is here presented again in his memory, to take the opportunity for showing to young generation of engineers how applied research was performed and presented when the computer age was not still born. The topic is on landing gear shock absorber design guidelines, and it has been selected because of the importance of such device for airplanes, which represents a very important system for the efficiency of the entire aircraft. The original paper [1] has represented a milestone for the design and dimensioning of landing gear shock absorbers highlighting parameters which often have not been discussed so clearly in papers which came later in the scientific literature and therefore the idea of collecting those information and revisiting them in a modern framework has been particularly exciting. It is in the idea of the authors that revisiting fundamental classic papers and projecting them in a modern scenario could be beneficial for the real understanding of the physical aspects of aircraft systems, covering calculations which could not being performed because of low computing power. Classic papers were forced to strongly rely on physical understanding from which creating simple models to correlate experimental data and theoretical calculations. Such physical background should not be lost, but hopefully improved by the actual computer power and this paper is an attempt proposed to the scientific community for discussing on the validity of such an approach.

Introduction

The aircraft landing gear is one of the most critical part of an aircraft, being this system responsible for ensuring the safety of the payload during take-off, landing and for the taxiing procedures, too. The general arrangement of the landing gear consists of the shock absorbers, retraction mechanism, steering, shimmy control, tires, wheels and brakes. It represents about 3.5 to 7 percent of the gross weight and from 2 to 4 percent of the aircraft sales price.

The design of landing gears has been considered one of the more challenging and technically satisfying engineering task, since it demands expertise in mechanical and structural engineering, hydraulics, kinematics, materials and a very good understanding of detail design.

For these reasons, but even more to bring back memories, we remember, in the year of the first centenary of the Italian Air Force, Eng. Ermanno Bazzocchi, the designer of one of the most iconic aircraft, the MB-339, which still successfully equips the national aerobatic team, the PAN.

In 1955 Eng. Bazzocchi publishes in the magazine L'Aerotecnica a work on the design of one of the main elements of the landing gear of an aircraft, the shock absorber, based on a presentation held the previous year at a scientific congress in Paris.

This work has been taken up again in this article as evidence of its technical-scientific validity, after almost seventy years, and above all for the organization and setting given by the author to this work. An attentive technician who reads this work with dedication comes out capable of designing and realizing the structural component under discussion and with the modern tools of calculation and assisted design, can enhance concepts that at the time of its first draft could not be optimized due to lack of calculation tools.

The main wish behind recalling this work, underlining its importance and highlighting its merits, is to show young researchers how significant it can be to revisit past experiences, when the low computing power was overcome by knowledge of the physics of the problem as well as by a thorough ability in the use of engineering tools. From the authors of this article viewpoint, there is the hope to have been able to convey the pleasure of having revisited an important scientific document, [1], that still represents a milestone in the design of aircraft landing gear, together with other “well-seasoned” papers, [2] and [3].

Mechanics of the landing gear

One of the possible schemes of the landing gear considers that it is attached to a rigid mass which has a degree of freedom for the vertical displacement, only. Both the systems, mass of the airplane and landing gear constitute a 2-dof system, fig. 1(a). To obtain energy dissipation, the hydraulic fluid is forced to flow at high velocity because of the telescoping strut. To maximize such dissipation, the passage of the hydraulic fluid through the orifice should be properly designed by defining a variation of the orifice area by introducing a metering strut which controls the size of the orifice and governs the performance of the shock absorber, fig. 1(b). The balance of the forces is reported in fig. 1(c) which shows the mutual interaction between the tire and the strut.

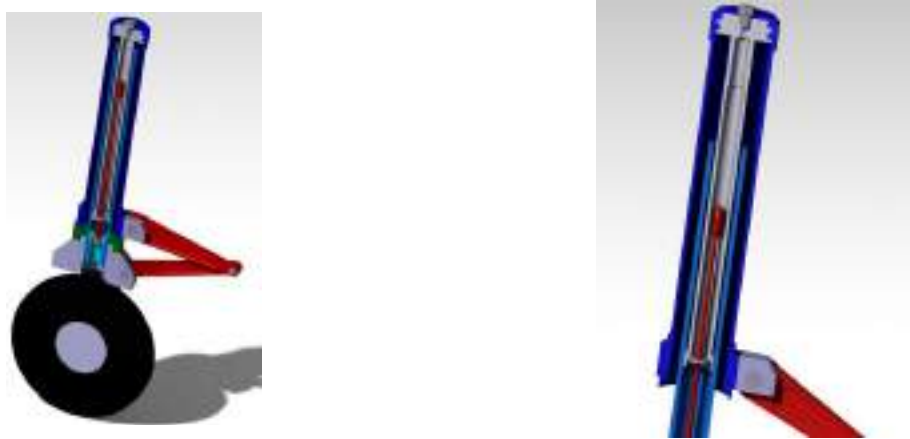


Figure 1 – Schematic of a typical landing gear (left) and shock absorber (right)

One of the most interesting aspects emerging by comparing the results of [1] and [2] is the choice of the plane for their representation. Ref. [1] uses a force versus displacement representation for the behavior of the landing gear. Ref. [2], on the other hand, presents the results in force, or displacement, versus time plots. This latter could appear more intuitive, as generally is for a time behavior of parameters, while the force versus displacement may appear a bit more difficult, but it is result (and efficiency) related, regarding the design of the landing gear because it gives an easy representation of its efficiency and opens to opportunities for improvements, if any.

Equations of motion

The approach for writing the equations of motion follows a common path which initially studies each component separately, then they come together for assessing the full behavior of the landing gear. This general approach may be split in modelling a passage from one to two degree of freedom system-or, which is equivalent, to an initial motion of the tire only and, reaching a certain force, activating the shock absorber, too. In [1] this latter approach is followed along with an engineering procedure which assumes, due to the short time, a static behavior of the tire, before defining the complex behavior of the shock absorber. Ref. [2] instead, employs the passage from 1 to 2-dof system in a chronological sequence which computes also the initial conditions for the beginning of the second phase, when the inertia, weight and lift forces become sufficiently large to overcome the preloading force in the shock strut due to the initial air pressure and internal friction.

The overall dynamic non-linear equilibrium equation for a 2-dof system is given by the following relationship:

$$\frac{W_1}{g} \ddot{z}_1 + \frac{W_2}{g} \ddot{z}_2 + F_{V_g}(z_2) + L = W_1 + W_2$$

where the subscripts 1 and 2 refer, respectively, to the upper mass (typically the partial mass of the airplane on the shock absorber) and the lower mass (typically the tire with its systems mass), L is the lift force and F_{V_g} is the vertical force on tire.

The previous equation uses physical degrees of freedom for representing the equilibrium. Clearly it needs to be manipulated for explicitly showing the main parameters before being integrated and becoming effectively useful for designing the shock absorber.

A different approach, more energy based, is used in [1], ending with one scalar non-linear equation which is stepwise integrated according to the time evolution of the physical phenomenon. Such equation, appeared at the time of Ref. [1] as impossible to solve, is written as

$$vv_a^2 \frac{dv_a}{dC_a} + v_a(A + B) - A = 0$$

where $v = v_p + v_a$ is the sum of the velocity of the tire and the shock absorber, and A and B are variables grouping several parameters as the stiffness of the tire and the shock absorber.

Results

Based on the previous equations, mainly those of Ref. [2], computer codes, [8], have been developed, tested and used for correlating laboratory measurements and numerical results. Fig. 2 presents the results obtained from the discussed methodologies and applied in comparing predictions with experimental measurements for a general aviation landing gear.

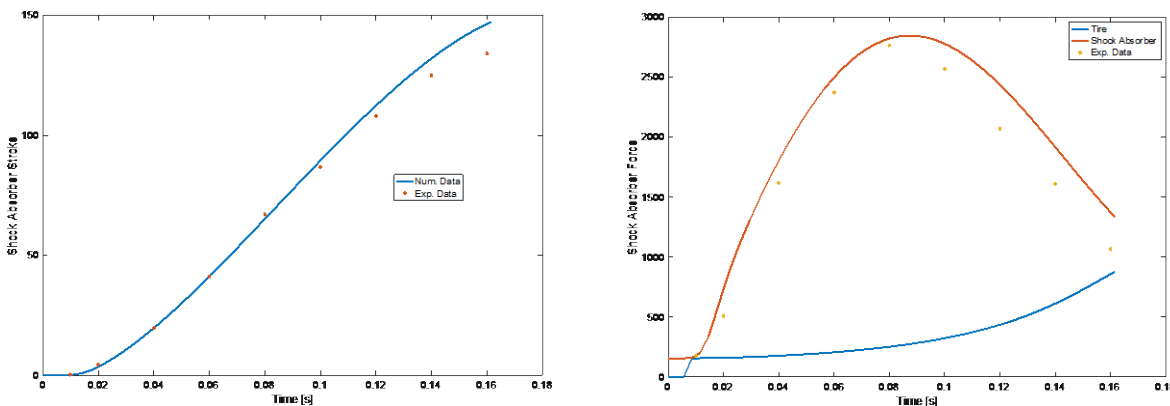


Figure 2 – Numerical-Experimental correlation of shock absorber stroke (left) and force (right) versus time, according to Ref. [2]

Figure 3 shows the results which can be obtained during the design phase of the main elements of a landing gear equipped with a shock absorber, together with the definition, for example, of the geometry of the metering pin, fig. 4, for reaching a specified value of the absorbing efficiency in some specific landing condition.

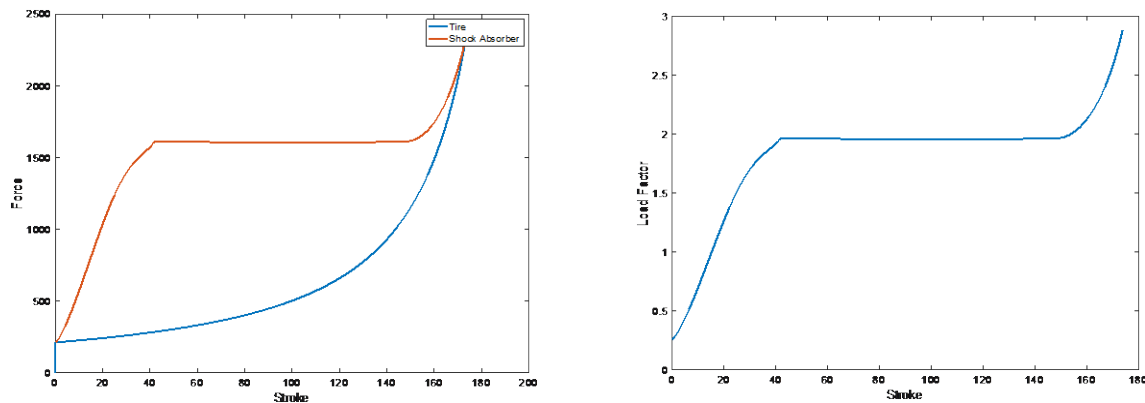


Figure 3 – Force and load factor versus landing gear stroke for designing and verification purposes, according to Ref. [1]

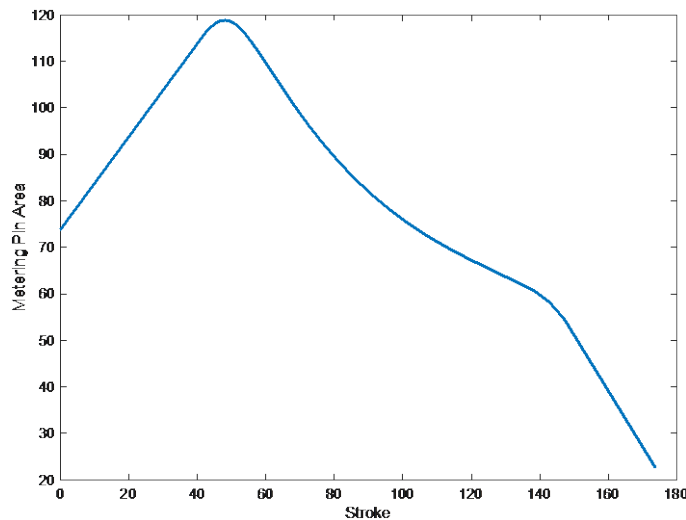


Figure 4 – Metering pin area versus landing gear stroke

Conclusions

The main purpose of this article has been to resume some old papers on the design and analysis of landing gear and to review considering modern computer technologies, trying to evidence the importance of their content and how they are still useful in the actual environment.

Acknowledgements

The authors are indebted with Prof. Fabrizio Ricci for having shared the basic idea of this work, for having encouraged its writing, for the interesting resulting discussions and for allowing the use of experimental data and Matlab scripts which are not reported here for sake of brevity, but very useful for summing up the main approaches described throughout the paper.

References

- [1] Ermanno Bazzocchi, “Metodo di calcolo degli ammortizzatori oleopneumatici e confronti con i risultati ottenuti alle prove”, L’Aerotecnica, Vol. XXXV, fasc. 3°, 1955
- [2] Benjamin Milwitzky, Francis E. Cook, “Analysis of Landing-Gear Behavior”, NACA Report 1154, Langley Field, Va., USA, 1953
- [3] Ladislao Pazmany, Landing Gear Design for Light Aircraft Vol. I, Pazmany Aircraft Corporation, San Diego, Ca, USA, 1986

- [4] Norman S. Currey, Aircraft Landing Gear Design: Principles and Practices, AIAA Education Series, Washington D.C., USA, 1988. <https://doi.org/10.2514/4.861468>
- [5] Benjamin Milwitzky, Francis E. Cook, “Analysis of Landing-Gear Behavior”, NACA Report 1154, Langley Field, Va., USA, 1953
- [6] AGARD Landing Gear Design Loads, CP-484, Portugal, 1990
- [7] Military Specifications, Landing Gear Systems, MIL-L-87139, July 1979
- [8] Rinaldi F., “Metodologie di progetto di un ammortizzatore oleopneumatico”, Tesi di Laurea, Dipartimento di Progettazione Aeronautica, a.a. 1994-‘95

Experiments and simulations for the development of a dual-stator PMSM for lightweight fixed-wing UAV propulsion

Aleksander Suti^{1,a,*}, Gianpietro Di Rito^{1,b}, Roberto Galatolo^{1,c},
Luca Sani^{2,d}, Giuseppe Mattei^{3,e}

¹Università di Pisa, DICI, Largo Lucio Lazzarino 2, 56122, Pisa, Italy

²Università di Pisa, DESTEC, Largo Lucio Lazzarino 2, 56122, Pisa, Italy

³Sky Eye Systems, Via Grecia 52, 56021, Cascina, Italy

^a aleksander.suti@dici.unipi.it, ^b gianpietro.di.rito@unipi.it, ^c roberto.galatolo@unipi.it,

^d luca.sani@unipi.it, ^e giuseppe.mattei@skyeyesystems.it

Keywords: UAV, Full-Electric Propulsion, Axial-Flux PMSM, Simulation, Testing

Abstract. The work summarizes the experimental and simulation studies carried out on the full-electric propulsion system of a lightweight fixed-wing UAV developed in the research program TERSA. The electric motor, specifically designed for the project, is a double-stator axial-flux PMSM with single output shaft, directly connected to a twin-blade fixed-pitch propeller. The system dynamics is firstly addressed by nonlinear simulation, modelling the motor and related sensors, the propeller and the digital controllers, to design the closed-loop control architecture. Successively, an experimental campaign is defined to identify/substantiate the main motor parameters (resistance and inductance of phases, torque and speed constants, back-electromotive force waveforms) and to validate the closed-loop control design.

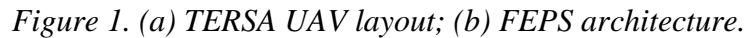
Introduction

In the air transport sector, Full-Electric Propulsion Systems (FEPSs) are expected to obtain large investments in forthcoming years, aiming to replace/support the operation of conventional internal combustion engines, especially in small-size power applications [1]. Even if immature nowadays in terms of reliability and energy density (e.g., gasoline energy density is about 100 times higher than lithium-ion battery packs [2], typically ranging about 300 kJ/kg), the design of the next-generation long-endurance UAVs is moving toward the use of FEPSs, pulled by the wider objectives of aerospace electrification. In this context, the Italian Government and the Tuscany Regional Government funded the research program TERSA¹ [3], led by Sky Eye Systems (Italy) in collaboration with University of Pisa and other Italian industries. The TERSA project aims to develop a Unmanned Aerial System (UAS) based on a lightweight fixed-wing UAV (Fig. 1), having the following main characteristics:

- Main performance data: MTOW from 35 to 50 kg; Endurance >6 h; Range >3 km;
- Take-off/landing systems: pneumatic launcher and parachute/airbags;
- Propulsion system: FEPS with a twin-blade fixed-pitch propeller;
- Payloads: SAR (Synthetic Aperture Radar) and SAAS (Sense-And-Avoid System).

¹ Tecnologie Elettriche e Radar per Sistemi aeromobili a pilotaggio remoto Autonomi, Fund ID F/130088/01-05/X38





Two test campaigns with different experimental setup have been carried out to identify/substantiate the main parameters of the propulsion system model and to validate the closed-loop regulators. In the first campaign, since the motor model identification requires three parameters (the motor speed constant k_m , the resistance R and the inductance L of the phases) and three BEMF waveforms as functions of the electrical angle ($k_{ex}(\theta_e) = e_x/k_m\dot{\theta}_e$, where e_x is the BEMF of the phase x ($= a, b, c$) and θ_e is the electrical angle), two tests have been designed. The

first one is done with blocked rotor to identify R and L , and the second one with the rotor dragged by the bench motor to identify k_m and k_{ex} . In the second campaign, a first test has been done by blocking the rotor while commanding the motor current with step inputs of different amplitudes, and a second test (Fig. 2) has been performed by connecting the propeller and by commanding the angular speed with tracking signals of different amplitudes. Figure 3 reports the motor speed constant and the BEMF waveforms for both stators. Figure 3(a) highlights that the dependency of the speed constant on the angular speed is more relevant in the stator 1 (S1), even if the maximum variation is about 1%. In addition, Fig. 3(b) shows an electrical angle phase misalignment (about 15 deg) in the BEMF waveforms. Figure 4 summarizes the simulation results. Figure 4(a) points out the validation of the current controller, accomplished by requesting step commands of quadrature current (40 A and 60 A, respectively) while the output shaft is blocked. The model exhibits a slight delay (1 ms) when the command signal is applied, but the prediction error rapidly diminishes (within 5ms). The validation of the speed controller is finally reported in Fig. 4(b), and it is performed by requesting two ramped-step speed commands, with 2 and 4 krpm amplitudes, both characterised by a 1 krpm/s slope. In both cases, the test ends by removing the electrical power and letting the motor passively decelerate (thus permitting a more direct identification/substantiation of system inertias). Apart from a low frequency (about 8 Hz) harmonic disturbance due to imperfect rig grounding, the model behaves satisfactorily during both controlled and uncontrolled phases.

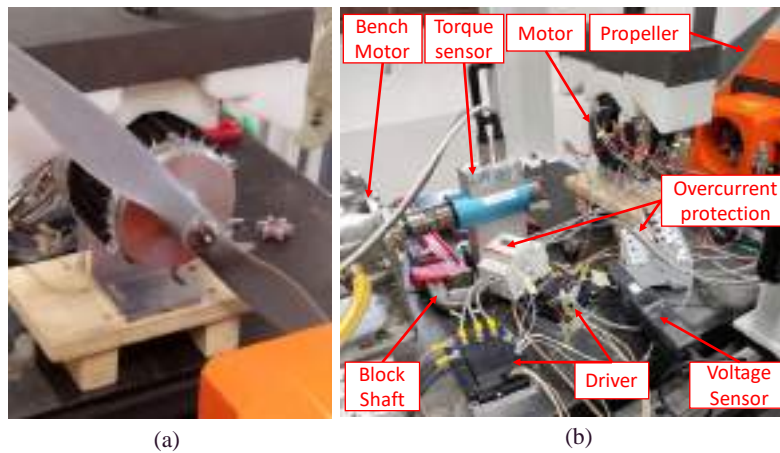


Figure 2. Experimental setup for speed tracking tests: (a) connected propeller (b) rig layout.

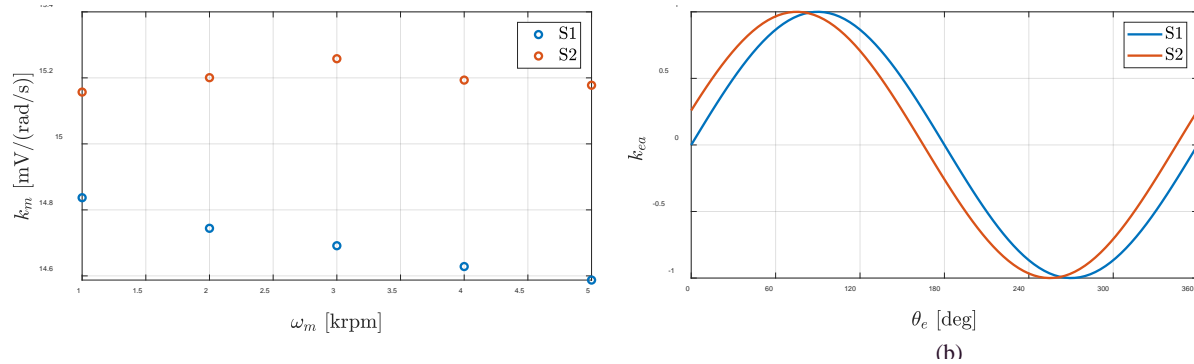


Figure 3. BEMF of motor modules: (a) speed constant; (b) BEMF wrt electrical angle.

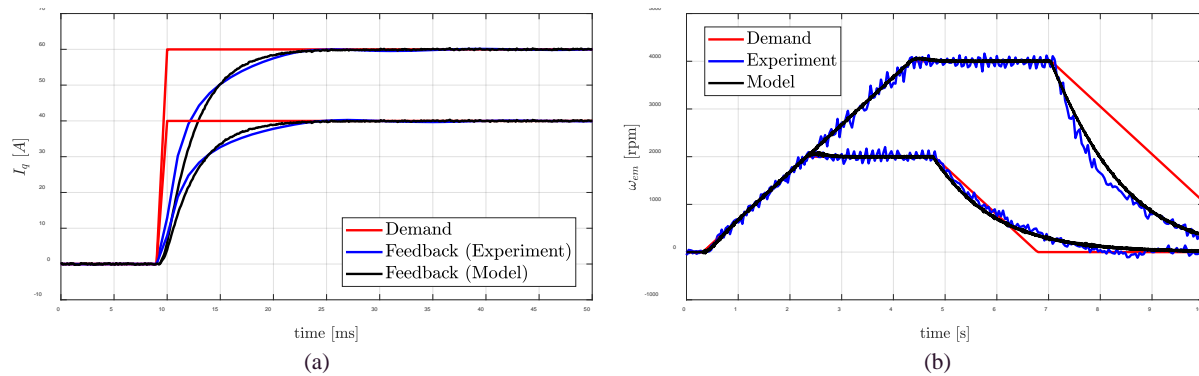


Figure 4. Closed-loop control validation: (a) current (b) angular speed.

Summary

The main parameters of the nonlinear model of the TERSA UAV propulsion system are identified/substantiated through experiments and the closed-loop control performances are validated. Due to manufacturing imperfections, the BEMF of the stator modules are misaligned wrt the motor angle and they have different torque constants. The asymmetry, though partially compensated by the control actions, can cause a reduction of the propulsion system efficiency and high-frequency torque ripples that, affecting bearings and seals, can potentially lead to premature failure. The FEPS model can be used to develop advanced model-based monitoring techniques, for the enhancement of the system diagnostics and prognostics.

References

- [1] A. Suti, G. Di Rito, and R. Galatolo, "Climbing performance enhancement of small fixed-wing UAVs via hybrid electric propulsion," in *2021 IEEE Workshop on Electrical Machines Design, Control and Diagnosis (WEMDCD)*, IEEE, Apr. 2021, pp. 305–310. <https://doi.org/10.1109/WEMDCD51469.2021.9425638>
- [2] C. C. Chan, "The state of the art of electric and hybrid vehicles," *Proceedings of the IEEE*, vol. 90, no. 2, pp. 247–275, 2002. <https://doi.org/10.1109/5.989873>
- [3] A. Suti, G. Di Rito, and R. Galatolo, "Fault-Tolerant Control of a Dual-Stator PMSM for the Full-Electric Propulsion of a Lightweight Fixed-Wing UAV," *Aerospace*, vol. 9, no. 7, p. 337, Jun. 2022. <https://doi.org/10.3390/aerospace9070337>
- [4] R. Huang, C. Liu, Z. Song, and H. Zhao, "Design and Analysis of a Novel Axial-Radial Flux Permanent Magnet Machine with Halbach-Array Permanent Magnets," *Energies (Basel)*, vol. 14, no. 12, p. 3639, Jun. 2021. <https://doi.org/10.3390/en14123639>
- [5] A. ; R. N. , A. ; H. W. , P. Mahmoudi, "Axial-flux permanent-magnet machine modeling, design, simulation and analysis," *Scientific Reseach and Eassays*, vol. 6, no. 12, pp. 2525–2549, 2011.
- [6] Z. Wang, J. Chen, and M. Cheng, "Fault tolerant control of double-stator-winding PMSM for open phase operation based on asymmetric current injection," in *2014 17th International Conference on Electrical Machines and Systems (ICEMS)*, IEEE, Oct. 2014, pp. 3424–3430. doi: 10.1109/ICEMS.2014.7014114
- [7] G. Liu, Z. Lin, W. Zhao, Q. Chen, and G. Xu, "Third Harmonic Current Injection in Fault-Tolerant Five-Phase Permanent-Magnet Motor Drive," *IEEE Trans Power Electron*, vol. 33, no. 8, pp. 6970–6979, Aug. 2018. <https://doi.org/10.1109/TPEL.2017.2762320>

- [8] A. Suti, G. Di Rito, and R. Galatolo, "Fault-Tolerant Control of a Three-Phase Permanent Magnet Synchronous Motor for Lightweight UAV Propellers via Central Point Drive," *Actuators*, vol. 10, no. 10, p. 253, Sep. 2021. <https://doi.org/10.3390/act10100253>
- [9] R. Zhang, V. H. Prasad, D. Boroyevich, and F. C. Lee, "Three-dimensional space vector modulation for four-leg voltage-source converters," *IEEE Trans Power Electron*, vol. 17, no. 3, pp. 314–326, May 2002. <https://doi.org/10.1109/TPEL.2002.1004239>
- [10] M. Mazzoleni, G. Di Rito, and F. Previdi, *Electro-Mechanical Actuators for the More Electric Aircraft*. Cham: Springer International Publishing, 2021. doi: 10.1007/978-3-030-61799-8
- [11] Z. Wang, J. Chen, and M. Cheng, "Fault tolerant control of double-stator-winding PMSM for open phase operation based on asymmetric current injection," in *2014 17th International Conference on Electrical Machines and Systems (ICEMS)*, IEEE, Oct. 2014, pp. 3424–3430. doi: 10.1109/ICEMS.2014.7014114

Target localization with a distributed Kalman filter over a network of UAVs

Salvatore Bassolillo^{1,a}, Egidio D'Amato^{2,b}, Massimiliano Mattei^{3,c},
Immacolata Notaro^{1,d *}

¹Department of Engineering, University of Campania "L. Vanvitelli", 81031 Aversa, Italy

²Department of Science and Technology, University of Naples "Parthenope", Napoli, Italy

³Department of Electrical Engineering and Information Technology, University of Naples
"Federico II", Napoli, Italy

^asalvatorerosario.bassolillo@unicampania.it, ^begidio.damato@uniparthenope.it,

^cmassimiliano.mattei@unina.it, ^dimmacolata.notaro@unicampania.it

Keywords: Distributed Kalman Filter, Target Localization, UAV Formation

Abstract. Unmanned Aerial Vehicles (UAVs) have gained significant usage in various kinds of missions, including reconnaissance, search and rescue, and military operations. In rescue missions, timely detection of missing persons after avalanches is crucial for increasing the chances of saving lives. Using UAVs in such scenarios offers benefits such as reducing risks for rescuers and accelerating search efforts. Employing a formation of multiple drones can effectively cover a larger area and expedite the process. However, the challenge lies in achieving autonomous and scalable systems, as drones are typically operated on a one-to-one basis, requiring a large team of rescuers. To enhance situational awareness and distribute communication load, this paper proposes a decentralized Kalman filtering algorithm that exploits sensor data from multiple drones to estimate target positions and support guidance and control algorithms. The algorithm combines Consensus on Information and Consensus on Measurements techniques. Preliminary validation is conducted through numerical simulations in a sample scenario.

Introduction

In recent decades, the use of UAVs (Unmanned Aircraft Vehicles) has experienced exponential growth in both civil and military sectors. The widespread adoption of these aircraft can be attributed to their ease of use and versatility in various missions. However, in certain scenarios, a single UAV may not suffice, and a collaborative team of UAVs is preferred. Such formations offer comparable or even greater mission capabilities, along with improved flexibility and robustness [1]. According to the Center for Research on the Epidemiology of Disasters (CRED) [2], the issue of fatalities and disappearances due to natural events remains a significant concern globally. To mitigate risks for human rescuers, UAVs should be prioritized for initial rescue operations in hazardous environments. Collaborative efforts among multiple drones have garnered attention from researchers in recent years, as they provide an effective solution to expedite the search process [3]. The coordination and collaboration of UAVs are crucial to function as a unified entity, maintaining formation and directing their flight toward the target.

In this paper, a distributed estimation algorithm for a formation of UAVs is proposed to locate a possible missing skier under the snow. The situational awareness is obtained by equipping UAVs with on-board heterogeneous sensors. The distributed algorithm is based on a decentralized Kalman filtering technique that involves a set of local Kalman filters, one for each UAV. By considering the formation as a network of vehicles, every node provides onboard sensors data and contributes to the estimation of the overall state [4]. With respect to a centralized architecture, running on a leader, that receives information from the other nodes, the decentralized scheme



decreases the computational burden on the central node of the formation and it is less vulnerable against system failure, being not depending on a single aircraft.

The proposed sensor fusion algorithm receives measurements from a Global Positioning System (GPS) receiver and an Inertial Navigation System (INS), that represent the most widely used sensors for navigation purposes. To enhance system capabilities in hazardous environments and the robustness to sensors fault, each aircraft is equipped with a radio transponder to measure the relative distance between vehicles. Such device can be based on time-of-flight measurements over ultra-wideband radio signals or on the Received Signal Strength Indication (RSSI) of the same communication standard used to create the formation network. In order to find targets, each aircraft is equipped with a modern avalanche transceiver (ARTVA), typically used by back country skiers, whose signal power measurements, from multiple drones, can be used to perform triangulation and locate missed people.

Problem Statement

Let us consider a heterogeneous swarm of N UAVs, composed of aircraft in multi-rotor or fixed wing configurations. The swarm must survey a specific area in order to identify the presence of a snow-covered skier after an avalanche event. For first rescue mission in the search of a missing skier and for navigation purposes, UAVs must be able to estimate the position of the skier and their position in the airspace.

The discrete-time model of each UAV can be described in the inertial reference frame by the following equations:

$$\begin{cases} \mathbf{S}_i(k) = \mathbf{S}_i(k-1) + \mathbf{V}_i(k-1)T_s + \boldsymbol{\omega}_i^S(k) \\ \mathbf{V}_i(k) = \mathbf{V}_i(k-1) + \boldsymbol{\omega}_i^V(k) \end{cases} \quad \forall i = 1, 2, \dots, N \quad (1)$$

where k is the time step, $\mathbf{S}_i(k) = [X_i(k), Y_i(k), Z_i(k)]^T$ is the vector of the spatial coordinates, $\mathbf{V}_i(k) = [V_{X_i}(k), V_{Y_i}(k), V_{Z_i}(k)]^T$ is the velocity vector of the i -th UAV, $[\boldsymbol{\omega}_i^{S^T}(k), \boldsymbol{\omega}_i^{V^T}(k)]^T$ is a process noise vector, and T_s is the sample time.

The global state vector $\mathbf{x}(k) \in \mathbb{R}^m$ is defined as:

$$\mathbf{x}(k) = [\mathbf{S}_1^T(k), \mathbf{V}_1^T(k), \dots, \mathbf{S}_N^T(k), \mathbf{V}_N^T(k), \mathbf{S}_t^T(k)]^T \quad (2)$$

where the position of the missing skier is identified by $\mathbf{S}_t(k) = [X_t(k), Y_t(k), Z_t(k)]^T$.

Each UAV is equipped with a set of sensors composed of:

- a GPS, to measure its position in the airspace;
- $N - 1$ transponders, to evaluate the relative distance to each UAV in the swarm;
- an avalanche receiver antenna (ARTVA), to detect the signal from the skier avalanche transceiver.

Consider the measure provided by the GPS

$$\mathbf{z}_i^{GPS}(k) = [X_i(k), Y_i(k), Z_i(k)]^T + \mathbf{v}_i^{GPS}(k) \quad (3)$$

the measurement provided by the transponders

$$\mathbf{z}_i^{Tr}(k) = [d_{i1}(k), \dots, d_{iN}(k)]^T + \mathbf{v}_i^{Tr}(k) \quad (4)$$

and the measurement provided the ARTVA

$$\mathbf{z}_i^{AT}(k) = d_{it}(k) + \mathbf{v}_i^{AT}(k) \quad (5)$$

where $\mathbf{v}_i^{GPS}(k)$, $\mathbf{v}_i^{Tr}(k)$, and $\mathbf{v}_i^{AT}(k)$ are the corresponding sensor noises. The term $d_{ij}(k) = \|\mathbf{S}_j(k) - \mathbf{S}_i(k)\|_2$ represents the Euclidean between two aircraft, i and j , whereas $d_{it}(k) = \|\mathbf{S}_t(k) - \mathbf{S}_i(k)\|_2$ is the distance of the i -th aircraft from the target skier, with $\|\cdot\|_2$ denoting the Euclidean norm.

The measurement vector of the overall set of sensors is represented by

$$\mathbf{z}_i(k) = \left[\mathbf{z}_i^{GPS^T}(k), \mathbf{z}_i^{Tr^T}(k), \mathbf{z}_i^{AT}(k) \right]^T + \mathbf{v}_i^T(k) \quad (6)$$

with $\mathbf{v}_i(k) = \left[\mathbf{v}_i^{GPS^T}(k), \mathbf{v}_i^{Tr^T}(k), \mathbf{v}_i^{AT}(k) \right]^T$ as the overall measurement noise vector.

Consensus Estimation

At any time k , the communication structure of the formation can be represented by an undirected graph $\mathbb{G}(k) = \{\mathcal{V}, \mathcal{A}(k)\}$, where $\mathcal{V} = \{1, 2, \dots, N\}$ is the set of UAVs, and $\mathcal{A}(k) \subseteq \mathcal{V} \times \mathcal{V}$ is the set of edges describing the communication link between the aircraft i and j . The i -th UAV can receive data from the j -th vehicle if the arc $(i, j) \in \mathcal{A}(k)$. For each aircraft i , $\mathcal{M}_i(k) = \{j: (i, j) \in \mathcal{A}(k)\}$ is the set of its neighbors, including the i -th vehicle, and $D_i(k) = \text{card}(\mathcal{M}_i(k)) - 1$ represents its degree, with $\text{card}(\cdot)$ representing the cardinality of a generic set.

Let $\xi_i(k)$ be the generic information associated with the i -th agent. We assume that $\xi_i(k)$ is updated according to the Average Consensus Protocol [8]:

$$\xi_i^{(l+1)}(k) = \sum_{j \in \mathcal{A}} W_{ij}(k) \xi_j^{(l)}(k) \quad l = 0, 1, \dots, L - 1 \quad (7)$$

performed on L consensus steps for each time instant k .

Coefficients $W_{ij}(k)$ can be computed using the Metropolis formula [9]:

$$W_{ij}(k) = \begin{cases} \frac{1}{1 + \max\{D_i(k), D_j(k)\}} & \text{if } j \in \mathcal{M}_i(k) \\ 1 - \sum_{j \in \mathcal{M}_i(k)} W_{ij}(k) & \text{if } i = j \\ 0 & \text{otherwise} \end{cases} \quad (8)$$

So that, to determine the weight, each agent i does not need any knowledge of the communication graph but only the degrees of its neighboring nodes, $D_j(k)$, with $j \in \mathcal{M}_i$.

The UAVs asymptotically reach the consensus if, for any initial condition $\xi_i^0(k)$, $\lim_{l \rightarrow \infty} \|\xi_i^l(k) - \xi_j^l(k)\| \rightarrow 0$, for each $(i, j) \in \mathcal{A}(k)$, where l is the generic consensus step.

Results

The performance of the proposed algorithm was evaluated by means of numerical simulations. As reference, a centralized version of the KF was considered, in order to verify the performance cost of the decentralized technique. In this section, to resume results, only an example scenario is considered, with a formation of 9 UAVs, flying together and surveying an area of interest to look for a target. Each aircraft flies along the same direction, at a constant speed of 5 m/s, with an altitude of 100 m above the terrain. Every agent is able to communicate with two neighbors, in order to form a cycle graph and it is equipped with an avalanche receiver to sense the signal from the target skier. Such receiver has a detection range of $d_{sens} = 200$ m.

At the beginning of the simulation, each aircraft knows only its position, initializing the overall state estimate with random values. Such assumption was useful to evaluate the convergence of the algorithm to the correct estimate and the ability to reach the consensus.

Fig. 1 show the estimated components of the target position vector, comparing the real value, the centralized IKF and the proposed decentralized KF. As shown in Figures, at the beginning of the simulation, the target position is still unknown being outside UAVs sensor range.

At $t = 5.5s$, the target enters in the sensor range of UAV_1 , but it is not sufficient to be localized. Indeed, for localization problems using fusion algorithms, the measurements of at least three aircraft are required to effectively locate the target [5].

From $t = 17s$, the target is in the sensor range of UAV_1 , UAV_2 and UAV_3 and it becomes localizable. The skier estimated position definitively converge at $t = 26s$.

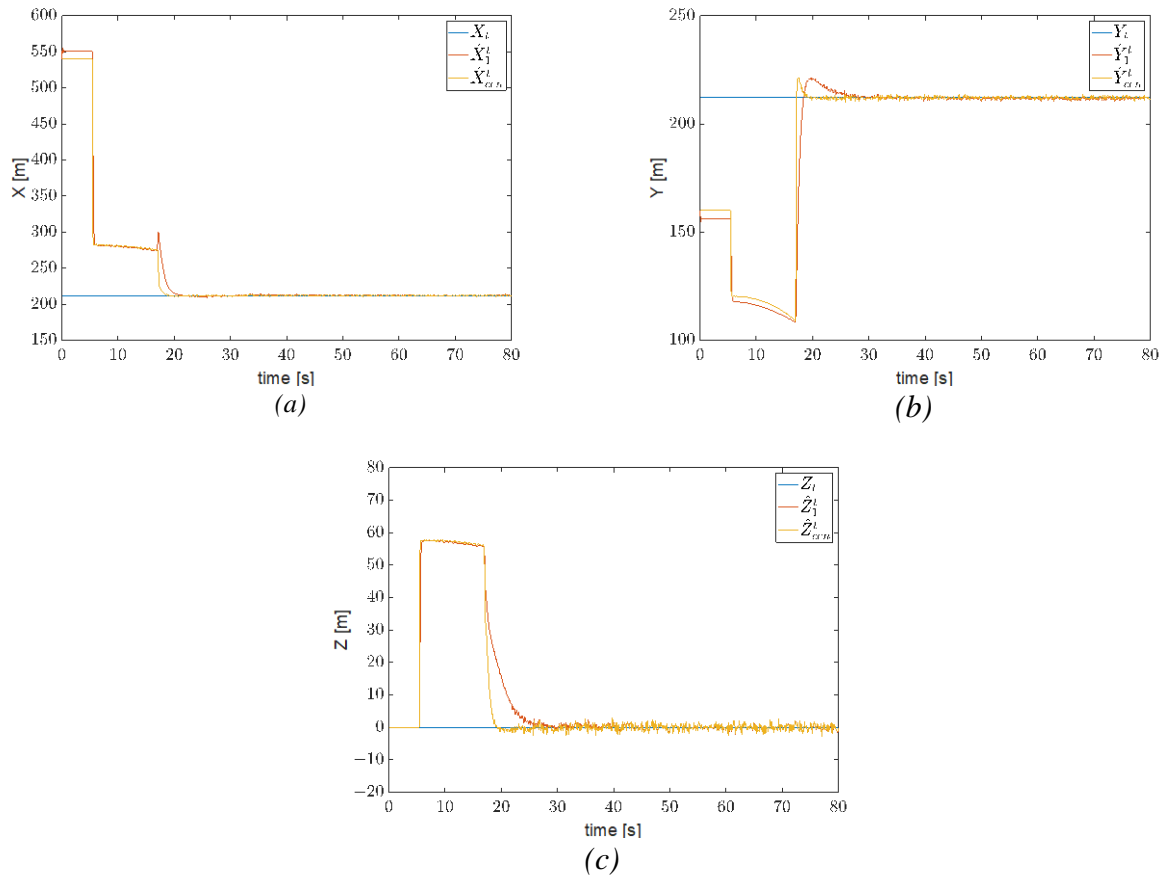


Figure 1- Comparison of the estimates of the skier's coordinates: (a) x-component, (b) y-component, (c) z-component .

References

- [1] F. Y. Hadaegh, S.-J. Chung, and H. M. Manohara, On Development of 100-Gram-Class Spacecraft for Swarm Applications, *IEEE Systems Journal*, vol. 10, no. 2, pp. 673–684, Jun. 2016. <https://doi.org/10.1109/JSYST.2014.2327972>
- [2] D. Guha-Sapir, F. Vos, and R. Below, *Annual Disaster Statistical Review 2011. 2012.*
- [3] L. Ruetten, P. A. Regis, D. Feil-Seifer, and S. Sengupta, Area-Optimized UAV Swarm Network for Search and Rescue Operations, in *2020 10th Annual Computing and Communication Workshop and Conference (CCWC)*, Jan. 2020, pp. 0613–0618. <https://doi.org/10.1109/CCWC47524.2020.9031197>
- [4] M. Cicala, E. D'Amato, I. Notaro, and M. Mattei, Scalable Distributed State Estimation in UTM Context, *Sensors*, vol. 20, no. 9, Art. no. 9, Jan. 2020. <https://doi.org/10.3390/s20092682>
- [5] M. A. Azam, S. Dey, H. D. Mittelman, and S. Ragi, Average Consensus-Based Data Fusion in Networked Sensor Systems for Target Tracking, in *2020 10th Annual Computing and Communication Workshop and Conference (CCWC)*, Jan. 2020, pp. 0964–0969. <https://doi.org/10.1109/CCWC47524.2020.9031250>

Air Traffic Control, Aircraft Operations and Navigation

Integration in controlled airspace: definition and validation of link loss contingency procedures for RPAS in terminal manoeuvring areas

G. D'Angelo^{1,a,*}, G. Pompei^{2,b}, A. Manzo^{3,c}, G. Riccardi^{3,d}, and U. Ciniglio^{4,e}

¹Leonardo, C.so Francia, 426 – Torino 10146, Italy

²Leonardo, Via Tiburtina km 12,400 – Roma 00131, Italy

³ENAV, Viale Fulco Ruffo. di Calabria – Napoli 80144, Italy

⁴CIRA, Via Maiorise – Capua 81043, Italy

^agiuseppe.dangelo@leonardo.com, ^bgino.pompei@leonardo.com,

^calessandro.manzo.1@enav.it, ^dgiovanni.riccardi.1@enav.it, ^eu.ciniglio@cira.it

Keywords: RPAS Integration, Terminal Manoeuvring Area (TMA), Contingency

Abstract. Remotely Piloted Aircraft Systems (RPAS) are increasingly becoming a part of our day-to-day lives. The vast range of possible applications in both military and civil contexts (e.g. border surveillance, search and rescue, civil protection) is creating a new industry with a large economic potential that, consequently, is pushing the rulemaking and standardization authorities to define and publish the rules, standards and procedures the industry has to comply with in order to integrate its products with the Air Traffic Management System. From an operational perspective, the challenge lies in integrating the worlds of manned and unmanned aircraft in a safe and efficient way allowing both types of aircraft to share the same airspace. An aspect of this challenge consists in defining and validating operational procedures and technical capabilities that allow to manage safely the RPAS even when a (Command and Control and/or ATC radio) link loss occurs. This paper is aimed at describing the procedures for the management of link loss events that affect RPAS flying under Instrument Flight Rules (IFR) in a Terminal Manoeuvring Area (TMA). This paper also describes the distributed facility used to validate such procedures by means of real time simulations in an Italian operational scenario with pilots and Air Traffic Controller (ATCO) in the loop. Positive feedback was provided by both ATCO and Remote Pilots (RPs) on the overall acceptance of the proposed operational procedures which were considered satisfactory even in non-normal conditions (e.g.: degradation of the communication channel quality). The insertion of RPAS in TMA was considered feasible, even in case of single or multiple Command and Control Link Loss (C2LL) contingencies. The experiment described in this paper was part of the SESAR 2020 Programme, PJ13 ERICA project.

Background

In 2012, experts in the RPAS field were called upon by the European Commission to develop a European roadmap for the integration of civil RPAS. In 2013, in response to the 'Roadmap for the integration of civil RPAS into the European aviation system', the SESAR Joint Undertaking launched a set of projects within the SESAR1 framework, then continued in the frame of SESAR 2020 in 2019 [4]. Bringing partners together from across ATM and Europe, the projects aimed at validating emerging RPAS technologies and operational procedures in non-segregated airspace and supporting the update of the related avionic standards and flight rules ([2][3][6]). Overall, these projects perceived no significant difference between the behaviour of an RPAS and a general aviation aircraft of the same (small or medium) category, when operating in the Air Traffic Control (ATC) environment. However, the following threads needed to be addressed before integration could be considered:



- Updated and well-established civil regulation and certification system by the required certification authorities [7];
- Policies and procedures on how ATC should interact with RPAS to ensure efficient operations and to meet safety-level requirements [1];
- A detect & avoid (D&A) capability and compliance with European aircraft equipage requirements;
- A reliable Command & Control (C2) link as well as voice link together with contingency procedures in case of link failures.

Operational context and user needs

Accepting the integration of RPAS into the ATM system poses many challenges and the need to address operational, performance and safety concerns for each of the flight phases of the RPA and considered ATM scenarios. The operational context considered in this paper is the integration of civil RPAS in the ‘certified’ category flying under IFR in low/medium density non-segregated airspaces from class A to C. The considered ATM scenario was a TMA wherein RPAS and manned aircraft operate simultaneously (mixed traffic), flying Standard Initial Departure and Standard Arrival Route procedures (SID/STAR) and responding to ATCOs clearances and instructions (vectoring included).

In such context two main user needs can be identified:

- Ensure that the RPA are able to flow the same SIDs and STARs designed for manned aviation without penalizing the traffic operations (e.g. by introducing delays or degrading the overall flight safety) in the involved ATC sector¹;
- Ensure that a C2 link-loss or voice loss condition affecting an RPA, has an acceptable impact on RP and ATC in terms of workload and procedures.

Simulation objectives

This paper describes a specific Real Time Simulation (RTS) campaign executed in the frame of SESAR 2020 W2 PJ13 ERICA project, Solution 117 [5][8], aimed at defining and validating the long-term operational, procedural and technical capabilities required to allow the integration of certified MALE and Tactical RPAS into the Italian Area of the Brindisi Control Centre (Brindisi ACC), by using the BARI-PALESE (LIBD) as main airport and BRINDISI-CASALE (LIBR) as alternate one.

The validation experiment described in this paper is the last step of an extensive validation activity which comprised two other propaedeutic RTS campaigns. The final RTS campaign, based on a set of four defined validation scenarios, considered both nominal and link loss contingency situations [5][8]. The experiment aimed at proving the feasibility of mixed operations in nominal conditions, as well as at the acceptance by RPs and Traffic Controllers of the implemented Human System Interfaces and automatic C2LL contingency procedures. It was also used to define a specific ATC phraseology for handling such C2LL contingencies. The simulation framework as well as the functions and procedures used, the outcomes and the resulting recommendations, main scope of this paper, are reported in the next sections.

Distributed simulation framework

To get significative results against the validation objectives, several complex scenarios were built and executed by using the Capua-Roma-Torino Air Ground Operation (CARTAGO) simulation framework depicted in Figure 1.

¹ A defined airspace region for which the *associated* controller(s) has ATC responsibility.

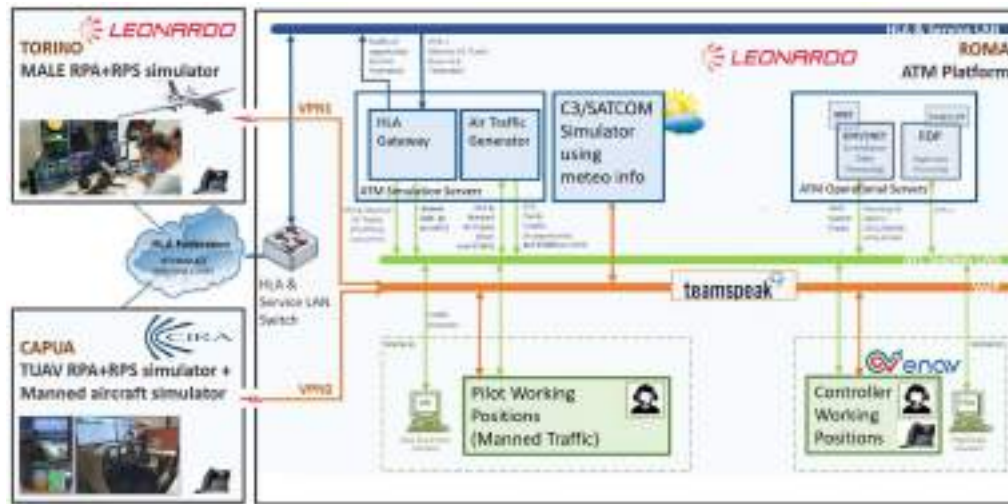


Figure 1 - The CARTAGO Real Time, geographically distributed, simulation facility

CARTAGO consisted of a Real Time geographically distributed simulation facility including:

- A Leonardo real ATC platform equipped with a Short-Term Conflict Alert (STCA) tool and upgraded to manage C2LL contingencies.
- A Leonardo MALE RPAS (10 tons of MTOW, 325 kt of maximum speed) full simulator hosting a Flight Management System model and a C2LL contingency function.
- A CIRA fixed wing Tactical RPAS (550 Kg of MTOW, 90 kt of maximum speed) simulator.
- A CIRA General Aviation manned aircraft simulator.
- A SATCOM model used by RPS to exchange both C2 messages with RPA and voice messages with ATCO. The model allowed to simulate the effects of different weather conditions on the link in terms of delay and degradation.

The geographically distributed simulation platforms were integrated by using the High Level Architecture (HLA) standard [9], specifically customized for ATM data run time exchange so as to keep under neglectable limits the related site-to-site transmission latency. In addition, as shown in Figure 1, the voice communication between RPs and ATCO was implemented by using the open-source TeamSpeak IP-based framework, adequately modified to emulate realistic disruptions over VHF radio link.

Technical functions, operational procedures and scenarios

An automatic C2LL contingency function was developed and tested together with a set of contingency procedures designed to allow the handling of a link loss condition in a wide range of possible situations.

Figure 2 shows the most complex operational scenario that was simulated where the MALE RPA lost the C2 link via SATCOM and the Tactical RPA lost the VHF radio. It can be noted the presence of a ground-ground voice link between the RPS and the ATC. Indeed, it is assumed that the integration of the RPAS into the ATM also requires a ground-ground voice link as essential enabler in order to ensure a back-up link in case of a VHF radio loss. It is still under discussion if this ground-ground link will be implemented by upgrading the existing telephone lines (quick solution) or by creating a dedicated ATM VoIP infrastructure (medium-term solution but with the advantage to avoid the communication latencies introduced by the SATCOM link).



Figure 2. Link loss contingency - Complex scenario

Figure 3 shows one of the C2LL contingency procedures automatically executed by the RPA under the control of the on-board C2LL contingency function. The light blue arrow represents the direction from where the RPA could arrive. If the RPA loses the C2 Link (C2L) before the BAR Initial Approach Fix (IAF), it shall continue to fly in automatic way to BAR waypoint by maintaining the last authorized speed and Flight Level (FL). Once BAR IAF is reached, the RPA turns right (yellow path) direct to APFIB fix, then the RPA enters the holding pattern (red path) and holds it for 7 minutes. If the C2L is not recovered during the holding, the RPA shall go direct to BAR IAF (brown arrow) continuing to maintain speed and flight level. Once BAR IAF is reached, the RPA enters a second holding pattern to recover the IAF altitude if needed (green path). As soon as the IAF altitude is reached, the RPA flies to BD554 and starts an automatic RNP approach (purple path) and auto-landing procedure.



Figure 3. C2LL Procedure for SID and STAR, RWY25

The orange arrow represents, instead, the direction from where the RPA could come if the RPA lost the C2L before the Final SID Fix (FSF). In fact, if the C2L is lost during the departure phase, the C2LL contingency function will take the control of the RPA and, by maintaining the last authorized speed and FL, will complete the climb phase. Once the FSF is reached, the RPA flies automatically direct to APFIB (orange arrow) then enters the holding pattern (red path) and continue the procedure as already described above.

The C2LL contingency function is working properly even when the C2L is lost during the execution of a vectoring instruction. In that case, the C2LL contingency function maintains the last assigned instruction for two minutes then it commands the RPA to rejoin the original flight plan and reach the FSF or IAF as applicable, by maintaining the last authorized speed and FL. Once the FSF or IAF is reached, the RPA flies automatically direct to APFIB and continue the procedure as already described above.

Validation results and recommendations

Throughout the exercise, human performance and safety related aspects were investigated using a range of qualitative and quantitative assessment techniques including post run and post simulation questionnaires, debriefings sessions and operational expert observations annotated during the runs.

Operational acceptance. Positive feedback was provided by both ATCO and RPs on the overall acceptance of the concept and the procedures, even in case of single or multiple C2LL contingencies.

Human performance and perceived level of safety. Both ATCO and RPs stated that the overall workload was tolerable. Single and multiple C2LL contingencies generated a moderate workload but no concerns were raised about potential increase in human error linked to management of RPAS traffic. Positive feedback was provided by the ATCO in terms of impact on safety in both nominal and non-nominal conditions regarding the nominal and C2LL operational procedures, indeed the safety levels were not degraded.

Recommendation and future studies. As additional outcome of the exercise, the following set of recommendations was collected and reported by the ATCO and the RPs, suggested to be addressed in future studies and validations:

- in case a first C2LL procedure is already in place and another RPA is arriving at the same TMA, it was proposed that the ATCO (if needed) instructs this second RPA (with the C2 link still working) to update the pre-programmed C2LL trajectory in order to avoid potential overlapping on the same contingency path.
- to implement the automatic execution of the “open loop” clearances² with a flight level limit. In fact, only automatic execution of open loop clearances with time limit were validated, but the ATCO reported that this kind of clearance is rarely used, while flight level limit is more commonly used.
- to implement the automatic execution of “closed loop” clearances. In fact, despite the implementation of “open loop” clearance with limit was acceptable, ATCOs would prefer this implementation to allow them to specify the re-join waypoint together with a vectoring instruction.
- to implement an on-board emergency function to handle an FMS failure under a C2LL condition.

References

- [1] CANSO, ANSP CONSIDERATIONS FOR UNMANNED AIRCRAFT SYSTEMS (UAS) OPERATIONS, 2019. <https://canso.org>
- [2] ICAO, Doc 10019 Manual on Remotely Piloted Aircraft Systems (RPAS), February 2019.
- [3] SESAR 2020, PJ.10-05-W1 V2 OSED SPR/INTEROP v01.00.00, July 2020. <https://doi.org/10.5005/pid-2-1-iv>
- [4] EUROCONTROL, RPAS ATM CONOPS V4.0, February 2017.
- [5] Alessandro Manzo et al 2023 J. Phys.: Conf. Ser. 2526 012103. <https://doi.org/10.1088/1742-6596/2526/1/012103>
- [6] EASA, Advance Notice of Proposed Amendment, 2015-10.
- [7] EASA, Commission Implementing Regulation (EU) No 923/2012. <https://www.easa.europa.eu>
- [8] SESAR 2020, PJ13-W2-117 Validation Report (VALR) for V2, December 2022.
- [9] Richard M. Fujimoto (Georgia tech) & Richard M. Weatherly (MITRE), HLA TIME MANAGEMENT AND DIS, 1999.

² An ATC clearance that does not include a specified or implied point where the restriction on the trajectory ends.

Hybrid graph-clothoid based path planning for a fixed wing aircraft

Luciano Blasi^{1,a *}, Egidio D'Amato^{2,b}, Immacolata Notaro^{1,c}, Gennaro Raspaolo^{1,d}

¹Department of Engineering, University of Campania "L. Vanvitelli", Via Roma, 29, Aversa, 81031, Italy

²Department of Science and Technology, University of Naples "Parthenope", Centro Direzionale di Napoli, isola C4, Napoli, 80143, Italy

^aluciano.blasi@unicampania.it, ^begidio.damato@uniparthenope.it,

^cimmacolata.notaro@unicampania.it, ^dgennaro.raspaolo@studenti.unicampania.it

Keywords: Path Planning, Clothoids, RRT, UAVs

Abstract. Planning of safe and efficient trajectories is a critical task in the operation of unmanned aerial vehicles (UAVs), especially in urban or complex environments. With the increasing use of UAVs for various applications, such as surveillance, delivery, and inspection, it is becoming more important to automatically generate collision-free paths that also consider aircraft dynamics. This paper proposes an algorithmic approach based on the Rapidly exploring random tree (RRT) algorithm combined with a clothoid-based smoothing procedure to account for aircraft performance.

Introduction

The Rapidly exploring random tree (RRT) is a path planning algorithm commonly used in robotics and other applications where complex path planning is necessary. The algorithm constructs a tree of randomly generated exploration locations, iteratively adding nodes connected to existing ones if they do not cause collisions with their surrounding environment. RRT is particularly useful for trajectories planning in high-dimensional spaces or with complex obstacle spaces as it can quickly find approximate solutions to such problems. Typically, the solution produced by this algorithm is a piecewise linear path that overlooks the aircraft inability to follow instantaneous heading changes between segments. In literature, RRT is often hybridized with smoothing techniques based on Dubins circles or optimal control methods. The proposed method follows this idea, using clothoid curves to smooth the path. Clothoids, also known as Euler spirals, are mathematical curves that have a constant rate of curvature change along their length. They are widely used in various fields, including engineering, robotics, and transportation, due to their unique properties. Clothoids are particularly useful in path planning problems because they allow for smooth and continuous changes in curvature, enabling vehicles or robots to follow complex trajectories without abrupt changes in direction, which can be detrimental to performance and efficiency. The aim is to provide UAVs with the ability to navigate challenging environments while optimizing a flyable path that minimizes fuel consumption and avoids no-fly zones. In our approach, clothoid construction is integrated into an enhanced RRT procedure, with a reduction algorithm to avoid too many heading changes during flight.

Single aircraft clothoid-based path planning

To follow a sequence of waypoints, a flight trajectory can use straight and circular paths [1]. However, switching from one to the other is hard for fixed wing aircrafts because of the sudden change in yaw rate and bank angle. To track paths with continuous curvature and limits to maximum curvature and sharpness, clothoids can be used [2, 3]. These curves can achieve the desired direction with a linear relationship between curvature and arc length.

Spatial position coordinates x and y can be expressed as a function of the arc length s as follows [4]:



$$x(s) = x_0 + \int_0^s \cos\left(\frac{1}{2}\sigma\zeta^2 + \kappa_0\zeta + \psi_0\right) d\zeta \quad (1)$$

$$y(s) = y_0 + \int_0^s \sin\left(\frac{1}{2}\sigma\zeta^2 + \kappa_0\zeta + \psi_0\right) d\zeta \quad (2)$$

where σ is the sharpness, κ_0 represents the initial curvature, ψ_0 defines the initial heading and ζ is the integration variable. Multiple clothoids can be combined into a spline to create a continuous curvature path [5, 6, 7, 8] by matching the curvature at the tips of clothoid segments.

The maximum bank angle ϕ_{max} and the maximum bank angle rate $\dot{\phi}_{max}$ are important factors for setting the curvature and sharpness boundaries. The maximum path curvature depends on the aircraft speed v , the gravity acceleration g and the maximum bank angle ϕ_{max} [9]. The maximum sharpness can be obtained by taking the derivative of the curvature function with respect to time.

$$\kappa_{max} = \frac{g}{v^2} \tan(\phi_{max}) \quad (3)$$

$$\sigma_{max} = \frac{g}{v^2} \dot{\phi}_{max} \sec^2(\phi_{max}) \quad (4)$$

Being curvature a linear function with the arc length, the lowest and highest curvature values are found at the endpoints of a clothoid segment.

Rapidly exploring random tree (RRT)

In this chapter a RRT based path planning procedure is presented, combined with a reduction algorithm and clothoid smoothing curves to make the final paths more compliant with aircraft dynamics. RRT represents a wide spectrum of search algorithm extensively used in path planning [10]. Each RRT is based on a graph whose shape resembles a tree, built incrementally by adding random samples chosen from the search space. RRT is often build so that the graph tends to expand towards less explored areas; however, it is possible to properly guide the search towards specific areas of interest.

Let \mathcal{C} be the search space, α an infinite sequence of samples in \mathcal{C} and $\alpha(i)$ the i -th sample. The first vertex of the graph is q_0 and, starting from it, the tree is generated for k iterations. At every iteration a random sample is picked and linked to the nearest node of the graph, thus becoming a node itself.

To avoid too many changes of flight attitude a reduction algorithm is implemented inside the RRT. In a traditional RRT each new sample, out of the obstacle region, is linked only with the nearest node of the graph. With a reduction algorithm for each new point the most convenient path is searched; the starting point is the nearest node, then the search proceeds backwards by assigning a cost to each link between the new point and the nodes of the graph, provided the link does not enter an obstacle zone.

Only the link with the lesser cost is added to the graph and become one of its edges. During this phase the clothoids are inserted. Each edge between two nodes is composed by a linear path and two clothoids, one for each node. This is done to obtain a feasible trajectory without the need of a post processing phase.

Test case

The algorithm has been tested taking a real-world scenario. In particular, the city of Padova is considered and two of its squares, piazza Cavour and piazza degli Eremitani are chosen, respectively, as the starting point and the ending point, with a minimum height considered for the obstacles of 10 meters.

Since RRT is based on random samples, it is reasonable to expect some minor differences between different run of the algorithm, given that a solution (i.e. a path between the starting and ending points) is always found. A test was done by running the algorithm 100 times. The mean path length found was 456.62m while 200.24s was the mean computational time. On the other

hand, the minimum and maximum path length were, respectively, 417.52m and 606.34m, whereas the minimum and maximum time were, respectively, 44.04s and 806.32s. Figure 1 (Left) shows the effect of the reduction procedure. Without reduction the path (blue dashed line) would have been too long and convoluted, whereas the path obtained applying the reduction algorithm (red solid line) has just a few direction changes. In Figure 1 (Right) a detail of the smooth transition between different directions obtained with clothoid curves is shown.

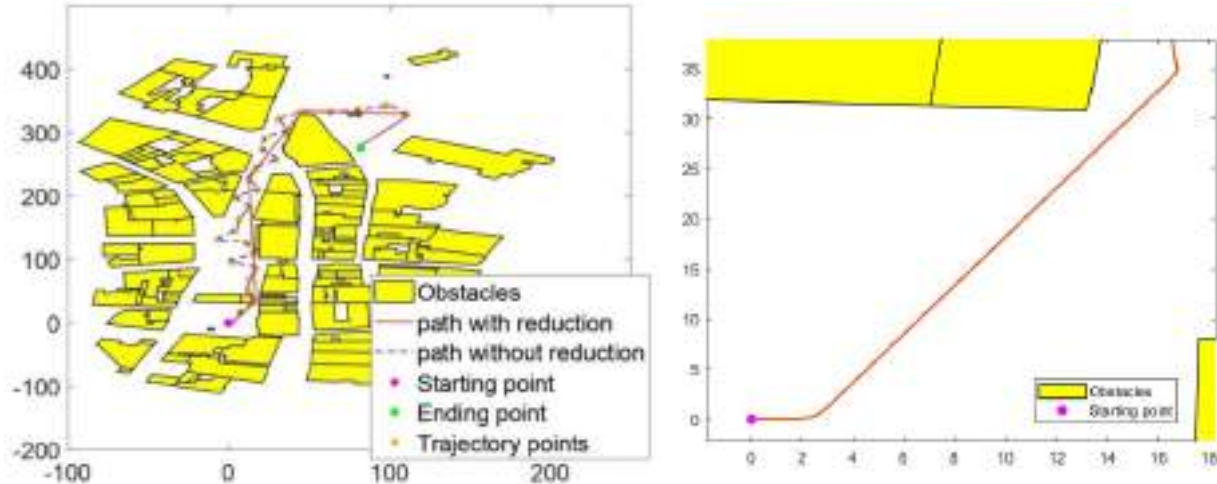


Figure 1 - (Left): comparison between paths obtained with (red solid line) and without (blue dashed line) the reduction algorithm; (Right): detail of the smooth transition between different directions obtained with clothoid curves.

Conclusions

This paper proposes an air vehicle path planner based on the Rapidly exploring random tree (RRT) algorithm combined with a clothoid-based smoothing procedure to better account for aircraft performance. The analysis carried out in the paper proved the effectiveness of the proposed procedure also in complex real-world scenarios, where the use of clothoids ensures the path compliance with aircraft dynamics. Moreover, the application of a reduction algorithm allows to avoid an excessive number of direction changes, although it increases the computational burden.

Future developments will be focused on the edge-adding procedure, being the basis of the algorithm, to guide the creation of new nodes more efficiently and minimize the length of the edges.

References

- [1] L. Blasi, E. D'Amato, M. Mattei e I. Notaro, «UAV Path Planning in 3D Constrained Environments Based on Layered Essential Visibility Graphs,» IEEE Transactions on Aerospace and Electronic Systems, pp. 1-30, 2022. <https://doi.org/10.1109/TAES.2022.3213230>
- [2] M. Al Nuaimi, Analysis and comparison of clothoid and Dubins algorithms for UAV trajectory generation, 2014.
- [3] T. Tuttle e J. P. Wilhelm, «Minimal length multi-segment clothoid return paths for vehicles with turn rate constraints,» Frontiers in Aerospace Engineering, vol. 1, 2022. <https://doi.org/10.3389/fpace.2022.982808>
- [4] E. Bertolazzi e M. Frego, «Interpolating clothoid splines with curvature continuity,» Mathematical Methods in the Applied Sciences, vol. 41, p. 1723–1737, 2018. <https://doi.org/10.1002/mma.4700>

- [5] D. S. Meek e D. J. Walton, «Clothoid spline transition spirals,» *Mathematics of computation*, vol. 59, p. 117–133, 1992. <https://doi.org/10.1090/S0025-5718-1992-1134736-8>
- [6] T. Fraichard e A. Scheuer, «From Reeds and Shepp's to continuous-curvature paths,» *IEEE Transactions on Robotics*, vol. 20, p. 1025–1035, 2004. <https://doi.org/10.1109/TRO.2004.833789>
- [7] D. K. Wilde, «Computing clothoid segments for trajectory generation,» in *2009 IEEE/RSJ International Conference on Intelligent Robots and Systems*, 2009. <https://doi.org/10.1109/IROS.2009.5354700>
- [8] S. Gim, L. Adouane, S. Lee e J.-P. Derutin, «Clothoids composition method for smooth path generation of car-like vehicle navigation,» *Journal of Intelligent & Robotic Systems*, vol. 88, p. 129–146, 2017. <https://doi.org/10.1007/s10846-017-0531-8>
- [9] T. McLain, R. W. Beard e M. Owen, «Implementing dubins airplane paths on fixed-wing uavs,» 2014.
- [10] S. M. LaValle, «Rapidly-exploring random trees : a new tool for path planning,» *The annual research report*, 1998.

Navigation services from large constellations in low earth orbit

Giovanni B. Palmerini^{1,a *} and Prakriti Kapilavai^{2,b}

¹Scuola di Ingegneria Aerospaziale, Sapienza Università di Roma, via Salaria 851 – 00138 Roma, Italy

²Dipartimento di Ingegneria Astronautica, Elettrica ed Energetica, Sapienza Università di Roma, via Salaria 851 – 00138 Roma, Italy

^a giovanni.palmerini@uniroma1.it, ^b prakriti.kapilavai@uniroma1.it

Keywords: Global Navigation Satellite Systems, Large Constellation Design, Dilution of Precision (DOP), Doppler Observable

Abstract. Very large satellite constellations in Low Earth Orbits (LEO) devoted to data broadcast could also help in providing navigation services. Lacking a specific payload onboard, the downlink can be exploited as a signal of opportunity, as an example looking at the carrier's Doppler shift. The number of sources and the short distance to users, enabling indoor positioning, are significant advantages of this option. However, recent studies confirmed that commercially-oriented designs partly miss the advantage on the number of sources by directing just one or two beams at a given time to any area on the Earth: it is enough for communication services, it is not for navigation when several signals need to be received by the user at the same time. Looking at a possible service combining downlinks from more than one system to achieve the requested minimum of four signals, this work focusses on the dilution of precision proper to the novel concept. Therefore, the paper updates previous studies - concerning the effects of the orbital configuration of a single LEO system - extending the results to the new scenario.

Introduction

Satellite-based navigation services are a technological asset everyday more present in our life. Starting from GPS, continuing with GLONASS, Galileo and Beidou, these systems, continuously updated and increasingly completed by regional additions (e.g. EGNOS, QZSS) are quickly becoming an essential infrastructure. All of these Global Navigation Satellite Systems (GNSS) work on the time-of-arrival (TOA) principle, measuring the distances from the observer to at least four signal sources. The TOA principle calls for a specialized nature of the payload, including atomic time sources of exceptional stability onboard. Furthermore, a rich control segment is requested to achieve great accuracy in position and timing [1]. GNSS constellations are mainly deployed in Medium Earth Orbits (MEO) to reduce the number of spacecraft and the effect of perturbations: their large orbital radius, between 25000 and 30000 km, makes signals reaching users quite low in power, limiting the capability to receive in certain environments.

The recent appearance of extremely large constellation, with hundreds or thousands of platforms in LEO devoted to data broadcasting, suggested alternatives to traditional systems. In fact, the widespread distribution of these satellites offers a huge number of signal sources at a far shorter distance, enabling indoor service (see [2] and references therein). The interest for LEO systems is proofed also by some emerging commercial venture explicitly devoted to navigation and timing [3]; however, the huge number of satellites requested to provide an effective service suggested the idea of using instead the rich set of sources already in orbit for successful and large data broadcast systems, so called big-LEOs. Work has been done on the way to exploit the relevant signals from big-LEOs [4] as well as on the quality of the service attainable as function of their orbital geometry [5], [6]. These studies considered that Big-LEOs, not devoted – until now – to navigation, should be better seen as sources of signals of opportunity and the service completed



by tracking and timing functions adds-on. More recent studies [7] changed the scenario making it far more complex. In fact, it has been observed that the more developed big-LEO, i.e. Starlink, provides at most two beams for any location on the Earth, with a dynamic distribution of resources focusing on current clients' demand. Indeed, the expected rich coverage is definitely apparent, ending up to be similar or even worse with respect to first generation large telecommunication constellations as Iridium or Globalstar. Notwithstanding this strong limitation, the large number of satellites into orbit still calls for the analysis of services combining signals of opportunity from different systems. This paper aims indeed to update the results referred to orbital aspects of the navigations solution presented in [6] by considering the integrated contribution of the two nowadays larger systems, i.e. Starlink and OneWeb. As the same idea could be applied with proper caution to other systems too, it is expected that findings will be useful independently on the current, still limited, development status of data broadcasting constellations. Focusing on the orbital aspects only, this approach acknowledges that several other, more important technical issues ([6], [7]) should be also considered.

Doppler as observable

Basic goal while navigating a standard terrestrial user (i.e. where high performance should not be requested) is the definition of a 4x1 set of unknowns given by the coordinates and the time

$$X = [x_u \ y_u \ z_u \ t]^T \quad (1)$$

(notice that this reduced kinematic state, missing velocity variables, perfectly fits stationary or very low-dynamics users). As recalled, traditional TOA technique is not exploitable from current LEO platforms due to the need of a specialized payload. Instead, it would be possible to extract the carrier of the (complex) modulated data broadcast signal [4]. Neglecting errors and noise, the carrier from source i recovered from a user u will be Doppler-shifted in frequency:

$$\Delta f_i = \frac{f_i}{c} (\vec{v}_i - \vec{v}_u) \cdot \vec{e}_i = \dot{\rho}_i \quad (2)$$

leading to the following relation between the range rate (expressed in Hz) and the variables:

$$\dot{\rho}_i = \frac{f_i}{c d} [(\dot{x}_i - \dot{x}_u) \cdot (x_i - x_u) + (\dot{y}_i - \dot{y}_u) \cdot (y_i - y_u) + (\dot{z}_i - \dot{z}_u) \cdot (z_i - z_u)] + \Delta f_u + \varepsilon \quad (3)$$

where $d = \sqrt{(x_i - x_u)^2 + (y_i - y_u)^2 + (z_i - z_u)^2}$ is the distance between the source and the user, Δf_u the frequency error at the receiver and ε the other errors affecting the measurement. Considering a linearization, it is possible to focus on the corrections with respect to the reference condition, obtaining a relation as

$$\Delta \dot{\rho} = H \Delta X, \quad \Delta X = [\Delta x_u \ \Delta y_u \ \Delta z_u \ \Delta f_u]^T \quad (5)$$

where the time variable has been substituted by the drift of the receiver's oscillator with respect to the nominal frequency, from which the time is computed. According to Eq.3, the terms in H will clearly differ from the ones proper of the TOA scheme (i.e., the direction cosines of the line of sight of the sources with respect to the receiver, with the last column given by unity terms). Specifically, also following [8], it is possible to write

$$H_{i1} = -\frac{f_i}{c d_i^3} (x_i - x_u) [(\dot{x}_i - \dot{x}_u)(x_i - x_u) + (\dot{y}_i - \dot{y}_u)(y_i - y_u) + (\dot{z}_i - \dot{z}_u)(z_i - z_u)] - \frac{f_i}{c d_i} (\dot{x}_i - \dot{x}_u)$$

$$H_{i2} = -\frac{f_i}{c d_i^3} (y_i - y_u) [(\dot{x}_i - \dot{x}_u)(x_i - x_u) + (\dot{y}_i - \dot{y}_u)(y_i - y_u) + (\dot{z}_i - \dot{z}_u)(z_i - z_u)] - \frac{f_i}{c d_i} (\dot{y}_i - \dot{y}_u)$$

$$H_{i3} = -\frac{f_i}{cd_i^3} (z_i - z_u) [(\dot{x}_i - \dot{x}_u)(x_i - x_u) + (\dot{y}_i - \dot{y}_u)(y_i - y_u) + (\dot{z}_i - \dot{z}_u)(z_i - z_u)] - \frac{f_i}{cd_i} (\dot{z}_i - \dot{z}_u)$$

$$H_{i4} = 1 \quad (6)$$

The relation for Doppler observables (Eq. 5) can be processed as done for pseudorange observables in TOA systems [1], to obtain an approximated error evaluation as the product of the error in measurements (σ_{UERE}) and a geometric factor known as dilution of precision (GDOP):

$$\varepsilon_{GNSS} = GDOP \sigma_{UERE} \quad (7)$$

GDOP includes the effects of the relative geometry between satellites and receiver, indeed collecting the properties of the orbital configuration of the sources. Assuming the hypotheses of a stationary geometry during the measurements, of an uncorrelated behaviour in terms of errors among satellites and of a common error statistics among them, it can be computed as:

$$GDOP = \sqrt{\text{tr}(H^T H)^{-1}} \quad (8)$$

The correctness of the hypotheses leading to GDOP definition should be re-evaluated in the case of the Big-LEO. Specifically, the first hypothesis is certainly more relevant due to the higher velocity of the lower-altitude platforms, while the second hypothesis is in some way relaxed as platforms belong to different systems. The third hypothesis should be fully re-considered as the sources could even have different possible causes of errors (as an example, they can adopt different frequencies and very different hardware), and the condition of an equal value of the overall standard deviation of the error is really difficult to judge. If, pending some specific analysis, the hypotheses can be preliminarily accepted, it is possible to numerically evaluate the GDOP in the frame of an orbital propagation for some selected BigLEOs. In such a way, GDOP can be evaluated in time for any site, defining indeed the amplification factor on the error due to the specific, considered orbital configurations.

Simulations and discussion

Figures 1-6 refer to the configurations of Starlink and OneWeb constellations, currently the two largest big-LEOs, as per Fall 2022, when Starlink included 3049 satellites in various inclinations and altitudes, and OneWeb featured 424 satellites mostly at 1200 km altitude and 87° inclination. More recent data (July 2023) provide 4347 Starlink's and 631 OneWeb's spacecraft, not really changing the rationale of the analysis. The ephemerides requested for the orbital propagation have been obtained from Two Lines Elements (TLE) sets available online [9]. It can be first confirmed that large LEO have the possibility to provide navigation services. Fig. 1 shows the coverage in Padua area (45.41N, 11.88E) limited to sources above 15° elevation. As expected, Starlink is offering most of the coverage, even if, due to the nature of the constellation, in a way which is definitely non uniform in time. Notice that the coverage from OneWeb has a significant periodic behavior, with repetitive gaps: it reflects the more ordered nature of the OneWeb architecture, with higher, less perturbed orbits and a more regular spacing of the orbital planes.

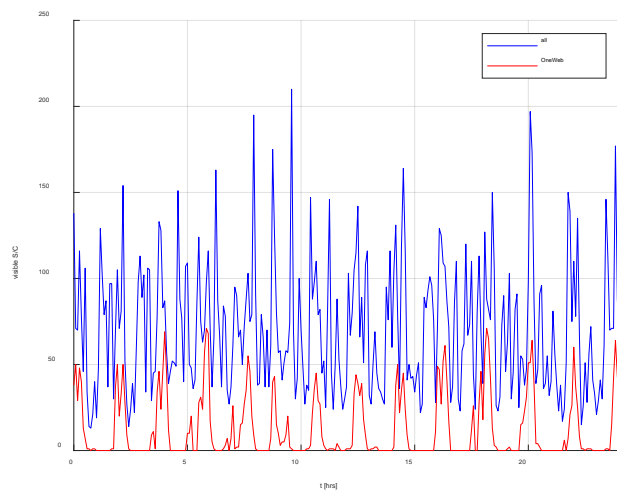


Fig. 1 – S/C above 15° from Padua (cumulative Starlink/OneWeb and OneWeb only)

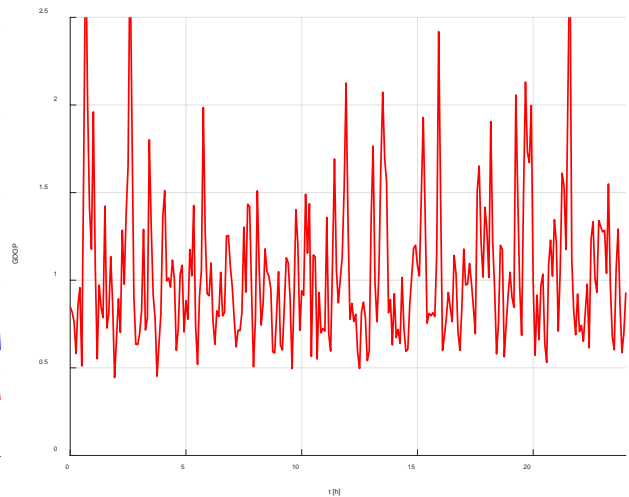


Fig. 2 – GDOP(Time of Arrival observables), full set of visible S/C

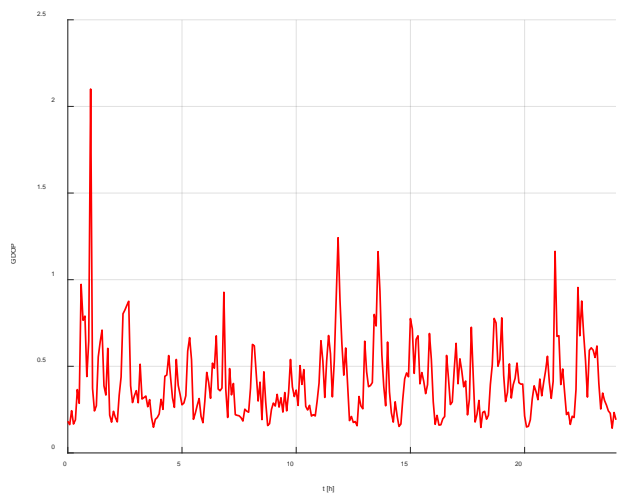


Fig. 3 – GDOP(Doppler), full set of visible S/C

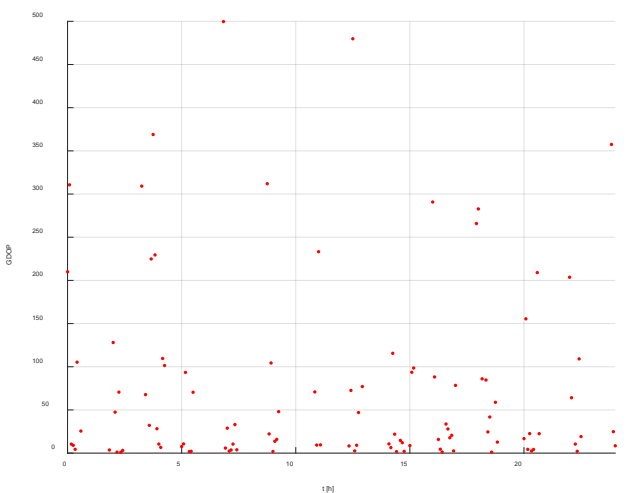


Fig. 4 – GDOP(Doppler), 4 satellites case

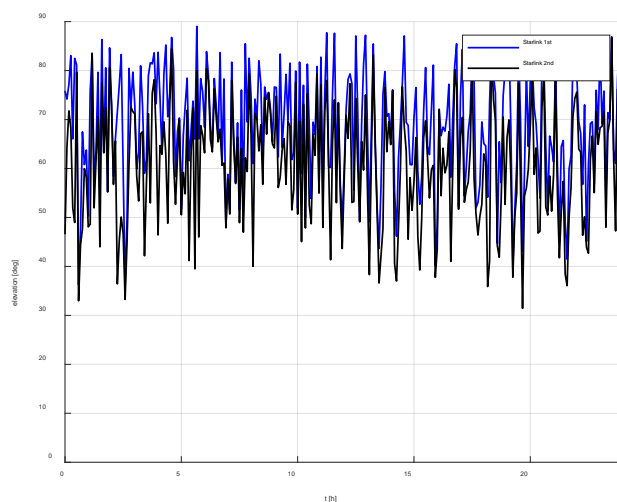


Fig. 5 – Elevation of the best and second best visible S/C of the Starlink constellation.

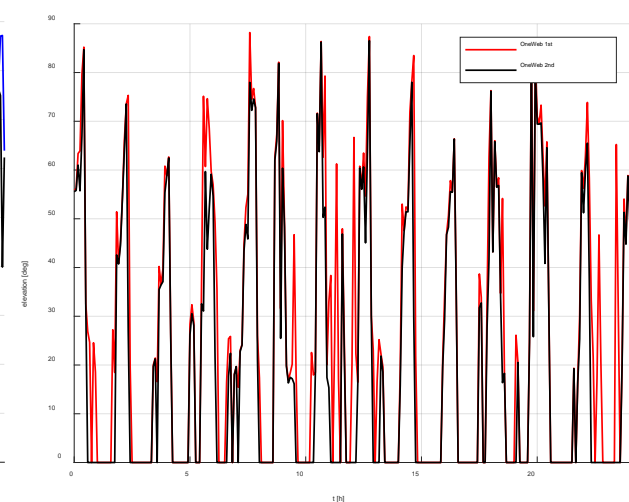


Fig. 6 – Elevation of the best and second best visible S/C of the OneWeb constellation.

Comparable plots referred to July 2023 constellation would show these gaps disappearing with at least one satellite visible above the horizon (elevation threshold equal to 0°). Fig. 2 and Fig. 3 show extremely low, and indeed good, values of GDOPs, for both time-of-arrival and Doppler observable cases, if all sources are considered: and obvious result of the rich coverage offered. If, looking at the new findings about signal distribution [7], the focus is instead on the case of 2-sources only from each constellation, Fig. 4 clarifies that spotted GDOP is higher and the coverage is non continuous. Only the Doppler observable case is here reported, but the behavior does not change for the traditional time-of-arrival case except for the magnitude of values, which is by the way not too significant as observable themselves do have a different magnitude. In fact, active satellites would be the same, i.e. the two from each constellation seen by the receiver with the higher elevation (indeed the closest one at the site). Fig. 5 clarifies that the rich, yet non regular, distribution of Starlink perfectly satisfy the coverage request, with even the second best always above 30° , and generally 40° elevation. Instead, Fig. 6 reports the spaced-out distribution of OneWeb, with the gaps where not even a satellite was available (as previously reported, OneWeb current configuration would offer a single coverage in these intervals, still not enough for a navigation service). Notice that, notwithstanding the (far from trivial) issues in capturing and elaborating different signals, the same approach could be extended to more than two constellations (as an example by adding Orbcomm or Iridium), achieving in such a way the requested coverage without gaps.

Conclusion

Big-LEOs systems can be helpful in providing navigation services in addition, or as a back-up, of existing GNSS, if considered as sources of signals of opportunity. The paper reports the evaluation of the geometry matrix for the Doppler shift observable and the simulations for the GDOP in case of two large (Starlink and OneWeb) systems, considering their current configuration and their specific limited irradiation characteristics.

References

- [1] E.D. Kaplan, C.J. Hegarthy, Understanding GPS Principles and Applications, 2nd ed., Artech House, Norwood (MA, USA), 2006.
- [2] T.G.R. Reid et al. (part 1), and Z.M. Kassas (part 2), Navigation from Low Earth Orbit, in: J. Morton, F. van Diggelen, J. Spilker, Jr., B. Parkinson (Eds.), Position, Navigation, and Timing Technologies in the 21st Century: Integrated Satellite Navigation, Sensor Systems, and Civil Applications, Volume 2, Wiley–IEEE, 2021, pp. 1359 ff.
- [3] T. Reid, Commercial Satnav from LEO, Inside GNSS, May 2022.
- [4] J.J. Khalife, Z.M. Kassas, Receiver Design for Doppler Positioning with Leo Satellites, IEEE International Conference on Acoustics, Speech and Signal Processing (ICASSP), 2019. <https://doi.org/10.1109/ICASSP.2019.8682554>
- [5] G.B. Palmerini, P. Kapilavai, Navigation Services from LEO Constellations, paper IAC-22-B2.7.8, 73rd International Astronautical Congress (IAC), Paris, France, 18-22 September 2022.
- [6] G.B. Palmerini, P. Kapilavai, Orbital Configurations for Large LEO Constellations Providing Navigation Services, IEEE Aerospace Conference Proceedings, 2023. <https://doi.org/10.1109/AERO55745.2023.10115563>
- [7] P.A. Iannucci, T.E. Humphreys, Fused Low-Earth-Orbit GNSS, IEEE Transactions on Aerospace and Electronic Systems (2020, *in press*). <http://doi.org/10.1109/TAES.2022.3180000>. <https://doi.org/10.1109/TAES.2022.3180000>
- [8] M. Di Mauro, Doppler Positioning Satellite System, EWP1959, ESA ESTEC 1997.
- [9] <https://celestrak.org/NORAD/elements/>

Aircraft Design and Aeronautical Flight Mechanics

A tool for risk assessment after a catastrophic event during suborbital flight operations

Giulio Avanzini^{1a,*}, Giovanni Curiazio^{2b}, Lorenzo Vampo^{2c}

¹ Department of Engineering for Innovation, University of Salento, Campus Ecotekne (Building "O"), Via per Monteroni, 73100 Lecce (Italy)

² Course in Engineering of Aerospace Systems, Politecnico di Bari (Centro Magna Grecia), Via del Turismo, 74123 Taranto (Italy)

^agiulio.avanzini@unisalento.it, ^bg.curiazio@studenti.poliba.it, ^cl.vampo@studenti.poliba.it

Keywords: Suborbital Flight; Risk Analysis; Space Flight Boundaries

Abstract. Suborbital flights represent a new frontier for the aerospace industry. Together with technological challenges and legal aspects, suitable tools for risk analysis are required to evaluate the potential damage produced by a catastrophic event during a suborbital flight. In particular, an explosion during the powered acceleration phase can cause dispersion of a large number of debris over a wide area, potentially harming the population living close to the launch site. A tool for the determination of the impact footprint of debris after an explosion is proposed, with the objective of supporting the definition of suitable ascent trajectories which reduce the risk for third parties below a publicly acceptable threshold. Legal aspects are also discussed.

Introduction

Suborbital flight is being envisaged as a new market for space tourism and as a means for low-cost access to microgravity environment (although for time intervals limited to a few minutes). Safety issues are a primary concern for full commercial development of this novel class of activities at the threshold between atmospheric and space flight. This is relevant not only for people on board of the suborbital vehicle, but also for third parties on the ground. Vehicle reliability should be high enough for commercial operations, with a risk level adequate for public acceptance. Simultaneously, tools are needed for evaluating the risk of third parties exposed to the passage of this novel class of vehicles in case of a (hopefully unlikely, but not impossible) catastrophic event. In this respect, also legal aspects require to be taken into due consideration, possibly requiring *ad hoc* regulations defined at a national as well as international level. During the descent phase, suborbital ballistic flight is less critical than conventional re-entry trajectories. Assume as a reference the configuration of Space Ship II, developed by Virgin Galactic: after release from its mother-plane, the vehicle accelerates by means of a solid-fuel rocket, reaching its apogee in proximity of the Kármán line at 100 km with a velocity close to zero. Thermal loads and peak values of deceleration during descent remain within bounds which does not require a heat shield, nor it produces extreme structural loads. This makes the possibility of a major catastrophic event with vehicle fragmentation less likely during this phase. Conversely, failure of the solid rocket during the ascent may result into an explosion, with vehicle fragments impacting the ground on a large area. This implies that a risk analysis for third parties on the ground requires evaluating the impact footprint of debris produced by an explosion at different points along the trajectory.

The objective of the present paper is focused on this latter issue. Several potential explosion points are evaluated along the trajectory. A cloud of fragments and velocity increments along tangential, normal to the trajectory, in the vertical plane, and transverse directions are randomly generated. A correction is applied, in order to enforce that the total linear momentum after the explosion equals the momentum of the vehicle at the instant before the explosion. The magnitude



of the increments is then scaled in order to match an estimate of the kinetic energy increase due to the energy released by the explosion. This energy is higher, at early stages of the ascent trajectory, when more unburned fuel is present in the rocket, decreasing close to zero at rocket burnout. Stemming from previous experience with risk analysis for remotely piloted vehicle operations over inhabited areas [1], statistical properties of impact footprints in terms of number of fragments per unit area and kilograms of debris per unit area are determined, together with the distance of the centroid of the footprint. Combining this information with population density in the areas possibly interested by the fallout allows one to evaluate the risk for communities and individuals in the region, making it possible to design the ascent trajectory in such a way that the probability of damage to people on the ground remains within acceptable levels.

Legal aspects

Before the end of World War II, technologies developed for long-range bomber aircraft were paving the way towards the blossoming of commercial flight. At the same time it was clear that a supranational set of regulations was required for the sake of harmonization of flight procedures, aircraft certification and crew licensing, together with other activities essential for civil commercial flight. The Convention on International Civil Aviation, usually referred to as the Chicago Convention, signed in 1944, features as many as 19 Annexes, covering issues from meteorology to accident investigation, from aircraft noise and engine emissions to safety and security aspects. Although other Conventions followed, such as the Convention on Offences and Certain Other Acts Committed on Board Aircraft in 1963 (known as the Tokyo Convention), The Hague Hijacking Convention (formally the Convention for the Suppression of Unlawful Seizure of Aircraft), signed in 1970, and The Montreal Convention (formally, the Convention for the Unification of Certain Rules for International Carriage by Air) signed in 1999, the Chicago Convention, updated in 2006, is still the backbone of international regulations for Civil Aviation.

Unfortunately, such an effort for providing an internationally recognized set of regulations for space activities has yet to be undertaken. The Outer Space Treaty, signed in 1967 [3], is an early attempt, formally accepted by all Nations with relevant space activities, which states only basic principles, such as the freedom for all Nations to access space or the impossibility to claim portion of space under a single Nation sovereignty. Coming to more specific and technically relevant issues, there is no set of space rules, which can be the counterpart of the Rules of the Air listed in Annex 2 of the Chicago Convention. As an example, the United Nations delivered guidelines for the mitigation of the danger related to the increasing number of space debris [4], but these guidelines only provide a set of non-binding recommendations, without any actual constraints (let alone, sanctions) for potentially dangerous space activities of sovereign states.

There are two major aspects that pose a serious obstacle to the development of a supranational space law. First of all, the concept of airspace extends the sovereignty of a state to the volume where aeronautical activities are carried out above its territory and an airplane can follow a trajectory which avoids the airspace of war zones, as it is currently happening over Ukraine. This is not possible in space, where orbits follow a prescribed pattern due to gravity and perturbing forces, and a continuous trajectory control is not available. Hence it is impossible to prescribe boundaries in space which follow in any form those present on the Earth surface and extended vertically for conventional air operations. A second issue is represented by the definition of an unambiguous threshold for separating the domains of atmospheric and space flight. Conventionally, the Kármán line, placed at 100 km, is often adopted as the boundary that marks the entry into space flight, but air traffic never gets even close to those altitudes, most air activities being limited to altitudes well below 30 km. Conversely, spacecraft orbit the Earth at an altitude higher than 250 km for avoiding a fast orbit decay. Conventional space vehicles rapidly cross the region between 30 and 250 km during launch and, much less frequently, reentry. The development of suborbital flight operation

will soon require to adequately regulate activities taking place in the region of space between those used for conventional air and space operations.

Model for explosion, fragmentation and fallout

Among many other aspects, tools for risk analysis are required in order to define safe operations which do not result into a hazard for communities living in the neighborhood of the spaceport. This requires the identification of an impact footprint of debris in case of a catastrophic event that causes the fragmentation of the vehicle during the powered ascent trajectory. Flight data for Virgin Galactic SpaceShip 2 were used as a reference, which allow for the determination of suitable initial conditions in terms of vehicle speed and climb rate at different altitudes.

At the time of the catastrophic event, t_0 , the velocity components of the vehicle are equal to $V_{x,0} = V_0 \cos \gamma_0$, $V_{y,0} = 0$, and $V_{z,0} = V_0 \sin \gamma_0$, with $\sin \gamma_0 = \dot{h}/V_0$. We assume that the explosion generates a cloud of N fragments. A uniform distribution of N random numbers r_k between 0 and 1 is generated. Assuming a vehicle mass of approximately $M = 4535$ kg and letting $R = \sum_{k=1}^N r_k$ and $f = M/R$, the mass of the k -th fragment is $m_k = f r_k$. Three sets of N Gaussian distributed velocity increments $\Delta v_{x,k}$, $\Delta v_{y,k}$, and $\Delta v_{z,k}$, are also generated. Provided that the momentum of fragments after t_0 must equate vehicle momentum right before t_0 , three corrections, $\Delta v_{x,C}$, $\Delta v_{y,C}$, and $\Delta v_{z,C}$ are introduced, which satisfy the relation

$$\sum_{k=1}^N m_k (\Delta v_{x,k} + \Delta v_{x,C}) = 0; \quad \sum_{k=1}^N m_k (\Delta v_{y,k} + \Delta v_{y,C}) = 0; \quad \sum_{k=1}^N m_k (\Delta v_{z,k} + \Delta v_{z,C}) = 0$$

Velocity increments are then multiplied by a factor K_E , related to the intensity of the explosion, higher, when more unburned fuel is present in the rocket, and smaller at engine shut off. Assuming an explosion intensity proportional to kinetic energy increase, K_E is obtained solving

$$\sum_{k=1}^N \mathcal{E}_k - \mathcal{E}_0 = \Delta \mathcal{E}_{expl}$$

where $\Delta \mathcal{E}_{expl}$ is the increment of kinetic energy due to the explosion, $\mathcal{E}_0 = \frac{1}{2} M V_0^2$ is the kinetic energy of the vehicle just before t_0 and the kinetic energy of the k -th fragment after t_0 is

$$\mathcal{E}_k = \frac{1}{2} m_k \left\{ [V_{x,0} + K_E (\Delta v_{x,k} + \Delta v_{x,C})]^2 + [K_E (\Delta v_{y,k} + \Delta v_{y,C})]^2 + [V_{z,0} + K_E (\Delta v_{z,k} + \Delta v_{z,C})]^2 \right\}$$

A simple ballistic trajectory is assumed after the explosion. This allows to analytically determine the time of impact on the ground of the k -th fragment, $t_{k,F}$, from the equation

$$h_0 + [V_{z,0} + K_E (\Delta v_{z,k} + \Delta v_{z,C})] t_{k,F} - \frac{1}{2} g t_{k,F}^2 = 0$$

The distance flown in the along track and cross track directions are thus respectively equal to

$$x = [V_{x,0} + K_E (\Delta v_{x,k} + \Delta v_{x,C})] t_{k,F}; \quad y = [V_{y,0} + K_E (\Delta v_{y,k} + \Delta v_{y,C})] t_{k,F}$$

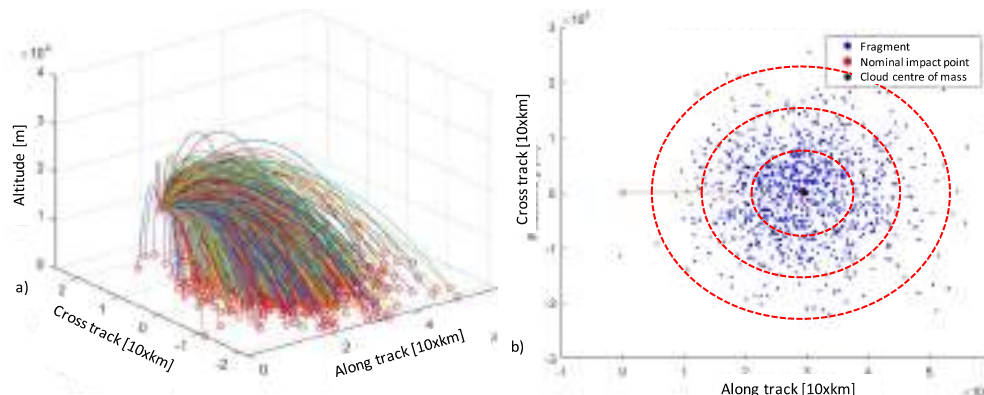


Figure 1. Fragment impact footprint: trajectories (a) and $3 - \sigma$ ellipses (b).

Results

The last equations are used for the determination of the impact footprint of the N fragments, when they hit the ground. Figures 1.a and b represent the parabolic trajectory and the impact footprint after a fragmentation due to an explosion at an altitude of 21 640 m, after 20 s from rocket engine ignition. In this preliminary analysis only the position of the fragments at impact is considered, neglecting the effects of aerodynamic drag on the resulting trajectory (hence also wind and turbulence). Regardless of these simplifying assumptions, it is possible to determine the standard deviation σ_x and σ_y in the along-track and cross-track directions of the positions of impact points with respect to the nominal point, represented by the impact point of the center of mass of the fragment cloud. The relevant data for a bivariate Gaussian distribution become thus available, which represents the possibility of the impact of a fragment in a given area. As it was done in [1], the three ellipses with 1σ , 2σ , and 3σ semiaxes contain 39%, 87%, and 99% of the fragments, respectively. These allows one to estimate the number of fragments per unit area expected to fall in each circular region. By matching these data with population density it is possible to derive the probability of hitting somebody on the ground. Future studies will address the effect of aerodynamic drag, wind and turbulence on the dispersion of the fragments. Moreover, together with the number of fragments per unit area, other risk parameters will be evaluated, such as the mass of debris per unit area and the kinetic energy of the fragments at impact, which are significantly affected by the deceleration due to drag.

Conclusions

A procedure for the determination of the impact footprint of fragments generated by the explosion of a suborbital vehicle during its powered ascent phase is outlined and some preliminary results proposed. Once the altitude and velocity profile of the mission are known, it is possible to perform a statistical analysis of the expected impact points of a cloud of debris, thus identifying the number of fragments per unit area expected to fall on the ground after a catastrophic event at a given altitude.

References

- [1] G. Avanzini, D.S. Martí nez, Risk assessment in mission planning of uninhabited aerial vehicles, *Proc. I.Mech.E. Part G: J. Aerosp. Eng.*, 233:10 (2019) 3499-3518.
<https://doi.org/10.1177/0954410018811196>
- [2] Various Authors, Convention on International Civil Aviation, Doc. 7300/9, 9th edition, International Civil Aviation Organization, 2006
- [3] Various Authors, Treaty on Principles Governing the Activities of States in the Exploration and Use of Outer Space, including the Moon and Other Celestial Bodies, United Nations Office for Disarmament Affairs, 1967
- [4] Various Authors, Space Debris Mitigation Guidelines of the Committee on the Peaceful Uses of Outer Space, United Nations Office for Outer Space Affairs, 2010

Cruising by air and sea: brief history, status and outlook for a submersible aircraft

Sergio De Rosa^{1,2,*}, Marco Cinque¹, Giuseppe Petrone^{1,2} and Leonardo Lecce³

¹ Department of Industrial Engineering, Università di Napoli Federico II, Italy

² WaveSet S.r.l., Napoli, Italy

³ Novotech S.r.l., Casoria (NA), Italy

* sergio.derosa@unina.it

Keywords: Submersible Aircraft, Innovative Design, Transitional Configuration

Abstract. Even in a post-modern era, some possible new configurations for aircrafts and spacecrafts remain to be explored. Normally, the main attention was given detaching from ground and by looking at the sky, but the sea should not be forgotten and thus the possibility to go from/to the sky to/from the sea should have to be considered. This paper is just centered around the historical first developments for the submersible aircraft and the possible future developments. Market segments for manned aircraft seems to be largely unexplored.

Introduction and Historical References

In the field of aeronautics, there exists an aircraft configuration that remains unrealized, only existing as a concept in works of fiction such as books and movies. This refers to the idea of a craft capable of cruising through both air and sea. As far back as 1904, Jules Verne, a visionary who shaped the modern era through his fictional writings, had already imagined a machine called *l'Épouvante*, which could transform and adapt for terrestrial, aerial, or marine motion [1].

Not surprisingly, there is a long-standing tradition of attempting to tackle this challenge. The emergence of unmanned vehicles has reinvigorated the research in this fascinating area [2-12]. It is worth noting that in 2008, DARPA made a statement regarding the potential design of a manned version, as shown in Figure 1, [13].

Looking at the historical context, the initial concepts for these configurations emerged in the military sectors of both the United States and Russia, which is a common trend in the history of aeronautics and aerospace [14-16].

Crouse [17] delves into the conceptual design of a submersible airplane, and notably, Longobardi's patent [18] is explicitly mentioned for proposing the incorporation of foldable wings in such a configuration. This patent, dating back to 1918, also envisioned the vehicle functioning as a car.

Manned configurations and a Possible New Market

Living in Napoli, the idea was to have a mission profile really related to the land, sky and sea in order to give a full range of opportunities for tourists. Let's image a small aircraft which can

- (i) take-off and land over a small field;
- (ii) take-off and land over a sea area and
- (iii) submerge and cruise underwater the fantastic natural and archeological scenarios in Baia or the blue sea around Capri.

The task at hand is highly demanding due to the evident conflict between the requirements for air and sea domains. However, recent indications suggest that the design issues may have been

Nonetheless, the primary challenge lies in devising and determining the feasibility of potential new configurations for the aircraft.

The Seagull

A suitable starting point for analysis could be the Seagull aircraft, recently developed by Novotech (Italy). This aircraft features a main hull, two auxiliary side floats (sponsons), and a V-tail, as depicted in Figure 2.

The Seagull is a hybrid-electric, two-seater (side by side) amphibian aircraft with a pusher propeller. It stands out for its automated folding wing system and incorporates extensive use of composite structures manufactured through eco-compatible production processes.

The Seagull program commenced in January 2018, and the production of the first prototype was completed by December 2020. As shown in Figure 2, the Seagull aircraft underwent initial water tests in the early part of 2021 to evaluate maneuverability and floating capabilities. Currently, the aircraft is in the process of obtaining flight permits from the Italian Civil Aviation Authority, while the second prototype is nearing completion.

Designed to facilitate communication between individuals and overcome existing barriers in public and private transport, the Seagull can autonomously moor at common seaports thanks to its folding wing system. The high-wing configuration enables panoramic views both in the air and over the sea, while the sponsons can be adapted and transformed into water tanks for loading and unloading. Indeed, thanks to the folding wing system, it can be moored in a common seaport.

The high-wing configuration allows the possibility to look around in both air and over sea, while the sponsons can be adapted and transformed in two tanks able to load and unload water for diving and emerging from water. Now, this vehicle in air

- can accommodate 1 passenger and 1 pilot;
- has foldable wings for increasing maneuverability in the water taxiing;
- can fly 220 km at 4000 ft altitude;

- has an estimated cruise speed of 185 km/hr;
- can accommodate up to 700 kg;
- can be equipped with hybrid electric or I.C. engine with a power up to 100 HP @5800 RPM.

It should be modified so to allow a transit under surface for about 45 minutes at a cruise speed of 4 knots (about 7 km/hr). This goal will be achieved if these design problems will be faced and solved:

- immersion and emersion phases
- additional engine/propeller for underwater cruise
- estimation of the increased weight and installed power
- management of the breathable air for the pilot and the passenger
- sealing of the interiors and the air systems (engine, electrical wiring, etc.)



Fig. 2. Seagull: (top) sketch and (bottom) picture of the prototype in marine configuration

Managing these challenges is undoubtedly complex, but it is seeming emerging from the literature that utilizing foldable wings represents the most promising starting point for exploring the possibilities.

It is also important to keep in mind that the market segment associated with this submersible aircraft is highly specific, well-defined, and somewhat limited in scope.

Concluding Remarks

As humankind sets its sights on returning to the moon and embarking on the first manned mission to Mars, along with the advent of super- and hypersonic transportation, it seems that the time is ripe for exploring underwater cruising as well, despite the design challenges that remain largely theoretical at this point.

References

- [1] Jules Verne, https://en.wikisource.org/wiki/The_Master_of_the_World, 1904

- [2] P. Marks. *A sub takes to the skies*. New Scientist, 3 July 2010: 32-35. [https://doi.org/10.1016/S0262-4079\(10\)61629-6](https://doi.org/10.1016/S0262-4079(10)61629-6)
- [3] P. Drews-Jr, et alii, *A Survey on Aerial Submersible Vehicles*. (2009). <https://www.researchgate.net/publication/263314909>
- [4] Q. Wang, et alii, *Submersible Unmanned Aerial Vehicle: Configuration Design and Analysis is Based on Computational Fluid Dynamics*, MATEC Web Conf., 95 (2017) 07023. <https://doi.org/10.1051/mateconf/20179507023>
- [5] Y. Xu, W. Son, *Conceptual design of a submersible aircraft with morphing technology*, Asian Workshop on Aircraft Design Education, AWADE 2016, Nanjing University of Aeronautics and Astronautics (NUAA).
- [6] L. Qiu, W. Song, *Efficient Decoupled Hydrodynamic and Aerodynamic Analysis of Amphibious Aircraft Water Takeoff Process*. Journal of Aircraft, 2015, 50(5): p. 1369-1379. <https://doi.org/10.2514/1.C031846>
- [7] M. Maia, et alii, *Demonstration of an Aerial and Submersible Vehicle Capable of Flight and Underwater Navigation with Seamless Air-Water Transition*, <https://arxiv.org/pdf/1507.01932.pdf>, 2015.
- [8] X. Yang, et al., *Survey on the novel hybrid aquatic-aerial amphibious aircraft: Aquatic unmanned aerial vehicle (AquaUAV)*, Progress in Aerospace Sciences. Beihang University, China, 2014. <https://doi.org/10.1016/j.paerosci.2014.12.005>
- [9] T. A. Weisshaar, *Morphing Aircraft Systems: Historical Perspectives and Future Challenges*, Journal of Aircraft, Vol. 50, No. 2 (2013), pp. 337-353. <https://doi.org/10.2514/1.C031456>
- [10] H.X. Liu. *Investigation on the mechanism of a bionic aquatic-aerial aircraft and prototype aircraft project*, Beihang University, Beijing, 2009
- [11] A. Gao, A. H. Techet, 2011. *Design considerations for a robotic flying fish*. Proceedings of Oceans 2011, Washington D.C., IEEE, pp. 1-8. <https://doi.org/10.23919/OCEANS.2011.6107039>
- [12] L. Dong et alii, *Numerical Study on the Water Entry of a Freely Falling Unmanned Aerial-Underwater Vehicle*. J. Mar. Sci. Eng., 2023. <https://doi.org/10.3390/jmse11030552>
- [13] DARPA. *Submersible Aircraft*, DARPA-BAA-09-06. October 3, 2008.
- [14] G. Petrov, *Flying submarine*, Journal of fleet, 1995 (http://www.airforce.ru/aircraft/miscellaneous/flying_submarine/index.htm)
- [15] B. Reid. *The Flying Submarine: The Story of the Invention of the Reid Flying Submarine, RFS-I*. Heritage Books, 2004
- [16] N. Polmar and K. J. Moore. *Cold War Submarines: The Design and Construction of U.S. and Soviet Submarines*. Potomac Books Inc., 2003
- [17] G. L. Jr. Crouse. *Conceptual Design of a Submersible Airplane*. Auburn University, 2010, 48th AIAA Aerospace Sciences Meeting. <https://doi.org/10.2514/6.2010-1012>
- [18] F. Longobardi. *Combination Vehicle*. US Patent #1,286,679, Issued Dec. 3, 1918. <https://patentimages.storage.googleapis.com/17/4a/c4/bbd85eb1cbb025/US1286679.pdf>

Low-boom supersonic business jet: aerodynamic analysis and mission simulation towards a CO₂ emission standard

Giacomo Richiardi^{1,a*}, Samuele Graziani^{1,b}, Oscar Gori^{1,c} and Nicole Viola^{1,d}

¹Politecnico di Torino, Torino, Italy

^a s296139@studenti.polito.it, ^b samuele.graziani@polito.it, ^c oscar.gori@polito.it,

^d nicole.viola@polito.it

Keywords: Supersonic Aircraft, Environmental Sustainability, CO₂ Emission Standard

Abstract. This study aims at investigating the aerodynamic characteristics and mission performance of a supersonic business jet at a conceptual design stage. Moreover, the environmental impact of such concept is analyzed to support the development of a potential CO₂ emissions standard for supersonic transport aircraft. The case study considered for the analysis is a supersonic business jet.

Introduction

High-speed transport has gained a renewed interest within the aerospace community during the past few decades. However, concerns about environmental impact, specifically CO₂ emissions, require a thorough analysis of aerodynamics and mission performance. This study focuses on a Mach 1.5 low-boom supersonic business jet, analyzing its aerodynamic characteristics and mission simulation to support the development of a CO₂ emissions standard for supersonic transport aircraft. CFD simulations are exploited to examine lift, drag, and pitching moment coefficients. Mission simulation is used to evaluate the performance in terms of fuel consumption and maximum range. The study also assesses CO₂ emissions standards, which are compared to subsonic limits and other supersonic concepts. The findings are expected to contribute to the design and regulation of environmentally sustainable future supersonic aircrafts.

Case Study

The case study is a Mach 1.5 low-boom supersonic business jet, 100% SAF-powered. An isometric view of the aircraft is presented in Fig. 1, while the main data are reported in Table 1.

The vehicle's configuration is derived from the *Nasa X-59 QueSST* [1], which is a configuration specifically studied for minimizing the sonic boom signature, ensuring a modest far-field pressure distribution and a reduced time distance between the two peaks of the N-wave [2].

However, to accommodate up to twelve passengers and three members of the crew, the central part of the fuselage has been enlarged, assuming a seat pitch of *1.4m*. This change in geometry generated a gap between the leading edge of the root chord of the wing and the cockpit, that were originally at the same longitudinal coordinate from the front of the vehicle, allowing the placement of the passengers' entrance door. Moreover, due to the necessity of having two thrusters for range and safety-related reasons, the two state of the art turbofan engines have been moved from the tail, under the vertical stabilizer, to the wing of the plane.





Table 1 Aircraft main data

Payload [kg]	1500
MTOW [kg]	39283
Empty weight [kg]	19048
Fuel mass [kg]	18434
Wing surface [m ²]	112
Wingspan [m]	14
Fuselage diameter [m]	2.2
Length [m]	44
Range [km]	3800
Mach cruise	1.5

Fig. 1 Isometric view of the airplane

Aerodynamic analysis

To investigate the aerodynamic characteristics of the case study, inviscid and steady *CFD* simulations are performed. Two different mesh grids are generated, one for the subsonic domain (about 5.2 million elements) and the second one for the supersonic one (about 2.8 million elements). *ANSYS ICEMCFD* [3] is used to generate the mesh grids, while *ANSYS FLUENT 2022R2* [4] is used as pre-processor and solver. An overview of the mesh grid is shown in Fig. 2.

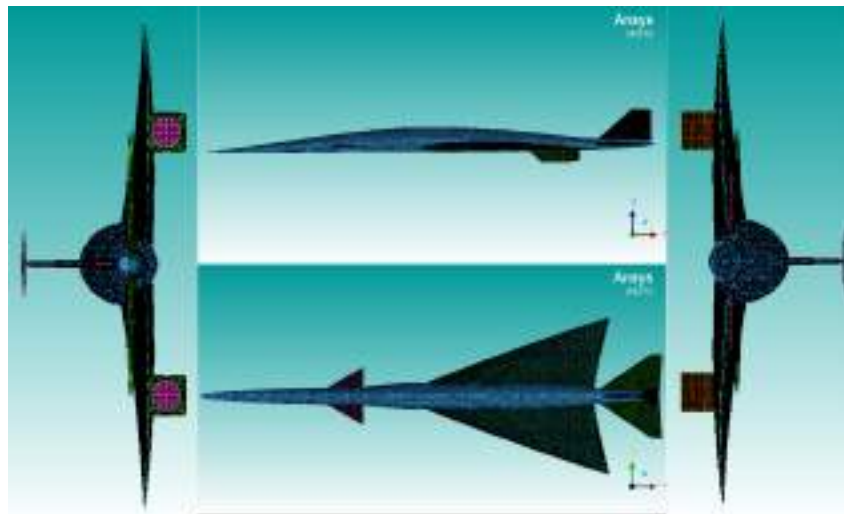


Fig. 2 Mesh grid

The resulting lift and drag coefficients as a function of the angle of attack and for different Mach numbers are reported in Fig. 3 and Fig. 4, respectively. The drag polar is also reported in Fig. 5, while the pitching moment coefficient trend for different angles of attack is shown in Fig. 6.

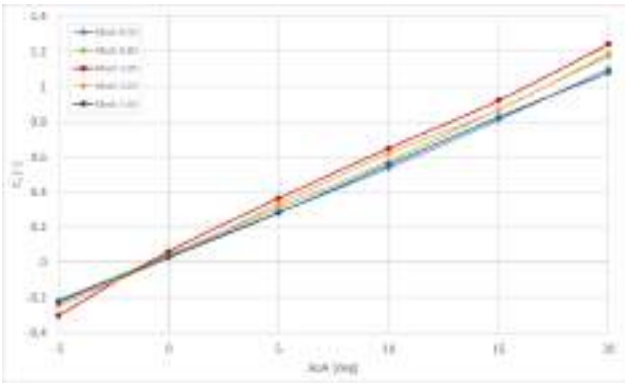


Fig. 3 Lift coefficient vs Angle of Attack for different Mach numbers

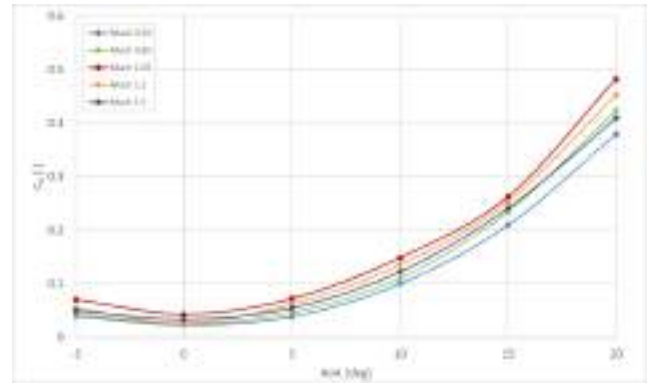


Fig. 4 Drag coefficient vs Angle of Attack for different Mach numbers

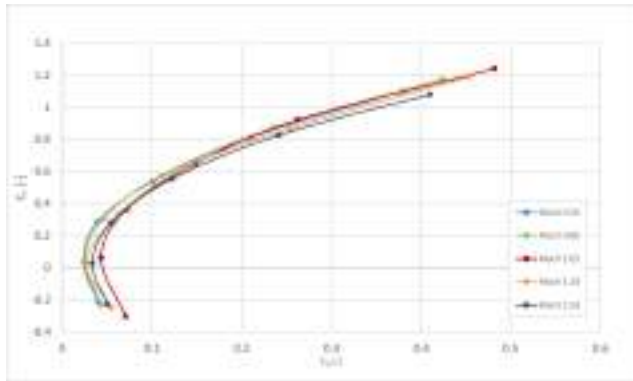


Fig. 5 Lift coefficient vs Drag coefficient for different Mach numbers

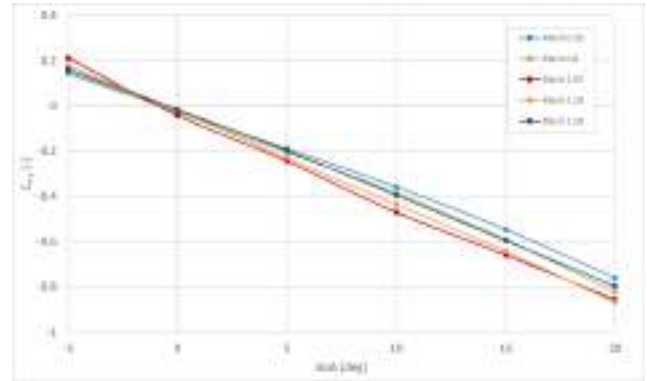


Fig. 6 Pitching moment coefficient vs Angle of Attack for different Mach numbers

Mission simulation

Once the aerodynamic database is available, the aircraft's performance along the reference mission can be studied using the ASTOS software. The main results of the mission simulation are presented in this section. The altitude and Mach profiles during the mission are reported in Fig. 7, while the total and propellant mass variation over time is shown in Fig. 8. The aircraft performs the cruise at Mach = 1.5, while the altitude varies from 14 to 17 km. The propellant on-board is sufficient to cover a range of 3800 km. The angle of attack variation during the mission is reported in Fig. 9, while the L/D ratio is shown in Fig. 10.

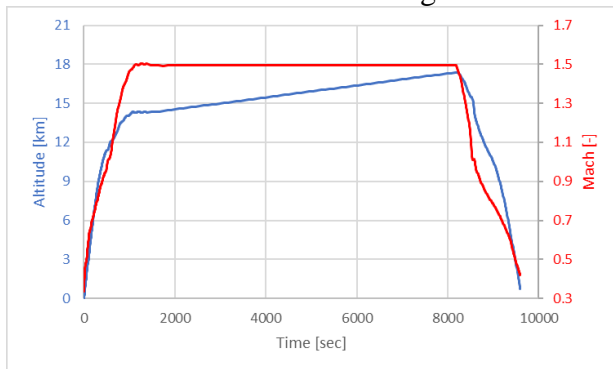


Fig. 7 Altitude and Mach profile during the mission

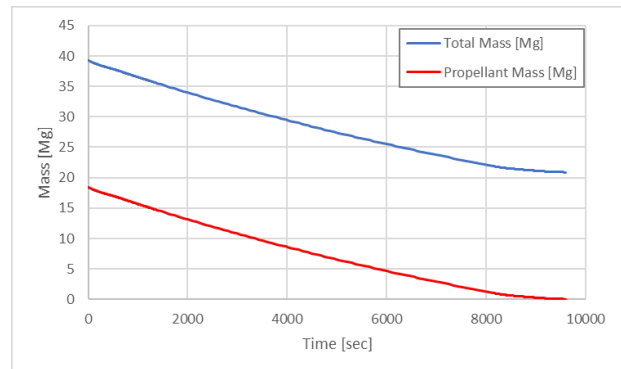


Fig. 8 Total and propellant mass variation during the mission

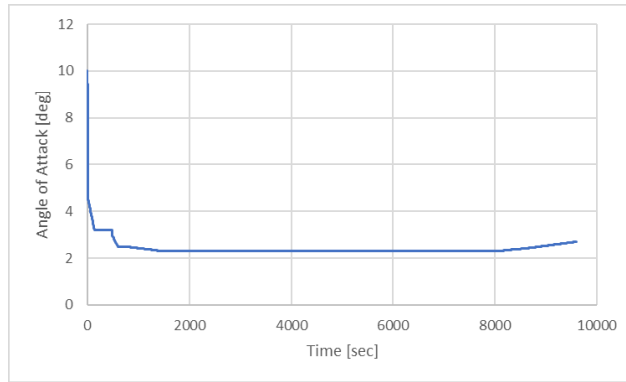


Fig. 9 Angle of attack vs time

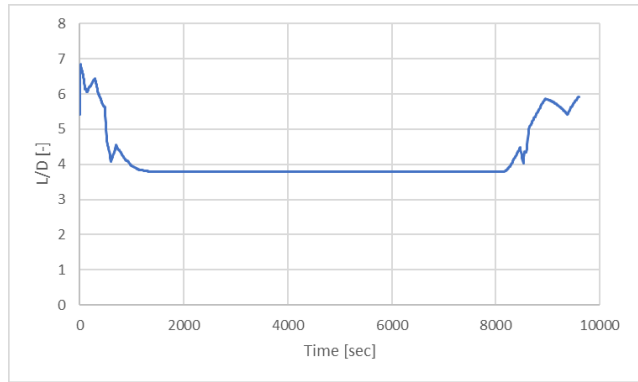


Fig. 10 Lift to Drag ratio vs time

CO₂ emission standard

The CO₂ emission standard is based on *Specific Air Range (SAR)* in cruise flight and *Reference Geometric Factor (RGF)* as presented in the following equation [5], [6]:

$$CO_2 \text{ Metric Value} = \frac{\left(\frac{1}{SAR}\right)_{avg}}{RGF^{0.24}}$$

Where *SAR* = kilometer range/unit of kg fuel is a cruise point fuel burn performance while *RGF* is just a measure of cabin size. In line with requirements for subsonic airplanes, *SAR* values were computed for 3 specific reference points, which are function of Maximum Take-Off Mass (MTOM) and are presented in Fig. 11:

1. High mass point = $0.92 \cdot MTOM$
2. Low mass point = $(0.45 \cdot MTOM) + (0.63 \cdot MTOM^{0.924})$
3. Mid mass point = average of high and low

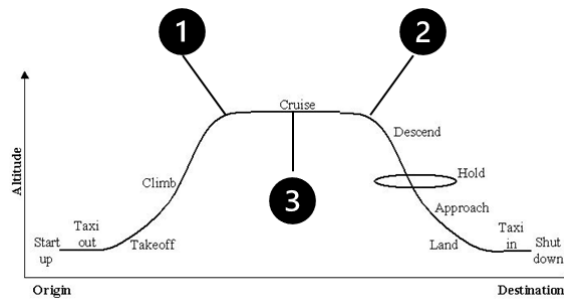


Fig. 11 Mass points for a subsonic mission

Since for supersonic aircrafts these reference points may not be representative of cruise conditions, *SAR* was evaluated at modified points, so that the high and low mass points coincided with the actual cruise start and end conditions. The evaluated CO₂ metric value for both the subsonic reference mass points and the modified ones is reported in Fig. 12. These results are compared to the CO₂ limits for subsonic aircrafts (reported with continuous lines) and to other supersonic concepts, such as a Mach 2 passenger aircraft, a Mach 1.4 and a Mach 1.6 business jet concepts.

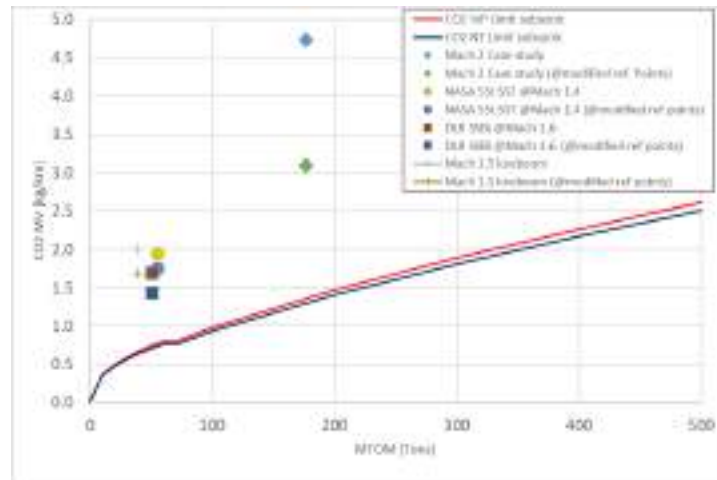


Fig. 12 CO₂ Metric value

Conclusion

A Mach 1.5 low-boom supersonic business jet concept has been analyzed in this study. The aerodynamic characteristics and mission performance of such aircraft have been computed at a preliminary design level. The capability to cover a range up to 3800 km was verified. Moreover, the Co₂ metric value has been computed according to present regulations. Eventually, a comparison with other supersonic concepts has shown that the evaluated metric value has some similarities with the values computed for those aircrafts.

References

- [1] D. Durston, "NTRS - NASA Technical Reports Server," 12 June 2022. [Online]. Available: <https://ntrs.nasa.gov/api/citations/20220009235/downloads/Supersonics%20talk%20to%20AirVenture%2C%20Durston%20July%202022%20no%20vid.pdf>.
- [2] Y. Sun and H. Smith, "Low-boom low-drag solutions through the evaluation of different supersonic business jet concepts," *The Aeronautical Journal*, vol. 124, no. 127, pp. 76-95. <https://doi.org/10.1017/aer.2019.131>
- [3] I. ANSYS, ANSYS ICEM CFD Tutorial Manual, Canonsburg, PA 15317, 2012.
- [4] I. ANSYS, ANSYS FLUENT User's Guide, Canonsburg, PA 15317, 2010.
- [5] ICAO, ICAO Annex 16 Vol III.
- [6] ICAO, "ICAO Aircraft CO₂ Emissions Standard," [Online]. Available: <https://www.icao.int/environmentalprotection/Documents/CO2%20Metric%20System%20-%20Information%20Sheet.pdf>. [Accessed 30 06 2023].

Effects of different drag laws on ice crystals impingement on probes mounted on a fuselage

A. Carozza^{1*}, P.L. Vitagliano¹, G. Mingione¹

¹Centro Italiano Ricerche Aerospaziali, Dipartimento di Meccanica dei Fluidi, via Maiorise snc, Capua, Italia

*a.carozza@cira.it

Abstract. In this work the effects of different drag laws regarding the ice crystals impingement on the fuselage of a regional aircraft are investigated. Different probes are considered on the surface of interest. Along each of these instrumentations the collection efficiency has been calculated by using a RANS structured solver named UZEN and an eulerian impingement code IMP3D, both developed internally at CIRA. The solvers are parallelized and well assessed. The computational grid has been generated with ICEM CFD. Results show the strong influence of the shape considered for the ice crystal particles. Results are shown in terms of collection efficiency and total ice mass collected.

Keywords: Impingement, Probes, Ice Crystals, Eulerian Scheme

Nomenclature

Latin symbols

A	surface area of the particle	[m ²]
d	particle diameter	[μm]
MVD	mean volume diameter	[μm]
X	x axis - coordinate of probe	[m]
Y	y axis - coordinate of probe	[m]
Z	z axis - coordinate of probe	[m]
V	ice crystals velocity	[m/s]

Greek symbols

β_{inst}	installation coefficient, ratio of the local particle concentration to the upstream particle concentration, is calculated along the direction normal to the fuselage	
y+	dimensionless wall distance	[m]
Φ	$\frac{\pi d_p^2}{A}$	[0,1]

Subscripts

p	particle
---	----------

Introduction

Icing is a major hazard for aviation safety. In flight icing is caused by water droplets that froze after impacting on aircraft surface. Ice crystals were assumed to not be an hazard for in flight aircraft operations, nevertheless in the last decades an additional risk has been identified when flying in clouds with high concentrations of ice-crystals where ice accretion may occur on warm parts of the engine core, resulting in engine incidents such as loss of engine thrust, strong vibrations, blade damage, or even the inability to restart engines. Ice crystals can also accumulate on probe: on July 2029 an A320 from Paris to Rio de Janeiro had a fatal incident, investigators demonstrated that the main cause of the incident was ice formation on pitot tube due to a very strong concentration of ice crystals, that caused provision of false information on pilots

instruments that caused the incident. Performing physical engine tests in icing wind tunnels is extremely challenging, expensive and currently limited to partial tests for engine components and in addition very few facilities are able to simulate ice crystals.

The need for the European aeronautics industry to use numerical simulation tools able to accurately predict ICI (Ice Crystal Icing) is therefore urgent and paramount, especially regarding the development of the new generation engines (UHBR, CROR, ATP) which are expected to be even more sensitive to the ICI threat than current in-service engines and for which comparative analysis methods will not be applicable any more.

MUSIC-HAIC research project is devoted to complete the development of ICI models, implement them in existing industrial 3D multidisciplinary tools, and perform extensive validation of the new ICI numerical capability through comparison of numerical results with both academic and industrial experimental data.

The resulting capability will allow the replacement of physical tests by cheaper virtual tests, which would be easier to configure and run, allowing substantial gains in development costs and more design choices to be explored and de-risked.

Most importantly, MUSIC-HAIC will provide the aeronautical sector with the confidence to move away from a step-by-step incremental evolution of engine design to a more radical breakthrough approach, because the ability to simulate the behaviour of ICI on these designs with a high degree of confidence will be available. This will reinforce the competitiveness of the European aircraft and engine manufacturers. MUSIC-HAIC will also enhance the expertise of the scientific and research community on ICI.

The scope of this work is to show the effects of the sphericity and deformation of a particle on the collection efficiency when ice crystals with high MVD are considered. At this aim different drag laws have been implemented in the Eulerian impingement code developed at CIRA IMP3D.

Methods

Since the end of the 1990s CIRA has invested in the study, development and application of numerical methods for the analysis of in flight icing conditions. Over the years, the presence of the in-house IWT facility has promoted the development of tools for supporting experiments as well as offering a viable and low-cost means to industrial customers. Besides, the participation in EU-funded projects has implied a continuous upgrade of in-house competences, allowing at the same time the monitoring of the most promising finds. Currently, almost all the project's proposals on the icing topic include, in addition to the experimental measurements, work packages dedicated to numerical analyses and/or the study of new simulation techniques.

For 2D ice accretion a very fast low-order model, was developed, the Multi-Ice tool, which solves two-dimensional potential flow. It is a classic panel method often used for the aerodynamic analysis of single- and multi-element airfoils, capable to compute impingement and ice accretion on each component. In case of 3D complex geometries two software have been developed at CIRA: UZEN and SIMBA [7][8]. They solve the compressible RANS equations on two- and three-dimensional block-structured (UZEN), and Cartesian meshes (SIMBA).

Water droplets trajectories can be calculated by using IMP3D and SIMBICE-ICE, respectively coupled to UZEN and SIMBA. They both solve the water phase by using a Eulerian approach.

For the objective of this study the in-house Eulerian solver named IMP3D is available to estimate the ice crystal impingement around 2D and 3D geometries. Several models can be used for the drag coefficient C_d of the ice crystals as a function of the particle sphericity [2] and the Reynolds number based on the particle equivalent diameter. It is crucial for the trajectories of ice crystals.

In this work the following drag correlations have been used:

1. Clift and Gauvin [1][3], with no sphericity ($\Phi=1$)
2. Ganser et al. [4],
3. Haider and Levenspiel [5],
4. Hölzer and Sommerfeld [6],
5. Nakayama et al. with the effect of the surface tension (EXTICE) on Φ .

On the other hand, evaporation and melting processes have been simulated within an Eulerian formulation by means of source terms for mass and energy transfer.

Results and Discussion

A research configuration of fuselage has been considered with five probe locations. Indeed, the probe blockage represents a risk pilots face when they travel in icing conditions. In order to have a representative overview of what recent numerical tools can predict on these instrumentations in terms of ice impingement the effects of several drag correlations are shown.

Four probes were considered: a pitot probe, a total temperature probe and two angle of attack probes. In addition, it was decided to add a fifth location for post-processing at the nose of the fuselage.

The probes locations on the aircraft nose are provided in Table 1.

Table 1: Coordinates of the probes on the fuselage configuration for post-processing purposes

	X [m]	Y [m]	Z [m]
PT2	8.9195	1.2950	-1.1660
TAT2	9.5832	0.6389	-1.9203
AoA1	13.7037	2.6183	-0.6364
AoA2	13.6996	2.5187	-0.9685
Nose	6.3825	0	0.2925

The aircraft is assumed to be flying at Mach number 0.78 at altitude 34000 ft. corresponding to an atmospheric pressure of 25000 Pa. The angle of attack is 2.05 degree (Table 2).

Table 2: Flight conditions

Altitude [ft]	Angle of attack [°]	Mach	Pressure [Pa]	Temperature [K]
34000	2.05	0.78	25000.	233.15

The impingement has been computed considering the MMD and the IWC indicated in Table 3 without considering droplets but only ice crystals.

Table 3: Ice crystal characteristics

Mean Mass Diameter [μm]	Ice Water Content [g/m^3]
336.5	1.15

Only half of the configuration is meshed and a symmetry plane condition is used. The geometry shown in the Figure 1 is meshed using ANSYS/ICEMCFD. The limits of the computational domain surrounding the geometry are located at a distance of 30 times the length of the nose. The ratio between two adjacent cells is equal or lower than 1.2. The height of the first cell at the vicinity of the wall is 0.006 mm. 50 cells have been used to capture the boundary layer characteristics near the wall and in direction perpendicular to it. A Navier-Stokes multiblock structured mesh of about 18 Million of cells and 26 blocks has been generated.

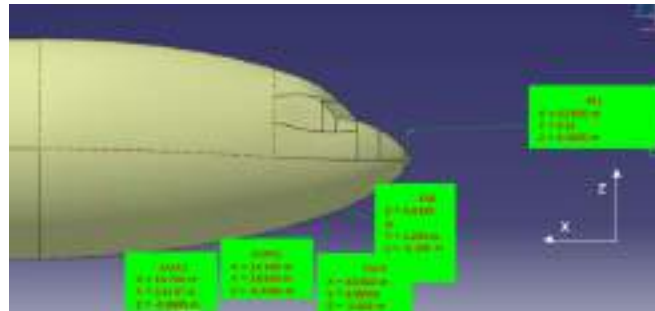


Figure 1: nose fuselage configuration

Results show that the wall y^+ lies between 0.5 and 1.0, Figure 2. Pressure coefficient is shown in Figure 3 while a collection efficiency distribution is plotted in Figure 4.

The computation of the aerodynamic flow field around the geometry made of nose and fuselage is realized using the in house UZEN Multi-block CFD simulation software. The Reynold number based on the length of the geometry nose is 5.9×10^6 . The aerodynamic flow field is computed using RANS modelling with TNT $k-\omega$ turbulence model in fully turbulent approach.

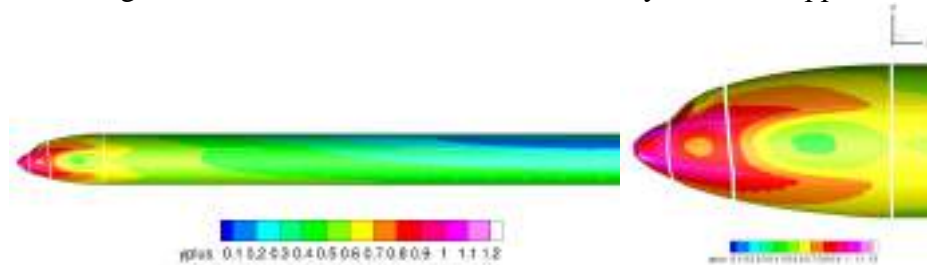


Figure 2 y^+ contours

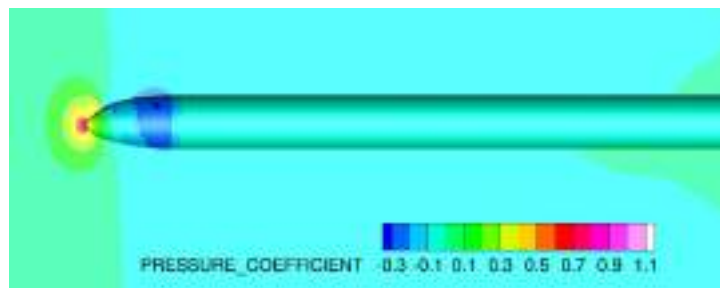
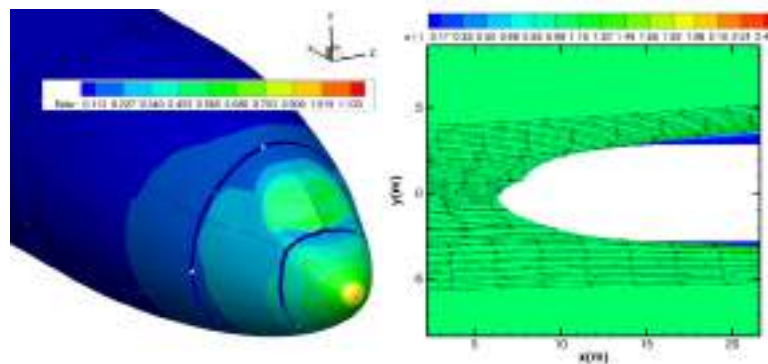


Figure 3 Pressure coefficient C_p contours



Bucknell (with fragmentation threshold)

Figure 4 Ice crystals collection efficiency using the Bucknell impact model

Observing the collection efficiency contours, see Figure 4, it is possible to state that the two zones mainly affected by the problem of ice crystals impact are the nose and the glass in front of the cabin. The maximum value of the collection efficiency does not go over 1.15 also for this simulation, while the total mass flux deposited on the surface is about 2.12 kg/s on the whole surface. In the Figure 5 the installation coefficient β_{inst} , ratio of the local particle concentration to the upstream particle concentration, IWC, is calculated along the direction normal to the fuselage, calculated by using the Bucknell model [9] including the fragmentation without re-emission are shown.

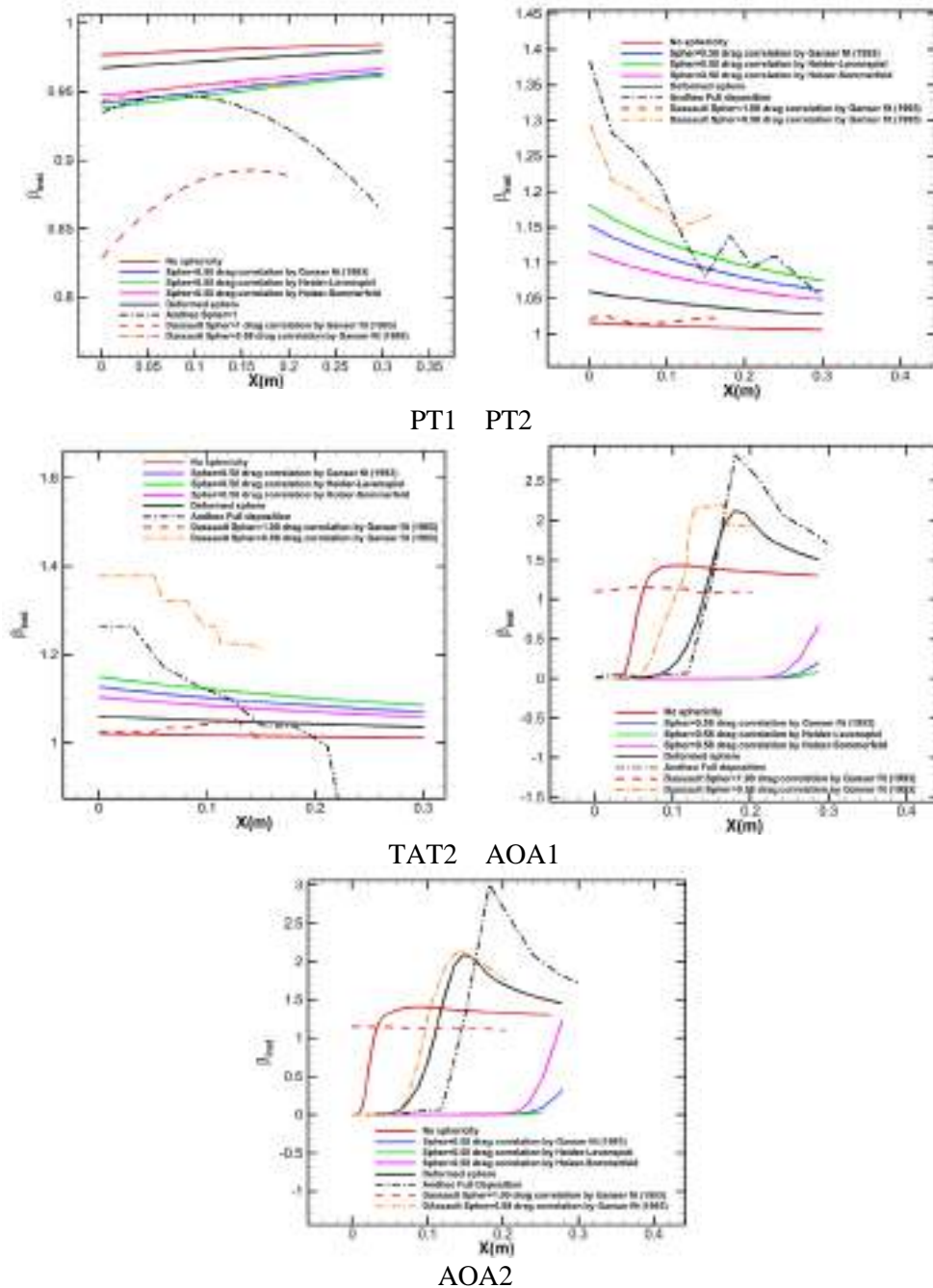


Figure 5 Installation coefficient for different shapes of ice crystals along the probes axis

The installation coefficients can be looked at. Probes AoA1 and AoA2, that are the furthest ones from the nose, show the more relevant impact of the ice crystals shapes and related correlations on the installation coefficient and mass deposition along the probes. The ice crystals current is subjected to fragmentation with a larger mass loss when compared to the case with ice crystals modelled like simple spheres. Moreover, it has to be noticed that there are strong over concentrations of ice crystal particles on the probes AoA1 and AoA2 without considering the effect of particle shape. This behaviour is inverted when probes Nose, PT2 and TAT2 are considered.

Some comparisons have also been added in the installation coefficient plots, considering data coming from Andheo or Dassault companies. They are in agreement with data computed by the authors.

Conclusions

An impingement study has been carried out on some probes installed on a fuselage. At this aim a RANS finite difference code and a Eulerian scheme impingement 3D code have been used on the same computational grid generated around a fuselage. Different drag laws related to the ice crystals injected in the domain have been adopted in order to assess the sphericity importance in the collection efficiency of a specific geometry of aeronautical interest. The main conclusions are:

1. Sphericity has a relevant rule into determining the impingement values and the shadow zones
2. It generates a variable water concentration of ice crystals along the probes axis

Acknowledgments

Authors would thank Andheo and Dassault for their support and permission to use the data collected in the Eu project Music-haic.

References

- [1] Clift R, Grace JR, Weber ME. Bubbles, drops, and particles. New York: Academic Press 1978.
- [2] E. Loth, Drag of non-spherical solid particles of regular and irregular shape, Powder Technology 182 (2008) 342–353
- [3] Clift, R., and Gauvin, W.H., The motion of particles in turbulent gas streams, Proceedings CHEMECA 1970, Butterworth, Melbourne, 1, 14-28, 1970.
- [4] G.H. Ganser, A rational approach to drag prediction of spherical and nonspherical particles, Powder Technol. 77 (1993) 143.
- [5] A. Haider, O. Levenspiel, Drag coefficient and terminal velocity of spherical and non-spherical particles, Powder Technol. 58 (1989) 63–70.
- [6] A. Hölzer, M. Sommerfeld, New simple correlation formula for the drag coefficient of non-spherical particles, Powder Technology 184 (2008) 361–365
- [7] C. Marongiu, P. Catalano, M. Amato, G. Iaccarino, U-ZEN : A computational tool solving U-RANS equations for industrial unsteady applications, 34th AIAA FluidDynamics Conference, Portland (Or), June 28 -July 1 2004, AIAA Paper 2004–2345.
- [8] Capizzano et al., CIRA contribution to the first AIAA Ice Prediction Workshop, AIAA AVIATION 2022 Forum, <https://doi.org/10.2514/6.2022-3400>
- [9] Bucknell, A., McGilvray, M., Gillespie, D., Yang, X. et al., "ICICLE: A Model for Glaciated & Mixed Phase Icing for Application to Aircraft Engines," SAE Technical Paper 2019-01-1969, 2019, <https://doi.org/10.4271/2019-01-1969>.

Morphing technology for gust alleviation: an UAS application

Fernando Montano^{1,a*}, Vincenzo Gulizzi^{1,b} and Ivano Benedetti^{1,c}

¹Department of Engineering, University of Palermo, Viale delle Scienze, Edificio 8, 90128, Palermo, Italy

^afernando.montano@unipa.it, ^bvincenzo.gulizzi@unipa.it, ^civano.benedetti@unipa.it

Keywords: Gust Alleviation, Morphing Wings, UAVs

Abstract. Atmospheric turbulence can significantly affect aircraft missions in terms of aerodynamic loads and vibration. These effects are particularly meaningful for MALE-HALE UAS because of their high aspect ratios and because of their low speed, sometimes comparable with that of the gust itself. Many studies have been conducted to reach the goal of efficient gust alleviation. A viable solution appears the application of morphing technology. However, the design of morphing aircraft is a strongly multidisciplinary effort involving different expertise from structures to aerodynamics and flight control. In this study, a multidisciplinary wing-and-tail morphing strategy is proposed for attaining gust attenuation in UAVs. The strategy is based on the combined use of: i) an automatic detection system that identifies gust direction and entity and ii) an aeroelastic model stemming from the coupling between a high-order structural model that is able to resolve the motion and the strain and stress distributions of wings with complex internal structures and a Vortex Lattice Method (VLM) model that accounts for the aerodynamics of the wing-tail system. The gust alleviation strategy employs the information from the detection system and the aeroelastic model to determine the modifications of the wing and the tail surfaces aimed at contrasting wind effects, reducing induced loads and flight path errors. Numerical results are presented to assess the capability of the framework.

Introduction

UAS flight is widely affected by atmospheric turbulence for two principal motivations: small dimensions and slow speed. This is more pregnant especially for small UAS because they flight at low altitude and have speed components comparable with atmospheric ones. For the above-mentioned reasons, it is very important to devise an efficient gust alleviation strategy to achieve safe flight conditions. This requires a two-step process: first, wind components need to be accurately identified. Second, suitable actions must be taken on the lifting surfaces to counteract the effect of the gust. Among the various approaches proposed in the literature, morphing appears a viable option to implement the latter step [1, 2].

Morphing covers all those technologies that result in a continuous shape variation of one or more elements of the aircraft during flight, aimed at obtaining maximum performance in multiple flight phases. For example, morphing technologies are increasingly applied in micro unmanned aircraft (MAVs) [3].

Airfoil modifications are morphing technologies that allow to change the camber or the thickness of the wing profile during flight.

This approach could be efficiently applied to gust alleviation modifying aerodynamic surfaces to generate aerodynamic coefficient modification to contrast wind induced ones.

Wind identification algorithm

An accurate non-linear mathematical model based on the classical rigid body equations of motion in body axes has been used [4]. The identification algorithm is based on an Extended Kalman Filter (EKF) [5, 6, 7], in which the corrector employs a set of measurements gathered in turbulent air.

The measurement vector is composed of the airspeed (V), pitch rate (q), elevation angle (θ) and the spatial coordinate of the center of mass ($x; h$).

As it is well known, the wind components modify the airspeed (V), the angle of attack (α) and the pitch rate (q) as follows:

$$V = \sqrt{(u + u_g)^2 + (w + w_g)^2} \quad (1)$$

$$\alpha = \text{atan} \frac{w + w_g}{u + u_g} \quad (2)$$

$$q = q + q_q \quad (3)$$

where (u_g, w_g, q_g) are the unknown wind components in body axes.

To tune the EKF, an optimization procedure, based on the control of prediction errors, has been used. In previous paper [6, 7] authors demonstrated the robustness of the tuning procedure, which allows to identify various kind of atmospheric disturbances with appreciable accuracy. In fact, it has been demonstrated that the algorithm is able to identify either infinite step gusts or finite ones.

Vortex Lattice Method

The aerodynamic model is based on the Vortex Lattice Method (VLM). As it is well known, VLM is a numerical method used in computational fluid dynamics based on the following assumptions:

- the flow field is incompressible, inviscid and irrotational;
- the lifting surfaces are thin, the influence of thickness on aerodynamic forces are neglected;
- the angle of attack and the angle of sideslip are both small, small angle approximation;
- the wing (or tail) is replaced by a lifting surface.

Morphing technology

In this research a combined wing and tail morphing technique is proposed. The morphing approach allows to modify wing and tail camber either simultaneously or not, in terms of both position of maximum camber and camber itself, depending on the gust entity and loads.

In Fig. °1 and Fig. °2 examples of camber modification of wing airfoil are reported.

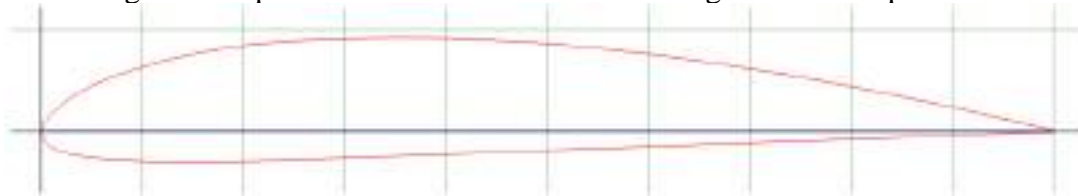


Figure 1: Clark Y wing airfoil

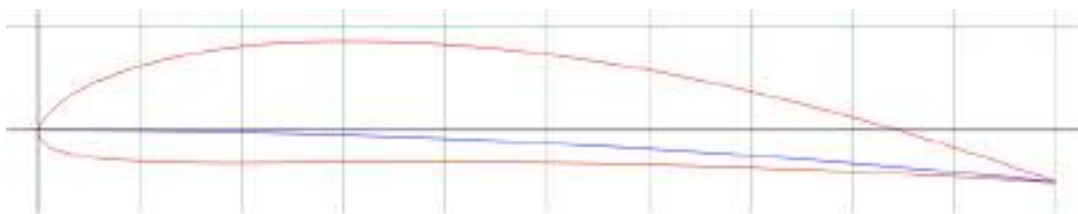


Figure 2: Clark Y wing airfoil with maximum camber variation

Simulations and results

The proposed procedure has been applied to a UAS that is a 1:5 scale model of a real airplane. Its geometrical and weight features are well known as it is the same model studied in previous applications [5, 6, 7].

Using VLM, various wind-tail geometric configurations have been modeled. These ones can be applied to the UAS during flight with morphing techniques. All obtained data has been analyzed and a polynomial relationship between the C_L and camber has been extracted.

The obtained relationship has been inserted in an algorithm developed in MATLAB environment. Such an algorithm identifies the configuration that UAS needs to reject the external disturbance.

Various simulations have been performed and results show that, when the wind identification procedure identify the external disturbance (in few time steps), the gust alleviation system comes into operation modifying aerodynamic surfaces to reach the goal of the reduction of gust induced variation of angle of attack.

Fig.°3 shows the desired flight path and the real flight path for a landing procedure in turbulent air, while Fig.°4 shows the tracking error.

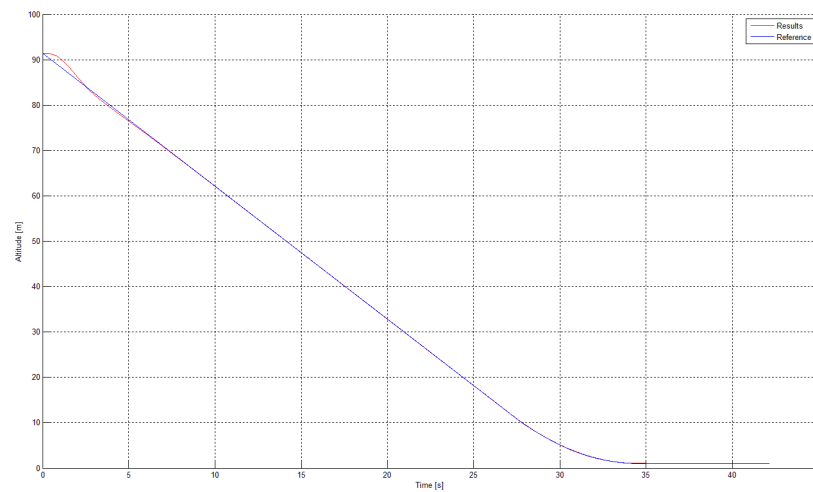


Figure 3: Desired and controlled flight path

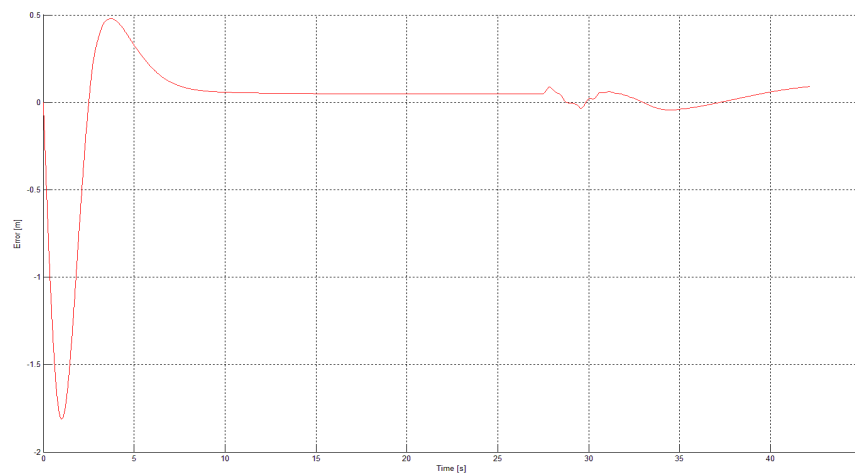


Figure 4: Tracking error

Acknowledgements

FM and IB acknowledge the support of the European Union through the FESR o FSE, PON Ricerca e Innovazione 2014-2020 - DM 1062/2021 co-funding scheme.

References

- [1] D. Li, S. Zhao, A. Da Ronch, J. Xiang, J. Drofelnik, Y. Li, L. Zhang, Y. Wu, M. Kintscher, H. P. Monner, A. Rudenko, S. Guo, W. Yin, J. Kirn, S. Storm, R. De Breuker, A review of modelling and analysis of morphing wings, *Progress in Aerospace Sciences*, 100 (2018), 46-62. <https://doi.org/10.1016/j.paerosci.2018.06.002>
- [2] R. M. Ajaj, M. S. Parancheerivilakkathil, M. Amoozgar, M. I. Friswell, W. J. Cantwell, Recent developments in the aeroelasticity of morphing aircraft, *Progress in Aerospace Sciences*, 120 (2021), 100682. <https://doi.org/10.1016/j.paerosci.2020.100682>
- [3] R. Bardera, A. Rodríguez-Sevillano, A. García-Magariño, Aerodynamic investigation of a morphing wing for micro air vehicle by means of PIV, *Fluids*, Volume 5, issue 4 191 (2020). <https://doi.org/10.3390/fluids5040191>
- [4] B. Etkin, *Dynamics of atmospheric flight*, J. Wiley & Sons, New York, 1972
- [5] C. Grillo, F. Montano, F., Automatic EKF tuning for UAS path following in turbulent air, *International Review of Aerospace Engineering*, 11(6) (2018), 241-246. <https://doi.org/10.15866/irease.v11i6.15122>
- [6] C. Grillo, F. Montano, Wind component estimation for UAS flying in turbulent air, *Aerospace Science and Technology*, Volume 93 (2019), 105317. <https://doi.org/10.1016/j.ast.2019.105317>
- [7] F. Montano, I. Benedetti, Automatic wind identification for UAS: a case study, *Modelling Progress in Aerospace Science (MPAS 2022)* in ICNAAM 2022, Heraklion, Greece, 19th-25th September 2022

Multidisciplinary design, analysis and optimization of fixed-wing airborne wind energy systems

Filippo Trevisi^{1,a,*}, Alessandro Croce^{1,b} and Carlo Emanuele Dionigi Riboldi^{1,c}

¹Department of Aerospace Science and Technology, Politecnico di Milano, Via La Masa 34, 20156 Milan, Italy

^afilippo.trevisi@polimi.it, ^balessandro.croce@polimi.it, ^ccarlo.riboldi@polimi.it

Keywords: AWE, MDAO, Wind Energy, Flight Mechanics

Abstract. Airborne wind energy (AWE) is the second generation of wind energy systems, an innovative technology which accesses the large untapped wind resource potential at high altitudes. It enables to harvest wind power at lower carbon intensity and, eventually, at lower costs compared to conventional wind technologies. The design of such systems is still uncertain and companies and research institutions are focusing on multiple concepts. To explore the design space, a new multidisciplinary design, analysis and optimization framework for fixed-wing airborne wind energy systems (T-GliDe) is being developed. In this work, the framework of T-GliDe and its problem formulation are introduced.

Introduction

Airborne Wind Energy (AWE) refers to the field of wind energy in which tethered airborne systems are used to harvest wind power at high altitudes. Compared to conventional wind energy, AWE opens new areas for energy from wind, offers increased energy generated per square kilometer, has the potential to provide energy at lower cost and has lower environmental impact [1].

Airborne Wind Energy Systems (AWESs) are typically classified based on their flight operations, which can be crosswind, tether-aligned and rotational as described by Vermillion et al. [2]. Electric power is generated with onboard wind turbines and transferred to the ground through the tether (Fly-Gen) or generated directly on the ground by a moving or fixed ground station (Ground-Gen). This work focuses on crosswind AWESs and the results are applicable to both Ground-Gen and Fly-Gen systems which are characterized by a single fixed wing.

The design of such systems is still uncertain and companies and research institutions are focusing on multiple concepts. To explore the design space and perform a robust design, the usage of MDAO techniques is crucial. This paper aims at introducing the underdevelopment MDAO framework T-GliDe (Tethered Gliding systems Design) [3] and the related problem formulation.

T-GliDe architecture and problem formulation

T-GliDe features an optimization module and an uncertainty quantification module, allowing for a number of algorithm-based design techniques (Fig. 1). The disciplines currently involved are related to the flight dynamics [4], to the optimal control [5], to the structural design, to the aerodynamics [6] and to the economics [7].



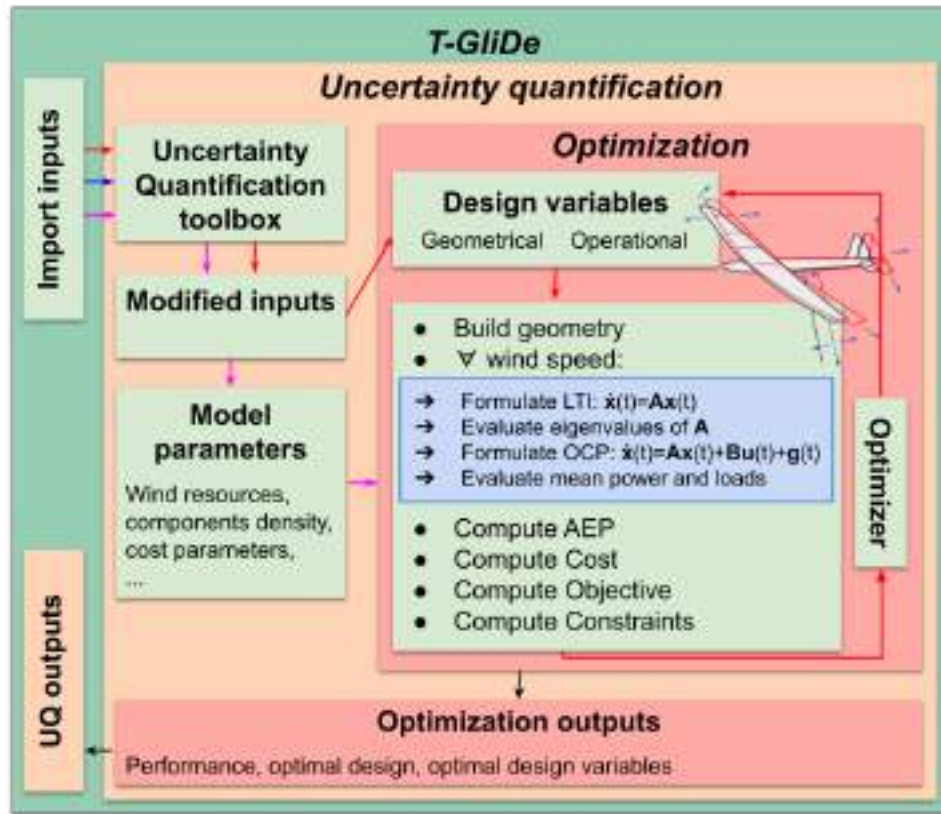


Figure 1: T-GliDe architecture.

The flight dynamics is modelled by linearizing the 6 d.o.f. equations of motion about a fictitious steady state on the circular trajectory where the fluctuating terms $\mathbf{g}(t)$ (e.g. gravity) are treated as disturbances. In this way, the dynamics is reduced to a linear time-invariant system

$$\dot{\mathbf{x}}(t) = \mathbf{A}\mathbf{x}(t) \quad (1)$$

and the eigenvalues of \mathbf{A} are designed to be stable by the optimizer.

The fluctuating terms and the control inputs $\mathbf{u}(t)$ are added to formulate the optimal control problem (OCP)

$$\dot{\mathbf{x}}(t) = \mathbf{A}\mathbf{x}(t) + \mathbf{B}\mathbf{u}(t) + \mathbf{g}(t). \quad (2)$$

Since the OCP is periodic for a steady inflow, it is solved in the frequency domain, reducing the problem size and enhancing the physical understanding of optimal trajectories. Small circular-shaped trajectories, obtained by decreasing the airborne mass, are found to be beneficial for the dynamics, as they decrease the gravitational potential energy exchange over the loop.

Tight trajectories, however, increase the aerodynamic induction and thus decrease the aerodynamic power potential. To model this, an analytical vortex-based aerodynamic model, validated with the lifting line free vortex wake method implemented in QBlade [8], is included. These disciplines are coupled to an underdevelopment economic model based on companies' data.

The optimization problem is being built with a monolithic architecture in a “all-at-once” fashion [9], employing a gradient-based algorithm with algorithm differentiation for the derivative calculation. The uncertainty quantification module allows to study how the optimization problem is influenced globally by uncertainties in the model parameters and in the modelling, to achieve a robust design.

Both Ground-Gen and Fly-Gen Airborne Wind Energy Systems (AWESs), with fixed wing, can be designed with T-GliDe. The optimal designs are expected to perform well in the energy market, while having good dynamic qualities which could enable “soft” trajectories and relieve the control system in presence of turbulence and gusts.

Summary

In this work, the underdevelopment MDAO framework T-GliDe (Tethered Gliding systems Design) and the related problem formulation are introduced. T-GliDe features an optimization module and an uncertainty quantification module, allowing for a number of algorithm-based design techniques. The disciplines currently involved are related to the flight dynamics, to the optimal control, to the structural design, to the aerodynamics and to the economics. T-GliDe will be used to explore the design space and achieve robust conceptual designs of fixed-wing crosswind AWESs.

References

- [1] Getting airborne – the need to realise the benefits of airborne wind energy for net zero. Tech. rep. BVG Associates on behalf of Airborne Wind Europe, Sept. 2022. url: <https://airbornewindeurope.org/wp-content/uploads/2023/03/BVGA-Getting-Airborne-White-Paper-220929.pdf>
- [2] Vermillion, C., Cobb, M., Fagiano, L., Leuthold, R., Diehl, M., Smith, R. S., Wood, T. A., Rapp, S., Schmehl, R., Olinger, D., and Demetriou, M.: Electricity in the air: Insights from two decades of advanced control research and experimental flight testing of airborne wind energy systems, *Annual Reviews in Control*, 52, 330–357, 2021. <https://doi.org/10.1016/j.arcontrol.2021.03.002>
- [3] Trevisi, F., Riboldi, C. E. D., and Croce, A.: Sensitivity analysis of a Ground-Gen Airborne Wind Energy System design., *Journal of Physics: Conference Series*, 2265, 042 067, 2022. <https://doi.org/10.1088/1742-6596/2265/4/042067>
- [4] Trevisi, F., Croce, A., and Riboldi, C. E. D.: Flight Stability of Rigid Wing Airborne Wind Energy Systems, *Energies*, 14, 2021. <https://doi.org/10.3390/en14227704>
- [5] Trevisi, F., Castro-Fernández, I., Pasquinelli, G., Riboldi, C. E. D., and Croce, A.: Flight trajectory optimization of Fly-Gen airborne wind energy systems through a harmonic balance method, *Wind Energy Science*, 7, 2039–2058, 2022. <https://doi.org/10.5194/wes-7-2039-2022>
- [6] Trevisi, F., Croce, A. and Riboldi, C. E. D.: Vortex model of the aerodynamic wake of airborne wind energy systems, *Wind Energy Science*, 8, 999-1016, 2023. <https://doi.org/10.5194/wes-8-999-2023>
- [7] R. Joshi, R., Trevisi, F., Schmehl, R., Croce, A., and Riboldi, C.: A Reference Economic Model for Airborne Wind Energy Systems, Presented at the Airborne Wind Energy Conference (AWEC 2021), Milan, 22-25 June, 2022. <http://resolver.tudelft.nl/uuid:3e9a9b47-da91-451b-b0af-2c26c7ff9612>
- [8] Marten, D., Lennie, M., Pechlivanoglou, G., Nayeri, C. N., and Paschereit, C. O.: Implementation, Optimization and Validation of a Nonlinear Lifting Line Free Vortex Wake Module Within the Wind Turbine Simulation Code QBlade, Volume 9: Oil and Gas Applications; Supercritical CO2 Power Cycles; Wind Energy, 2015. <https://doi.org/10.1115/GT2015-43265>
- [9] Martins, J. R. R. A. and Lambe, B.: Multidisciplinary Design Optimization: A Survey of Architectures, *AIAA Journal* 2013 51:9, 2049-2075

Artificial Intelligence Application

Refinement of structural theories for composite shells through convolutional neural networks

Marco Petrolo^{1,a,*}, Pierluigi Iannotti^{1,b}, Mattia Trombini^{1,c} and Mattia Melis^d

¹MUL2 Lab, Department of Mechanical and Aerospace Engineering, Politecnico di Torino,
Corso Duca degli Abruzzi 24, 10129, Torino, Italy

^amarco.petrolo@polito.it, ^bpierluigi.iannotti@polito.it, ^cmattia.trombini@polito.it,

^dmattia.melis@studenti.polito.it

Keywords: CUF, Structural Theories, Neural Networks, FEM

Abstract. This study examines the use of Convolutional Neural Networks (CNN) to determine the optimal structural theories to adopt for the modeling of composite shells, to combine accuracy and computational efficiency. The use of the Axiomatic/Asymptotic Method (AAM) on higher-order theories (HOT) based on polynomial expansions can be cumbersome due to the amount of Finite Element Models (FEM) virtually available and the problem-dependency of a theory's performance. Adopting the Carrera Unified Formulation (CUF) can mitigate this obstacle through its procedural and lean derivation of the required structural results. At the same time, the CNN can act as a surrogate model to guide the selection process. The network can inform on the convenience of a specific set of generalized variables after being trained with just a small percentage of the results typically required by the AAM. The CNN capabilities are compared to the AAM through the Best Theory Diagram (BTD) obtained using different selection criteria: errors over natural frequencies or failure indexes.

Introduction

The modeling of composite structures involves the balancing between accuracy and computational costs. Focusing on 2D models, using refined theories based on higher-order polynomial thickness expansions [1,2] is particularly useful in describing crucial aspects such as transverse anisotropy and shear deformability. However, their accuracy is strictly problem-dependent, and their variety is virtually unlimited.

The Axiomatic/Asymptotic Method [3-6] can be used to identify the best models for different levels of numerical complexity. The AAM starts with selecting a maximum order for the polynomial expansion and then gradually suppresses its terms. The resulting models are then compared to a reference using a control parameter, e.g., displacements or frequencies. Different theories can emerge as optimal for the same structural problem depending on the control parameter chosen. Implementing the AAM may be cumbersome due to the vast number of results required, becoming even less manageable for complex structures. The numerical efficiency of AAM can be augmented by Machine Learning (ML), more specifically through Convolutional Neural Networks [7]. By exploiting feature extraction capabilities, CNN can create surrogate models that identify the best theories at a fraction of the cost required by the AAM. This result is achieved by drastically reducing the FEM analyses needed to train the network successfully.

The new methodology presented in this paper is based on the Carrera Unified Formulation (CUF) [6] for deriving the finite element results used to train the network and to perform the comparison with the outcome expected from the AAM. For the structural case presented here, the best models were selected based on the accuracy in estimating different natural frequencies and failure indexes, with the results summarized through the Best Theory Diagram (BTD).



CUF and FEM Formulation

CUF efficiently obtains the governing equations and the finite element formulations for virtually any higher-order theory. For shells, the displacement field is expressed as

$$u(\alpha, \beta, z) = F_\tau(z)u_\tau(\alpha, \beta) \quad \tau = 1, \dots, M \quad (1)$$

$F_\tau(z)$ are the expansion functions adopted along the thickness, $u_\tau(\alpha, \beta)$ is the vector of the generalized unknown displacements, and M is the total number of expansion terms. The Einstein notation is used on τ . As an example of displacement field formulation stemming from a higher-order theory, a complete fourth-order model (E4) is reported herein extended format,

$$\begin{aligned} u_\alpha &= u_{\alpha_1} + zu_{\alpha_2} + z^2u_{\alpha_3} + z^3u_{\alpha_4} + z^4u_{\alpha_5} \\ u_\beta &= u_{\beta_1} + zu_{\beta_2} + z^2u_{\beta_3} + z^3u_{\beta_4} + z^4u_{\beta_5} \\ u_z &= u_{z_1} + zu_{z_2} + z^2u_{z_3} + z^3u_{z_4} + z^4u_{z_5} \end{aligned} \quad (2)$$

From the geometrical and constitutive relations described in [8], and by applying the Principle of Virtual Displacements (PVD), the governing equation for the free-vibration problem can be derived for the k -th layer:

$$m_{\tau i s j}^k \ddot{u}_{\tau i}^k + k_{\tau i s j}^k u_{\tau i}^k = 0 \quad (3)$$

$k_{\tau i s j}^k$ and $m_{\tau i s j}^k$ are 3x3 matrices known as fundamental nuclei of the stiffness and mass matrices, respectively. By assembling all nodes and elements and introducing the harmonic solution, the complete formulation of the eigenvalue problem can be obtained,

$$(-\omega_n^2 M + K)U_n = 0 \quad (4)$$

Using the same approach for the static case, the governing equation reads:

$$k_{\tau i s j}^k u_{\tau i}^k = p_{s j}^k \quad (5)$$

Here, $p_{s j}^k$ is the fundamental nucleus for the external mechanical load. Similarly, the well-known static problem formulation is derived through the assembly procedure.

$$KU_n = P \quad (6)$$

For a more in-depth description of the assembly procedure and other mathematical details, the reader can refer to [8].

Axiomatic/Asymptotic Method

AAM selects the optimal set of expansion terms, or generalized variables, to adopt for a specific problem configuration. The aim is to find the most convenient structural theory to provide the best accuracy at the lowest computational cost. Dealing with polynomial expansions, this procedure's first step is defining the maximum order allowed. For the work presented in this paper, a maximum order of four was considered, leading to a total amount of possible theories equal to 2^{15} . This number was reduced to 2^{12} by always considering the constant terms for each of the three displacement components. The accuracy of each model can be evaluated by choosing a reference solution, e.g., the full fourth-order expansion, E4, and a control parameter. The first one

considered in this paper was the percentage error over the single natural frequency, defined as follows:

$$\%E_{f_i} = 100 \times \frac{|f_i - f_i^{E4}|}{f_i^{E4}} \quad (7)$$

where f_i^{E4} is the i -th frequency evaluated using the reference full fourth-order Taylor expansion. The second indicator adopted was the percentage error over a failure index evaluated at a specific location in the structure. The 3D Hashin criterion [9] was selected for this purpose. For example, the percentage error over the index for the matrix tension (MT) mode is

$$\%E_{MT} = 100 \times \frac{|MT - MT^{E4}|}{MT^{E4}} \quad (8)$$

The outcome of this selection procedure is summarized by the BTD, a graphical representation of the accuracy achievable by varying the number of generalized variables adopted. Each point of the BTD corresponds to the best theory, given the number of active expansion terms.

Convolutional Neural Network

A CNN able to handle multi-dimensional inputs and outputs was used. The input is represented by the set of active generalized variables identifying a specific structural theory. This information is first encoded into a series of 0 and 1, corresponding to a deactivated and active term, respectively. An example of this procedure is presented here,

$$\begin{aligned} u_\alpha &= u_{\alpha_1} + zu_{\alpha_2} + z^4u_{\alpha_5} \\ u_\beta &= u_{\beta_1} + zu_{\beta_2} + z^3u_{\beta_4} \\ u_z &= u_{z_1} + zu_{z_2} + z^2u_{z_3} \end{aligned} \quad \Rightarrow \quad [111001010100] \quad (9)$$

Note that the three constant terms were not included in the sequence because they were always considered active. This sequence is then re-shaped into a 3x4 matrix, constituting the actual input to the network. The output consists of the percentage errors over the first ten natural frequencies or the two evaluated failure indexes. The complete architecture is presented in Table 1. The training of the network was performed only using 10% of all possible theories and related errors.

Table 1. Parameters and architecture of the adopted CNN.

Layer Type	Filters (Size) / Neurons	Activation Function
Convolutional	128 (3x3)	ReLU
Convolutional	128 (3x3)	ReLU
Convolutional	128 (3x3)	ReLU
Flatten	-	-
Dense	128	ReLU
Dense	128	ReLU
Output	10 or 2	Sigmoid

Numerical Results

A simply-supported shell with $[0^\circ/90^\circ/0^\circ]$ stacking sequence was considered. The curvature radii were kept equal along the two curvilinear coordinates α and β , imposing $R/a=5$. A thickness ratio $a/h=10$ was used, and the following material properties were employed: $E_{11}/E_{22}=25$, $G_{12}/E_{22}=G_{13}/E_{22}=0.5$, $G_{23}/E_{22}=0.2$, $\nu_{12}=\nu_{13}=\nu_{23}=0.25$. Only a quarter of the shell was modeled to reduce computational costs further. This choice required the use of symmetry boundary conditions, thus allowing to consider symmetrical vibration modes exclusively. A 4x4 mesh of Q9 elements was adopted.

Starting with the free-vibration problem, Figs. 1 and 2 show the BTDs for the first and third natural frequencies, respectively. In each of them, the results obtained from the direct application of the AAM are compared to those obtained by the CNN. Table 2 shows the best theories provided by CNN for the first five frequencies having eight active degrees of freedom; an active term is indicated by a black triangle, with their order increasing from left to right, up to the fourth.

In the case of failure indexes as control parameters, a static analysis was performed on the same structure. A bi-sinusoidal pressure of unit amplitude was applied to the top surface. Failure indexes were evaluated at the center of the top and bottom edges, for the compressive and tensile modes, respectively. Figure 3 shows the resulting BTD. In each diagram, some of the resulting best models are presented.

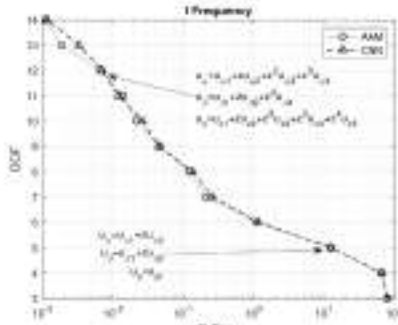


Figure 1. BTD for the 1st frequency.

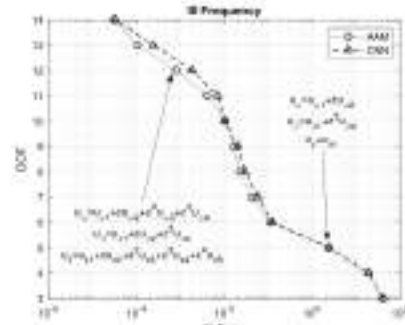


Figure 2. BTD for the 3rd frequency.

For the free-vibration case, the CNN accurately reproduced the BTD for different frequencies while also correctly providing indications regarding the relevance of specific terms. The results obtained over the failure indexes show similar levels of accuracy, with just a slight reduction when dealing with larger amounts of degrees of freedom. This behavior is related to the influence of each expansion term on the various stress components involved in the failure index estimation.

Table 2. Best models with eight active terms for the first five frequencies.

I					II					III				
u_α	▲	▲	△	▲	△	u_α	▲	▲	△	▲	△	△	△	△
u_β	▲	▲	△	▲	△	u_β	▲	▲	△	▲	△	▲	▲	△
u_z	▲	△	▲	△	△	u_z	▲	△	△	△	▲	▲	△	▲
IV					V									
u_α	▲	▲	△	▲	△	u_α	▲	▲	△	▲	△	△	△	△
u_β	▲	▲	△	▲	△	u_β	▲	▲	△	▲	△	△	△	△
u_z	▲	△	△	△	▲	u_z	▲	△	△	△	△	△	△	▲

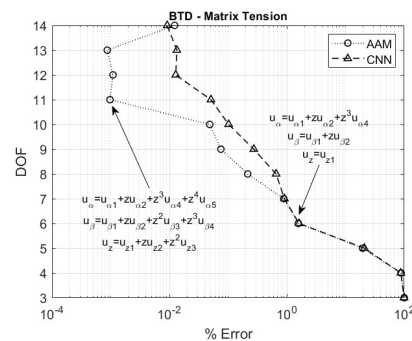
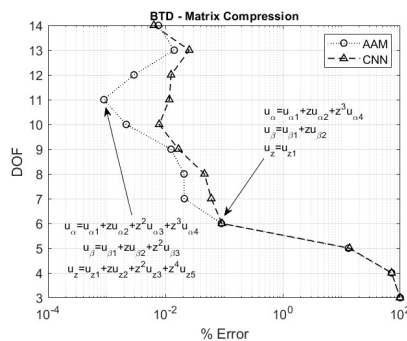


Figure 3. BTD based on the failure index

Summary

This paper explores the use of Convolutional Neural Networks in the analysis of composite shells. Focusing on higher-order theories obtained through polynomial expansions, CNN can identify the best models for various structural configurations with a fraction of the computational overhead required by the Axiomatic/Asymptotic Method. This new efficient approach can be extended to different families of problems maintaining consistent precision levels in providing the optimal modeling strategy.

References

- [1] F.B. Hildebrand, E. Reissner, G. B. Thomas, Notes on the foundations of the theory of small displacements of orthotropic shells, Technical Report, Massachusetts Institute of Technology, 1949.
- [2] J. N. Reddy, A simple higher-order theory for laminated composite plates, *Journal of Applied Mechanics*, December 1984, 51(4) 745–752. <https://doi.org/10.1115/1.3167719>
- [3] D. S. Mashat, E. Carrera, A. M. Zenkour, S. A. Al Khateeb, Axiomatic/asymptotic evaluation of multilayered plate theories by using single and multi-points error criteria, *Composite Structures*, 106 (2013) 393–406. <https://doi.org/10.1016/j.compstruct.2013.05.047>
- [4] M. Petrolo, M. Cinefra, A. Lamberti, E. Carrera, Evaluation of mixed theories for laminated plates through the axiomatic/asymptotic method, *Composites Part B: Engineering*, 76 (2015) 260–272. <https://doi.org/10.1016/j.compositesb.2015.02.027>
- [5] M. Petrolo, P. Iannotti, Best Theory Diagrams for Laminated Composite Shells Based on Failure Indexes, *Aerotecnica Missili & Spazio*, In Press. <https://doi.org/10.1007/s42496-023-00158-5>
- [6] M. Petrolo, E. Carrera, Best Spatial Distributions of Shell Kinematics Over 2D Meshes for Free Vibration Analyses, *Aerotecnica Missili & Spazio*, 99 (2020) 217-232. <https://doi.org/10.1007/s42496-020-00045-3>
- [7] S. Albawi, T. A. Mohammed, S. Al-Zawi, Understanding of a convolutional neural network, 2017 International Conference on Engineering and Technology (ICET), Antalya, Turkey, 2017. <https://doi.org/10.1109/ICEngTechnol.2017.8308186>
- [8] E. Carrera, M. Cinefra, M. Petrolo, E. Zappino, Finite element analysis of structures through unified formulation, Wiley, Chichester, 2014. <https://doi.org/10.1002/9781118536643>
- [9] Z. Hashin, Failure criteria for unidirectional fiber composites, *Journal of Applied Mechanics*, 47 (1980) 329–334. <https://doi.org/10.1115/1.3153664>

Decision trees-based methods for the identification of damages in strongly damped plates for aerospace applications

Alessandro Casaburo^{1,a,*}, Cyril Zwick^{1,b}, Pascal Fossat^{1,c}, Mohsen Ardabilian^{2,d},
Olivier Bareille^{1,e}, Franck Sosson^{3,f}

¹ Laboratoire de Tribologie et Dynamique des Systèmes (LTDS), École Centrale de Lyon, 36
Av. Guy de Collongue, 69134 Écully, France

² Laboratoire d'Informatique en Image et Systèmes d'Information (LIRIS), École Centrale de
Lyon, 36 Av. Guy de Collongue, 69134 Écully, France

³ Materials Departement, SMAC S.A.S., 66 Impasse Edouard Branly, 83079 Toulon, France

^aalessandro.casaburo@ec-lyon.fr, ^bcyril.zwick@ec-lyon.fr, ^cpascal.fossat@ec-lyon.fr,

^dmohsen.ardabilian@ec-lyon.fr, ^eolivier.bareille@ec-lyon.fr, ^ffranck.sosson@smac.fr

Keywords: Composite Plate, Vibration Test, Damage Identification, Machine Learning

Abstract. Damage identification and localization is fundamental in industrial engineering, since it helps perform corrective actions in time to reduce as much as possible system downtime, operational costs, perform quick maintenance and avoid failure. Recently, structural health monitoring has found in machine learning an extremely useful tool, making the monitoring of complex systems more manageable. In this work, composite plates manufactured with the purpose of damping vibrations in aerospace structures are experimentally tested; the strong damping suddenly reduces the vibrations, leading to responses very similar to one another, without noticeable or structured differences between undamaged and damaged plates. To overcome this issue, machine learning methods are applied. Decision trees-based methods are chosen since they provide a combination of feature selection capabilities and robust classification performances. The used methods are decision trees themselves and two boosting methods: AdaBoost and RUSBoost. All three methods perform well in identifying damaged plates, the type (thickness damage and debonding) and sub-type of damage (thickness/debonding of types A and B).

Introduction

Damage is defined as an intrinsic change in geometrical or material characteristics of an engineering system that negatively affects its operational life, safety, reliability, and performance [1]. The detection, diagnosis, and prognosis of failure can be performed through Structural Health Monitoring (SHM). The most challenging step in SHM is damage detection, interpreted as the systematic and automatic process of finding the existence of a damage. As Yuan et al. [2] report, damage detection has been performed in SHM with two approaches up to now: physics-based and data-driven. The former becomes unreliable as the system complexity increases. Improvements in computational power and advances in information and sensing technologies allow monitoring of many parameters, which opens the path to data-driven approaches. As reported by Avci et al. [3], during the last decades, Machine Learning (ML) has been widely applied to SHM, with the objective of generating models mapping input patterns in measured sensor data to output targets for damage assessment.

This work is executed in the framework of IDEFISC (IDentification de FISSures dans les Composites) project, aimed at the identification and quantification of damages in composite structures with the aid of machine learning methods. The test articles under investigation are composite plates consisting of three layers: a metallic, an elastomeric and a composite one, aiming to damp the vibrations in aerospace vehicles. Such strong damping leads to a sudden reduction of



vibration amplitude, making the responses remarkably similar between healthy and damaged plates, impairing the damage identification task. The need of fast and reliable methods paves the way to the powerful classification capabilities of machine learning methods, exploited here to distinguish which plate is damaged and which not, but also to identify the types (reduction or debonding) and sub-types (changes in position) of damages.

Theoretical framework

Three machine learning methods are used in this work. The first method is decision trees. They have a flowchart-like structure, characterized by nodes, in which a test on an attribute is executed, and branches representing the outcome of the test [4]. Each split is executed to maximize the information gain, so that the most informative feature is used to determine the status of the sample. Decision trees are attractive models because of interpretability, they allow mixing feature types, and automatic selection of the optimal feature. However, they tend to overfit when trees are too deep. A typical approach to fight overfitting is to build a more robust model through ensemble methods: they combine several weak classifiers into a meta-classifier having better generalization performances than an individual classifier alone. There are different types of ensemble learning; the one used herein is AdaBoost (Adaptive Boosting), in which several decision trees are trained in series so that, at each iteration, the training examples are re-weighted to build a more robust classifier which learns from the errors of the previous classifier in the ensemble. The final prediction combines the outputs of all the weak learners and is taken by majority voting. A modification of AdaBoost is used as third method: RUSBoost (Random UnderSampling Boosting). It is very effective when the classes are not evenly distributed in the dataset. Instead of involving the entire training set (like AdaBoost), RUSBoost takes the basic unit for sampling equal to the number of members N in the class with the smaller number of instances in the training data.

Experimental tests and application of machine learning

The plates may present two types of purposely made damages: thickness damage, and debonding between the aluminum and elastomeric layers. In turn, each damage type appears in two sub-types, labeled A and B, in which size and location of the damages change. Eleven plates are tested, in total. Three plates are undamaged, while the remaining ones have one sub-type of damage.

Global vibration tests are executed on the plates to obtain their response in both the time and frequency domains. The test articles are clamped on the short side, they are excited with a 1.5 second sweep sine signal provided through an electrodynamic shaker on the aluminum part, ranging from 5 to 5000 Hz. Velocity measurements are performed with a Polytec LDV (Laser Doppler Vibrometer) on the composite part in 187 points. The frequency response of one point is displayed in Fig. 1: there are no noticeable differences among the several damage conditions.

The dataset is made of 10 plates and 25 features, extracted from both time and frequency measurements, such as summary statistics, frequency centroid, roll-off frequency, time of flight, etc. The features are estimated for all the measured points, thus the entire training set contains 1870 observations. Three identification tasks are performed: damage identification, damage type identification, and damage sub-type identification. Thus, a label is assigned to each observation, corresponding to the status of the plate. The generalization capabilities of the machine learning methods are checked considering one plate at time for testing. Hence, all the observations of one plate are extracted from the dataset to generate the test set, and all the remaining observations, belonging to all the other plates, are shuffled and constitute the training set. This procedure is performed several times, one for each plate.

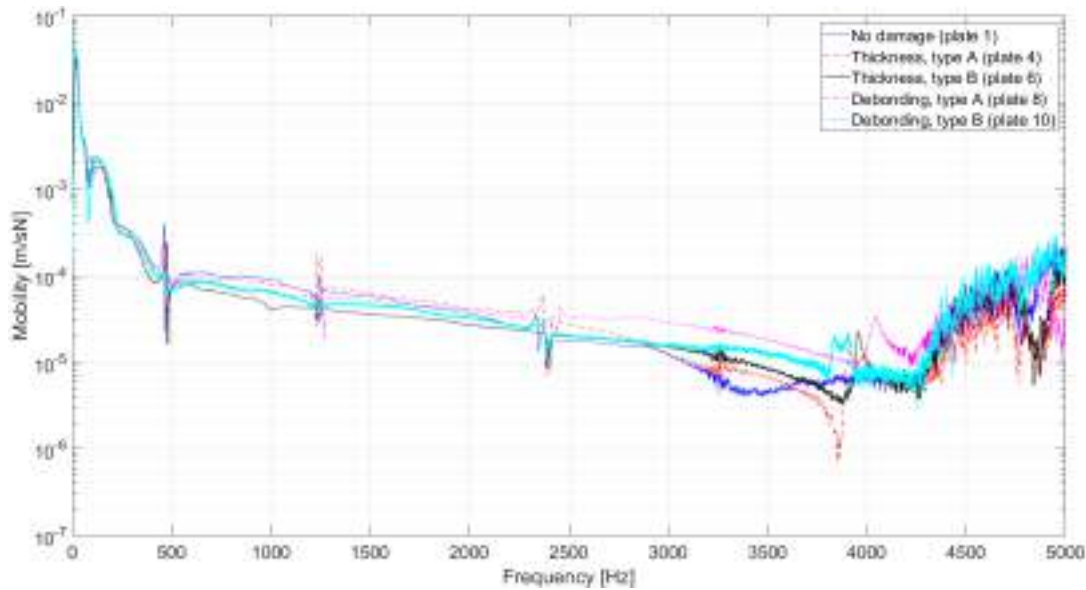


Figure 1 - Mobility of the tested plates.

For sake of brevity, the results of all the tasks are summarized in Tables 1-3, where the acronyms DT, AB, and RUSB stand for Decision Trees, AdaBoost, and RUSBoost, respectively. Plate 1, without damage, is used as baseline for the estimation of those features requiring the comparison of the test plate with an undamaged plate, thus it cannot be used for machine learning. The test plates are reported along the rows, the columns refer to the methods; each cell provides the proportion of correctly classified measurements with respect to the total number of measurements performed for each plate. The results show that not all the labels are correctly predicted: Plate 8 always provide misclassifications, and the ratio of wrong predictions increases as the complexity of the task increases. However, the overall performance capabilities are very good, since the majority of the measurements are associated with a correct prediction of the status of the plates.

Plate ID	DT	AB	RUSB
Plate 2	187/187	187/187	187/187
Plate 3	187/187	0/187	187/187
Plate 4	187/187	187/187	187/187
Plate 5	187/187	187/187	187/187
Plate 6	187/187	187/187	187/187
Plate 7	187/187	187/187	187/187
Plate 8	0/187	0/187	0/187
Plate 9	187/187	187/187	187/187
Plate 10	187/187	187/187	187/187
Plate 11	187/187	187/187	187/187

Table 1 - Classification performances of DTs, AB, and RUSB, undamaged-damaged classification task.

Plate ID	DT	AB	RUSB
Plate 2	187/187	187/187	187/187
Plate 3	187/187	0/187	187/187
Plate 4	187/187	187/187	187/187
Plate 5	187/187	187/187	187/187
Plate 6	187/187	187/187	187/187
Plate 7	187/187	187/187	187/187
Plate 8	0/187	0/187	0/187
Plate 9	187/187	187/187	187/187
Plate 10	187/187	0/187	187/187
Plate 11	0/187	187/187	187/187

Table 2 - Classification performances of DTs, AB, and RUSB, damage type identification task.

Table 3 - Classification performances of DTs, AB, and RUSB, damage subtype identification task.

Plate ID	DT	AB	RUSB
Plate 2	187/187	187/187	187/187
Plate 3	187/187	0/187	187/187
Plate 4	187/187	187/187	187/187
Plate 5	187/187	187/187	187/187
Plate 6	187/187	187/187	187/187
Plate 7	187/187	187/187	187/187
Plate 8	0/187	0/187	0/187
Plate 9	187/187	187/187	187/187
Plate 10	187/187	0/187	187/187
Plate 11	0/187	0/187	187/187

Conclusions

This work's main aim is to classify the health status of plates characterized by strong damping. Such a damping explains the responses of experimental vibration tests, remarkably similar among plates with and without damages. However, what is undistinguishable for the human eye provides valuable information for machine learning techniques. In fact, the application of three methods, namely decision trees, AdaBoost, and RUSBoost, proves that data-driven methods have excellent classification capabilities: the presence of damage itself, damage type and sub-type are correctly predicted with high accuracy. This opens the way to new, more advanced types of tasks, such as identification of smaller damages, as well as their localization.

Acknowledgments

Regarding the here-reported works, the authors would like to gratefully acknowledge for the financial support to the Region Auvergne Rhône Alpes through the scientific program RDI BOOSTER 2019 - RRA 20 010276 01 – IDEFISC.

References

- [1] D. Frangopol, J. Curley, Effects of damage and redundancy of structural reliability, journal of Structural Engineering 113(7) (1987) 1533-1549. [https://doi.org/10.1061/\(ASCE\)0733-9445\(1987\)113:7\(1533\)](https://doi.org/10.1061/(ASCE)0733-9445(1987)113:7(1533))
- [2] F. Yuan, S. Zargar, Q. Chen, S. Wang, Machine learning for structural health monitoring: challenges and opportunities, in: H. Huang (Ed.), Sensors and Smart Structures Technologies for Civil, Mechanical, and Aerospace Systems 2020, International Society for Optics and Photonics (SPIE), 2020, pp. 1-23. <https://doi.org/10.1117/12.2561610>
- [3] O. Avci, O. Abdeljaber, S. Kiranyaz, M. Hussein, M. Gabbouij, D. Inman, A review of vibration-based damage detection in civil structures: From traditional methods to machine learning and deep learning applications, Mechanical Systems and Signal Processing 147 (2021). <https://doi.org/10.1016/j.ymssp.2020.107077>
- [4] T. Mitchell, Machine Learning, McGraw-Hill Education, New York, 1997.
- [5] S. Raschka, Y. Liu, V. Mirjalili, Machine Learning with PyTorch and Scikit-Learn, Packt, Birmingham, 2022.

SHM implementation on a RPV airplane model based on machine learning for impact detection

G. Scarselli^{1,a,*}, F. Dipietrangelo^{1,b}, F. Nicassio^{1,c}

¹Department of Engineering for Innovation, University of Salento, Building O, Ekotekne,
Via per Monteroni, Lecce 73100, Italy

^agennaro.scarselli@unisalento.it, ^bflavio.dipietrangelo@unisalento.it,

^cfrancesco.nicassio@unisalento.it

Keywords: Lamb Waves, RC Airplane, Impact Detection, Machine Learning

Abstract. In this work an on-working Structural Health Monitoring system for impact detection on RC airplane is proposed. The method is based on the propagation of Lamb waves in a metallic structure on which PZT sensors are bonded for receiving the corresponding signals. After the detection, Machine Learning algorithms (polynomial regression and neural networks) are applied to the data obtained by the processing of the acquired ultrasounds in order to characterize the impacts. Furthermore, this work presents the development of a mini-equipment for acquisition and data processing based on a Raspberry Pi micro-computer.

Introduction

The localisation of impacts on aerospace structures is one of the main goals of Structural Health Monitoring (SHM) systems [1]. Even a small impact at low speed can cause a crack that can become serious damage in the long run. Therefore, SHM has reached a certain level of maturity for what concerns the choice of the best sensor network for the impact detection [2],[3]. Furthermore, other works focus on the application of machine learning (ML) algorithms for the elaboration of acquired data and the prediction of the impact localisation and of the damage [4]-[8]. In the present work a ML model is built in order to characterize the real impacts on a fixed specimen in laboratory and then it is tested in the presence of vibrations due to the engine of a balsa wood RC model of the Piper J3 CUB airplane.

Experimental Setup

In a first activity, low speed impacts were performed on a 25×25 cm specimen made of aluminium alloy with density 2700 kg/m³, elastic modulus $E = 72$ GPa, Poisson's ratio $\nu = 0.33$ and thickness = 1.2 mm. Four piezoelectric ceramic PZT Pb[Zr_xTi_{1-x}]O₃ sensors [9] (diameter equal to 10 mm) were bonded on the surface, at the four vertices of a 12.5×12.5 cm square area. The impacts were performed inside the area above by dropping a steel ball from the top of a "drop tower" built up in the AeroSpace Structural Engineering Lab (AS.S.E. Lab – University of Salento) [10]. The waves generated by the impacts were processed by a Picoscope 6402D oscilloscope connected to an Intel CPU workstation running Picoscope6 software. The processed data became the input for a ML model implemented in MATLAB, as described below. In a second activity, the vibration due to the engine were detected by the sensors bonded on the fuselage and the wings of a balsa wood RC model of the Piper J3 CUB airplane (Fig. 1). The vibrations were processed by a Pimoroni HAT Explorer Pro connected to an ARM CPU Raspberry Pi minicomputer running Python software. The processed data became the input for a ML model implemented in C++ through MATLAB Coder, run on the same Raspberry Pi.





Fig. 1. Experimental setup: acquisition of the vibrations via Raspberry Pi

Machine Learning Application

In the first activity, L impacts were performed and, for each impact, four ToFs (Time of Flight) were calculated on the basis of the Lamb waves detected by the four PZT sensors. The ToF was defined as the arrival time of A0 mode of the Lamb wave to a sensor, in the range 0-40 kHz, where the A0 mode is dominant, while the S0 can be considered neglectable [11-12]. The ToF was calculated by evaluating the Short Time Fourier Transform (STFT) of the signals in the range 0-40 kHz. Because of the absence of an absolute clock signal, the differences t_1, t_2, t_3 between the ToFs at three sensors and the ToF at one reference sensor were chosen as the features for the ML application. After the evaluation of the ToFs, a dataset was built, made of L rows corresponding to the samples (impacts points) and five columns containing, for each sample, the actual coordinates (x,y) and the three ToF differences t_1, t_2, t_3 . Two supervised ML algorithms, polynomial regression (PR) and artificial neural network (ANN), were applied to this dataset, in order to build models able to predict the position of an unknown impact, and to identify the best one. Considering a PR algorithm, the coordinates (x,y) of the impact are polynomial functions of the three ToF differences t_1, t_2, t_3 . The building of the model consists of identifying the degree d and the coefficients θ in order to best fit a set of given data:

$$x = \theta_{x_0} + \sum_{i=1}^3 \theta_{x_i} t_i + \sum_{j=1}^3 \sum_{k=1}^3 \theta_{x_{jk}} t_j t_k + \dots \quad (1)$$

$$y = \theta_{y_0} + \sum_{i=1}^3 \theta_{y_i} t_i + \sum_{j=1}^3 \sum_{k=1}^3 \theta_{y_{jk}} t_j t_k + \dots \quad (2)$$

Fixing the polynomial degree d and extending the above equations to L impacts, it is possible to use the matrix form:

$$\mathbf{U} = \mathbf{T}\mathbf{B} \quad (3)$$

where: \mathbf{U} is $L \times 2$ matrix, in which the columns contain the coordinates for the L impacts respectively; \mathbf{T} is $L \times p$ matrix, in which the p columns contain the so-called polynomial features (ToF differences, their power and relative cross multiplication); \mathbf{B} is $p \times 2$ Design Matrix of weight coefficients θ . A subset of M impacts was used as training data, in order to calculate the design matrix \mathbf{B} as specified in [13]. The model was validated by estimating the Mean Radial Error (MRE) over the M training data, the N test and total L data, where the Radial Error (RE) was defined as the Euclidean distance between the actual coordinates (x_i, y_i) and the coordinates (\bar{x}_i, \bar{y}_i) calculated by the algorithm for the i^{th} impact. Considering an ANN, the coordinates (x,y) of the impact are calculated in the basis of the three ToF differences t_1, t_2, t_3 by computations in succession through connected nodes called neurons. Each neuron performs the computation of an intermediate output

z using the input vector t , the vector of weights w and the vector of biases b and the computation of the output a as an activation function g (a linear function in a regression problem, like a *sigmoid* one) of z :

$$z = w^T t + b \quad (4)$$

$$a = g(z) \quad (5)$$

The neurons are aggregated into layers and a shallow neural network (SNN) was chosen, consisting of only one hidden layer. As for PR, a subset of M impacts was used for the training phase of the network, that consists of an iterative procedure in order to set the weights w and the biases b of each neuron. For this procedure, three learning algorithms were compared: Levenberg-Marquardt, Bayesian Regularization and Scaled Conjugate Gradient [14]-[16]. As for PR, the model was validated by estimating the Mean Radial Error (*MRE*).

Analysis and Results

About the PR, in order to generalise the model, the calculation of B and the corresponding *MRE* was performed by the mean in a *K-Fold* cross validation procedure, considering the polynomial degrees from 1 to 7 and, for each degree, 5 different combinations of training/test sets with an 80/20 ratio. In this calculation, L (total number of impacts) was equal to 167, M (number of training impacts) was equal to 134, N (number of test impacts) was equal to 33. The best model, in terms of generalising, was chosen considering both minimum total *MRE* and minimum gap between training and test *MREs*: this condition occurred with degree equal to 3. Moreover, the threshold 110 appeared to be the best training size: for bigger values of size there was no littler *MRE*. After the evaluation of the best degree and training size, 50 test cases were implemented, with a main result in terms of *MRE* on the entire dataset equal to **1.50** mm. About the SNN, the performances were evaluated considering all the three learning algorithms above, increasing the complexity of the model in terms of number of neurons in the hidden layer (10, 20, 30, 40, 50). The increasing in neurons number did not lead to a significant improvement of *MRE*, while the best training algorithm was the Bayesian Regularization. After the evaluation of the best neurons number and training algorithm, 50 test cases were implemented in MATLAB [17], with a training/test ratio equal to 70/30 ($L = 167$, $M = 117$, $N = 50$) and a main result in terms of *MRE* on the entire dataset equal to **1.20** mm. In a second activity, the vibrations due to the engine of a balsa wood RC model were acquired and processed by a Pimoroni HAT Explorer Pro connected to an ARM CPU Raspberry Pi minicomputer. The processed waveforms were used to reproduce the same vibrations on the 25×25 cm specimen using a LMS Test Lab shaker. The best ML model (based on SNN algorithm) trained and built during the first activity was then tested in presence of vibrations, obtaining a similar *MRE*. The ML model was implemented in C++ through MATLAB Coder, run on the same Raspberry Pi.

Conclusions

This work focused on the implementation of a SHM system on a balsa wood RC model of the Piper J3 CUB airplane. A machine learning model able to predict the location of low-speed impacts on aluminium plate was built and it was tested in the presence of the vibrations due to the engine of the airplane model. The best algorithm was found to be a shallow neural network trained with Bayesian Regularization procedure. The best *MRE* value was equal to 1.20 mm, configuring the model with a 70% training sample ratio and 10 hidden neurons, and a similar *MRE* was calculated in the presence of the vibrations. The results can be considered excellent, because the mean radial error falls in an acceptable range if compared to the size of the plates. Furthermore, this work presents the development of two innovative mini-equipment: (i) impact detection and wave acquisition system via Pimoroni HAT Explorer Pro; (ii) data processing and prediction via ML

learning software running on a Raspberry Pi micro-computer. These two mini-systems can be considered very efficient because of their performance in terms of precision and for their little size, that allows to install it on unmanned aerial vehicles.

References

- [1] V. Giurgiutiu, "Structural health monitoring (SHM) of aerospace composites," *Polymer Composites in the Aerospace Industry*, pp. 491–558, Jan. 2020. <https://doi.org/10.1016/B978-0-08-102679-3.00017-4>.
- [2] S. Carrino, A. Maffezzoli, and G. Scarselli, "Active SHM for composite pipes using piezoelectric sensors," *Mater Today Proc*, vol. 34, pp. 1–9, 2019. <https://doi.org/10.1016/J.MATPR.2019.12.048>.
- [3] F. Nicassio, S. Carrino, and G. Scarselli, "Elastic waves interference for the analysis of disbands in single lap joints," *Mech Syst Signal Process*, vol. 128, pp. 340–351, Aug. 2019. <https://doi.org/10.1016/J.YMSSP.2019.04.011>.
- [4] L. Capineri and A. Bulletti, "Ultrasonic Guided-Waves Sensors and Integrated Structural Health Monitoring Systems for Impact Detection and Localization: A Review," *Sensors* 2021, Vol. 21, Page 2929, vol. 21, no. 9, p. 2929, Apr. 2021. <https://doi.org/10.3390/S21092929>.
- [5] N. D. Boffa, M. Arena, E. Monaco, M. Viscardi, F. Ricci, and T. Kundu, "About the combination of high and low frequency methods for impact detection on aerospace components," *Progress in Aerospace Sciences*, vol. 129, p. 100789, Feb. 2022. <https://doi.org/10.1016/J.PAEROSCI.2021.100789>.
- [6] D. F. Hesser, G. K. Kocur, and B. Markert, "Active source localization in wave guides based on machine learning," *Ultrasonics*, vol. 106, Aug. 2020. <https://doi.org/10.1016/j.ultras.2020.106144>.
- [7] S. Carrino, F. Nicassio, and G. Scarselli, "Development and application of an in-flight structural health monitoring system," in *Proceedings of Meetings on Acoustics*, 2019, vol. 38, no. 1. <https://doi.org/10.1121/2.0001177>.
- [8] R. Gorgin, Z. Wang, Z. Wu, and Y. Yang, "Probability based impact localization in plate structures using an error index," *Mech Syst Signal Process*, vol. 157, Aug. 2021. <https://doi.org/10.1016/j.ymssp.2021.107724>.
- [9] "Piezoelectric Discs." <https://www.physikinstrumente.com/en/products/piezoelectric-transducers-actuators/disks-rods-and-cylinders/piezoelectric-discs-1206710/#downloads> (accessed Mar. 01, 2022).
- [10] "<https://asselab.unisalento.it/en/>."
- [11] G. B. Santoni, L. Yu, B. Xu, and V. Giurgiutiu, "Lamb Wave-Mode Tuning of Piezoelectric Wafer Active Sensors for Structural Health Monitoring," *J Vib Acoust*, vol. 129, no. 6, pp. 752–762, Dec. 2007. <https://doi.org/10.1115/1.2748469>.
- [12] P. M. Schindler, R. G. May, R. O. Claus, and J. K. Shaw, "Location of impacts on composite panels by embedded fiber optic sensors and neural network processing," *Smart Structures and Materials 1995: Smart Sensing, Processing, and Instrumentation*, vol. 2444, pp. 481–489, Apr. 1995. <https://doi.org/10.1117/12.207698>.
- [13] C. M. Bishop, "Pattern Recognition And Machine Learning - Springer 2006," *Antimicrob Agents Chemother*, vol. 58, no. 12, pp. 7250–7, 2014.

- [14] X. Glorot and Y. Bengio, “Understanding the difficulty of training deep feedforward neural networks”, Accessed: Feb. 24, 2022. [Online]. Available: <http://www.iro.umontreal>.
- [15] M. Kayri, “Predictive abilities of Bayesian regularization and levenberg-marquardt algorithms in artificial neural networks: A comparative empirical study on social data,” *Mathematical and Computational Applications*, vol. 21, no. 2, May 2016. <https://doi.org/10.3390/MCA21020020>.
- [16] M. F. Møller, “A scaled conjugate gradient algorithm for fast supervised learning,” *Neural Networks*, vol. 6, no. 4, pp. 525–533, Jan. 1993. [https://doi.org/10.1016/S0893-6080\(05\)80056-5](https://doi.org/10.1016/S0893-6080(05)80056-5).
- [17] M. Paluszek and S. Thomas, *MATLAB machine learning recipes: A problem-solution approach*, Second edition. Apress Media LLC, 2019. <https://doi.org/10.1007/978-1-4842-3916-2>.

Fluid-Dynamics

Assessment and optimization of dynamic stall semi-empirical model for pitching aerofoils

Enrico Galli^{1,a}, Gregorio Frassoldati^{2,3,b}, Davide Prederi^{2,c}, Giuseppe Quaranta^{1,d,*}

¹Politecnico di Milano, Dipartimento di Scienze e Tecnologie Aerospaziali, via La Masa, 34, 20156, Milano, Italy

²Leonardo S.p.A., Helicopter Division, via Giovanni Agusta, 520, Cascina Costa (VA), Italy

³Università di Roma Tre, Department of Engineering, via della Vasca Navale, 79, 00146, Roma, Italy

^aenrico5.galli@mail.polimi.it, ^bgregorio.frassoldati@leonardo.com,

^cdavide.prederi@leonardo.com, ^dgiuseppe.quaranta@polimi.it

Keywords: Dynamic Stall, Helicopter Rotors, Optimization

Abstract. Dynamic stall is a phenomenon affecting aerofoils in unsteady flows which is particularly relevant in the helicopter field. Semi-empirical models are reliable tools to simulate this phenomenon, especially during preliminary design phases and for aeroelastic assessments. However, they need a large number of tuning parameters to provide reliable estimations of unsteady airloads. To face this problem, a parameter identification procedure based on sequential resolutions of optimization problems by means of a Genetic Algorithm is developed and it is applied to the state-space formulation of a modified version of the so-called "Second Generation" Leishman-Beddoes model. The effects of the optimal parameters on the model prediction capabilities are discussed and the variability of the parameters with reduced frequency is studied. The estimations of the unsteady airloads obtained by applying the optimization of parameters show a great improvement in the correlation of the experimental data if compared to the predictions obtained by using the parameters provided in literature, especially for pitching moments where the negative peaks are very well described. These improvements justify the need for optimization to set the parameters.

Introduction

Dynamic stall is a very impacting phenomenon in the helicopter field because it is the main cause of the occurrence of large blade torsional airloads and rotor in-plane vibrations which are usually limiting factors both for design purposes and for performance evaluation. So, a reliable prediction of unsteady airloads is paramount.

Mathematical tools, aiming at modelling the effects of dynamic stall, range from semi-empirical models to sophisticated CFD methods. Despite the continuously increasing applications of the CFD methods for research purposes and their capability of providing physically realistic simulation of the rotor flow field, their daily use during the design process is still impractical nowadays due to the huge computational costs, the large memory requirements and the numerical issues.

It is here that semi-empirical models, developed since the eighties and the nineties of the last century, return as competitive and trustworthy prediction tools. Indeed, although they are based on simplified nonlinear equations, they can provide very quickly reliable predictions of unsteady airloads if properly tuned. Therefore, their application could be fundamental, especially in those cases where many predictions of unsteady airloads are needed in a short time, as is the case of aeroelastic assessments.



Among all the semi-empirical models available in the literature, the Leishman-Beddoes model is chosen for the present investigation because it is one of the most used by the industries and it is one of those which has known a great number of modifications and improvements over the years. Moreover, differently to the models developed starting from the ONERA model [1] or from the Peters model [2], the Leishman-Beddoes is more physically based since it is easier giving a physical interpretation to the involved parameters. The state-space formulation of the modified version of the "Second Generation" of the LB model which is considered in the present investigation is extensively explained in [3].

One of the main drawbacks of semi-empirical models is the necessity to identify many parameters that have to be extracted from experimental measurements or very reliable numerical simulations. Unfortunately, there are a couple of issues about the available parameters:

- the parameters can be applied with confidence only for the combinations of aerofoil shapes, Mach and Reynolds numbers used for their identification, limiting the extrapolation capability of semi-empirical models.
- the ranges of the parameters reported in the literature have a very limited extension in terms of aerofoil shapes and aerodynamic conditions. So, the number of experimental test cases where they can be used decreases.

To solve this issue, it has been decided to focus on the development of a parameter identification procedure based on optimization problems that aims at identifying the proper tuning parameters of the considered version of the Leishman-Beddoes model. The goal of this investigation is to provide a general methodology which could be applied routinely to aerodynamic conditions and aerofoil shapes different from those already assessed in the past, allowing to enlarge the range of effective applicability of the Leishman-Beddoes model.

Optimization of tuning parameters for the Leishman-Beddoes model

The considered version of the model needs sixteen parameters depending on aerofoil shapes, Mach and, Reynolds numbers which can be extracted from the static curves of normal force and pitching moment coefficients and from the unsteady airloads of a few selected pitching motions performed at different combinations of mean angle, oscillation amplitude and reduced frequency. The developed parameter identification procedure has some characteristics:

- it is a sequential procedure because the parameters are not identified simultaneously by means of a unique optimization, instead, they are divided into smaller groups and then they are identified performing successive optimizations. Indeed:
 - the slope of the static normal force coefficient ($C_{N/\alpha}$), the maximum of the normal force coefficient ($C_{N_{max}}$), the angle of attack at zero lift (α_{zL}) and the pitching moment coefficient at null incidence (C_{M_0}) are easily extracted from the static curves of the coefficients and therefore they are not identified by means of any optimization,
 - the first optimization allows to identify parameters α_1 , S_1 , S_2 which are used for the approximation of the curve of the static trailing edge separation point,
 - then, the second optimization allows to identify parameters m , K_0 , K_1 , K_2 which approximates the static curve of the pitching moment coefficient,
 - finally, the last optimizations are performed to extract parameters T_p , T_f , T_v , T_{vl} , δ_{α_1} which account for all the delays occurring during dynamic stall due to: evolution of the unsteady pressure distribution (T_p), evolution of the unsteady boundary layer (T_f), vortex formation (T_v), vortex travel over aerofoil upper surface (T_{vl}) and flow reattachment (δ_{α_1}).

- The optimization problems are bounded problems, and the design spaces of the variables are defined by exploiting the physical interpretation of the parameters. The parameters reported in [4] are used as guess values around which the design spaces are set.
- The objective functions of the optimization problems are error functions computed between the static curves of the aerodynamic coefficients or the unsteady airloads from pitching motions and their numerical approximations.
- The bounded optimization problems are solved by means of the Genetic Algorithm Toolbox provided by Matlab [5]. A genetic algorithm is chosen to solve the problems due to the high non-linearity and the complexity of the objective functions.

Approximation static trailing edge separation point curve. The LB model uses the Kirchhoff-Helmholtz theory to account for the nonlinear airloads due to flow separation at the trailing edge. In particular, the static normal force coefficient is related to angle of attack α and to the effective trailing edge separation point, f :

$$C_N = C_{N/\alpha}(\alpha - \alpha_{zL}) \left(\frac{1+\sqrt{f}}{2} \right)^2 \quad (1)$$

By measuring the experimental static behavior of the normal force coefficient and by manipulating Eq.(1), it is possible to obtain an experimentally derived distribution for the static trailing edge separation point. Then, this distribution can be fitted by the following exponential approximation:

$$f(\alpha) = \begin{cases} 1 - 0.3e^{\frac{\alpha - \alpha_1}{S_1}}, & \alpha \leq \alpha_1 \\ 0.04 + 0.66e^{\frac{\alpha_1 - \alpha}{S_2}}, & \alpha > \alpha_1 \end{cases} \quad (2)$$

To extract α_1 , S_1 and S_2 , the fitting problem of Eq.(2) is considered as an optimization problem where the optimal set of parameters is the one which minimizes the fitting error against the distribution of the separation point f previously obtained by inverting Eq.(1).

Approximation pitching moment static curve. The LB model suggests the following expression for the approximation of the static curve of the pitching moment where the non-linearity of the airloads is accounted by means of the effective separation point, f :

$$\frac{C_M - C_{M_0}}{C_N} = K_0 + K_1(1 - f) + K_2 \sin(\pi f^m) \quad (3)$$

Since the parameters for the exponential approximation of Eq. (2) and the static curves of the aerodynamic coefficients are available from experimental measurements, then the parameters for the pitching moment approximation can be extracted by considering the problem of Eq. (3) as an optimization problem where the optimal set of parameters is the best one over many optimization problems. The total error to be minimized is the sum of a fitting error between static pitching moment curve and its numerical approximation, the error between the maxima and the minima of the experimental curve and its numerical approximation.

Time constants computation. To identify the non-dimensional time constants, the bounded optimization problems are performed by considering the time history of the unsteady airloads

coming from pitching oscillations. The objective function to be minimized is complex and it is the sum of a total error on the lift coefficient and a total error on the pitching moment coefficient. These total errors are themselves the sum of a global error between the time history of the coefficient and its numerical approximation and an error between the maximum and an error between the minimum over the pitching cycle. To limit the interdependent effects between the variables, the identification is further split in two successive steps:

- At first, a unique optimization is performed by considering the unsteady airloads of a pitching motion in a condition of moderate stall with mean angle lower than the static stall one and a large variation of incidence both under and above static stall angle ($\pm 10^\circ$) at high reduced frequency ($k = 0.1$). This specific condition is assumed to be appropriate because all the stages of dynamic stall can have enough time to develop, all the involved delays can occur and the vortex shedding effects are not yet too much strong. This first optimization is performed by using all the five variables but only T_p , T_f and δ_{α_1} are correctly computed.
- Then, to identify parameters T_v and T_{v1} , which describe vortex-induced effects, many optimizations are performed by considering the unsteady airloads from pitching motions at different conditions of deep stall characterized by a mean angle greater than the static stall one, a large variation of incidence both under and above static stall angle ($\pm 10^\circ$) and different values of reduced frequency smaller than the previous one. The condition of deep stall is considered suitable to compute vortex-related parameters because in this case the vortex is very strong. These computations are performed by keeping fixed the values of T_p , T_f and δ_{α_1} obtained by previous resolution and allowing only parameters T_v and T_{v1} to vary. It is interesting to note that performing the optimizations considering the unsteady airloads at different reduced frequencies allows to study the variability of T_v and T_{v1} with this parameter which is defined as $k = \frac{\omega c}{2V}$ (where ω is the frequency of the pitching oscillation of the aerofoil, c is the chord length and V is the constant free stream velocity). So, by modifying k , it is possible to explore the widest possible range of conditions that a blade section could encounter on the rotor disk during operative conditions.

Results

The previously described identification procedure is applied to NACA 0012 at conditions of $Ma = 0.3$ and $Re = 3.8 \cdot 10^6$. All the static curves of the aerodynamic coefficients and the experimental unsteady airloads come from the database of [6].

The predictions of the unsteady airloads obtained by applying the optimization of parameters are shown in Fig. 1 and Fig. 2. It is possible to see how the predictions obtained by the optimal set of parameters (red curves) allow a great improvement in the correlation of the experimental data (black dashed lines), if compared to the predictions obtained by using the parameters provided in literature (blue curves). The improvement applies especially for pitching moments where the negative peaks are very well described and for small values of the reduced frequency. These improvements justify the need for optimization in the parameters setting.

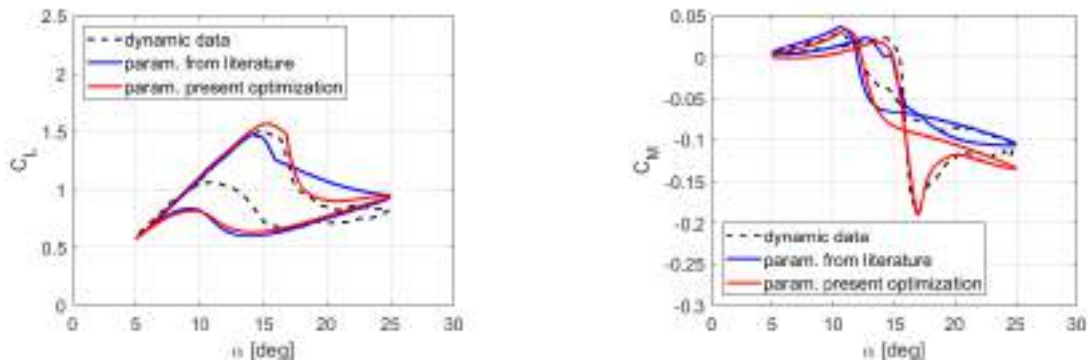


Figure 1: Comparison of the unsteady airloads (C_L on the left, C_M on the right) by means of LB model for NACA 0012 oscillating in pitch with $\alpha = 15^\circ + 10^\circ \sin(\omega t)$ and $k = 0.025$.

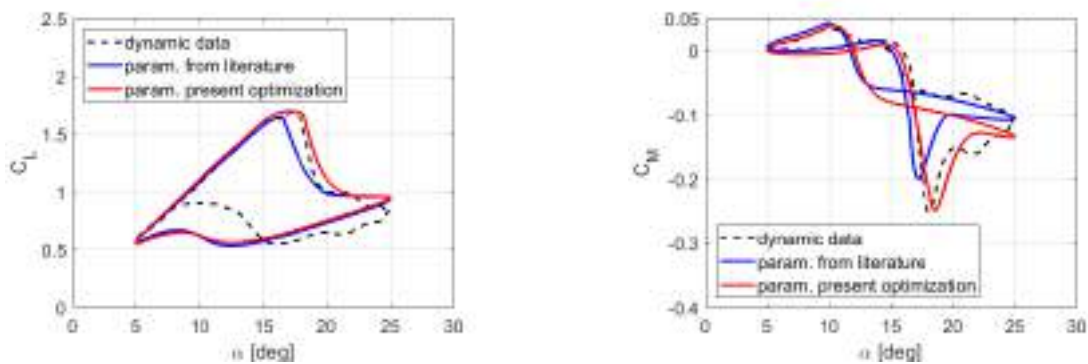


Figure 2: Comparison of the unsteady airloads (C_L on the left, C_M on the right) by means of LB model for NACA 0012 oscillating in pitch with $\alpha = 15^\circ + 10^\circ \sin(\omega t)$ and $k = 0.05$.

References

- [1] C. T. Tran, D. Petot, Semi-empirical model for the dynamic stall of airfoils in view of the application to the calculation of the responses of a helicopter blade in forward flight, Vertica 5 (1981) 35-53.
- [2] D. A. Peters, Toward a unified lift model for use in rotor blade stability analysis, Journal of the American Helicopter Society 30 (1985) 32-42. <https://doi.org/10.4050/JAHS.30.3.32>
- [3] G. Dimitriadis, Introduction to nonlinear aeroelasticity, first edition, John Wiley & Sons Ltd, Chichester, West Sussex, UK, 2017.
- [4] J. G. Leishman, G. L. Crouse, State-space model for unsteady airfoil behavior and dynamic stall, Technical Report Paper 89-1219, AIAA, 1989. <https://doi.org/10.2514/6.1989-1319>
- [5] Matlab, Genetic Algorithm Toolbox, <https://it.mathworks.com/help/gads/genetic-algorithm.html>.
- [6] W. J. McCroskey, K. W. McAlister, L. W. Carr, S. L. Pucci, An experimental study of dynamic stall on advanced airfoil sections, Volume 1, 2, 3, Technical Memorandum TM-84245, NASA, 1982.

Pattern recognition of the flow around a pitching NACA 0012 airfoil in dynamic stall conditions

Giacomo Baldan^{1,a *}, Alberto Guardone^{1,b}

¹Department of Aerospace Science and Technology, Politecnico di Milano, Via La Masa 34, Milano 20156, Italy

^agiacomo.baldan@polimi.it, ^balberto.guardone@polimi.it

Keywords: Dynamic Stall, Proper Orthogonal Decomposition, Pitching Airfoil, Pattern Recognition, Helicopters, Wind Turbines

Abstract. The present work numerically investigates the flow evolution of a pitching NACA 0012 airfoil incurring in deep dynamic stall phenomena. The experimental data at Reynolds number $Re = 1.35 \cdot 10^5$ and reduced frequency $k = 0.1$, provided by Lee et al., are compared to numerical simulation using different methods. Firstly, 2D URANS with different turbulence models are explored highlighting the advantages and the drawbacks of each strategy. On the one hand, simulations are able to describe most characteristic flow features of dynamic stall. On the other hand, numerical models still struggle in describing the inherent complexity of instability and transition from laminar to turbulence, resulting in a misprediction of the angle of attack at which the dynamic stall vortex (DSV) is generated and convected rearward. Finally, a Proper Orthogonal Decomposition (POD) is proposed to analyze the main flow features and to recognize flow patterns. The decomposition of both velocity magnitude and pressure fields shows a high frequency content requiring a large portion of the modes to recover most of the flow energy.

Introduction

Dynamic stall is a complex unsteady aerodynamic phenomenon that is present in a large range of engineering applications such as retreating blades of helicopter rotors, wind turbines, turbomachinery and maneuvering fixed wing aircraft [1]. Compared to static stall, it is characterized by a temporary delay of the boundary layer separation followed by a large flow detachment on the suction side of the profile. This results in a loss of lift, a strong pitch down moment, and an increase in drag. Before the flow reattachment, the profile underlays varying loads due to the chaotic nature of the involved phenomena.

Especially during the last decade, many experiments and computational simulations have been performed to further investigate dynamic stall phenomena and study the flow around pitching and plunging airfoils [2]. Low-fidelity tools are still unable to capture the main features of the flow and computational fluid dynamics should be leveraged [3]. Most difficulties rely in the modelling of the laminar separation bubble (LSB) and the subsequent creation of the dynamic stall vortex (DSV). Laminar to turbulent transition plays a major role in the formation and the convection of the DSV that influences a significant portion of the flow evolution.

In this paper, the flow around a pitching NACA 0012 profile underlying deep dynamic stall regime is numerically investigated. Firstly, a space and time convergence study is conducted using 2D RANS equations. Then, three different turbulent models are compared focusing on the LSB and DSV description. Finally, a Proper Orthogonal Decomposition (POD) is performed using the pressure and velocity magnitude fields.

Numerical setup

The numerical setup aims at reproducing the experimental campaign presented in Lee et al. [4]. A NACA 0012 profile with $c=0.15$ m chord underlying a sinusoidal pitching motion, at reduced



frequency $k=0.1$ ($k=\omega \cdot c/2 / V_\infty$) and Reynolds number $Re = 1.35 \cdot 10^5$, is investigated. The free-stream velocity is $V_\infty = 14$ m/s with a turbulent intensity equal to 0.08%, pressure is $P_\infty = 1$ atm, and the pitching frequency ω is set equal to 18.67 Hz. Three different O-grids have been generated as reported in Tab. 1, where N_x is the number of points around the profile and N_y in the normal direction. All grids respect the $y^+ < 1$ requirement at the wall.

Table 1: NACA 0012 O-grid specifications

O-Grids	N_x	N_y	$\Delta x_{le} (\cdot 10^{-3}c)$	$\Delta x_{te} (\cdot 10^{-4}c)$
G1	384	96	3.3	8.4
G2	512	128	2.0	5.0
G3	1024	256	0.67	3.6

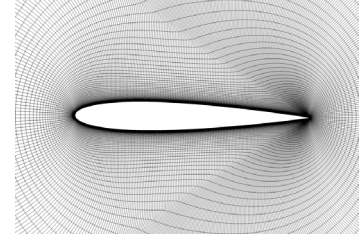


Figure 1: O-grid detail

Numerical simulations are performed using ANSYS Fluent 2023R1. The unsteady incompressible RANS equations are solved using second-order upwind discretization and second-order implicit time integration scheme. Gradients are retrieved through a least square cell-based method and fluxes are obtained with the Rhie-Chow momentum-based formulation. Pressure-velocity equations are solved using the SIMPLE method. A rigid motion of the entire grid is prescribed to allow the airfoil pitching, $\alpha(t) = 10^\circ + 15^\circ \sin(\omega t)$.

The POD decomposition is chosen, in this work, because it is the linear decomposition that, on average, minimize the energy loss considering a subset of k modes and it also grants the orthogonality of the modes [5]. The POD is computed using the Singular Value Decomposition (SVD) method.

Results

As a first step, time and grid independence study is performed. For each mesh three different simulations have been computed using 900, 1800, and 3600 time steps per pitching cycle. SST model with intermittency equation close the RANS equations system. All simulations are run until the solution of subsequent cycles overlaps, usually requiring three or four cycles. In Fig. 2 the last converged cycle is reported. The convergence has to be mainly verified in the upstroke part and on the angle at which the DSV generates the peak in lift and drag. All three grids show a good agreement in the aforementioned points but G1 should not be used since the low resolution does not satisfactory describe the DSV evolution, resulting in a larger mismatch in the downstroke part.

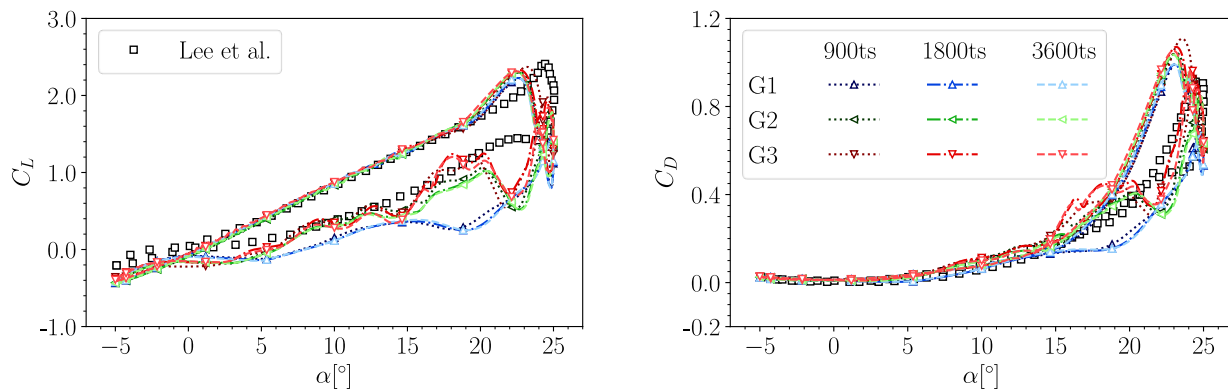


Figure 2: Space and time convergence study. Experimental data [4].

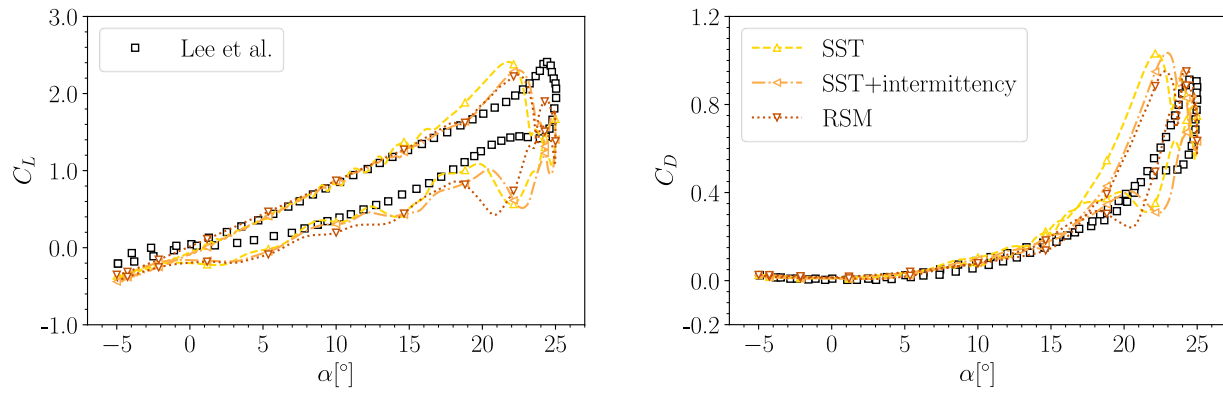


Figure 3: Turbulence model comparison using G2 grid and 3600 time steps per cycle. Experimental data [4].

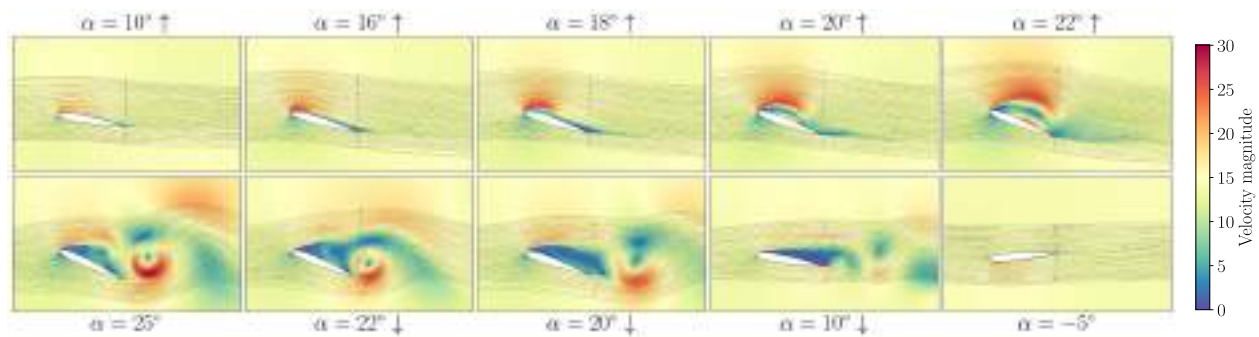


Figure 4: Velocity magnitude contours and streamlines at different pitch angles.

Another critical aspect in dynamic stall simulations is turbulence modelling. SST, SST with intermittency equation, and RSM models are tested using the G2 grid and 3600 time steps per cycle. In Fig. 3, it can be noted that standard SST model fails to describe the LSB and results in oscillation in the DSV formation. The same behavior is present in the RSM even if the effect is weaker since the individual components of the Reynolds stress tensor are computed. The SST model coupled with the intermittency equation describes in more detail the transition from laminar to turbulent giving more accurate results. For this last case, the velocity magnitude contour and streamlines are reported in Fig. 4 to represent the dynamic stall phenomena.

Finally, the POD decomposition is computed for pressure and velocity magnitude fields in the airfoil reference frame during an entire cycle. In Fig. 5 the eigenvalues are shown while in Fig. 6 the first ten modes are represented. The first mode, which is the most energetic one, represent the mean flow over the entire cycle. The following modes confirm the crucial role of the DSV evolution. As the number of the mode increases higher frequency content is represented. It is visible how the DSV that detaches from the leading edge interacts with the stall that originates from the trailing edge. The high frequency content of the flow is confirmed by the cumulative eigenvalue spectrum in which the number of modes required to represent 99% of the energy are 155 and 503 for pressure and velocity, respectively.

Conclusion

In this work, a pitching NACA 0012 underlying dynamic stall phenomena is investigated using 2D URANS with three turbulence models. Numerical simulations are able to describe the LSB and the DSV, showing a good agreement with experiments in the upstroke phase but are not able to capture the angle at which the DSV is convected rearwards anticipating the drag and lift picks. The LSB is shown to play a crucial role in the flow evolution requiring a turbulence model capable of describing the transition from laminar to turbulent, as in the case of SST with intermittency

equation. In addition, a POD is provided for both pressure and velocity magnitude fields to extract the main flow features and to emphasize the interactions of leading and trailing edge stall.

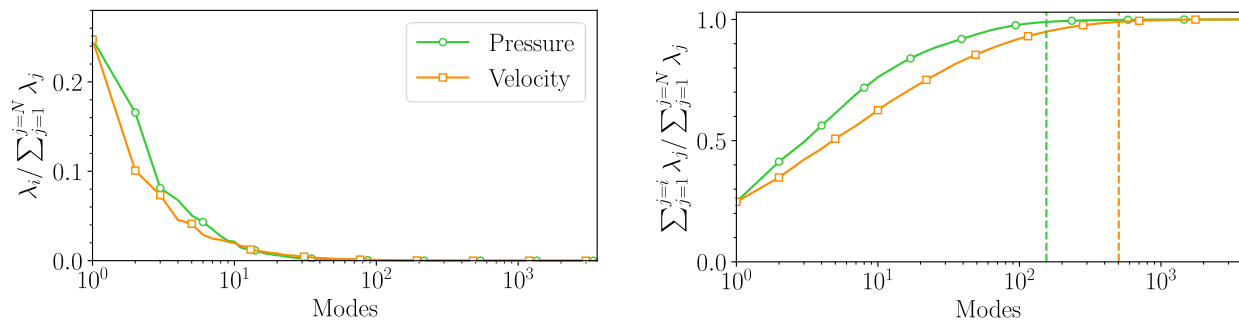


Figure 5: Pressure and velocity magnitude POD eigenvalues and cumulative eigenvalue spectrum. The dashed lines show the number of modes required to represent 99% of the energy.

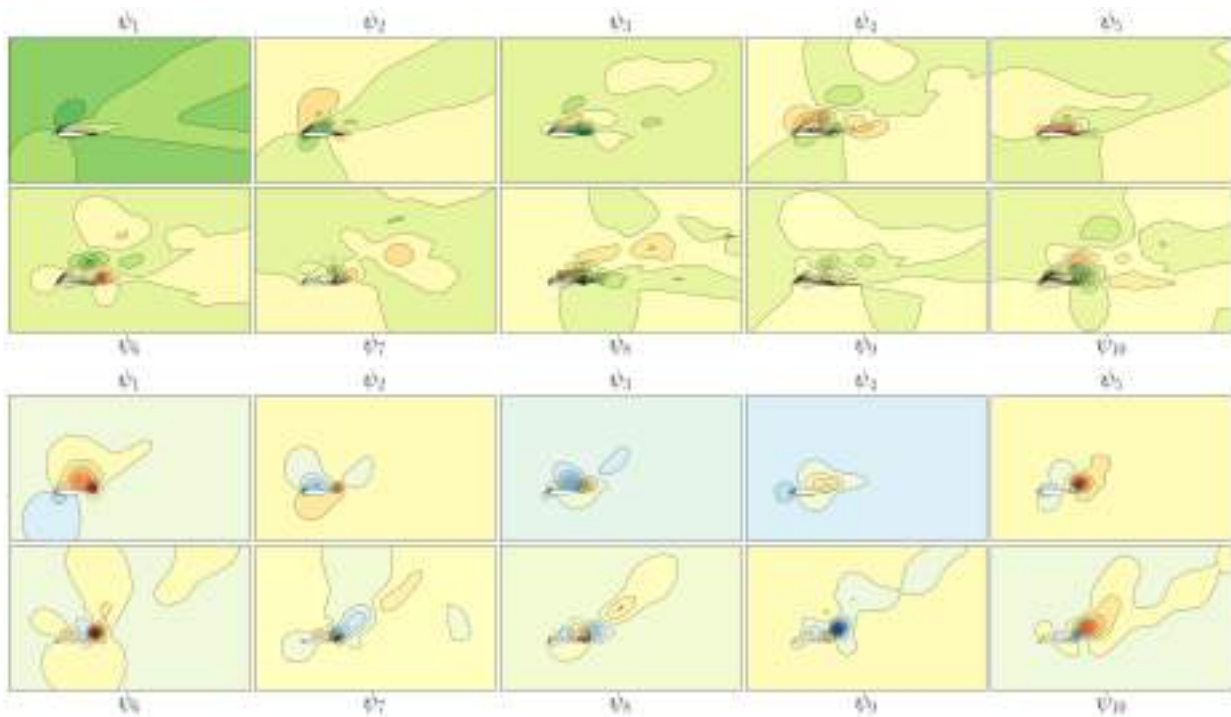


Figure 6: First ten POD modes of velocity magnitude (above) and pressure (below) fields.

References

- [1] M. Visbal, D. Garmann, "Analysis of Dynamic Stall on a Pitching Airfoil Using High-Fidelity Large-Eddy Simulations". AIAA Journal 2018; 56(1):46-63.
<https://doi.org/10.2514/1.J056108>
- [2] F. Avanzi, F. de Vanna, Y. Ruan and E. Benini, "Enhanced Identification of Coherent Structures in the Flow Evolution of a Pitching Wing". AIAA 2022-0182. AIAA SCITECH 2022 Forum. <https://doi.org/10.2514/6.2022-0182>
- [3] A. D. Gardner, A. R. Jones, K. Mulleners, J. W. Naughton, M. J. Smith. "Review of rotating wing dynamic stall: Experiments and flow control". Progress in Aerospace Sciences 2023; 137:100887. <https://doi.org/10.1016/j.paerosci.2023.100887>

- [4] T. Lee, P. Gerontakos, "Investigation of flow over an oscillating airfoil". *Journal of Fluid Mechanics* 2004; 512:313–341. <https://doi.org/10.1017/S0022112004009851>
- [5] H. Eivazi, S. Le Clainche, S. Hoyas, R. Vinuesa. "Towards extraction of orthogonal and parsimonious non-linear modes from turbulent flows". *Expert Systems with Applications* 2022; 202:117038. <https://doi.org/10.1016/j.eswa.2022.117038>

RANS transition model predictions on hypersonic three-dimensional forebody configuration

Luigi Cutrone^{1,a*}, Antonio Schettino^{1,b}

¹ CIRA (Centro Italiano Ricerche Aerospaziali), Unità di Aerotermodinamica, Via Maiorise, 81043 Capua (CE), Italy.

^al.cutrone@cira.it, ^ba.schettino@cira.it

Keywords: Laminar-to-Turbulent Transition, CFD, Hypersonic Flows

Abstract. Future space transportation systems will heavily rely on predicting and understanding Boundary Layer Transition (BLT) during atmospheric entry, especially in the hypersonic phase. Several models, compatible with RANS solvers, have yet been proposed, but not validated in the hypersonic regime. This paper focuses on evaluating prediction capabilities for such models on complex 3D geometries, using the International Boundary Layer Transition (BOLT) Flight Experiment as a test case.

Introduction

The success of future “Apollo” or “Shuttle”-like spacecraft programs and other concepts based on air-breathing propulsion will require an accurate prediction of Boundary Layer Transition (BLT) given that a boundary layer turbulence can amplify surface heating by a factor in excess of five with respect to laminar conditions. The Reynolds-averaged Navier–Stokes equations (RANS equations) are widely used for modeling turbulent flows, but they can’t predict laminar-to-turbulent transition. This limitation arises from the RANS averaging procedure itself, which effectively removes the influence of linear disturbance growth—an essential factor in the transition process. A common approach is then to combine the turbulence model with a transition criterion based on experimental correlations. Correlation-based models are frequently linked to an intermittency transport equation, such as that developed by Steelant and Dick [1] or more complex formulations as proposed by Suzen et al. [2], even though these models require nonlocal information to trigger the transition. More recently, several local correlation-based transition modeling (LCTM) methods have been developed and implemented into modern parallel RANS code. Examples include models developed by Menter [3][4], based on solving one or more differential equations or even based on fully algebraic frameworks [5]. Furthermore, based on the LCTM framework, extensions targeting the hypersonic flow regime have been developed [6]. In all cases, these models have only been partially explored for hypersonic flows, and rely on a large number of constants to tune the results.

Expanding on the prior research conducted in a previous paper [9], we will now apply the 2015 and 2021 Menter's models to a three-dimensional configuration. The primary goal is to validate their predictive abilities when multiple transition mechanisms such as Mack waves, crossflow instabilities, Goertler vortices, and others may simultaneously occur. The configuration selected is the one proposed in the International BOUNDARY Layer Transition (BOLT) Flight Experiment, which was specifically designed to have multiple mechanisms to transition that interact with each other. The geometry was extensively tested in several wind tunnels, including full-scale tests at the CUBRC LENS II wind tunnel, [7].



Models description

The 2015 Menter γ transition model[4], from now on referred as Model-1, is based on the solution of the $k - \omega$ equations (accordingly to the SST turbulence model [8]) and an additional transport equation for intermittency:

$$\frac{\partial(\rho\gamma)}{\partial t} + \frac{\partial(\rho U_j \gamma)}{\partial x_j} = P_\gamma - E_\gamma + \frac{\partial}{\partial x_j} \left[\left(\mu + \frac{\mu_t}{\sigma_f} \right) \frac{\partial \gamma}{\partial x_j} \right]. \quad (1)$$

The transition to turbulence is controlled by the F_{onset} factor in the intermittency production term, $P_\gamma = F_{length} \rho S \gamma (1 - \gamma) F_{onset}$, which can be triggered from both the streamwise and crossflow transition modes:

$$F_{onset} = \max(F_{onset,sw}, F_{onset,cf}). \quad (2)$$

The model can effectively incorporate information from freestream turbulence and the streamwise pressure gradient using only local variables, and, by activating the cross-flow transition term, it can also account for local variations in the flow direction. The labels Model-1A and Model-1B will refer to the version without and with the crossflow transition term, respectively.

Menter recently introduced a new algebraic correlation for intermittency in the 2021 version of his γ transition model [5], thus avoiding the solution of an independent transport equation for it. Similar to Model-1, this new fully algebraic γ transition model, referred to as Model-2 from now on, can consider the streamwise pressure gradient, but currently not the crossflow transition.

Application to 3D geometry

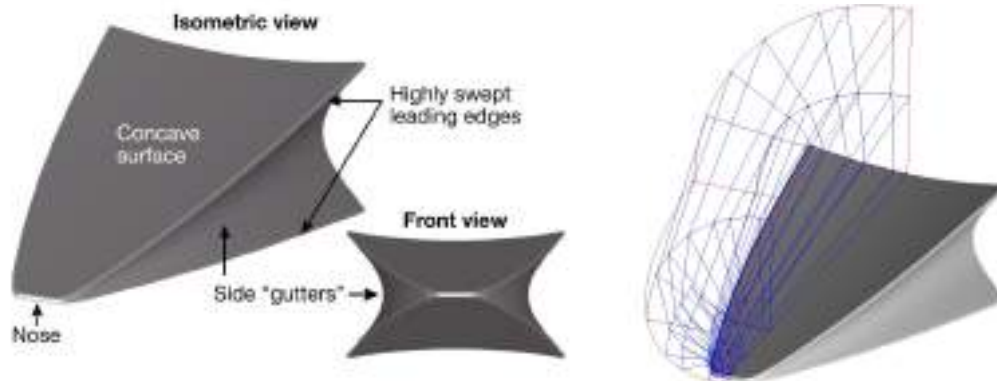


Fig. 1 (left) BOLT geometry, from [7]; (right) domain decomposition for a quarter of the body.

Test case consists in the numerical rebuilding of some of the ground experiments carried out on the geometry of the BOLT (BOundary Layer Transition) project which was designed to investigate the hypersonic boundary layer transition on a low-curvature concave surface with highly swept leading edges, Fig. 1. A full-scale model of the BOLT geometry underwent extensive ground test experimentation in the LENS-II hypervelocity reflected shock tunnel at CUBRC, and here the conditions of RUN-03 in [7] will be used as reference. These conditions are here briefly summarized: $M = 5.17$, $Re_L = 3.92 \cdot 10^6 [\text{m}^{-1}]$, with stagnation pressure and temperature equal to 1.5[MPa] and 1130[K], respectively. A wall temperature of 294.4[K] was imposed. Four inlet values of the turbulent intensity level, $Tu_\infty = [0.1, 0.3, 0.5, 1.0]\%$, were selected to study the effect of freestream turbulence intensity on the transition onset, provided that no specific information on tunnel noise or specific freestream turbulence measures are available. A quarter of the forebody was meshed (exploiting both symmetries). Two shock-fitted structured multi-blocks meshes with 3.5M and 24M cells were used. All the BOLT simulations presented in this paper are based on the 24M cell mesh. All the simulations have been carried out using Ansys Fluent 2021R2.

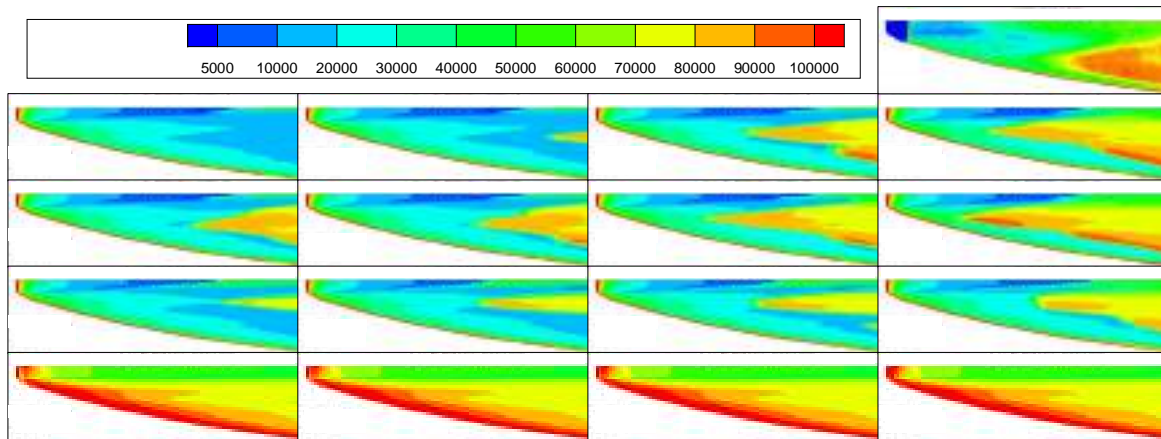


Fig. 2 Heat flux contour map on the primary surface, progressing from Model-1A at the top to Model-2 at the bottom. It showcases various levels of freestream turbulent intensity, ranging from 0.1% leftmost to 1.0% rightmost. Fully turbulent results are also reported for comparisons.

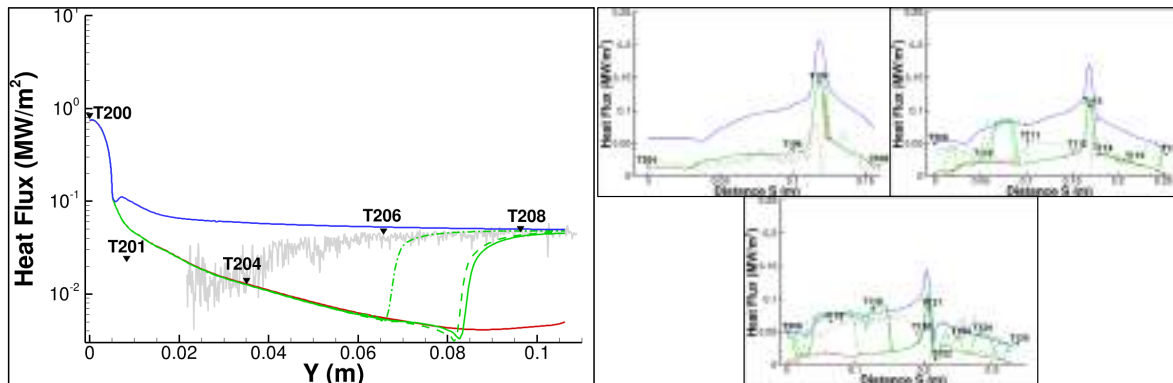


Fig. 3 (left) Heat flux profiles on primary symmetry line; (right) Heat flux profiles at $x=10, 20$, and 30 inches sections. —: TSP heat flux, \blacktriangledown thin-films heat flux, —: Fully laminar, —: Fully turbulent, —: Model-1A, —: Model-1B, —: Model-2. Numerical results for $Tu = 0.5\%$.

Results from computations using different transition models can be seen in Fig. 2. Here, four set of results per freestream turbulence intensity level are available, three sets employing a different transition model and one fully turbulent. An experimental heat flux map obtained with TSP for this run is also shown.

Figure 2 shows quite clearly the dependence of the transition front position on the transition model choice. It is also evident that Model-1A and Model-2 show a significant dependence of their transition front position on Tu_{∞} , with a trend towards earlier transition for increasing Tu_{∞} levels as expected, [10][9]: at extremely low Tu_{∞} levels, both transition models tend to converge towards the laminar solution (not reported here for the sake of brevity). On the other hand, when the correction for cross-flow transition is activated by using Model-1B (and BOLT geometry was specifically designed to experience this mode of transition) the solutions seem to be less sensitive to the Tu_{∞} levels, suggesting that crossflow term is entirely responsible for predicting a transition front even at very low Tu_{∞} levels: only at the highest value considered, $Tu_{\infty} = 1\%$, the streamwise onset terms became predominant and shift significantly forward the transition front.

With respect to the TSP contour map reported in the top right corner of Fig. 2, it seems that all the three transitional results provide the best alignment with the experiment when the Tu_{∞} is set at 0.5% : notably, the transition front obtained with Model-1B demonstrates a tendency to be closer to the lateral leading edge, similar to what observed in the experimental map. Then, a significant difference between the models appears in central part of the primary surface (a symmetry plane in the simulations), where Model-2 systematically predicts an earlier transition.

The aforementioned tendency becomes more apparent in Fig. 3(left), which provides a quantitative comparison between experimental and numerical heat flux profiles. Here, the heat flux at the stagnation point (T200) is accurately predicted, but at the second point (T201) location, where the flow is still laminar, all the numerical results consistently overestimate the experimental value. The authors intend to investigate the effects of a non-homogeneous wall temperature distribution, closer to the experimental conditions. Additionally, when observing the temperature-sensitive paint (TSP) data on the same graph, it becomes evident that the transition needs approximately 0.04 m to fully take place, being extensively distributed across the surface. Conversely, the simulations predict a rapid but delayed transition to turbulence onset, with only Model-2 displaying slightly less delay. Finally, the cross-cut sections in Fig. 3(right) clearly show that Model-1B is everywhere capable of predicting a wider transition zone with respect to all the other models.

Summary

Two transition models have been investigated, one of which equipped with a specific term for crossflow transition. This latter proves to be especially valuable at lower Tu_{∞} values, although an accurate turbulence characterization of the experiment is mandatory for reducing uncertainties.

References

- [1] Steelant, J., Dick, E., Modelling of Bypass Transition with Conditioned Navier–Stokes Equations Coupled to An Intermittency Transport Equation. *J. Num. Meth. Fluids*, 23:193-220. [https://doi.org/10.1002/\(SICI\)1097-0363\(19960815\)23:3%3C193::AID-FLD415%3E3.0.CO;2-2](https://doi.org/10.1002/(SICI)1097-0363(19960815)23:3%3C193::AID-FLD415%3E3.0.CO;2-2)
- [2] Suzen, Y. B., and Huang, P. G., Modeling of Flow Transition Using an Intermittency Transport Equation. *ASME. J. Fluids Eng.* June 2000; 122(2): 273–284. <https://doi.org/10.1115/1.483255>
- [3] R. B. Langtry and F. R. Menter. Correlation-Based Transition Modeling for Unstructured Parallelized Computational Fluid Dynamics Codes. *AIAA Journal*. 47(12), 2009, pp. 2894–2906. <https://doi.org/10.2514/1.42362>
- [4] Menter, F. R., Smirnov, P. E., Liu, T., and Avancha, R., A One-Equation Local Correlation-Based Transition Model, *Flow, Turbulence and Combustion*, Vol. 95, No. 4, 2015, pp. 583–619. <https://doi.org/10.1007/s10494-015-9622-4>
- [5] Menter, F. R., Matyushenko, A., Lechner, R., Stabnikov, A., and Garbaruk, A., An Algebraic LCTM Model for Laminar–Turbulent Transition Prediction, *Flow, Turb. Comb.*, Vol. 109, No. 4, 2022, pp. 841–869. <https://doi.org/10.1007/s10494-022-00336-8>
- [6] Liu, Z., Lu, Y., Li, J., and Yan, C. Local correlation-based transition model for high-speed flows. *AIAA Journal*, 60(3):1365–1381, 2022. <https://doi.org/10.2514/1.J060994>
- [7] Berridge, D. C., McKiernan, G., Wadhams, T. P., Holden, M., Wheaton, B. M., Wolf, T. D., and Schneider, S. P., Hypersonic Ground Tests in Support of the Boundary Layer Transition (BOLT) Flight Experiment, *Fluid Dynamics Conference*, 2018, p. 2893. <https://doi.org/10.2514/6.2018-2893>
- [8] Menter, F. R., "Two-Equation Eddy-Viscosity Turbulence Models for Engineering Applications," *AIAA Journal*, Vol. 32, No. 8, August 1994, pp. 1598-1605. <https://doi.org/10.2514/3.12149>
- [9] Infante, G. M., Cutrone, L., Schettino, A., Numerical methods for laminar/turbulent transition prediction in Hypersonic regime, *ESA FAR conference*, 2020.
- [10] J. I. Cardesa, G. Delattre Comparison of RANS transition model predictions on hypersonic three-dimensional forebody configurations 57th 3AF International Conference on Applied Aerodynamics 29-31 March 2023, Bordeaux – France

A finite-volume hybrid WENO/central-difference shock capturing approach with detailed state-to-state kinetics for high-enthalpy flows

Francesco Bonelli^{1,a,*}, Davide Ninni^{1,b}, Gianpiero Colonna^{2,c} and
Giuseppe Pascazio^{1,d}

¹DMMM & CEMeC, Politecnico di Bari, Bari, 70125, Italy

²CNR-ISTP, Via Amendola 122/D, 70126 Bari, Italy

^afrancesco.bonelli@poliba.it, ^bdavide.ninni@poliba.it, ^cgianpiero.colonna@cnr.it,
^dgiuseppe.pascazio@poliba.it

Keywords: WENO, Hybrid Schemes, Hypersonics, Thermochemical Non-Equilibrium

Abstract. This work shows novel space discretization capabilities of an innovative fluid dynamics solver able to deal with thermochemical non-equilibrium by using a detailed state-to-state model. The implementation of a WENO hybrid scheme is verified and thermochemical non-equilibrium effects are investigated by considering a high temperature shock tube test case. The work represents a first step to enable the solver to perform LES and DNS simulations of turbulent hypersonic flows.

Introduction

The investigation of high enthalpy flows is important in several fields, e.g., hypersonic flows in the context of entry objects (space capsules, reusable space vehicles, debris, meteoroids, etc.), laser applications (laser induced breakdown spectroscopy, etc.), high-enthalpy wind tunnels, rocket engines, etc. [1]. Such flows can involve different phenomena (e.g., strong shock waves, thermochemical non-equilibrium, turbulence, etc.) each of which requires a specific expertise and adequate modeling. In the last years, the authors have developed a finite-volume solver of the Navier-Stokes equations for the simulation of hypersonic flows in thermochemical non-equilibrium, see, e.g. [2,3]. From a numerical point of view the solver is based on conventional approaches that have demonstrated to be robust and affordable. A third order Runge-Kutta scheme and the flux vector splitting of Steger and Warming, with a second order MUSCL reconstruction, were employed for time and space discretization, respectively. On the other hand, to deal with thermochemical non-equilibrium an accurate state-to-state (StS) approach, in addition to the classical multi-temperature Park's model, makes the software a unique tool in the present scene. In order to extend code capabilities to problems that involve both shocks and turbulence, a hybrid WENO/central-difference scheme has been implemented. Indeed, this approach has shown to be among the most convincing when dealing with problems involving shocks and turbulence interacting dynamically [4]. In the present implementation, the popular fifth-order WENO scheme is coupled with a sixth-order central scheme with a shock sensor that limits the use of the shock capturing scheme to region of strong gradients, thus reducing numerical dissipation in smooth regions. To verify the algorithm implementation and to show code capabilities, the one dimensional Sod [5] and Shu–Osher [4] problems, and the two dimensional double Mach reflection (DMR) [5] have been analyzed. Finally, a high temperature shock tube has been investigated by using the hybrid scheme along with the StS approach.



Governing Equations and Numerical Method

The system of Euler equations is solved for a calorically perfect gas ($\gamma = c_p/c_v = 1.4$) or, to consider high temperature effects, for a reacting mixture in thermochemical non-equilibrium.

A cell centered finite-volume (FV) approach is employed and the method of lines is used to separate space and time discretization. Upwind space discretization can be performed either by the Steger and Warming (SW) or by the Lax-Friedrichs (LF) Flux Vector Splitting (FVS). The accuracy of the upwind scheme is increased by a fifth order WENO reconstruction following a characteristic-wise FV method [6]. Then, to reduce numerical dissipation, the WENO scheme is hybridized with a numerical flux built from a sixth order central scheme (CD6). The hybrid approach switches from CD6 to WENO when a shock sensor (χ) [7] is larger than a threshold (χ_L). Time integration is performed by a third order explicit Runge-Kutta scheme [5]. In the case of reacting mixtures an operator splitting approach is applied to deal with stiff source terms [2,3]. Finally, thermochemical non-equilibrium is handled by a StS approach for a N_2 -N mixture [2].

Results

Code verification has been performed by considering 1D and 2D test cases. All problems have been solved by using the SW-FVS except for the double Mach reflection for which the LF-FVS has been employed.

The first test is represented by Sod's shock tube [5]. In Fig. 1 (left) the exact solution is compared with the results obtained by the WENO scheme with three different resolutions: a very good agreement is obtained. Figure 1 (right) shows the results of the hybrid scheme with three different χ_L using 100 cells. Oscillations due to dispersive error increase with χ_L .

The Shu-Osher problem [4] is a benchmark for studying shock turbulence interactions being the propagation of a shock in a perturbed density field. A reference solution has been obtained by using the WENO scheme with mesh size $\Delta x = 6.25 \cdot 10^{-3}$ (1600 cells). Figure 2 shows that with the same resolution ($\Delta x = 5 \cdot 10^{-2}$, 200 cells) the hybrid scheme provides better results with respect to the WENO approach in terms of density profiles, whereas no difference emerges from velocity profiles.

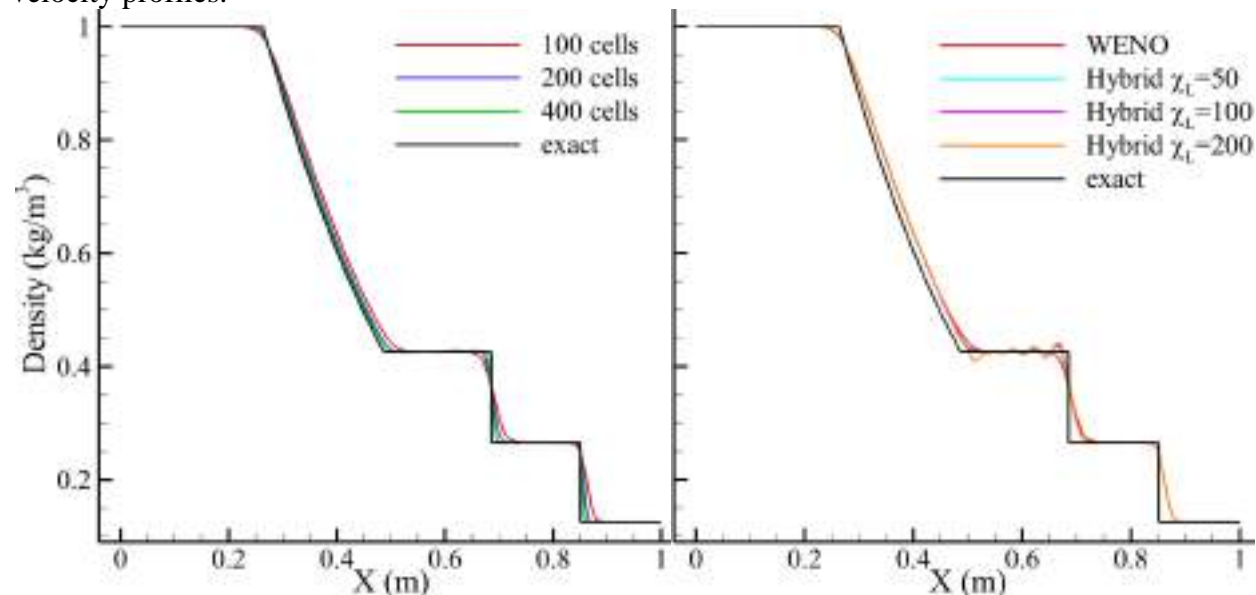


Fig. 1 Sod's shock tube at $t=0.2$: (left) WENO scheme; (right) WENO/CD6 hybrid scheme.

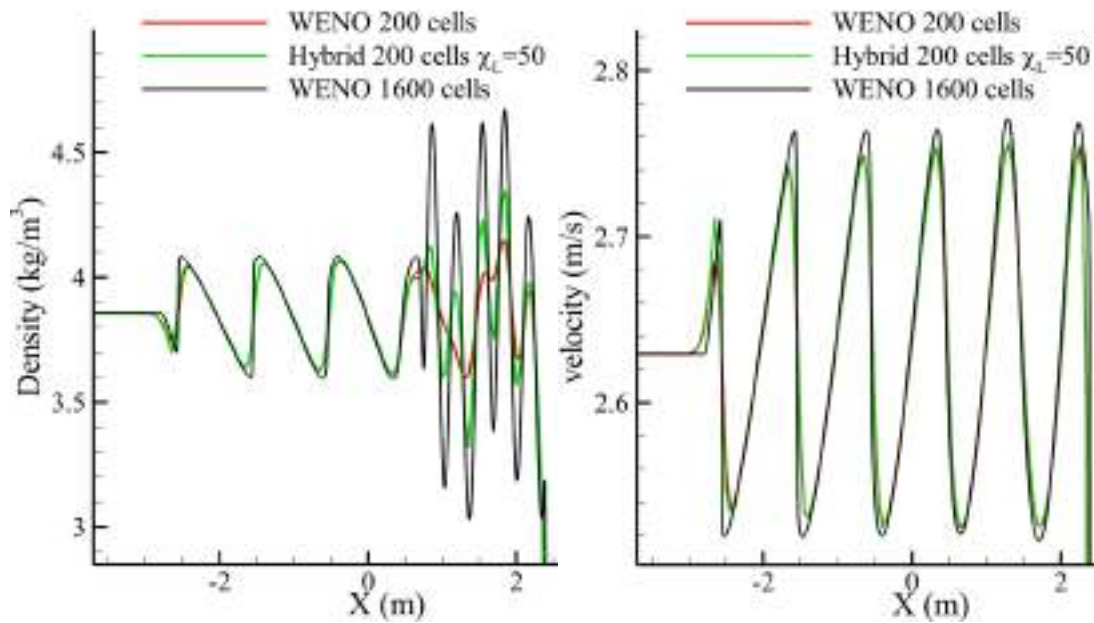


Fig. 2 Shu-Osher problem: (left) density profiles; (right) velocity profiles.

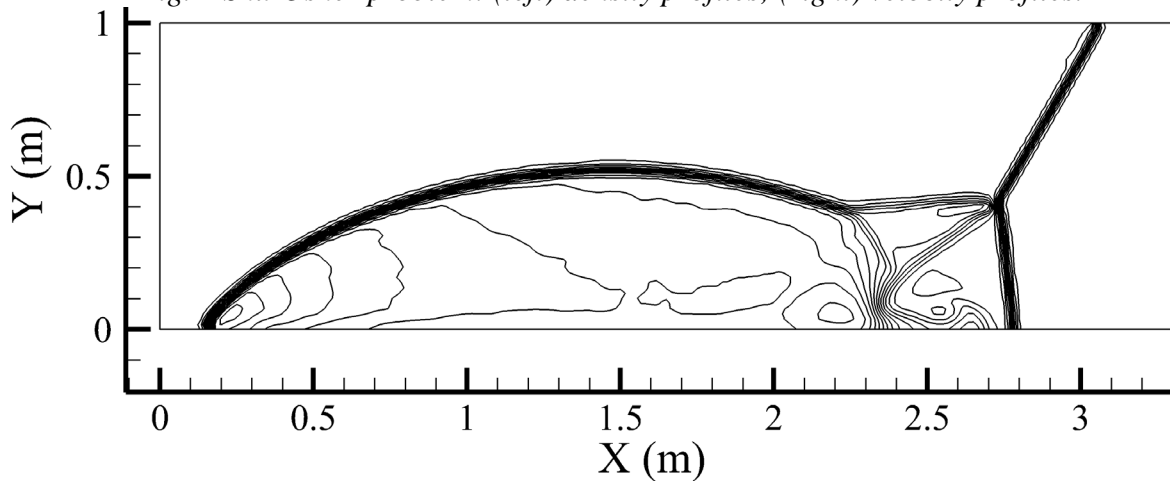


Fig. 3 DMR: 240x59 cells, $t=0.2$, $CFL=0.6$, 30 levels from 1.731 to 20.92, $\chi_L = 200$.

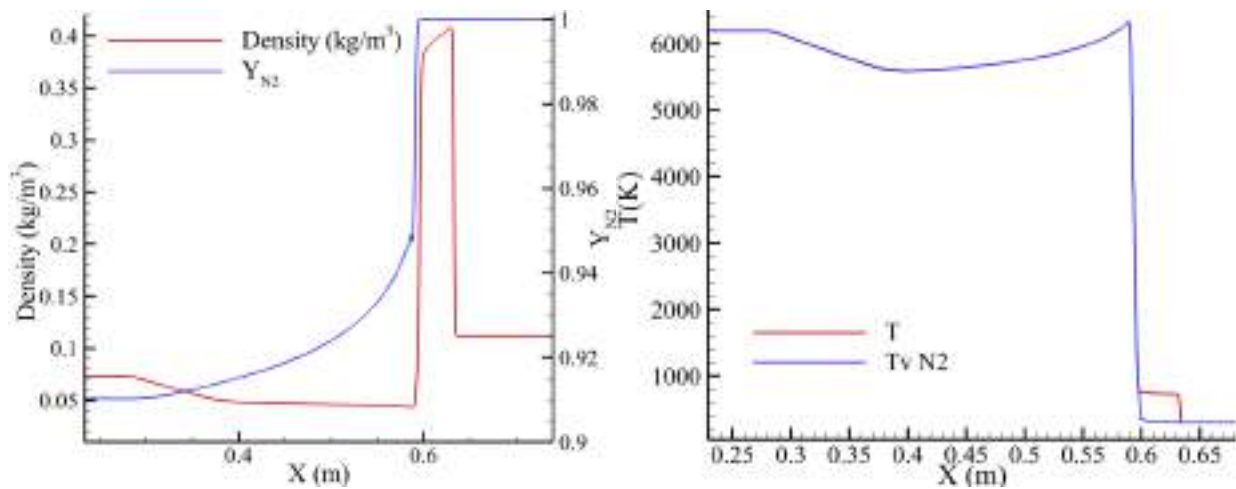


Fig. 4 High temperature shock tube at $t = 1.3 \cdot 10^{-4}$ s: (left) density and Y_{N_2} ; (right) T and Tv_{N_2}

Figure 3 shows the density isolines for the double Mach reflection problem (hybrid scheme). A very good agreement is obtained with Jiang and Shu [5]. Finally, a high temperature shock tube has been simulated by using the StS approach. The initial conditions are those given in Grossmann

and Cinnella [8] except for the initial mixture composition that here is a pure N_2 mixture (mass fraction $Y_{N_2}=1$). The hybrid scheme with $\chi_L=100$ has been employed. Figure 4 shows an important N_2 dissociation which causes a temperature reduction in the upstream region. The translational (T) and the vibrational (T_{vN_2}) temperature differ in the region between the shock wave and the contact discontinuity thus showing a small thermal non-equilibrium.

Conclusions

In this work a WENO/CD6 hybrid scheme was implemented in a fluid dynamics solver able to deal with thermochemical non-equilibrium by using a StS approach. The solver was verified by considering benchmark test cases. Finally, a high temperature shock tube was analyzed showing the ability of the scheme to deal with high temperature gases in thermochemical non-equilibrium.

Acknowledgement

D. N., F. B. and G. P. were partially supported by the Italian Ministry of Education, University and Research under the Program Department of Excellence Legge 232/2016 (Grant No. CUP - D93C23000100001). F. B. was supported by PON “Ricerca e Innovazione” 2014-2020 Azione I.2 “Mobilità dei Ricercatori” - Avviso di cui al D.M. n. 407 del 27/02/2018 AIM “Attraction and International Mobility” Linea 1 Grant No. AIM1895471 - CUP D94I18000210007

References

- [1] J.D. Anderson Jr., Hypersonic and High-Temperature Gas Dynamics, second ed., American Institute of Aeronautics and Astronautics, Inc., Reston, Virginia, 2006.
- [2] G. Pascasio, D. Ninni, F. Bonelli, G. Colonna, Hypersonic flows with detailed state-to-state kinetics using a GPU cluster. In Plasma Modeling (Second Edition): Methods and applications. IOP Publishing. Bristol, UK, 2022, pp. 10-1–10-41. <https://doi.org/10.1088/978-0-7503-3559-1>
- [3] D. Ninni, F. Bonelli, G. Colonna, G. Pascasio, On the influence of non equilibrium in the free stream conditions of high enthalpy oxygen flows around a double-cone. Acta Astronaut., 201 (2022) 247-258. <https://doi.org/10.1016/j.actaastro.2022.09.017>
- [4] E. Johnsen et al., Assessment of high-resolution methods for numerical simulations of compressible turbulence with shock waves, J. Comput. Phys. 229.4 (2010) 1213-1237. <https://doi.org/10.1016/j.jcp.2009.10.028>
- [5] G.S. Jiang, C.W. Shu, Efficient implementation of weighted ENO schemes. J. Comput. Phys., 126.1 (1996) 202-228. <https://doi.org/10.1006/jcph.1996.0130>
- [6] CW. Shu, Essentially non-oscillatory and weighted essentially non-oscillatory schemes for hyperbolic conservation laws. in: Quarteroni, A. (eds) Advanced Numerical Approximation of Nonlinear Hyperbolic Equations. Lecture Notes in Mathematics, vol 1697. Springer, Berlin, Heidelberg, 1998, pp. 325-432 <https://doi.org/10.1007/BFb0096355>
- [7] D.J. Hill, D.I. Pullin, Hybrid tuned center-difference-WENO method for large eddy simulations in the presence of strong shocks, J. Comput. Phys. 194 (2004) 435–450. <https://doi.org/10.1016/j.jcp.2003.07.032>
- [8] B. Grossman, P. Cinnella, Flux-split algorithms for flows with non-equilibrium chemistry and vibrational relaxation. J. Comput. Phys. 88.1 (1990) 131-168. [https://doi.org/10.1016/0021-9991\(90\)90245-V](https://doi.org/10.1016/0021-9991(90)90245-V)

Quantum computing CFD simulations: state of the art

Giulio Malinverno^{1,a*}, Javier Blasco Alberto^{2,b} and Jon Lecumberri SanMartin^{2,c}

¹Engineering Department, FIMAC S.p.A., via Piemonte 19, 20030 Senago (MI) - Italy

²Departamento de Ciencia y Tecnología de Materiales y Fluidos, Universidad de Zaragoza, calle Marie de Luna 3, 50018 Zaragoza, Spain

^ag.malinverno@fimac.aero, ^bjablasal@unizar.es, ^cjonlecum@gmail.com

Keywords: Quantum Computing, CFD, Scientific Machine Learning, Lattice Boltzmann Method, Hydrodynamic Schrödinger Equation, Navier Stokes Equations

Abstract. This document is meant to review and discuss the possible applications of Quantum computing in the area of computational fluid dynamics (CFD). A review of the current state-of-the-art of quantum computing applied to computational fluid dynamics has been carried out, highlighting how the technology is promising but still in an early stage of development. Furthermore, within the approaches developed to solve CFD problems with the use of quantum algorithms and / or quantum computers, this article discusses a quantum algorithm approach, based on the Lattice Boltzmann Method and developed to the study of 2D flow around a cylinder, a model which can be related to several industrial problems and, in the future, modified to simulate the refrigeration cycle used in aeronautical environmental control systems (ECS). This preliminary code helped to highlight the inherent difficulties to implement a quantum algorithm but helped also to demonstrate the applicability of quantum computing.

Introduction

Quantum computing is a type of computation that harnesses the collective properties of quantum states, such as superposition, interference, and entanglement, to perform calculations [1]. The devices that perform quantum computations are known as quantum computers.

Quantum Computing is currently a very active field of study and development, with expected applications in various fields ranging from the classical computer science problem, like cryptography and search problem, to engineering application, like structural optimization [2] and mechanical dynamics [3], but additional applications in different fields have been identified and developed [4], also for pure financial investments [5].

Indeed, several approaches have been proposed for the solutions of CFD problems with the use of quantum algorithms and / or quantum computers, as summarized in [6], being the rationale of the development the estimated scalability of quantum computing [7] and the analogy between Navier Stokes equations (NSE) with the Schrödinger equation through the Madelung transform, i.e., the Hydrodynamic Schrödinger equation (HSE) [8].

Known methodologies review and related works.

Basically, three approaches can be envisioned to solve fluid mechanics problems, namely the algorithmic approach, in which is focused on the development of numerical algorithms to be run on quantum computers, the analog approach, which can be described as the “design” of a quantum mechanical system able to “mimic” the fluid mechanic problem, and, last and not least, the development of machine learning codes for quantum computer.

An example of the “algorithmic” or “circuitual” approach, implicitly demonstrating the applicability of quantum computing to the classical computational fluid dynamics equations despite the inherent complexity of these equations [7], is the resolution of classical Navier-Stokes equations for a typical De Laval nozzle, described by Gaitan [9].



Another examples of the algorithmic approach are the solution of the vortex-in-the-cell method in a parallel environment by Steijl and Barakos [10] or the solution of Collisionless Boltzmann Equations by Steijl and Todorova [11], which highlights how the streaming operations can be effectively implemented in a quantum circuit by the use of one of elementary quantum gate, i.e., the controlled NOT (shortly CNOT) logic gates, under the assumed periodic boundaries conditions.

It is worth to noting that the problem associated with a (classical) lattice gas can be equivalently solved with a quantum computer implementing the “analog” approach, i.e., the use of a lattice gas quantum computer in which quantum bits replace classical bit and are arranged in a lattice-based array [12], whereas the “streaming” operations are carried out by the quantum system evolution.

Contributions of present work.

To verify the applicability of quantum computer to industrial problem, a relatively simple fluid dynamic problem has been considered, i.e., the flow around a cylinder in a 2D domain, solved with a quantum algorithm based on a two dimensional approach on nine variables (streaming/collision directions), or D2Q9, configuration of the Lattice Boltzmann Method (see the following figure for the calculation mesh), extending the previous works with a non-rarified fluid and consequently including collisions.

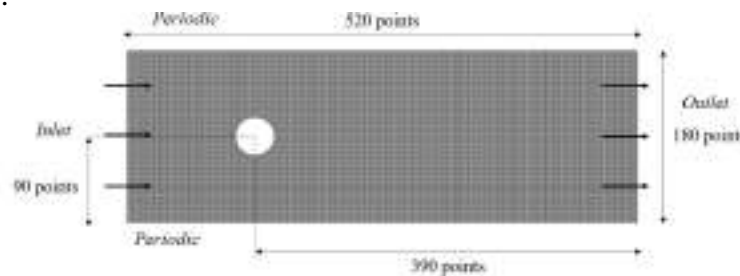


Figure 1 – Lattice mesh

The rationale of this selection is that flow around a cylinder is routinely used as benchmark problem for CFD algorithms because of the phenomena it exhibits but it is representative, in its simplicity, of many applications such as heat exchangers design or subsea pipeline assessment [13], as well as the modelling of porous media [14].

Indeed, the Lattice Boltzmann method has been considered due to the opportunity of extension of this study to porous media (as the filtering mesh used in aeronautical refrigerant system can be modelled) or to the refrigeration cycle itself (due to the presence of multiphase flow).

The flow is considered unsteady, incompressible, laminar, and with constant fluid properties. Inlet has been modelled imposing the flow velocity, whereas the outlet is a simple opening, with periodic boundary conditions on the upper and lower edge. The cylinder wall has been modeled with the bounce back technique to model the non-slip condition.

The equations regulating the flow can be summarized by the classical Lattice Boltzmann Equations with the BGK (Bhatnagar–Gross–Krook) approximation [15]:

$$f_k(\mathbf{x} + \Delta\mathbf{x}, t + \Delta t) = f_k(\mathbf{x}, t) \cdot (1 - \omega) + \omega \cdot f_k^{eq}(\mathbf{x}, t)$$

where \mathbf{x} is the position vector, ω is the relaxation time, f_k is the particle distribution function, and f_k^{eq} is the local equilibrium distribution function defined as:

$$f_k^{eq}(\mathbf{x}, t) \doteq w_k \cdot \rho(\mathbf{x}, t) \cdot \left(1 + 3 \cdot \frac{\mathbf{c}_k \cdot \mathbf{u}}{c_s^2} + \frac{9}{2} \cdot \frac{(\mathbf{c}_k \cdot \mathbf{u})^2}{c_s^4} - \frac{3}{2} \cdot \frac{\mathbf{u}^2}{c_s^2} \right)$$

Where \mathbf{u} is the particle velocity vector, w_k a weighting factor, while c_s is the isothermal speed of sound and \mathbf{c}_k is the unitary velocity vector along the streamlines [15].

In the quantum algorithm, the equilibrium distribution function expression has been truncated to the first order terms respect the velocity to avoid non linearities for this first algorithm and rely only on linear operations, introducing an averaged expected velocity vector \mathbf{u}_0 :

$$f_k^{eq}(x, t) \simeq w_k \cdot \rho(x, t) \cdot \left(1 + 3 \cdot \frac{c_k \cdot u}{c_s^2} + \frac{9}{2} \cdot \frac{(c_k \cdot u) \cdot (c_k \cdot u_0)}{c_s^4} - \frac{3}{2} \cdot \frac{u \cdot u_0}{c_s^2} \right)$$

The numerical expected error is quite small due to the range of velocity considered. Please note that the classical code has been implemented considering the full expression of the distribution function.

The full state of the quantum system is given by:

$$|\psi\rangle \equiv |a\rangle|F\rangle|y\rangle|x\rangle = |a_0 a_1 a_2\rangle|F_0 F_1 F_2 F_3 F_4\rangle|y_0 y_1 y_2\rangle|x_0 x_1 x_2 x_3\rangle$$

where $|a\rangle$, $|F\rangle$, $|y\rangle$, and $|x\rangle$ represent respectively the state vector relative to the ancilla qubits, the distribution function qubits, the macroscopic variables, and the spatial (x, y) coordinates.

The quantum algorithm has been developed and tested using the IBM's quantum computing software development framework *Qiskit* [16], and it can be generally discretized in five major steps [17]: initialization, collision, propagation, boundary condition implementation and, calculation of macroscopic quantities.

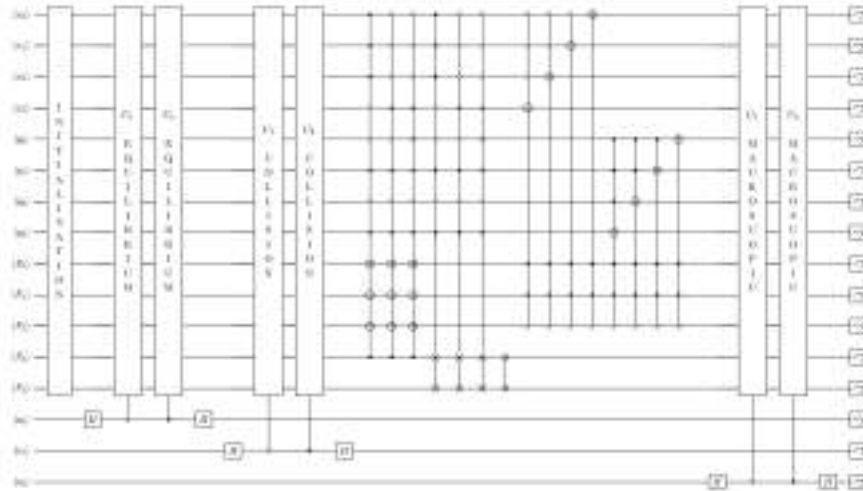


Figure 2 – Quantum algorithm scheme for the single iteration (simplified)

It is worth noting that, after one time step simulation is finished, it is necessary to re-initialize the quantum state for the next step. Indeed, classical programming tools like for-cycles or variables overwriting cannot be implemented into a quantum system.

Results, comparison, and validation

To assess the quantum algorithm, a verification of the implementation of the Lattice Boltzmann equations on classical computer has been carried for several Reynolds numbers, to verify the correctness of the underlying theoretical algorithm, retrieving not only the velocity and vorticity distribution but also evaluating the drag coefficient on the cylinder. Results are in accordance with available data from bibliography and results obtained through the solution of the classical Navier Stokes equations.

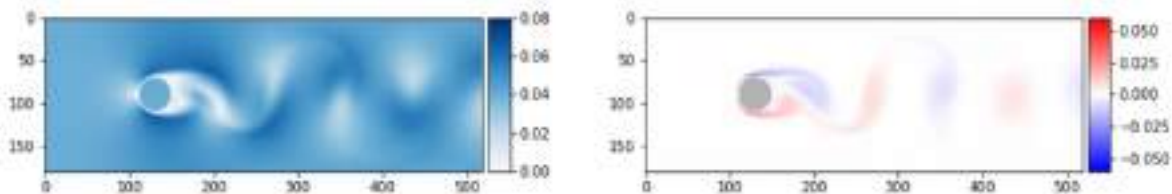


Figure 3 –Classical LBM algorithm results: velocity and vorticity profiles for $Re=1000$

The quantum algorithm is still under investigation, but on-going preliminary results seem to be (at least qualitatively) in accordance with the results obtained at the previous step, even considering the strong simplification introduced by the linearization of equilibrium function.

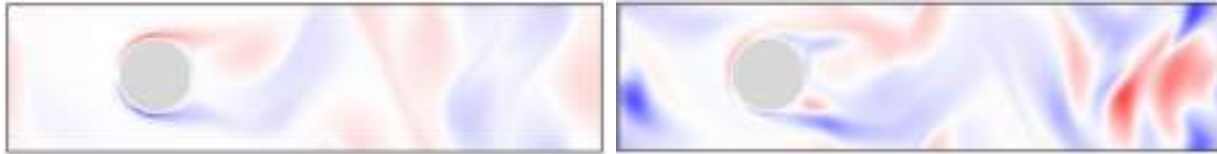


Figure 4 –Classical vs. quantum LBM algorithms results (vorticity)

Unfortunately, a significant drawback (beside the numerical error introduced by the linearization) is the time required to run the above-described algorithm, i.e., execute the algorithm on a quantum computer simulator, mainly due to the initialization and measurement process (roughly 2 minutes for iteration instead of few tenths of seconds for the classical algorithm) [18].

Conclusions

This paper summarized the three approaches that can be envisioned to solve fluid mechanics problems, namely the algorithmic or circuitual approach, the analog or annealing approach and, finally, the machine learning applied to quantum computers.

A quantum algorithm for solving a classical two-dimensional fluid mechanic problem is introduced in the present work, based on the “translation” to a quantum computing framework of the numerical procedure known as Lattice Boltzmann method. The rationale of this choice is that the method shows similarities with the quantum operations themselves and it can be extended to multiphase flows and to complex geometrical domains, typical conditions of interesting industrial problems such as the modeling of aeronautical heat exchangers and in general, the refrigeration cycle of aircraft environmental control system.

Very preliminary results show that the quantum algorithm is able to achieve (even if under heavy mathematical simplifications) a result which is comparable with the results obtained with classically implemented Lattice Boltzmann codes, but the implementation shows the inherent difficulties to translate a classical code into a quantum framework (e.g., linearization, time required to simulate the quantum system on classical hardware) and the discrepancies due to the linearization.

Future steps include the implementation of nonlinear distribution function as well as the extension of algorithm to more sophisticated problem, including heat exchanges, also to confirm that the algorithm works fine even outside the range of unitary velocities. Furthermore, another aspect that requires a strong improvement is the numerical implementation in order to avoid the re-initialization of the code at each iteration, which is a major bottleneck in the current implementation.

References

- [1] Wikipedia, “Quantum Computing”, https://en.wikipedia.org/wiki/Quantum_computing (Last visited: February 23rd, 2022)
- [2] Wils, K.A., Quantum Computing for Structural Optimization, M.Sc. thesis, TU Delft, (2020).
- [3] Smaili A. & Alt., Application of the flexible link model (FLM) and quantum computing-based algorithm for the optimum synthesis of partially compliant mechanism, ESDA2012-82467, (2012). <https://doi.org/10.1115/ESDA2012-82467>
- [4] Palmer J., Quantum technology is beginning to come into its own”, The Economist, <https://www.economist.com/news/essays/21717782-quantum-technology-beginning-come-its-own> (Last visited: February 23rd, 2022)), (2017).
- [5] Walters R., Early quantum computing investors see benefits, Financial Times, <https://www.ft.com/content/b2f1c0ea-e4ff-11e7-a685-5634466a6915>, (2018).

- [6] Bharadway S.S. et Alt., Quantum Computation of Fluid Dynamics, *Pramana-Journal of Physics*, (2020), DOI 12.3456/s78910-011-012-3.
- [7] Chen et alt., “Quantum Finite Volume Method for Computational Fluid Dynamics with Classical Input and Output”, *arXiv:2102.03557* (2021) [quant-ph].
- [8] Meng and Yang, Quantum computing of fluid dynamics using the hydrodynamic Schrödinger equation., *arXiv:2302.09741* (2023) [physics.flu-dyn].
<https://doi.org/10.1103/PhysRevResearch.5.033182>
- [9] Gaitan F., Finding flows of a Navier -Stokes fluid through quantum computing, *npj Quantum Information*, (2020), s41534-020-00291-0. <https://doi.org/10.1038/s41534-020-00291-0>
- [10] Steijl, R. and Barakos, G. N., Parallel evaluation of quantum algorithms for computational fluid dynamics. *Computers and Fluids*, 173, (2018), pp. 22-28.
<https://doi.org/10.1016/j.compfluid.2018.03.080>
- [11] Todorova B. and Steijl R. (2020), “Quantum Algorithm for the Collisionless Boltzmann Equation”, *Journal of Computational Physics*, 409, (2020), 109347.
<https://doi.org/10.1016/j.jcp.2020.109347>
- [12] Yepez J. (1998), “Quantum Computation of Fluid Dynamics”, *Quantum Computing and Quantum Communications Lecture Notes in Computer Science*, Colin P. Williams (Ed.) Vol. 1509 Springer-Verlag Berlin (1999). https://doi.org/10.1007/3-540-49208-9_3
- [13] Doreti, L. and Dineshkumar, L. Control techniques in flow past a cylinder- A Review. *IOP Conference Series: Materials Science and Engineering*. 377, 012144 (2018,6).
<https://doi.org/10.1088/1757-899X/377/1/012144>
- [14] Fattahi et alt., Lattice Boltzmann methods in porous media simulations: From laminar to turbulent flow. *Computers Fluids*. 140 pp. 247-259 (2016).
<https://doi.org/10.1016/j.compfluid.2016.10.007>
- [15] Mohamad A.A., *Lattice Boltzmann method - Fundamentals and Engineering Applications with Computer Codes*, Springer-Verlag (London), 2011. <https://doi.org/10.1007/978-0-85729-455-5>
- [16] <https://qiskit.org/>
- [17] Budinski L., Quantum algorithm for the Navier Stokes equations by using the stream function vorticity formulation and the lattice Boltzmann method, *Quantum Physics*, 2022, <https://doi.org/10.48550/arXiv.2103.03804>
- [18] Lecumberri J., Quantum computing implementation of LBM, thesis, Universidad de Zaragoza, B.Sc. Physics degree, 2023

Analysis of plasma formation during hypersonic flight in the earth atmosphere

Salvatore Esposito^{1,a*}, Domenic D' Ambrosio^{2,b}

¹Dipartimento di Elettronica e Telecomunicazioni, Politecnico di Torino, Torino, Italy

²Dipartimento di Ingegneria Meccanica e Aerospaziale, Politecnico di Torino, Torino, Italy

^asalvatore_esposito@polito.it, ^bdomenic.dambrosio@polito.it

Keywords: Hypersonic Aerodynamics, Plasma, Non-Equilibrium, Thermo-Chemistry

Abstract. In this study we investigate the formation of plasma in hypersonic flight and its impact on radio communications and radar tracking. The transfer of kinetic energy from the vehicle to the surrounding gas in the hypersonic regime leads to the formation of plasma, which can cause interference with electromagnetic waves. By conducting a numerical simulation campaign using Computational Fluid Dynamics (CFD), we are determining the critical Mach number and altitude conditions that lead to plasma formation. The plasma generated at the nose of the vehicle and its subsequent convection along the body and in the wake are the main subjects of our investigation. The simulations include physical models that account for chemical, vibrational and electron-electron energy non-equilibria, using a two-temperature approach. The results indicate the Mach numbers and altitudes at which plasma formation can significantly affect the propagation of electromagnetic waves.

Introduction

Hypersonic flight presents a significant challenge to aircraft design and operation due to the highly complex gas flow characteristics that occur when objects travel at speeds well in excess of the speed of sound. In hypersonic flight, the transfer of kinetic energy from the object to the surrounding gas creates a region of high temperature around the body, leading to the formation of plasma [1], which can greatly affect the propagation of electromagnetic waves. If the charge density in the plasma is high enough, the wave can be completely reflected. Specifically, if the collision frequency tends to zero and the frequency of the radio link is less than or equal to the plasma frequency (satisfying the cut-off condition), the real part of the permittivity tends to zero or becomes negative. As a result, the electromagnetic wave becomes evanescent, resulting in an exponential decay of its intensity as it traverses that region of space [2]. The plasma surface thus replaces the surface of the body, distorting the reflected radiation and altering the radar trace. Even if the plasma frequency is below the cut-off values, refraction and absorption can still occur, causing a redistribution of electromagnetic waves and a reduction in re-radiation.

Understanding and predicting plasma formation around hypersonic vehicles is therefore critical for accurate tracking and evaluation of radio communication capabilities.

We present a numerical simulation campaign based on CFD tools focused on the prediction of plasma formation in suborbital hypersonic flight. The aim of the research is to determine the Mach number and altitude conditions that could produce regions around the vehicle where the plasma frequency, collision frequency (and hence permittivity) reach critical levels. For this purpose, we consider a test matrix with Mach numbers between 8 and 16 and altitudes between 20 and 70 km. We analyze the plasma formation at the nose of the vehicle and its subsequent convection along the conical nose and in the wake. We use this data to show the flight regimes in which plasma formation can interfere with the propagation of electromagnetic waves, and we superimpose this



with surface temperature data to eliminate flight conditions that are not feasible for thermal protection reasons.

Physical Model and Numerical Method

The adopted physical model is based on the Navier-Stokes equations and includes non-equilibrium phenomena involving vibrational and electronic energy relaxation, as well as chemical and ionization reactions. We consider air as a gas mixture potentially composed of 7 chemical species, namely monoatomic oxygen and nitrogen, O and N , nitric oxide, NO , diatomic oxygen and nitrogen, O_2 , N_2 , the positive ion NO^+ , and electrons, e^- . The effects of non-equilibrium energy on air chemistry are represented by a two-temperature model. The rates of the chemical reactions are derived from [4,5], while the thermodynamic properties of each chemical species are taken from [6].

Due to the flight conditions, a non-magnetized, inhomogeneous, collisional cold plasma model is assumed. Under this premise, the relative permittivity, ϵ_r , which determines the wave transmission in a medium, can be approximatively described by the Drude model [2]:

$$n^2 = \epsilon_r = 1 - \frac{(f_{pe}^2)}{(f(f + if_c))} = 1 - \frac{(f_{pe}^2)}{(f^2 + f_c^2)} + \frac{i(f_{pe}^2 f_c)}{(f(f^2 + f_c^2))}. \quad (1)$$

In Eq. (1), n is the refractive index at the frequency of the electromagnetic wave, f . The electron number density, n_e , determines the electron plasma frequency as in Eq. (2):

$$f_{pe} = \frac{1}{2\pi} \sqrt{e^2 n_e / \epsilon_0 m_e}. \quad (2)$$

where e is the electric charge, m_e is the effective mass of the electron, and ϵ_0 is the permittivity of free space.

The term f_c is the collision frequency between electrons and neutral particles, defined as:

$$f_c = \frac{1}{2\pi} \sum_i n_i \sigma_{i,e} \sqrt{\frac{8k_b T}{\pi m_e}}. \quad (3)$$

where n_i and $\sigma_{i,e}$ are respectively the number density and the neutral-electron scattering cross section for the neutral species i , T is the temperature and k_b is the Boltzmann constant.

The real part of ϵ_r governs the wave propagation, while the imaginary part controls the collisional absorption, i.e., the transfer of energy from electrons to neutral species.

The mathematical formulation of the physical model is solved numerically using the CFD software ICFD++ by Metacomp Technologies. It utilizes a finite volume discretization approach, employing a Harten-Lax-van Leer-Contact (HLLC) approximate Riemann solver with Total Variation Diminishing (TVD) limited second-order reconstruction for the convective fluxes. The diffusive fluxes are computed using a naturally second-order centered scheme. The computational mesh is unstructured and consists primarily of polyhedral cells, except for the wall region where a structured, stretched quadrilateral grid is employed to accurately capture the boundary layer. The mesh undergoes local refinement through an Adaptive Mesh Refinement technique based on the magnitude of the Mach number gradient. The total number of cells in the mesh varies between 350,000 and 400,000, depending on the specific test case. We apply the model to an axi-symmetric blunt-nosed cone exposed to hypersonic flow. The body has an overall length of 1.125 m. The nose of the cone is an ellipsoid with minor and major radii of 2.5 cm and 5.5 cm, respectively. This is followed by a cylindrical section that is 2.5 cm long, and finally, a cone with a semi-opening angle of approximately 8.2047° , as described in [3]. Despite its simplicity, this geometric

configuration serves as a suitable starting point for representing plasma formation around a slender body in hypersonic atmospheric flight. To capture the plasma in the wake, the computational domain extends up to 2.875 m behind the nose.

Results

The results were obtained considering non-catalytic and radiation-adiabatic wall conditions, assuming a zero angle of attack to ensure axisymmetric flow. Applying a radiation-adiabatic wall boundary condition implies that the wall is considered adiabatic, but it can radiate heat received from the flow. Such a condition is known as 'radiative equilibrium.' It is assumed that the gas is fully transparent to the radiation flowing away from the wall, while the wall benefits from radiative cooling. Previous research has demonstrated that, in many scenarios, this condition provides a reasonably accurate estimate of surface temperature compared to flight data [7]. The radiative equilibrium condition states that the heat transfer into the wall is determined by the approximate relation:

$$q_w = \epsilon \sigma T_w^4 \quad (4)$$

implying that the wall will reject all heat from the flow, except for what it can radiate away. In Eq. (4), $\sigma = 5.67 \times 10^{-8} \text{ W/m}^2/\text{K}^4$ is the Stefan-Boltzmann constant, while ϵ is the surface emissivity, which we assumed to be equal to 0.8 in this work.

The permittivity was calculated for an electromagnetic wave frequency of 1 GHz, which is typical for land-based long-range surveillance radars [8]. Setting the maximum possible temperature at the vehicle surface to 3500 K, Table 1 shows that the Mach 14 and 16 conditions at 20 km altitude and the Mach 16 condition at 30 km altitude are not feasible. The results also show that no thermochemical phenomena are observed at an altitude of 70 km for Mach numbers between 8 and 10, and therefore these observations have not been reported.

Table 1 – Maximum wall temperature in Kelvin degrees.

z[Km]\M	8	9	10	12	14	16
70	/	/	/	1.47E+03	1.68E+03	1841
50	1.56E+03	1.74E+03	1.91E+03	2.05E+03	2.27E+03	2.51E+03
30	2041	2.30E+03	2.43E+03	2.82E+03	3.29E+03	3761
20	2.25E+03	2.43E+03	2.83E+03	3.34E+03	3845	4.44E+03

Figures 1 to 4 indicate that along the symmetry axis in the region of the cone nose and at four different stations in the wake, the plasma frequency and the collision frequency reach their maximum values, and the real part of the permittivity reaches its minimum values. For the highest Mach numbers (at least M=12), the permittivity decreases below unity even in the wake, indicating refraction of electromagnetic waves in this region. However, significant permittivity values are only observed at altitudes of 30 and 50 km.

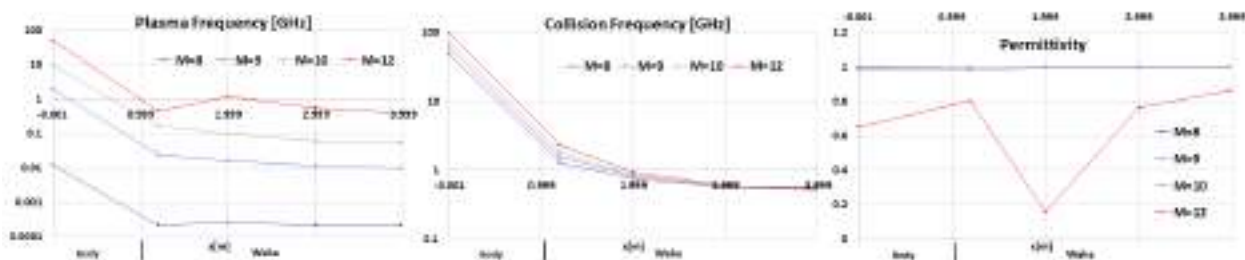


Figure 1. Maximum plasma and collision frequencies, and minimum real part of permittivity at 20 km altitude.

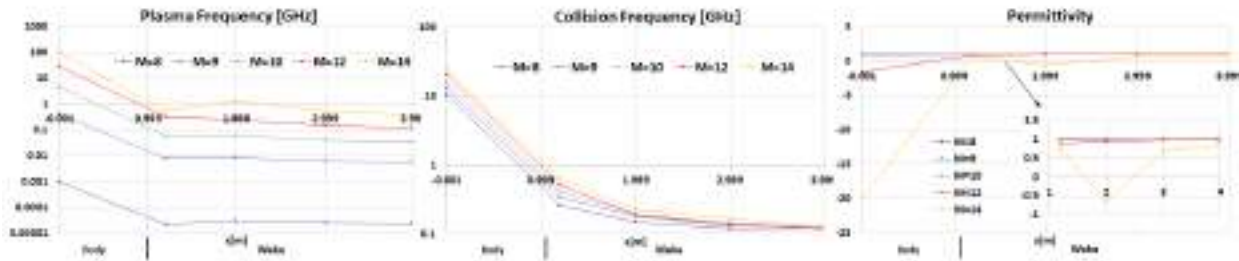


Figure 2. Maximum plasma and collision frequencies, and minimum real part of permittivity at 30 km altitude.

Specifically, the results presented in Fig. 1 indicate that the conditions at 20 km altitude correspond to highly collisional regimes with relevant collision frequencies. Significant permittivity values are observed only at Mach 12. Regarding the results in Fig. 4, the very low pressure at 70 km altitude limits the thermodynamic activity, resulting in relevant conditions only for Mach 16 and at the nose, while plasma formation in the wake remains negligible.

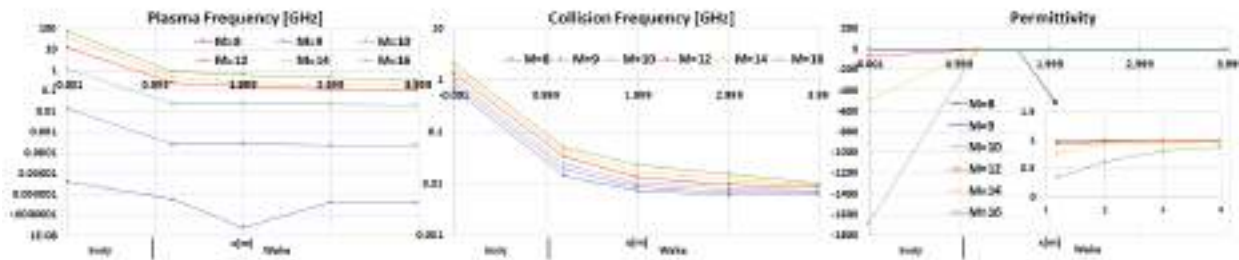


Figure 3. Maximum plasma and collision frequencies, and minimum real part of permittivity at 50 km altitude.

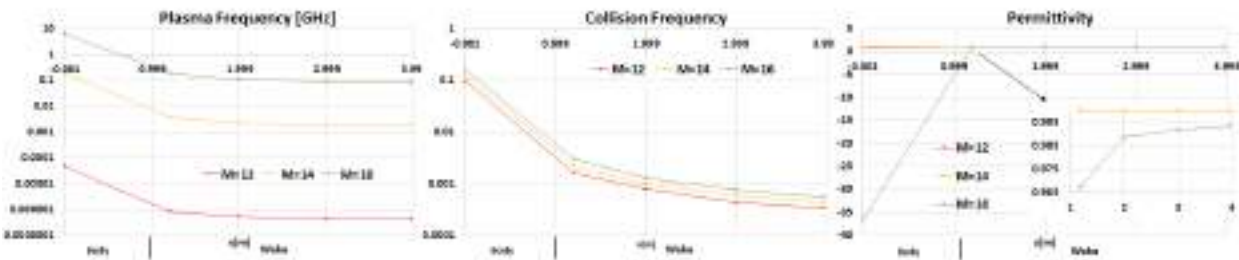


Figure 4. Maximum plasma and collision frequencies, and minimum real part of permittivity at 70 km altitude.

Conclusions

The objective of this study was to understand plasma formation during hypersonic flight and its impact on radio communications and radar tracking using CFD tools and non-equilibrium thermochemical models. The results showed that at altitudes between 30 and 50 kilometers and Mach numbers above 12, the plasma sheath can have a significant effect on the propagation of electromagnetic waves. Subsequent research will include an analysis of the scattering of electromagnetic waves induced by the plasma, with focus on the study of the radar cross section.

References

- [1] Anderson, John David. Hypersonic and high temperature gas dynamics. AIAA, 1989.
- [2] Stix, Thomas H. Waves in plasmas. Springer Science & Business Media, 1992.

- [3] Qian, Ji-Wei, Hai-Li Zhang, and Ming-Yao Xia. "Modelling of Electromagnetic Scattering by a Hypersonic Cone-Like Body in Near Space." *International Journal of Antennas and Propagation* 2017 (2017), Article ID 3049532. <https://doi.org/10.1155/2017/3049532>
- [4] Park, Chul. "Review of chemical-kinetic problems of future NASA missions. I - Earth entries." *Journal of Thermophysics and Heat transfer* 7(3), 1993: 385-398. <https://doi.org/10.2514/3.431>
- [5] Park, Chul, Richard L. Jaffe, and Harry Partridge. "Chemical-Kinetic Parameters of Hyperbolic Earth Entry." *Journal of Thermophysics and Heat transfer* 15(1), 2001: 76-90. <https://doi.org/10.2514/2.6582>
- [6] Gupta, Roop N., et al. "A review of reaction rates and thermodynamic and transport properties for an 11-species air model for chemical and thermal nonequilibrium calculations to 30000 K." NASA-RP-1232, 1990.
- [7] Gnoffo, Peter A., Johnston, Christopher O., and Thompson, Richard A. "Implementation of Radiation, Ablation, and Free Energy Minimization in Hypersonic Simulations." *Journal of Spacecraft and Rockets*. 47(2), 2010: 251–257. <https://doi.org/10.2514/1.44916>
- [8] Skolnik, Merrill I. *Radar handbook*. McGraw-Hill Education, 2008.

Multi-step ice accretion on complex three-dimensional geometries

Alessandro Donizetti^{1,a*}, Tommaso Bellosta^{1,b}, Mariachiara Gallia^{1,c},
Andrea Rausa^{1,d}, Alberto Guardone^{1,e}

¹Politecnico di Milano, Department of Aerospace Science and Technology, Via Privata
Giuseppe La Masa, 34, 20156 Milano, Italy

^aalessandro.donizetti@polimi.it, ^btommaso.bellosta@polimi.it, ^cmariachiara.gallia@polimi.it,
^dandrea.rausa@polimi.it, ^ealberto.guardone@polimi.it

Keywords: In-Flight Icing, Multi-Step, Level-Set Method, Unstructured Grids, Mesh Adaptation

Abstract. This work presents the Politecnico di Milano Icing Research Group's contribution to developing new numerical tools and methodologies for simulating long-term in-flight icing over complex three-dimensional geometries. PoliMIce is an in-house ice accretion software that includes state-of-the-art solvers for the dispersed phase to compute the droplets' impact on the aircraft, and ice accretion models, including the exact local solution of the unsteady Stefan problem. PoliMIce has also been extensively developed for the simulation and robust design optimization of thermal ice protection systems. A crucial aspect that characterizes and makes numerical simulations challenging is the formation, and evolution in time of complex ice geometries, resulting from the ice accretion over the body surface and/or previously formed ice. A multi-step procedure is implemented since the aerodynamic flow field is coupled with ice accretion. The total icing exposure time is subdivided into smaller time steps. At each time step, a three-dimensional body-fitted mesh suitable for the computation of the aerodynamic flow field around the updated geometry is generated automatically. The novel remeshing procedure is based on an implicit domain representation of the ice-air interface through a level-set method and Delaunay triangulation to generate a new conformal body-fitted mesh. In this work, the unique capabilities of the PoliMIce suite are employed to perform automatic multi-step ice accretion simulations over a swept wing in glaze ice conditions. Numerical simulations are hence compared with the available experimental data.

Introduction

In-flight icing is a complex problem that involves various disciplines, including aerodynamics, multi-phase flows, thermodynamics, and meshing capabilities.

It is a critical safety issue in aeronautics since it disrupts the aircraft's aerodynamics. Computational fluid dynamics techniques are valuable for simulating different and potentially extreme conditions that complement experimental and in-flight campaigns, better understanding how ice accretion affects aerodynamic performances, and designing optimal ice protection systems [1].

For the numerical simulation of in-flight ice accretion, most of the icing tools, such as LEWICE [2], FENSAP-ICE [3], SIMBA-ICE [4], rely on a standard and well-established segregated approach as multi-step approach. Under a quasi-steady assumption, the total icing exposure time is divided into smaller time steps. The aerodynamic flow field, the amount and distribution of the cloud water droplets impinging on the selected surfaces, and the ice growth rate are computed sequentially at each step. Then, the new geometry and the corresponding surrounding mesh must be updated. This operation is usually the most critical phase of the multi-step loop, especially if a fully automated procedure is desired.



The following sections describe how the in-house code PoliMIce [5] computes the aerodynamic flow field, the amount and distribution of the cloud water droplets impinging on the selected surfaces, the ice growth rate, and the updating of the geometry and corresponding surrounding mesh.

Flow solver

Aerodynamic simulations of the external airflow are performed here using SU2 [6]. A node-centered finite volume method (FVM) is applied on arbitrary unstructured meshes using a standard edge-based data structure on a dual grid with median-dual control volumes. Convective fluxes are discretized at each edge mid-point using either centered or upwind schemes. The aerodynamic field is computed as a solution to the Reynolds-averaged Navier-Stokes (RANS) equations, used in this study in tandem with the Spalart–Allmaras (SA) turbulence model.

Collection efficiency solver

Due to the scales at play in ice accretion and the concentration of water droplets, their effects on the solution of the airflow field can usually be neglected so that the computation of the aerodynamics can be performed independently of the water droplets. This assumption leads to the so-called one-way coupled approach; only the airflow field can affect the motion of water droplets. The in-house particle tracking code is based on a Lagrangian framework and simulates clouds containing supercooled water droplets [7, 8].

The Lagrangian framework allows straightforward modeling of supercooled water droplets' effects, such as splashing, aerodynamic breakup, and deformation, and can deal with secondary particles. As the result depends on the particle resolution, a strategy was developed to automatically refine the seeding region by adding new particles where needed. Elements are incrementally split at each iteration, evolving the current cloud front, and computing the collection efficiency on the surface. The simulation stops when the difference in the L_2 norm between two consecutive collection efficiency calculations is below a user-supplied threshold.

Thermodynamic solver

The in-house code PoliMIce [5] is used for computing the ice accretion. Computing the thickness of the forming ice layer amounts to solving a phase change problem over the body surface. Typically surfaces are first discretized in computational cells, and a one-dimensional Stefan problem is solved for each control volume. Early icing tools rely on the approximate solution of the Stefan problem proposed by Messinger in 1953 [9] for aeronautical applications. In 2001 Myers [10] proposed an improved version of Messinger's model, obtaining a better representation of the transition between the rime and the glaze ice. A further modification to Myers' model, based on the exact local solution of the unsteady Stefan problem, is implemented in the current version of PoliMIce [11]. PoliMIce can also perform numerical simulation of Electro-Thermal Ice Protection Systems (ETIPS) [12], both in the anti-icing and de-icing mode, identifying six different icing conditions and the transition between one and the other, including accretion, melting of ice, and water evaporation.

The surface roughness is estimated a-priori with the empirical formula of Shin, as a function of liquid water content (LWC), static air temperature, and freestream velocity. It provides an equivalent sand-grain roughness, k_s , which is needed by the Spalart–Allmaras turbulence model.

In the multi-step procedure, the water film distribution and all the icing data are interpolated from the previous step through a nearest-neighbor search algorithm.

Updating geometry module

To avoid mesh entanglement and grid intersections typical of standard mesh deformation techniques, PoliMIce updating geometry module [13, 14] is based on an implicit domain

remeshing strategy to obtain a robust and automatic remeshing procedure that permits long-term in-flight icing simulations without the user intervention.

At each step, the new ice-air interface is represented as the zero-contour level of a level-set function defined over the computational volume, such that $\varphi < 0$ in the portion of the domain occupied by material, $\varphi > 0$ in the portion of the domain not occupied by material, and $\varphi = 0$ at the interface. Keeping the clean body elements untouched, only the ice-air interface ones are then isotropically remeshed to obtain a body-fitted surface mesh with good-quality elements, which is finally used as a base for generating the volume grid required for the next time step computations.

Results

This section presents a 10 steps ice accretion simulation over a 30° degree swept NACA0012 wing in glaze ice conditions, taken from the 1st Ice Prediction Workshop. Numerical results are compared with the experimental results obtained at NASA Glenn Icing Research Tunnel (IRT).

Test conditions are reported in Table 1. The inputs to the problem are the angle of attack (AoA), the freestream velocity, temperature and pressure, the liquid water content (LWC) of the cloud, i.e. the grams of water contained in a cubic meter of air, the droplet median volume diameter (MVD) and the total icing exposure time.

Table 1: Icing test conditions.

Case	Sweep Angle [deg]	AoA [deg]	Vel [m/s]	Temp [K]	Pres [Kpa]	LWC [g/m ³]	MVD [μm]	Time [s]
362	30	0	103	266	92.32	0.5	34.7	1200

The simulated ice shape is characterized by high temperatures near the stagnation point, which result in thin ice layers at the leading edge, and runback water driven by shear stresses.

The length and the angle of the horns are well predicted, although there is an underprediction in the overall mass of ice accreted, particularly near the stagnation point.

The final ice shape and the evolution of the geometry represented through a slice perpendicular to the leading edge are represented in Figure 1 and Figure 2, respectively. Comparing the solution obtained with the single-step approach with the multi-step one, it is evident how the latter is fundamental to correctly capture the glaze ice shape, accounting for the progressive modification of the flow field around the wing.

Conclusions and future work

This paper briefly presented the PoliMIce toolkit, which can perform multi-step simulations of in-flight ice accretion over three-dimensional geometries, avoiding mesh entanglement and allowing for long-term simulations necessary to simulate full aircraft configurations and bringing the possibility of certification by simulation in the near future.

In the future, PoliMIce will be employed for multi-step simulations around other swept wings with different sweep angles, testing new roughness and density models to better understand ice accretion's physics and consequently improve its modeling. Finally, complex three-dimensional ice shapes, easily managed by the proposed methodology, will be adopted to evaluate the aerodynamic losses due to ice formation on commercial and military aircraft.



Figure 1: Glaze ice shape at $t = 1200$ s.

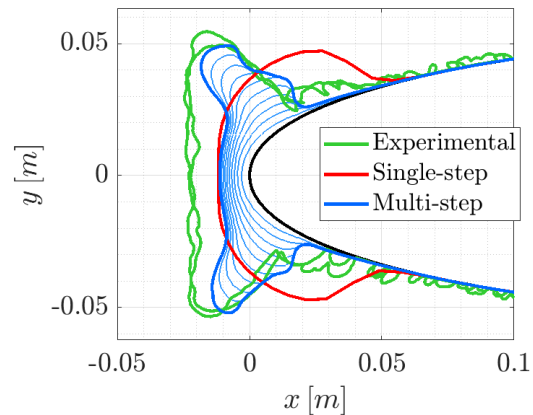


Figure 2: Ice shape evolution.

References

- [1] M. Gallia, B. Arizmendi Gutierrez, G. Gori, A. Guardone et P. M. Congedo, «Robust Optimization of a Thermal Anti-Ice Protection System in Uncertain Cloud Conditions,» *Journal of Aircraft*, pp. 1-15, 2023. <https://doi.org/10.2514/1.C037223>
- [2] W. B. Wright, «User Manual for the NASA Glenn Ice Accretion Code LEWICE,» 2002.
- [3] H. Beaugendre, W. Habashi et F. Morency, «FENSAP-ICE's three-dimensional in-flight ice accretion module: ICE3D,» *Journal of Aircraft*, vol. 40, pp. 239-247, 2003. <https://doi.org/10.2514/2.3113>
- [4] D. de Rosa, F. Capizzano et D. Cinquegrana, «Multi-step Ice Accretion by Immersed Boundaries,» chez *International Conference on Icing of Aircraft, Engines, and Structures*, 2023. <https://doi.org/10.4271/2023-01-1484>
- [5] M. Morelli, B. Tommaso, A. Donizetti et A. Guardone, «Assessment of the PoliMice toolkit from the 1st AIAA Ice Prediction Workshop,» chez *AIAA AVIATION 2022 Forum*, 2022. <https://doi.org/10.2514/6.2022-3307>
- [6] T. D. Economon, F. Palacios, S. Copeland, T. Lukaczky et J. Alonso, «SU2: An Open-Source Suite for Multiphysics Simulation and Design,» *AIAA Journal*, vol. 54, pp. 828-846, 2015. <https://doi.org/10.2514/1.J053813>
- [7] T. Bellosta, G. Baldan, G. Sirianni et A. Guardone, «Lagrangian and Eulerian algorithms for water droplets in in-flight ice accretion,» *Journal of Computational and Applied Mathematics*, vol. 429, 2023. <https://doi.org/10.1016/j.cam.2023.115230>
- [8] G. Baldan, T. Bellosta et A. Guardone, «Efficient Lagrangian particle tracking algorithms for distributed-memory architectures,» *Computers & Fluids*, vol. 256, 2023. <https://doi.org/10.1016/j.compfluid.2023.105856>
- [9] B. Messinger, «Equilibrium Temperature of an Unheated Icing Surface as a Function of Air Speed,» *Journal of the Aeronautical Sciences*, vol. 20, pp. 29-42, 1953. <https://doi.org/10.2514/8.2520>
- [10] T. Myers, «Extension to the Messinger model for aircraft icing,» *AIAA Journal*, vol. 39, pp. 211-218, 2001. <https://doi.org/10.2514/3.14720>
- [11] G. Gori, G. Parma, M. Zocca et A. Guardone, «Local Solution to the Unsteady Stefan Problem for In-Flight Ice Accretion,» *Journal of Aircraft*, vol. 55, pp. 251-262, 2018. <https://doi.org/10.2514/1.C034412>

- [12] M. Gallia, A. Rausa, A. Martuffo et A. Guardone, «A Comprehensive Numerical Model for Numerical Simulation of Ice Accretion and Electro-Thermal Ice Protection System in Anti-icing and De-icing Mode, with an Ice Shedding Analysis,» chez *International Conference on Icing of Aircraft, Engines, and Structures*, 2023. <https://doi.org/10.4271/2023-01-1463>
- [13] A. Donizetti, T. Bellosta, A. Rausa, B. Re et A. Guardone, «Level-Set Mass-Conservative Front-Tracking Technique for Multistep Simulations of In-Flight Ice Accretion,» *Journal of Aircraft*, pp. 1-11, 2023. <https://doi.org/10.4271/2023-01-1467>
- [14] A. Donizetti, A. Rausa, T. Bellosta, B. Re et A. Guardone, «A Three-Dimensional Level-Set Front Tracking Technique for Automatic Multi-Step Simulations of In-Flight Ice Accretion,» chez *International Conference on Icing of Aircraft, Engines, and Structures*, 2023. <https://doi.org/10.4271/2023-01-1467>

Large Eddy simulations and Reynolds-averaged Navier-Stokes simulations of separation-induced transition using an unstructured finite volume solver

Manuel Carreño Ruiz^{1,a,*} and Domenic D'Ambrosio^{1,b}

¹ Department of Mechanical and Aerospace Engineering, Politecnico di Torino, C.so Duca degli Abruzzi, 24, 10124 Torino, Italy

^amanuel.carreno@polito.it and ^bdomenic.dambrosio@polito.it

Keywords: Laminar Separation Bubbles (LSB), Large Eddy Simulation (LES), Transition Modelling, Reynolds Averaged Navier Stokes (RANS)

Abstract. The study aims to assess the capability of different methodologies in capturing the separation-induced transition phenomenon. This transition mechanism occurs when the flow separates from the airfoil surface, and transitions from a laminar to a turbulent state due to the amplification of the Kelvin-Helmholtz instability developed in the separated shear layer. The simulations employ high-order numerical methods for solving the Navier-Stokes equations, while the transition modeling for RANS is based on the $\gamma - Re_\theta$ transition model. LES enables prediction of the onset and location of transition and provides turbulent flow statistics.

Introduction

Predicting flow transition on airfoils is crucial for designing unmanned aerial systems, as it directly impacts their aerodynamic performance, stability, and control. However, accurately predicting flow transition remains challenging due to the complex nature of flow physics and the limited availability of high-fidelity experimental data, especially in the very-low Reynolds number regime. One extensively studied benchmark case in this regard is the SD7003 airfoil. Galbraith et al. [1] carried out Implicit Large Eddy Simulations (ILES) using a Discontinuous Galerkin method to study flow transition on the SD7003 airfoil. Uranga et al. [2] corroborated the good performance of ILES in computing separation-induced transition, testing Reynolds numbers as low as 22,000. Catalano et al. [3] presented LES results using a second-order scheme for the chordwise and wall-normal directions, employing Fourier collocations in the spanwise direction. They contested the conclusions of [1], which claimed the necessity of a high-order scheme to capture laminar separation bubbles. In fact, second-order schemes can adequately capture separation-induced transition, albeit with extremely refined grids. RANS approaches have also been employed for studying the SD7003 airfoil. Windte et al. [4] coupled a $k-\omega$ model with an e^N transition model to predict transition around the airfoil. Catalano et al. [5,6] proposed modifications to the $k-\omega$ SST turbulence model to better capture lower Reynolds number flows, applying it to this specific airfoil. De Santis et al. [7] recently introduced a modification of the γ transition model [8] to enhance turbulent kinetic energy production within separation bubbles. Carreño et al. [9] also attempted to increase turbulent kinetic energy production in separation bubbles by tuning the s_1 parameter in the $\gamma - Re_\theta$ transition model [10].

This study uses LES to predict flow transition on the SD7003 airfoil at Reynolds number 60,000 and Mach number of 0.2. We examine different numerical settings for LES, focusing on the impact of selecting higher-order and less dissipative schemes. We compare the velocity field created by the separation bubble using the RANS model described earlier and LES. Additionally, we present a comparison between the WALE and dynamic Smagorinsky subgrid-scale models.



Numerical Methods

Numerical simulations in this paper were conducted using the commercial software STAR-CCM+. The SD7003 airfoil geometry at an angle of attack of 4 degrees was employed for this analysis. To minimize the influence of the far-field boundary, the computational domain was extended to approximately 100 chords. The RANS equations were solved on a two-dimensional grid. A time-accurate implicit second-order integration was utilized to capture the vortex shedding that occurs behind the trailing edge of low Reynolds number airfoils at low angles of attack prior to transition. The time-step was set to 0.01 convective turnovers. Further details regarding the numerical setup of the RANS simulations and the implementation of the $\gamma - Re_\theta$ transition model can be found in [9]. For LES, the SD7003 geometry was extruded in the spanwise direction for 0.1 chords, which has been determined by [1] as sufficient for computing flow statistics at low and moderate angles of attack. The lateral boundaries were meshed conformally and assigned periodic boundary conditions. Several grids were tested to evaluate the influence of resolution on capturing small-scale structures, with the finest grid consisting of approximately 15 million cells. The grid ensures y_+ values below 0.2 and x_+ and z_+ values below 5 near the airfoil. Furthermore, we verified that the grid resolves at least 80% of the turbulent kinetic energy in the spectrum. Simulations were performed using 128 cores of 4 Intel Xeon Scalable Processors Gold 6130 2.10 GHz. The time step employed in our simulation was 0.002 convective turnovers. The inner solver executed 10 iterations per time step, resulting in residuals dropping between 2 and 3 orders of magnitude. Simulations were conducted for 20 turnovers, and statistics were computed within the last 10. The Wall Adaptive Local Eddy-viscosity (WALE) sub-grid turbulence model and the Dynamic Smagorinsky approach were compared. The recommended spatial discretization in STAR-CCM+ is the second-order Bounded Central Difference (BCD) scheme. This scheme was compared with a third-order Central Difference (CD3) scheme, a third-order Monotonic Upwind Scheme for Conservation Laws (MUSCL3), and a hybrid scheme that combines third-order central difference and upwind schemes (CD/MUSCL3). Third-order schemes demonstrated no significant overhead compared to the bounded central difference scheme implemented in STAR-CCM+. Compared to the standard second-order upwind scheme, the overhead was approximately 10%. Despite these small overheads, the enhanced accuracy of third-order schemes, as demonstrated by Ricci et al. [11], could outweigh the additional computational costs.

Results and Discussion

Figure 1 illustrates the Q-criterion iso-surface obtained using the CD3 scheme, revealing an artificial structure outside the boundary layer resulting from solver instability. Conversely, the hybrid CD/MUSCL3 scheme with a blending factor of 0.15 proved to be stable and robust. In Figure 2, the friction coefficient for our simulations is compared to the results presented by Galbraith & Visbal [1]. It is important to note that their simulations were conducted at a Mach number of 0.1. However, we believe this discrepancy is likely insufficient to account for the variations observed in Figure 2. Our simulations exhibit a delayed separation transition and reattachment, with separation bubbles of the same length but shifted toward the trailing edge. These differences indicate that dissipation remains a significant factor, necessitating further grid refinements to ensure that grid-related issues do not influence this phenomenon. Nevertheless, some intriguing observations can still be made. Firstly, reducing the blending factor clearly decreases dissipation, which is associated with an artificially rapid decay of turbulent kinetic energy when using upwind schemes. Additionally, we can observe that the Dynamic Smagorinsky approach demonstrates a higher level of turbulent kinetic energy production, anticipating the reattachment of the boundary layer.

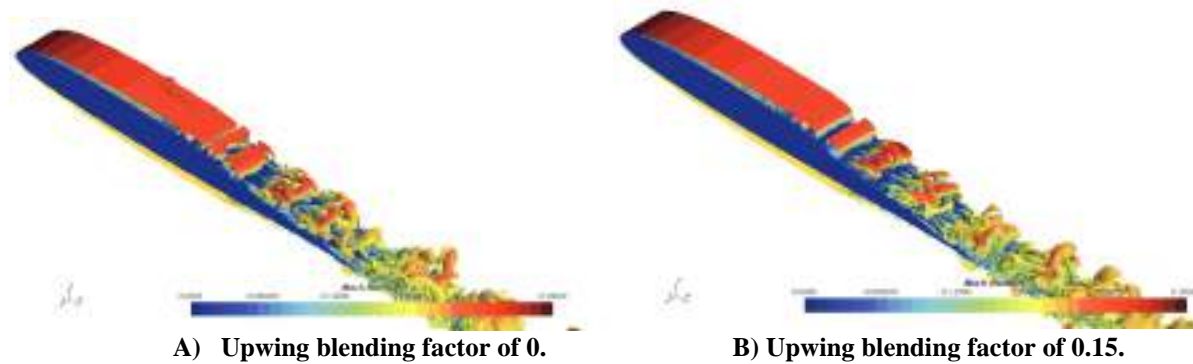


Figure 1. Q -criterion=500 Isosurface coloured with Mach number. CD3/MUSCL3 Scheme.

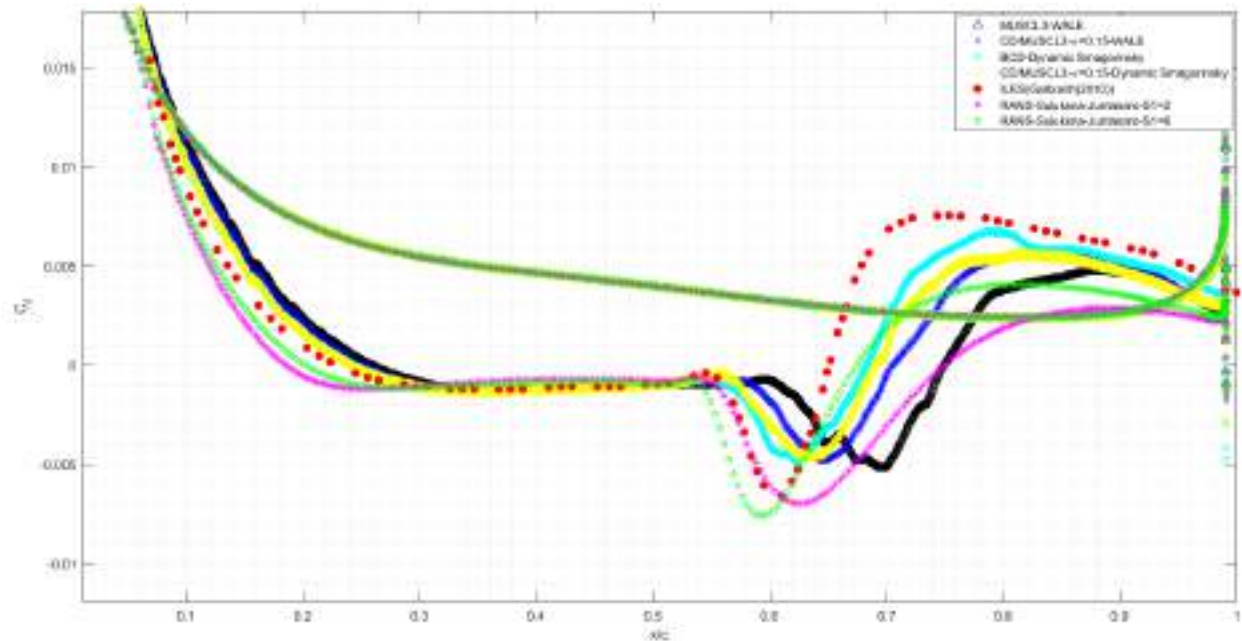


Figure 2. Time-averaged friction coefficient at the mid-span plane.

When comparing our RANS and LES approaches, we observe a noticeable shift of the separation bubble towards the trailing edge. This discrepancy arises because the RANS model follows the recalibration performed in reference [9], which utilized the Galbraith ILES results [1] as a reference. Nevertheless, the overall agreement is satisfactory. Figure 3 depicts the averaged velocity fields, revealing the presence of a separation bubble in both cases. Once again, we observe a slight shift of the bubble towards the trailing edge in the LES simulation. Notably, the LES simulation predicts a much sharper closure of the separation bubble, leading to a higher friction coefficient after reattachment. This discrepancy in skin friction under-prediction becomes more pronounced at lower Reynolds numbers [9] and is associated with excessive damping of turbulent kinetic energy production near the airfoil wall in the RANS model. Despite these discrepancies, Figure 3 highlights the usefulness of a well-tuned transition model, enabling accurate performance predictions with two-dimensional simulations that require a computational cost of approximately 1 CPU-hour, compared to around 40,000 CPU-hours for the 3D LES simulations. Furthermore, it opens up the possibility of enhancing the accuracy of RANS simulations in complex three-dimensional scenarios, such as flow over a rotor, where LES remains currently unaffordable.

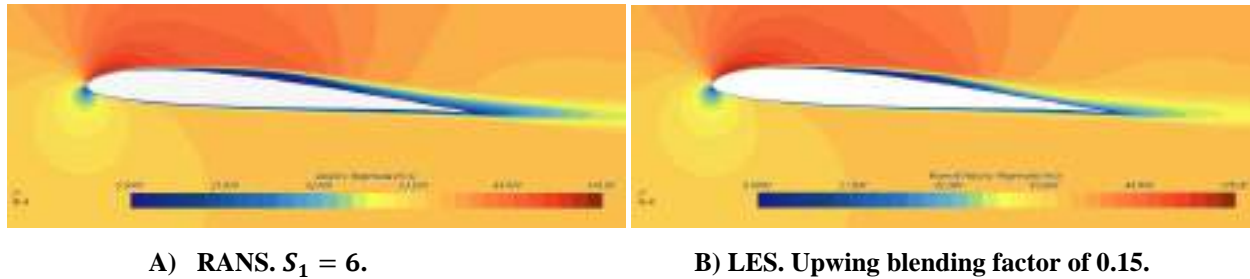


Figure 3. Time-averaged velocity magnitude fields at the mid-span plane.

References

- [1] Galbraith, M., & Visbal, M, Implicit large eddy simulation of low-Reynolds-number transitional flow past the SD7003 airfoil. In 40th fluid dynamics conference and exhibit (2010) AIAA-4737. <https://doi.org/10.2514/6.2010-4737>
- [2] Uranga, A., Persson, P. O., Drela, M., & Peraire, J. Implicit large eddy simulation of transitional flows over airfoils and wings. In 19th AIAA Computational Fluid Dynamics (2009) AIAA- 4131. <https://doi.org/10.2514/6.2009-4131>
- [3] Catalano, P., & Tognaccini, R. Large eddy simulations of the flow around the SD7003 airfoil. In AIMETA Conference (2011) pp. 1-10.
- [4] Windte, J., Scholz, U., and Radespiel, R., “Validation of RANS Simulation of Laminar Separation Bubbles on Airfoils,” Aerospace Science and Technology Journal, Vol. 10, No. 7, 2006, pp. 484–494. <https://doi.org/10.1016/j.ast.2006.03.008>
- [5] Catalano, P. and Tognaccini, R., “Turbulence Modelling for Low Reynolds Number Flows,” AIAA Journal, Vol. 48, No. 8, 2010, pp. 1673–1685. <https://doi.org/10.2514/1.J050067>
- [6] Catalano, P. and Tognaccini, R., “RANS analysis of the low-Reynolds number flow around the SD7003 airfoil,” Aerospace Science and Technology Journal, 2011. <https://doi.org/10.1016/j.ast.2010.12.006>
- [7] De Santis, C., Catalano, P., & Tognaccini, R. (2022). Model for enhancing turbulent production in laminar separation bubbles. AIAA Journal, 60(1), 473-487. <https://doi.org/10.2514/1.J060883>
- [8] Menter, F. R., Smirnov, P. E., Liu, T., & Avancha, R. (2015). A one-equation local correlation-based transition model. Flow, Turbulence and Combustion, 95, 583-619. <https://doi.org/10.1007/s10494-015-9622-4>
- [9] Carreño Ruiz, M., D’Ambrosio, D. Validation of the γ -Re θ Transition Model for Airfoils Operating in the Very Low Reynolds Number Regime. Flow Turbulence Combust 109, 279–308 (2022). <https://doi.org/10.1007/s10494-022-00331-z>
- [10] Langtry, R. B., & Menter, F. R. (2009). Correlation-based transition modeling for unstructured parallelized computational fluid dynamics codes. AIAA journal, 47(12), 2894-2906. <https://doi.org/10.2514/1.42362>
- [11] Ricci, F. & Strobel, P. & Tsoutsanis, P. & Antoniadis, A. Hovering rotor solutions by high-order methods on unstructured grids. Aerospace Science and Technology. (2019). <https://doi.org/10.1016/j.ast.2019.105648>

High-fidelity simulation of the interaction between the wake of a descent capsule and a supersonic parachute

Luca Placco^{1*}, Giulio Soldati³, Alessio Aboudan¹, Francesca Ferri¹,
Matteo Bernardini³, Federico Dalla Barba² and Francesco Picano²

¹ Centro di Ateneo di Studi e Attività Spaziali 'Giuseppe Colombo' (CISAS), Università degli Studi di Padova, via Venezia 15, 35131 Padua, Italy

² Department of Industrial Engineering, Università degli Studi di Padova, via Venezia 1, 35131 Padua, Italy

³ Department of Mechanical and Aerospace Engineering, Sapienza Università di Roma, via Eudossiana 18, 00184 Rome, Italy

*luca.placco@unipd.it

Keywords: Supersonic Parachute, Supersonic Flows, Large Eddy Simulation, Unsteady

Abstract. The objective of the project is to analyze the unsteady dynamics of the parachute-capsule system in a supersonic airflow while descending during planetary entry. Currently, a combination of Large-Eddy Simulation and an Immersed-Boundary Method is being utilized to examine the evolving flow of a rigid supersonic parachute trailing behind a reentry capsule as it descends through the atmosphere of Mars. The flow is simulated at $Ma = 2$ and $Re = 10^6$. A massive GPU parallelization is employed to allow a very high fidelity solution of the multiscale turbulent structures present in the flow that characterize its dynamics. We show how strong unsteady dynamics are induced by the interaction of the wake turbulent structures and the bow shock which forms in front of the supersonic decelerator. This unsteady phenomenon called 'breathing instability' is strictly related to the ingestion of turbulence by the parachute's canopy and is responsible of drag variations and structure oscillations observed during previous missions and experimental campaigns. A tentative one-dimensional model of the flow time-evolving dynamics inside the canopy is proposed.

Introduction and case approach

The recent unsuccessful European missions (i.e. ExoMars 2016) proved how the prediction and the understanding of the dynamics of the descent capsule under the effect of a supersonic decelerator is still an open question in the active research scene that revolves around space exploration. The failure of Schiaparelli EDM landing indeed was ultimately caused by an improper evaluation of the coupled oscillatory motions existing between the descent module and the deployed parachute. The models and the experimental evaluations that were employed to predict the general behaviour of the capsule under the effect of a supersonic decelerator proved to be insufficient, triggering the premature end of the mission [1]. In this context, the main aim proposed by this research activity is to develop a novel technique to study effectively how compressible and turbulent flows interact with non-rigid structures, to properly evaluate and predict their non-steady behaviour. The description of this phenomenon is very elaborate, being affected by several uncertainties such as atmosphere fluctuations, unsteady flow dynamics and structure oscillations [2],[3]. The proposed approach involves Large-Eddy Simulations (LES) [4] for solving the multi-scale flow dynamics and Immersed Boundary Methods to deal effectively with moving solid boundaries [5]. A novel technique to deal with the fluid-structure interaction of compressible flows and thin membranes is in the process of development, starting from the existing IBM strategies. As a starting point for the implementation of the final configuration, a Large-Eddy simulation of



a rigid mock-up parachute trailing behind a reentry capsule has been performed, showing both the potential of the LES approach and the primary dependence of the breathing phenomenon to the interaction of the turbulent wake of the module with the bow shock produced by the parachute.

Computational approach and simulation setup

Compressible Navier-Stokes equations are solved with the high-order finite difference solver STREAmS [4]. Turbulent structures are ultimately identified using the implicit large eddy simulation (ILES) approach; in this way, conventional LES turbulence modeling has been omitted, using instead the numerical dissipation given by the numerical discretization as artificial viscosity acting at small scales. Thus, the 3D Navier-Stokes equations solved are the following:

$$\begin{aligned}\frac{\partial \rho}{\partial t} + \frac{\partial(\rho u_j)}{\partial x_j} &= 0 \\ \frac{\partial(\rho u_i)}{\partial t} + \frac{\partial(\rho u_j u_i)}{\partial x_j} + \frac{\partial p}{\partial x_i} - \frac{\partial}{\partial x_j} \left(\mu \left(\frac{\partial u_i}{\partial x_i} + \frac{\partial u_j}{\partial x_i} - \frac{2}{3} \frac{\partial u_k}{\partial x_k} \delta_{ij} \right) \right) &= 0 \\ \frac{\partial(\rho E)}{\partial t} + \frac{\partial(\rho E u_j + p u_j)}{\partial x_j} + \frac{\partial}{\partial x_j} \left(\lambda \frac{\partial T}{\partial x_j} \right) + \frac{\partial}{\partial x_j} \left(\mu \left(\frac{\partial u_i}{\partial x_i} + \frac{\partial u_j}{\partial x_i} - \frac{2}{3} \frac{\partial u_k}{\partial x_k} \delta_{ij} \right) u_i \right) &= 0\end{aligned}\quad (1)$$

where ρ is the density, u_i denotes the velocity component in the i Cartesian direction ($i=1,2,3$) and p is the thermodynamic pressure. With the intent of reproducing the effect of Mars' atmosphere, the fluid is considered as an ideal gas of CO_2 ; the ratio between the specific heat at constant pressure C_p and the specific heat at constant volume C_v is set to 1.3 while Prandtl number is 0.72. $E = C_v T + u_i^2/2$ represents the total energy per unit mass and the dynamic viscosity μ is assumed to follow the generalized fluid power-law. The thermal conductivity λ is related to μ via the Prandtl number with the following expression: $\lambda = C_p \mu / Pr$. Convective and viscous terms are discretized using a sixth-order finite difference central scheme while flow discontinuities are accounted through a fifth-order WENO scheme. Time advancement of the ODE system is given by a third-order explicit Runge-Kutta/Wray algorithm. No-slip and no-penetration wall boundary conditions on the body are enforced through an Immersed-Boundary Method (IBM) algorithm.

The simulation was performed at $Ma = 2$ and $Re = 10^6$ to simulate the condition at which the parachute deploys. The reference fluid properties associated to the free-stream condition correspond to an altitude of about 9 km from the planet surface and have been obtained using a simulated entry and descent trajectory through the Mars atmosphere of a generic reentry probe [2].

The flow domain selected to perform this first simulation has a size of $L_x = 20D$, $L_y = 5D$, $L_z = 5D$, where $D=3.8\text{ m}$ is the maximum diameter of the descent module; parachute diameter is set to $2.57D$. the mesh is a rectilinear structured grid that consists of $N_x \cdot N_y \cdot N_z = 2560 \cdot 840 \cdot 840$ nodes. The grid density changes in both axial and transverse directions, gaining resolution in the central portion of the domain; the position of the capsule nose is set at $[1D, 0, 0]$ while the parachute center lies at $[10D, 0, 0]$. Computations have been carried out on CINECA Marconi100 cluster, allowing the domain parallel computing on a total of 64 GPUs.

Results

In figure 1 we observe the two-dimensional instantaneous flow field obtained by isolating the $y=0$ slice from the full 3D domain; Mach number contours are shown. Subsonic flow regions (in red), sonic regions (in white) and supersonic areas (in blue) can be identified. We observe the generation of two bow shocks ahead of the capsule and the canopy and the wake produced by the two bodies. The flow at the vent section is sonic. Pushed by the high pressure within the canopy and finding a larger passage section, it rapidly accelerates to the highest Mach number of the flow field. The breathing motion involves inhomogeneous fluctuations in pressure and density, resulting in

substantial variations in drag, even though the canopy area remains constant. The primary cause of the breathing cycle appears to be the aerodynamic interaction between the wake of the capsule and the bow shock created by the parachute canopy.

Figure 2 shows density ratio contours in the area around the canopy. Different phases of the cycle that surrounds the periodic motion of the front bow shock along the flow direction: an increasing density inside the canopy pushes the shockwave away, allowing a larger flux to escape from the canopy (from [1] to [2]). Thus, this creates a decrease in the density that in turn draws back in the shockwave ([2] to [3]) and restarts the cycle ([3] to [4]). The

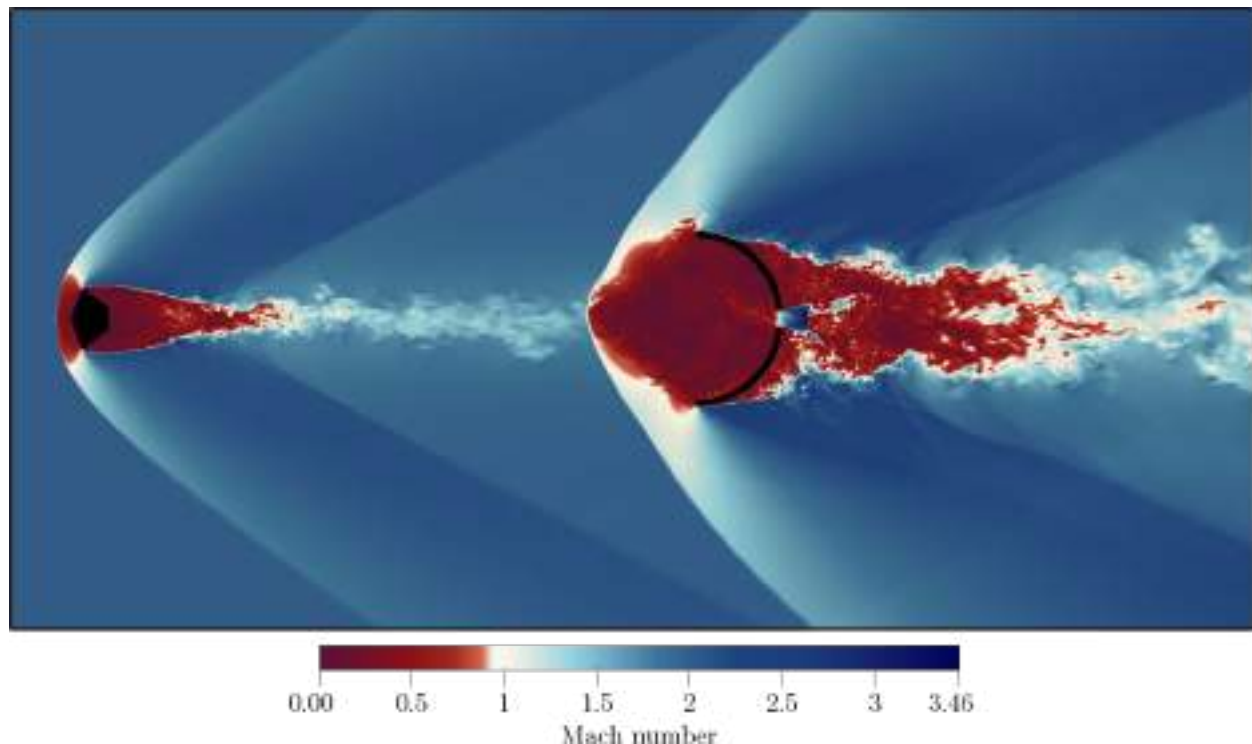


Figure 1: Instantaneous Mach contours ($y = 0$ cross section) of the simulated flow domain.

Conclusions

The present work proposes a high-fidelity time-evolving simulation of the interaction between the turbulent wake of a supersonic descent module and a generic rigid mock-up thick decelerator. We show how the critical ‘breathing’ instability associated to supersonic parachutes is intrinsically connected to the interaction of the turbulent wake flow of the descent module and the front bow shock produced by the decelerator. To overcome the limitation of the current setup and further extend the representation of its dynamics, the implementation of a novel immersed boundary method technique is in progress. This will require the solution of fluid-structure interaction of compressible supersonic flows and flexible thin membranes. The new framework will involve an extension of the current IBM module and a finite element method model to deal with flexible moving boundaries (zero-thickness), representing the very thin structure of the simulated decelerator. In this way, the approach in development will allow to represent properly both the entire deployment sequence and the system unsteadiness in all its components, thus providing the full representation of the ‘breathing’ phenomenon. The oscillation cycles align with the dynamics of the wake, as observed in previous experimental studies [3]. These cycles exhibit a frequency that is consistently around 0.16 in terms of the Strouhal number.

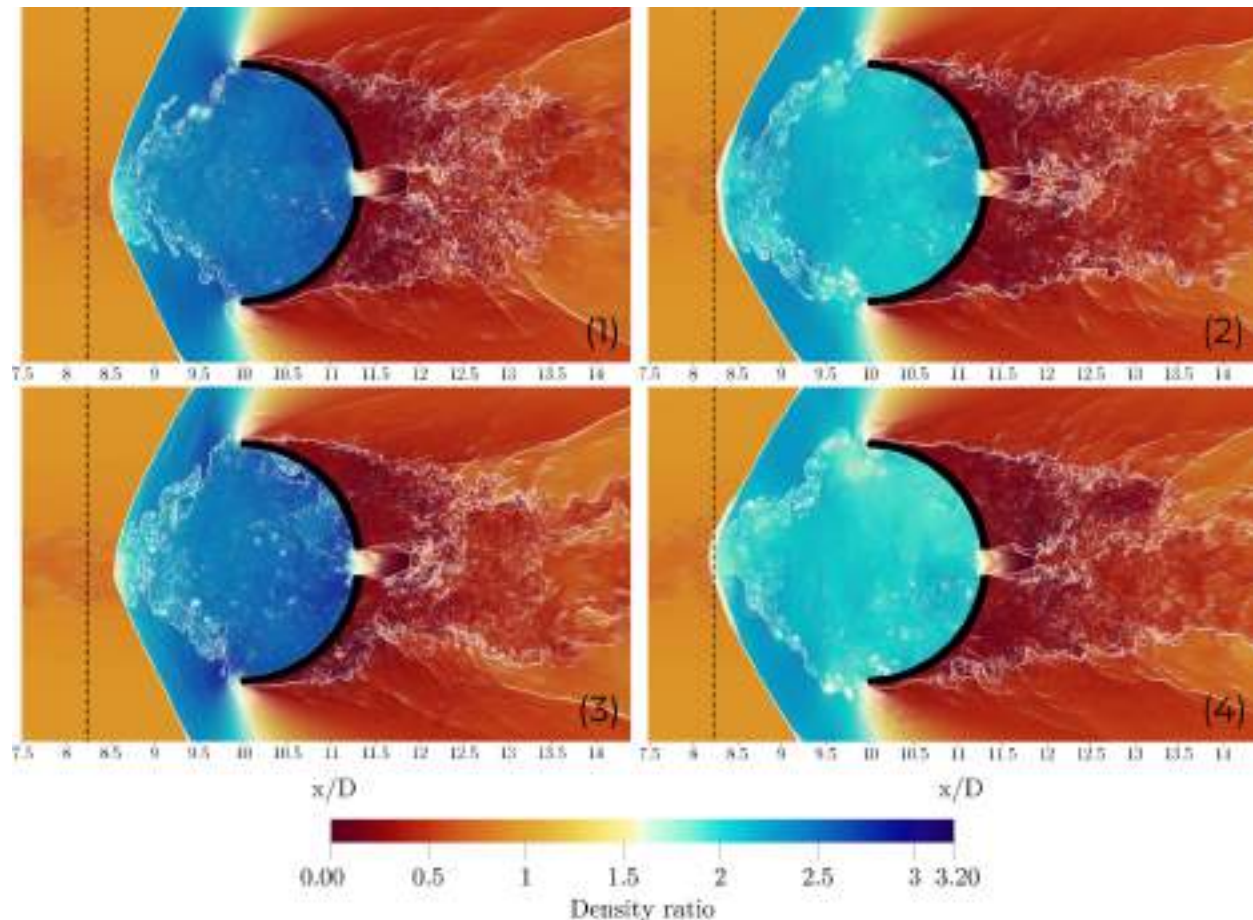


Figure 2: Instantaneous density ratio contours ($y = 0$ cross section) at different progressive timestep around the parachute canopy.

References

- [1] T. Tolker-Nielsen. EXOMARS 2016 - Schiaparelli Anomaly Inquiry, 2017.
- [2] A. Aboudan et al. ExoMars 2016 Schiaparelli module trajectory and atmospheric profiles reconstruction. *Space Science Reviews*, 214: 97, 08 2018. <https://doi.org/10.1007/s11214-018-0532-3>
- [3] X. Xue and Chih-Yung Wen. Review of unsteady aerodynamics of supersonic parachutes. *Progress in Aerospace Sciences*, 125:100728, 2021. <https://doi.org/10.1016/j.paerosci.2021.100728>
- [4] M. Bernardini, D. Modesti, F. Salvatore, and S. Pirozzoli. Streams: a high-fidelity accelerated solver for direct numerical simulation of compressible turbulent flows. *Co.Ph.Co.*, 263, 2021. <https://doi.org/10.1016/j.cpc.2021.107906>
- [5] H. Yu and C. Pantano. An immersed boundary method with implicit body force for compressible viscous flow. *Journal of Computational Physics*, 459:111125, 2022. <https://doi.org/10.1016/j.jcp.2022.111125>

Impact of a wedge in water: assessment of the modeling keyword, presence of cavitation and choice of the filter most suitable for the case study

D. Guagliardo^{1,a}, E. Cestino^{1,b*}, G. Nicolosi^{1,a}, E. Guarino^{1,a}, A. Virdis^{1,a},
A. Alfero^{1,a}, D. Pittalis^{1,a} and M.L. Sabella^{1,a}

¹Politecnico di Torino (DIMEAS), Corso Duca degli Abruzzi, 24 10129 Torino, Italy

^ateams55.polito@gmail.com, ^benrico.cestino@polito.it

Keywords: Fluid-Structure Interaction, SPH, Cavitation, Pressure Filter

Abstract. The purpose of this paper is to compare the results obtained from a rigid wedge impacting water that is modelled using different techniques based on the SPH (Smoothed Particle Hydrodynamics) method. The study aims to evaluate the quality of the results, optimizing the computational time, which is obtained when the wedge is discretized as a section or as a half of it. The comparison of the results obtained considers the different materials that the ANSYS LS-DYNA software allows to assign to water through different keywords. The effect of cavitation on the pressures reached during the vertical impact was evaluated as a function of ambient temperature. Finally, given the high noise recorded in the pressure files, the study uses a filter created in MATLAB. The latter involves a double pass through the Kalman filter first and the Gauss filter later. All results obtained through the numerical method are compared with Von Karman and Wagner analytical theories.

Introduction

The student team "TEAM S55" of Politecnico of Turin was born in 2017 to rebuild the SIAI-Marchetti S55 seaplane on a 1:8 scale [1-3]. The following paper is created by the FSI section which studies the interaction between the aircraft and the water at ditching. The purpose of this paper is to describe through ANSYS LS-DYNA the water impact of a wedge, at a vertical speed of 5.8 m/s, to evaluate the effect of various parameters in wedge and water modelling. Due to the high computational requirements inherent in the SPH method, the influence of air is neglected to reduce the computational time, since it doesn't have an influence on the accuracy of stress prediction [4]. The analysis results are purified from numerical noise through a filter implemented in MathWorks MATLAB.

Model description

Full model. The model under study is composed of two parts, here under described. The first one is the wedge, it has a width of 254.8 mm, a height of 105 mm, a thickness of 2 mm and a dihedral angle of 30°, as shown in *Fig. 1*. The item is discretized in 1320 shell elements, mainly concentrated in the impacting wall. The material used is an infinitely rigid steel, modelled through the keyword *020 MAT_RIGID*. The boundary conditions forced the wedge to translate only along the z-direction and lock any rotation.

The second one is the water. The water box has dimensions $x = 1200$ mm, $y = 40$ mm, $z = 300$ mm, and it got an SPH number of 56000. It has got **BOUNDARY_SPH_NON_REFLECTING* plans in the bottom and perpendicular to the x-direction, and **BOUNDARY_SPH_SYMMETRY-PLANE* perpendicular to the y-direction. It's possible to use three different materials to model the water [5]: *009 MAT_NULL*, *001 MAT_FLUID-ELASTIC_FLUID* and *010 MAT_ELASTIC_PLASTIC_HYDRO*. For each material, it's possible to define the cavitation pressure. The phenomenon of cavitation is a function of the ambient temperature through vapor



pressure, and it is defined differently for each material. For materials 009 and 010 cavitation is indicated by the pressure cut-off, while for materials 001 it is defined by the cavitation pressure parameter.

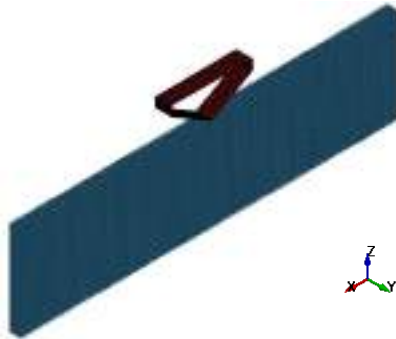


Figure 1. Wedge and water

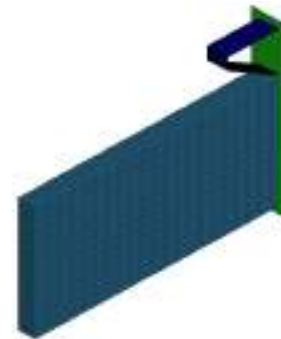


Figure 2. Half wedge with symmetry plane

Model description

Half model. The geometry in this case turns out to be the exact half as shown in Fig. 2; both the wedge and the water box were halved along the x direction and a symmetry wall was then added via the keyword `*BOUNDARY_SPH_SYMMETRY_PLANE`, green in Fig. 2, as used by [4].

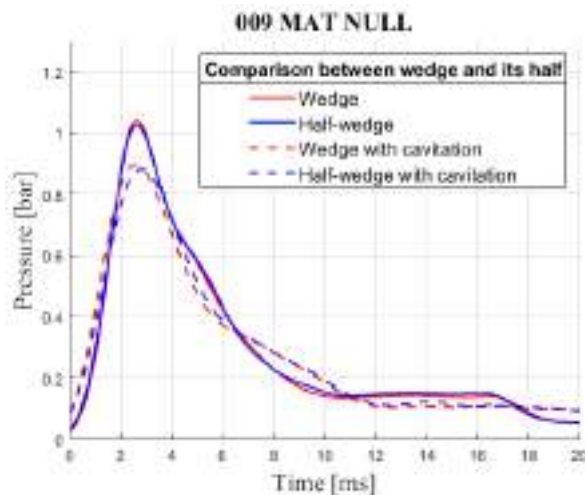


Figure 3. Comparison using MAT_NULL

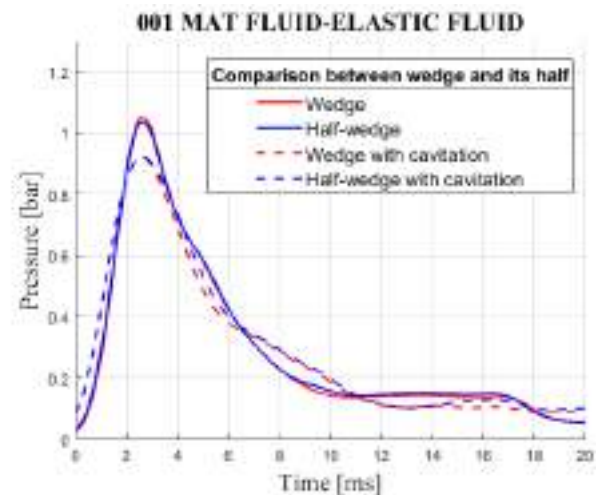


Figure 4. Comparison using MAT_ELASTIC

Between a complete model and a halved one there is a time saving of 48% with a discrepancy in the results, as regards the peak pressure in `001 MAT_FLUID-ELASTIC_FLUID`, of 1% for the results in which cavitation is neglected and almost nothing as regards the case in which cavitation is considered. The pressure peaks for `009 MAT_NULL` differ by 1.34% when cavitation is ignored and by 1.84% when cavitation is considered. The pressure detection sensor, in all analyses, is positioned at 13.93 mm along the x direction; this position will be the same one considered for the analytic theories of von Karman [6] and Wagner [7].

The pressure results for the cases just mentioned are shown in Fig. 3 and Fig. 4 and are related respectively to the materials `009 MAT_NULL` and `001 MAT_FLUID-ELASTIC_FLUID`. Furthermore, the vertical impact velocity of the wedge is 5.8 m/s and the vapor pressure considered for cavitation is referred to standard conditions (25 °C).

Water keyword comparison

As studied by Q.W. Ma and D.J. Andrews [7] the water can be defined in three different ways. `009 MAT_NULL` and `010 MAT_ELASTIC_PLASTIC_HYDRO` need an EOS (Equation Of State), it was chosen the `*EOS_GRUNEISEN` for both materials. In modelling a fluid, it can be observed

that some keywords can be advantageous due to computational cost, the *001 MAT_FLUID-ELASTIC_FLUID* appears to be the fastest in computation, because it's the only one without an EOS. The *009 MAT_NULL* is 6% slower, and the *010 MAT_ELASTIC_PLASTIC_HYDRO* is even 26% slower. *Fig. 5* shows the results obtained for the three different keywords, in the absence of cavitation, compared with the maximum values predicted by the analytical theories of von Karman [6] and Wagner [7]. It's noteworthy that in the peak pressure zone, which is the most important in terms of structural strength, the values are consistent among the various materials, with an error lower than 2%.

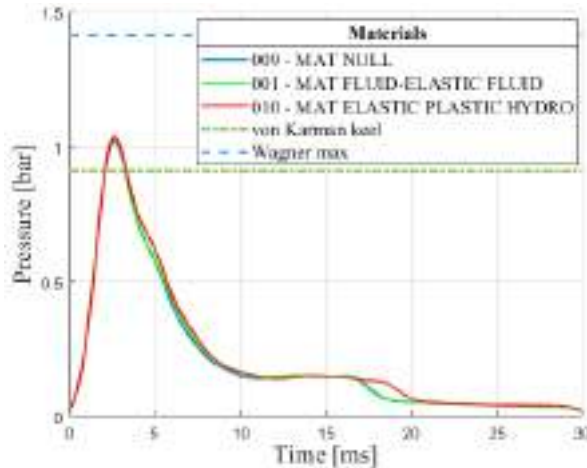


Figure 5. Water keyword comparison

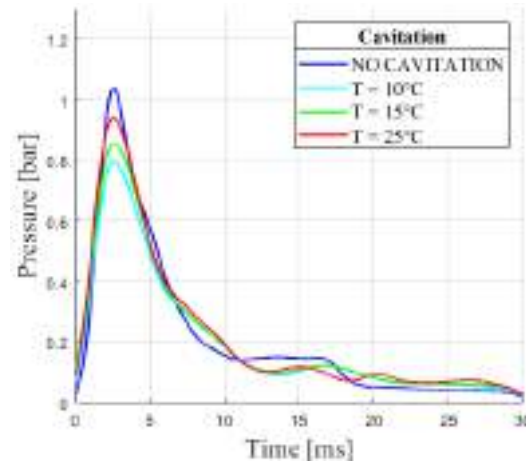


Figure 6. Pressure as function of temperature

Effect of cavitation

Cavitation is a phenomenon that can occur when an object impacts a liquid, causing its phase change to gas due to the variation in fluid pressure, as predicted by Wagner [8]. That condition is verified in the study, but it was found a similar phenomenon even with velocities that don't verify the relation. This phenomenon is defined by Korobkin [9] as interface cavitation. The study shows that in a zone close to the first impacting object part, the hydrodynamic pressure is smaller than the atmospheric pressure. This leads to the formation of a cavity that, however, does not extend to the peripheral zones. The formation of this cavity, whose shape and size are described analytically in [9], changes the liquid flow and the pressure distribution. On the LS-DYNA software [10], pressure cut-off (PC) is defined to allow for a material to "numerically" cavitate. In other words, when a material undergoes dilatation above a certain magnitude, it should no longer be able to resist this dilatation. Since dilatation stress or pressure is negative, setting PC as the vapor pressure value, for the desired temperature, would allow for the material to cavitate once the pressure in the material goes below this negative value. Cavitation pressure (CP) is also defined in *001 MAT_FLUID-ELASTIC_FLUID*, but in this case the chosen value is positive. Analysis have been carried out by comparing the pressure trend in the case where the cavitation is not considered and if the cavitation is considered at the temperatures of 10°C, 15°C and 25°C. For the comparison the material *001 MAT_FLUID-ELASTIC_FLUID* is used. As can be seen in *Fig. 6* the pressure peak without cavitation is greater with respect to the cases where cavitation is considered, but after the peak, signal noise is lower. Considering that the vapor pressure decreases as the temperature decreases, it was found that the peak pressure decreases with decreasing water temperature and the effect of cavitation becomes more significant.

Filter choice and effects

The pressure results contained in the outputs provided by LS-DYNA are very noisy due to the unstable nature of the SPH. From previous studies [11], the importance of data filtering in this type of experiment was understood; so, the new goal was to search for the best filter that approximated data accurately with a lower error correlation. The choice was the Kalman filter following the indications given by [12] as it also reconstructs the trend without adding delays. From experimental results, Kalman filter is superior in terms of filtering accuracy, it's implemented in two iterative repeated phases: prediction and update. The *prediction* part consists in predicting the estimated state variable and the predicted state variance variable; the update part includes the Kalman gain and inside it the filtered data corresponds to the *updated* estimated state variable and is shown as the output of the algorithm. However, filtering performance depend on the parameters R, measurement constant, and Q, process variance constant. As reported by [13], the parameters $R = 1$ and $Q = 0.01$ experimentally provide the best filter results because noise is reduced but the original characteristics of the data are preserved. In general, the ratio of R to Q should not exceed 100 to avoid excessively filtered results. After the application of the Kalman filter, the graph is still partially affected by noise, for this reason a Gaussian filter is also applied to further smooth the curves (Fig. 7).

A Gaussian filter attenuates the high-frequency components in the signal and passes the low-frequency components. It is based on input signal convolution with a Gaussian function. The input signal is convoluted with the Gaussian filter kernel. This involves point-by-point multiplication

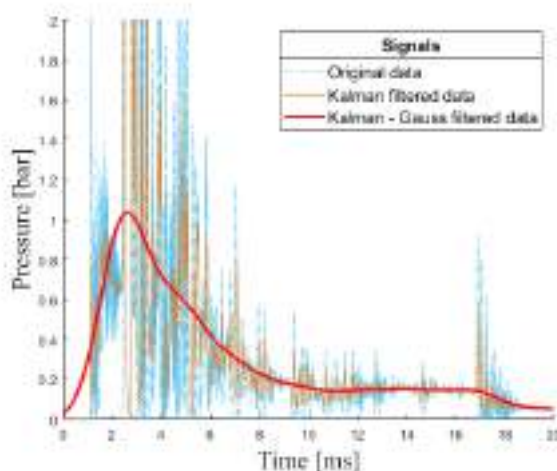


Figure 7. Kalman – Gauss filter

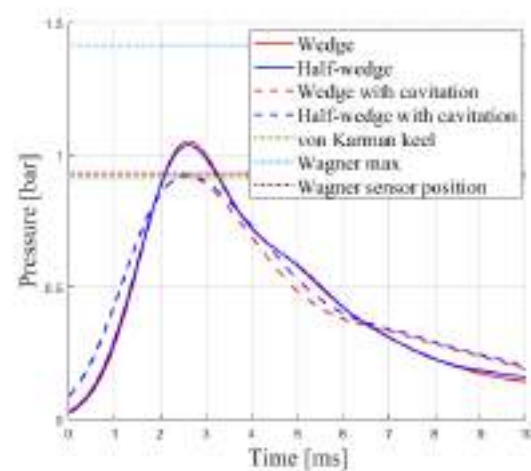


Figure 8. Numerical-analytical comparison

between kernel samples and input signal samples, followed by the sum of the results. The smoothing effect produced by a Gaussian filter will depend on the width of the kernel, which is controlled by the sigma parameter, standard deviation, automatically calculated by MATLAB.

Conclusions

Using a half geometry, it's worth choice to maintain the precision in the results and to reduce the computational cost. The cavitation effect or the cavity formed under the wedge reduce the pressure peak, but it can produce undesired vibrations. It's highlighted the importance of the cavitation as function of temperature variation in the range from 25 °C to 10 °C. A lower water temperature can produce a lower pressure due to the reduction of vapor pressure and bulk modulus. The reduction of these two values prevails over the increase of density and viscosity coefficient. Furthermore, the peak pressure, obtained in the analyses considering cavitation with the water temperature at 25 °C, well fit with the pressure values predicted by the analytical theories of Wagner and von Karman for the sensor position (Fig. 8), that were based, especially the von Karman theory, on practical experiments in which is naturally included the cavitation effect.

Acknowledgement

The authors thank the Politecnico di Torino and the DIMEAS department for the provision of resources and facilities. We would thank ANSYS and EnginSoft SpA for the support and for providing us with the software licenses.

References

- [1] Cestino, E.; Frulla, G.; Sapienza, V.; Pinto, P.; Rizzi, F.; Zaramella, F.; Banfi, D. (2018) Replica 55 Project: A Wood Seaplane in The Era Of Composite Materials, In: Proc of 31st ICAS 2018 Congress, 9-14 September 2018, Belo Horizonte (Brasil)
- [2] Nicolosi G., Valpiani F., Grilli G., Saponaro Piacente A., Di Ianni L., Cestino E., Sapienza V., Polla A., Piana P. Design Of A Vertical Ditching Test. Proc. 32nd ICAS Congress 6-10 September 2021 - Shanghai, China
- [3] Cestino, E., Frulla, G., Polla, A., Nicolosi, G. (2023). Equivalent Material Identification in Composite Scaled Hulls Vertical Impact Tests. In: Lopresto, V., Papa, I., Langella, A. (eds) Dynamic Response and Failure of Composite Materials. DRAF 2022. Lecture Notes in Mechanical Engineering. Springer, Cham. https://doi.org/10.1007/978-3-031-28547-9_6
- [4] Fragassa C, Topalovic M, Pavlovic A, Vulovic S. Dealing with the Effect of Air in Fluid Structure Interaction by Coupled SPH-FEM Methods. *Materials*. 2019; 12(7):1162. <https://doi.org/10.3390/ma12071162>
- [5] Q.W. Ma and D.J. Andrews. On techniques for simulating effects of cavitation associated with the interaction between structures and underwater explosions using LS-DYNA. 3rd European LS-DYNA Conference, Paris, 2001.
- [6] von Kármán T. The impact on seaplane floats during landing. NACA Technical Notes N.321, 1929.
- [7] Wagner H. Über Stoß- und Gleitvorgänge an der Oberfläche von Flüssigkeiten. Zeitschrift Für Angewandte Mathematik Und Mechanik, Vol. 12, No. 4, 1932. <https://doi.org/10.1002/zamm.19320120402>
- [8] Panciroli R, Pagliaroli T, Minak G. On Air-Cavity Formation during Water Entry of Flexible Wedges. *Journal of Marine Science and Engineering*. 2018; 6(4):155. <https://doi.org/10.3390/jmse6040155>
- [9] "Korobkin, A. Cavitation in liquid impact problems. In Proceedings of the Fifth International Symposium on Cavitation (CAV2003), Osaka, Japan, 1 January 2003; Volume 2, pp. 1–7."
- [10] Keyword Manual, 1999, "LS-DYNA keyword user's manual", Livermore Software Technology Corporation.
- [11] F. Valpiani, P. Cicolini, D. Esposto, A. Galletti & D. Guagliardo. Numerical modeling of Fluid-Structure Interaction of a 3D wedge during water impact with variation of velocity and pitch angle. 33rd ICAS Congress 4-9 September 2022 – Stockholm, Sweden
- [12] V, Kutz J N, Brunton B W. Numerical differentiation of noisy data: A unifying multiobjective optimization framework. *IEEE Access*, Vol. 8, 2020. <https://doi.org/10.1109/ACCESS.2020.3034077>
- [13] Ma'arif, Alfian & Iswanto, & Nuryono, Aninditya & Alfian, Rio. (2020). Kalman Filter for Noise Reducer on Sensor Readings. *Signal and Image Processing Letters*. 1. 11-22. <https://doi.org/10.31763/simple.v1i2.2>

Thermal fluid-structure interaction by discontinuous Galerkin methods

Vincenzo Gulizzi^{1,a*}

¹Department of Engineering, University of Palermo, Viale delle Scienze, 90128, Palermo

^avincenzo.gulizzi@unipa.it

Keywords: Thermal Fluid-Structure Interaction, Discontinuous Galerkin Methods, High-Order Accuracy

Abstract. This research study presents a novel high-order accurate computational framework for thermal fluid-structure interaction problems. The framework is based on the use of block-structured Cartesian grids where level set functions are employed to define both the fluid and the solid regions. This leads to a mesh that consists of a collection of standard d -dimensional rectangular elements and a relatively smaller number of irregular elements at the fluid-solid interface. The embedded boundaries are resolved with high-order accuracy thanks to the use of high-order accurate quadrature rules for implicitly-defined regions. The fluid is assumed compressible and governed by the inviscid Navier-Stokes equations, whilst the solid region obeys the equations of thermo-elasticity within the small-strain regime. Numerical examples are provided to assess the capability of the proposed approach.

Introduction

The interest in developing reliable, sustainable and reusable transportation systems that are capable of flying at Mach numbers ranging from 0 to 12 is continuously growing. It is well-known that, within such a wide flight regime, the aircraft structure must endure extreme conditions in terms of pressure and temperature loads. These loads induce a complex thermo-elastic interaction that is generally resolved via the aid of numerical methods as analytical solutions exist for very special combinations of boundary conditions and material properties.

In the context of computational methods, the Finite Volume (FV) method is the industry-standard numerical approach to fluid mechanics problems and is found in many open-source and commercial software libraries; on the other hand, thermo-mechanical problems are very often tackled by the Finite Element (FE) method. Both the FV and the FE methods are extremely robust and widely employed in science and engineering; however, their coupling may become involved and may represent the bottleneck for fluid-structure interaction simulations.

Among the various alternatives to FV- or FE-based approaches, the discontinuous Galerkin (DG) method has proved a powerful numerical technique for both fluid- and solid-mechanics; see, e.g., [1], among several recent contributions. With respect to other techniques, DG-based formulations use spaces of discontinuous basis functions to approximate the solution fields; this naturally enables high-order accuracy with generally shaped mesh elements, block-structured mass matrices and massive parallelization. Additionally, as DG methods enforce both boundary and interface conditions in a weak sense, the coupling between different formulations for the same or for different sets of partial differential equations is significantly simplified. This includes the coupling between different DG formulations or between a DG formulation and a FVM scheme, see Ref.[2].

This study introduces a novel formulation for unsteady thermal fluid-structure interaction problems coupling a shock-capturing FV scheme and a high-order DG scheme. Numerical tests are presented for a thermo-elastic cylinder moving at supersonic speed in an inviscid gas.



Geometry representation and discretization

The coupled thermal fluid-structure interaction problem involves the modeling of two regions consisting of a fluid domain and a solid domain. Here, the geometry is represented via a level set function φ defined in a rectangular domain $\mathcal{R} \subset \mathbb{R}^d$, such that the fluid domain \mathcal{D}^g and the solid domain \mathcal{D}^s are identified by the points belonging to \mathcal{R} where φ is negative and where φ is positive, respectively. It follows that the interface \mathcal{J} between the fluid and the solid domains is identified by $\{x \in \mathcal{R} : \varphi(x) = 0\}$. To illustrate, Fig.(1a) shows a level set function defining a circle in a square domain, whilst Fig.(1b) shows the corresponding fluid and solid regions.

The fluid and the solid domains are eventually discretized. Here, we use the implicitly-defined mesh approach developed in Refs.[2,3,4], which is based on intersecting a structured grid with the zero-contour of the level set functions and allows resolving the curved boundaries with high-order accuracy. Fig.(1c) shows the implicitly defined mesh for the geometry shown in Fig.(1b); in the figure, the darker elements represent the extended elements that prevent the presence of overly small elements in the mesh. See Refs.[2,3,4] for further detail on this meshing strategy.

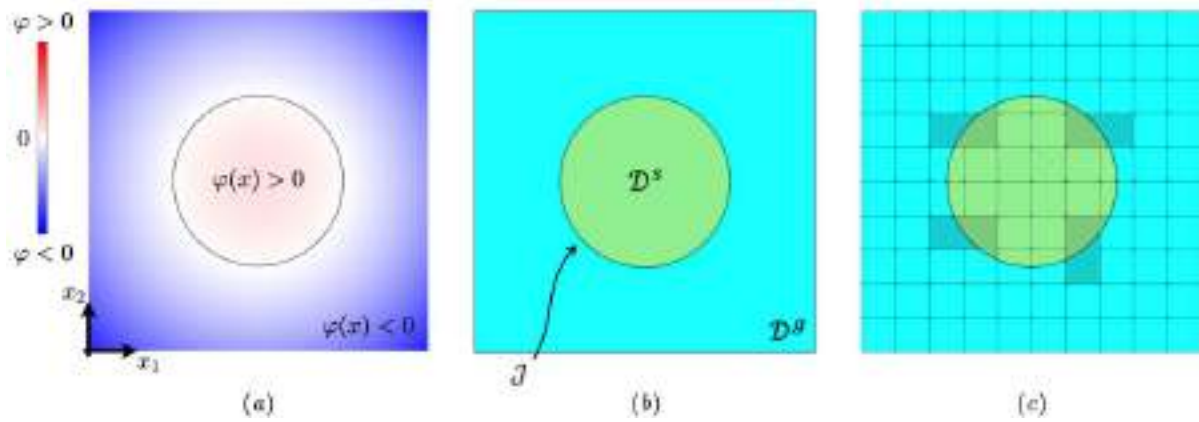


Fig. 1: (a). Level set function defined in a two-dimensional square and (b) corresponding fluid and solid regions identified by the sign of the level set function. (c) Implicitly defined mesh.

Fluid dynamics model

The considered fluid is a compressible gas assumed to obey the Euler equations, which are expressed as the following conservation law:

$$\frac{\partial \mathbf{U}^g}{\partial t} + \frac{\partial \mathbf{F}_k^g}{\partial x_k} = 0, \quad (1)$$

where t is time, x_k is the k -th spatial component, and \mathbf{U}^g and \mathbf{F}_k^g denote the $(d+2)$ -dimensional vectors of the conserved variables and the flux in the k -th direction, respectively; these are

$$\mathbf{U}^g \equiv \begin{pmatrix} \rho^g \\ \rho^g \mathbf{v}^g \\ \rho^g e_0 \end{pmatrix} \quad \text{and} \quad \mathbf{F}_k^g \equiv \begin{pmatrix} \rho^g v_k^g \\ \rho^g v_k^g \mathbf{v}^g + p \delta_k \\ (\rho^g e_0 + p) v_k^g \end{pmatrix}, \quad (2)$$

where ρ^g is the fluid density, $\mathbf{v}^g \equiv (v_1^g, \dots, v_d^g)^T$ is the gas velocity vector, e_0 is the gas total energy and p is the gas pressure. The governing equations are closed by the ideal-gas equation of state with ratio γ of specific heats. In Eq.(1) and in the remainder of the paper, Latin indices will take value in $\{1, \dots, d\}$ and, when repeated, imply summation.

Thermo-mechanical model

The thermo-mechanical model considered here is based on the theory of linear elasticity and Fourier's law of heat conduction. In absence of external sources, it is possible to show that the governing equations of coupled, unsteady thermo-elasticity may be written as:

$$\frac{\partial \mathbf{U}^s}{\partial t} - \frac{\partial}{\partial x_k} \left(\mathbf{Q}_{kl} \frac{\partial \mathbf{U}^s}{\partial x_l} + \mathbf{R}_k \mathbf{U}^s \right) + \mathbf{R}_k^* \frac{\partial \mathbf{U}^s}{\partial x_k} + \mathbf{S} \mathbf{U}^s = \mathbf{0}, \quad (3)$$

where

$$\mathbf{U}^s \equiv \begin{pmatrix} \mathbf{u}^s \\ \mathbf{v}^s \\ \vartheta \end{pmatrix}, \quad \mathbf{Q}_{kl} \equiv \begin{pmatrix} \mathbf{0} & \mathbf{0} & \mathbf{0} \\ \frac{\mathbf{c}_{kl}}{\rho^s} & \mathbf{0} & \mathbf{0} \\ \mathbf{0} & \mathbf{0} & \frac{\kappa_{kl}}{c^s} \end{pmatrix}, \quad \mathbf{R}_k \equiv \begin{pmatrix} \mathbf{0} & \mathbf{0} & \mathbf{0} \\ \mathbf{0} & \mathbf{0} & -\frac{\mathbf{m}_k}{\rho^s} \\ \mathbf{0} & \mathbf{0} & 0 \end{pmatrix}, \quad \mathbf{R}_k^* \equiv \begin{pmatrix} \mathbf{0} & \mathbf{0} & \mathbf{0} \\ \mathbf{0} & \mathbf{0} & \mathbf{0} \\ \mathbf{0} & \frac{T_0 \mathbf{m}_k^T}{c^s} & 0 \end{pmatrix} \quad (4a)$$

and

$$\mathbf{S} \equiv \begin{pmatrix} \mathbf{0} & -\mathbf{I}_d & \mathbf{0} \\ \mathbf{0} & \mathbf{0} & \mathbf{0} \\ \mathbf{0} & \mathbf{0} & 0 \end{pmatrix}. \quad (4b)$$

In Eq.(4), $\mathbf{u}^s \equiv (u_1^s, \dots, u_d^s)^T$ is the solid displacement vector, $\mathbf{v}^s \equiv (v_1^s, \dots, v_d^s)^T$ is the solid velocity vector, $\vartheta \equiv T^s - T_0$ represents the variation of the solid temperature field T^s with respect to a reference temperature T_0 , ρ^s and c^s are the density and the heat capacity per unit volume, respectively, of the solid domain, \mathbf{c}_{kl} is a $d \times d$ matrix collecting subsets of elastic coefficients, see, e.g., Refs.[5], κ_{kl} is the kl -th entry of thermal conductivity tensor, \mathbf{m}_k is the d -dimensional vector containing components of the thermo-elasticity tensor, and \mathbf{I}_d is the $d \times d$ identity matrix. It is noted that the thermo-elastic properties of the solid are assumed temperature independent.

Thermal fluid-structure coupling

The coupling between the gas region and the solid region occurs at the interface between the two domains, i.e. at \mathcal{J} shown in Fig.(1b). Recalling that the solid is assumed to undergo small deformations, its interface with the gas do not change with time and, as such, behaves like a fixed wall for the gas dynamics equations. Additionally, as the gas is assumed inviscid and non-conducting, its temperature T^g is determined by the equation of state.

The thermal fluid-structure coupling problem is then solved as follows: the conserved variables of Eq.(1) are updated from the time instant t to the time instant $t + dt$ using an explicit time-integration algorithm; then, at the time $t + dt$, the computed values of the gas pressure and temperature provide the required boundary conditions at the gas-solid interface to solve the unsteady thermo-elastic problem.

Discontinuous Galerkin formulation

The governing equations of the gas domain, i.e. Eq.(1), are numerically solved via the time-explicit Runge-Kutta discontinuous Galerkin formulation coupled to a shock-capturing second-order FV scheme [2,4]. On the other hand, the equations governing the thermo-elastic solid are solved by extending the DG formulation for elliptic PDEs developed in Refs.[5] with suitably-defined terms accounting for the temporal derivatives in Eq.(3). See Ref.[6] for further detail.

Results

Numerical results are presented for a cylinder with radius $r = 0.2$ m moving at a Mach number $\mathbf{M}_\infty = 2$ at an altitude $h = 10$ km; the geometry and the boundary conditions of the problem are sketched in Fig.(2a). The final time of simulation is $I_t = 3$ ms. The gas is assumed perfect with $\gamma = 1.4$, while the solid is assumed isotropic with properties: density 2700 kg/m³, Young's

modulus 70 GPa, Poisson's ratio 0.33, thermal conductivity coefficient 210 W/(m K), thermal expansion coefficient 24×10^{-6} 1/K and volumetric heat capacity 2.43×10^6 J/(m³ K).

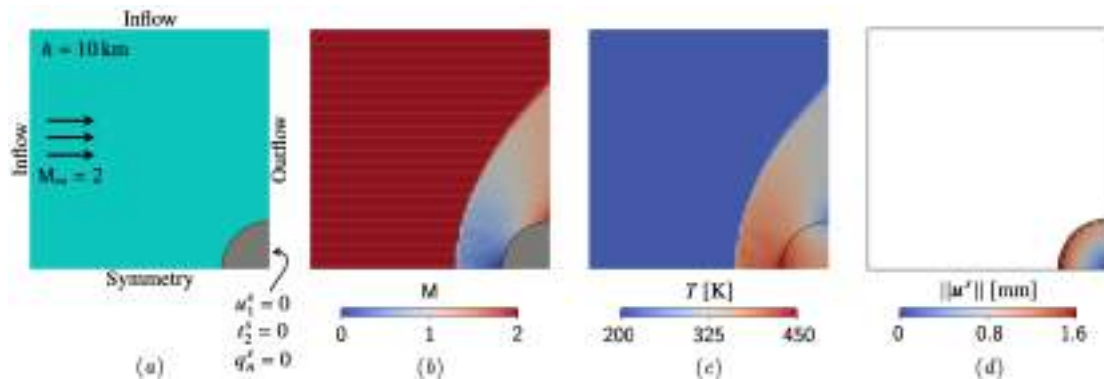


Fig. 2: (a) Geometry and boundary conditions. (b) Mach number. (c) Temperature. (d) Displacement magnitude (the dashed line denotes the undeformed shape).

Fig.(2b) shows the distribution of the Mach number, Fig.(2c) shows the temperature distribution within both the gas and the solid, while Fig.(2d) shows the displacement magnitude of the solid. The figures confirm the ability of the formulation to capture the shock wave, the thermal loads induced by the fluid flow and the deformation of the body.

Conclusions

A novel formulation for unsteady thermal fluid-structure interaction problems has been presented. The formulation uses a high-order accurate representation of embedded geometries, a shock-capturing FV scheme to resolve flow discontinuities, and a high-order accurate DG scheme for the thermo-elastic problem. Numerical results have been presented for a thermo-elastic cylinder moving at $M = 2$ and have showed the capability of the proposed approach.

References

- [1] Z.Cai and B. Thornber. A high-order discontinuous Galerkin method for simulating incompressible fluid-thermal-structural interaction problems. *International Journal of Heat and Fluid Flow*, 83 (2020), p.108572. <https://doi.org/10.1016/j.ijheatfluidflow.2020.108572>
- [2] V. Gulizzi, A.S. Almgren and J.B. Bell. A coupled discontinuous Galerkin-Finite Volume framework for solving gas dynamics over embedded geometries. *Journal of Computational Physics*, 450 (2022), p.110861. <https://doi.org/10.1016/j.jcp.2021.110861>
- [3] R. Saye. Implicit mesh discontinuous Galerkin methods and interfacial gauge methods for high-order accurate interface dynamics, with applications to surface tension dynamics, rigid body fluid-structure interaction, and free surface flow: Part I. *Journal of Computational Physics*, 344 (2017), pp.647-682. <https://doi.org/10.1016/j.jcp.2017.04.076>
- [4] V. Gulizzi and R. Saye. Modeling wave propagation in elastic solids via high-order accurate implicit-mesh discontinuous Galerkin methods. *Computer Methods in Applied Mechanics and Engineering*, 395 (2022), 114971. <https://doi.org/10.1016/j.cma.2022.114971>
- [5] V. Gulizzi, I. Benedetti and A. Milazzo. A high-resolution layer-wise discontinuous Galerkin formulation for multilayered composite plates. *Composite Structures*, 242 (2020), 112137. <https://doi.org/10.1016/j.compstruct.2020.112137>
- [6] V. Gulizzi, I. Benedetti and A. Milazzo. Discontinuous Galerkin Methods for Solids and Structures. in: M.H. Ferri Aliabadi, W.O. Soboyejo (Eds.), *Comprehensive Structural Integrity* 2nd edition, Oxford: Elsevier, 2023, pp. 348-377. <https://doi.org/10.1016/B978-0-12-822944-6.00024-4>

Conjugate heat transfer applied to transitory analysis for rocket engine cooling systems design

Vincenzo Barbato^{1,a*}, Matteo Fiore^{1,b}, Francesco Nasuti^{1,c}

¹University La Sapienza of Rome, Department of Mechanical and Aerospace Engineering, Via Eudossiana 18, Rome, Italy

^abarbato.1739632@studenti.uniroma1.it, ^bmatteo.fiore@uniroma1.it,
^cfrancesco.nasuti@uniroma1.it

Keywords: Conjugate Heat Transfer, Liquid Rocket Engine, Regenerative Cooling Systems

Abstract. This study investigates the use of an in-house Conjugate Heat Transfer (CHT) numerical solver for the modelling of transient phenomena in liquid rocket engines active cooling systems. Heat transfer considerations place great limitations in the development of rocket engines and transient operative conditions are amongst the most critical. The current lack of models and numerical tools capable of accounting for the complexities of this time-dependent multi-physics problem, results in oversized cooling systems, long development times and increased risk of failure. The fine modelling of all the involved phenomena and their interaction with each other is crucial to achieve a correct prediction of the thermal fluxes and wall temperatures involved. Hence, CHT simulations are the state-of-the-art for this application. The CHT solver proposed in this work utilizes a partitioned coupling strategy where two extensively validated single-physics solvers exchange information through their interfaces at discrete time steps. A simplified version of the RL-10A-3-3A regenerative cooling jacket is considered as reference to test the strengths and the limits of this approach. Both a complete chilldown of the engine and part of the start-up transient have been simulated. The analyses performed show the ability of the solver proposed to deal with transient phenomena where fluid-structure interaction occurs. In addition, they provide a complete overview of the numerical issues related to the partitioned coupling approach. These preliminary results pave the way for further developments aimed at increasing the reliability of the solutions and extending the application field of the software developed.

Introduction

Transient heat transfer conditions can be encountered during thrust build-up (engine start-up) and engine shutdown in all rocket propulsion systems. These phases of the rocket engine operational life are amongst the most critical and thus, must be carefully analysed to avoid failures: a cooling system sized on the engine nominal conditions is not sufficient to guarantee overall safety and integrity. During the start-up or shut-down transients, the chamber or nozzle walls may reach temperatures higher than those recorded at steady-state, as well as experience large temperature gradients. Furthermore, transient analysis is particularly important for reusable engines, where the knowledge of the thermal loads involved, can be crucial to guarantee safety through the engine thermal cycles. The aim of the present work is to present a numerical solver for the CHT problem completely developed by the authors, to study transient phenomena occurring in rocket engine regenerative cooling jackets. This multi-physics solver is based on a partitioned coupling approach, where two separate single-physics solvers exchange information through the boundary conditions at their interfaces. Two transient conditions have been analysed, engine chilldown and engine start-up, assuming a simplified version of the cooling jacket of the RL-10A liquid rocket engine as a reference for both geometry and operative conditions.



Conjugate Heat Transfer

All active cooling techniques, such as regenerative cooling, are characterized by the interaction between the fluid coolant and the solid chamber walls. To model such interaction and to predict accurate values of temperature and heat flux, one must focus on conjugating the boundary conditions at the fluid-solid interface through coupled heat transfer analysis. Such a coupled field of study is termed Conjugate Heat Transfer (CHT) analysis [1]. Over the years, CHT has evolved as the most effective method of heat transfer study. A review of the coupling techniques currently adopted in the CHT community together with a thorough analysis of the stability of each method, can be found in the work of Verstraete and Scholl [2]. Amongst the various alternatives, a *partitioned approach with a serial coupling and a Dirichlet-Neumann boundary exchange method* has been selected for the present work. As suggested by M.B. Giles [3], this coupling strategy guarantees overall stability through the coupling iterations, thus resulting in the best choice for the first implementation of a new CHT solver.

Reference Case

The CHT approach for transient analyses developed in the present work has been tested on a simplified version of the cooling jacket of the RL-10A LOX/LH₂ liquid rocket engine [4]. Two transient operative conditions have been simulated: the complete chilldown of the engine and the start-up transient. The RL-10A has been chosen as reference because a great number of details are available for this engine. However, since the scope of the present work is to investigate the limits of the CHT approach proposed, a simplified version of the RL-10A cooling jacket has been considered to neglect multiple phenomenology arising from a complex geometry (i.e., curvature effects, variable cross section, etc.). As a result, a rectified version of the cooling jacket is considered, assuming a constant rectangular cross section for each of the 180 tubes that make up the cooling jacket, made of Type-347 Stainless Steel. Channel dimensions have been chosen equal to the dimensions of the real channel section at the nozzle throat [5].

Numerical Setup

A conjugate heat transfer model based on the coupled numerical integration of the Navier-Stokes equations for the coolant flow and the Fourier's law of conduction for the heat transfer within the solid has been adopted [6], exploiting in-house validated solvers [7]. The flow solver integrates the Reynolds Averaged Navier Stokes Equations, written in the conservation form, by a Godunov-type finite volume scheme, which is second order accurate in space. Turbulence is computed with the one-equation model of Spalart-Allmaras [8].

The fundamental hypothesis on which the coupling strategy is based, is that the heat capacity of the solid is much greater than that of the fluid. This translates in the assumption that when the flow field reaches equilibrium, the structural thermal conduction has not yet begun. In terms of the coupling logic, this implies that at each time step, the steady flow analysis and the unsteady thermal analysis are implemented in turn, as shown in Fig. 1. Steady flow field computed by an isothermal boundary condition and uniform temperature field in the solid are specified as initial conditions for the coupled flow-thermal analysis. Thereafter, the thermal boundary condition for the flow analysis is updated after every thermal conduction calculation for the solid. A maximum temperature variation ΔT is considered as stopping criteria for the transient solid simulation: when at least one cell in the solid domain changes its temperature by an amount greater than the ΔT selected, the unsteady thermal analysis is stopped and the solution is evaluated. From the analysis carried out, it results that this method is first order accurate in time. This is probably a consequence of keeping the heat flux constant during the unsteady thermal analysis in the solid.

Given the symmetry of the problem, to reduce the computational cost of the simulations, only half of the channel has been simulated. The solid is divided in five 3D blocks whereas for the fluid, a single 3D component is sufficient to characterize the entire domain. The number of cells adopted for the fluid domain and its cell-clustering parameters have been chosen to guarantee that $y_+ \leq 1$. Instead, for the solid domain, the discretization has been chosen to include a sufficiently high number of cells to reduce the mapping error in the coupling phase caused by non-matching grids.

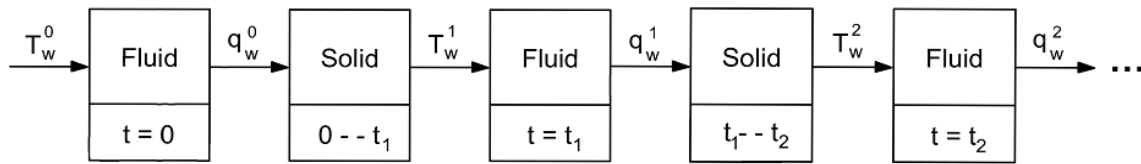


Figure 1 - Schematic representation of the coupling procedure adopted.

Results

To investigate the capabilities of the proposed CHT approach, a complete chilldown of the engine cooling jacket has been simulated. The analysis has been conducted assuming the following constant operative conditions for the fluid: inlet temperature $T_{in} = 25$ K, inlet mass flow rate $m_{in} = 0.01$ kg/s and outlet pressure $p_{out} = 40$ bar. Moreover, all external walls of the solid domain have been assumed adiabatic and the initial wall temperature is set to $T_w = 240$ K. With this study, the sensitivity of the solution to the variation of the stopping criteria (i.e., ΔT) has been investigated. Four different simulations have been realized with the same initial and boundary conditions, but with different simulation parameters. The results obtained showed that, for a simple problem as chilldown where the heat transfer process is monotonous, the variation of ΔT only slightly affects the overall time needed to simulate the same phenomenon. One of the major non-physical phenomena introduced by the discretization of the problem is the possible occurrence of *heat flux inversion*. In the case under analysis, heat flux inversion may occur towards the end of the chilldown process, when the temperature difference between the solid and the fluid approaches zero. When this happens, in the same time in which any cell of the solid changes its temperature of the ΔT required by the stopping criteria, the temperature of one or more of the wall cells, may become lower than the local fluid temperature. Thus, in the successive iteration, the heat flux locally changes its sign and rather than having the fluid cooling the solid, the inverse happens. Once heat flux inversion is triggered, solutions lose their validity and start oscillating because the

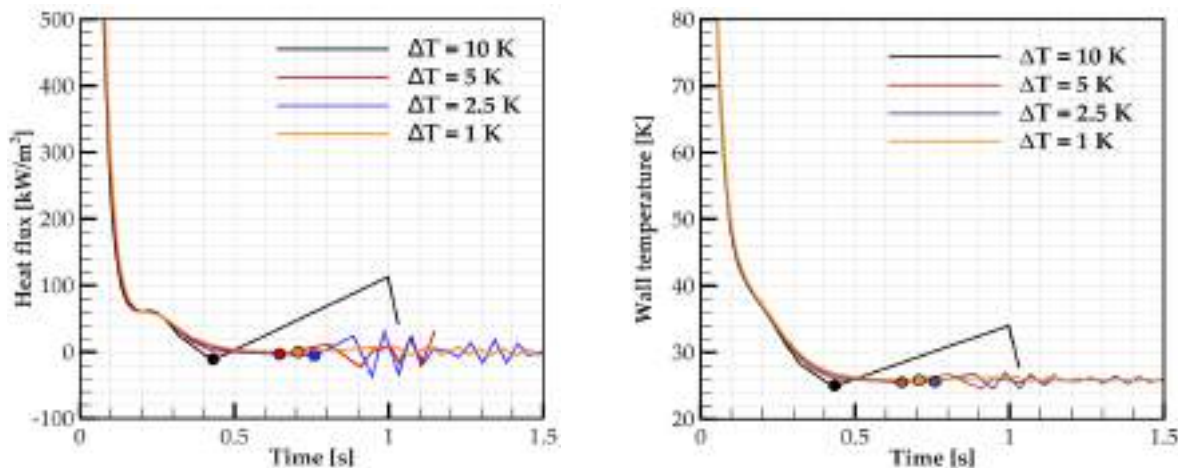


Figure 2 - Oscillations induced by the heat flux inversion phenomenon.

heat flux reverses its sign alternatively from one coupling iteration to the other (Fig. 2). Furthermore, the use of decreasing values of ΔT suggested the possibility of a convergence

analysis analogous to the ones usually carried out for the spatial convergence. It has been found that the pseudo-order of convergence in time of this coupling strategy is approximately one.

Transient operative conditions in liquid rocket engines are generally much more complex than those characterizing a simple engine chilldown. During start-up and shut-down, cooling channels are subject to time-varying inflow and outflow conditions, as well as asymmetrical heating caused by the burning of fuel and oxidizer in the combustion chamber. In this work, part of the start-up transient of the RL-10A has been simulated. Several assumptions have been made to adapt the real start-up transient of the engine to the simplified geometry utilized. Not all the relevant quantities could be found in literature [4,5], thus a best-guess approach has been adopted to account for the missing or partial data. In particular, the heat flux value enforced on the hot-gas-side wall at each time $q_w(t)$ has been approximated by scaling the steady-state heat flux $q_{w,ss}$, through a function of the chamber pressure (Eq. 1) utilizing the information available in literature [5].

$$q_w(t) = q_{w,ss} (p_c(t) / p_{c,ss})^{0.8} \quad (1)$$

It is crucial to emphasize that the scope of the present work is not to represent the real conditions of the start-up transient of the RL-10A. Instead, the aim of this further transient analysis is to show the ability of the solver to correctly represent the physical phenomena occurring in a much more complex scenario. Because of the wide temperature range involved in this simulation, an intermediate value of $\Delta T = 5K$ has been considered as stopping criteria, to reduce the number of couplings performed and the solutions evaluated. To show the consistency of the results obtained, in Fig. 3, the final solution of the transient simulation has been compared to a steady-state solution obtained with a parallel validated steady-state CHT solver [9]. In particular, the temperature field is shown along the channel symmetry plane. The presence of an intense monotonically increasing external heat flux, leads to a major modelling problem: the external heat flux is always underestimated. Indeed, the temperature distribution shows the same pattern suggesting that the solver is heading in the right direction. However, by constantly underestimating the real heat flux, lower temperatures are obtained with respect to the actual steady-state solution. To reduce this modelling error, a smaller ΔT should be adopted. However, for a simulation demanding as the one presented, this choice implies a non-negligible increase in the computational cost. Thus, to obtain a better trade-off between solution accuracy and computational time, a logic that automatically modifies the ΔT depending on the current solution of the problem, could be introduced. Given the multiple problems related to the constancy of the heat flux, such logic should be based on the percentage change, from one iteration to the next, of the magnitude of the heat flux itself.

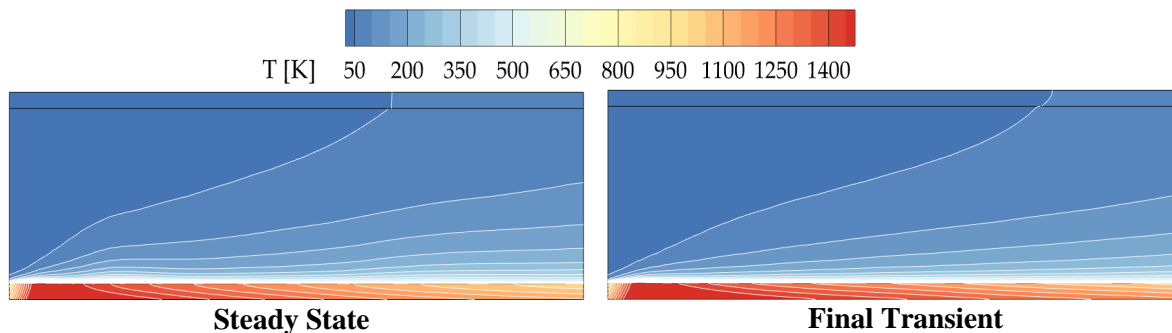


Figure 1 – Temperature field comparison for steady-state and final transient solutions.

Conclusions

This study presented a thorough analysis of the main limits of the in-house Conjugate Heat Transfer numerical solver developed by the authors. Overall, the partitioned approach proved to be a viable way of developing a new multi-physics solver, allowing for reuse of already existing validated tools. The results obtained show the capability of this CHT solver of dealing with the modelling of transient phenomena in liquid rocket engines active cooling systems. Despite the reported results being only preliminary, the methodology here proposed is quite general and can be easily extended to a wide range of problems where fluid-solid interaction occurs.

References

- [1] John B., Senthilkumar P. and Sadasivan S., “Applied and theoretical aspects of conjugate heat transfer analysis: A review,” *Archives of Computational Methods in Engineering*, Vol. 26, 2019, pp. 475–489. <https://doi.org/10.1007/s11831-018-9252-9>
- [2] Verstraete, T., and Scholl, S., “Stability analysis of partitioned methods for predicting conjugate heat transfer,” *International Journal of Heat and Mass Transfer*, Vol. 101, 2016, pp. 852–869. <https://doi.org/10.1016/j.ijheatmasstransfer.2016.05.041>
- [3] Giles, M. B., “Stability analysis of numerical interface conditions in fluid–structure thermal analysis,” *International journal for numerical methods in fluids*, Vol. 25, No. 4, 1997, pp. 421–436. [https://doi.org/10.1002/\(SICI\)1097-0363\(19970830\)25:4%3C421::AID-FLD557%3E3.0.CO;2-J](https://doi.org/10.1002/(SICI)1097-0363(19970830)25:4%3C421::AID-FLD557%3E3.0.CO;2-J)
- [4] Binder, M., Tomsik, T., and Veres, J. P., “RL10A-3-3A rocket engine modeling project,” Tech. rep., 1997.
- [5] Binder, M., “A transient model of the RL10A-3-3A rocket engine,” 31st Joint Propulsion Conference and Exhibit, 1995, p. 2968. <https://doi.org/10.2514/6.1995-2968>
- [6] Pizzarelli, M., Nasuti, F., and Onofri, M., “Coupled wall heat conduction and coolant flow analysis for liquid rocket engines,” *Journal of Propulsion and Power*, Vol. 29, No. 1, 2013, pp. 34–41. <https://doi.org/10.2514/1.B34533>
- [7] Pizzarelli, M., Urbano, A., and Nasuti, F., “Numerical analysis of deterioration in heat transfer to near-critical rocket propellants,” *Numerical Heat Transfer, Part A: Applications*, Vol. 57, No. 5, 2010, pp. 297–314. <https://doi.org/10.1080/10407780903583016>
- [8] Spalart, P., and Allmaras, S., “A one-equation turbulence model for aerodynamic flows,” 30th aerospace sciences meeting and exhibit, 1992, p. 439. <https://doi.org/10.2514/6.1992-439>
- [9] Nasuti, F., Torricelli, A., and Pirozzoli, S., “Conjugate heat transfer analysis of rectangular cooling channels using modeled and direct numerical simulation of turbulence,” *International Journal of Heat and Mass Transfer*, Vol. 181, 2021, p. 121849. <https://doi.org/10.1016/j.ijheatmasstransfer.2021.121849>

Assessment of aerodynamics of low Martian atmosphere within the CIRA program TEDS

Francesco Antonio D'Aniello^{1,a,*}, Pietro Catalano^{1,b} and Nunzia Favaloro^{1,c}

¹Cira, Via Maiorise, Capua (CE), Italy

^af.daniello@cira.it, ^bp.catalano@cira.it, ^cn.favaloro@cira.it

Keywords: RANS, Low Reynolds Number, Compressible, Martian Atmosphere

Abstract. The space exploration and colonization Roadmap, and the growing interest of the international scientific community toward the Mars colonization, are highlighting the need to develop, or improve to higher TRLs, those technologies enabling human exploration and colonization. In this framework, the CIRA - PRORA research program TEDS has identified some of the most promising technologies and research areas for human/robotic exploration, and human survivability in hostile environments in future space missions. In this contest, Aerodynamics in the Martian low atmosphere, characterized by low Reynolds number and high Mach number, is one of the research areas to investigate. The compressible aerodynamics of low Reynolds number flow (Reynolds number of orders of magnitude 10^4 - 10^5 and Mach number of 0.2-0.7) characterizes the low altitude Martian atmosphere. The need in the exploration of the Martian surface has increased the interest in this "particular" aerodynamic regime, currently, scarcely investigated, and an assessment of the numerical methods is necessary. Three suitable airfoils for compressible low-Reynolds aerodynamics in Martian atmosphere have been selected through a bibliographic study: Triangular, NACA 0012-34 and Ishii airfoils. The experiments in the low-density CO₂ facility of the Mars Wind Tunnel, at Tohoku University, over a Triangular, NACA0012-34 and Ishii airfoils with global forces and local PSP measurements, have been considered. The CIRA in-house developed flow solver UZEN (Unsteady Zonal Euler Navier-Stokes) code has been applied by employing several turbulence models. The flow over the Triangular airfoil has been simulated inside the wind tunnel and the free air flow over the NACA 0012-34 and Ishii airfoils have been simulated, and in this paper many results are reported.

Introduction

During the last years, the interest of the international scientific community in space exploration and colonization is growing up, particularly toward Mars. For this scope the CIRA-PRORA research program TEDS [1] has identified some of the most promising technologies and research areas for human/robotic exploration, and human survivability in hostile environments in future space missions. Within this program, focusing on Mars exploration and colonization, the study of Aerodynamics in the Martian low atmosphere, characterized by low Reynolds number (10^4 - 10^5) and high Mach number in the compressible or transonic range (0.2 - 0.7), is one of the research areas to investigate. The task concerns the evaluation of the aerodynamic characteristics, of airfoils and wings, in the low Martian atmosphere. Numerical results will also support the feasibility study of a Martian rotorcraft for future survey and exploration missions.

Unfortunately, the pair of compressible/transonic Mach and low Reynolds does not occur in the Earth's atmosphere which is characterized by the incompressible regime. For this reason, low-Reynolds number compressible flows were scarcely investigated so far, and thus the experimental data of airfoils, flying in this Aerodynamics, are very limited. Only NASA and JAXA agencies have experimentally studied this aerodynamic regime as in *Errore. L'origine riferimento non è stata trovata.*, therefore, an assessment of the numerical methods has been necessary.



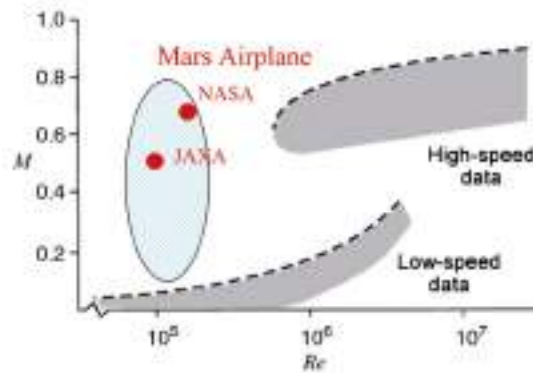


Figure 1 Martian atmospheric flight [2,3].

RANS numerical simulations through the CIRA built in-house UZEN code has been conducted on three suitable airfoils, for compressible low Reynolds aerodynamics in Martian atmosphere, that have been selected through a bibliographic study: Triangular, NACA 0012-34 and Ishii airfoils. The experiments in the low-density CO₂ facility of the Mars Wind Tunnel of Tohoku University over a NACA0012-34, Triangular and Ishii airfoils (sketched in Fig. 2, considering [2,4,5], respectively) with global forces and local PSP measurements, have been considered to first assess the UZEN code.

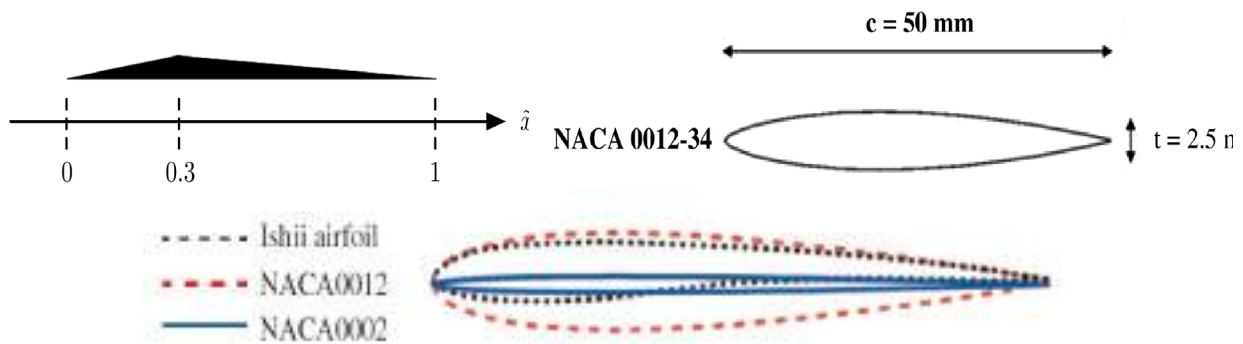


Figure 2 Triangular (top left), NACA0012-34 (top right) and Ishii airfoils (bottom).

Mars Low atmosphere and Aerodynamics

Martian low atmosphere is more rarefied than Earth's one, in fact it mostly consists of carbon dioxide CO₂ (95%) and it is characterized by low pressure ($p \sim 0.0075 \times 101.3$ kPa) low density ($\rho \sim 0.017$ kg/m³) and low temperature, at the surface, respect to the Earth surface. In the low Reynolds number compressible regime, the flow on the upper wing surface is prone to separate forming the laminar separation bubble (LSB), and after the transition zone the flow reattaches in turbulent manner (as shown in Fig. 3). This complicated flow field scenario strongly affects aerodynamic performances of airfoils and wings. Because of these unusual flow characteristics, the airfoil shape largely impacts on the aerodynamic characteristics, in fact in [3,6] it has suggested three shape characteristics involving high aerodynamic performances in low Reynolds number compressible regime:

- sharp leading edge to fix the separation point at the edge and can improve its Reynolds-number dependence on the aerodynamic performance;
- flat upper surface to reduce the separation region;
- cambered airfoil to gain a higher lift than a symmetric airfoil.

Following the trace of prescribed suggestions, Triangular, NACA 0012-34 and Ishii airfoils have been selected to be numerically simulated.

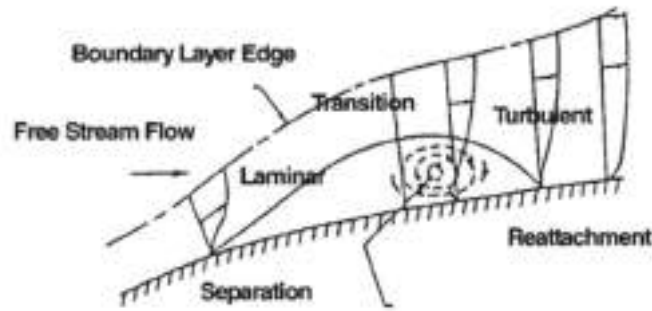


Figure 3 Flow field development when separation bubble occurs [7,8].

Numerical method

The numerical analysis is conducted by using the CIRA in-house code UZEN. The code UZEN [9] solves the compressible 3D steady and unsteady RANS equations on block-structured meshes. The spatial discretization adopted is a central finite volume formulation with explicit blended 2nd and 4th order artificial dissipation. The dual-time stepping technique is employed for time accurate simulations [10,11]. The pseudo-time integration is carried out by an explicit hybrid multistage Runge-Kutta scheme. Classical convergence acceleration techniques, such as local time stepping and implicit residual smoothing, are available together with multigrid algorithms. Turbulence is modelled by either algebraic or transport equation models [12]. Structured multi-block grids were built by using ICEM CFD[®] commercial code for all the selected airfoils. Both RANS and URANS numerical simulations were conducted to reproduce the MWT experimental data collected in the selected bibliography for all three airfoils, with large interest in the aerodynamic performance coefficients, i.e. lift coefficient (C_L) and drag coefficient (C_D), to better understand how the aerodynamic performance change in the Mars atmosphere respect to the Earth one.

Triangular wing has been simulated within the MWT, while NACA 0012-34 and Ishii airfoils has been exclusively simulated in bi-dimensional domains. In Table 1, the level of grid mesh and the number of cells, for each level and for the three considered airfoils, are listed. Where not specified, the number of cells in spanwise direction is equal to 1 (i.e. $n_k = 1$); otherwise the choice of n_k is due to the tri-dimensional grid construction.

Table 1 Grid levels and number of cells ($n_i \times n_j \times n_k$) for Triangular, NACA 0012-34 and Ishii airfoils.

	1 st lev	2 nd lev	3 rd lev	4 th lev
Triangular	2×10^6 ($n_k = 64$)	15×10^6 ($n_k = 130$)	/	/
NACA 0012-34	$200 \times 25 = 5000$	$400 \times 50 = 20000$	$800 \times 100 = 80000$	$1600 \times 200 = 320000$
Ishii	$64 \times 32 = 2048$	$128 \times 64 = 8192$	$256 \times 128 = 32768$	$512 \times 256 = 131072$

Numerical results and discussion

In Fig. 4, the dimensionless wall distances (y^+) on Triangular wing ($M=0.5$, $Re=1.0 \times 10^4$, $\alpha=5^\circ$), and over the upper region of NACA 0012-34 ($M=0.2$, $Re=1.1 \times 10^4$, $\alpha=0^\circ$) and Ishii ($M=0.2$, $Re=2.3 \times 10^4$, $\alpha=0^\circ$) airfoils, obtained by RANS calculations, are reported.

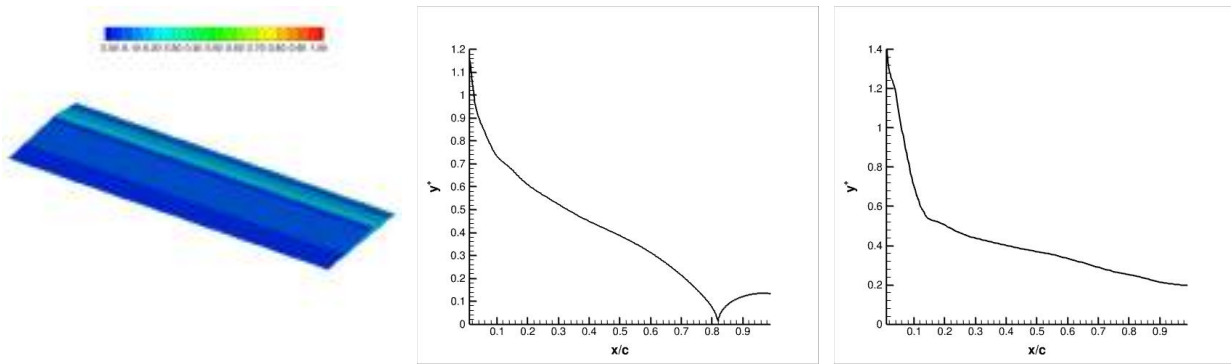


Figure 4 Dimensionless wall distance (y^+) on Triangular wing (left), over the upper region of NACA 0012-34 airfoil (centre) and over the upper region of Ishii airfoil (right).

Through the comparison with the available experimental data, numerical results for the three selected airfoils, globally confirm experimental reports, highlighting that the Mars aerodynamic regime strongly affects aerodynamic performances of airfoils. In fact, looking at Fig. 5, Fig. 6 and Fig. 7, convergence simulations have been discretely reproduced the global trend of polar curves or C_D curves for all the Reynolds and Mach numbers considered. The differences between numerical results and MWT experimental data are due to the used computational grids (bi-dimensional in the case of NACA 0012-34 and Ishii) because their coarsening or design (Ishii trailing edge is open). Turbulence models were not always be able to reproduce exactly the very complex flow field (vortex structures, laminar separation bubble, etc) generated around the wing or on the airfoils. For the Triangular wing (refer to Fig. 5), at Reynolds number equal to 1.0×10^4 , numerical results are in good agreement with the experiments at $\alpha = 5^\circ$, at all the three Mach numbers considered. As the incidence increases, the comparison gets worse. For NACA 0012-34 airfoil (refer to Fig. 6), polar curves are partially reproduced due to the lack of numerical convergence. Numerically reproduced polars are slightly underestimated in terms of C_D than those experimentally recorded. The comparison between numerical results and experimental data slightly improves at high Mach numbers, perhaps as a result of the compressibility effect introduced. At Mach number equal to 0.61, a good agreement with experimental data is reached through the $\kappa - \omega$ SST. For Ishii airfoil (refer to Fig. 7), a globally slight underestimation is detectable in terms of C_D with respect to the experimental data. The $\kappa - \omega$ turbulence models used does not allow to reproduce perfectly the complex flow field that occurs on this airfoil, already at low angles of attack. The $\kappa - \omega$ SST model gave a good agreement with experimental data, and also respect to the LES numerical simulations reported in literature, for almost all the considered incidences.

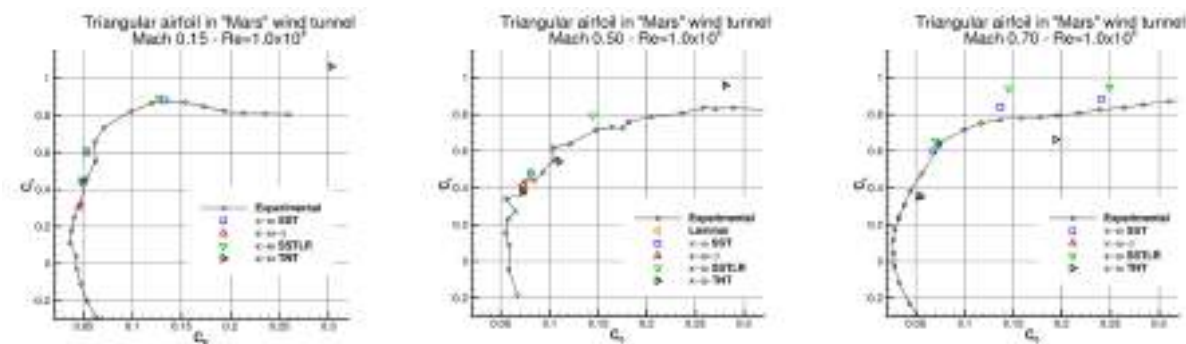


Figure 5 Triangular wing: Drag Polars at Reynolds number 1.0×10^4 , at $M = 0.15$ (left), $M = 0.50$ (centre) and $M = 0.70$ (right), calculated with different $\kappa - \omega$ turbulence models.

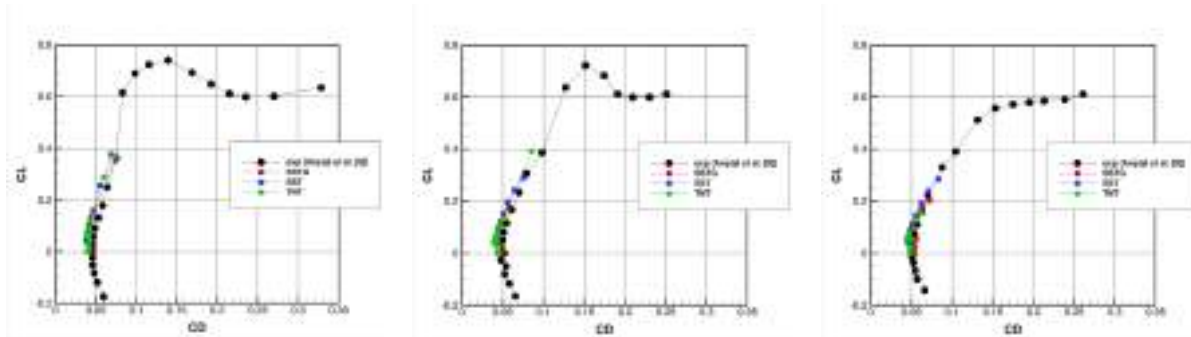


Figure 6 NACA 0012-34 airfoil: Drag Polars at $Re = 1.1 \times 10^4$, at $M = 0.20$ (left), $M=0.48$ (centre) and $M=0.61$ (right), calculated with different $\kappa - \omega$ turbulence models.

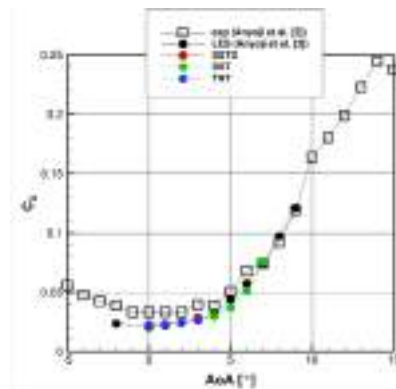


Figure 7 Ishii airfoil: Drag Coefficient versus angle of attack at Reynolds number 2.3×10^4 and at Mach number 0.20, calculated with different $\kappa - \omega$ turbulence models.

Focusing on Triangular airfoil, the flow field around the wing, inside the wind tunnel, provided by the numerical simulations is actually very complex, above all at high incidence. Flow structures forming at the side-ends of the body and developing in the wake can be also appreciated in Fig. 8 that, following the Q-criterion, reports an iso-surface of $Q = \frac{1}{2}(\Omega_{i,j}\Omega_{i,j} - S_{i,j}S_{i,j})$, where $\Omega_{i,j}$ is the vorticity magnitude and $S_{i,j}$ is the rate of strain (Q-criterion defines vortices as areas where the vorticity magnitude is greater than the magnitude of the rate of strain). The vortex regions in the central part are visible. It can be also noted as the side-end structures tend to disappear at the highest Reynolds number.

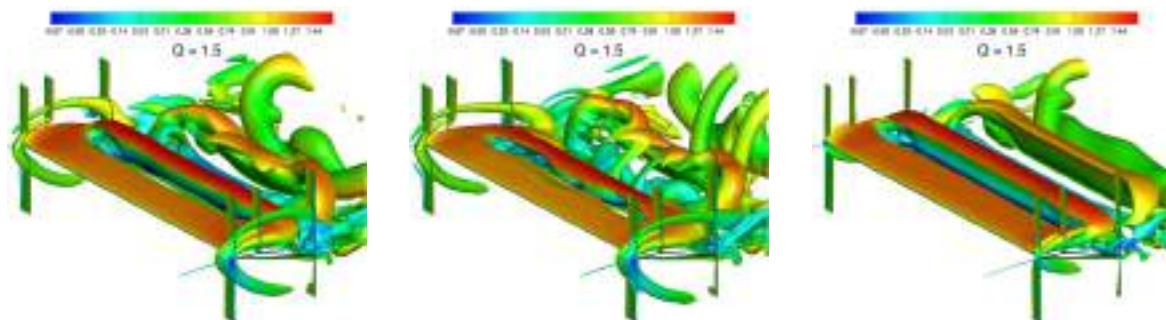


Figure 8 Iso-surface of Q at $\alpha = 15^\circ$, $M=0.15$, $Re=3.0 \times 10^3$ (left), $M=0.50$, $Re=3.0 \times 10^3$ (centre), $M=0.15$, $Re=1.0 \times 10^4$ (right).

Summary

Numerical simulations conducted with CIRA built in-house UZEN code through all the employed κ - ω turbulence models, have been partially reproduced the flow field around the wing in the wind tunnel (Triangular airfoil) and around the airfoils in free air (NACA0012-34, Ishii) and with a global good agreement with the experimental data in terms of aerodynamic performances (i.e. lift and drag coefficients), especially at low and medium incidences.

Although the scarce 3D simulations conducted on the wing based on the Triangular airfoil, they allow to underline the strongly 3D structure of the flow field that influences the aerodynamic performance degradation, above all at high incidences.

NACA 0012-34 and Ishii are more feasible to fly airfoils than the Triangular one. Their design has been thought to fly at high incidences in a low-Reynolds environment and, at the same time, to allow the flow to reattach downstream the formation of the laminar separation bubble.

The influence of the Mach number has been also investigated. The numerical results have shown that the increase in Mach numbers seems to energize the flow, that is more able to withstand the adverse pressure gradients and becomes less prone to the separation.

References

- [1] N. Favaloro, G. Saccone, F. Piscitelli, R. Volponi, P. Leoncini, P. Catalano, A. Visingardi and M. C. Noviello, "Enabling Technologies for Space Exploration Missions: The CIRA-TEDS Program Roadmap Perspectives," *Aerotecnica Missili & Spazio*, 2023.
<https://doi.org/10.1007/s42496-023-00159-4>
- [2] Anyoji, Numata, Nagai and Asai, "Effects of Mach Number and Specific Heat Ratio on Low-Reynolds-Number Airfoil Flows," *AIAA Journal*, vol. 53, no. 6, 2015.
<https://doi.org/10.2514/1.J053468>
- [3] F. W. Schmitz, "Aerodynamics of the Model Airplane Part1," NASA, Technical Rept., NASA-TM-X-60976, 1967.
- [4] Munday, Taira, Suwa, Numata and Asai, "Nonlinear Lift on a Triangular Airfoil in Low-Reynolds-Number Compressible Flow," *Journal of Aircraft*, 2015.
<https://doi.org/10.2514/1.C032983>
- [5] Anyoji, Nonomura, Aono, Oyama, Fujii, Nagai and Asai, "Computational and Experimental Analysis of a High-Performance Airfoil Under Low-Reynolds-Number Flow Condition," *Journal of Aircraft*, vol. 51, no. 6, 2014. <https://doi.org/10.2514/1.C032553>
- [6] F. W. Schmitz, "The Aerodynamics of Small Reynolds number," NASA TM, 1980.
- [7] Tsukamoto, Yonemoto, Makizono, Sasaki, Tanaka, Ikeda and Ochi, "Variable-Pressure Wind Tunnel Test of Airfoils at Low Reynolds Numbers Designed for Mars Exploration Aircraft," *Trans. JSASS Aerospace Tech. Japan*, vol. 14, no. 30, pp. 29-34, 2016.
https://doi.org/10.2322/tastj.14.Pk_29
- [8] Rinoie and Kamiya, "Laminar Separation Bubbles Formed on Airfoils," *Journal of Japan Society of Fluid Mechanics*, no. 22, pp. 15-22, 2003.
- [9] Catalano and Amato, "An evaluation of RANS turbulence modelling for aerodynamic applications," *Aerospace Science and Technology*, vol. 7, no. 7, pp. 493-509, 2003.
[https://doi.org/10.1016/S1270-9638\(03\)00061-0](https://doi.org/10.1016/S1270-9638(03)00061-0)
- [10] Marongiu, Catalano, Amato and Iaccarino, "U-ZEN: A computational tool solving U-RANS equations for industrial unsteady applications," in *34th AIAA FluidDynamics Conference and Exhibit*, 2004. <https://doi.org/10.2514/6.2004-2345>

- [11] Capizzano, Catalano, Marongiu and Vitagliano, “URANS modelling of turbulent flows controlled by synthetic jets,” in 35th AIAA FluidDynamics Conference and Exhibit, 2005.
<https://doi.org/10.2514/6.2005-5015>
- [12] Catalano, Mele and Tognaccini, “On the implementation of a turbulence model for low Reynolds number flows,” Computers and Fluids, vol. 109, pp. 67-71, 2015.
<https://doi.org/10.1016/j.compfluid.2014.12.009>

A combustion-driven facility to study phenomenologies related to hypersonic sustained flight

Antonio Esposito

Dept. of Industrial Engineering, University of Naples Federico II, Via Claudio 21, 80125 Napoli (Italy)

antespos@unina.it

Keywords: Combustion-Driven Facility, Oxy-Fueled Guns, Hypersonics

Abstract. This paper reports on the development of a new Blowdown-Induction Facility driven by two different Oxy-Fueled Guns. The facility is conceived and realized to simulate different phenomenologies and flow conditions related to hypersonic sustained flight.

Introduction

Plasma Guns used in the context of Thermal Spray are often engineered versions of similar devices originally designed for aerospace research; for these applications the plasma gun is particularly relevant because it couples the reliability of an industrial device with the desired operating conditions, i.e. very high temperatures and very low pressures of the considered gas (heated by the electric arc). Nowadays however, new applications emerging in the general fields of Aerothermodynamics and Propulsion require (a) lower temperatures and higher pressures, (b) different process gases (Methane or Hydrogen) and (c) different operational modes (combustion instead of electric arc) respect to those generated by plasma torches. All these requirements call for the design and development of facilities with combustion-driven Thermal Spray Guns, and the present study may be regarded as a relevant effort along these lines; in particular, here we describe the development of a new facility based on two different Oxygen-Fueled guns (DJ2700 and 6P-II) that exhausts into a low pressure ambient. Unique properties of this facility are its ability to simulate different phenomenologies and flow conditions related to hypersonic sustained flight.

Experimental apparatus

Figure 1 shows the overall Vacuum Oxy-fueled Facility (VOF).

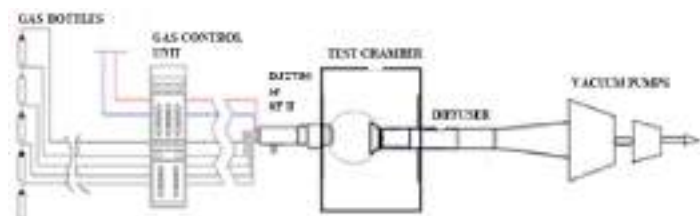


Figure 1 – VOF –Picture (left) and Layout (right).

Main facility components can be listed as:

1. Gas Supply Systems
2. Gas Control Units
3. Hybrid HVOF gun (DJ2700) / LVOF gun (6P-II)
4. Test Chamber and Diffuser

5. Vacuum Tanks and Vacuum Pump System

Gas Supply System

The details of the gas supply systems are shown in Fig. 2. In both systems Nitrogen is used only to prevent melting of the powder injectors in the guns.

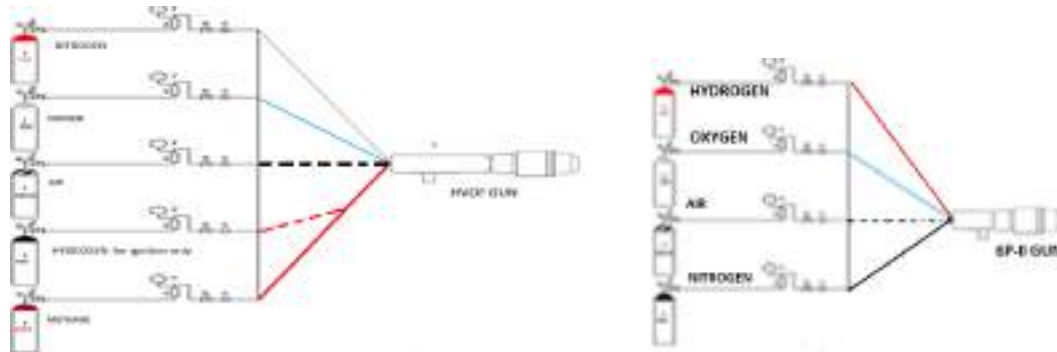


Figure 2 – Layout of the gas supply system for DJ2700 (left) and 6P II (right).

For the DJ2700 gun the gas flow requirements are: Oxygen 340 NLPM at 12 bar - Methane 200 NLPM at 7 bar - Air 439 NLPM at 7 bar - Nitrogen 18 NLPM at 12 bar - Hydrogen 8 NLPM at 10 bar. For the 6P-II gun the gas flow requirements are: Oxygen 45 NLPM at 2.6 bar - Hydrogen 170 NLPM at 2.4 bar - Air 50 NLPM at 6 bar - Nitrogen 15 NLPM at 5 bar.

Gas Control Units

A sketch of the Gas Control Units is shown in Fig. 3, with some relevant details being made evident through the associated legend. Both the units are realized in the laboratory.

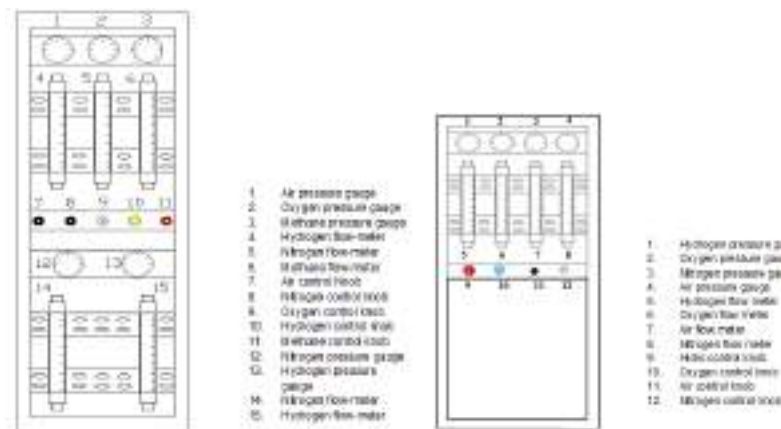


Figure 3 – Gas Control Units Front Panels for DJ2700 (left) and 6P-II (right)

HVOF gun (DJ2700) and LVOF gun (6P-II)

The Sulzer-Metco Diamond Jet (DJ) 2700 has been chosen as HVOF gun, the reader being referred to Figure 4 for a detailed sectional drawing of the gun. The DJ gun relies on a combination of oxygen, fuel and air to produce a high pressure annular flame, which is characterized by a uniform temperature distribution. The exhaust gases, together with the air injected from the annular inlet orifice, expand through the nozzle to reach a supersonic state. The air cap is cooled by both water and air to prevent it from melting.



Figure 4 – DJ 2700 Hybrid Thermal Spray torch.

The Flame Spray Technology 6P-II has been chosen as LVOF gun, the reader being referred to Figure 5 for a detailed sectional drawing of the gun. The 6P-II can be used with Hydrogen as fuel gas. A siphon plug system mixes fuel and oxygen in precise volumetric proportions at the gun to provide consistent operation and prevents the possibility of backfire. A reversible air cap is used to create a parallel air flow to cool the gun or as a convergent pinch air flow.

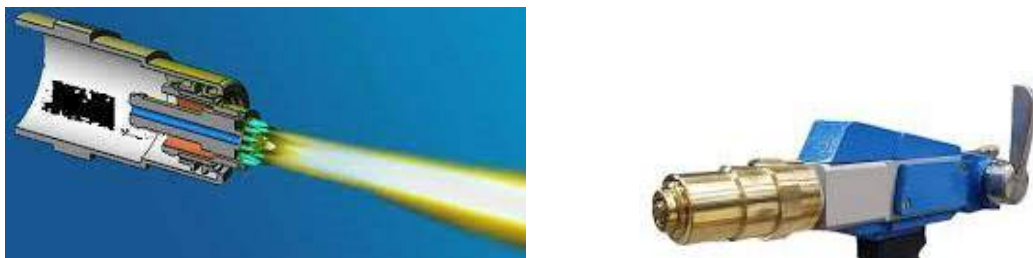


Figure 5 – 6P II Flame Spray torch.

Test Chamber and Diffuser

The test chamber is a iron cylinder with a diameter of 600 mm (Fig. 8), flanged at the ends and hosted inside the first section of the supersonic diffuser, Figs. 6(left) and (right).



Figure 6 – VOF Test Chamber (left) and Diffuser (right).

Vacuum Tank and Vacuum Pumps system

Vacuum pumps are a Stokes Microvac 212H (220 m³/h) and a Edwards E2M275 (292 m³/h); they evacuate the facility and the tank in a relatively brief time -5 minutes about - up to 100 (Pa) ultimate pressure.

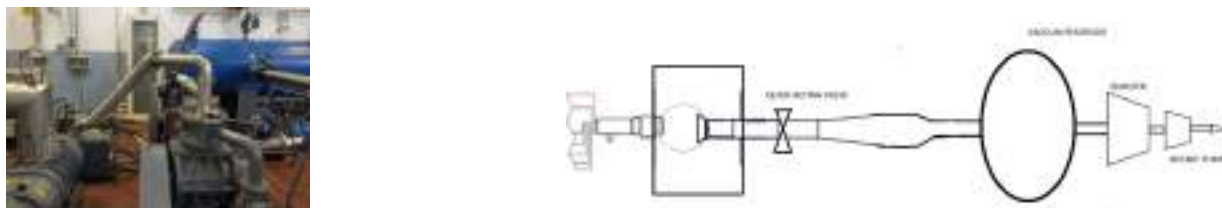


Figure 7 – Vacuum System: Rotary pumps (left) and system layout (right).

Applications and preliminary results

DJ2700 – HVOF

The HVOF gun (DJ700) produces a supersonic, overexpanded flow at atmospheric pressure ($p \sim 0.7$ (bar) at nozzle exit) of residual exhaust gases from Methane-Oxygen combustion; this flow is suitable for simulating the jet at the exit of a supersonic combustor (e.g. ramjet) if added with air and brought to the correct expansion conditions by means of a particular starting procedure of the facility set up in [1], see Figure 8.



Figure 8 – HVOF gun at ambient pressure (left) and in the VOF Test Chamber (right).

6P – II LVOF

As for the 6P-II gun, this device produces a subsonic, high velocity flow in which Hydrogen and Oxygen burn generating thermal energy (and a residual water vapour), which heats Air (flowing in the cooling cap) and Nitrogen (flowing in the injector); by correcting the composition with Oxygen in the right percentage, Air at high temperature and atmospheric pressure is therefore obtained which can be used as a source for a hypersonic tunnel of the blowdown-induction type (see figure 7, right side). At the time of writing this paper ignition tests with hydrogen have begun and great precaution is needed.

References

[1] A. Esposito, C. Allouis, M. Lappa “A new facility for hypersonic flow simulation driven by a high velocity oxygen fuel gun” - ICAS 2022, 33rd Congress of the International Council of the Aeronautical Sciences, Stockholm Sweden 4 -9 September 2022.

Development of a DNS solver for compressible flows in generalized curvilinear coordinates

Giulio Soldati^{1,a,*}, Alessandro Ceci^{1,b} and Sergio Pirozzoli^{1,c}

¹ Via Eudossiana 18, Rome 00184, Italy

^agiulio.soldati@uniroma1.it, ^balessandro.ceci@uniroma1.it, ^csergio.pirozzoli@uniroma1.it

Keywords: Generalized Curvilinear Coordinates, Shock-Wave/Boundary Layer Interaction, Turbulent Compression Ramp, Curved Channel Flow

Abstract. We present a solver for DNS of turbulent compressible flows over arbitrary shaped geometries. The code solves the compressible Navier-Stokes equations in a generalized curvilinear coordinates system, using high-order central finite-difference schemes combined with WENO reconstruction for shock-waves treatment. An innovative stabilization strategy for central schemes based on skew-symmetric-like splitting of convective derivatives is used. The code is oriented to modern HPC platforms thanks to MPI parallelization and the ability to run on GPU architectures. The robustness and accuracy of the present code is assessed both in the low-subsonic case and in the supersonic case. We show here the results of a turbulent curved channel flow and a turbulent supersonic compression ramp, which proved to be in excellent match with previous studies.

Introduction

Compressible flows over curved surfaces are ubiquitous in the aerospace field, both in external (e.g., aircraft wings) and internal (e.g., turbomachinery) configurations. The dynamics of these flows involves complex phenomena, such as shock-wave boundary layer interactions, which still need further investigation, and make it challenging to accurately estimate skin friction and wall heat transfer. A key tool in this context is the DNS, which demands high-order numerical schemes and good shock-capturing capabilities to accurately describe high-speed flows. However, due to the numerical complications arising from geometric complexities, the application of the DNS is often limited to simple Cartesian cases [1,2]. Dealing with complex geometries leads to the use of local mesh refinement or unstructured meshes, which in turns causes high computational cost or decreased accuracy, respectively [3]. Another approach to deal with such geometries is the use of body fitted mesh in a generalized curvilinear coordinates system, which guarantee an accurate simulation of the fluid dynamics near the wall at a competitive computational cost. In this work, we developed a solver for DNS of turbulent compressible flows over complex geometries, using high-order central finite-difference schemes in a generalized curvilinear coordinate system. Central approximations of the Navier-Stokes equations, being non-dissipative, exhibit numerical instability when used at small viscosity. To address this problem, we implemented energy-preserving schemes [4], allowing to accurately simulate the wide range of turbulent scales without relying on artificial diffusivity [5] or filtering of physical variables [6]. Moreover, those schemes can be efficiently combined with modern shock-capturing methods as WENO reconstructions, yielding hybrid schemes that currently represent an optimal strategy for the computation of shocked flows [7].

Methodology

The code solves the compressible Navier-Stokes equations for a perfect gas in a generalized curvilinear coordinate system:



$$\frac{1}{J} \frac{\partial \mathbf{Q}}{\partial t} + \frac{\partial \mathbf{F}_j}{\partial \xi_j} = \frac{\partial \mathbf{F}_j^v}{\partial \xi_j}$$

where \mathbf{Q} is the vector of conservative variables, \mathbf{F}_j is the vector of convective fluxes, \mathbf{F}_j^v is the vector of viscous fluxes and J is the Jacobian of the coordinate transformation. Here, we consider stationary grids. A full description of the fluxes vectors can be found in [8]. A curvilinear body-fitted mesh is first represented in the physical space, x_i . Through the transformation $x_i(\xi_j)$ it is then mapped to the computational space, ξ_j , where it can be seen as a regular hexahedron. Non-uniform skewed input cells of the mesh are thus re-stretched into uniform cubical cells. Finite-difference schemes are applied in the computational space to approximate spatial derivatives, which must be reconstructed in the physical space by using the metrics, $\partial \xi_j / \partial x_i$. Since the mesh is directly described in the physical space, first we compute the inverse of the metrics, $\partial x_i / \partial \xi_j$, by numerically deriving the physical mesh coordinates; then the metrics are obtained with a matrix inversion. To guarantee free-stream preservation, we use the same approximation for both metric and convective derivatives [9].

In smooth regions of the flow, a skew-symmetric-like splitting of the convective derivatives is employed. This approach guarantees preservation of kinetic energy in the semi-discrete, inviscid low-Mach-number limit. A computationally effective implementation of convective derivatives cast in split form was proposed by Pirozzoli [10]. The locally conservative formulation allows straightforward hybridization of central schemes with classical shock-capturing reconstructions. In our case, shock-capturing capabilities rely on WENO reconstruction of the numerical flux in the proximity of discontinuities. To judge on the local smoothness of the numerical solution and switch between the energy preserving and the shock capturing discretization, our code relies on a modified version of the Ducros shock sensor [11]. As for the viscous terms, they are expanded to Laplacian form to avoid odd-even decoupling phenomena. Spatial derivatives are approximated in the computational space with central formulas and reconstructed in the physical space by applying the chain-rule. The accuracy order of each scheme can be selected by the user and goes up to eight in the case of central schemes, up to seventh for WENO ones. The system is advanced in time using a three-stage, third order Runge-Kutta scheme [12].

The code is designed to efficiently work on the most common HPC architectures operating today. MPI parallelization and CUDA-Fortran porting enable the use of multi-GPUs architectures, while retaining the possibility to compile and use the code on standard CPU-based systems.

Results

We simulated low-Reynolds-number, mildly curved, turbulent channel flow. The computational domain is bounded by sectors of concentric cylinders, with a centreline radius of curvature $r_c = 79h$, where h is the channel semi-height. An imposed mean-pressure gradient in the azimuthal direction drives the flow. Periodic boundary conditions are imposed in the streamwise and spanwise directions, so that the simulated flow is fully evolved. The resolution is $216 \times 72 \times 144$ in the streamwise, wall-normal and spanwise directions, respectively. Mach number and Reynolds number based on the bulk velocity are set to $M_b = 0.1$ and $Re_b = 2600$. The Reynolds numbers based on the inner and outer friction velocities resulted in $Re_\tau^i = 156$ and $Re_\tau^o = 178$, respectively. Fig. 1 illustrates an instantaneous field of the velocity magnitude U normalized with respect to bulk velocity U_b . Fig. 2 shows the root-mean-square (rms) of the velocity fluctuations of the present DNS (STREAmS) together with the data from Moser and Moin [13] and Brethouwer [14]. The excellent agreement of the results can be noted.

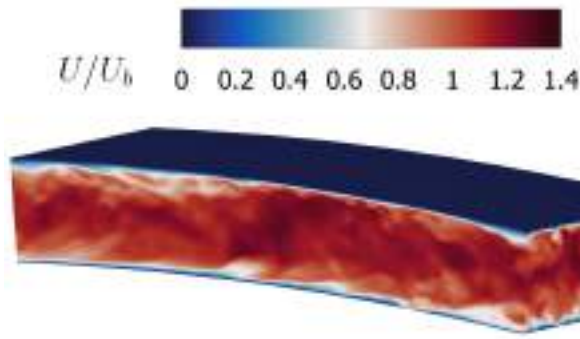


Fig. 1 Instantaneous field of the velocity magnitude.

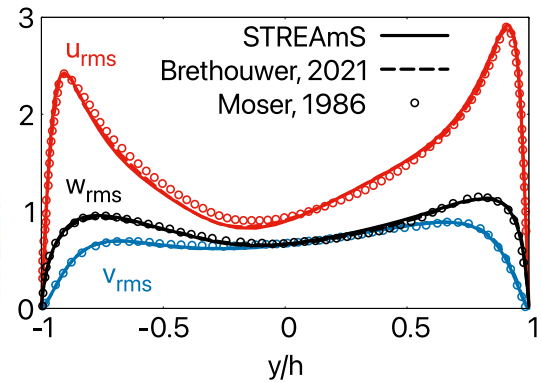


Fig. 2 Rms of the velocity fluctuations.

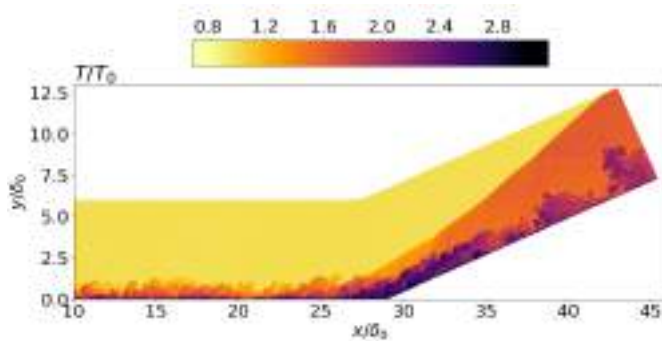


Fig. 3 Instantaneous field of the temperature.

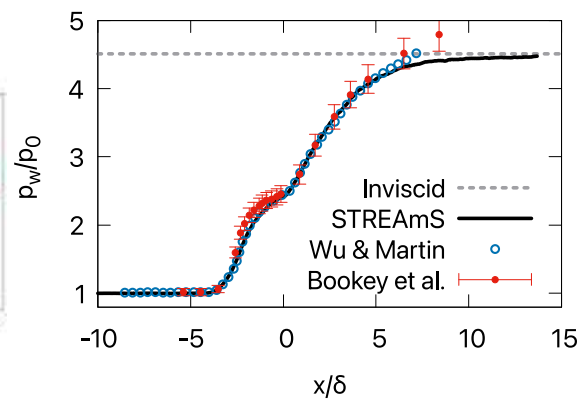


Fig. 4 Mean wall-pressure distribution.

Shock wave/turbulent boundary layer interaction is investigated by simulating a supersonic flow over a 24° compression ramp. Incoming flow conditions are Mach number $M = 2.9$ and Reynolds number $Re_0 = 2300$ based on the inflow boundary layer momentum thickness. Synthetic turbulence is imposed at the inflow using a recycling and rescaling method. Supersonic outflow boundary conditions with non-reflecting treatment are used at the outlet and the top boundary. Non-slip condition is imposed at the wall, which is isothermal. The number of grid points used is $2432 \times 256 \times 160$ in the streamwise, spanwise, and wall-normal directions, respectively. Fig. 3 illustrates an instantaneous field of the normalized temperature. Fig. 4 shows the mean wall-pressure distribution of the present DNS (STREAMS) together with the data from Wu and Martin [15] and Bookey et al. [16]. Again, results are in excellent agreement.

Conclusions

We developed an in-house solver for DNS of turbulent compressible flows over complex geometries in the framework of the generalized curvilinear coordinates. The code is based on high-order central finite-difference schemes hybridized with WENO reconstruction for shock capturing. The high-fidelity of the solver is ensured by the innovative stabilization technique of central schemes, which relies on physical principles related to the preservation of the total kinetic energy from convection, without the addition of any artificial viscosity. The optimization to run on multi-GPUs architectures makes our solver capable to perform large-scale DNS of a wide range of different flow configurations. The validation of the code was carried out by simulating a subsonic

turbulent curved channel flow and a supersonic turbulent compression ramp flow. In both cases, the results proved to be in excellent agreement with previous numerical and experimental studies.

References

- [1] Bernardini, M., Modesti, D., Salvatore, F., & Pirozzoli, S. (2021). STREAmS: a high-fidelity accelerated solver for direct numerical simulation of compressible turbulent flows. *Computer Physics Communications*, 263, 107906. <https://doi.org/10.1016/j.cpc.2021.107906>
- [2] Li, Y., Fu, L., & Adams, N. A. (2021). A low-dissipation shock-capturing framework with flexible nonlinear dissipation control. *Journal of Computational Physics*, 428, 109960. <https://doi.org/10.1016/j.jcp.2020.109960>
- [3] Piquet, A., Zebiri, B., Hadjadj, A., & Safdari Shadloo, M. (2020). A parallel high-order compressible flows solver with domain decomposition method in the generalized curvilinear coordinates system. *International Journal of Numerical Methods for Heat & Fluid Flow*, 30(1), 2-38. <https://doi.org/10.1108/HFF-01-2019-0048>
- [4] Pirozzoli, S. (2010). Generalized conservative approximations of split convective derivative operators. *Journal of Computational Physics*, 229(19), 7180-7190. <https://doi.org/10.1016/j.jcp.2010.06.006>
- [5] Kawai, S., & Lele, S. K. (2008). Localized artificial diffusivity scheme for discontinuity capturing on curvilinear meshes. *Journal of Computational Physics*, 227(22), 9498-9526. <https://doi.org/10.1016/j.jcp.2008.06.034>
- [6] Visbal, M. R., & Gaitonde, D. V. (2002). On the use of higher-order finite-difference schemes on curvilinear and deforming meshes. *Journal of Computational Physics*, 181(1), 155-185. <https://doi.org/10.1006/jcph.2002.7117>
- [7] Pirozzoli, S. (2011). Numerical methods for high-speed flows. *Annual review of fluid mechanics*, 43, 163-194. <https://doi.org/10.1146/annurev-fluid-122109-160718>
- [8] Chandravamsi, H., Chamarthi, A. S., Hoffmann, N., & Frankel, S. H. (2023). On the application of gradient based reconstruction for flow simulations on generalized curvilinear and dynamic mesh domains. *Computers & Fluids*, 258, 105859. <https://doi.org/10.1016/j.compfluid.2023.105859>
- [9] Gaitonde, D., & Visbal, M. (1999, January). Further development of a Navier-Stokes solution procedure based on higher-order formulas. In *37th Aerospace Sciences Meeting and Exhibit* (p. 557). <https://doi.org/10.2514/6.1999-557>
- [10] Pirozzoli, S. (2011). Stabilized non-dissipative approximations of Euler equations in generalized curvilinear coordinates. *Journal of Computational Physics*, 230(8), 2997-3014. <https://doi.org/10.1016/j.jcp.2011.01.001>
- [11] Ducros, F., Ferrand, V., Nicoud, F., Weber, C., Darracq, D., Gacherieu, C., & Poinot, T. (1999). Large-eddy simulation of the shock/turbulence interaction. *Journal of Computational Physics*, 152(2), 517-549. <https://doi.org/10.1006/jcph.1999.6238>
- [12] Spalart, P. R., Moser, R. D., & Rogers, M. M. (1991). Spectral methods for the Navier-Stokes equations with one infinite and two periodic directions. *Journal of Computational Physics*, 96(2), 297-324. [https://doi.org/10.1016/0021-9991\(91\)90238-G](https://doi.org/10.1016/0021-9991(91)90238-G)
- [13] Moser, R. D., & Moin, P. (1987). The effects of curvature in wall-bounded turbulent flows. *Journal of Fluid Mechanics*, 175, 479-510. <https://doi.org/10.1017/S0022112087000491>
- [14] Brethouwer, G. (2022). Turbulent flow in curved channels. *Journal of Fluid Mechanics*, 931, A21. <https://doi.org/10.1017/jfm.2021.953>
- [15] Wu, M., & Martin, M. P. (2007). Direct numerical simulation of supersonic turbulent boundary layer over a compression ramp. *AIAA journal*, 45(4), 879-889. <https://doi.org/10.2514/1.27021>
- [16] Bookey, P., Wyckham, C., Smits, A., & Martin, P. (2005). New experimental data of STBLI at DNS/LES accessible Reynolds numbers. In *43rd AIAA Aerospace Sciences Meeting and Exhibit* (p. 309). <https://doi.org/10.2514/6.2005-309>

Numerical tank self-pressurization analyses in reduced gravity conditions

Francesca Rossetti^{1,a,*}, Marco Pizzarelli^{2,b}, Rocco Pellegrini^{2,c}, Enrico Cavallini^{2,d}, and Matteo Bernardini^{1,e}

¹Department of Mechanical and Aerospace Engineering, "Sapienza" University of Rome, Via Eudossiana 18, Rome, 00184, Italy

² Italian Space Agency (ASI), Via del Politecnico s.n.c., Rome, 00133, Italy

^af.rossetti@uniroma1.it, ^bmarco.pizzarelli@asi.it, ^crocco.pellegrini@asi.it, ^denrico.cavallini@asi.it, ^ematteo.bernardini@uniroma1.it

Keywords: VOF, Tank Self-Pressurization, Cryogenic, Reduced Gravity

Abstract. In this study, a suitable numerical methodology to study the self-pressurization phenomenon inside a cryogenic tank, in a reduced gravity environment is proposed. This methodology is validated with the results of a benchmark self-pressurization experiment, carried out in the liquid hydrogen tank of the second stage of the Saturn IB AS-203 vehicle. The time-varying acceleration and heat flux due to solar radiation to which the tank was exposed during the experiment, have been modeled in our analysis. Finally, the numerical results show that the proposed methodology allows to reproduce the experimental data with a reasonably good accuracy.

Introduction

Studying the thermo-fluid-dynamics behavior of cryogenic propellant in reduced gravity is crucial for the design of upper stage cryogenic storage tanks. Cryogenic propellant, having a low boiling point, is very sensitive to the heat leaks to which the tank is unavoidably subjected. These heat leaks in a closed, no-venting tank, cause propellant boil-off, self-pressurization, and thermal stratification. The gravity level, g , influences the boiling process, in particular, according to Fritz expression [1], the bubble diameter at departure varies as $g^{-1/2}$ on an upward-facing horizontal surface. Not only the boiling process, but also the dynamics of the free-surface is influenced by the gravity level. Indeed, in case of low Bond number, the free-surface tends to go up along the tank walls. This phenomenon must be countered, through settling strategies, in cases when in-orbit engine start-up and operation is necessary. Important results on propellant behavior in tanks under reduced gravity conditions have been provided by the experiments, nevertheless, the uncertainty of the experimental data and the cost and complexity associated to experiments carried out in a reduced gravity environment highlight the potentialities of CFD simulations. The first self-pressurization experiment in reduced gravity, with data sufficiently detailed for validating storage tank models, was carried out in the liquid hydrogen (H₂) tank of the second stage of the Saturn IB AS-203 vehicle [2]. In the present study, a state-of-the-art numerical methodology [3], which allows to describe the main thermo-fluid-dynamics phenomena occurring in cryogenic tanks during self-pressurization in reduced gravity, is presented. This methodology is validated with the experimental data of Ward et al. [2].

Mathematical formulation and thermophysical properties

Mathematical formulation. The Volume-of-Fluid (VOF) method [4] is used to track the two-phase fluid interface. Moreover, to compute the mass transfer due to phase change, the Lee model [5] is selected. In addition, the Continuum Surface Force (CSF) model [6] is used to address the effects of surface tension force. The flow is modeled as turbulent, being the modified Rayleigh number



(based on the liquid height) of liquid H_2 of the order of 10^{14} , so highly above the critical value of 10^{11} . In particular, the SST $k-\omega$ model of Menter [7] is selected.

Thermophysical properties. For the liquid H_2 , the Boussinesq approximation is selected for the density, and constant thermophysical and transport properties, taken from the NIST [8] database, at the average pressure and liquid temperature, are used. The gaseous H_2 is modeled as an ideal gas, with temperature dependent specific heat, thermal conductivity, and viscosity. The latter are modeled as a piecewise linear fit of NIST data, at the average pressure. The H_2 saturation curve is approximated with a piecewise linear fit of NIST data.

Computational setup and preliminary results

Test case description. The test case under consideration is a self-pressurization experiment carried out in the liquid H_2 tank of the second stage of the Saturn IB AS-203 vehicle [2]. This tank has a height, H , of 11.3 m, a radius, R , of 3.3 m. The initial liquid mass is 7103.3 kg, corresponding to an initial liquid height, h_l , of 4.1 m, and the ullage contains only evaporated H_2 . The tank characteristic dimensions are schematized in Fig. 1 (a). The tank shares a common bulkhead with the liquid oxygen (O_2) tank, which is placed below it. The test tank was in a circular low Earth orbit, and, thus, absorbed a time-varying heat flux due to solar radiation. Moreover, it was subjected to a time-varying axial acceleration resulting from the balance between an axial thrust and the drag force.

Flow solver. The pressure-based solver of the commercial CFD software Ansys Fluent® [9] is used to simulate the transient self-pressurization phenomenon. The flow is modeled as 2D axisymmetric, a minimum time step of 0.01 s is used in order to keep the residuals below a proper limit. Second order upwind schemes are used for spatial discretization of the convective terms in the governing equations. Ansys Fluent®'s Compressive scheme [9] is used for the volume fraction equation. The chosen pressure-velocity coupling scheme is SIMPLE. An interpolation of the experimental time-varying heat flux is imposed, as boundary condition, on each part of the tank wall, instead the walls of the baffles are treated as adiabatic. The different parts of the tank wall are indicated in Fig. 1 (a). Fig. 1 (b) represents the evolution of both the experimental and the interpolated heat transfer rate on the different parts of the tank wall. The tank axial acceleration level is modeled as an interpolation of its experimental values. This interpolation, together with the experimental acceleration, are represented in Fig. 1 (c). The tank is initialized at a pressure of 85495 Pa, the initial liquid temperature is 19.72 K, the ullage is initialized using a linear stratification between the liquid temperature and a temperature of 22.5 K [2].

Grid independence study. A grid independence study has been carried out, comparing the results obtained with two grids, a coarse one, having 23401 cells, and a medium one, having 34017 cells. For both grids the height of the first cell at the wall and at the interface is of 4 mm. Fig. 2 (a) shows the experimental and the numerical pressure evolutions obtained with the two grid levels. The pressure rise rate obtained during the first 500 s is in good agreement with the experimental one. Unfortunately, experimental data are lacking in the period between 500 s and 4350 s, so it is not possible to verify the accuracy of the numerical prediction in that time

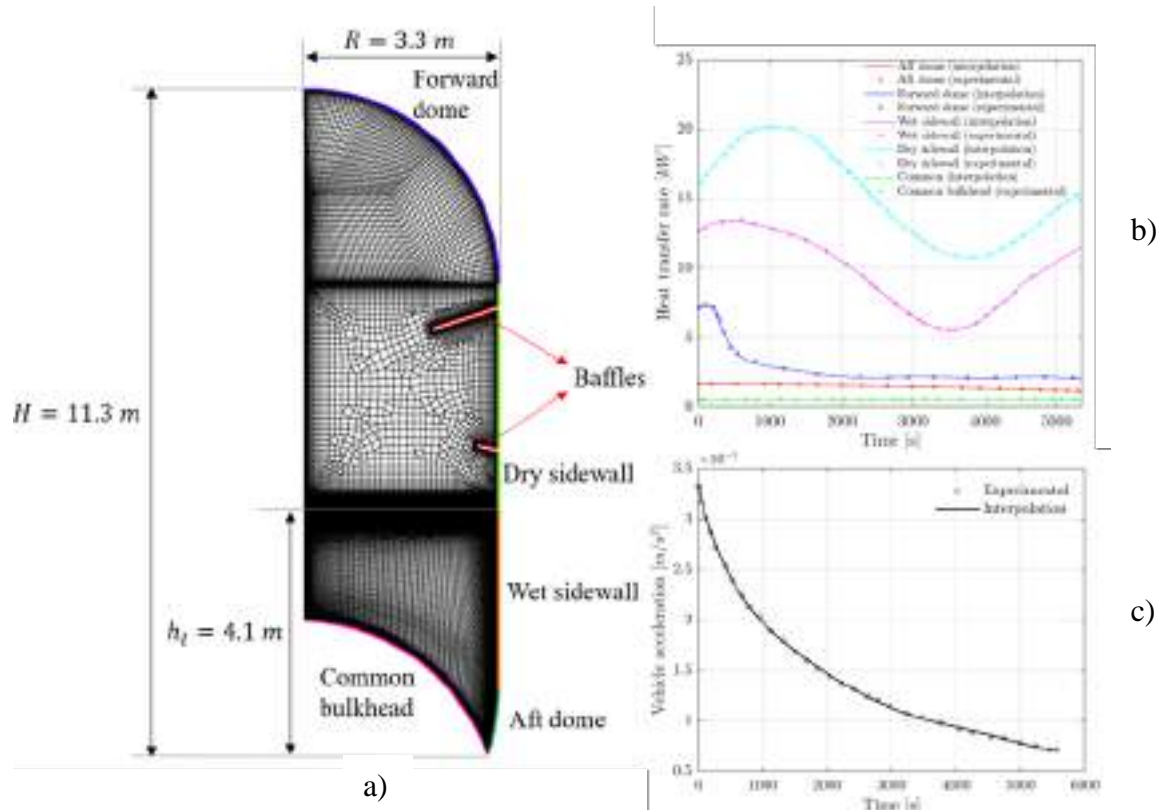


Figure 1: (a) Selected computational grid with the indication of the tank characteristic dimensions and of the names of the different parts of the tank wall, (b) Experimental [2] and interpolated heat transfer rates, (c) Experimental [2] and interpolated vehicle acceleration.

interval, but, certainly, some discrepancies with the experimental data arise, as it is confirmed by the numerical underestimation of the pressurization rate, in the last part of the experiment. The difference between the self-pressurization rates obtained with the two grids is negligible, but the finest grid is considered more appropriate because it allows a better representation of the vapor bubbles generating at the wall, as it will be clear in the following paragraph.

Preliminary results. Fig. 2 (b) shows the contours of the liquid H_2 volume fraction at 330 s, obtained with the coarse grid (left) and with the medium grid (right). Bubble nucleation is visible at the wall for both grid levels, and the resolution of the finest grid is able to better represent the shape of the bubbles. Nucleate boiling develops due to the high heat flux imposed at the wall. The liquid-ullage interface remains settled during the whole simulation, in agreement with the experiment [2]. Indeed, even if the tank was in orbital flight, the low acceleration imposed to it was sufficient to keep the propellant stabilized. This behavior is explained by the estimation of the Bond number based on the liquid level, which is of the order of 10^3 , evidencing the prevalence of the gravity force over the surface tension force.

Conclusions

In this work, a numerical methodology to study the self-pressurization of cryogenic propellant in tanks characterized by reduced gravity conditions is proposed, and validated with experimental data from [2]. The agreement between the numerical and the experimental data is reasonably good, but further analyses are necessary in order to refine the methodology, and assess its applicability to test cases with different propellants, dimensions, and operating conditions.

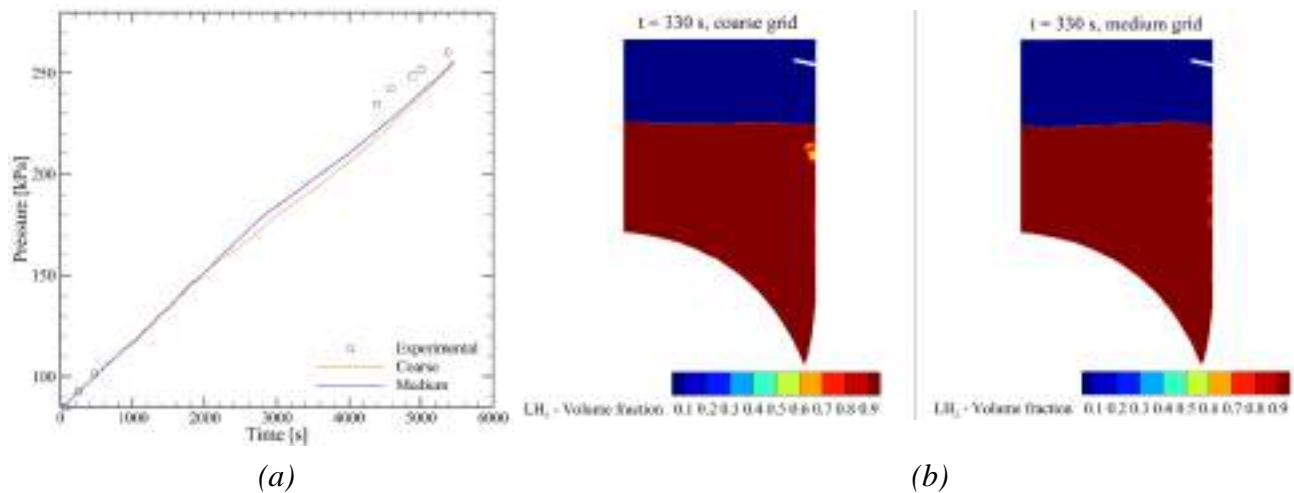


Figure 2: (a) Experimental [2] and numerical pressure evolutions obtained with the two grid levels used for grid independence study. (b) Contours of the liquid H_2 volume fraction at 330 s, obtained with the coarse grid (left) and with the medium grid (right).

Acknowledgments

This research was jointly funded by Sapienza University and the Italian Space Agency - Agenzia Spaziale Italiana (ASI) as part of the research project: "Technical Assistance for launchers and propulsion" N.2019-4-HH.0 carried out under a framework research agreement CUP:F86C17000080005.

References

- [1] W. Friz, Maximum volume of vapor bubbles, J. Physic. Zeitsch. 36 (1935) 354-379.
- [2] W. D. Ward, et al., Evaluation of AS-203 low-gravity orbital experiment, NASA CR 94045 (1967) 13.
- [3] F. Rossetti, et al., Setup of a numerical methodology for the study of self-pressurization of cryogenic tanks, submitted to Journal Cryogenics (2023).
- [4] C. Hirt, B. Nichols, Volume of fluid (VOF) method for the dynamics of free boundaries, J. Comput. Phys. 39 (1981) 201–225. [https://doi.org/10.1016/0021-9991\(81\)90145-5](https://doi.org/10.1016/0021-9991(81)90145-5)
- [5] W. H. Lee, A pressure iteration scheme for two-phase flow modeling, Computational Methods for Two-Phase Flow and Particle Transport (2013) 61–82. https://doi.org/10.1142/9789814460286_0004
- [6] J. Brackbill, et al. A continuum method for modeling surface tension, J. Comput. Phys. 100 (1992) 335–354. [https://doi.org/10.1016/0021-9991\(92\)90240-Y](https://doi.org/10.1016/0021-9991(92)90240-Y)
- [7] F. R. Menter, Two-equation eddy-viscosity turbulence models for engineering applications, AIAA J. 32 (1994) 1598–1605. <https://doi.org/10.2514/3.12149>
- [8] M. M. Lemmon, E.W., D. Friend, Thermophysical properties of fluid systems, NIST Chemistry WebBook, NIST Standard Reference Database Number 69, Eds. Linstrom, P.J., and Mallard, W.G., National Institute of Standards and Technology, Gaithersburg MD, 20899. URL: <https://webbook.nist.gov>
- [9] Ansys Fluent documentation, release 2022 R1, 2022.

Aerodynamic analysis of a high-speed aircraft from hypersonic down to subsonic speeds

Giuseppe Pezzella^{1,a} and Antonio Viviani^{1,b*}

¹ Università della Campania “Luigi Vanvitelli”, Dipartimento di Ingegneria, via Roma 29, 81031 Aversa (CE), Italy

^agiuseppe.pezzella@unicampania.it, ^bantonio.viviani@unicampania.it

Keywords: Subsonic, Hypersonic, CFD, Aerodynamics, Flying Test Bed

Abstract. Unmanned flying-test bed aircraft are fundamental to experimentally prove and validate next generation high-speed technologies, such as aeroshape design, thermal protection material and strategy; flight mechanics and guidance-navigation and control. During the test, the aircraft will encounter realistic flight conditions to assess accuracy of new design choices and solutions. In this framework, the paper focuses on the longitudinal aerodynamic analysis of an experimental aircraft, with a spatuled body aeroshape, from subsonic up to hypersonic speeds. Computational flowfield analyses are carried out at several angles of attack ranging from 0 to 15 deg and for Mach numbers from 0.1 to 7. Results are detailed reported and discussed in the paper.

Introduction

Advancements in high-speed technologies strongly rely on the development of flying-test beds [1].

In fact, performing flight and Wind Tunnel (WT) test campaigns represent the only and ultimate proof to demonstrate the technical feasibility of next generation high-speed aircraft (HAS) concepts and technologies [2], [3]. In this framework, the paper reports on the longitudinal aerodynamics of the Vanvitelli-one (V-one) flying test bed, shown in Figure 1 [4],[5].

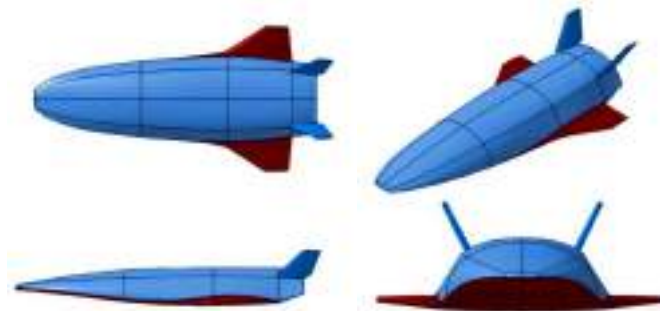


Figure 1 – Four views of the concept aeroshape [4], [5].

The V-one aircraft aims to provide a research platform suitable for a step-by-step increase of the readiness level of several enabling hypersonic technologies by means of both WT and in-flight experimentations. The V-one aeroshape features a classical lifting-body aeroshape which embodies all the features of an operational HSA, such as a low aspect ratio double-delta wing, two full movable vertical stabilizers in butterfly configuration, a spatuled fuselage forebody, characterized by a rounded off two-dimensional leading edge, mated on top of the wing. The wing flap, which must be actuated as elevon and aileron, is shown in purple in Figure 2 along with the complete moving fins (ruddervators) in green. The ruddervators pivot point is located at 50% of the root chord length.



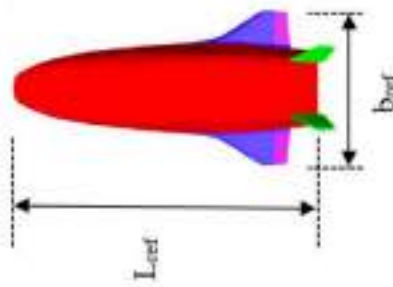


Figure 2 – Elevons and ruddervators of the aeroshape [4],[5].

The spatuled-body architecture allows to validate hypersonic aerothermodynamic design databases and passenger experiments, including thermal shield and hot structures, suitable for the successfully development of full-scale HSA [6],[7]. Within a typical mission scenario, in fact, HSA will encounter free-stream flows ranging from hypersonic to low subsonic speed.

The assessment of V-one longitudinal aerodynamics is undertaken with a Computational Fluid Dynamics (CFD) analysis with the goal to provide aerodynamic database (AEDB) to feed Flight Mechanics analyses. Both low speed and high-speed conditions were investigated at several angles of attack, α . Indeed, CFD analyses, carried out with ANSYS FLUENT[®] tool, address the flowfield past the aircraft for α ranging from 0 to 15 deg, for Mach from 0.1 to 7 and for clean configuration (i.e., no aerodynamic surfaces deflected) only.

Aerodynamic Flowfield Analysis

Concept longitudinal aerodynamics is addressed in terms of force and moment coefficients, according to the ISO-1151 standard. Lift (C_L), drag (C_D), and pitching moment (C_{M_x}) coefficients are calculated according to the following equations.

$$\begin{cases} C_i = \frac{F_i}{q_\infty S_{ref}} & i = L, D \\ C_{M_x} = \frac{M_x}{q_\infty L_{ref} S_{ref}} \end{cases} \quad (1)$$

The moment coefficient refers to the aircraft moment reference centre (MRC), and the reference length, L_{ref} , coincides with the fuselage length, see Fig. 2. Then, the vehicle planform area is considered as reference surface, S_{ref} . Aerodynamic coefficients are obtained by means of steady state Reynolds Averaged Navier-Stokes (RANS) flowfield computations. The pressure-based coupled solver was used for all CFD analyses carried out at free-stream Mach number lower than $M_\infty=0.3$; for Mach higher than this threshold (i.e., $M_\infty=0.3$) the density-based solver was considered. In this case, the Flux Difference Splitting (FDS) second-order upwind scheme (least square cell based) has been used for the spatial reconstruction of convective terms, while for the diffusive fluxes a cell-centred scheme has been applied. An implicit scheme has been considered for time integration. For both incompressible and compressible simulations, the $k-\omega$ SST turbulence model was used for Reynolds stress closure due to its ability to model separated flows and regions of flow circulation. Further, the ideal gas model was assumed for air. Recall that, even though CFD simulations have been carried out at hypersonic flow conditions (up to $M_\infty=7$), the ideal gas assumption was still valid. The reason is that the aeroshape features a very slender configuration and shall fly at rather low AoA (i.e., weak attached shock waves). A temperature-dependent formulation was considered for the specific heat at constant pressure, c_p , to accommodate the rather high flow energy at hypersonic speed [6]. Both unstructured and multi-block structured grids with an overall number of about 10M cells (half body) were considered for

the flowfield computations. For each mesh, a body of influence surrounding the vehicle for grid refinement was considered, with the condition of $Y^+ = O(1)$ at wall. Adiabatic wall is assumed at subsonic flow conditions, while the radiative cooled wall ($\epsilon=0.8$) was assumed in the other cases. Sixty-four fully three-dimensional flowfield simulations were carried out and results, in terms of lift and drag coefficients, are summarized in Fig. 3.

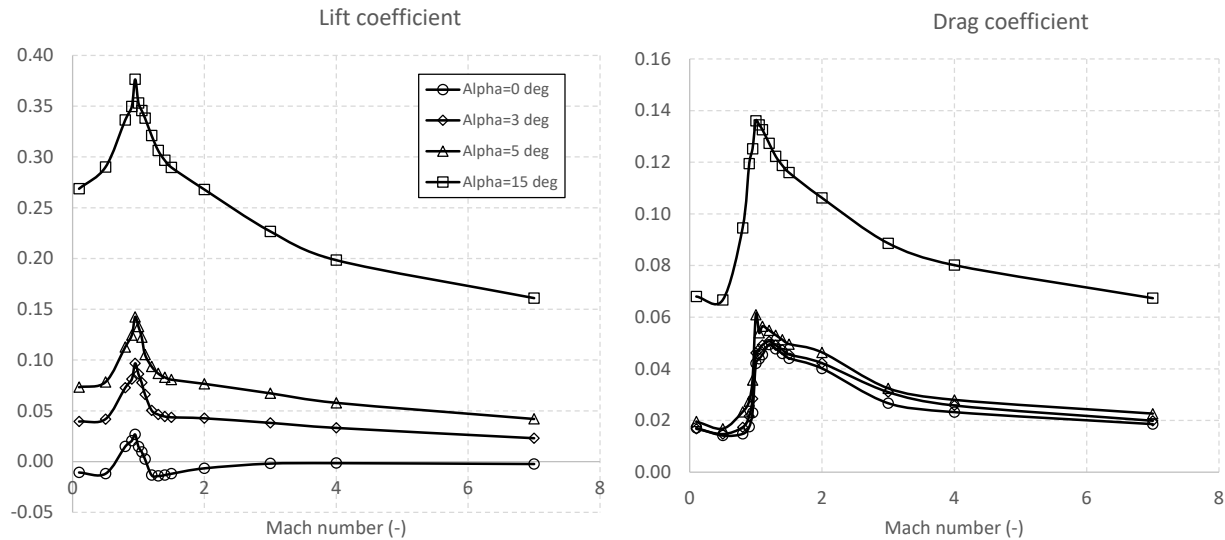


Figure 3 – Lift and drag coefficients versus Mach at $\alpha=0^\circ$, 3° , 5° , and 15° .

Figure 3 provides aircraft C_L and C_D versus Mach at four angles of attack, namely $\alpha=0^\circ$, 3° , 5° , and 15° . As shown, lift and drag coefficients rise in the transonic region and as expected increase as α increases. In particular, shock waves take place in the flowfield and determine a large increase of aerodynamic drag due to both wave drag and base drag which, in this speed regime, reach their maximum values. On the contrary, when Mach number further increases up to hypersonic flow conditions, aerodynamic coefficients decrease and reach a limit value, according to the Mach number independence principle.

Summary

Flying test bed vehicles are an efficient way to experimentally validate next generation high-speed technologies. In this framework, the paper focused attention on the appraisal of the longitudinal aerodynamic performance of a streamlined flying test bed aircraft with a spatuled-forebody aeroshape. Several computational flowfield analyses are carried out at angles of attack ranging from 0 to 15 deg and for Mach numbers from 0.1 to 7.

Initial findings for the hypersonic speed range pointed out that the high streamlined sharp leading edges of the V-one aeroshape led to a rather low wave drag component. In fact, up to 5 deg angle of attack the drag coefficient is equal to about 0.02; while aerodynamic lift at this attitude is close to 0.05.

Low speed aerodynamic analyses show that the lift coefficient features a mostly linear lift curve slope as expected for this flow regime and wing profile. The rounded leading edges of the double-delta planform prevent the formation of strong vortices, which would otherwise result in sharp changes in lift curve slope at high AoA. Vortices were instead observed forming along the forebody of the aircraft, which would contribute to aerodynamic forces and stability. A comparison of a structured domain with an unstructured showed little difference in extracted coefficients.

References

- [1] McClinton, C. R., Rausch, V. L., Nguyen, L. T., Sitz, J. R., “Preliminary X-43 flight test results”, *Acta Astronautica*, Volume 57, Issues 2–8, 2005, Pages 266-276, ISSN 0094-5765, <https://doi.org/10.1016/j.actaastro.2005.03.060>
- [2] Jeyaratnam, J., Bykerk, T., Verstraete, D., “Low speed stability analysis of a hypersonic vehicle design using CFD and wind tunnel testing” (2017) 21st AIAA International Space Planes and Hypersonics Technologies Conference, Hypersonics 2017, 10 p. <https://doi.org/10.2514/6.2017-2223>
- [3] Bykerk, T., Verstraete, D., Steelant, J., Low speed lateral-directional dynamic stability analysis of a hypersonic waverider using unsteady Reynolds averaged Navier Stokes forced oscillation simulations (2020) *Aerospace Science and Technology*, 106, art. no. 106228. <https://doi.org/10.1016/j.ast.2020.106228>
- [4] Bykerk, T., Pezzella, G., Verstraete, D., Viviani, A., “High and Low Speed Analysis of a Re-usable Unmanned Re-entry Vehicle”. HISST. International Conference on High-Speed Vehicle Science and Technology. Moscow. Russia. November 25-29, 2018. hisst-2018_1620897.
- [5] Bykerk, T., Pezzella, G., Verstraete, D., Viviani, A., “Lateral-Directional Aerodynamics of a Re-Usable Re-Entry Vehicle”. 8th European Conference for Aeronautics and Space Sciences (Eucass-2019). July 2019. Madrid. Spain.
- [6] Scigliano, R., Pezzella, G., Di Benedetto, S., Marini, M., Steelant, J., “Hexafly-Int Experimental Flight Test Vehicle (EFTV) Aero-Thermal Design”. Proceedings of the ASME 2017 International Mechanical Engineering Congress & Exposition IMECE 2017. November 3-9, 2017, Tampa, Florida, USA. ASME 2017 International Mechanical Engineering Congress and Exposition Volume 1: Advances in Aerospace Technology Tampa, Florida, USA, November 3–9, 2017. Conference Sponsors: ASME. ISBN: 978-0-7918-5834-9. Paper No. IMECE2017-70392, pp. V001T03A022; 14 pages. <https://doi.org/10.1115/IMECE2017-70392>
- [7] Schettino, A., Pezzella, G., Marini, M., Di Benedetto, S., Villace, V.F., Steelant, J., Choudhury, R., Gubanov, A., Voevodenko, N. “Aerodynamic database of the HEXAFLY-INT hypersonic glider”. (2020) *CEAS Space Journal*, 12 (2), pp. 295-311. <https://doi.org/10.1007/s12567-020-00299-4>

General Session

Virtual testing application to ESA micro vibrations measurement system

Lorenzo Dozio^{1,a *}, Leonardo Peri^{2,b}, Michele Pagano^{3,c} and Pietro Nali^{4,d}

¹Politecnico di Milano, Department of Aerospace Science and Technology, via La Masa, 34, 20156, Milano, Italy

²Politecnico di Milano, Department of Aerospace Science and Technology, via La Masa, 34, 20156, Milano, Italy (currently employed as PhD student at KU Leuven, Dept. Mech. Eng.)

³Politecnico di Milano, Department of Aerospace Science and Technology, via La Masa, 34, 20156, Milano, Italy (currently employed as Mechanical Environment Engineer at CNES)

⁴Thales Alenia Space, Domain Observation & Navigation Italy, Strada Antica di Collegno, 253, 10146, Torino, Italy

^alorenzo.dozio@polimi.it, ^bleonardo.peri@kuleuven.be, ^cmichelepagano919@gmail.com, ^dpietro.nali@thalesaleniaspace.com

Keywords: Virtual Testing, Microvibrations, MOR Techniques, Enhanced Craig-Bampton, Balanced Truncation

Abstract. The challenging application of Virtual Testing (VT) to ESA's six-degree-of-freedom Micro Vibrations Measurement System (MVMS) is described in this work. The digital replicate of MVMS is first obtained from a high-fidelity finite element model, whose order is later appropriately reduced. A state-space model representative of the dynamic behaviour of the MVMS is finally obtained. MVMS VT simulations are thus exploited as a key enabling technology to perform the ad-hoc design of MVMS control system design. This work focuses on different model-order reduction techniques applied to MVMS, which were evaluated and compared in terms of performance and computational issues. Classical and more recent approaches belonging to the family of Component Mode Synthesis (CMS) methods are addressed. State-space based techniques are considered as well, also in two-stage combination with CMS methods. Challenges and advantages of VT are lastly discussed.

Introduction to MVMS and virtual testing methodology

MVMS is a novel 6DOFs microvibration facility developed for the European Space Agency (ESA) by the UK's National Physical Laboratory. It is designed to measure/impose microvibration accelerations, forces, and moments in the frequency range from 0.03 Hz to 100 Hz, thus allowing both the characterisation of potential microvibration source and the assessment of an item's performance subjected to a microvibration environment [1]. Figure 1 shows MVMS, which is composed of three main components: a base support (BS), the VIBration ISolation platform (VIBISO), and the vibration Measurement PLatform (MPLAT). The base support interfaces with the ground, and it is mechanically connected to VIBISO through a MINUS-K device which acts as a passive mechanical low-pass filter. The function of BS is to sustain the upper MVMS components and to hold the seismometers and the fixed parts of the voice coil actuators, which form the set of sensors/actuators used by VIBISO to complement and improve the passive isolation provided by the MINUS-K with an active control action. Indeed, the aim of VIBISO is to actively isolate the upper part of the facility from vibrations transferred via the ground such as seismic disturbance. The function of MPLAT is to measure/impose the microvibration environment from/to the test specimen. It interfaces VIBISO through a second MINUS-K device and an additional set of voice coil actuators.



The digital replicate of MVMS is obtained by a properly correlated high-fidelity finite element model of the facility. A set of reduced-order models are later derived by retaining only the most relevant dynamics information, with the final aim of using the resulting state-space representation for the control system design. Figure 2 provides an overview of the computational methodology put in place for MVMS Virtual Testing in line with [2].

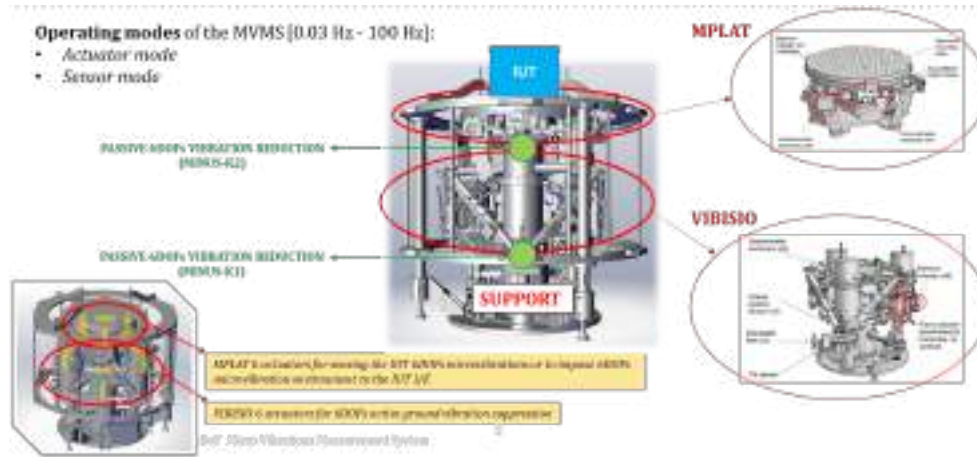


Figure 1. General description of the MVMS facility.

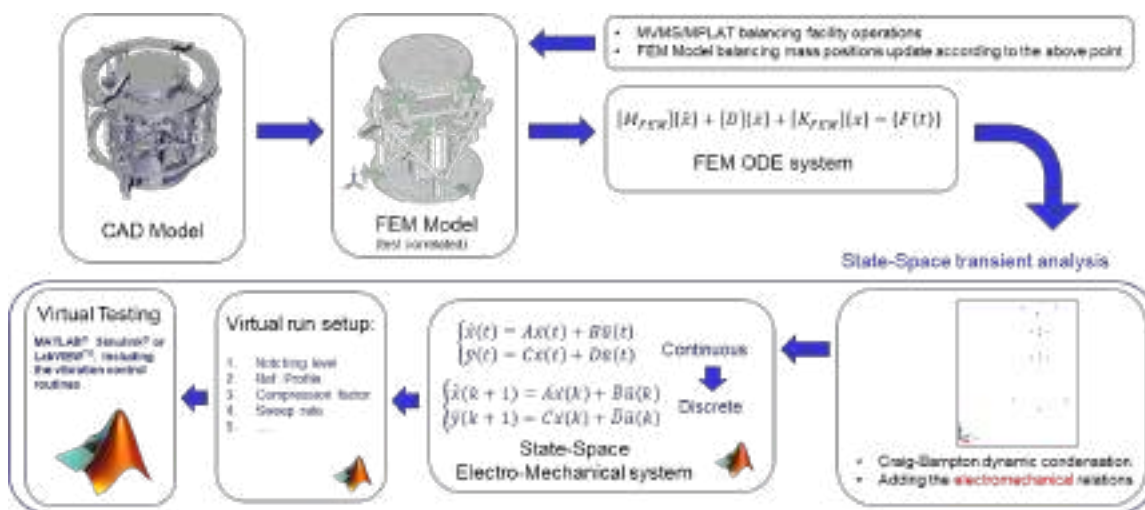


Figure 2. Overview of the computational methodology of MVMS Virtual Testing.

Assessment of model-order reduction techniques

In this work, several different model-order reduction techniques are considered, evaluated, and compared in terms of performance and computational issues. Classical and more recent approaches belonging to the family of Component Mode Synthesis (CMS) methods are applied to MVMS, as well as state-space based techniques such as the simple modal truncation (MT) and the powerful balanced truncation (BT). A hybrid technique consisting in a two-stage reduction combining CMS methods with BT or MT is also developed to overcome the numerical difficulties associated with the direct application of BT to very high-order problems [3]. A very restricted selection of results is presented below to give a concise comparison of the various methodologies, along with advantages or disadvantages of the adopted techniques.

Concerning CMS methods, in addition to the classical Craig-Bampton (CB) method [4], the Rubin (RU) method [5] and the Enhanced Craig-Bampton (ECB) [6] technique are evaluated. The

reductions are carried out by considering as substructures the three main components of MVMS. Both ECB and RU aim to improve CB reduction performance by taking into account a contribution coming from discarded modes in the transformation matrix. While in RU this is achieved by approximating the dynamic behaviour via free-interface normal modes, ECB considers fixed-interface modes as in the original CB formulation. The selection of component modes to be retained for the three substructures is carried out by resorting to the Effective Interface Mass criterion [7], resulting in 15, 37 and 4 modes, respectively, for BS, VIBISO and MPLAT, along with 60 boundary DOFs.

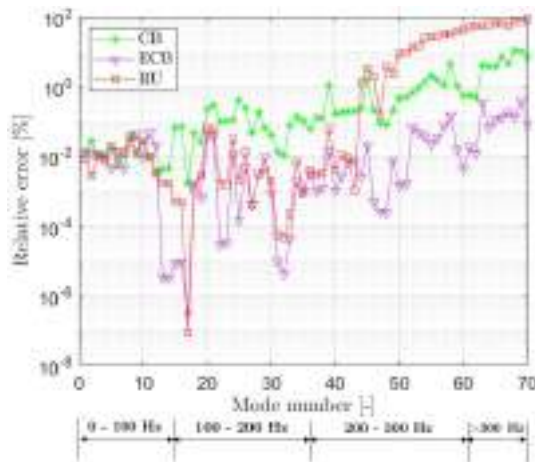


Figure 3. Relative error on natural frequencies among CMS methods.

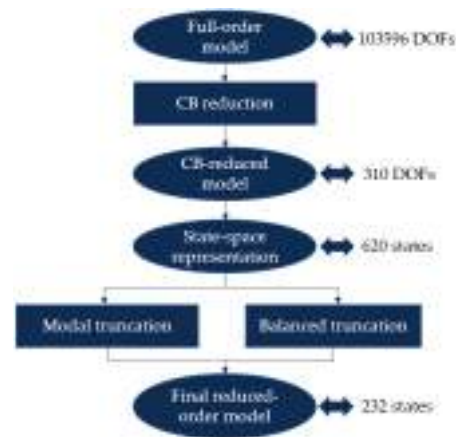


Figure 4. Two-stage reduction workflow.

Figure 3 reports the relative error between the natural frequencies computed by the high-fidelity FE model and those obtained from the reduced models. Both RU and ECB provide higher accuracy with respect to the classical CB reduction. In particular, ECB maintains superior performance in approximating both low and higher frequency modes, while a significant worsening is experienced with RU above approximately 250 Hz.

A similar analysis was carried out by employing MT and BT methods [8]. The latter is particularly appealing in the present VT approach, as it allows the input-output behaviour of the system to be preserved as much as possible. However, the high computational effort required by BT prevents its direct application to large-scale systems. This issue is overcome in this work by resorting to a hybrid two-stage reduction approach [9], envisaging a preliminary reduction via one of the CMS methods (CB is considered here), followed by either MT or BT, as reported in Fig. 4. The performance of the various reduction methods is assessed by comparing the frequency response in terms of the transmissibility from a longitudinal seismic disturbance to the item under test as shown in Fig. 5. All the methods, except for the hybrid MT, provide a high-performance approximation of the system response. The lack of a notable difference among the methods is explained by the peculiar dynamic behaviour of MVMS. Indeed, the low-pass filtering action of the MINUS-K devices strongly affects the dynamic response, which is dominated by a few low-frequency structural modes. With the aim of providing a deeper insight into the performance of the reduction techniques, the same analysis is carried out by retaining a significantly lower amount of DOFs. Figure 6 reports the relative error in the transmissibility function between the full-order and the reduced models. The largest improvements with respect to the classical CB method performance are provided by ECB and hybrid BT techniques.

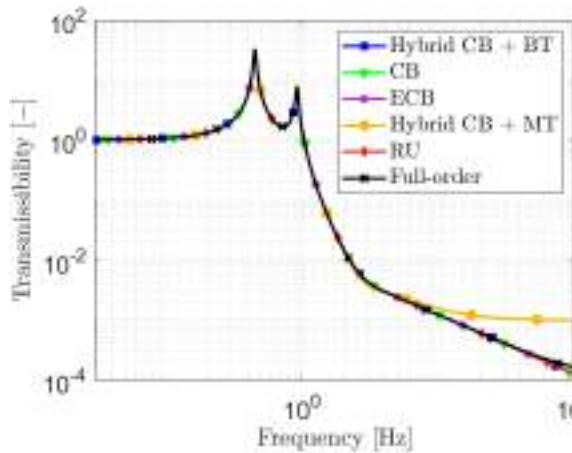


Figure 5. Comparison of the frequency responses.

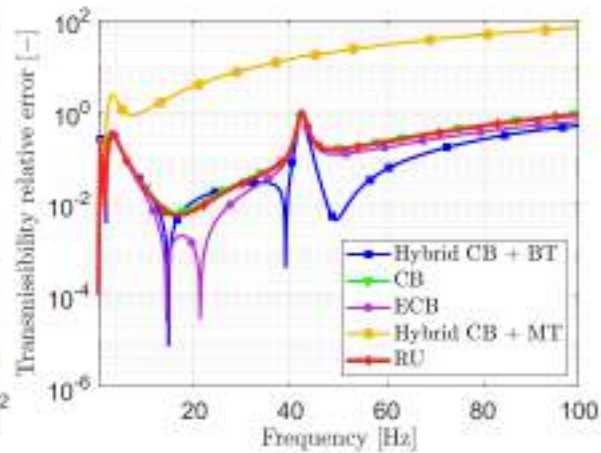


Figure 6. Relative error on the transmissibility.

In conclusion, referring to the MVMS application, hybrid BT and ECB appear as the most promising methods in terms of performance improvements with respect to classical reduction techniques typically adopted in the VT framework.

References

- [1] Statement of Work ESA Express Procurement – EXPRO SOW 6DOF MVMS Simulation Model, SA-TEC-MXE-MECH-SOW-00147.
- [2] P. Nali, et al., A virtual shaker testing experience: modeling, computational methodology and preliminary results, ECSSMET 2016 (European Conference on Spacecraft Structures, Materials & Environmental Testing), Toulouse, France, 27-30 September 2016.
- [3] B. Besselink, et al., A comparison of model reduction techniques from structural dynamics, numerical mathematics and systems and control, J Sound Vib., 332 (2013), 4403–4422. <https://doi.org/10.1016/j.jsv.2013.03.025>
- [4] R.R. Craig, M.C.C. Bampton, Coupling of Substructures for Dynamic Analyses, AIAA Journal, 6 (1968), 1313–1319. <https://doi.org/10.2514/3.4741>
- [5] S. Rubin, Improved Component-Mode Representation for Structural Dynamic Analysis, AIAA Journal, 13 (1975), 995–1006. <https://doi.org/10.2514/3.60497>
- [6] J. Kim and P. Lee. An enhanced Craig–Bampton method, International Journal for Numerical Methods in Engineering, 103 (2015), 79–93. <https://doi.org/10.1002/nme.4880>
- [7] D. Kammer, M. Triller, Selection of component modes for Craig–Bampton substructure representations, ASME J Vib. Acoust., 118 (1996), 264–270. <https://doi.org/10.1115/1.2889657>
- [8] A. Antoulas. Approximation of Large-Scale Dynamical Systems, SIAM, Philadelphia, USA, 1 edition, 2005. ISBN 978-0-89871-529-3.
- [9] J. Spanos and W. Tsuha. Selection of Component Modes for Flexible Multibody Simulation, J Sound Vib., 14 (1991), 278–286. <https://doi.org/10.2514/3.20638>

Nonlinear transient analyses of composite and sandwich structures via high-fidelity beam models

Matteo Filippi^{1,a,*}, Rodolfo Azzara^{1,b} and Erasmo Carrera^{1,c}

¹MUL2 Group, Department of Mechanical and Aerospace Engineering, Politecnico di Torino,
Corso Duca degli Abruzzi 24, 10129, Torino, Italy

^amatteo.filippi@polito.it, ^brodolfo.azzara@polito.it, ^cerasmo.carrera@polito.it

Keywords: Finite Element Method, Transient Nonlinear Analyses, One-Dimensional Formulations, Carrera Unified Formulation

Abstract. In this study, we employ low and high-fidelity finite beam elements to conduct geometrical nonlinear transient analyses of composite and sandwich structures. The equations of motion for various structural theories are derived in a total Lagrangian scenario using the Carrera Unified Formulation. The unified formalism's three-dimensional nature enables us to include all components of the Green-Lagrange strain tensor. To solve the equations, we utilize the Hilber-Hughes-Taylor (HHT)- α algorithm in conjunction with a Newton-Raphson procedure. We present the dynamic response of a sandwich stubby beam subjected to a step load, calculated using both equivalent-single layer and layer-wise approaches. Additionally, we discuss the effects of geometrical nonlinearity.

Introduction

In recent decades, the aerospace, automotive, and other engineering fields have faced new challenges that necessitate the adoption of sophisticated and lightweight components. These highly flexible structures are extensively utilized in various engineering applications as they can exhibit large displacements and rotations without undergoing plastic deformations. Furthermore, many of these components comprise sandwich structures made of composite materials to ensure a significant strength-to-weight ratio. As highlighted in numerous scientific papers [1,2], analyzing these structural configurations requires refined kinematic theories that can overcome the well-known limitations of the Euler-Bernoulli and the first-order-shear deformation theories.

This research aims to analyze the nonlinear dynamic behavior of composite and sandwich structures using variable-fidelity one-dimensional finite elements. The mathematical models are derived using the Carrera Unified Formulation (CUF). This hierarchical formalism enables the selection of the order of the structural model as an input of the analysis. Therefore, any theory can be obtained by arbitrarily expanding the generalized variables. Specifically, this work employs Lagrange (LE) and Taylor (TE) polynomials to develop kinematic expansions. According to the layer-wise concept, the LE models allow for the independent discretization of each lamina. In contrast, the Taylor-based models homogenize the cross-section properties with polynomials of arbitrary orders. Regardless of which theory is adopted, the governing equations and the related finite element arrays are formulated in terms of *Fundamental Nuclei* (FNs), the invariants of the methodology. The nonlinear equations are formulated using the total Lagrangian approach and solved using a suitable Newton-Raphson method. We utilize the Hilber-Hughes-Taylor (HHT)- α algorithm as the implicit time integration scheme to evaluate the nonlinear dynamic response. This algorithm proves particularly effective in stabilizing the time integration process under highly nonlinear effects.

To highlight the relevant discrepancies between low- and high-fidelity solutions in studying the response of laminated beams, we consider a stubby sandwich structure characterized by a

significant degree of anisotropy between the core and external layers. Moreover, we have compared geometrical linear and nonlinear solutions for two different load magnitudes.

Unified formulation of geometrical nonlinear beam theory

The theoretical basis required for solving transient analyses in geometrically nonlinear regimes can be found in [3]. However, to ensure the self-contained nature of this work, we provide some basic equations here. Based on the one-dimensional finite element unified formulation, we express the displacement vector $\mathbf{u}^T(x, y, z, t) = (u_x, u_y, u_z)$ as a sum of products between cross-sectional (defined over the x-z plane) functions $F_\tau(x, z)$, finite element shape functions $N_i(y)$ (defined over the y-axis) and the nodal unknown vector $\mathbf{q}_{\tau i}(t)$

$$\mathbf{u}(x, y, z, t) = F_\tau(x, z)N_i(y)\mathbf{q}_{\tau i}(t) \quad \tau = 1, \dots, M \text{ and } i = 1, \dots, nn_{el} \quad (1)$$

In Eq. 1, the subscripts indicate summation, while M and nn_{el} represent the number of functions included in the structural model and the number of nodes belonging to a single finite beam element, respectively. As previously mentioned, the geometrically nonlinear FE governing equations are obtained according to a total Lagrangian formulation by including all Green–Lagrangian strain tensor components. The strain–displacement relation and the constitutive law reported in Eq. 2 are obtained using the linear and nonlinear differential operators, \mathbf{b}_l and \mathbf{b}_{nl} , respectively, and the stiffness matrix for linear elastic materials, \mathbf{C} .

$$\boldsymbol{\varepsilon} = (\mathbf{b}_l + \mathbf{b}_{nl})\mathbf{u} \quad \boldsymbol{\sigma} = \mathbf{C} \boldsymbol{\varepsilon} \quad (2)$$

By substituting Eq. 1 and Eq. 2 into the principle of virtual work, it becomes possible to express the virtual variations of both strain energy (δL_{int}) and the work done by inertial forces (δL_{ine}) and external loads (δL_{ext}) in the CUF formalism.

$$\begin{aligned} \delta L_{int} &= \delta \mathbf{q}_{sj}^T \mathbf{K}_s^{ij\tau s} \mathbf{q}_{\tau i} \\ \delta L_{ine} &= \delta \mathbf{q}_{sj}^T \mathbf{M}^{ij\tau s} \ddot{\mathbf{q}}_{\tau i} \\ \delta L_{ext} &= \delta \mathbf{q}_{sj}^T \mathbf{F}^{sj} \end{aligned} \quad (3)$$

The FNs of the secant stiffness and mass matrix are denoted as $\mathbf{K}_s^{ij\tau s}$ and $\mathbf{M}^{ij\tau s}$, respectively, while \mathbf{F}^{sj} represents the fundamental nucleus of the loading vector. Here, the indexes s and j are adopted for the virtual variations of the displacements and have the same bounds as τ and i . The assembled matrices and vectors associated with any arbitrary structural model are constructed by permuting these four indexes. Based on this notation, the equations of motion are

$$\mathbf{M}\ddot{\mathbf{q}}(t) + \mathbf{K}_s(\mathbf{q})\mathbf{q}(t) = \mathbf{F}(t) \quad (4)$$

Equation 4 is solved by using the Newton-Raphson method and the HHT- α implicit time integration scheme. For a dynamic conservative problem, the linearization of the residual nodal forces leads to

$$\begin{aligned} \delta(\delta L_{int} + \delta L_{ine} - \delta L_{ext}) &= \delta \mathbf{q}_{sj}^T (\mathbf{K}_0^{ij\tau s} + \mathbf{K}_{T1}^{ij\tau s} + \mathbf{K}_\sigma^{ij\tau s}) \delta \mathbf{q}_{\tau i} + \delta \mathbf{q}_{sj}^T \mathbf{M}^{ij\tau s} \delta \dot{\mathbf{q}}_{\tau i} = \\ &= \delta \mathbf{q}_{sj}^T \mathbf{K}_T^{ij\tau s} \delta \mathbf{q}_{\tau i} + \delta \mathbf{q}_{sj}^T \mathbf{M}^{ij\tau s} \delta \dot{\mathbf{q}}_{\tau i} \end{aligned} \quad (5)$$

In Eq. 5, $\mathbf{K}_T^{ij\tau s}$ represents the FN of the tangent stiffness matrix (see [4]).

Results

Figure 1 and Table 1 present the dimensions, material properties, boundary conditions, and loading conditions of the sandwich beam. The structure was subjected to a pressure load that was constant in time but variable in magnitude.

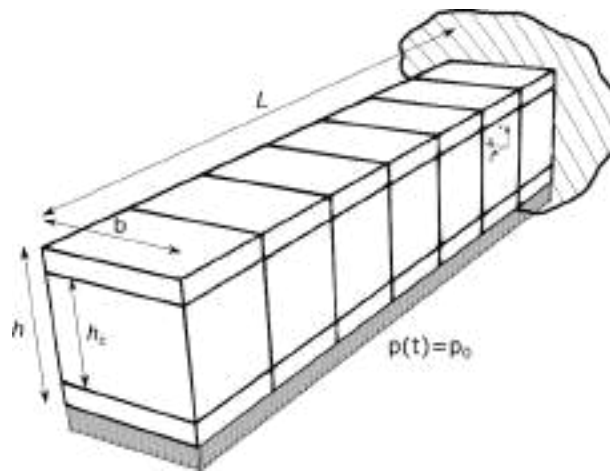


Figure 1: the cantilever sandwich beam.

Table 1: dimensions and material data of the sandwich beam.

Geometrical data	Material data	Face	Core
$L = 0.1$ [m]	Young's modulus, E [GPa]	200	0.66
$h = b = 0.02$ [m]	Poisson's ratio	0.27	0.3
$h_c = 0.014$ [m]	Density [kg/m^3]	7800	60

The finite element models utilized in this study consisted of seven 4-node beam elements placed along the longitudinal axis. Transient analyses were performed using the Taylor-based expansions of second (TE2) and third order (TE3) - as well as a layer-wise model consisting of three (one per layer) bi-cubic Lagrange elements (3-LE16) placed over the cross-section. The degrees of freedom (d.o.f.) corresponding to the TE2, TE3 and 3LE16 solutions were 396, 660, and 2640, respectively. In Figure 2, the transverse deflection of the sandwich beam is depicted for two different values of the applied pressure. As expected, the equivalent-single-layer solutions, although improved compared to classical beam models, significantly underestimate the deformation of the structure when compared to the layer-wise prediction. Additionally, it is noteworthy that both geometrically linear and nonlinear approaches provide almost indistinguishable results for relatively small values of p_0 , irrespective of the structural theory employed. However, it can be observed that with the increase of the load value, the linear and nonlinear curves obtained using the 3-LE16 model differ significantly. This effect can be attributed to the superior ability of the layer-wise model to accurately describe the deformation and stress fields compared to the equivalent-single-layer kinematics.

Summary

This work presented preliminary results concerning composite and sandwich structures' geometrical nonlinear transient responses calculated with one-dimensional finite element models based on various kinematic assumptions. The comparisons between low- and high-fidelity solutions demonstrated the importance of accurately describing the cross-section deformations, especially in the nonlinear regime. Further results will be provided on composite laminated structures subjected to different loads.

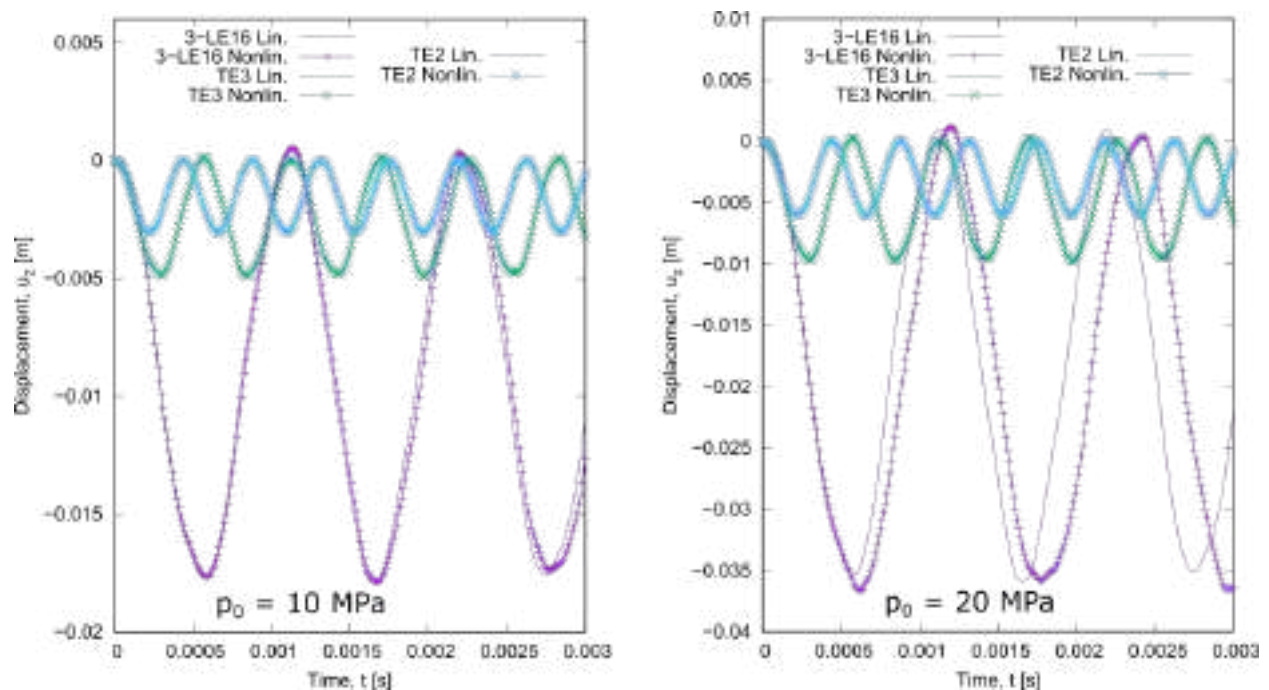


Figure 2: transient responses of the sandwich beam for two pressure values.

References

- [1] T. Kant, C.P. Arora, J.H. Varaiya, Finite element transient analysis of composite and sandwich plates based on a refined theory and a mode superposition method, *Composite Structures*. 22 (1992) 109-120. [https://doi.org/10.1016/0263-8223\(92\)90071-J](https://doi.org/10.1016/0263-8223(92)90071-J)
- [2] J.R. Kommineni, T. Kant, Large Deflection Elastic and Inelastic Transient Analyses of Composite and Sandwich Plates with a Refined Theory, *Journal of Reinforced Plastics and Composites*. 12 (1993) 1150-1170. <https://doi.org/10.1177/073168449301201102>
- [3] R. Azzara, M. Filippi, A. Pagani, Variable-kinematic finite beam elements for geometrically nonlinear dynamic analyses, *Mech. Adv. Mater. Struct.* (2022). <https://doi.org/10.1080/15376494.2022.2091185>
- [4] A. Pagani, E. Carrera, Unified formulation of geometrically nonlinear refined beam theories, *Mech. Adv. Mater. Struct.* 25 (2018) 15-31. <https://doi.org/10.1080/15376494.2016.1232458>

BEA: Overview of a multi-unmanned vehicle system for diver assistance

Leonardo Barilaro^{1*}, Jason Gauci², Marlon Galea², Andrea Filippozzi³,
David Vella², Robert Camilleri²

¹ The Malta College of Arts, Science & Technology, Aviation Department, Paola PLA 9032, Malta

² Institute of Aerospace Technologies, University of Malta, Msida, MSD 2080, Malta

³Divers Code Ltd., St Paul's Bay, SPB 2080, Malta

* leonardo.barilaro@mcast.edu.mt

Keywords: Swarm Unmanned Vehicles, UAV, USV, UUV, Safety at Sea

Abstract. This paper presents an overview of a solution to address the issue of marine traffic endangering scuba diving and free diving. Diving is a popular recreational activity, and it is estimated that there are around six million active scuba divers worldwide. When diving, it is essential to signal one's presence with universal markers, however, boat drivers do not always recognize them and can speed too close to dive zones, posing a risk to divers. To mitigate these risks, a multi-unmanned vehicle system consisting of an Unmanned Aerial Vehicle (UAV), an Unmanned Surface Vehicle (USV), and an Unmanned Underwater Vehicle (UUV) has been developed. The proposed system works in synergy to monitor and protect divers. The UAV monitors the surface of the sea near the dive zone for any traffic, while the USV tracks the UUV, communicates with the other unmanned vehicles, and provides a takeoff/landing surface for the UAV. The USV can also be used to tow divers and equipment to/from the shore. Finally, the UUV tracks the diver and warns them if it is unsafe to surface. The paper provides an overview of the design and system's architecture, algorithms for boat detection, precision landing and UUV tracking, as well as preliminary tests carried out on the prototype. The proposed system is found to be suitable for the intended application. The BEA (Buoy Eau Air) system is the first in the world to use a multi-drone system to create a geo-fence around the diver and monitor the area within it. The paper also highlights the potential benefits of such a system for the touristic sector, especially for countries where diving is a popular recreational activity.

Introduction

The project presented in this paper develops the first system in the world composed of a multi-drone system: BEA. Before the global pandemic due to Covid-19, the touristic sector in Malta contributed to approximately 25% of GDP and to 28% of fulltime employment. Around 5% of inbound tourists have engaged in diving activities such as snorkelling, scuba diving and freediving [1]. However, such activities have an element of risk. With the recovery of the economic situation worldwide it is important to investigate ways to reboost the touristic sector with new solution to improve the safety at sea. To mitigate the risks associated, BEA proposes a system of drones, one operating in the air, one on the water surface and one underwater to support and monitor the safety of divers. While the hovering UAV creates a geo-fence around the diver, therefore offering protection against boat incursions [2, 3]. The self-propelled Buoy acts as a resting platform while hosting critical support. It also acts as the communication link between the hovering drone and the underwater ROV. Finally, the ROV is able to follow the diver emulating the “buddy philosophy”, while providing reassurance to the diver. The multi-drone system works in synergy, with the sub-systems being in communication with each other, and have the ability to relay a message to the



diver. The buddy system is set of safety procedures to improve the chances of avoiding accidents in or under water by having divers in a group of at least two. The group dive together and co-operate, so that they can help or rescue each other in the event of an emergency. The key point is to respond in time, which is related with the experience of the divers. The multi-drone system enhances this, working in synergy, with the sub-systems being in communication with each other, and having the ability to relay a message to the diver.

The use of a group (or swarm) of unmanned vehicles to perform a task is advantageous because it makes it possible to overcome the limitations of individual vehicles and improves overall performance, flexibility and fault-tolerance, amongst other things. Various instances of collaboration between unmanned aerial, ground, surface and underwater vehicles are available in the literature. For instance, collaborations are reported between Unmanned Ground Vehicles (UGVs) and UAVs [4-7]; between USVs and UAVs [8-10]; and between UAVs, USVs and UUVs [11, 12]. The applications for such collaborations are endless and include: maritime patrol [10], power pylon inspection [7], search and rescue [11], object transportation [5] and terrain navigation [6]. BEA will contribute towards maintaining the safety track record of the local Maltese industry while offering a novelty which boosts the diving experience.

The rest of the paper is organized as follows. Section 2 describes the BEA concept overview while Sections 3 detail the architecture of the proposed system and, finally, Section 4 concludes the paper and describes future work.

BEA concept overview

The BEA system is composed of 3 main modules, the Buoy, developed from scratch, a drone monitoring the geo-fence around the diver and an underwater drone.

More in detail, the primary objectives of BEA are to develop a functional prototype of the multi-drone system and to conduct comprehensive testing under various ambient conditions, including different sea and diving scenarios. By capturing data from test campaigns, divers, and engineers, the secondary objective of BEA is to facilitate design improvements and industrialization while creating a valuable database of average diving safety conditions.

The engineering and divers' requirements have been captured to ensure the system's effectiveness and usability. Figure 1 illustrates the conceptual architecture of the system, outlining the roles and interactions of each component.

The UAV plays a critical role in detecting boat traffic through an onboard camera. It takes off from the Unmanned Surface Vehicle (USV) and hovers at a specified altitude. The UAV can initiate its flight either at the beginning of a dive or a few minutes prior to the expected end, during the divers' safety stop. Upon detecting a boat or vessel, the UAV transmits a warning signal to the USV, which subsequently activates a light indicator located on its underside. The warning signal is also relayed to the Underwater Unmanned Vehicle (UUV), triggering a light indicator for the divers. This system ensures that divers are visually alerted to the presence of boats, enabling them to exercise caution before surfacing.

Throughout the dive, the UUV closely follows the divers, detecting their movements and adapting its speed and direction accordingly, while avoiding obstacles such as rocks. Simultaneously, the USV tracks the UUV's position, maintaining a fixed distance from it by maneuvering and propelling itself. Furthermore, the UAV continuously tracks the current position of the USV. These three vehicles maintain mutual tracking during the dive, ensuring comprehensive surveillance and support.

At the conclusion of the dive, as the divers surface, the UAV descends and lands on the USV by accurately detecting and tracking fiducial markers. Additionally, the UUV docks with the USV, facilitating seamless retrieval. Prior to or after a dive, the USV can be manually operated by the divers, allowing them to tow themselves and their equipment to or from the shore or a boat. In rescue situations, the USV can also serve as a towing mechanism for divers requiring assistance.

Figure 2 shows the 3D model of the finalized conceptual design.



Fig 1: BEA system concept

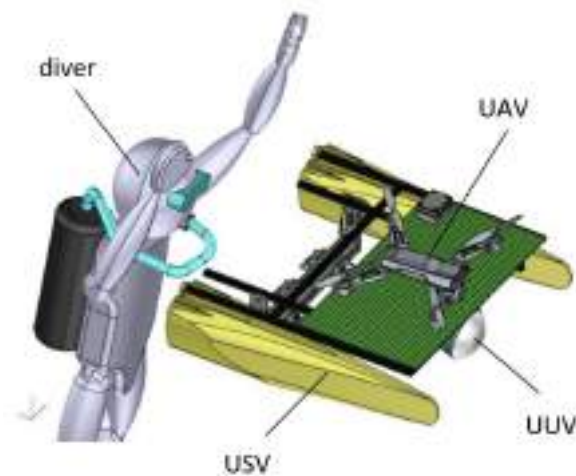


Fig 2: BEA conceptual design

System architecture

This paragraph will describe in detail the system architecture.

UAV: The UAV is the Cuta-Copter EX-1 drone. This quadcopter has an IP67 rating, a payload capacity of 2 kg and an endurance of 23 minutes (without a payload). It is equipped with a Pixhawk 2.4.8 flight controller (running ArduPilot autopilot software) and supports manual and automatic flight. For this application, additional components were added to the Cuta-Copter. The first of these is a Raspberry Pi 4 (Model B) companion computer with 8 GB of RAM. This computer exchanges MAVLink messages with the flight controller via a Universal Asynchronous Receiver-Transmitter (UART) communication interface. It also exchanges data with the USV via a wireless, half-duplex, serial communication link. Two sensors are connected to the Raspberry Pi: a visible light camera module and a distance sensor. The camera is a Raspberry Pi camera module (v1) with a weight of 3 g, a sensor resolution of 2592 x 1944 pixels, a horizontal Field of View (FoV) of 53.5 degrees and a vertical FoV of 41.4 degrees. The camera is mounted beneath the Cuta-Copter and points downwards. It is used both for boat detection and precision landing. The distance sensor is a Benewake TF02-Pro IP65 LiDAR with an outdoor range of 13.5 m and a weight of 50 g. This

sensor is mounted next to the camera and measures the height of the UAV above the USV. This sensor is used for precision landing.

USV: The USV was custom-built for this work (Fig. 3). It is made of fiberglass and consists of two hulls; a takeoff/landing pad measuring 1 x 1 m; a waterproof compartment for the electronics; and a handle bar for manual control. Its overall size is 110 x 80 x 15 cm. The USV is controlled by an Arduino Mega 2560 microcontroller and is powered by a 14.8 V 46 Ah LiPo battery pack, complete with a Battery Management System (BMS). Propulsion is provided by four BlueRobotics T200 thrusters at the bottom of the USV – two in front and two at the back. The speed and direction of the USV is controlled by varying the Pulse Width Modulation (PWM) signals to these thrusters. The GPS position of the USV is determined by an Adafruit Ultimate GPS module which provides the controller with NMEA-0183 messages. The position of the USV is transmitted to the UAV via the wireless communication link, and this position is sent to the UAV's autopilot as a new waypoint. Thus, the UAV can follow the USV and remain overhead. Two BlueRobotics ping sonar altimeters and echosounders are mounted in front of the USV, 70 cm apart. Each sensor operates at 115 kHz and has a beam width of 30 degrees and can detect objects up to 50 m underwater. The output of each sensor consists of a distance measurement and a confidence value. These sensors are used to estimate the position of the UUV. An underwater Light Emitting Diode (LED) – whose brightness can be controlled by means of a PWM signal – is mounted beneath the USV. This LED can be turned on by the controller to warn the divers in the event of boat traffic. The USV and UUV communicate via Water Linked M64 underwater modems which provide a wireless half-duplex acoustic communication link.



Fig 3: USV

UUV: The UUV is the iBubble Evo. This is an untethered drone with seven thrusters, an endurance of one hour, and a maximum operating depth of 60 m. The iBubble has a proprietary sonar positioning system. This is capable of tracking a diver by using four hydrophones to pick up the acoustic signal transmitted by a remote controller worn by the diver. The iBubble can also detect and avoid obstacles by means of an integrated visible light camera module. As in the case of the UAV, additional electronic components were added to the iBubble. A Water Linked M64 acoustic modem relays warning messages from the USV to an Arduino Mega 2560 microcontroller which, in turn, turns on an LED indicator to warn the diver in the event of marine traffic.



Fig 4: BEA system with Cutacopter, iBubble EVO, Buoy (from left to right)

Conclusions

This paper presented a multi-unmanned vehicle system consisting of a UAV, a USV and a UUV, to assist divers and warn them of boat traffic in their proximity. By integrating the Buoy, UAV, and ROV modules, this multi-drone system, Figure 4, effectively tracks and supports divers throughout their underwater activities. The requirements capture process, functional architecture and versatile surface operation capabilities collectively position BEA as a promising solution for improving diving safety conditions. The initial simulations and real-world test results have showcased the system's suitability and effectiveness for the intended application. Future developments will focus on the full integration of the three vehicles, enabling further real-world testing with divers to evaluate the system's performance in a wider range of diving scenarios.

Acknowledgement

The work described in this paper was carried out as part of the BEA (R&I-2018-005T) project which was financed by the Malta Council for Science & Technology, for and on behalf of the Foundation for Science and Technology, through the FUSION: R&I Technology Development Programme.

References

- [1] "How Many Divers Are There? 8 Reasons Make Diving Is So Popular." Blue Calmness. <https://bluecalmness.com/how-many-divers-are-there-8-reasons-make-diving-is-so-popular/> (accessed Jan. 31, 2023).
- [2] "Safe Boating Guidelines." DAN World. <https://world.dan.org/safety-prevention/diver-safety/psa/safe-boating-guidelines/> (accessed Jan. 31, 2023).
- [3] M. Agius. "Vessels caught speeding next to diving flags." Newsbook. <https://newsbook.com.mt/en/vessels-caught-speeding-next-to-diving-flags/> (accessed Jan. 31, 2023).
- [4] F. Cocchioni et al., "Unmanned Ground and Aerial Vehicles in extended range indoor and outdoor missions," 2014 International Conference on Unmanned Aircraft Systems (ICUAS), Orlando, FL, USA, 2014, pp. 374-382. <https://doi.org/10.1109/ICUAS.2014.6842276>.
- [5] E. H. C. Harik, F. Guérin, F. Guinand, J. -F. Brethé and H. Pelvillain, "UAV-UGV cooperation for objects transportation in an industrial area," 2015 IEEE International Conference on Industrial Technology (ICIT), Seville, Spain, 2015, pp. 547-552. <https://doi.org/10.1109/ICIT.2015.7125156>.
- [6] T. Miki, P. Khrapchenkov and K. Hori, "UAV/UGV Autonomous Cooperation: UAV assists UGV to climb a cliff by attaching a tether," 2019 International Conference on Robotics and Automation (ICRA), Montreal, QC, Canada, 2019, pp. 8041-8047. <https://doi.org/10.1109/ICRA.2019.8794265>.

- [7] A. Cantieri et al., "Cooperative UAV–UGV Autonomous Power Pylon Inspection: An Investigation of Cooperative Outdoor Vehicle Positioning Architecture," *Sensors*, vol. 20, no. 21, p. 6384, Nov. 2020. <https://doi.org/10.3390/s20216384>.
- [8] M. Zhu and Y. Wen, "Design and Analysis of Collaborative Unmanned Surface-Aerial Vehicle Cruise Systems," *Journal of Advanced Transportation*, vol. 2019, Jan. 2019. <https://doi.org/10.1155/2019/1323105>.
- [9] G. Shao, Y. Ma, R. Malekian, X. Yan and Z. Li, "A Novel Cooperative Platform Design for Coupled USV–UAV Systems," in *IEEE Transactions on Industrial Informatics*, vol. 15, no. 9, pp. 4913-4922, Sept. 2019. <https://doi.org/10.1109/TII.2019.2912024>.
- [10] W. Li, Y. Ge, Z. Guan, and G. Ye, "Synchronized Motion-Based UAV–USV Cooperative Autonomous Landing," *Journal of Marine Science and Engineering*, vol. 10, no. 9, p. 1214, Aug. 2022. <https://doi.org/10.3390/jmse10091214>.
- [11] C. Ke and H. Chen, "Cooperative path planning for air–sea heterogeneous unmanned vehicles using search-and-tracking mission," *Ocean Engineering*, vol. 262, Oct. 2022. <https://doi.org/10.1016/j.oceaneng.2022.112020>.
- [12] J. Ross, J. Lindsay, E. Gregson, A. Moore, J. Patel and M. Seto, "Collaboration of multi-domain marine robots towards above and below-water characterization of floating targets," 2019 IEEE International Symposium on Robotic and Sensors Environments (ROSE), Ottawa, ON, Canada, 2019, pp. 1-7. <https://doi.org/10.1109/ROSE.2019.8790419>.

Requirements definition in support of digital twin platform development

Castrese Di Marino^{1,a}, Valeria Vercella^{1,b*}, Rocco Gentile^{1,c}, Giacomo Nasi^{1,d}
and Stefano Centomo^{1,e}

¹Leonardo Labs, Leonardo S.p.A, C.so Castelfidardo 22, 10138 Torino, Italy

^acastrese.dimarino.ext@leonardo.com, ^bvaleria.vercella.ext@leonardo.com,

^crocco.gentile.ext@leonardo.com, ^dgiacomo.nasi.ext@leonardo.com,

^estefano.centomo.ext@leonardo.com

Keywords: Digital Twin Platform, User Experience, Aeronautics, Requirements

Abstract. This paper discusses the exploitation of a System Engineering approach and, specifically, of Requirements Engineering to derive a set of desired features based on stakeholders' needs to be implemented into a Digital Twin (DT) platform. Key focus is on the development of a collaborative and highly integrated simulation environment tailored for the design of breakthrough aeronautical products and able, in principle, to cover all the phases of product lifecycle. Specifically, a preliminary list of platform requirements is elicited and from them a set of desired features to be implemented is derived. Then, basing on these features, a Kano questionnaire is set up and used to question a pool of engineers and experts in the aeronautical field. Eventually, by analysing the questionnaire results, the list of desired characteristics is prioritized and used to provide guidelines for the development of the front-end interface of the collaborative platform.

Introduction

The high competitiveness within the aeronautical sector drives the ambitions for shortening the time to market of advanced aircraft concepts. In a context of increasing digitalization, the emerging Digital Twin (DT) technology can play a key role in supporting the introduction of cost-effective innovative solutions since the early design phases thanks to collaborative DT platforms able to facilitate the exchanges among involved stakeholders all along the aircraft life cycle. The DT concept is based on the idea that a physical system can be represented as a digital information or a "twin" of the information originally embedded into the physical system itself [1, 2]. Applications of the DT span all the phases of product lifecycle, starting from design, through manufacturing and service, up to retire phase [3]. In the aviation industry framework, all major aviation companies have been developing DT platforms [4] to be made available internally. A noteworthy example is the Digital Design, Manufacturing & Services (DDMS) platform by Airbus, providing a complete end-to-end process from preliminary design to final assembly to "reduce costs and time to market for our products, while meeting our customers' expectations for quality, safety and environmental performance" [5]. Supposing to be in charge of developing a custom DT environment to be used to assess the feasibility of highly innovative aeronautical products, the substantial lack of manufacturing and in-service data for such breakthrough solutions can hamper the development of a comprehensive DT platform like DDMS. However, this limitation can be turned into a chance to focus on the establishment of the design component of the DT (i.e. the Design DT), paving the way to potential cost savings in the subsequent phases of "real" product development. Indeed, it is well established that the cost to introduce a change into design direction increases along the product lifecycle phases [6]. Therefore, the possibility to fully explore all feasible design alternatives at early design stages can avoid the introduction of an abrupt and costly design change during manufacturing.



On this basis, with the goal to support the development of a DT platform for the aviation sector, Section 2 will discuss the derivation of main platform requirements basing on a possible set of stakeholders' needs. The proposed list of requirements, grouped in five macro-groups, is exploited by means of brainstorming and a Use Case Analysis to obtain a list of features to be implemented into the platform. Basing on these features, Section 3 describes the exploitation of Kano questionnaire to investigate a platform user experience and extract a set of basic information (attractive, must be, indifferent, etc.) useful for defining the features to be implemented and leading the development of the front-end Graphical User Interface (GUI) of the platform. Eventually, main conclusions will be drawn and ideas for future works will be elicited.

Digital Twin Platform Requirements

The System Engineering approach can support the definition of key DT platform characteristics in a structured way [7]. In particular, Requirements Engineering can be used to list high-level platform requirements basing on stakeholders' needs and expectations. For the current application, after internal discussion with involved stakeholders, the set of requirements is derived and represented through SysML (Fig. 1).

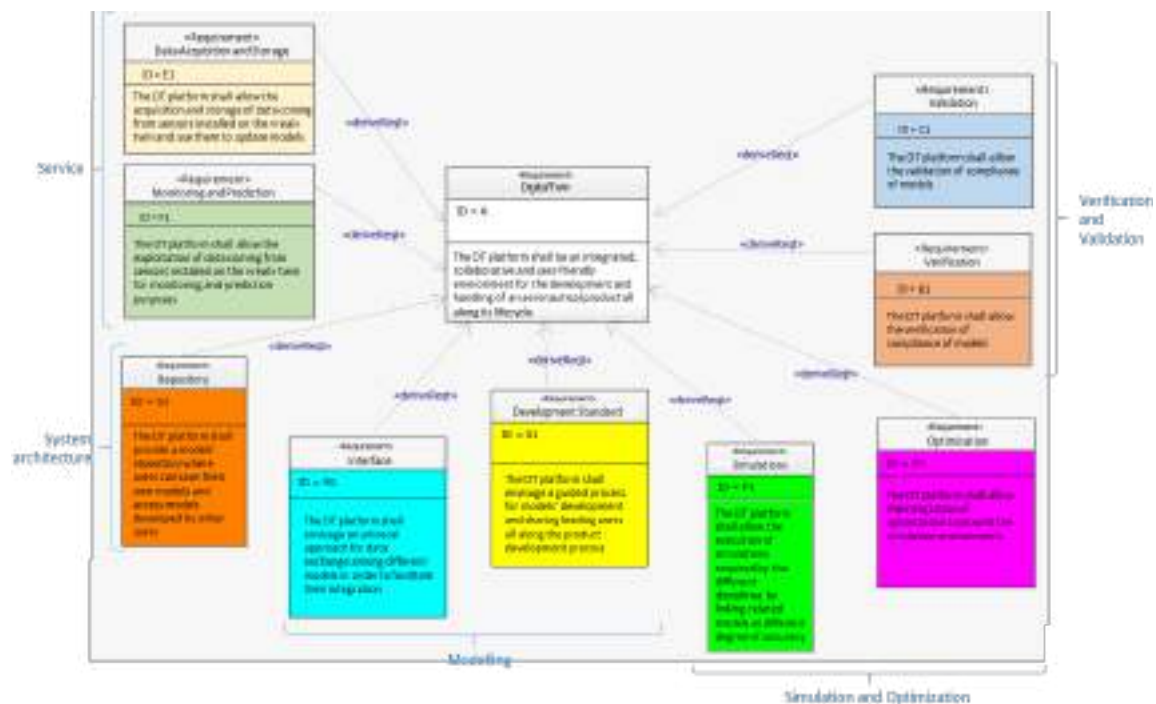


Fig. 1 Requirements and Pillars related to DT platform

According to Fig. 1 and considering the current focus on Design DT, the platform shall be a collaborative simulation environment allowing the user to build the aircraft DT by exploiting the simulation models loaded by himself or by other users. For sake of clarity, the two requirements connected to the in-service component of the DT (i.e. “Data Acquisition and Storage” and “Monitoring and Prediction”) are here reported just to strengthen the link between the DT and the “real” twin, basing on the idea to exploit real in-service data to improve the simulation models used during design activities. The requirements under analysis can be grouped into five macro-categories herein considered as the pillars of DT platform development:

1. *System Architecture*, describing how the platform should work;
2. *Modelling*, including all modelling processes, protocols and rules to be followed within the platform;

3. *Simulation and Optimization*, connected to the need of performing simulation and optimization from the platform;
4. *Verification and Validation*, related to the possibility to verify and validate the models loaded into the platform;
5. *Service*, representing the need to link the DT with the «real» twin.

Basing on the pillars and related requirements, it is then possible to derive a set of desired features to be implemented into the DT platform (Fig. 2).

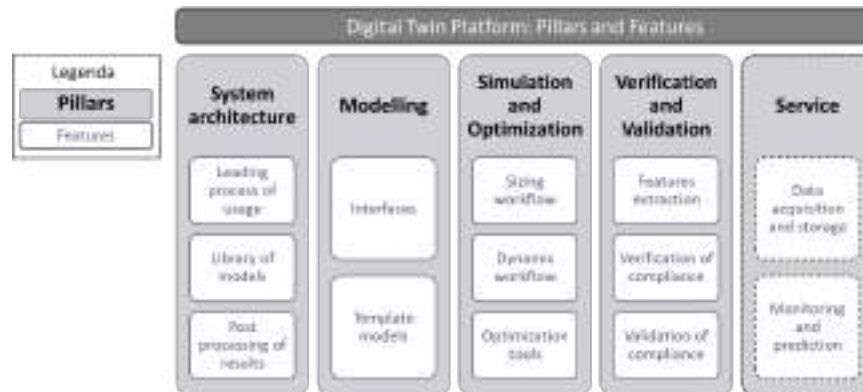


Fig. 2 Pillar and Features connected to DT platform

For sake of clarity, the leading process of usage is intended as a guided sequence of steps that leads the user alongside the whole process. This feature, like the one linked to the capability to provide a proper post-processing of results, is strictly connected to the need to deliver a user-friendly environment. As a result, the DT platform should embed the following features:

- 1) The user should be guided through the platform usage,
- 2) Access to the library of simulation models and
- 3) Easy visualization and manipulation of simulation results within the platform.

Dealing with the “Modelling” pillar, the platform should be able to:

- 1) Manage the interfaces and signals (inputs and outputs) of the models and their position and value within the database and
- 2) Guide the users by providing a set of predefined coding rules to be used while developing models (i.e. to provide coding templates for models development).

Eventually, for “Simulation and Optimization” pillar, by means of the DT platform, the user should be able to:

- 1) Analyse simulation results and perform feature extraction activities [8],
- 2) Automatically verify models compliance to System Requirements (i.e. the model “works” within the platform),
- 3) Validate models compliance to Stakeholders’ Requirements (i.e. the model “works well” within the platform).

User Experience Investigation Through Kano Questionnaire

Since the current work points to develop an innovative platform for designing and exploring complex systems, it shall be characterized by collaboration among developers and usability. The first analysis conducted on Stakeholders’ needs led to a set of requirements consequently exploded into a list of features as reported in the previous section. To select the most valuable features, a very powerful tool reported in literature for requirements analysis and prioritization is adopted.

The Kano Model [8] is a framework that allows exploring customer satisfaction with respect to product functions. A feature is presented in positive (functional) and negative (dysfunctional) form to measure the degree of satisfaction from the user in order to extract an opinion that can fall into a category: A (Attractive), M (Must-have), O (One-dimensional), R (Reverse), Q (Questionable), or I (Indifferent). The developers shall focus on Attractive to improve satisfaction of the customer and Must-have to avoid dissatisfaction. Concurrently, the features classified as One-dimensional (also named Performance) are characterized by a linear trend between satisfaction and functional and are the valuable to implement. On another hand, it may turn out that a feature considered valuable results indifferent for customer. If it happens, the developers can decide to invest time according to team needs. An example of a questions couple is reported in the following:

- If to develop a model you are asked to follow predefined coding rules, how would you feel?
- If to develop a model you are not asked to follow predefined coding rules, how would you feel?

The acceptable answers are: I like it!; I expect it; I'm neutral; I can live with it; or I dislike it.

The Kano Matrix [8] compares the answers of a single feature per customer. The sum of all answers provide the main category where a feature falls. The categories with second and third frequency can be considered for a detailed analysis. In Table 1 the answers of a pool of engineers is presented reporting not only the category, but also a Satisfaction Coefficient (S) and Dissatisfaction Coefficient (DS). The combination of S and DS provides the Overall Satisfaction Coefficient (OS) that indicates how much the satisfaction increases and decreases if the requirement is implemented or not. Some results are commented as sample of this preliminary analysis.

- *Feature extraction*: it results the only M category, that means it does not improve customer satisfaction but it must be implemented in order not to reduce the degree of satisfaction since the customer expects to find it.
- *Leading process of usage*: it results to be A on the first frequency, O and I on the second and third. This indicates that designers are available to work on this platform, appreciating the potential benefits even though usability is still not ready.
- *Sizing Workflow/Dynamic Workflow*: the majority of customers consider that features as O. Since the high importance in a DT for design as well as for simulation, it will be further implemented through innovative methods and agnostic tools.
- *Template of models*: although this feature results indifferent for customers, it is an outcome of an analysis of possible compliance within the DT platform, therefore, in future application it can be explored and implemented without producing dissatisfaction in customers.

The majority of the features are considered O, so they are well suited to be constantly improved during development.

Table 1 Results of Kano questionnaire (A: Attractive, M: Must-have, O: One-dimensional, R: Reverse, Q: Questionable, I: Indifferent, S: Satisfaction, DS: Dissatisfaction, OS: Overall satisfaction)

FEATURE	A	M	O	R	Q	I	CATEGORY	S	DS	OS
LEADING PROCESS OF USAGE	39%	17%	22%	0%	0%	22%	A	0,61	-0,39	0,22
LIBRARY OF MODELS	17%	33%	44%	0%	0%	6%	O	0,61	-0,78	-0,17
POST PROCESSING OF RESULTS	28%	17%	50%	0%	0%	6%	O	0,78	-0,67	0,11
INTERFACES	17%	17%	33%	0%	0%	33%	O	0,50	-0,50	0,00
TEMPLATE MODELS	17%	6%	17%	6%	0%	56%	I	0,35	-0,24	0,12
SIZING WORKFLOW	33%	11%	44%	0%	0%	11%	O	0,78	-0,56	0,22
DYNAMIC WORKFLOW	22%	11%	67%	0%	0%	0%	O	0,89	-0,78	0,11
OPTIMIZATION TOOLS	44%	17%	28%	0%	0%	11%	A	0,72	-0,44	0,28
FEATURES EXTRACTION	22%	39%	28%	0%	0%	11%	M	0,50	-0,67	-0,17
VERIFICATION OF COMPLIANCE	22%	11%	50%	0%	0%	17%	O	0,72	-0,61	0,11
VALIDATION OF COMPLIANCE	22%	17%	33%	0%	0%	28%	O	0,56	-0,50	0,06
DATA ACQUISITION AND STORAGE	33%	11%	39%	0%	0%	17%	O	0,72	-0,50	0,22
MONITORING AND PREDICTION	17%	11%	33%	0%	0%	39%	I	0,50	-0,44	0,06

Conclusions and Future Works

In conclusion, this research work presents a preliminary analysis towards the development of a collaborative and integrated environment for design and simulation of a DT. One of the main goals is to provide an environment where users can collaborate alongside all the design and production steps and where the integration and validation of models can be easily carried out. Currently, a set of requirements and features are identified and classified according to Kano Model. In the next step, a more complex questionnaire may support the decision making process considering a demographic section where roles of users are highlighted and functions and features of different application and phases of development are reported in order to extract more precise information about the real needs of involved people.

References

- [1] L. Li, S. Aslam, A. Wileman and S. Perinpanayagam, Digital twin in aerospace industry: a gentle introduction, *IEEE Access*, 10 (2021) 9543-9562.
<https://doi.org/10.1109/ACCESS.2021.3136458>
- [2] H. Aydemir, U. Zengin and U. Durak, The digital twin paradigm for aircraft review and outlook, *AIAA Scitech 2020 Forum* (2020). <https://doi.org/10.2514/6.2020-0553>
- [3] M. Liu, S. Fang, H. Dong and C. Xu, Review of digital twin about concepts, technologies, and industrial applications, *Journal of Manufacturing Systems*, 58 (2021) 346-361
<https://doi.org/10.1016/j.jmsy.2020.06.017>
- [4] H. Meyer, J. Zimdahl, A. Kamtsiuris, R. Meissner, F. Raddatz, S. Haufe and M. Bassler, Development of a digital twin for aviation research, *Deutscher Luft- und Raumfahrt Kongress*, Hamburg, 2020
- [5] Information on <http://www.airbus.com/en/innovation/disruptive-concepts/digital-design-manufacturing-services>
- [6] S. J. Kapurch, *NASA systems engineering handbook*, Diane Publishing, 2010.
- [7] B. Vogel-Heuser, D. Schütz, T. Frank. and C. Legat, Model-driven engineering of Manufacturing Automation Software Projects – A SysML-based approach, *Mechatronics*, 24, n. 7 (2014) 883-897. <https://doi.org/10.1016/j.mechatronics.2014.05.003>
- [8] K. Samina, T. Shehryar and S. Nasreen, A survey of feature selection and feature extraction techniques in machine learning, in *Proceedings of 2014 Science and Information Conference*, SAI 2014, 2014
- [9] N. Kano, Attractive quality and must-be quality, *Journal of the Japanese society for quality control*, 31, n. 4 (1984) 147-156

Coupling effect of acoustic resonators for low-frequency sound suppression

G. Catapane^{1,a*}, L.M. Cardone^{1,b}, G. Petrone^{1,c}, O. Robin^{2,d}, F. Franco^{1,e}

¹ PASTA-Lab (Laboratory for Promoting experiences in Aeronautical Structures and Acoustics), Università degli Studi di Napoli "Federico II", Via Claudio 21, Napoli, 80125, Italy

² Centre de Recherche Acoustique-Signal-Humain, Université de Sherbrooke, 2500 boulevard de l'Université, Sherbrooke, J1K 2R1, Quebec, Canada

^agiuseppe.catapane@unina.it, ^bluigimaria.cardone@unina.it, ^cgiuseppe.petrone@unina.it,
^dolivier.robin@USherbrooke.ca, ^efrancof@unina.it

Keywords: Sound Absorption, Acoustic Resonators, Noise Suppression

Abstract. Acoustic resonators like Helmholtz resonators, micro-perforated panels and quarter wavelength tubes are employed to suppress tonal noise for several industry application. The issue related to the design of these resonators is their bulkiness for low-frequency application and their narrow band behaviour. In this paper, microperforated panels and coiled quarter wavelength tubes are coupled in series and in parallel, tested inside impedance tube for sound absorption. The experimental samples are 3D printed with filament (PLA) additive manufacturing technique. The two acoustic devices are coupled and tested to reach broadband low-frequency noise suppression just by positioning one respect to the other in series or in parallel. The reported results demonstrate that the tonal behaviour of the acoustic devices can lead to enlarged absorption if they are tuned at similar frequencies. The disposition of the acoustic resonators and their frequency tuning hardly impact absorption: indeed, anti-resonance and filtering effect are experienced for series configuration, while parallel configuration is the sum of the two acoustic devices standalone absorption behaviour.

Introduction

Transport engineering has to develop vehicles, planes and ships with limited CO₂ and noise emissions. With regards to noise, sound absorbing structures are designed to suppress disturbance produced by acoustic sources and vibrating devices. Typical solutions include porous materials, Micro-Perforated Panels (MPPs), Helmholtz Resonators (HRs) and Quarter Wavelength Tubes (QWTs). Porous materials like fibers and foams are mostly used in transportation and building applications; MPPs are used for the design of acoustic liners that find several applications in the reduction of aircraft engine or automotive noise, but also in building acoustics. MPPs are composed by a thin plate with perforations followed by a backing cavity. Although a hole diameter of the order of 1 mm guarantees a large acoustic resistance and a reduced acoustic mass reactance, which results in a wide-band sound absorption [1], this cannot cover more than one or two octaves at low frequency [2]. Their micro-perforated structure can also be beneficial to suppress the sound disturbance without affecting the source performance: for instance, the small drag produced by a micro-perforated panel in the acoustic liners is the best compromise to reduce the engine noise without affecting the flow-path.

The main aim of this communication is to investigate the effect of the coupling of an MPP with a QWT in series and in parallel. Quarter wavelength tubes exhibit multiple resonance frequency when the length of the tube is an odd-multiple integer of the quarter of the wavelength (λ). Multiple resonance frequencies are exploited to extend the low-frequency region of influence of a hybrid model made by MPP and the tube. To cope with their excessive length requirement for low-



frequency application, their channel is stretched into a spiral. In this paper, spiral-coiled quarter wavelength tubes (spiral resonator) are coupled with different MPPs to highlight interesting coupling properties like filtering, anti-resonance behavior and general low-frequency wide sound absorption. Generally, MPPs are made in titanium or steel; for this testing phase, they are herein 3D printed with PLA, and post-drilled to avoid manufacturing imperfection effects.

Definition of The Problem

An absorber based on the micro perforated panel has a perforated plate followed by a cavity (Figure 1a). An MPP, a perforated plate followed by a cavity (see Figure 1(a)) with holes diameter d and plate thickness t , has an impedance equal to $Z_{plate} = R_{plate} + j\omega M_{plate}$, with the resistance $R_{plate} = (32\eta t/\sigma d^2)([1 + (k^2/32)]^{1/2} + (\sqrt{2}/32)k(d/t))$ and $M_{plate} = (\rho_0\omega t/\sigma)(1 + [1 + (k^2/2)]^{-1/2} + 0.85(d/t))$, with ρ_0 and c_0 density and speed of sound of air, η is the dynamic viscosity of air, σ is the perforation ratio and the generic coefficient $k = d\sqrt{\omega\rho_0/4\eta}$. The backing cavity is function of its dept D , with impedance: $Z_{cavity} = -jZ_0 \cot(\omega D/c_0)$ [1].

An Archimedean-spiral quarter wavelength tube (Figure 1b) is modeled as a perforated plate modelled with Johnson-Champoux-Allard (JCA) approach [3], followed by a QWT, defined following the Low Reduced Frequency (LRF) model [4]. LRF theory studies the sound propagation inside the QWT with a lossy Helmholtz equation, where the density ρ_{eff} and speed of sound c_{eff} are modelled taking into account visco-thermal dissipation inside the narrow tube, and so the effective impedance $Z_{eff} = \rho_{eff}c_{eff}$ and the effective wavenumber $k_{eff} = \omega/c_{eff}$. The impedance of the QWT of length L writes $Z_{QWT} = -jZ_{eff} \cot(k_{eff}L)$. The impedance of the spiral resonator writes $Z_{SR} = 1/\phi_{inlet} \left[Z_{d_{in,JCA}} \frac{-jZ_{QWT} \cot(k_{d_{in,JCA}}t_{in}) + Z_{d_{in,JCA}}}{Z_{QWT} - jZ_{d_{in,JCA}} \cot(k_{d_{in,JCA}}t_{in})} \right]$, with $Z_{d_{in,JCA}} = \rho_{JCA}c_{JCA}$ and $k_{d_{in,JCA}} = \omega/c_{JCA}$ impedance and complex wavenumber of a perforated plated of thickness t_{in} and a circular inlet hole of diameter d_{in} , with $c_{JCA} = \sqrt{K_{JCA}/\rho_{JCA}}$, ρ_{JCA} and K_{JCA} effective speed of sound, density and bulk modulus. $\phi_{inlet} = A_{hole}/A_{plate}$ is the perforation ratio between the hole and the plate areas. The MPP is coupled with the spiral resonator in series (Figure 1c) and in parallel (Figure 1d), with the impedance of both systems evaluated through electro-acoustical analogy:

$$Z_{series} = Z_{plate} + \left[\frac{1}{Z_{cavity}} + \frac{1}{Z_{SR}} \right]^{-1}, \quad Z_{parallel} = \frac{(Z_{plate} + Z_{cavity}) \cdot Z_{SR}}{(Z_{plate} + Z_{cavity}) + Z_{SR}}. \quad (1)$$

MPP and QWT coupling is evaluated through analytical, numerical and experimental viewpoints. Experimental tests are made to measure sound absorption coefficient α_{exp} inside a 100 mm diameter impedance tube: a speaker placed at one end of the tube excites the tube with a normal plane wave radiation; the sample is placed at the opposite end, backed by a rigid cavity. The dimension of the tube D_{tube} is a design parameter for any samples, that must have circular cross section with a 100 mm diameter. Therefore, the perforation ratio of the MPPs can be written as $\sigma = N_{holes}d/D_{tube}$, with N_{holes} number of the MPP holes. The sound absorption coefficient is estimated following the ISO 10534-2 1998 standard. Acoustic simulations mimic this experimental measurement with the impedance tube and the wall of both the MPP and the spiral resonator are considered rigid. The analyses are made with COMSOL Multiphysics, *Pressure Acoustics Module*. The geometrical properties of the four tested configurations are listed in Table 1.

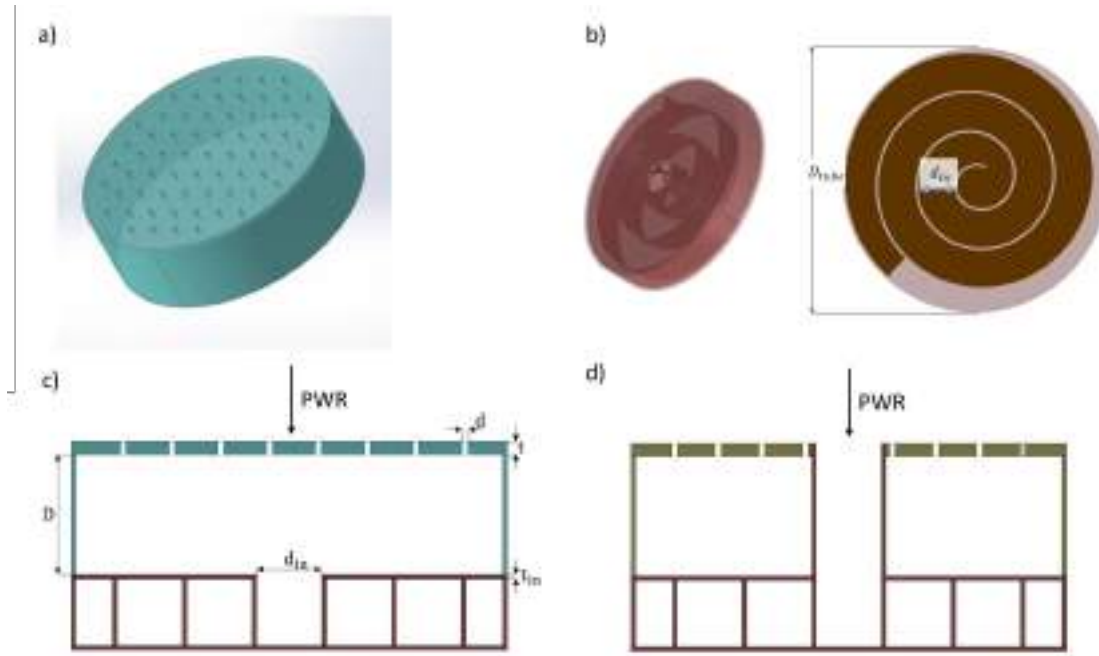


Figure 1: coupling scheme of the MPP and coiled QWT in a) series and in b) parallel.

Table 1: geometrical properties of the objects of study.

	d [mm]	N_{holes}	D [mm]	t [mm]		d [mm]	N_{holes}	D [mm]	t [mm]
$MPP_{1,series}$	1.0	33	27	3.0	$MPP_{2,series}$	1.4	65	27	3.0
$MPP_{1,parallel}$	1.0	32	27	3.0	$MPP_{2,parallel}$	1.4	64	27	3.0
	d_{in} [mm]					t_{in} [mm]		L [mm]	
SR_{series}	15					1.0		451	
$SR_{parallel}$	15					1.0		481	

Samples are 3D printed with PLA, and post-drilled to maximize the accuracy of holes diameter. Spiral resonators are different for series and parallel configuration: while for the first one the length L represents the length of the spiral path, for the parallel configuration is the sum of the length of the spiral path and the elongation to have the inlet at the top of the perforated plate, as it is possible to see in Figure 1b. Respective lengths L for SR in series and in parallel are reported in Table 1. The SR_{series} has first two harmonics at 190 and 570 Hz; $SR_{parallel}$ has first two harmonics at 178 and 535 Hz. MPP_1 has resonance peak around 283 Hz, hence between the first and the second SR harmonics. MPP_2 has resonance peak around 560 Hz, and it is designed to see resonance interaction effects between the second SR harmonics and the MPP characteristic frequency.

Results

Experimental sound absorption of the aforementioned samples is plotted in Figure 2 and each test shows a good match with theoretical and numerical predictions, which are nearly superimposed. The series coupling shows interesting properties: when the spiral and the MPP has no superimposed resonances, any spiral harmonics after the MPP resonance is filtered, and poor absorption peaks are visible (Figure 2a); on the other hand, when the MPP resonance is tuned at a similar frequency of the SR second harmonics, their interaction implies an anti-resonance effect, with the peak split in two and with a drop down of the sound absorption in correspondence of the

resonance (Figure 2a). Filtering and antiresonance effect completely disappear in the parallel configurations (Figure 2c-d), with each peak preserved by their coupling.

Conclusions

Coupling an MPP and a QWT can extend the bandwidth of the acoustic efficiency. The parallel configuration induces properties that are deemed more useful with respect to the series

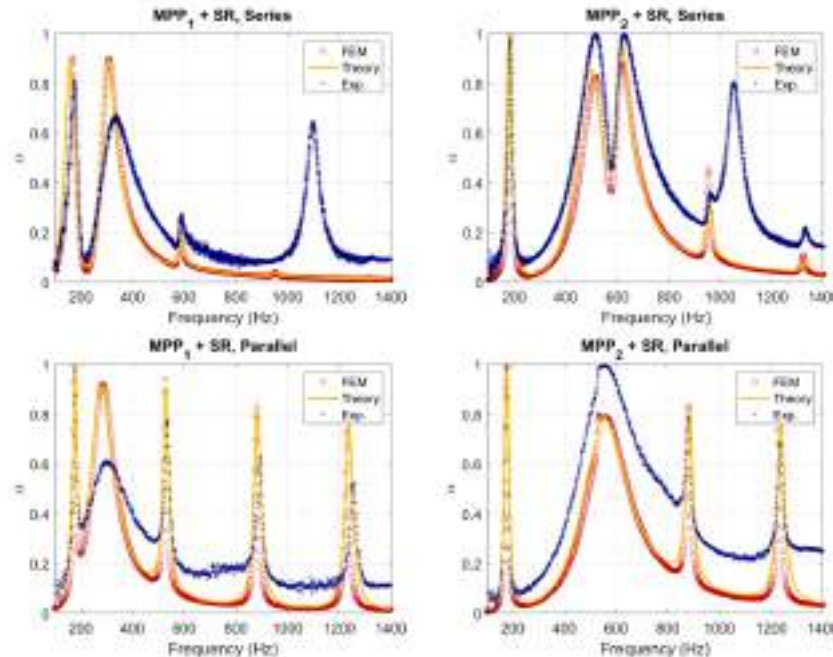


Figure 2: Sound absorption plot of the series and parallel coupling of two **MPP_s** coupled with 190Hz SR.

configuration. The larger inlet dimension that is required for the parallel configuration nevertheless limits its application. For instance, an engine acoustic liner cannot accept a 15 mm opening, because it would be unacceptable for aerodynamic and engine performance reasons. The series configuration could be easier implemented for an acoustic liner, but the relative position of each absorption peak brought by the MPP and the QWT is crucial. Future developments will involve different materials and manufacturing considerations.

References

- [1] D.-Y. Maa, "Potential of microperforated panel absorber," *J Acoust Soc Am*, vol. 104, no. 5, pp. 2861–2866, 1998. <https://doi.org/10.1121/1.423870>.
- [2] C. Wang and L. Huang, "On the acoustic properties of parallel arrangement of multiple micro-perforated panel absorbers with different cavity depths," *J Acoust Soc Am*, vol. 130, no. 1, pp. 208–218, 2011. <https://doi.org/10.1121/1.3596459>.
- [3] N. Atalla and F. Sgard, "Modeling of perforated plates and screens using rigid frame porous models," *J Sound Vib*, vol. 303, no. 1–2, pp. 195–208, 2007. <https://doi.org/10.1016/j.jsv.2007.01.012>.
- [4] A. Magnani, C. Marescotti, and F. Pompoli, "Acoustic absorption modeling of single and multiple coiled-up resonators," *Applied Acoustics*, vol. 186, 2022. <https://doi.org/10.1016/j.apacoust.2021.108504>.

New UAV ice tunnel characterization

Arrigo Avi^{1,a,*}, Giuseppe Quaranta^{1,b} and Riccardo Parin^{2,c*}

¹Politecnico di Milano, Milano, Italy

²Eurac Research – terraXcube, Bolzano, Italy

^aarrigo.avi@polimi.it, ^bgiuseppe.quaranta@polimi.it, ^criccardo.parin@eurac.edu

Keywords: UAV, Ice Tunnel, Ice Accretion, System Characterization, Climatic Chamber, Hypobaric Chamber

Abstract. In the recent years, the field of unmanned aircraft vehicles (UAVs) has shown great technological progresses and many new applications have born. To assess the potential of this technology and to improve the availability and reliability of the rising services it is critical to overcome operational limitations. One key operational hazard is atmospheric in-flight icing, resulting in large aerodynamic penalties, unbalances and other detrimental phenomena that sometimes can lead to catastrophic consequences. In this paper, a new ice tunnel developed in the large hypobaric and climatic chamber of the terraXcube facility of Eurac will be presented. A preliminary characterization and calibration of the system has been also performed following the EASA regulation reported in the Easy Access Rules for Large Rotorcraft (CS-29) (Amendment 6).

Introduction

While UAV systems offer numerous features and performance capabilities, there are areas in need of improvement, particularly in terms of reliability. Unmanned aircraft are often deployed on high-risk missions, operating in marginal weather conditions for purposes such as search and rescue or military operations. Therefore, the development of an effective tool to assess performance in these challenging conditions would be highly valuable. Currently, only a few unmanned aircraft are specifically designed to address the challenges of icing. These aircraft are primarily large military UAVs developed for long-range missions in harsh environments. While smaller UAVs may have some level of rainproof or snowproof certification, there is generally no specific consideration for icing (EU 2019/945 EU 2019/947). In the aviation industry, there are well-known and established facilities dedicated to icing testing, however, these facilities are both complex and expensive. Consequently, integrating an icing testing program during the development of a small or mini-UAV can be highly challenging. For example, the estimated cost of regional transport aircraft icing tests, as mentioned in the IPHWG Task 2 WG Report - Appendix J, is approximately 700,000 € [1]. Here we propose a more cost-effective alternative, a home-made ice tunnel developed in our climatic chamber. This new facility could allow for the testing of a full-scale UAV under realistic icing conditions.

Experimental setup and Methods

Facility

TerraXcube is an infrastructure for research and testing that leverages a multi-dimensional approach for environmental simulation part of Eurac Research Institution. With a useable volume of 360 m³, the climatic chamber Large Cube can simulate the most extreme environmental conditions on the Earth's surface, allowing the synchronous control of multiple complex environmental parameters for long duration analysis.



Wind tunnel

Inside the climatic chamber an open-loop wind tunnel was developed. The chamber was hypothetically divided into two sections as showed in Fig. 1: testing section on the right and production section on the left. The testing section is the volume where the UAV is placed and the subcooled cloud is fully developed. The production section is composed by the wind tunnel, fan and nozzles which contributes to the formation of the ice conditions.

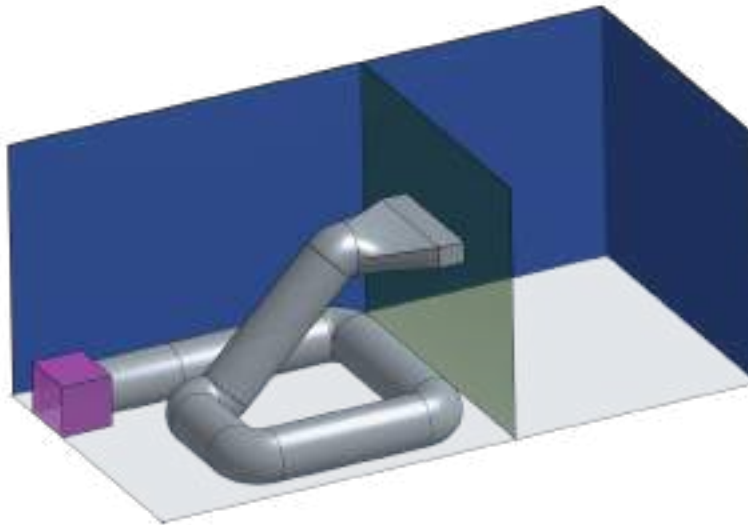


Fig. 1 - Layout



Fig. 2 - Setup

The climatic chamber works as a closed loop system. The air is extracted from the wall on the right side of Fig. 1 (North side), it is treated by heat exchangers and it returns from the left side (South side) inside the chamber. Almost all the flow treated by the chamber is streamed to the axial fan, depicted in purple on Fig. 1. The fan (volume purple in Fig 1) controls the air speed inside the wind tunnel. Immediately after the fan there are 25 nozzles which can be controlled in terms of air and water pressure leading to different subcooled cloud properties described in the next section. The ice tunnel allows to test UAV platforms up to 2 m³ (Fig. 2).

The main characteristics of the open-loop wind tunnel are briefly reported in the following Table 1.

Table 1 Technical data of wind tunnel

Fan	Konz Lufttechnik
Speed [m/s]	0 ÷ 30
Diameter [m]	1
Length [m]	About 18 m

Icing system

The icing system is composed by 25 nozzles supplied by pressurized air and water and managed as prescribed in [2-3] to produce different icing conditions. The main aspects of subcooled clouds are the mean volume droplets (MVD), which refers to the average size or diameter of water droplets, and the LWC, liquid water content, which refers to the amount or concentration of liquid water present in a given volume of air or cloud. Modifying the number of nozzles involved, the air pressure and the water pressure, MVD and LWC can be varied as desired. The water supplied is

ultrapure water ($18 \text{ M}\Omega \cdot \text{cm}$) which allows to the water to remain in the liquid state until the impact with the UAV surface. The technical data are as follows:

Table 2 Technical data of icing system

LWC [g/m^3]	$0 \div 3$
MVD [μm]	$15 \div 40$
Operating temperature [$^{\circ}\text{C}$]	$-40 \div +0$
Nozzles	Spraying System SUJ-12

Droplets measurements

The real time droplets measurements system consists in a low-cost optical system [4,5]. Based on shadowgraph, it is composed by a telecentric objective coupled with an industrial CMOS camera. After a proper calibration, the system takes pictures of the stream, an OpenCV algorithm detects droplets and measures their diameter. With such method, it is possible to have a real time measurement of MVD and LWC (indirect estimate) of the stream.

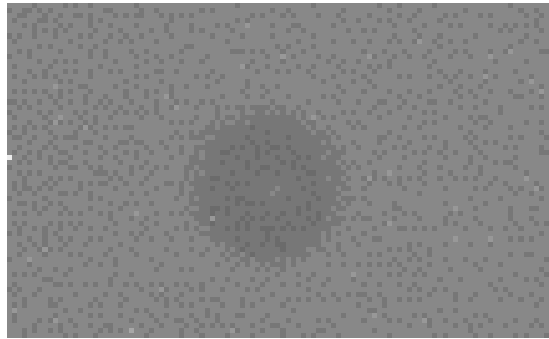


Fig. 3 - Example of a droplet detected by the optical system.

Results

The characterization and calibration of the system has been performed following the standard for calibration and acceptance of icing wind tunnel described by EASA [6] with the cylinder collection method. Three set of parameters were analyzed, the duration of each test was fixed at 10 minutes.

Table 3 System parameters

	Test #A	Test #B	Test #C
Temperature [$^{\circ}\text{C}$]	-10 ± 2	-10 ± 2	-10 ± 2
Air pressure [bar]	3.1 ± 0.3	2.3 ± 0.3	1.1 ± 0.3
Water pressure [bar]	1.5 ± 0.3	1.5 ± 0.3	0.7 ± 0.3
Number of nozzles	4	4	4

Mean Volume Diameter. MVD data, collected with the optical measurement system, were compared to calibration chart as in [3].

Table 4 MVD measurement comparison

	Test #A	Test #B	Test #C
MVD theoretical [μm]	15	25	35
MVD measured [μm]	20 ± 4	31 ± 4	38 ± 4

Liquid Water Content. LWC data, obtained by the ice cylinder method, showed a good agreement between the technical datasheet of nozzles and [6].

Table 5 LWC measurement comparison

	Test #A	Test #B	Test #C
LWC datasheet [g/m^3]	0.16	0.23	0.18
LWC cylinder [g/m^3]	0.11	0.19	0.25

Conclusion

The preliminary characterization of the icing wind tunnel in the terraXcube facility yielded promising outcomes. The primary advantage of this new system lies in its potential to conduct full-scale UAV trials within the real operational environment. However, further refinements and investigations are required to ensure a complete understanding of its capabilities. Additionally, an important area for exploration involves the simultaneous utilization of the icing system and hypobaric capabilities of the chamber. This integration holds the potential to significantly impact UAV testing within icing conditions at high altitudes (up to 9000 m).

References

- [1] Ice Protection Harmonization Working Group, Task, 2, appendix J (2005).
- [2] EASA CS-25 Appendix O
- [3] Ludovico Vecchione et al., Cloud calibration update of the CIRA Icing Wind Tunnel, (2003). <https://doi.org/10.2514/6.2003-900>
- [4] Arrigo Avi, “Development of icing testing tools for large climatic chamber”, MSc thesis, Politecnico di Milano, Milano, Italy (2019)
- [5] Staffan Rydbloom. “Measuring Water Droplets to Detect Atmospheric Icing”. PhD thesis, Mid Sweden University, Sundsvall, Sweden, (2017)
- [6] SAE (Society of automotive engineers) Aerospace Recommended Practice (ARP), (2015)

Remote sensing validation with in-situ measurements for efficient crop irrigation management

I. Terlizzi^{2,3,a*}, F. Morbidini^{2,b}, C. Maucieri^{2,c}, C. Bettanini^{1,3,d}, G. Colombatti^{1,3,e},
S. Chiodini^{1,3,f}, F. Toson^{1,g}, M. Borin^{2,h}

¹ CISA G. Colombo, University of Padova, Via Venezia, 15, Padova (PD), Italy

² DAFNAE, University of Padova, Viale dell'Università, 16, Legnaro (PD), Italy

³ DII, University of Padova, Via Venezia, 1, Padova (PD), Italy

^airene.terlizzi@unipd.it, ^bfrancesco.morbidini@unipd.it, ^ccarmelo.mauceri@unipd.it,

^dcarlo.bettanini@unipd.it, ^egiacomo.colombatti@unipd.it, ^fsebastiano.chiodini@unipd.it,

^gfederico.toson@phd.unipd.it, ^hmaurizio.borin@unipd.it

Keywords: Vegetation Index, Satellite, Multi-Spectral, Remote Sensing

Abstract. The multi-spectral data acquired with either satellite imagery, UAV or tethered and stratospheric balloons can be used to calculate vegetation indices directly related to the well-being of the crops providing a quantitative information about its health and growth. The vegetation indices are calculated combining measurements from different parts of the electromagnetic spectrum, typically in the visible and near-infrared ranges. The aim of this work is to integrate the remote sensing data with in-situ collected measurements in order to validate remote observations for monitoring soybean water status and requirements. The study is conducted in Italy on a field of 160 x 40 m², divided into four plots of 40 x 40 m²; two of them are irrigated at 100% of the CRW (Crop Water Requirement) and two irrigated at 70% of CWR. In each plot tensiometers and capacitive probes directly measure the soil moisture, along with a climate station used to monitor environmental parameters. The in-situ data are correlated with multi band satellite images by the PlanetScope constellation providing a ground resolution of 3 m. The use of UAV or balloons is needed to monitor the diurnal variation of the indices, as the satellite revisit time is once per day around 9:00 and 10:00 UTC on the site. The balloon payload is equipped with commercial cameras and dedicated filters to acquire images in the same spectral bands as satellites. The importance of this study lies in the possibility of managing the fields irrigation basing on the actual physiological need of the crop rather than relying on a predefined timetable, resulting in a more efficient and environmentally responsible irrigation. The article will present the methodology and the instruments applied, together with the results obtained.

Introduction

Soybean is one of the most important crops worldwide as it is used not only for livestock feed and human nutrition, but also assumes it has key role in the biofuel sector [1]. Moreover, the need to expand and increase irrigated agriculture appears to be extremely necessary in view of the increased demand for food in the coming decades [2].

For correct irrigation management, it is necessary to know the crop evapotranspiration index (ET_c) and the right value of the crop coefficient (K_c).

$$K_c = \frac{ET_c}{ET_0} \quad (1)$$

where ET_c is the evapotranspiration of the crop under optimal conditions and ET₀ is the potential evapotranspiration of the reference crop calculated with the Pennam-Withman equations.



A linear relationship between K_c values and some vegetative indices, first of all NDVI, has been observed from several studies [3]. Agronomical indices can be obtained from remote-sensing images from cameras aboard instrumentation such as tethered balloon and satellites. Remote sensing can provide useful information with high accuracy regarding optimal irrigation management allowing to obtain information not only of the crop but also of the soil and environmental factors [4].

Study area

The study was conducted in Castelfranco Veneto (IT) on a field constituted of 4 plots of 40 x 40 m² each. Two different irrigation regimes were applied: full irrigation (application of 100% of the CWR) and regulated deficit irrigation (application of 70% of the CWR with 100% restoration between the beginning of flowering and the beginning of pod formation) as can be seen in *Figure 1*.



Figure 1: Field of study in Castelfranco veneto

Irrigation was managed by referring to probes capable of measuring soil moisture at three different depths (at 20, 40 and 60 cm) and with the data collected was calculated the water balance. Then consumption by evapotranspiration was obtained with the equation:

$$ET = I + P \pm \Delta S - R - D \quad (2)$$

Where ET is the evapotranspiration (in mm), I is the irrigation water (in mm), P is precipitation (in mm), ΔS is the change in soil water storage (in mm), R is surface runoff and D is deep percolation. Then with (1) was obtained K_c .

Satellite data and vegetation index calculation using multiband images

Images from Planetscope constellation have been used to calculate the indices. Planetscope is a constellation of 130+ Cubesat in sun-synchronous orbits which permits a revisit time of 24h on the field.

The satellites' camera operates in eight bands each one with a resolution of 3 m: Coastal Blue (431 - 452 nm), Blue (465 - 515 nm), Green I (513 - 549 nm), Green (547 - 583 nm), Yellow (600 - 620 nm), Red (650 - 680 nm), Red-Edge (RE) (697 - 713 nm), Near-Infrared (NIR) (845 - 885 nm).

The bands given by the camera allow to calculate numerous indices, each of these utilizes specific combination of spectral bands to capture different aspects of the crop health and vigour:

- Normalized Difference Vegetation Index (NDVI): used to assess the health and vitality of plants, allowing the recognition of areas with development issues. [5]

$$NDVI = \frac{NIR - Red}{NIR + Red} \quad (3)$$

- Green Normalized Difference Vegetation Index (GNDVI): GNDVI is a variant of NDVI that uses reflectance in the green band instead of the red band. This index is more sensitive to chlorophyll concentration and is used to determine the presence of water and humidity. [5]

$$GNDVI = \frac{NIR - Green}{NIR + Green} \quad (4)$$

- Normalized Difference Red Edge (NDRE): NDRE is an index combines reflectance in the Red Edge band with reflectance in the NIR band. This index is particularly sensitive to the presence of chlorophyll and is useful for assessing crop health and detecting water stress. [5]

$$NDRE = \frac{NIR - RE}{NIR + RE} \quad (5)$$



Figure 2: NDVI index of 15 July 2022

The purpose was to identify which index exhibited the strongest correlation with K_c .

The correlations aimed to determine which index could provide the most accurate estimation of K_c to study and compare the health of the two subplot.

Correlation of satellite based vegetation indexes and in situ based

The linear correlation was performed by considering the pixel mean value calculated for each of the two plots and the K_c data obtained from the water balance for each day when satellite data was available. The correlation coefficients were very close to each other, as can be seen in *Table 1*, so further analysis need to be conducted. In the meantime, this study helped defining the payload for the tethered balloon which will fly the next months to collect data on the variation of the indices over one day.

Table 1: Correlation coefficients between K_c and NDVI, GNDVI, NDRE for the two subplot

	70%CWR	100%CWR
NDVI	0,231445	0,23948
GNDVI	0,251871	0,23865
NDRE	0,272279	0,24143

Integration of balloon based multispectral images

The tethered balloon will fly over the field approximately once a month throughout the crop development phase. It will acquire data for at least one day at a height of 50 meters, providing a

field of view of about 100 x 100 m², it will be positioned at the center of the field, acquiring with half of his Field Of View the field at 70% CWR and with the other half the field at 100% CWR.

It is equipped with a thermal camera, to measure the temperature of the crop and of the soil, and with two other cameras: a monochrome camera with a Red-Edge filter and a colored camera with a triple band filter in the bands of Blue, Green and NIR, to obtain data on the bands respectively of 735 nm, 475 nm, 550 nm and 850 nm.

In this way, the bands will be acquired to measure GNDVI, NDRE, and ENDVI (Enhanced Normalized Difference Vegetation Index) as substitutes for NDVI.

$$ENDVI = \frac{((NIR + GREEN) - 2BLUE)}{((NIR + GREEN) + 2BLUE)} \quad (6)$$

Conclusions

In conclusion, after acquiring data from the balloon and conducting a more detailed analysis of the correlations, it will be possible to effectively utilize the indices to assess the health status of the crop and optimize irrigation practices. This is especially crucial during a time when water resources are more critical than ever. By leveraging the information provided by the indices, farmers and irrigation can make informed decisions to ensure efficient water usage and maximize crop productivity while considering the limited water availability.

Acknowledgments

Image data services were provided by Planet team (2017), Planet Application Program Interface: in Space for Life on Earth, San Francisco, Ca. <https://api.planet.com>

References

- [1] Aydinsakir K. “Yield and quality characteristics of drip-irrigated soy bean under different irrigation levels”. In: *Agronomy Journal* 110 (2018),pp. 1473–1481. <https://doi.org/10.2134/agronj2017.12.0748>
- [2] Massari C et al. “A review of irrigation information retrievals from space and their utility for users.” In: *Remote Sensing* 13 (20 2021), p. 4112. <https://doi.org/10.3390/rs13204112>
- [3] Campos I et al. “Estimation of total available water in the soil layer by integrating actual evapotranspiration data in a remote sensing-driven soil water balance.” In: *Hydrology* 534 (2016), pp. 427–439. <https://doi.org/10.1016/j.jhydrol.2016.01.023>
- [4] Ahmad U, Alvino A, and Marino S. “A review of crop water stress assessment using remote sensing. *Remote Sensing*”. In: *Agronomy Journal* 13 (2021), p. 4155. <https://doi.org/10.3390/rs13204155>
- [5] Information on <https://leonardolaureti.wordpress.com/2021/01/08/interpretazione-degli-indici/>

DUST mitigation technology for lunar exploration and colonization: existing and future perspectives

Guido Saccone^{1,a*}, Nunzia Favaloro^{1,b}

¹Italian Aerospace Research Centre (CIRA), Space Exploration Technologies Lab, Via Maiorise snc, 81043, Capua (CE), Italy

^ag.saccone@cira.it, ^bn.favaloro@cira.it

Keywords: Moon, Dust Mitigation, Space Exploration, High-Performance Polymers

Abstract. Micrometric dust particles of lunar regolith represent one of the most serious issues of the harsh moon environment. Indeed, the extremely high vacuum conditions expose the lunar soil minerals to intense ultraviolet and galactic cosmic rays' bombardment during the Moon's daylight producing photoionization of the constituent's atoms and electron release. Moreover, Moon periodically interacts with the surrounding solar wind which generates a continuous flux of charged particles is generated accompanied by electric fields around the terminator region able to lift off the lunar regolith dust up to ~100 km above the geometrical surface. In this way, micrometric granular matter forms a subtle veil of contaminants. This electrically charged and extremely adhering dust environment can cause various critical drawbacks not only to several robotic parts e.g., mechanical components, electronic devices, solar panels, thermal radiators, rovers seals and bearings, etc. but also can dramatically damage the respiratory systems of humans if accidentally inhaled. For these reasons, lunar dust was recognised, by several agencies including NASA and ESA, as one of the main potential showstoppers for the ongoing robotic and manned exploration and colonization of our natural satellite. For overcoming or at least mitigating these issues, several technologies were developed and assessed ranging from the active ones requiring a source of energy e.g., mechanical, fluidal and, above all, electric devices, to the passive technologies involving suitable material design and development. In the work here reported, the design and development of innovative high-performance polymers simultaneously exhibiting outstanding thermo-mechanical properties and superior non-sticking capacity i.e., *abhesion* to be applied for structural purposes on the Moon is presented. Further improvement of these suitable designed materials with the addition of appropriate electric properties will make them ideal candidates as dielectric substrates of a combined passive and electroactive system able to repel micrometric regolith particles i.e., lunar dust shield.

Introduction

Dust in space environments, especially Moon and Mars has been recognized by several Space Agencies, including NASA and ESA, as a major concern for the successful robotic and manned exploration and colonization of extra-terrestrial bodies.

Indeed, the Lunar surface is covered by regolith i.e., a loose granular material, consisting of a broad range of shapes, sizes, and types of sediments [1]. It mainly consists of silicate minerals e.g., olivine, pyroxene, plagioclase, and non-silicate minerals such as ilmenite [2], crushed by meteoric bombardment causing the fracturing, scattering and agglutination of lunar regolith in the form of micrometric (approximately 50% of the lunar regolith consists of granular, dust particle with diameters less than 60 μm [3]), sharp, abrasive, porous, chemically reactive dust particles. These granulometric particles are electrostatically charged by the interactions with the local plasma environment and the solar ultraviolet (UV) radiations as well as the solar wind due to the photoelectric effect i.e., the UV and X-ray induced photoemission of electrons of the grain-materials [4,5]. Even without any mechanical activities, the dust grains are levitated by the



electrostatic fields and transported away from the surface in the near vacuum environment of the Moon. Above all, the lunar, regolith dust particles can adhere strongly to the exposed surfaces.

As verified during the Apollo missions, these particles were an unforeseen problem and caused several issues [6] including vision obscuration during landing [7]], abrasion of visors, gloves and boots of astronaut's suits [9], degradation of radiators and thermal control surfaces, deterioration of solar panels efficiency, deposition on optical surfaces, vision obscuration, creation of wrong responses from measuring devices and false instrument reading, interference with the operation of Extra-Vehicular Activity (EVA) systems including suits, airlocks, suitports tools, etc. [8].

In order to efficiently overcome the serious issues represented by the challenging lunar and Martian dust environments (or small bodies like asteroids, comets, and Near-Earth Objects), innovative technologies/approaches have to be investigated and employed.

They can be generally subdivided into passive and active approaches:

- **Passive dust mitigation technologies:** they consist in preventing the sticking and adherence of the loose granular fraction of lunar or Martian regolith i.e., micrometric dust (on the Moon the term dust usually refers to particles with a Sauter mean diameter $< 25 \mu\text{m}$). This ambitious and challenging goal is achieved without the application of any kind of external source of energy, by means of suitable design and development of special materials with the lowest possible surface energy, thanks to a tailored modification of the chemical structure further improved by a suitable alteration of the topographical/morphological features of the material's external layers due to application of several possible chemical and physical strategies.
- **Active dust mitigation technologies:** they foresee the direct cleaning of the examined surfaces or the protection of them from dust deposition and contamination. Active technologies utilize external forces: electrodynamic, electrostatic, fluidal, mechanical, etc. But the most effective ones are based on regolith particle charge. In detail, solar radiation and the solar wind produce a "plasma scabbard" near the lunar surface and lunar grains acquire charge in this environment and can exhibit unusual behaviour, including levitation and transport across the surface because of electric fields in the "plasma scabbard".

Results and Discussion

In order to solve or mitigate the dust issue, CIRA aims to pursue a hybrid strategy consisting of the simultaneous application of passive and active methods as depicted in Figure 1.



Figure 1. Scheme of the CIRA dust mitigation approach.

In particular, it can be accomplished by the design and development of a suitable material exhibiting at the same time minimum surface energy, i.e., *abhesion* capacity consisting of non-sticking ability against micrometric lunar dust particles, and excellent dielectric properties making it a good candidate as an insulating substrate of electrodynamic or electrostatic dust mitigation devices.

The harsh Moon environment requires also the design and development of a material endowed with outstanding thermo-mechanical properties in order to resist the strong temperature

fluctuations, UV and galactic cosmic rays' irradiation, micro-meteoritic bombardment and ultra-vacuum conditions. Moreover, low density is another appealing characteristic for every material, which has to be transported from Earth and fly as payload within a space launcher. Considering also these constraints, the class of high-performance polymers has been recognized to be the most appropriate for lunar applications. In particular, aromatic polyimides (PI) have been selected as starting materials for achieving hybrid dust mitigation capacity.

According to this approach, CIRA has designed innovative aromatic PIs consisting of monomers endowed with a greater amount of trifluoromethyl groups in order to successfully employ the dipole-dipole repulsion forces exerted by the C-F groups, due to the highest electronegativity of the fluorine atom among all the elements. Furthermore, monomers containing a limited number of benzene rings have been identified since they guarantee the achievement of superior thermo-mechanical properties. Moreover, specially designed additives, Surface Migrating Agents (SMA) based on silicon moieties, have been formulated and they are able to spontaneously migrate toward the outermost layers of the material drawn by thermodynamic forces and react with the dianhydrides, used for the PI synthesis, forming a co-polyimide as shown in Figure 2.

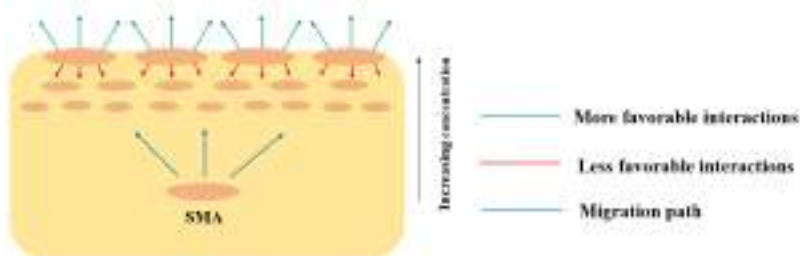


Figure 2. Schematic representation of the SMA migration mechanism.

The SMAs, reaching the external layers of the material, contribute to further lowering the surface energy, already minimized by the presence of elevated $-CF_3$ groups. This behaviour has been experimentally observed by the increase of the contact angles these coupons form with micrometric water droplets.

In order to realize a device endowed with passive and active dust mitigation capacity, this innovative PI has to be combined with a suitable electrodynamic system consisting of an array of thin conducting electrodes (Figure 3), embedded in the surface, and separated among them by an insulating material, designed to prevent electrical breakdown between the independent electrodes [7].

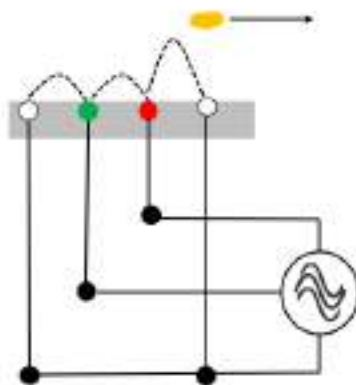


Figure 3: Schematic depicting dust particle motion on an electrodynamic system.

Electrodes are connected to a multi-phase low-frequency AC power supply, able to generate pulsed standing waves to shift, lift and transport far away charged particles, approaching the

protected surface. Electrostatically charged particles, such as those encountered on the Moon, Mars, or on asteroids, are carried along by the traveling field due to the actions of Coulomb and dielectrophoretic forces.

Innovative materials developed by CIRA can be optimal candidates as insulating materials for electrodynamic devices for hybrid dust mitigation technology due to their inherent low dielectric strength.

References

- [1] Wohl, C.J., Atkins, B.M., Belcher, M. A., Connell, J.W., Copoly(imide siloxane) Adhesive Materials with Varied Siloxane Oligomer Length, International SAMPE Symposium and Exhibition (Proceedings), (2010).
- [2] Fateri, M., Gebhardt, A., Gabrielli, R.A., Herdrich, G., Fasoulas, S., Großmann, A., Schnauffer, P., Middendorf, P., Additive Manufacturing of Lunar Regolith for Extra-terrestrial Industry Plant, 30th ISTS Conference, Kobe, Japan, (2015).
- [3] Taylor, L.A., Schmitt, H.H., Carrier, W.D., Nakagawa, M., The Lunar Dust Problem: From Liability to Asset, in 1st Space Exploration Conference: Continuing the Voyage of Discovery, American Institute of Aeronautics and Astronautics, Orlando, FL., (2005). <https://doi.org/10.2514/6.2005-2510>
- [4] Abbas, M., Tankosic, D., Craven, P.D., Spann, J.F., LeClair, A., West, E.A., Lunar dust charging by photoelectric emissions, *Planetary and Space Science* 55, 953-965, (2007). <https://doi.org/10.1016/j.pss.2006.12.007>
- [5] Stubbs, T.J., Vondrak, R.R., Farrell, V.M., A dynamic fountain model for lunar dust, *Advanced in Space Research* 37, 59-66, (2006). <https://doi.org/10.1016/j.asr.2005.04.048>
- [6] Afshar-Mohajer, N., Wu, C.-Y., Curtis, J., Gaier, J. R., Review of Dust Transport and Mitigation Technologies in Lunar and Martian Atmospheres, *Advances in Space Research*, (2015). <https://doi.org/10.1016/j.asr.2015.06.007>
- [7] Calle, C.I., Buhler, C.R., McFall, J.L., Snyder, S.J., Particle removal by electrostatic and dielectrophoretic forces for dust control during lunar exploration missions, *Journal of Electrostatics* 67, 89-92, (2009). <https://doi.org/10.1016/j.elstat.2009.02.012>
- [8] Gaier, J.R., The effects of lunar dust on EVA systems during the Apollo missions, NASA/TM 213610: (2005).
- [9] Goodwin, R., 2002. Apollo 17: The NASA Mission Reports, vol. 1. Apogee Books, Ontario, Canada.

A static, refractive and monolithic Fourier spectrometer for an HEMERA balloon flight

Fabio Frassetto^{a1*}, Lorenzo Cocola^{b1}, Paola Zuppella¹, Vania Da Deppo¹,
Riccardo Claudi² and Luca Poletto¹

¹ CNR-IFN Via Trasea, 7 – 35131 Padova, Italy

² Astronomical Observatory, INAF, Padova, Italy

^afabio.frassetto@cnr.it, ^blorenzo.cocola@cnr.it

Keywords: Fourier Transform Spectroscopy, Space Instruments, Interferometry

Abstract. In this work we present the characteristics of a static Fourier transform spectrometer designed for a balloon flight and meant to test the instrument in an actual working environment. The flight campaign has been provided within the HEMERA Research Infrastructure. The interferometric assembly, the core of the instrument, is made with only refractive and reflective surfaces, without diffraction gratings. It is realized with four glass elements that are glued in a single monolithic structure with no spacers or framed supports. There are no hollow spaces, thus improving the mechanical stiffness. The spectral band accessible to the presented optical design is 450 – 850 nm and the working spectral region can be chosen to be either 550 – 850 nm or 450 – 550 nm. The spectral resolution is variable as it is driven by the refractive index of the used glasses in the considered spectral region. In this design, the resolution varies from 1500 at 550 nm to 200 at 800 nm and to 4000 at 450 nm. The total field of view of the instrument is 3 degrees. All the optical elements used to operate the spectrometer are installed on a 3D printed structure. This is possible due to the low sensitivity of the instrument to vibrations. The interferometric assembly has undergone thermal test to quantify the temperature range it can tolerate. We will present the instrument design and the first results of the flight campaign.

Introduction

Static Fourier transform spectroscopy is nowadays a well-documented technique [1-3], the interested reader is invited to start from the references for a description of the technique. Here is sufficient to recall that the technique is based on the recording, via a 2D detector, of an image signal, called interferogram, whose Fourier transform returns the spectrum of the light that has produced the interferogram itself. What we have tested in this flight campaign is the possibility to realize the interferometer as a monolithic optical assembly in which the beam-splitter and the retro-dispersive elements, two Littrow's prisms [4-6], are glued together forming a compact structure (hereafter the interferometric assembly, IA) with no hollow volumes in the optical path.

Being the IA realized by gluing together glasses with different coefficients of thermal expansion (BK7 and SF57), the proposed optical concept has been tested to evaluate the possible occurrence and effect of thermal stresses in the interferometric assembly. The spectrometer, with the indication of all its major parts, is shown in Fig. 1a; Fig. 1b shows the instrument, closed with its cover, during the pre-flight tests. The supporting base is realized via SLS 3D printing technology in Nylon 12.



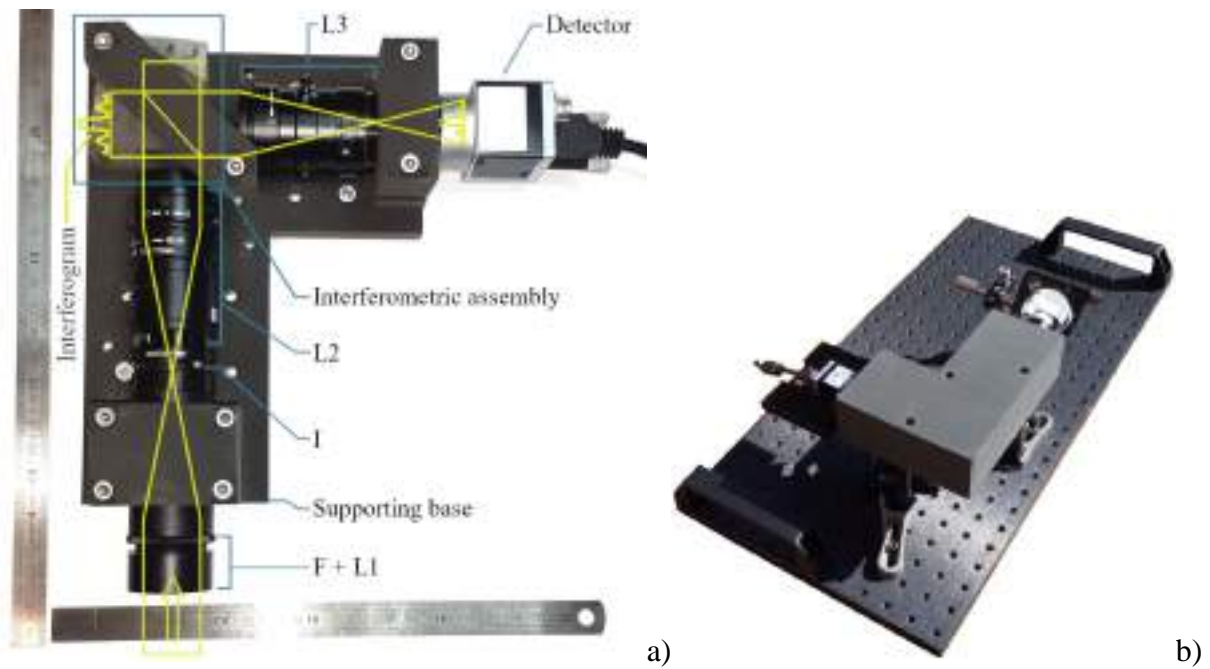


Fig. 1. Image of the realized instrument. a) The spectrometer without the cover and with all the main parts indicated. The yellow overlay mimics the light path and illustrates the imaging action of L3, which projects the interferogram on the detector focal plane. b) The spectrometer installed on a breadboard, during the pre-flight tests.

The flight

As in the first flight [7], the spectrometer, prepared for the flight campaign, has been installed inside a polystyrene box with 1 cm thick walls. The box contains also all the electronics and the power source, see Fig. 2 for details on the internal sub-assembly arrangement. The flight took place the 11th of May 2023 in the morning at the Aire-Sur-L'Adour "Centre d'Opérations Ballons" - CNES. The ascending phase lasted about 1 hour and 30 minutes and the descending one 50 minutes, for a total flight duration of about 2 hours and 20 minutes. The maximum reached altitude, as inferred from the internal sensor (Bosch BME680) with its default calibration curve, was 26 km. Pressure altitude and temperature as measured from the internal transducers are plotted in Fig. 3.

An interferogram has been acquired every second. Fig. 4a presents a 2D map of the acquired spectra during the entire ascending and descending phase. To obtain a spectrum, the interferogram is line by line multiplied with a "Blackman" window, then for each line the squared absolute value of the 1-D Fourier transform is calculated. The results are then averaged on the full frame. For each acquisition the spectrum is normalized to its maximum value. Fig. 4b shows in detail three spectra acquired after 1031 s, 3007 s and 5504 s.

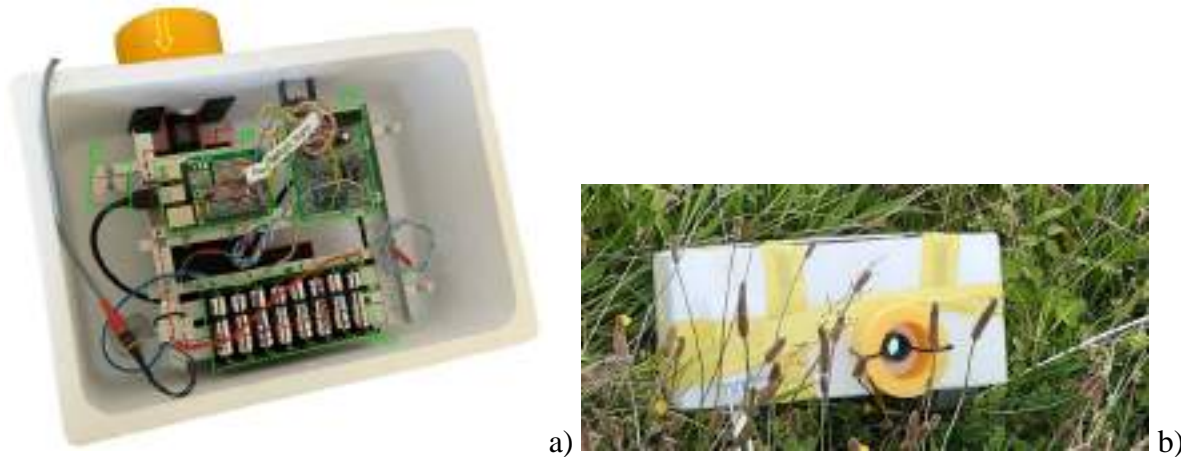


Fig. 2. The instrument assembled for the flight campaign. a) Internal view: the arrow indicates the entering direction of the light. A) the instrument, partially hidden behind the two PCBs, B) the single board computer, C) the power and environmental sensing unit, D) the batteries, E) one of the four connecting pylons between the instrument and the external box in polystyrene. b) The instrument, landed in an open field, after the flight.

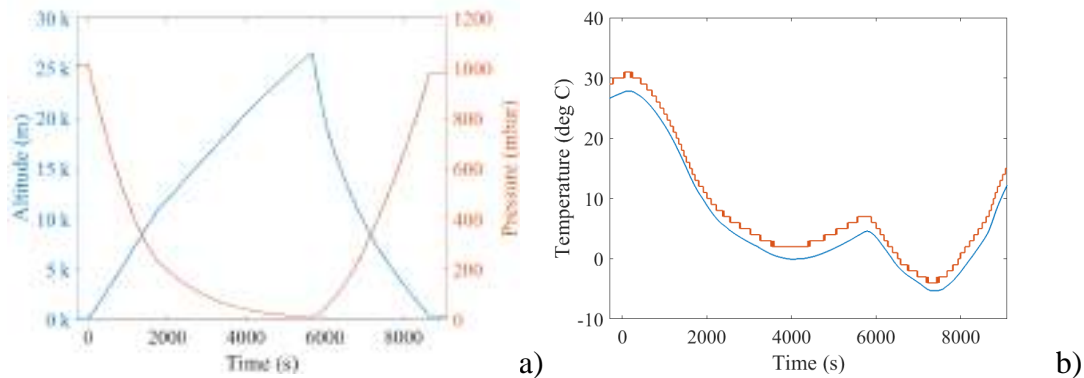


Fig. 3. Environmental parameters acquired during the flight. a) Altitude and pressure from Bosch BME680. b) Temperature inside the polystyrene box measured by two distinct transducers.

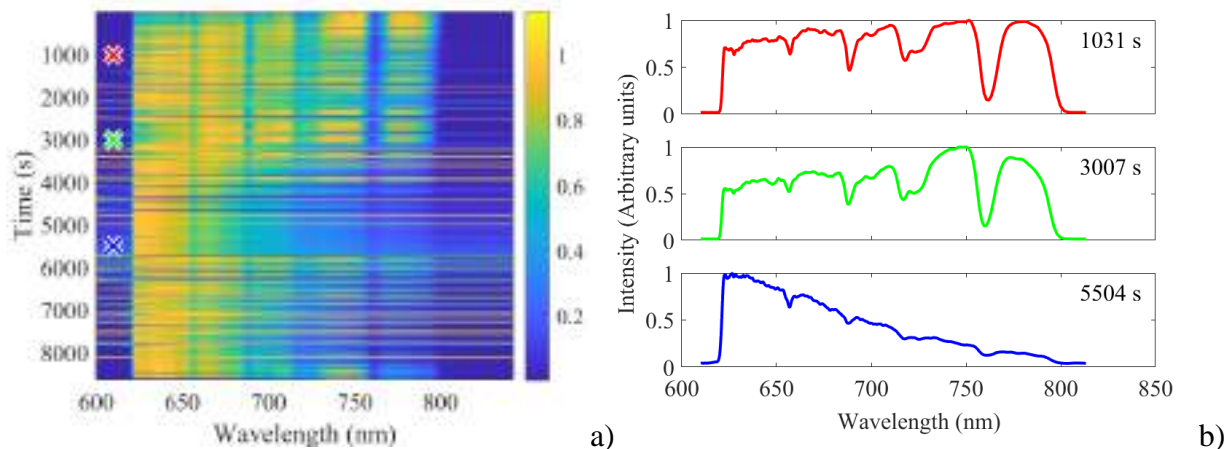


Fig. 4. Spectra acquired during the flight. A) 2D map: each spectrum is normalized to its maximum value. B) for the three horizontal cuts corresponding to the crosses in figure a), the corresponding spectra are plotted. The spectra are acquired after 1031, 3007, 5504 seconds from the beginning of the flight.

Conclusions

The proposed optical design proved to operate in a real flight environment showing negligible thermal drift effects. Moreover, compared to the previous spectrometer design [7] which featured separate prisms and beam splitter on an aluminum optical bench, this new layout showed an improved mechanical stability. Despite the lightweight 3D printed supporting base, the new design enabled operation with longer integration times without any spectral degradation due to loss of contrast in the interferogram.

Acknowledgments

We desire to thank all the people from CNES, ASI and INAF that supported us during the realization of the instrument and the flight campaign. In particular, and knowing we are mentioning just a few, André Vargas, Cruzel Serge, all the CNES operation team, Angela Volpe, Lorenzo Natalucci, Pietro Ubertini and all the HEMERA community.

Fundings

This work has been supported by ASI, Agenzia Spaziale Italiana, Agreement n. 2019-33- HH.0, for the payload realization and the flight opportunity has been provided by the European Commission in the frame of the INFRAIA grant 730790-HEMERA.

References

- [1] J. M. Harlander, Spatial Heterodyne Spectroscopy: Interferometric Performance at any Wavelength Without Scanning, Thesis (Ph.D.) University of Wisconsin, Madison, 1991, <https://ui.adsabs.harvard.edu/abs/1991PhDT.....62H>
- [2] J. Harlander, F. Roesler, J. Cardon, C. Englert and R. Conway, Shimmer: a spatial heterodyne spectrometer for remote sensing of Earth' middle atmosphere, *Appl. Opt.* 41, 1343-1352 (2002). <https://doi.org/10.1364/AO.41.001343>
- [3] M. Kaufmann, F. Olschewski, K. Mantel, B. Solheim, G. Shepherd, M. Deiml, J. Liu, R. Song, Q. Chen, O. Wroblowski, D. Wei, Y. Zhu, F. Wagner, F. Loosen, D. Froehlich, T. Neubert, H. Rongen, P. Knieling, P. Toumpas, J. Shan, G. Tang, R. Koppmann and M. Riese, A highly miniaturized satellite payload based on a spatial heterodyne spectrometer for atmospheric temperature measurements in the mesosphere and lower thermosphere, *Atmos. Meas. Tech.*, 11, 3861–3870. <https://doi.org/10.5194/amt-11-3861-2018>
- [4] F. Frassetto, L. Cocola, V. Da Deppo, L. Poletto and P. Zuppella, High signal-to-noise ratio spectrometer based on static Fourier transform interferometer (for hemera balloon flight), Italian Association of Aeronautics and Astronautics, XXV International Congress, 9-12 September 2019, Rome, Italy
- [5] F. Frassetto, L. Cocola, R. Claudi, V. Da Deppo, P. Zuppella and L. Poletto, Low noise Fourier transform spectrometer for a balloon borne platform, Italian Association of Aeronautics and Astronautics, XXVI International Congress, 31 August -3 September 2021, Pisa, Italy. <https://doi.org/10.5194/egusphere-egu22-11428>
- [6] F. Frassetto, L. Cocola, P. Zuppella, V. Da Deppo and L. Poletto, High sensitivity static Fourier transform spectrometer, *Opt. Express* 29, 15906-15917 (2021). <https://doi.org/10.1364/OE.422645>
- [7] F. Frassetto, L. Cocola, R. Claudi, V. Da Deppo, P. Zuppella and L. Poletto, Report on a refractive static Fourier transform spectrometer flown on a stratospheric balloon for the HEMERA program, ICSO International Conference on Space Optics 3-7 October 2022, Dubrovnik, Croatia. <https://doi.org/10.5194/egusphere-egu22-11428>

Ascent trajectory of sounding balloons: dynamical models and mission data reconstruction

C. Bettanini^{1,2 *}, M. Bartolomei², A. Aboudan² and L. Olivieri²

¹ Department of Industrial Engineering, University of Padova, via Venezia 1, Padova (Italy)

² CISAS - Center for Studies and Activities for Space "Giuseppe Colombo", University of Padova, via Venezia 15, Padova (Italy)

carlo.bettanini@unipd.it

Keywords: Sounding Balloon Dynamics; Trajectory Reconstruction, Linear Quadratic Estimation Method

Abstract. Small sounding balloons are a fast and cost-effective transport system to lift up scientific payloads up to stratospheric burst altitudes below 40 kilometres; during ascent and descent phase dedicated instruments may be operated to monitor atmospheric parameters and optical payloads may be used for remote observation. This work will focus on the reconstruction of the trajectory of the ascent phase, which is the longest and dynamically less perturbed part of the flight; in this section the dynamics of the flight system is determined by the lift of the balloon guiding the vertical motion and the local winds controlling the horizontal motion. The presented reconstruction algorithm is based on a linear quadratic estimation predictor corrector using the standard equations of motions in ECEF system to propagate the simulation and the measurement of the on-board sensors (triaxial accelerometer, GPS, pressure and temperature sensors) to correct the estimation and reduce the uncertainty in the reconstruction, which is mainly related to the value of balloon canopy drag coefficient C_d , the lifting gas volume and local wind perturbations. Two different balloon flights, both launched within a joint effort between teams by University of Padova and University of Pisa, are considered: one conducted during daytime, the other in night time. The different environmental conditions and in particular the different temperature evolution within the lifting balloon in the day flight due to Sun heating provide a good proving ground to investigate sensitivity of algorithm to environmental conditions. The prediction of flight dynamic models implementing horizontal and vertical equations of motion are compared with real mission data acquired by on board systems, highlighting the influence of local perturbations on the foreseen ascent trajectory.

Introduction

Stratospheric sounding balloons are small high-altitude balloons that can reach altitudes below 40 kilometres before burst; to date thanks to the availability of powerful low-cost command and data acquisition systems it is possible to carry scientific instruments, experiments or complex autonomous systems with an overall payloads mass below 3 kilograms to high altitudes and conduct in situ research and remote observation of ground targets. [1] [2].

One of the key challenges associated with stratospheric balloon flights is the accurate prediction and reconstruction of the balloon's trajectory; an accurate prediction is needed since launch decisions must be based on the likelihood of landing in a desirable location for safety issues and recovery; post flight reconstruction is both used to tune the parameters of the prediction algorithms and to provide along with attitude data georeferentiation for remote sensing data.

The simplest dynamic model utilised in the simulation of balloon trajectory is a lumped mass 3 DOF system and is the one applied in several freely available trajectory prediction software tools [3][4] or in the more complex Monte Carlo based simulation codes[5].



Several factors may affect the accuracy of these prediction algorithms: environmental conditions and atmosphere layering above the launch site may differ from the nominal standard atmosphere profile and the ascent profile depends strongly on the temperature reversal near the tropopause (about 15 km) [6]. Wind variations and atmospheric turbulence, along with cloud presence and changing ground albedo can affect also the accuracy of the prediction; the last two contributions affect lifting gas equilibrium temperature inside the canopy [7] [8] and ,as a consequence, the temperature inside the balloon may differ from surrounding atmosphere of more than 30 K due to balloon radiative heating both from the Sun and from the Earth's surface[5].

During daytime launches it is therefore critical to develop a thermal model for the balloon to investigate internal temperature variation and consequently calculate balloon volume and shape along ascent trajectory. [9] For the typical size of latex balloons temperature and pressure gradients can be disregarded and density considered constant over the volume of the balloon.

Furthermore, although helium gas mass at launch may be inferred by measuring the lift at the hook, the value is usually not accurate since is calculated by reaching the floating condition using a ballast mass; this requires to reconstruct the correct ascent velocity by mission data. Finally flight Reynolds numbers span within the so called "drag crisis" zone and accurate modelling of the balloon's ascent rate requires that the C_d be treated as a function of Reynolds number and therefore iteratively calculated depending on altitude and ascent velocity [10]. Adjustments and corrections are therefore needed to improve the accuracy of the dynamical model and due to the variability of the environmental conditions a reconstruction process is usually performed relying on mission data from a variety of sensors and instruments, including GPS receivers, accelerometers, magnetometers and external temperature sensors. Such exercise is particularly important when optical systems are part of the payload and no active control is present to guarantee platform's stability; an accurate trajectory reconstruction along with the elaboration of inertial attitude may minimise the error on pointing and therefore on the data extracted for targeted areas on ground.

Equations of motion for balloon ascent phase

The balloon ascent dynamic is a result of the lift, drag and gravitational forces on the flight train. The balloon's motion is mainly driven by the atmosphere winds governing the horizontal motion and the net lift force of the balloon determining the variation of altitude versus time and so the vertical motion. Usually the horizontal velocity of the balloon can be assumed as equal to the atmospheric wind so the drag created by relative motion between the atmosphere and the balloon system may be limited to the vertical motion into the atmosphere.

This assumption is essentially correct for lightly loaded balloons, especially at lower altitudes, but becomes less accurate at higher altitudes where inertia of the accelerated balloon must be taken into consideration. [11]

During the motion into the atmosphere, surrounding air is assumed to behave like a perfect gas in hydrostatic equilibrium. This assumption in the Earth's atmosphere is justified by the fact that the deviation from the perfect gas equation of state is negligible within the range of density and temperature conditions between the ground and a 40 km maximum altitude

The free lift force , also called net buoyancy of the balloon, is a function of the density of the lifting gas and the volume of the balloon and can be expressed as

$$\overrightarrow{F_{FL}} = (\rho_A V - m_{tot})\vec{g} \quad (1)$$

where ρ_A is ambient air density, V is the volume of the balloon, g is the gravitational acceleration vector and m_{tot} is the total mass for lift. Total mass m_{tot} is the sum of the flight train mass (payload mass, harness mass and balloon fabric mass), helium mass and the added mass which is the inertia of the mass of fluid displaced by the body, since the balloon must shift some volume of surrounding fluid as it moves through it

$$m_{ftrain} = m_{pay} + m_{harness} + m_{ball} ; \quad m_{tot} = m_{ftrain} + m_{gas} + m_{add} \quad (2)$$

The added mass for the sounding balloon may be typically approximated as 40% of the mass of the displaced air volume of the balloon [12][13]

$$m_{add} = 0.4 \rho_A V \quad (3)$$

It can be noted that due to added mass contribution, effective mass of the balloon system varies with altitude and must be properly updated especially if high volume balloons are considered. In zero pressure balloons (like the sounding balloons) the elastic latex canopy does slightly compress the lifting gas, but internal and external pressure remain within 1% of each other on average over the course of the flight, so treating the interior and exterior pressures as equal is reasonable and treating the lifting gas as an ideal gas, the density may be solved for by using the ideal gas law for balloon volume calculation.

The drag force of the aerostat is a function of the relative velocity of the balloon and atmosphere, the ambient density, the size of the balloon, and the drag coefficient. It can be calculated as F_D using:

$$\vec{F}_D = \frac{1}{2} \rho_A S v_{rel}^2 C_D \vec{u}_{vrel} \quad (4)$$

where S is the top projected area of the balloon, and C_D is the drag coefficient representative of the balloon flight train and can be considered as the one related to balloon canopy.

The C_D may be then assumed to be close to the one of a sphere and is a function of Reynolds number; Reynolds number must be therefore calculated using balloon diameter as reference dimension following the classical expression

$$Re = \frac{\rho_A v_{rel} D_{ball}}{\mu_{dyn}} \quad (5)$$

It may be underlined that velocity is given relative to the atmosphere, so a balloon's horizontal movement which is supposed to be similar to the horizontal wind does not affect the Reynolds number. As already mentioned balloon flight Reynolds numbers span the region where the coefficient of drag of the sphere decreases from 0.4-0.5 to 0.1; for the present work Conner's model was selected, as it is based on experimental data from latex balloon flights.[5]

Linear quadratic estimation model for Ascent trajectory reconstruction

The implemented model simulates the evolution of the balloon system considered as a point mass using a linear dynamic system of 12 variables (state) and considers the measures of on-board sensors as corrector building 7 observation parameters. The list of the variables is shown in listed the following equations (6)

The State is constituted by position (R_x, R_y, R_z) and velocity (V_x, V_y, V_z) of balloon system in ECEF Earth reference; Wind velocity (W_x, W_y, W_z) also expressed in ECEF is needed to calculate the vector expression for velocity relative to atmosphere as the difference of balloon velocity and local wind velocity and afterwards used in drag force evaluation. Atmospheric pressure and temperature are the last two parameters of the state and used to calculate balloon pressure and to estimate balloon temperature using a simplified thermal model for balloon canopy energy balance. [11]

The prediction of the system state at every time step performs the evaluation of total force on the balloon system (equations (2) and (4)) and calculates acceleration components (velocity time derivatives) for the trajectory.

$$State = (R_x|R_y|R_z|V_x|V_y|V_z|W_x|W_y|W_z|P_a|T_a)$$

$$Observation = (R_{x_{GPS}}|R_{y_{GPS}}|R_{z_{GPS}}|Alt_{GPS/BARO}|Ext_T|Ext_P|Acc_tot) \quad (6)$$

Standard Atmosphere models for atmospheric pressure (Pa) and temperature (Ta) are used to predict evolution depending on vertical velocity. The correction of the prediction is performed using GPS data acquired at 1 Hz sampling rate during the flight and transforming latitude and longitude data in cartesian coordinates in ECEF reference. Depending on flight altitude, the altitude measurement from GPS or inferred from IMU barometer is used as observation. At altitudes near 25 km ambient pressure falls close to barometer resolution so increases variance in the model is assigned to barometer readings forcing the algorithm to disregard the data. Atmospheric temperature and pressure observation are obtained by data from external sensors although as previously described pressure data need to be disregarded above a certain altitude. The module of total acceleration measured by IMU Triaxial accelerometer is used to estimate vertical accelerations linked to vertical turbulence. [14]

Flight data analysis

The data of two different sounding balloon flight have been analysed. The MINLU flight was launched on July 7th 2020 in an astronomical night condition with no Moon to investigate light polluting sources on ground. AREO flight was launched in day time on October 20th 2021 to provide remote observation with high resolution of crop fields providing calculation of vegetation indexes.

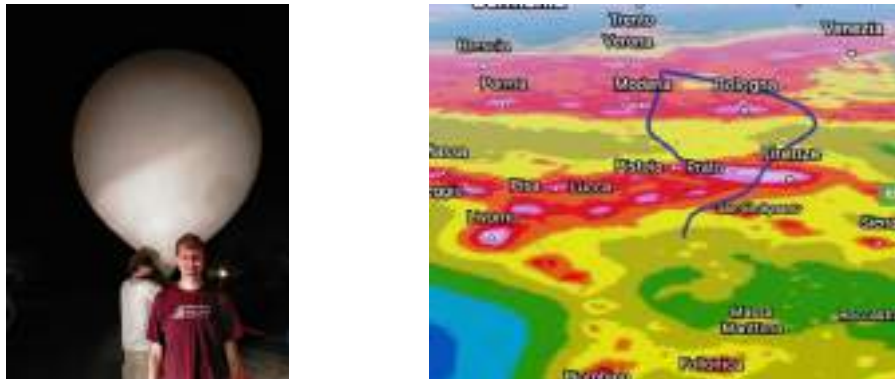


Figure 1 – MINLU night flight in the night of July 7th 2020 - Burst altitude 32104 m (3D trajectory reconstructed on satellite-based ground light pollution map)



Figure 2 – AREO flight on October 20th 2021 - Burst altitude 36907.9 m (3D trajectory reconstructed on Google Earth)

The elaboration of trajectory profiles and vertical velocities are reported in following figures 3 and 4 showing the ability of LQE model to predict system dynamic to fit real mission data.

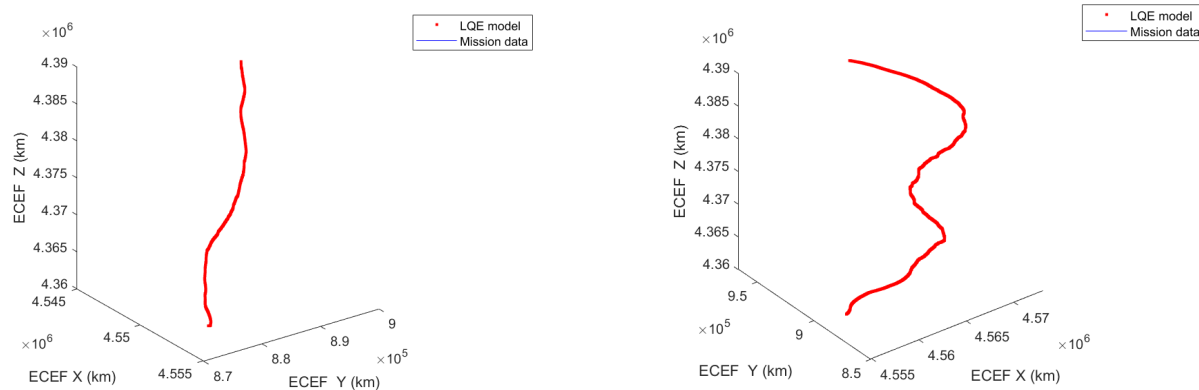


Figure 3 – Reconstructed trajectory from LQE model compared with GPS vertical velocity from mission data (left MINLU flight, right AREO flight)

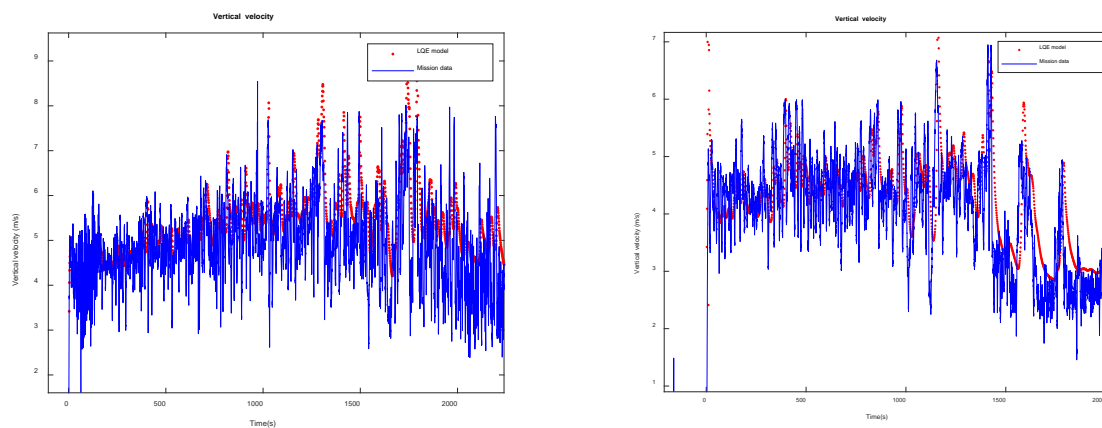


Figure 4 – Vertical ascent velocity from LQE model compared with GPS vertical velocity from mission data (left MINLU flight, right AREO flight)

LQE model is designed to adjust at every time step the parameters with higher uncertainty and no measured mission data (local Wind vector and Balloon drag coefficient C_d) allowing to estimate their time evolution

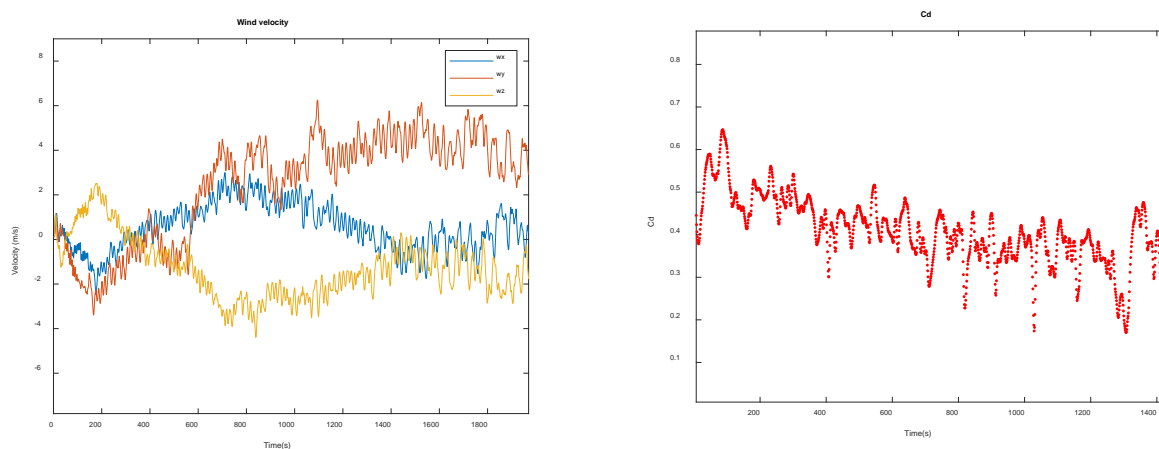


Figure 5 –LQE model estimation of local wind velocity and balloon C_d values (AREO flight)

Conclusions

LQE algorithms for trajectory reconstruction of ascent phase of high-altitude balloons have been developed to increase the accuracy of mission predictors and tested using real mission data. Post flight analysis has been conducted on two balloon-launched Earth observation payloads, one

dedicated to the determination of ground sources of Artificial Light at Night, the other to the analysis of vegetation Indexes. Although the presented results are preliminary and further validations shall be conducted, the algorithm allows to limit sudden changes in trajectory due to temperature variation and wind turbulences and improves the correct correlation of position and pointing direction needed to provide georeferentiation of images acquired during the balloon flights.

References

- [1] C. Bettanini, M. Bartolomei, P. Fiorentin, A. Aboudan and S. Cavazzani, "Evaluation of Sources of Artificial Light at Night With an Autonomous Payload in a Sounding Balloon Flight," *IEEE JOURNAL OF SELECTED TOPICS IN APPLIED EARTH OBSERVATIONS AND REMOTE SENSING*, vol. 16, pp. 2318-2326, 2023. <https://doi.org/10.1109/JSTARS.2023.3245190>
- [2] F. Toson, M. Pulice, M. Furiato, M. Pavan, S. Sandon, D. Sandu and R. Giovanni, "Launch of an Innovative Air Pollutant Sampler up to 27,000 Metres Using a Stratospheric Balloon," *Aerotecnica Missili & Spazio*, vol. 102, no. 2, pp. 127-138, June 2023. <https://doi.org/10.1007/s42496-023-00151-y>
- [3] L. W. Renegar, "A Survey of Current Balloon Trajectory Prediction Technology". <https://via.library.depaul.edu/cgi/viewcontent.cgi?referer=&httpsredir=1&article=1125&context=ahac>
- [4] A. Gallice, F.G. Wienhold, C.R. Hoyle, F. Immler and T. Peter "Modeling the ascent of sounding balloons: derivation of the vertical air motion", *Atmos. Meas. Tech.*, 4, 2235–2253, 201. <https://doi.org/10.5194/amt-4-2235-2011>
- [5] Luke W. Renegar "Development of a Probabilistic Trajectory Model for High-Altitude Scientific Balloons", University of Maryland, College Park
- [6] H.D. Voss, N.A. Ramm and J. Dailey "Understanding High-Altitude Balloon Flight Fundamentals", *Proceedings of 3rd Annual Academic High-Altitude Conference*
- [7] C. Olsson, "Sensitivity Analysis for Ascending Zero Pressure Balloons", Master thesis, 2019, Luleå tekniska universitet
- [8] Q. Dai, X. Fang, X. Li, L. Tian, "Performance simulation of high altitude scientific balloons", *Advances in Space Research* 49 (2012), 1045–1052. <https://doi.org/10.1016/j.asr.2011.12.026>
- [9] F. Kreith, J.F. Kreider "Numerical Prediction of the Performance of High Altitude Balloons", National Center for Atmospheric Research, Technical Note NCAR-TN/STR-65
- [10] J. Söder, M. Gerding, A. Schneider, A. Dörnbrack, H. Wilms, J. Wagner and F. Lübken "Evaluation of wake influence on high-resolution balloon-sonde measurements", *Atmos. Meas. Tech.*, 12, 4191–4210, 2019. <https://doi.org/10.5194/amt-12-4191-2019>
- [11] F.P. Camara, "Flight Dynamics of a High-Altitude Balloon," Master Thesis, 2018, Universidad Carlos III, Madrid
- [12] M. Tuveri, A. Ceruti, "Added masses computation for unconventional airships and aerostats through geometric shape evaluation and meshing"
- [13] W.J. Anderson, G.N. Shah, J. Park "Added Mass of High-Altitude Balloons", *JOURNAL OF AIRCRAFT* Vol. 32, No. 2, March-April 1995. <https://doi.org/10.2514/3.46714>
- [14] G. J. Marlton "On the development, characterisation and applications of a balloon-borne atmospheric turbulence sensor", Thesis Work, University of Reading, Department of Meteorology

Italian space agency space transportation activities and programs

Marta Albano^{1*}, Rocco Carmine Pellegrini¹, Roberto Bertacin¹,
Simone Ciabuschi¹, Simone Illiano¹, Rocco Maria Grillo¹, Enrico Cavallini¹

¹Italian Space Agency (ASI), Italy

marta.albano@asi.it

keywords: Launchers, Stratospheric Balloon, Hypersonic Vehicles, Suborbital Flight

Abstract Space transportation systems are the key elements for the space exploitation thought space-based services (for telecommunication, navigation and earth observation) and space exploration. As more government and commercial players show interest in effective and sustainable space transportation systems and services, affordable, regular and resilient transportation systems have become increasingly important for sustainable space services. Italy, through the activities of the Italian Space Agency, is increasingly investing in the space sector and it confirms to be one of the top players on the international scenario. The paper presents an overview of the activities of the Italian Space Agency in this sector, both through national and European framework.

Introduction

The Italian Space Agency has the role to promote and coordinate the space activities at national and international level. The main space transportation activities and programs will be presented in this paper showing the complexity and the variety of the Italian investments in this sector. The activities cover three main areas. Launchers: Italy through ASI, as National Space Agency with the aim of maintaining the national leadership in the sector participates to ESA launchers activities, such as VEGA family and develops, through ASI national programs, critical subsystems such as liquid and hybrid engines, avionics systems etc. Re-entry vehicles: Italy, through ASI, is the main contributor in Europe for the development of the first European re-entry and re-usable vehicle that will enable new type of services for institutional and commercial customers through Space Rider, based on the experience gained in IXV program. Sub-orbital, hypersonic and stratospheric flights: with the aim to perform missions, develop a national capacity in the specific sectors promotes collaboration with European entities for balloon borne launch campaigns, participates to European working groups dedicated to suborbital law and activities, works on the realization of a national hypersonic demonstrator.

Launchers

Italy, through the Italian Space Agency supports the development and exploitation of European launchers through its participation in ESA Programmes. The main support is to the VEGA family launchers (VEGA, VEGA-C and VEGA-E) where the leadership is Italian and the prime contractor is AVIO S.p.A. In particular, based on the successful development and exploitation of VEGA launch system entered into service in 2012, Italy has supported the development of the VEGA-C launcher[13] up to its maiden flight occurred in July 2022 with the successful release in orbit of LARES2 satellite (developed by ASI itself) and six CubeSats. After the successful maiden flight, Italy is now supporting the return to flight of VEGA-C after its failure on its second flight in December 2022, and its ramp-up in the stabilized exploitation phase, through a dedicated program aiming also at providing improved robustness to the Launch System in view of its commercial exploitation. Italy has also supported since long time the future evolution of VEGA, starting with ASI national Programs such as Lyra, fostering the introduction of a larger liquid propulsion upper



stage exploiting LOX-CH₄ propellant combination substituting Z9 and AVUM. In the frame of Lyra program, the basis for mastering this technology have been set up through a collaboration with Russia leading to the firing test of a 10 ton class engine demonstrator called MIRA [7]. Those achievements have been the basis for introducing within the ESA programmes the VEGA Evolution Preparatory Program aimed at developing VEGA-E that, starting from VEGA-C configuration, will substitute Z9 and AVUM+ with a new upper stage making use of M10 engine, developed in the frame of the same program. M10 [12] first development model (DM1) has been already successfully fire tested at engine level in the SPTF test facility located in Sardinia in 2022, while the second development model (DM2) will undergo a complete firing test campaign in the coming weeks. Italy has also a leading role in the P120C Solid Rocket Motor development program which constitutes a common element for the future VEGA and ARIANE launcher families, guaranteeing the synergy between the two launchers. P120C, indeed is used as first stage on VEGA-C and as strap-on booster on Ariane 6 in its version with 2 or 4 boosters. This will also allow higher production volume and cadence for the P120C production line, contributing to lowering the exploitation costs through an economy of scale and building blocks approach. In order to improve ARIANE 6 performances to allow the deployment of large constellations a further development of this SRM has been started in 2021 and then confirmed at the last Ministerial Conference 2022, for a more powerful version of the rocket called P120C+ (or P160C) with an extended length allowing to load a higher mass of solid propellant, increasing the overall total impulse of the motor.



Figure 1 First VEGA C -Lares 2 mission -courtesy of ESA.

In the logic of the P120C, the P120C+ (or P160) will maintain its characteristic of common building block of Ariane and Vega European family of launchers, increasing also the performance of Vega launchers, VEGA-C and VEGA-E. ASI conceived within the National PNRR and today supports the implementation of the so-called PNRR-STP project, funded by EU in the framework of the Italian PNRR. The project will be dedicated to the technology pushing towards the new generation of liquid propellant LOX-CH₄ launchers, through the in flight testing and demonstration of the innovative LoX-methane propulsion, based on M10 engine developed in the frame of VEGA-E Program, and the development of critical and enabling technologies. Those critical technologies consist of composite material cryogenic tanks, non-pyrotechnic separation systems and integrated avionics systems based on low-cost hardware. In addition, in the frame of the National PNRR funds, the development of a larger thrust class liquid rocket engine with respect to M10 has been started in the frame of an optional ESA Programme fully funded by Italy, so called High-Thrust Engine. This High thrust Engine (HTE), in the class of thrust and performance complementary and synergic with M10 and with Prometheus will constitute the base for future building blocks to be used in the next generation of European launchers fully based on Lox-Methane propulsion.

Avionic systems for Launchers

The development of future generation launchers is strongly characterized by the efficiency of the service offered both in terms of performance and competitiveness. This requires technological innovations aimed at improve the services provided on the market. The growing amount of data to be managed on board requires new concepts of avionic architectures. To innovate these systems, worldwide, various actions are undertaken such as the improvement of the hardware with the development of new on-board computers, the creation of new architectures such as for example the modular approaches or the implementation of new procedures aimed at streamline integration and ground testing activities with the use, for example, of wireless technologies or real-time simulations of environmental stimuli (rotation of the earth, gravity, sloshing of propellant tanks, temperature and thrust, weather conditions, etc.) . It should also be considered that avionics systems account for approximately 20-25% of the cost of the launch service and they are a fundamental element of innovation for the management of on-board data, launcher safety and state recovery. Therefore, avionics systems constitute a key element in order to place the launch service on the market in a strategic way. In order to promote the innovation and to consolidate the role of Italy in the launcher sector, avionic systems are in development through national programs. Wireless systems will allow to facilitate the ground procedures and the launcher design. Different GNC systems are in phase of study both for the re-entry of the launcher stages and for optimization of GNC systems itself by the means of data fusion. Neutralization systems are also in development phase in order to assure the safety of the flights. Communication systems based on Flexible TTEthernet are in early stage of development in order to lower the costs guaranteeing high reliability of those systems.[1]

Green Innovative propulsion and Technology Developements

Funded by EU in the framework of the Italian PNRR, ASI has contracted in April 2023 a major project to design, develop and on-ground qualify an innovative Multi-Purpose Green Engine (MPGE) to be exploited as “*building-block*” for the future Space Logistics scenarios, as element shared between the Space Transportation roadmap and the In-orbit servicing roadmap whose MPGE is part of. Thanks to an intrinsic versatility, mainly related to its throttability, MPGE will be able either to operate as propulsive module of orbiting platforms for next generation in-orbit services, also in reusable configurations (e.g. Space Rider), and to power the upper stages of VEGA-class launchers.

This kilo-Newton class engine will be designed to operate with an innovative combination of green liquid propellants, characterized by long-term storability. Main drivers of the project will be also the wide use of additive manufacturing processes, to optimize the layout and minimize the overall mass, and of a fast prototyping approach, by use of a large number of test campaign and development/qualification models.



Figure 2 First draft of MPGE.

In the field of Hybrid Propulsion, ASI has set up the PHAEDRA Program (Paraffinic Hybrid Advanced Engine Demonstrator for Rocket Application) [5] with the aim to gather the main Italian competences in the field of hybrid propulsion both in industry and in Universities and Research Centers in order to develop a technological demonstrator in relevant scale to be fire tested at the beginning of next year. The Demonstrator will devote particular attention to the re-ignition characteristics and throttling capabilities, adopting paraffin-based fuel in solid form as a single

port grain and oxygen peroxide (HTP) as liquid oxidizer. ASI has also funded research activities on solar sails propulsion with the aim to create highly specialized skills in various technological areas relating to the main issues of solar photonic propulsion such as mission analysis, materials development for membrane substrate and reflecting coating depositions, deployment structures (telescopic booms or memory form material booms) and attitude control system relying on photochromic materials. The activities on solar sails technologies are carried out in collaboration with some university departments and with specialized laboratories at Italian research institutes[3]. As a result of the activities carried out, material production processes have been set up, several samples at laboratory scale have been produced and characterized, both for the membrane substrate, reflecting coating optical properties, and boom subscale prototypes [6]. ASI participated also to project called “MAGIC”, funded by the Regione Lazio, which has developed enabling technologies aimed at the full industrialization of additive manufacturing processes (Additive Layer Manufacturing - ALM) of alloys and superalloys of nickel and copper for the production of aerospace components, complementary joining technologies, with a particular focus on laser welding, and certification and qualification protocols through Non-Destructive Testing (NDT). In particular components for the propulsion systems have been developed. ASI has supported the development of technologies for propulsion systems such as the study carried out for segmented solid rocket motor cases using composite materials culminated with the mechanical characterization tests of a sub-scale model applying this technology that can be of interest also for the application on inter-stage joints manufactured in composite materials with the aim to guarantee a more reliable and lightweight overall launch system.

Re-entry vehicles and technologies

Re-entry environment is the upmost challenging condition for a space vehicle. ASI has promoted over the years the development of technologies and system competences for re-entry. The national programs allowed Italy to have one of the most relevant European competence in this sector. Italy, through ASI, funded also ESA programs such as IXV, which successfully flew in 2015 and now is supporting with a primary role Space Rider.

The overarching objective of the Space Rider program is to develop a reusable, fully autonomous European space transportation system service, providing a European independent capability to routinely access and return from orbit with precise landing capability and a space vehicle serving as a platform for experimentation, in-orbit demonstration and validation with application missions in Low Earth Orbit. The Space Rider program is capitalizing the IXV experience and technological baseline qualified in flight. The Space Rider system is composed of two modules: the Re-entry Module (RM) and the Orbital Module (OM). The RM, being developed under the Design Authority of TAS-I, is a lifting body and it will be designed to embark experiments and payload inside a cargo bay and to return to Earth for landing and re-flight. The OM, under the Design Authority of AVIO, consists of the ALEK (AVUM Life Extension Kit) and acts as service module during the orbital phase of the system. The overall system is completed by a ground segment under the responsibility of ALTEC and TELESPAZIO and a landing site. The system has in orbit lifetime for a minimum duration of 2 months with the following applications: Micro-gravity experimentation laboratory, In-Orbit Demonstration and Validation for a wide range of technologies (e.g. Earth monitoring, satellite inspection, etc.). The vehicle shall be able to perform a high precision soft landing on ground on the landing site. The Space Rider system shall be designed to fly for 6 times. [10][11]

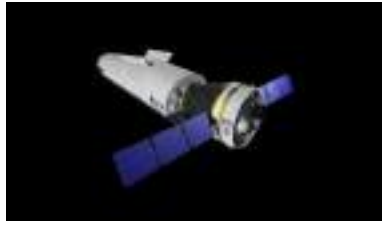


Figure 3 A possible configuration of Space Rider [2]

Suborbital, hypersonic and stratospheric flights

Complementary to classical space transportation topics, the Italian Space Agency funds and promotes national technological and research projects in the field of sub-orbital flights, meant as non-orbital, including support of their mid-stream component i.e. the spaceports, stratospheric platforms and suborbital-hypersonic vehicles. Stratospheric flights are operated by the means of platforms such as balloons at variable altitudes up to about 40km. ASI promoted these activities by its participation to the European project Hemera which developed technologies for the flight train and offered flights to the scientific community. ASI is continuing to keep in contact with the main European actors which participated also to the Hemera project[9]. Agreements and possible future European projects are ongoing. Suborbital flights have become over the years an interesting opportunity for both new space transportation services and research and development activities and a viable option for access to Space of nanosatellite systems. A suborbital flight usually does not exceed 100 km in height and will not orbit the Earth. In this sector ASI participate to discussions on the regulation of these flights. together with ENAC and to the European Commercial Spaceport Forum (ECSF), which brings together several European countries active in light spacecraft launch and suborbital flights. Hypersonic flights are performed by vehicles able to fly at Mach over 5. These flights conditions are typical of re-entry vehicles (winged such as the space shuttle or the aforementioned Space Rider or not winged such as Carina, ARD etc.) and of airbreathing cruise and acceleration vehicles (such as Sanger [4]). The last category, named also as CAV, is objective of many European studies in the recent years. Based on the high experience cumulated on these studies, the Italian Space Agency promoted a dedicated national agreement with CIRA in order to develop a small-scale propelled demonstrator. The project will develop the system and the necessary technologies focused on the propulsion[8].

Conclusions

Space transportation vehicles and technologies are of increasing interests at European and international level. ASI supports the development of the national capacities in order to maintain the strategic position of Italy in this field and to support though its national and ESA programs the European strategic independent access to space for Europe Space Program, both with its role in the frame of the ESA European launchers family and their exploitation and evolution in the European cooperation framework, and through R&D activities through its national programs. In this paper, a general overview of the main programs carried out at national and ESA level has been provided for the main lines of developments in the fields of Space Transportation, including Launchers, re-entry vehicles, suborbital, hypersonic and stratospheric flight and related technologies.

References

- [1] Flexible Time Triggered Ethernet: A Cost Efficient COTS-Based Technology for the Development of Launcher Networks “2023 IEEE INTERNATIONAL WORKSHOP ON Metrology for AeroSpace, Milano (Italy)
- [2] https://www.esa.int/Enabling_Support/Space_Transportation/Space_Rider_overview
- [3] Piano Triennale delle Attività dell’Agenzia Spaziale Italiana 2022-2024

- [4] Sanger II, A hypersonic flight and space transportation system, ICAS, 1988
- [5] A. Reina, M.L. Frezzotti, G. Mangioni, A. Cretella, F. Battista, C. Paravan, F. Nasuti, D. Pavarin, R. C. Pellegrini, E. Cavallini, Hybrid Propulsion System for future rocket applications, Space Propulsion Conference 2022,
- [6] Giovanni Vulpetti, Christian Circi, Rocco Pellegrini, Enrico Cavallini, Sailcraft Helianthus: a Solar-Photon Sail for Geostorm Early Warning, 6th International Symposium on Space Sailing (ISSS 2023)
- [7] M. Rudnykh, S. Carapellese, D. Liuzzi, L. Arione, G. Caggiano, P. Bellomi, E. D'Aversa, R. Pellegrini, S. D. Lobov, A. A. Gurtovoy, V. S. Rachuk Development of LM10-MIRA LOX/LNG expander cycle demonstrator engine, Acta Astronautica 126(2016)364–374. <https://doi.org/10.1016/j.actaastro.2016.04.018>
- [8] Sara Di Benedetto, Marco Marini, Pietro Roncioni, Antonio Vitale, P. Vernillo, Salvatore Cardone, Marta Albano, Roberto Bertacin, “Design of the Scramjet Hypersonic Experimental Vehicle”, Eucass 2023
- [9] HEMERA: a European Stratospheric Balloon Research Infrastructure, Raizonville P., S. Payan, K. Dannenberg, D. Hagsved, L. Stephane, P. Ubertini, K. Pfeilsticker, F.Vallon, M. Albano, IAC-21,A7,1,5,x66353, 25-29 October 2021, Dubai
- [10] Italian contribution to the esa ministerial conference 2016: next generation of the european vega launcher for new green and reusable space missions, IAC-17,D2,IP,22,x39093, A.Gabrielli; Mr. A. Cramarossa; E. D'Aversa; S. Ianelli; R.C. Pellegrini; M. Albano; IAC 2017
- [11] A. Fedele, G. Guidotti, G. Rufolo, G.Tumino et al, The Space Rider Programme: End user's needs and payload applications survey as driver for mission and system definition, Acta Astronautica, volume 152, nov 2018 pp. 534-541. <https://doi.org/10.1016/j.actaastro.2018.08.042>
- [12] D. Kajon, D. Liuzzi, C. Boffa, N.Ierardo et al., Development of the liquid oxygen and methane M10 rocket engine for the Vega-E upper stage, Eucass 2019
- [13] <https://www.arianespace.com/vega-c/>

Materials and Aerospace Structures

Nonlinear mechanical analysis of aerospace shell structures through the discontinuous Galerkin method

Giuliano Guarino^{1,a,*} and Alberto Milazzo^{1,b,*}

¹Department of Engineering, University of Palermo, Viale delle Scienze, Bld. 8, 90128, Palermo, Italy

^agiuliano.guarino@unipa.it, ^balberto.milazzo@unipa.it

Keywords: Multilayered Shells, Nonlinear Structural Behavior, Discontinuous Galerkin Method, High-Order Modelling

Abstract. The geometrically non-linear mechanical response of multilayer composite shells is addressed via an innovative discontinuous Galerkin formulation. In the framework of the Carrera Unified formulation, equivalent single layer kinematics with different through-the-thickness accuracy is adopted. The variational statement governing the shell nonlinear behavior is derived. The corresponding governing equations are solved via a discontinuous Galerkin approach, which employs the pure penalty method to weakly enforce the connection between the mesh elements. Numerical tests are presented to show the capabilities of the proposed approach.

Introduction

Multilayered composite shells are extensively employed as high-performance lightweight components in aerospace engineering. In advanced applications they may undergo large displacements, requiring non-linear analysis to characterize accurately their behavior. In this framework a fundamental role is played by the modelling and analysis of these structure that needs to be carried out with appropriate fidelity and cost effectiveness.

From the modelling point of view, besides fully three-dimensional models, shell structures are studied within the context of the so-called shell theories which can be classified into equivalent single layer (ESL) theories and layer-wise (LW) theories. Due to their complexity, the solution of shell theories models commonly requires the employment of numerical methods. The most common approach in the literature is the finite element method (e.g. Ref. [1]); the Ritz method [2], mesh-less solutions [3, 4] and the isogeometric analysis approach [5] have been also proposed.

Recently, the discontinuous Galerkin (dG) method emerged as a viable alternative showing interesting advantages in the use of nonstandard element and shape functions, in the application of non conformal meshes as well as high-order elements, in the implementation of meshing strategies such as hierarchical refinement and adaptativity and in scalable implementations [6, 7]. These features can underlie a robust treatment of complex problems as those involved in the analysis of multilayered shells [8, 9]. This motivate the present work in which high-order, equivalent single layer shell theories are solved through a pure penalty discontinuous Galerkin approach formulated accounting for geometrical nonlinear behavior [10].

Shell model and governing equations

In the context of a total Lagrangian approach, the shell deformation is described in terms of the displacement components expanded as [8, 9]

$$u_{\xi_i}(\xi_1, \xi_2, \xi_3) = \sum_{k=0}^{N_i} Z_k^i(\xi_3) U_{ik}(\xi_1, \xi_2) \quad (1)$$

where ξ_m are the curvilinear coordinates used to describe the shell geometry, N_i is the order of the assumed expansion, $Z_k^i(\xi_3)$ is the prescribed k -th function of the expansion and $U_{ik}(\xi_1, \xi_2)$ are the unknown generalized displacements. In Eq. (1) the N_i are considered as parameters whose different

values allow to build different order ESL shell theories. The shell theory corresponding to the expansion orders N_1 , N_2 and N_3 is denoted as $ED_{N_1N_2N_3}$.

To develop the proposed dG formulation, the shell reference domain Ω_ξ is partitioned into N_e elements Ω_ξ^e over which the generalized displacements $U_{ik}(\xi_1, \xi_2)$ are approximated via polynomial basis function.

Following Ref. [10] one obtains the following variational statement:

$$\begin{aligned} \sum_{e=1}^{N_e} \int_{\Omega_\xi^e} \left[\frac{\partial \mathbf{V}^T}{\partial \xi_\alpha} \left(\mathbf{Q}_{\alpha\beta} \frac{\partial \mathbf{U}_h}{\partial \xi_\beta} + \mathbf{R}_{\alpha 3} \mathbf{U}_h \right) + \mathbf{V}^T \left(\mathbf{R}_{3\alpha} \frac{\partial \mathbf{U}_h}{\partial \xi_\alpha} + \mathbf{S}_{33} \mathbf{U}_h \right) \right] d\Omega_\xi \\ + \sum_{i=1}^{N_i} \int_{\partial\Omega_{\xi 1}^i} \mu [\mathbf{V}]_\alpha^T [\mathbf{U}_h]_\alpha d\partial\Omega_\xi + \sum_{e=1}^{N_e} \int_{\partial\Omega_{\xi D}^e} \mathbf{V}^T \mathbf{U}_h d\partial\Omega_\xi \\ = \sum_{e=1}^{N_e} \int_{\Omega_\xi^e} \mathbf{V}^T \bar{\mathbf{B}} d\Omega_\xi + \sum_{e=1}^{N_e} \int_{\partial\Omega_{\xi N}^e} \mathbf{V}^T \bar{\mathbf{T}} d\partial\Omega_\xi + \sum_{e=1}^{N_e} \int_{\Omega_{\xi D}^e} \mu \mathbf{V}^T \bar{\mathbf{U}} d\partial\Omega_\xi \end{aligned} \quad (2)$$

where the Einstein's summation is assumed for $\alpha, \beta = 1, 2$, \mathbf{U}_h is the vector containing the dG approximation of the generalized displacements field, \mathbf{V} is the vector of the test functions chosen of the same form of the generalized displacements. In Eq (2), $\bar{\mathbf{B}}, \bar{\mathbf{T}}$ and $\bar{\mathbf{U}}$ are the generalized domain forces, the generalized boundary forces and the boundary prescribed generalized displacements, respectively, $\mathbf{Q}_{\alpha\beta}, \mathbf{R}_{\alpha 3}, \mathbf{R}_{3\alpha}$ and \mathbf{S}_{33} are the generalized stiffness matrices and $[\cdot]$ is the interelement jump operator. Finally, $\partial\Omega_{\xi 1}^i$, $\partial\Omega_{\xi D}^e$ and $\partial\Omega_{\xi N}^e$ are the inter-element interfaces and the elements portions of boundaries where the essential and natural boundary conditions are enforced, respectively. The definitions of the above-mentioned quantities can be found in Ref. [10], to which the reader is referred for the formulation details.

In the primal form of the proposed pure penalty dG method, namely Eq. (2), μ is the penalty parameter used to enforce the inter-elements continuity of the solution and the essential boundary conditions. The choice of μ is crucial for the method to be efficient as discussed in Refs. [7,10]

Applying the variational calculus procedures, the final nonlinear algebraic system is inferred, which is solved via a Newton-Raphson arc-length scheme. It is remarked that the use of a pure penalty formulation enables to compute the elements interface boundary integrals only once with the consequent computational time savings during the iterative solution scheme.

Numerical results

To illustrate the capabilities of the proposed method some results relative to the nonlinear analysis of cylindrical shells are proposed. The present results are representative of the proposed approach effectiveness that was proved by a lot of numerical tests whose results are not reported here for the sake of brevity.

Fig. 1a shows the geometry, boundary conditions and loads of the cylindrical shell having dimensions $L = 254$ mm, $R = 2540$ mm and $\theta = 0.1$ rad and subjected to a central pinch load \mathbf{F} . Only a quarter of the structure is modelled for symmetry conditions. Three different shell sections have been considered: i) a single-layer section of isotropic material (see Table 1) and thickness $\tau = 6.35$ mm, which is labeled as C1 case (thin shell); ii) a single-layer section of isotropic material M1 (see Table 1) and thickness $\tau = 12.7$ mm, which is labeled as C2 case (moderately thick shell); iii) a three-layer section with [0/90/0] layup of 4.233 mm thick plies having orthotropic properties as M2 material in Table 1, which is labeled as C3 case.

Table 1: Material properties.

	Isotropic M1	Orthotropic M2
Young's modulus E_1	75000 [MPa]	3300 [MPa]
Young's moduli $E_2 = E_3$	75000 [MPa]	1100 [MPa]
Shear Moduli $G_{12} = G_{13} = G_{23}$	28846 [MPa]	660 [MPa]
Poisson's coefficients $\nu_{12} = \nu_{13} = \nu_{23}$	0.3	0.25

Fig. 1b show the transverse displacement of the load application point u_3 versus the load amplitude F . These Equilibrium paths are computed using both the ED_{222} and ED_{333} shell theories and a 2×2 mesh grid of elements with polynomial trial and test function order $p = 5$. The results show that, as expected, snap-back or snap-through behavior occurs depending on the shell thickness ratio. The comparison of the present results with those of Refs [1], [11] and [12] shows very good agreement for both isotropic and multilayered shells, that proves the proposed approach effectiveness.

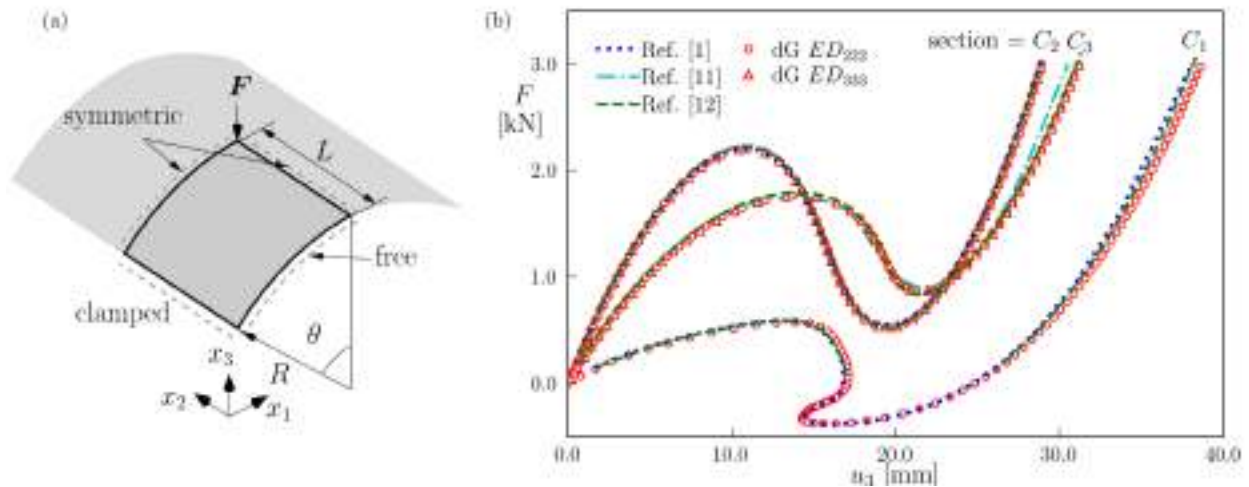


Figure 1: Cylindrical shells. (a) Geometry, boundary conditions and applied load. (b) Nonlinear equilibrium path for different shell sections.

Conclusions

A novel pure penalty discontinuous Galerkin method has been presented for the geometrically nonlinear static analysis of multilayered plates and shells described by refined equivalent single-layer kinematics with generality of the through-the-thickness resolution.

The numerical tests prove the ability of the method to deal with complex nonlinear behavior of shells and evidence very good agreement with literature results.

References

- [1] B.Wu, A. Pagani, W. Chen, E. Carrera, Geometrically nonlinear refined shell theories by Carrera Unified Formulation, Mechanics of Advanced Materials and Structures. 28 (2021) 1721–1741. <https://doi.org/10.1080/15376494.2019.1702237>

- [2] A. Milazzo, G. Guarino, V. Gulizzi, Buckling and post-buckling of variable stiffness plates with cutouts by a single-domain Ritz method, *Thin-Walled Structures*. 182 (2023) 110282. <https://doi.org/10.1016/j.tws.2022.110282>
- [3] M. Fouaidi, A. Hamdaoui, M. Jamal, B. Braikat, A high order mesh-free method for buckling and post-buckling analysis of shells, *Engineering Analysis with Boundary Elements*. 99 (2019) 89–99. <https://doi.org/10.1016/j.enganabound.2018.11.014>
- [4] S. Hosseini, G. Rahimi, D. Shahgholian-Ghahfarokhi, A meshless collocation method on nonlinear analysis of functionally graded hyperelastic plates using radial basis function, *ZAMM - Journal of Applied Mathematics and Mechanics*. 102 (2022) 202100216. <https://doi.org/10.1002/zamm.202100216>
- [5] Y. Guo, Z. Zou, M. Ruess, Isogeometric multi-patch analyses for mixed thin shells in the framework of non-linear elasticity, *Computer Methods in Applied Mechanics and Engineering*, 380 (2021) 113771. <https://doi.org/10.1016/j.cma.2021.113771>
- [6] D. N. Arnold, F. Brezzi, B. Cockburn, L. D. Marini, Unified analysis of discontinuous Galerkin methods for elliptic problems, *SIAM Journal on Numerical Analysis*. 39 (2002) 1749–1779. <https://doi.org/10.1137/S0036142901384162>
- [7] V. Gulizzi, I. Benedetti, A. Milazzo, Discontinuous Galerkin methods for solids and structures, in: F. M. H. Aliabadi, W. Soboyejo (Eds.), *Comprehensive Structural Integrity*, 2nd Edition, vol. 3, Elsevier, Oxford, 2023, pp. 348–377. <https://doi.org/10.1016/B978-0-12-822944-6.00024-4>
- [8] G. Guarino, A. Milazzo, V. Gulizzi, Equivalent-single-layer discontinuous Galerkin methods for static analysis of multilayered shells, *Applied Mathematical Modelling*, 98 (2021) 701–721. <https://doi.org/10.1016/j.apm.2021.05.024>
- [9] G. Guarino, V. Gulizzi, A. Milazzo, High-fidelity analysis of multilayered shells with cut-outs via the discontinuous Galerkin method, *Composite Structures*, 276 (2021), 114499. <https://doi.org/10.1016/j.compstruct.2021.114499>
- [10] G. Guarino, A. Milazzo, A discontinuous Galerkin formulation for nonlinear analysis of multilayered shells refined theories, *International Journal of Mechanical Sciences*, 255 (2023), 108426. <https://doi.org/10.1016/j.ijmecsci.2023.108426>
- [11] E. Carrera, A. Pagani, R. Azzara, R. Augello, Vibration of metallic and composite shells in geometrical nonlinear equilibrium states, *Thin-Walled Structures*. 157 (2020) 107131. <https://doi.org/10.1016/j.tws.2020.107131>
- [12] K. Sze, X. Liu, S. Lo, Popular benchmark problems for geometric nonlinear analysis of shells, *Finite Elements in Analysis and Design*. 40 (2004) 1551–1569. <https://doi.org/10.1016/j.finel.2003.11.001>

Exploring aerospace advancements and global collaborations: a comprehensive analysis of MCAST's aerospace program in Malta

Leonardo Barilaro^{1,a*}, Lorenzo Olivieri^{2,b}, Mark Wylie^{3,c}, Joseph Borg^{4,d}

¹ The Malta College of Arts, Science & Technology, Aviation Department, Paola PLA 9032, Malta

² CISAS "G.Colombo", University of Padova, Via Venezia 15, 35131 Padova (PD, Italy)

³ South East Technological University (SETU), Aerospace, Mechanical and Electronic Engineering Department, Carlow campus, Kilkenny Rd, Moanacurragh, Co. Carlow, Ireland

⁴ Department of Applied Biomedical Science, Faculty of Health Sciences, University of Malta, Msida MSD, 2080, Malta

^aleonardo.barilaro@mcast.edu.mt, ^blorenzo.olivieri@unipd.it, ^cmark.wylie@setu.ie,
^djoseph.j.borg@um.edu.mt

Keywords: Space Debris, Aerospace Structures, Satellites Shields, International Space Station

Abstract. This paper provides an overview of the Aerospace Program at the Malta College of Arts, Science and Technology (MCAST). The program comprises of four main projects that aim to address different challenges in the aerospace industry, in particular in the field of protection of aerospace structures and systems from space debris impacts. The first project focuses on the development of 3D printed Kevlar shields for aerospace applications. The outcome of this project is the development of repair strategies for inflatable manned modules in space and efficient small satellite shields. The second project describes the use of cold-welding phenomenon for spacecraft repair, in collaboration with South East Technological University (SETU), Ireland. The project aims to develop an experimental test rig to apply custom repair patches of different materials to pre-damaged metallic structures and monitor the performance of the adhered joint in low orbit and during re-entry. The third project presents a collaboration between MCAST and the University of Padova to develop a single stage Light-Gas Gun (LGG) impact facility in Malta. Finally, the paper discusses MCAST's participation in Malta's third space bioscience experiment launched to the International Space Station led by the University of Malta. The experiment aims to investigate how microgravity affects the behaviour of foot ulcer microbiomes in Type 2 Diabetes Mellitus patients. The project marks a significant milestone for both MCAST and the University of Malta. The projects presented in this paper reflect MCAST's commitment to contribute to the advancement of the aerospace industry and offer new opportunities for research, development, and commercialization.

Introduction

Over the past years, Malta has emerged as a promising player in the Space Sector, positioning itself as one of the up-and-coming nations in this field. This progress is underscored by Malta's Cooperation Agreement with the European Space Agency (ESA) on in 2012, aimed at establishing a framework for enhanced collaboration in ESA projects [1]. With its strategic location, access to the European Union (EU) market, administration and human capital, Malta presents a very good opportunity for the commercialization of space exploration. Guided by the central government, the Malta Council for Science and Technology (MCST) has taken on the crucial role of coordinating and governing space-related matters in the country since the signing of the Cooperation Agreement. MCST's Space Directorate actively fosters connections with foreign space agencies,



the Maltese government, businesses, and educational institutions. Recognizing the potential for space exploration to become a pillar of Malta's economy, the government has outlined its commitment through the National Space Strategy 2022. Drawing inspiration from the success achieved in the aviation sector and incorporating best practices from other countries, this strategy encompasses a wide range of initiatives undertaken in the Maltese space sector. It focuses on upstream and downstream activities and examines the economic possibilities for Malta. Furthermore, it is noteworthy that Malta is set to join the ESA Plan for European Cooperating States (PECS) in 2024, further solidifying its commitment to and integration with the European space community. In light of these developments, this paper aims to present a comprehensive analysis of the aerospace activities carried out at the Malta College of Arts, Science and Technology (MCAST) in Malta, in particular in the field of protection of aerospace structures and systems from space debris impacts. Section 2 will present the development of 3D printed Continuous Aramid Fibers (Kevlar^R) based shields for aviation and aerospace applications, Section 3 the use of cold-welding adhesion for spacecraft repairing, Section 4 presents a collaboration to develop a single stage Light-Gas Gun (LGG) impact facility in Malta and Section 5 provides an overview of Maleth 3 mission that was onboard the International Space Station.

Smart ballistic optimization for repairing of aerospace structures using 3d printed Kevlar

The SBORAEK project introduces an innovative concept by proposing the development of shields for aviation and aerospace applications using 3D printed Continuous Aramid Fibers (Kevlar^R). In the aviation industry, maintaining the structural integrity of aircraft is crucial for ensuring satisfactory performance [2]. The availability of repair materials and time often plays a significant role in deciding whether a part should be repaired or replaced. Repairable damage by patching refers to damage exceeding the limits that can be fixed by installing splice members to bridge the affected area of a structural component. Regarding aerospace applications and protection against impacts and hull damages, regulations and strategies for mitigation are currently under scrutiny. Active and passive debris removal technologies, as well as post-mission disposal techniques, are being developed. The current state and projected evolution of the debris environment necessitate the exploration and development of shields to protect active spacecraft. In crewed International Space Station (ISS) modules, mitigation techniques include reinforced hulls and shields to reduce the risk of hull perforation and subsequent depressurization [3]. Avoidance maneuvers are also performed for detected objects above a certain size threshold that may collide with the ISS. In contrast, unmanned systems utilize simpler and more cost-effective structures such as sandwich panels to mitigate the effects of space debris impacts. However, there is ongoing research to determine the best strategy for repairing damaged spacecraft hulls and shields while in orbit. In recent years, innovative processes like additive manufacturing have found applications in the satellite industry, enabling solutions that would have been challenging or expensive to implement using traditional manufacturing techniques. For instance, within the scope of the EU H2020 ReDSHIFT project [4], new 3D printed shields were developed for the protection of microsatellites. The SBORAEK will allow to go further, this will be the first time 3D printed Kevlar structures with optimized geometry will be applied to aviation and aerospace. There is currently no system targeting the same objectives of this project. SBORAEK, Figure 1, is however made from a number of subsystems, whose technology levels are mature enough so that they can be used and integrated together. The technology used for the SBORAEK project is divided into three segments: 3D printing, optimization algorithms and design techniques for high-energy impact conditions.

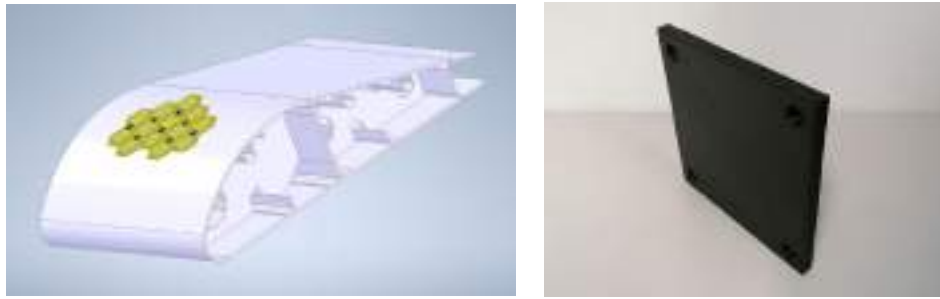


Fig 1: SBORAEK applications - Aviation structures (left), prototype spacecraft shields (right)

Cold welding adhesion for spacecraft repair

This research, in collaboration with South East Technological University (SETU), aims to explore the intentional cold-welding of metals as a method for spacecraft hull repair. This approach involves applying a repair patch to a perforated metal sample using an apparatus capable of applying combined axial and tangential forces [5]. Experimental evidence has shown that, in a near vacuum environment, cold-welding using this technique can be achieved with limited loads below 100 N. To validate this technique experimentally, it is necessary to recreate low orbit gravity and pressure conditions. The research plan consists of two phases: terrestrial experimentation and the subsequent development of an experimental payload to be tested in space. The terrestrial experimentation phase, Figure 2, establishes the primary system requirements, including perforation diameter and crater specifications, selection of material candidates for repair patches, mechanical interface design, actuation method (rotational, translational, or a combination), and applied forces. Secondary requirements encompass power needs and sensor specifications such as pressure transducers, load cells, and cameras. Currently, three non-ferrous materials are being considered as candidates: high ductility Indium foil (1-3 mm) shaped into a step tapered plug rivet, austenitic steels with a high Nickel content (Stainless Steel SS17-7PH plate), and a commonly used aerospace-grade Aluminum Alloy (AL AA-2024).

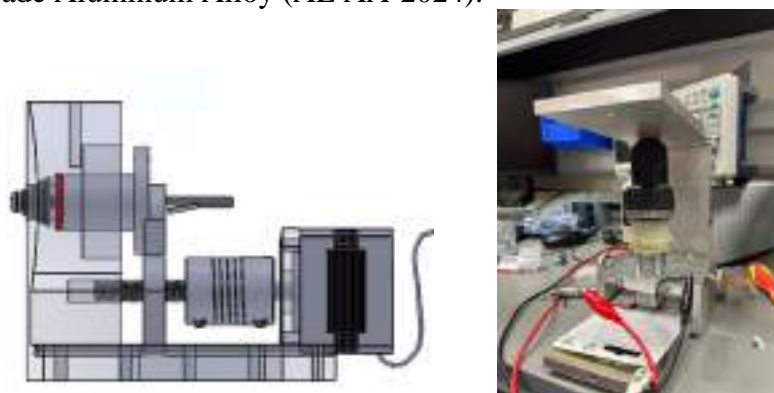


Fig 2: Test rig concept (left) and test rig prototype (right)

Single-stage Light-Gas Gun for high-velocity impacts

MCAST started a collaboration with the Center of Studies and Activities for Space (CISAS) at the University of Padova in Italy for the design of a hypervelocity research facility [6]. Considerable attention is directed towards essential components, such as the launch package and sabot-stopping system, in the construction of a hypervelocity impact facility. The launch package safeguards the projectile during acceleration, while the sabot-stopping system is responsible for terminating the sabot. Typically, Light Gas Guns (LGGs) employ an expandable sabot system to encase the

projectile. Subsequently, following the acceleration phase, the sabot separates from the projectile, fragmenting to prevent contamination of the target. However, this approach can inflict damage on the sabot-stopping system, necessitating either complete replacement or time-consuming maintenance. In order to establish a test facility capable of conducting high-velocity impact tests for the aviation and space sectors, a range of projectile velocities has been selected. This range is suitable for testing the impact of aircraft components as well as simulating low-speed impacts akin to those experienced in GEO orbit. The LGG is designed to primarily replicate impacts caused by metal impactors, particularly aluminum alloys. Its modular configuration can also be adapted to accommodate other types of projectiles, simulating space debris such as plastics and silica materials.

Maleth 3

The first-time collaboration for a space project between MCAST and the University of Malta, took place for the launch of the space bioscience experiment 'Maleth 3' on March 15th, 2023. The experiment was part of a commercial re-supply mission (CRS27) by SpaceX to the International Space Station (ISS). The objective of the experiment, titled "Microgravity effects on microbiome studies of Diabetic Patients", was to explore how microgravity influences the behavior of foot ulcer microbiomes, a major complication prevalent among patients with Type 2 Diabetes Mellitus, often requiring amputation surgeries [7]. The project entails a collaborative effort between also other institutions facilitated by Spaceomix in conjunction with Space Applications Services from Brussels, Belgium; Weill Cornell Medicine, New York, USA; King Faisal Specialist Hospital & Research Centre, Jeddah, Saudi Arabia; Metavisionaries based in Oxford, UK; and the Mohammed Bin Rashid Space Centre (MBRSC), whose astronaut is part of NASA's Crew-6 and handled Maleth 3 in space, Figure 3. The outcomes of this experiment have the potential to yield breakthroughs in life science research and treatment methods.

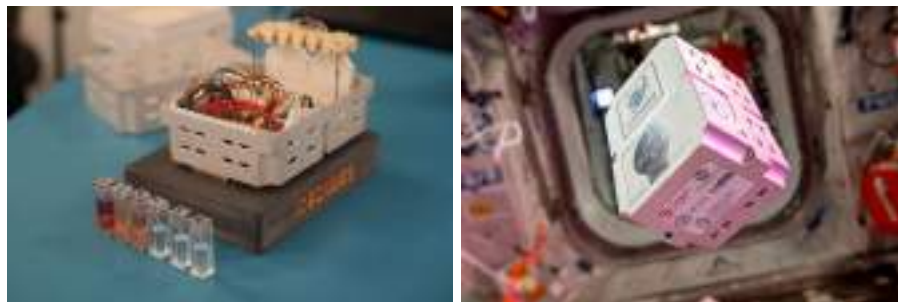


Fig 3: Maleth 3 experiment

Conclusions

This paper presented the Aerospace Program at MCAST, focusing on the protection of aerospace structures and systems from space debris impacts. The program consists of four main projects: 3D printed Kevlar shields, cold-welding for spacecraft repair, a single-stage Light-Gas Gun impact facility, and MCAST's participation in the Maleth 3 space bioscience experiment. The development of 3D printed Kevlar shields enables repair strategies for inflatable manned modules and efficient small satellite shields. Cold-welding adhesion shows promise as a method for spacecraft hull repair, with experiments conducted under near vacuum conditions. Collaboration with the University of Padova is designing a single-stage Light-Gas Gun facility for high-velocity impact testing in the aviation and space sectors. MCAST's collaboration with the University of Malta resulted in the successful launch of the Maleth 3 experiment, investigating the effects of microgravity on foot ulcer microbiomes in Type 2 Diabetes Mellitus patients. These projects

reflect MCAST's commitment to advancing the aerospace industry, contributing to research, development, and commercialization.

Acknowledgments

The work described in this paper was partially carried out as part of the SBORAEK (R&I-2022-002L) project which was financed by the Malta Council for Science & Technology, for and on behalf of the Foundation for Science and Technology, through the FUSION – Technology Development Programme LITE.

References

- [1] Malta Space strategy: <https://maltaspace.com>, last visited: 18th May 2023
- [2] Roach D., Rackow K. “Development and Validation of Bonded Composite Doubler Repairs for Commercial Aircraft”. Aircraft Sustainment and Repair (2018) pp.545-743.
<https://doi.org/10.1016/B978-0-08-100540-8.00011-X>
- [3] Barilaro L., Francesconi A. et al. “Impact damage and ballistic limit equations for flexible multilayer meteoroid and debris protection shields. ARA Congress (2010)
- [4] Rossi A. et al. “The H2020 ReDSHIFT project: a successful European effort towards space debris mitigation”. 70th International Astronautical Congress (2019)
- [5] L. Barilaro, M. Wylie, L. Olivieri, Cold welding adhesion for spacecraft repair: Experiment design and roadmap, Acta Astronautica, Vol. 210 (2023), pag 511-517.
<https://doi.org/10.1016/j.actaastro.2023.04.011>
- [6] L. Barilaro, L. Olivieri, R. Tiscio, A. Francesconi, Evaluation of a single-stage Light-Gas Gun facility in Malta: Business analysis and preliminary design, Aerotecnica Missili & Spazio 101(3) (2022). <https://doi.org/10.1007/s42496-022-00113-w>
- [7] C. Gatt et al., The Maleth Program: Malta’s first space mission discoveries on the microbiome of diabetic foot ulcers, Heliyon 8(639396) (2022).
<https://doi.org/10.1016/j.heliyon.2022.e12075>

Comparison of lattice core topologies in sandwich structures

G. Mantegna^{*1}, C.R. Vindigni¹, D. Tumino¹, C. Orlando¹, A. Alaimo¹

¹Kore University of Enna, Faculty of Engineering and Architecture, 94100 Enna, Italy

*giuseppe.mantegna@unikore.it

Keywords: Additive Manufacturing, Design for Manufacturing, Lattice Structures, Hybrid Structures

Abstract. Hybrid sandwich structures are often used in the aviation industry thanks to their high strength-to-weight ratio and resistance to bending and buckling. Today, through Additive Manufacturing technologies, it is possible to use different materials to create topology-optimized structures with complex shapes using lattice structures. In this work, a numerical approach is proposed to study the behaviour of a hybrid sandwich structure which can be used as a reinforcement for a control surface of a lightweight aircraft. A comparative analysis is conducted between a conventional honeycomb lattice core and lattice truss core structures.

Introduction

The use of sandwich structures in the aeronautics field has gained significant attention due to their high stiffness-to-weight ratio and buckling loads [1]. However, the reliability of the bond between the core and face-sheets remains a challenge, as adhesive bonding can limit the strength of the sandwich panel [2]. Additive Manufacturing (AM) allows a direct connection between the core structure and face sheets. Furthermore, thanks to its free-form tailoring ability, it is possible to create a topology-optimized core through the use of lattice cells. Multiple studies have demonstrated the structural advantages of truss core sandwich panels, which, owing to their open geometric configuration, can also be employed for multifunctional purposes. These types of structures have shown remarkable structural performance against bending and compression loads, as demonstrated by Wicks and Hutchinson [3]. Additionally, truss core sandwich panels can be used in heat transfer, such as anti-icing systems [4], and have proven effective in damping vibrations [5] and for impact absorption.

In this paper, the mechanical properties of three different lattice structures, namely lattice honeycomb, truss lattice Body Centred Cubic BCC and sine-Waved truss lattice Body Centred Cubic WBCC [6] are investigated. These lattice structures are evaluated in the context of an asymmetric sandwich core, which is intended for application in a new-generation tilt rotor control surface.

Lattice core homogenisation

In order to reduce the computational costs on the macro scale numerical analyses, the equivalent homogenised properties of the three selected lattice structures, shown in Figure 1, have been determined. All three specimens are manufactured through a standard Aluminium alloy, $E_{Al} = 71.0 \text{ GPa}$, $\nu = 0.33$ and have the same specific density $\rho^* = \text{Volume}_{cell} / \text{Volume}_{box} = 0.094$. The solid size length $L = 10 \text{ mm}$ is chosen, while the other geometric parameters are accordingly selected in order to guarantee the desired density.



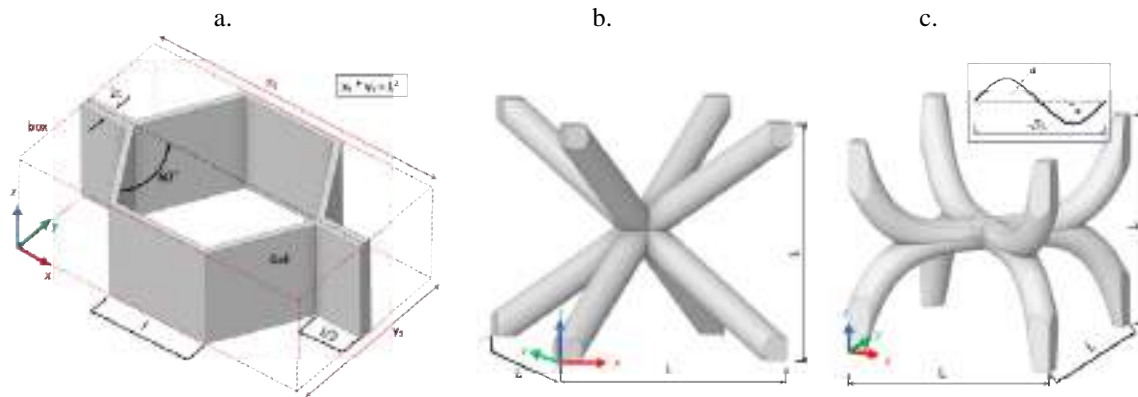


Figure 1 – Lattice cells configuration. a. Honeycomb (Hex) $l = 4.38 \text{ mm}$, $t = 0.29 \text{ mm}$, b. Body Centred Cubic (BCC) $d = 1.4 \text{ mm}$, $a = 0 \text{ mm}$, c. Waved Body Centred Cubic (WBCC) $d = 1.5 \text{ mm}$, $a = 2.0 \text{ mm}$.

The homogenised properties of the Hex cell are retrieved analytically from the work of Kumar et. al. [7], while an ad-hoc routine on Ansys Parametric Design Language (APDL) was developed for the BCC and WBCC lattice cells. More specifically, each node on the lateral faces is paired with its respective node on the opposite face through constraint equations:

$$u_{i^-} - u_{i^+} = \Delta u_p \quad (1)$$

with: u displacement along the x , y and z directions, i^- and i^+ nodes on two opposite faces sharing the same relative position. Δu_p is the difference in displacement of two pilot points chosen on the two faces.

The homogenised mechanical properties of each cell are reported in Table 1. It can be noted that the Hex and WBCC, whose material direction 3 is aligned with axis z in Figure 1, have an orthotropic behaviour.

Table 1 - Lattice cells homogenised mechanical properties.

	E_1 [Pa]	E_2 [Pa]	E_3 [Pa]	ν_{12}	ν_{23}	ν_{13}	G_{12} [Pa]	G_{23} [Pa]	G_{13} [Pa]
Hex	4.48E+07	5.10E+07	6.70E+09	9.24E-01	2.51E-03	2.21E-03	3.43E+07	1.05E+09	1.43E+09
BCC	1.11E+08	1.11E+08	1.11E+08	4.82E-01	4.82E-01	4.82E-01	9.08E+08	9.08E+08	9.08E+08
WBCC	1.61E+08	1.61E+08	1.11E+09	8.24E-01	7.46E-02	7.46E-02	8.51E+08	9.26E+07	9.26E+07

Finite element analysis comparison

To compare the mechanical properties of the three chosen lattice cores in asymmetric sandwich panels, a control surface of a new-generation Tiltrotor, illustrated in Figure 2.a, is selected. A schematic representation of the asymmetric sandwich panels placed on both the upper and lower skins is also depicted. The whole structure is modelled with two-dimensional surface elements using Ansys Composite PrepPost (ACP) module. The composite stabilizing and working skins use Epoxy-Carbon woven prepreg plies with the following properties: $E_{1,2} = 61.3 \text{ GPa}$, $E_3 = 6.9 \text{ GPa}$, $\nu_{12} = 0.04$, $\nu_{23,13} = 0.3$ and $G_{12} = 3.3 \text{ GPa}$, $G_{23,13} = 2.7 \text{ GPa}$.

In this preliminary study stage, a uniform pressure is applied to both the upper and lower skins, while displacement constraints are imposed as additional boundary conditions in accordance with the real aircraft model. The contour map deformation along the z -direction for the control surface with a honeycomb homogenised core is reported in Figure 2.b highlighting the most deformed region on the lower skin surface in accordance with the superimposed uniform load.

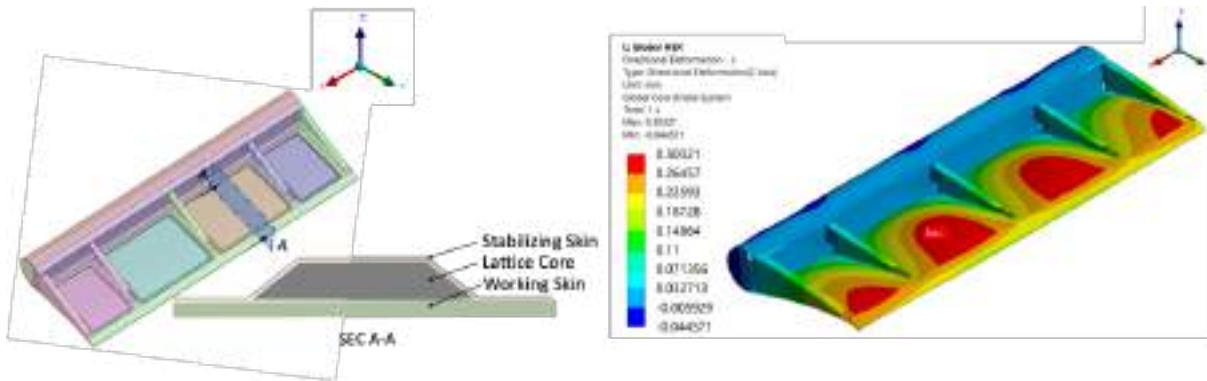


Figure 2 – a. Tiltrotor Control Surface: Schematic representation of asymmetric sandwich panel section view (Upper skin hidden). b. Hex-Core structure directional deformation [mm], z-direction (Upper skin hidden).

As shown in Table 1, the mechanical properties of the BCC cell are equivalent along the three cartesian directions; on the other hand, the WBCC, presents a preferred load direction along the three cartesian directions. For this reason, a second configuration WBCC2 is considered rotating the WBCC cell so that the material 3rd direction is parallel with global y-direction.

The z-direction displacements are investigated. Indeed, a global analysis of the homogenized core loses information on stress distribution in the lattice cell struts and the contact areas with the stabilizing and working skins. As a representative result in terms of stress, since no relevant difference appears in the four cases, Figure 3 presents the maximum stress values (σ_1) in the x-direction of the upper skin's 1st ply for the Hex configuration. No significant influence is appreciable on the σ_1 stress values at the observed layer. Figure 4 and Figure 5 show the z-direction deformation for upper and lower skins along the control surface span and chord. Overall, the Hex topology appears to be the more rigid solution, while WBCC1 is the least.

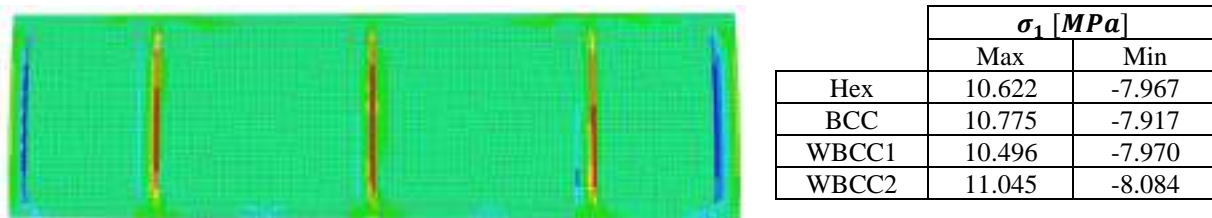


Figure 3 – Top skin 1st ply σ_1 stress contour map.

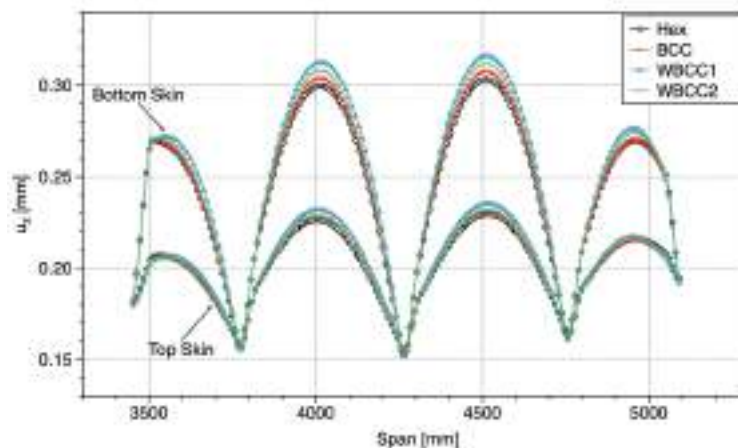


Figure 4 – Directional deformation along z-direction as a function of the control surface span. Top and Bottom skins.

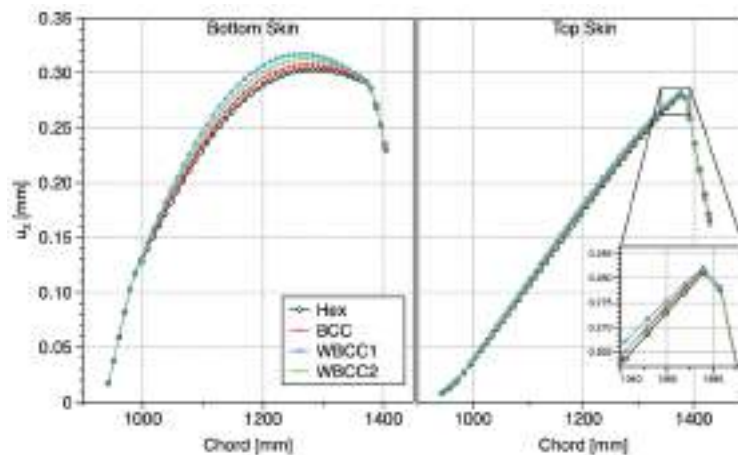


Figure 5 - Directional deformation along z -direction as a function of the control surface chord. Top and Bottom skins.

Conclusions

The DAVYD project sought novel structural configurations for the control surfaces of a new-generation tiltrotor. Various core options are proposed to reinforce the asymmetric sandwich panels. Displacements and stress contour maps indicate the potential use of topology-optimised lattice structures to enhance the overall response. Further studies will be carried out on the subject such as tailoring and optimising the orientation of the lattice cells.

Acknowledgements

The study was financially supported by M.U.R. for the DAVYD project (Grant ARS01_00940)

References

- [1] B. Castanie, C. Bouvet, and M. Ginot, "Review of composite sandwich structure in aeronautic applications," *Composites Part C: Open Access*, vol. 1, p. 100004, Feb. 2020. <https://doi.org/10.1016/j.jcomc.2020.100004>.
- [2] J. Bühring, M. Nuño, and K.-U. Schröder, "Additive manufactured sandwich structures: Mechanical characterization and usage potential in small aircraft," *Aerosp Sci Technol*, vol. 111, p. 106548, Feb. 2021. <https://doi.org/10.1016/j.ast.2021.106548>.
- [3] N. Wicks and J. W. Hutchinson, "Optimal truss plates," *Int J Solids Struct*, vol. 38, no. 30–31, 2001. [https://doi.org/10.1016/S0020-7683\(00\)00315-2](https://doi.org/10.1016/S0020-7683(00)00315-2).
- [4] C. G. Ferro, S. Varetti, G. De Pasquale, and P. Maggiore, "Lattice structured impact absorber with embedded anti-icing system for aircraft wings fabricated with additive SLM process," *Mater Today Commun*, vol. 15, 2018. <https://doi.org/10.1016/j.mtcomm.2018.03.007>.
- [5] K. Kohsaka, K. Ushijima, and W. J. Cantwell, "Study on vibration characteristics of sandwich beam with BCC lattice core," *Mater Sci Eng B Solid State Mater Adv Technol*, vol. 264, 2021. <https://doi.org/10.1016/j.mseb.2020.114986>.
- [6] D. Tumino, A. Alaimo, G. Mantegna, C. Orlando, and S. Valvano, "Mechanical properties of BCC lattice cells with waved struts," *International Journal on Interactive Design and Manufacturing (IJIDeM)*, 2023. <https://doi.org/10.1007/s12008-023-01359-9>.
- [7] A. Kumar, N. Muthu, and R. G. Narayanan, "Equivalent orthotropic properties of periodic honeycomb structure: strain-energy approach and homogenization," *International Journal of Mechanics and Materials in Design*, 2022. <https://doi.org/10.1007/s10999-022-09620-x>.

Thermal buckling analysis and optimization of VAT structures via layer-wise models

A. Pagani^{1,a,*}, E. Zappino^{1,b}, R. Masia^{1,c}, F. Bracaglia^{1,d}, and E. Carrera^{1,e}

¹Politecnico di Torino, DIMEAS, Corso Duca degli Abruzzi 24, Torino

^aalfonso.pagani@polito.it, ^benrico.zappino@polito.it, ^crebecca.masia@polito.it,

^dfrancesca.bracaglia@studenti.polito.it, ^eerasmo.carrera@polito.it

Keywords: Thermal Bucklin, Variable Angle Tow (VAT), Layer Wise (LW), High-Order Structural Theories

Abstract. The present study investigates the combination of different manufacturing parameters, such as the curvature radius of the single fiber along its path on a symmetric stacking sequence of the Variable Angle Tows composite (VAT). Moreover, the study objective is to individuate the VAT configuration to maximize the critical thermal buckling load of a thermal-loaded composite square plate. Numerical simulations are performed in the Carrera Unified Formulation (CUF) framework, which allows for a high-order two-dimensional (2D) theory based on the Finite Element Method (FEM), enabling the Layer Wise (LW) discretization of the model. The linearized buckling problem is involved in the formulation, and the resolution of the eigenvalue problem leads to finding the thermal buckling critical temperature.

Introduction

Composite materials have superior strength and stiffness properties compared to traditional materials but are often influenced by the environment. Those involving an increase in material temperature induce expansion strains, and consequently, the buckling critical load can be dramatically affected by an over-temperature. The thermal environment is particularly relevant for space applications with a consistent radiation heating. Instead, for high-speed aeronautical applications, the heating is usually imposed on the structures by the drag. Due to the applied overtemperature, buckling deflection may occur suddenly under specific load conditions, and the deformation of the plate can significantly influence the structure behavior. If a constant along the thickness temperature profile is applied, deflection occurs only at the unique critical temperature. Variable Angle Tows (VAT) materials exploit a new manufacturing technology introducing an additional degree of freedom in the fiber deposition that can follow curved shapes [1]. It is well known that VAT laminates can improve buckling performance compared to classical composites [2]. Furthermore, thermal buckling has been deeply studied for all the materials that can be subjected to thermal environments [3]. The present work focuses on the fiber deposition optimization of a thermally-loaded square plate to retard the thermal buckling phenomenon. The plate theory is applied within the Carrera Unified Formulation (CUF) framework combined with the Finite Element Method (FEM) approximation [4]. Different kinematic theories are employed, and the results are compared and discussed.

Model description

The decoupled approach is employed to describe the thermal problem. The primary variables of the problem are the displacements, denoted by \mathbf{u}^T :

$$\mathbf{u}^T(x, y, z) = (\mathbf{u}_x, \mathbf{u}_y, \mathbf{u}_z) \quad (1)$$



where the symbol T denotes transposition. As reported in Eq. (2), the strains $\boldsymbol{\varepsilon}$ can be obtained from the displacement by the geometrical relations using the non-linear differential operator \boldsymbol{b} . The stresses $\boldsymbol{\sigma}$ are calculated from the strains through the Hooke's law, by applying the material properties matrix \boldsymbol{C} as in Eq. (3). Note that in the VAT case, the matrix \boldsymbol{C} depends on the local fiber orientation and is not globally defined as in the case of classical configuration.

$$\boldsymbol{\varepsilon} = (\varepsilon_{xx}, \varepsilon_{yy}, \varepsilon_{zz}, \varepsilon_{xz}, \varepsilon_{yz}, \varepsilon_{xy})^T = \boldsymbol{b} \boldsymbol{u} \quad (2)$$

$$\boldsymbol{\sigma} = (\sigma_{xx}, \sigma_{yy}, \sigma_{zz}, \sigma_{xz}, \sigma_{yz}, \sigma_{xy})^T = \boldsymbol{C} \boldsymbol{\varepsilon} \quad (3)$$

The CUF introduces an indicial notation where the three-dimensional displacements are divided into two components, the first $\boldsymbol{F}_\tau(z)$ denotes the kinematic expansion function, and the second $\boldsymbol{u}_\tau(x, y)$ is the in-plane unknown vector. Furthermore, the FEM is employed, and $\boldsymbol{u}_\tau(x, y)$ can be expressed by combining the shape functions $\boldsymbol{N}_i(x, y)$ and the nodal displacement vector $\boldsymbol{q}_{i\tau}$ as represented in Eq. (4).

$$\boldsymbol{u}(x, y, z) = \boldsymbol{F}_\tau(z) \boldsymbol{u}_\tau(x, y) = \boldsymbol{F}_\tau(z) \boldsymbol{N}_i(x, y) \boldsymbol{q}_{i\tau} \quad \tau = 1, 2, \dots, M \quad i = 1, 2, \dots, N_n \quad (4)$$

where the double index means sum, M is the number of expansion terms, and N_n is the number of nodes. Via the CUF, high-order theories are employed to describe the in-thickness behavior of the analyzed plate, and among the various theories, Taylor Expansion (TE) and Lagrange Expansion (LE) functions are selected as $\boldsymbol{F}_\tau(z)$ for the present investigation. Furthermore, the laminate properties are described with the Equivalent Single Layer (ESL) approach in the TE case and using the Layer Wise (LW) approach in LE models.

The CUF allows an invariant formulation of the problem using the Fundamental Nuclei (FN) that are not formally mutated with the employed expansion or on the number of nodes [4]. The indicial notation lets the problem governing equation building. In the case of buckling, using the PVD, as reported in Eq. (5), to obtain a linearized formulation of the governing equation based on the tangent stiffness matrix \boldsymbol{K}_T is possible. Where \boldsymbol{K}_T is expressed in terms of FN, the complete procedure can be found in [5].

$$\delta^2(L_{int}) = \int_V \delta(\delta \boldsymbol{\varepsilon}^T \boldsymbol{\sigma}) dV = \delta \boldsymbol{q}_{sj}^T \boldsymbol{K}_T^{ij\tau s} \delta \boldsymbol{q}_{\tau i} = \delta \boldsymbol{q}_{sj}^T (\boldsymbol{K}_0^{ij\tau s} + \boldsymbol{K}_\sigma^{ij\tau s}) \delta \boldsymbol{q}_{\tau i} \quad (5)$$

The buckling critical temperature is considered coincident with the bifurcation point, which is the load point where two equilibrium configurations exist. As a result, an eigenvalue problem must be solved to obtain the critical load:

$$|\boldsymbol{K}_0 + \lambda_{cr} \boldsymbol{K}_\sigma| = 0 \quad (6)$$

Due to the linear approximation, the matrix \boldsymbol{K}_σ is supposed to be proportional to λ_{cr} , which is the buckling critical load factor. \boldsymbol{K}_σ is the geometric stiffness matrix strictly dependent on the internal pre-stress state due to the thermal over-temperature load.

Numerical results

In the present section, some numerical results about thermal buckling are presented. The VAT deposition angles are changed to obtain the best configuration retarding the buckling critical thermal load. Eq. (7) describes the fiber orientation θ . It depends on the three angles Φ , T_0 , and T_1 , which are, the reference system rotation angle, the fiber orientation in the center of the plate and,

the angle at the edge, respectively. The symbol d denotes a characteristic distance, and x' is the new reference direction [1].

$$\theta = \Phi + T_0 + \frac{T_1 - T_0}{d} x' \quad (7)$$

For the sake of simplicity, only T_0 and T_1 are changed during the optimization with Φ equal to zero, the stacking sequence is fixed at $[\theta/-\theta]_s$, and the plate is simply supported. The square plate has 150 mm edges and 1.016 mm thickness, and a one-degree constant over-temperature is applied on the whole plate. Two plates are analyzed, the first composed of Carbon/Epoxy whose properties are $E_1 = 147$ GPa, $E_2 = 10.3$ GPa, $\nu_{12} = 0.27$, $G_{12} = 7.0$ GPa, $\alpha_1 = -0.9 \times 10^{-6}$ 1/K, $\alpha_2 = 27.0 \times 10^{-6}$ 1/K. The second plate is E-Glass/Epoxy with $E_1 = 41$ GPa, $E_2 = 10.04$ GPa, $\nu = 0.28$, $G_{12} = 4.3$ GPa, $\alpha_1 = 7.0 \times 10^{-6}$ 1/K, $\alpha_2 = 26.0 \times 10^{-6}$ 1/K. Each plate presents a discretization of 20x20 Q9 in-plane elements, 2nd order TE and 3rd order LE are employed as expansion functions.

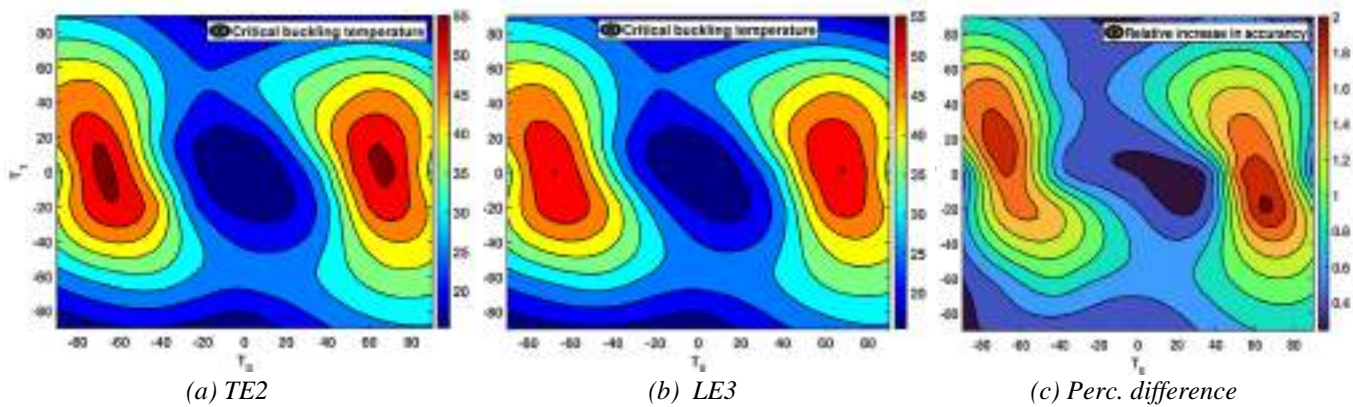


Figure 1: (a), (b) Carbon/Epoxy critical buckling temperature varying the path angles, 20 x 20 Q9 in plane mesh. (a): Present method with ESL and TE2, (b) Present method with LW and LE3. (c) Percentage relative increasing accuracy from LE to TE2 ($\frac{\theta_{TE} - \theta_{LE}}{\theta_{TE}} \times 100$). Carbon/Epoxy.

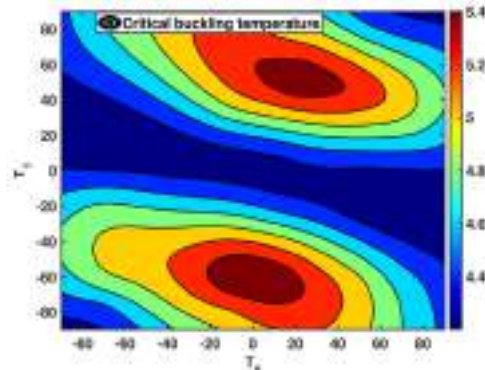


Figure 2: E-Glass/Epoxy critical buckling temperature varying the path angles, 20 x 20 Q9 in plane mesh, Present method with LW and LE3.

Table 1: Maximum critical buckling temperature for VAT and straight configuration with $\theta = 45^\circ$.

	T_0	T_1	ΔT_{cr}	$\Delta T_{straight}$
<i>Carbon/Epoxy</i>				
<i>20x20 Q9 LE3</i>	-68.29°	0.45°	55.11°	41.32°
<i>20x20 Q9 TE2</i>	-67.39°	0.45°	56.27°	41.87°
<i>Ref. [6]</i>	69.00°	-5.71°	57.79°	42.21°
<i>E-Glass/Epoxy</i>				
<i>20x20 Q9 LE3</i>	-4.97°	-60.15°	5.55°	5.38°
<i>Ref. [6]</i>	6.71°	58.04°	5.58°	5.43°

Conclusions

- As expected, the thermal buckling critical temperature graphs are symmetric to the line $T_0 = -T_1$ and present two maximum value zones for both configurations (Fig.1 and 2).
- Considering the adopted expansion theory, the 2nd-order TE model is more similar to the reference. Still, the LE model is more accurate even if it presents a greater computational cost. As depicted in Fig.1(c), the main difference is not in the critical temperature but mainly in the extension of the optimal zones. As a result, the zones with maximum temperature are abruptly reduced in the LE model reported in Fig.1(b) than in the less accurate model in Fig.1(a).
- Figure 1(c) clarifies that the increase in accuracy due to the LE model is not constant comparing different orientations angle but rises with the increase in the critical temperature.
- For the Carbon/Epoxy laminate, as collected in Table 1, the better path configuration allows reaching a critical over-temperature of 55.1° with a consistent gain to the straight deposition critical temperature of 41.3°.
- From Table 1 it is clear that E-Glass/Epoxy configuration does not present significant advantages using VAT deposition with a gain of 0.03% passing from a critical temperature of 5.384° to 5.55° in the VAT case.
- In the end, the choice of VAT deposition may be helpful to retard the buckling critical load, and, in Carbon/Epoxy case, the gain is more evident than in the Glass/Epoxy plate.

References

- [1]. *Accurate stress analysis of variable angle tow shells by high-order equivalent-single-layer and layer-wise finite element models*. A. R. Sánchez-Majano, R. Azzara, A. Pagani, E. Carrera. S. l.: Materials, 14(21), 2021. <https://doi.org/10.3390/ma14216486>
- [2]. *Prebuckling and buckling analysis of variable angle tow plates with general boundary conditions*. G. Raju, Z. Wu, B. C. Kim, P. M. Weaver. s.l.: Composite Structures.
- [3]. *Mechanical and thermal buckling loads of rectangular FG plates by using higher-order unified formulation*. M. Farrokh, M. Afzali. E. Carrera. s.l.: E. Mechanical of Advanced Materials and Structures, 2019.
- [4]. *Finite Element Analysis of Structures through Unified Formulation*. E. Carrera, M. Cinefra, M. Petrolo, E. Zappino. s.l.: Wiley & Sons, 2014.
- [5]. *Geometrically nonlinear refined shell theories by Carrera Unified Formulation*. B. Wu, A. Pagani, W. Q. Chen, E. Carrera. s.l.: Mechanics of Advanced Materials and Structures, 2021.
- [6]. *Thermal buckling of composite plates with spatial varying fiber orientation*. A. V. Duran, N. A. Fasanella, V. Sundararaghavan, A. M. Waas. s.l.: Composite Structures, 2015.

Surface node method for the peridynamic simulation of elastodynamic problems with Neumann boundary conditions

Francesco Scabbia^{1,a,*}, Mirco Zaccariotto^{1,2,b} and Ugo Galvanetto^{1,2,c}

¹Centro di Ateneo di Studi e Attività Spaziali “Giuseppe Colombo” (CISAS), Università degli Studi di Padova, Padova, 35131, Italy

²Industrial Engineering Department (DII), Università degli Studi di Padova, Padova, 35131, Italy

^afrancesco.scabbia@phd.unipd.it, ^bmirco.zaccariotto@unipd.it, ^cugo.galvanetto@unipd.it

Keywords: Peridynamics, Surface Node Method, Elastic Wave Propagation, Neumann Boundary Conditions

Abstract. Peridynamics is a nonlocal theory that can effectively handle discontinuities, including crack initiation and propagation. However, near the boundaries, the incomplete nonlocal regions are the cause of the peridynamic surface effect, resulting in unphysical stiffness variation. Additionally, imposing local boundary conditions in a peridynamic (nonlocal) model is often necessary. To address these issues, the surface node method has been proposed for improving accuracy near the boundaries of the body. Although this method has been verified for a variety of problems, it has not been applied for elastodynamic problems involving Neumann boundary conditions. In this work we show a numerical example of this case, comparing the results with the corresponding peridynamic analytical solution. The numerical results exhibit no stiffness variations near the boundaries throughout the entire simulation timespan. Therefore, we conclude that the surface node method allows to effectively solve elastodynamic peridynamic problems involving Neumann boundary conditions, with improved accuracy near the boundaries.

Introduction to peridynamics

Peridynamics (PD) is a nonlocal continuum theory based on integro-differential equations in which discontinuities, such as cracks, in the displacement field can arise and evolve without mathematical inconsistencies [1,2]. In a PD body B , two points interact through a so-called *bond* if their distance is smaller than δ , named *horizon size*. The PD equation of motion for a generic point x at a time instant t in a 1D, homogeneous, linear elastic body [3] is given as

$$\ddot{u}(x, t) = v^2 \int_{H_x} \frac{u(x', t) - u(x, t)}{\delta(x' - x)^2} dx', \quad (1)$$

where $H_x = \{x' \in B: |x' - x| \leq \delta\}$ is the set of points x' interacting with point x , u is the displacement, \ddot{u} is the acceleration, and v is the wave speed.

By using the meshfree method with a uniform grid spacing Δx [4], in which every node represents a cell of length Δx (see Fig. 1), Eq. 1 is discretized in space as

$$\ddot{u}(x_i, t) = \frac{v^2}{\delta} \sum_{j \in H_i} \frac{u(x_j, t) - u(x_i, t)}{(x_j - x_i)^2} \beta_{ij} \Delta x, \quad (2)$$

where x_i and x_j are respectively the coordinates of node i and any node j within the neighborhood H_i of node i , and β_{ij} is the quadrature coefficient, namely the fraction of cell of node j which lies within the neighborhood H_i [5]. The explicit central difference method is used for time integration [4]:



$$u(x_i, t_{n+1}) = 2u(x_i, t_n) - u(x_i, t_{n-1}) + \frac{(v\Delta t)^2}{\delta} \sum_{j \in H_i} \frac{u(x_j, t) - u(x_i, t)}{(x_j - x_i)^2} \beta_{ij} \Delta x, \quad (3)$$

where Δt is the time step size and n stands for the index of the current time step.

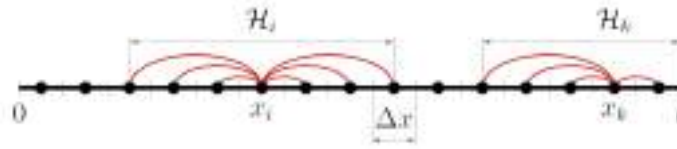


Figure 1: Each node (black dots) in the peridynamic body represents a cell of length Δx and interacts with all the nodes within its neighborhood through bonds (red lines).

As shown in Fig. 1, the nodes near the boundary of the body have an incomplete neighborhood. Due to this fact, the stiffness properties of the nodes close to the boundary are different from those of the nodes in the bulk. This undesired phenomenon is called *PD surface effect* [6-9]. Furthermore, boundary conditions in PD models should be imposed over a finite-thickness layer, in contrast with experimental measurements which are performed only at the boundary. Therefore, we use the Surface Node Method (SNM) to solve these issues [7-9].

Overview of the Surface Node Method

As shown in Fig. 2, the *fictitious nodes* (empty dots) are added in the peridynamic model to complete the neighborhoods of the interior nodes near the boundaries of the body. Furthermore, the *surface nodes* (solid squares) are introduced at the boundaries of the body to impose the boundary conditions.

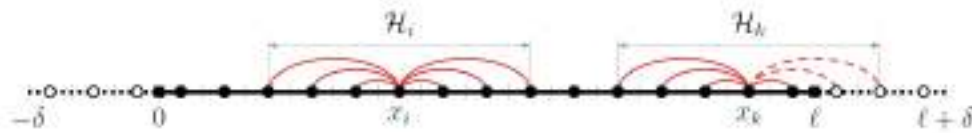


Figure 2: The fictitious nodes (empty dots) are introduced to reduce the PD surface effect by completing the neighborhoods of the interior nodes (solid dots). The surface nodes (solid squares) are introduced to impose the peridynamic boundary conditions through the fictitious bonds (red dashed lines).

The displacements of the fictitious nodes are determined by extrapolation from the displacements of the interior nodes. By using, for example, the linear Taylor-based method [7-9], the displacement of any fictitious node f is given as

$$u(x_f, t_n) = u(x_s, t_n) + (x_f - x_s) \frac{u(x_s, t_n) - u(x_p, t_n)}{x_s - x_p}, \quad (4)$$

where s is the index of the closest surface node and p is the index of the interior node closest to that surface node.

The surface nodes do not have interactions (bonds) with other nodes, the state of the fictitious bonds crossing them is governed by the equation of the force flux [7-9]:

$$\tau(x_s, t_n) = \frac{v^2}{\delta} \sum_{ij \in I} \frac{u(x_j, t_n) - u(x_i, t_n)}{(x_j - x_i)^2} \beta_{ij} \Delta x^2, \quad (5)$$

where $\tau(x_s, t_n)$ is the force flux at the surface node s and I is the set of all the fictitious bonds with positive direction crossing the boundary at x_s . Thanks to Eq. 5, constraints and loads can be applied to the surface nodes as one would do in a local model.

Numerical example

For the first time, we present a numerical example of a peridynamic model making use of the SNM to solve an elastodynamic problem involving Neumann boundary conditions. The initial boundary value problem is given as

$$\begin{cases} \ddot{u}(x, t) = \frac{v^2}{\delta} \int_{H_x} \frac{u(x', t) - u(x, t)}{(x' - x)^2} dx' & \text{for } 0 < x < \ell, \ t > 0, \\ u(0, t) = 0, \ \tau(\ell, t) = 0 & \text{for } t > 0, \\ u(x, 0) = 0.02e^{-100\left(\frac{x-0.5}{\ell}\right)^2}, \ \dot{u}(x, 0) = 0 & \text{for } 0 < x < \ell, \end{cases} \quad (6)$$

where \dot{u} is the velocity and ℓ is the length of the peridynamic body. The analytical solution is computed by means of the method of separation of variables [3]:

$$u(x, t) = \sum_{m=1,3,5,\dots}^{\infty} \frac{0.004\sqrt{\pi}}{\ell} \sin\left(\frac{k_m \ell}{2}\right) e^{\frac{-k_m^2}{400}} \sin(k_m x) \cos\left(vt \sqrt{\frac{2}{\delta^2} [k_m \delta \text{Si}(k_m \delta) + \cos(k_m \delta) - 1]}\right), \quad (7)$$

where $k_m = \frac{m\pi}{2\ell}$ and $\text{Si}(\cdot)$ is the sine integral function. The analytical solution in Eq. 7, truncated at $m = 80$, will be used as a comparison for the numerical results in Fig. 3.

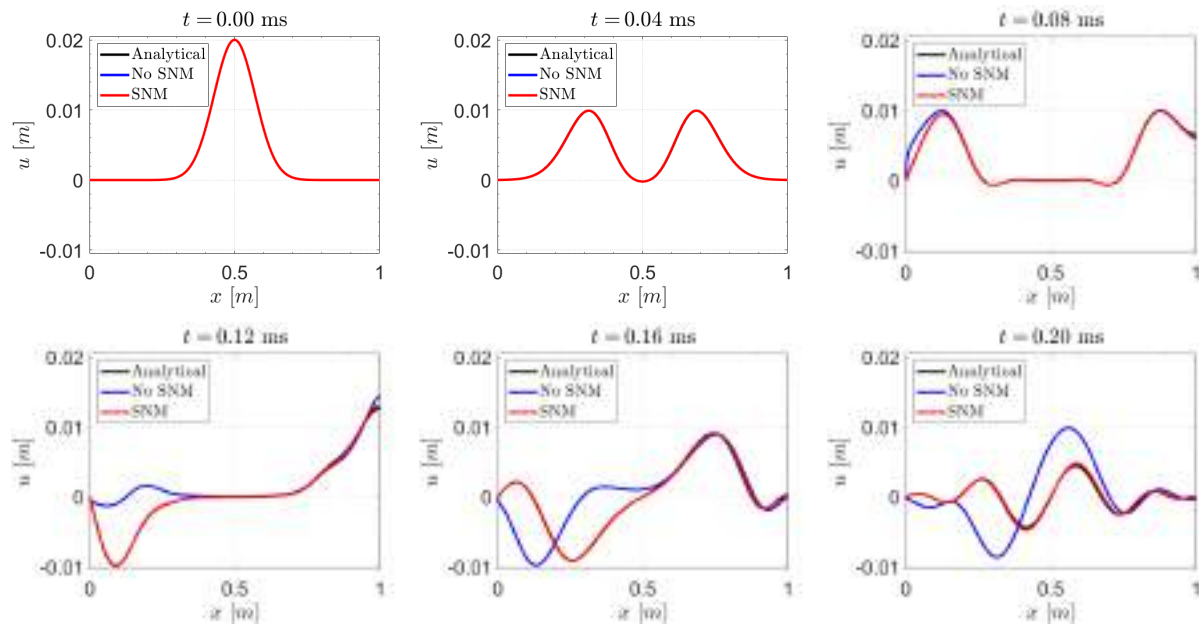


Figure 3: Plots of the propagating wave at different instants of time t for the analytical solution and the peridynamic models with and without the use of the Surface Node Method (SNM).

Fig. 3 shows the numerical results of the peridynamic model with and without the use of the SNM. If the SNM is not employed, the loads and the constraints are applied directly to the interior nodes closest to the boundary. The model parameters used to obtain those results are the following: $v = 5000$ m/s, $\ell = 1$ m, $\delta = 0.1$ m, $\Delta x = 0.001$ m, and $\Delta t = 0.2$ μ s. As shown in Fig. 3, it is evident that the model with the SNM provides results closer to the analytical peridynamic solution. The major differences are noticeable in the region near the end of the bar, where Dirichlet boundary conditions are imposed. However, without employing any boundary correction, non-negligible errors are also present at the other end of the bar, where Neumann boundary conditions are applied. Thus, the SNM allows to considerably reduce the numerical errors due to the PD surface effect and the imposition of the boundary conditions.

Conclusions

In this work, we numerically solved a 1D peridynamic elastodynamic problem involving Neumann boundary conditions by using the Surface Node Method (SNM) to mitigate the PD surface effect and impose the boundary conditions. The analytical solution to this problem has been derived thanks to the method of separation of variables. The numerical results show that the use of the SNM significantly reduces the errors near the boundaries of the body when compared to the corresponding model without boundary corrections, both where Dirichlet and Neumann boundary conditions are applied.

Acknowledgements. The authors would like to acknowledge the support they received from MIUR under the research project PRIN2017-DEVISU and from the University of Padova under the research project BIRD2020 NR.202824/20.

References

- [1] S.A. Silling, Reformulation of elasticity theory for discontinuities and long-range forces, *J. Mech. Phys. Solids* 48 (2000) 175-209. [https://doi.org/10.1016/S0022-5096\(99\)00029-0](https://doi.org/10.1016/S0022-5096(99)00029-0)
- [2] S.A. Silling, M. Epton, O. Weckner, J. Xu, E. Askari, Peridynamic states and constitutive modelling, *J. Elast.* 88 (2007) 151-184. <https://doi.org/10.1007/s10659-007-9125-1>
- [3] Z. Chen, X. Peng, S. Jafarzadeh, F. Bobaru, Analytical solutions of peridynamic equations. Part II: elastic wave propagation, *Int. J. Eng. Sci.* 188 (2023). <https://doi.org/10.1016/j.ijengsci.2023.103866>
- [4] S.A. Silling, E. Askari, A meshfree method based on the peridynamic model of solid mechanics, *Comput. Struct.* 83 (2005) 1526-1535. <https://doi.org/10.1016/j.compstruc.2004.11.026>
- [5] F. Scabbia, M. Zaccariotto, U. Galvanetto, Accurate computation of partial volumes in 3D peridynamics, *Eng. Comput.* 39 (2023) 959-991. <https://doi.org/10.1007/s00366-022-01725-3>
- [6] Q.V. Le, F. Bobaru, Surface corrections for peridynamic models in elasticity and fracture, *Comput. Mech.* 61 (2018) 499-518. <https://doi.org/10.1007/s00466-017-1469-1>
- [7] F. Scabbia, M. Zaccariotto, U. Galvanetto, A novel and effective way to impose boundary conditions and to mitigate the surface effect in state-based Peridynamics, *Int. J. Numer. Methods. Eng.* 122 (2021) 5773-5811. <https://doi.org/10.1002/nme.6773>
- [8] F. Scabbia, M. Zaccariotto, U. Galvanetto, A new method based on Taylor expansion and nearest-node strategy to impose Dirichlet and Neumann boundary conditions in ordinary state-based Peridynamics, *Comp. Mech.* 70 (2022) 1-27. <https://doi.org/10.1007/s00466-022-02153-2>
- [9] F. Scabbia, M. Zaccariotto, U. Galvanetto, A new surface node method to accurately model the mechanical behavior of the boundary in 3D state-based Peridynamics, *J. Peridyn. Nonlocal Model* (2023) 1-35. <https://doi.org/10.1007/s42102-022-00094-1>

Crack localization on a statically deflected beam by high-resolution photos

Andrea Vincenzo De Nunzio^{1,a*}, Giada Faraco^{1,b*}
Nicola Ivan Giannoccaro^{1,c} and Arcangelo Messina^{1,d}

¹Dipartimento di Ingegneria dell'Innovazione, Università del Salento, 73100 Lecce (LE), Italia

^aandrea.vincenzo.denunzio@unisalento.it, ^bgiada.faraco@unisalento.it,

^civan.giannoccaro@unisalento.it, ^darcangelo.messina@unisalento.it

Keywords: Structural Health Monitoring, Crack Detection, Image Processing, Optical Measurements

Abstract. In a context where the complexity of systems and their interconnection is increasing exponentially, the possibility of being able to monitor the structural integrity of crucial parts of structures is of considerable importance. In addition, the availability of modern and advanced tools opens the door to the advent of new diagnostic techniques. In this regard, the authors here deeply investigate and test a modern technique that allows to analyze a structure starting from a photo in order to identify and locate damage present in the structure in a rapid and non-destructive way. This allows to obtain an accurate location of the damage and consequently a quick evaluation of its state of integrity. Moreover, a further advantage lies in the possibility of carrying out the analysis in a non-invasive way without any physical interaction with the analyzed structure. The suitability of the technique is tested on a statically deformed beam in epoxy glass laminate. It has a notch, which represents the defect, and the goal is to determine the notch position, which is not visible in the photo. The basis of the proposed method is the correlation between the curvature that the beam presents under load conditions and its flexural stiffness. The damage on the beam, in fact, leads to a punctual alteration of its flexibility which is identified by sudden changes in the second derivative of the transversal deflection. The proposed methodology consists in taking a photo of the inflected beam; subsequently, the acquired photo is manipulated with specifically designed image processing tools, first to segment the beam shape and then to extract its axis. Finally, the second derivative is extracted using two different numerical differentiator filters (Lanczos filters and Gaussian wavelets) along with suitable processing to reduce the border distortions. The tests conducted demonstrate that it is possible to accurately detect the position of the notch. Although the authors realize that the technique can generally need sensibly large displacements, the results seem promising. Such a need is probably due to the resolution of the camera, which can sometimes represent a technological limit. It is believed that higher resolution would allow damage to be detected even for smaller displacements. A fundamental advantage is the speed of the methodology illustrated since it takes just a few moments from taking the photo to evaluating the results. This is accompanied by the ease of acquiring the measurement, which involves the use of the camera and its support without additional equipment.

Introduction

Structural health monitoring (SHM) is a crucial aspect of ensuring the safety and reliability of various engineering mechanical structures such as buildings, bridges etc. The ability to detect, assess, and manage structural degradation or damage is essential for preventing catastrophic failures and minimizing risks. SHM techniques generally consist in collecting data related to structure behavior, load distribution, vibrations, and material properties to analyze using sophisticated algorithms and models to detect any abnormalities or signs of deterioration [1].



Advantages of computer vision for SHM are several [2,3]: they are generally inexpensive, contactless, non-destructive and allow for the assessment of structural integrity without the installation of sensors directly on the structure, unlike traditional techniques that rely on data collection through accelerometers or strain gauges. Given the advantages, it is not surprising that vision-based SHM techniques are not limited to civil engineering structures but can also be extended to mechanical components (such as beam-type structures) characterized by operational conditions significantly different from those in civil engineering, such as small displacements and high vibration frequencies.

A computer-vision technique is adopted in [4–6] where a computer vision method for measuring the in-plane displacement field of cantilever beams is presented. The purpose of these articles is to carry out a structural health analysis starting from the deformed shape of the beam (acquired by the vision-based algorithm) by exploiting different damage detection techniques: second derivative algorithm, line segment algorithm and voting algorithm in [4], fractal dimension, wavelet transform and roughness methods in [5,6].

The authors' intent in this study is to develop and evaluate the potential of a vision-based method for SHM and damage detection. To achieve this goal, an algorithm was first developed to extract the deformation axis of a deflected beam starting from a photo of it. Then the acquired information is used as input for the damage detection procedure. Its basis is the correlation between the curvature that the beam exhibits under load conditions, and its flexural stiffness (e.g. [7,8]). The damage on the beam results in a localized change in its flexibility, manifesting as abrupt variations in the second derivative of the transverse deflection. Therefore, the proposed methodology can be summarized in two parts: first the acquisition and processing of the photo to extract the axis of the deformed beam, and second, the damage detection using the second derivative method. To conclude, the effectiveness of the proposed method was tested in the laboratory on a beam of which the structural integrity had already been evaluated in a previous study [9]. Furthermore, this allowed for a comparison between a traditional data acquisition methodology (PSD-triangular laser sensor) and a vision-based data acquisition technique.

Materials and Methods

The proposed methodology was tested on an epoxy glass laminate beam with dimensions equal to 500 x 10 x 25 mm; a notch, 2 x 5 x 25 mm, is made at 265 mm from the beam clamped end to simulate the damage.

With the purpose of evaluating suitability of the vision-based data acquisition methodology compared to a classical one (results are available in [9]), the beam was statically deformed to emulate its second mode shape.

The experimental setup (Fig. 1a) was composed by a frame, in which the beam was clamped at one end, two operating screws to impose the deflection shape, and a consumer-grade camera (Canon EOS 1200D) fixed on a tripod. Black cardboard was used as the background to make the beam more visible and to improve the segmentation processing.

The beam was deformed by setting its maximum displacements equal to those measured in [9]; subsequently, such an initial deflection was amplified by 2, 4, 6 and 10 times to test the method sensitivity.

In order to take non-distorted photos, camera calibration was carried out by the Matlab Camera Calibrator Toolbox.

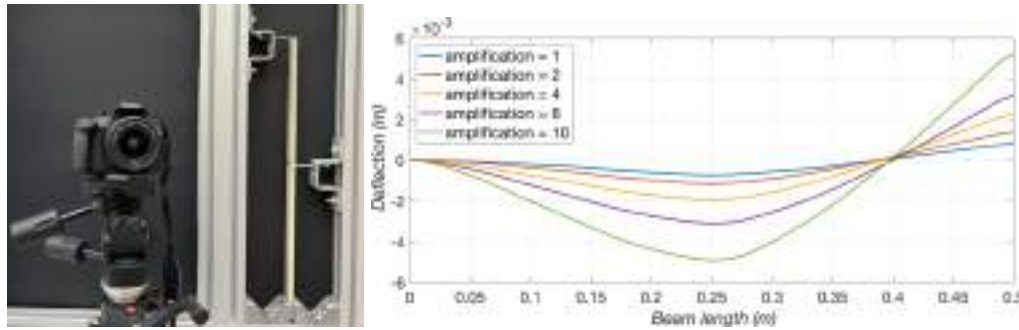


Figure 1: experimental setup (a) and extracted axis (b)

The segmentation algorithm was implemented in Matlab. Its output is a mask in which the beam is the foreground. The beam axis extraction algorithm is applied to this mask; such a procedure employs a $2\Delta_m \times 2\Delta_n$ pixel window moving along the beam profile by one pixel per step. At every iteration the axis point coordinates (in pixels) are calculated by (1):

$$(x_P, y_P) = \left(\frac{m_{max} + m_{min}}{2}, \frac{\sum_{i=1}^{4 \cdot \Delta_m \cdot \Delta_n} I_i \cdot n_i}{\sum_{i=1}^{4 \cdot \Delta_m \cdot \Delta_n} I_i} \right) \quad (1)$$

where m_{max} and m_{min} are the coordinates, along the beam axis direction, of the extreme pixels of the window, n_i is the coordinate of the i -th pixel in the transversal direction and I_i its intensity. Afterwards, a scale factor S [10] transformed pixel-coordinates into physical units [m]; in particular, photos having a resolution equal to 5184×3456 pixels produced $S \sim 0.1$ mm/pixels.

This procedure allowed the extraction of the bent beam axis $y(x)$ (Fig. 1) which was subsequently processed to estimate its second derivative (Fig. 2).

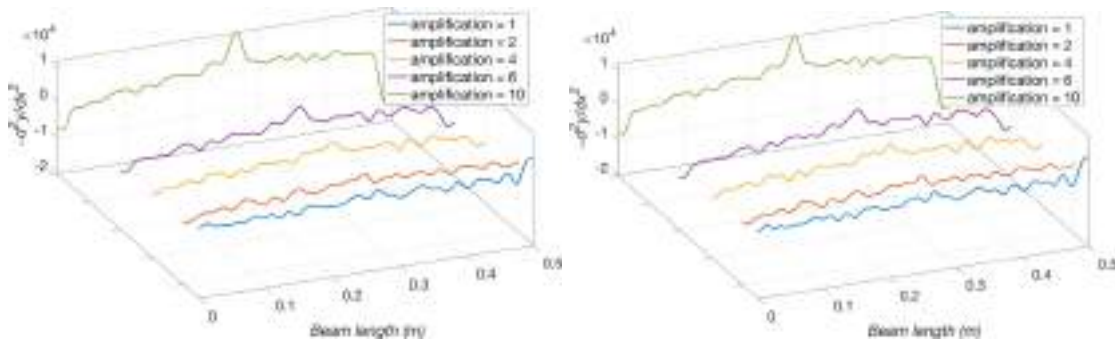


Figure 2: 2nd order derivative calculated by Lanczo's filter (a) and Continuous Wavelet Transform (b)

In particular, Figure 2 shows the second derivatives estimated with two different differentiator filters, i.e. Figure 2(a) represents the estimate through the Lanczos filter [11,12] while the estimate in Figure 2(b) is obtained by means of the continuous wavelet transform [12]. In both cases the second derivative was obtained by performing the numerical convolution (*) of the bent beam $y(x)$ twice through the respective filters of first derivative (h_1 in (2)). This to extend the physical signal through the *Rotation* option for each convolution step for reducing distortions at the edges [13]. Therefore, the following formula was applied for both filters.

$$\frac{d^2y}{dx^2} \cong h_1 * (h_1 * y_{ext})_{ext} \quad (2)$$

The length of the filters was calibrated through dilation parameters which provided similar performance to reject the experimental/numerical noise.

Results

It was observed that the displacements of the reference deformation [9] did not initially allow the damage to be identified with the proposed method. At least, this has been the case with the experimental setup herein used. Sensitivity analyses, based on different amplifications, suggested that a minimum deflection of 3 mm over a 500 mm long beam was needed to have a clear location of the damage.

Conclusions

The purpose of this work was to evaluate the suitability of a vision-based data acquisition method for damage detection compared to previous analyses. The results proved that the proposed vision-based method needs larger displacement than a PSD-triangular laser sensor to acquire valuable data. However, we found this technique is rather encouraging because it allowed to acquire a dense full-field displacement with a minimum effort in comparison to [9] which involved the acquisition of a large number of discrete points in a time consuming way.

Future research will be conducted by considering dynamic shapes of the beam excited by a shaker or, even, by environmental forces.

References

- [1]H.-N. Li, L. Ren, Z.-G. Jia, T.-H. Yi, D.-S. Li, State-of-the-art in structural health monitoring of large and complex civil infrastructures, *J Civil Struct Health Monit.* 6 (2016) 3–16. <https://doi.org/10.1007/s13349-015-0108-9>
- [2]C.-Z. Dong, F.N. Catbas, A review of computer vision–based structural health monitoring at local and global levels, *Structural Health Monitoring.* 20 (2021) 692–743. <https://doi.org/10.1177/1475921720935585>
- [3]D. Feng, M.Q. Feng, Computer vision for SHM of civil infrastructure: From dynamic response measurement to damage detection – A review, *Engineering Structures.* 156 (2018) 105–117. <https://doi.org/10.1016/j.engstruct.2017.11.018>
- [4]Z. Dworakowski, P. Kohut, A. Gallina, K. Holak, T. Uhl, Vision-based algorithms for damage detection and localization in structural health monitoring: Vision-based Algorithms for Damage Detection and Localization, *Struct. Control Health Monit.* 23 (2016) 35–50. <https://doi.org/10.1002/stc.1755>
- [5]J. Shi, X. Xu, J. Wang, G. Li, Beam damage detection using computer vision technology, *Nondestructive Testing and Evaluation.* 25 (2010) 189–204. <https://doi.org/10.1080/10589750903242525>
- [6]R. Kumar, S.K. Singh, Crack detection near the ends of a beam using wavelet transform and high resolution beam deflection measurement, *European Journal of Mechanics - A/Solids.* 88 (2021) 104259. <https://doi.org/10.1016/j.euromechsol.2021.104259>
- [7]A.K. Pandey, M. Biswas, M.M. Samman, Damage detection from changes in curvature mode shapes, *Journal of Sound and Vibration.* 145 (1991) 321–332. [https://doi.org/10.1016/0022-460X\(91\)90595-B](https://doi.org/10.1016/0022-460X(91)90595-B)
- [8]U. Andreaus, P. Casini, Identification of multiple open and fatigue cracks in beam-like structures using wavelets on deflection signals, *Continuum Mech. Thermodyn.* 28 (2016) 361–378. <https://doi.org/10.1007/s00161-015-0435-4>
- [9]B. Trentadue, A. Messina, N.I. Giannoccaro, Detecting damage through the processing of dynamic shapes measured by a PSD-triangular laser sensor, *International Journal of Solids and*

- Structures. 44 (2007) 5554–5575. <https://doi.org/10.1016/j.ijsolstr.2007.01.018>
- [10] A. Khaloo, D. Lattanzi, Pixel-wise structural motion tracking from rectified repurposed videos, Struct Control Health Monit. 24 (2017). <https://doi.org/10.1002/stc.2009>
- [11] C. Lanczos, Applied Analysis (1956), Dover Publications, New York
- [12] A. Messina, Detecting damage in beams through digital differentiator filters and continuous wavelet transforms, J. of Sound and Vib. 272(2004) 385-412. <https://doi.org/10.1016/j.jsv.2003.03.009>
- [13] A. Messina, Refinements of damage detection methods based on wavelet analysis of dynamical shapes, International Journal of Solids and Structures. 45 (2008) 4068–4097. <https://doi.org/10.1016/j.ijsolstr.2008.02.015>

Adaptive finite elements based on Carrera unified formulation for meshes with arbitrary polygons

Maria Cinefra^{1,a *} and Andrea Rubino^{1,b}

¹Politecnico di Bari, via Edoardo Orabona 4, Bari, Italy

^amaria.cinefra@poliba.it, ^bandrea.rubino@poliba.it

Keywords: Carrera Unified Formulation, Adaptive Finite Elements, 3D Elements, Node-Dependent Kinematics, Arbitrary Polygons

Abstract. The new Adaptive Finite Elements presented are based on Carrera Unified Formulation (CUF) that permits to implement 1D and 2D elements with 3D capabilities. In particular, by exploiting the node-dependent kinematic approach recently introduced and incorporating the FEM shape functions with the CUF kinematic assumptions in unique 3D approximating functions, it is demonstrated that new mesh capabilities can be obtained with the use of presented elements by easy implementation. A classical patch test is performed to investigate the mesh distortion sensitivity.

Introduction

To alleviate meshing issues due to FEM, more advanced techniques can be used, resorting to numerical methods that are designed from the very beginning to provide arbitrary order of accuracy on more generally shaped elements. These techniques are based, for instance, on the Virtual Element Method (VEM) [1]. In fact, in contrast to FEM in which elements are typically triangular and quadrilateral in 2D or tetrahedral and hexahedral in 3D, the VEM permits arbitrary two-dimensional polygonal and three-dimensional polyhedral elements [2]. This allows the problem domain to be discretized by elements represented by arbitrary polygons, which can be concave and convex. Moreover, different polynomial consistency is allowed within the method and non-conforming discretizations can be handled, mainly for local refinement and so on, representing the key aspect of this method.

The newly proposed Adaptive Elements, which are Finite Elements based on Carrera Unified Formulation (CUF), represent more agile and manageable elements, based on a well-known technique (FEM), easy to implement and can produce the same benefits of using VEM. Recently, in the framework of CUF, a novel approach called Node-Dependent Kinematics (NDK) has been proposed to further increase the numerical efficiency of the models [3]. The Node-Dependent Kinematics approach, along with the 3D modelling of non-orthogonal geometries [4], opens the possibility to create elements with a non-conventional number of nodes, complex geometrical shapes, and different polynomial approximations along different spatial directions, leading to a certain freedom in modelling the problem considered. In this way, 3D elements can be recovered with a non-regular shape that can adapt to the edges of the domain considered, when the geometrical constraints or the kinematic behavior of the structure requires that.

Adaptive Finite Elements

In traditional beam and plate theories, it is difficult to model beams with variable sections or sections that are not orthogonal to the axis, as well as plates with varying thickness or edges not perpendicular to the mid-surface. However, with the Node-Dependent Kinematic approach [3], it is possible to extend the Carrera Unified Formulation models to incorporate more complex geometries. This is achieved by incorporating the CUF kinematic assumption with the FEM discretization to create a unique 3D approximation, as follows:



$$\mathbf{u} = (F_{\tau}^i N_i) \mathbf{q}_{\tau i} = L_{\tau i}(\xi, \eta, \zeta) \mathbf{q}_{\tau i}$$

Where where ξ, η, ζ are the natural coordinates corresponding to x, y, z and $\mathbf{u} = \{u_x, u_y, u_z\}$ is the 3D displacement field. A double summation over the indices $i=1, \dots, N_n$ and $\tau=1, \dots, M$ is implied, where N_n is the number of the nodes in the element and M is the number of approximating functions adopted for the kinematic theory. F_{τ} and N_i are defined according to the type of element (beam or plate): N_i are the FEM shape functions that are used along the axis for beam elements or in the plane for the plate elements; F_{τ} are the approximating functions over the cross-section for the beam or along the thickness for the plate. Lagrange polynomials are chosen in this work for generating both F_{τ} and N_i , according to the CUF [4]. $q_{\tau i}$ are the generalized nodal displacements. Note that the function F_{τ} depends on the node 'i'.

The function $L_{\tau i} = (F_{\tau}^i N_i)$ represents a non-conventional 3D shape function in which the order of expansion can be different along one of the spatial directions. As a result, this approach overcomes the limitations of classical 3D finite element, related to its aspect ratio, with a consequent saving in degrees of freedom and the possibility to create polygonal elements.

In the following, the acronyms B2 (linear), B3 (quadratic) and B4 (cubic) are used both for the 1D discretization of the axis in beam models or for the approximation through the thickness in plate models; as well as the acronyms Q4 (linear), Q9 (quadratic) and Q16 (cubic) are used both for the 2D approximation of the cross-section in beam models and for the discretization of the in-plane domain in plate models.

Patch test

This standard test is classically used in order to investigate the mesh distortion sensitivity in plate bending problems. The in-plane dimensions of the square plate considered are $100 \times 100 \text{ m}^2$ and the thickness is 5 m. The boundary conditions are clamped (CC). A transverse concentrated force is applied at the center of the top surface $F = 4 \text{ N}$. The material is isotropic with the following properties: $E = 10.92 \text{ Pa}$, $\nu = 0.30$ and $\rho = 1 \text{ kg/m}^3$. The meshes initially used are a 4×4 Q4 elements and a 4×4 Q9 elements in the plane, with B3 approximation along the thickness in both cases.

Due to the symmetry of the problem, a quarter of the plate is considered. In particular, the bottom-left quarter of the plate is chosen and symmetry boundary conditions are applied along cut edges. $F = 1 \text{ N}$ is applied on the top-right corner. The resulting mesh of the plate quarter is 2×2 based on Q4 or Q9 plate elements.

Some beam elements are introduced in the mesh in order to obtain distorted elements with different number of nodes along the edges. Then, three different configurations are analyzed:

- 2xQ4 1xB2: in this configuration, the previous two elements at the top are substituted by a single 1D element with 2 nodes, having a Q9 approximation on the cross-section;
- 2xQ4 1xB3: as in the previous case, the two elements at the top are substituted by a single 1D element but having 3 nodes along the axis, where the cross-section is expressed as a Q9 element;
- 2xQ4 1xQ9: the number of nodes is identical with respect to the previous case, but the discretization of the two elements at the top is different, accounting for a single Q9 element having a B3 discretization along the thickness.

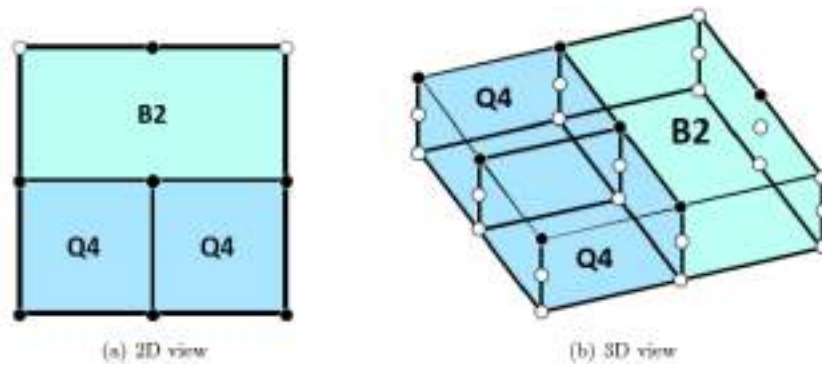


Figure 1: Quarter plate: 2xQ4 1xB2 mesh

In Fig. 1 it is possible to visualize one of the described configurations: the black dots are the FEM nodes, while the white dots represent the CUF nodes added considering the thickness and the cross-section of the plate and the beam elements, respectively.

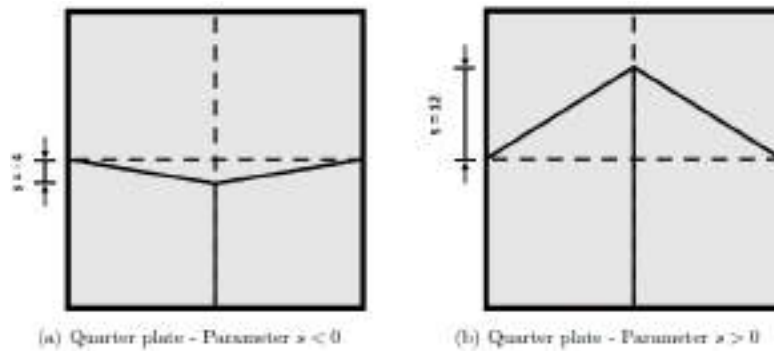


Figure 2: Quarter plate - mesh distortion defined by parameter 's'

The mesh distortion is characterized by the parameter $s \in \{-12, -10, -6, 0, 6, 10, 12\}$, which defines the coordinates of the central node of the plate quarter. Note that the parameter 's' can assume negative and positive values, as shown in Fig. 2: if the parameter s is negative, the considered element is convex; if the parameter s is positive, the element becomes non-convex.

A static analysis is performed and the results are computed in terms of transverse displacement $U_z = u_z(a, a, 0)$ (the center point on the midsurface of the entire plate) for the distorted mesh and it is normalized with respect to the reference value U_{z0} calculated for the regular mesh ($s = 0$). The results computed by varying the parameter s are reported in Fig. 3.

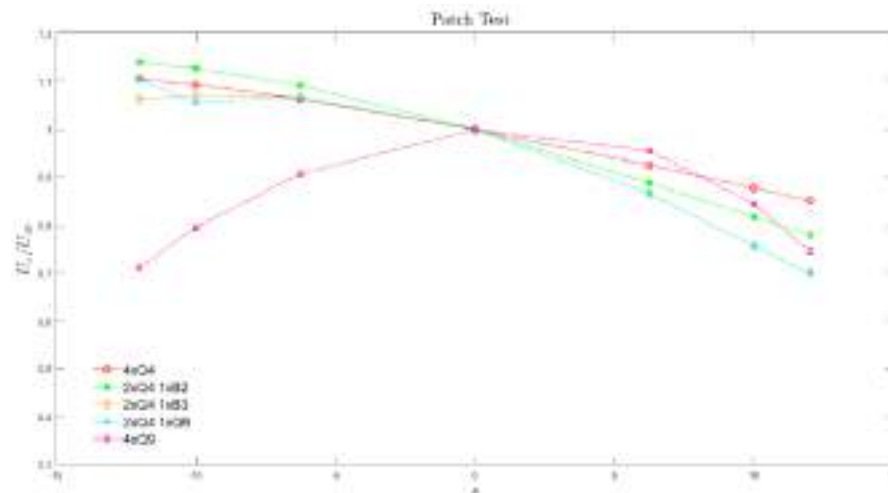


Figure 3: Variation of the ratio U_z/U_{z0} for CC quarter plate

One has to take into account that the 2x2Q9 solution is the most accurate with the highest number of degrees of freedom (DOFs=225), the 2x2Q4 (DOFs=81) is the least accurate and the other solutions are in the middle according to their related degree of approximation. The meshes 2xQ4 1xQ9 (DOFs=108) and 2xQ4 1xB3 (DOFs=108) are very similar to each other and they are compared to highlight that their solution are exactly the same, although the first uses a plate element (Q9) and the other one a beam element (B3).

Conclusions

The results demonstrate that the sensitivity to the distortion of the mixed meshes with beam elements is comparable to the regular meshes (2x2Q4 and 2x2Q9). In particular, the use of B2 beam element in the mesh 2xQ4 1xB2, with a number of DOFs equal to the mesh 2x2Q4 (DOFs=81), doesn't compromise the trend of the results when the mesh is distorted, although it permits to differentiate the number of nodes along the edges of the element (see Figure 3(a)) by reducing also the total number of the nodes in the element with respect to the other mixed meshes.

References

- [1] H. Chi, L. Beirão Da Veiga, G.H. Paulino, Some basic formulations of the Virtual Element Method (VEM) for finite deformations, *Comput. Methods Appl. Mech. Eng.* 318 (2017) 148-192. <https://doi.org/10.1016/j.cma.2016.12.020>
- [2] L. Beirão Da Veiga, F. Brezzi, L.D. Marini, A. Russo, The hitchhiker's guide to the virtual element method, *Math. Models Methods Appl. Sci.* 24:08 (2014) 1541-1573. <https://doi.org/10.1142/S021820251440003X>
- [3] G. Li, E. Carrera, M. Cinefra, A.G. De Miguel, A. Pagani, E. Zappino, An adaptable refinement approach for shell finite element models based on node-dependent kinematics, *Compos. B. Eng.* 210 (2019) 1-19. <https://doi.org/10.1016/j.compstruct.2018.10.111>
- [4] M. Cinefra, Non-conventional 1D and 2D finite elements based on CUF for the analysis of non-orthogonal geometries, *Eur. J. Mech. A Solids* 88 (2021) 104273. <https://doi.org/10.1016/j.euromechsol.2021.104273>

Analysis of the manufacturing signature on AFP-manufactures variable stiffness composite panels

Alfonso Pagani^{1,a *} and Alberto Racionero Sánchez-Majano^{2,b}

¹Mul2 Lab, Department of Mechanical and Aerospace Engineering, Politecnico di Torino, Corso Duca degli Abruzzi 24, Turin, Italy

^aalfonso.pagani@polito.it, ^balberto.racionero@polito.it

Keywords: Variable Stiffness Composites, Automated Fiber Placement, Unified Formulation, Defect Modeling

Abstract. Variable stiffness composites broaden the design space, in comparison with straight-fiber composites, to meet fixed mechanical performance. Nevertheless, the manufacturing of these advanced composites incurs into the presence of undesired fabrication defects such as gaps and overlaps, which alter the mechanical behavior of the laminated parts. In this work, the authors couple the Defect Layer Method, utilized to model defects, with the Carrera Unified Formulation in order to study how the manufacturing signature affects the fundamental frequency of variable stiffness laminates.

Introduction

Novel manufacturing techniques, such as Automated Fiber Placement (AFP), have permitted to conceive new families of laminated structures, namely Variable Stiffness Composites (VSC) or Variable Angle Tow (VAT), in which fiber tows are steered conforming curvilinear paths. Olmedo and Gürdal [1] investigated the buckling of VAT plates for different boundary conditions and rotations of the fiber path. Nevertheless, in the cases that Olmedo and Gürdal considered, the minimum turning radius, which determines whether a laminate is manufacturable or not, was not taken into account. Therefore, not all the solutions were feasible from a fabrication point of view. Besides, due to the manufacturing features inherent to AFP, imperfections are prone to arise during the fabrication process, namely gaps and/or overlaps, and affect the structural performance [2].

Many authors have proposed numerical methods to investigate the effect of gaps and/or overlaps on the mechanical properties of variable stiffness composites. Blom et al. [2] investigated how gaps affect the strength and stiffness of VAT using the Finite Element Method (FEM). They concluded that increasing the laminate's total gap area deteriorates strength and stiffness. Fayazbakhsh et al. [3] proposed the Defect Layer Method (DLM), which permits to capture the gap and/or overlap areas that appear in the laminate without incurring into an excessive computational burden as in [2].

In this manuscript, we tackle the influence of gaps and overlaps on VAT laminates by coupling DLM with the Carrera Unified Formulation (CUF) [4]. CUF permits obtaining the governing equations of any structural theory without making *ad hoc* assumptions. So far, CUF has proven to predict accurate stress states [5], as well as capture the influence of multiscale uncertainty defects on the mechanical performance of VAT plates [6].

Variable stiffness composite plates and defect modeling

VAT laminated components are fabricated by steering fiber bands along curvilinear paths. Throughout the years, different variation laws have been investigated. This work focuses on the linear variation, in which the local fiber orientation, θ , varies along the x' direction as follows:

$$\theta(x') = \phi + T_0 + \frac{T_1 - T_0}{d} |x'|. \quad (1)$$

The physical meaning the parameters involved above is depicted in [1], and are illustrated in Figure 1.

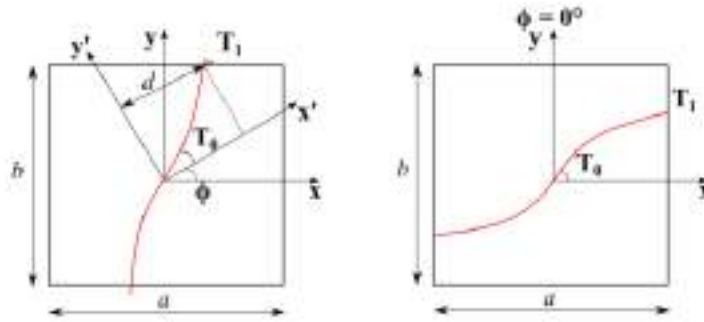


Figure 1. Representation of the fiber parameters involved in the definition of a VAT laminate.

Despite the steering capability of VAT plates, the AFP machines that manufacture them present some limitations, being one of them the curvature of the laid fiber path. A manufacturing feature inherent to AFP is the presence of gaps and overlaps in the final part, thereby affecting the structural performance. DLM [3] is considered to model these imperfections. As mentioned in [3], the defect area percentage is the only parameter to modify the elastic properties or the thickness associated to the finite element. Note that the elastic properties vary if gaps are considered, whereas an increase in the thickness is provided in the case of overlap.

Unified finite elements

2D FE are implemented within the CUF formalism. According to [4], the 3D field of displacement can be expressed in terms of arbitrary through-the-thickness expansion functions, $F_\tau(\mathbf{z})$, of the 2D generalized unknowns laying over the $\mathbf{x} - \mathbf{y}$ plane. That is,

$$\mathbf{u}(\mathbf{x}, \mathbf{y}, \mathbf{z}) = F_\tau(\mathbf{z})\mathbf{u}_\tau(\mathbf{x}, \mathbf{y}). \tau = 1, \dots, M \quad (2)$$

Therein, M denotes the number of expansion terms, and $\mathbf{u}_\tau(\mathbf{x}, \mathbf{y})$ is the vector containing the generalized displacements. The analysis of multi-layered structures is commonly conducted by following an Equivalent-Single-Layer (ESL) and Layer-Wise (LW) approach. In this manuscript, ESL models are built using Taylor polynomials as F_τ in the thickness direction. On the other hand, LW utilizes Lagrange polynomials over the single layers and then imposes the continuity of displacements at the layer interfaces, as in [7]. In this context, TE_n denotes a TE of the n -th order, whilst LE_n indicates the usage of an LE with n -th order polynomials. Moreover, XLE_n means that X Lagrange polynomials of n -th order are used to describe each layer of the laminate.

Utilizing the FE and shape functions $N_i(\mathbf{x}, \mathbf{y})$, the displacement field becomes:

$$\mathbf{u}(\mathbf{x}, \mathbf{y}, \mathbf{z}) = N_i(\mathbf{x}, \mathbf{y})F_\tau(\mathbf{z})\mathbf{q}_{\tau i}(\mathbf{x}, \mathbf{y}). i = 1, \dots, N_n \quad (3)$$

In Eq. (3), $\mathbf{q}_{\tau i}$ denotes the unknown nodal variables, and N_n indicates the number of nodes per element. In this work, 2D nine-node quadratic elements, referred to as Q9, are employed as N_i for the $\mathbf{x} - \mathbf{y}$ plane discretization. For the sake of brevity, the governing equations that calculate the fundamental frequency are not reported but can be found in [4].

Machine simulation: identification of defected regions

The steering of fiber bands along a fixed direction, and shifting the AFP head in its perpendicular direction to generate the subsequent fiber course, leads to the presence of gaps and/or overlaps. The location in which they appear depends not only on T_0 and T_1 but also on the steering strategy. Figure 2 illustrates the case of a $[[0,45]]$ plate in which the fiber courses touch each other at the

edge (Figure 2 left) and at the center of the plate (Figure 2 right). The yellow area indicates a gap area, whereas the green area highlights an overlap area.

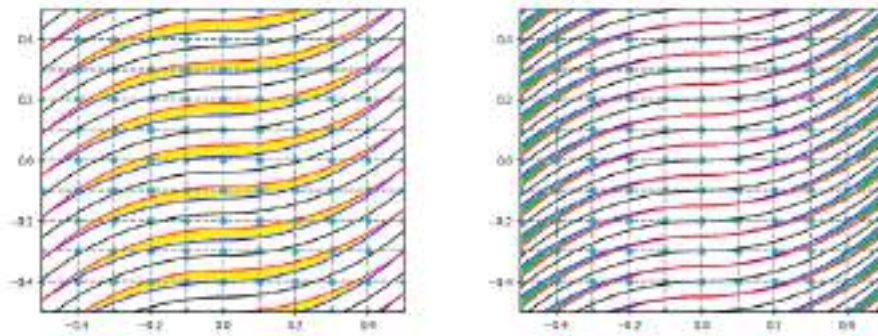


Figure 2. Example of a plate with $[(0, 45)]$ stacking sequence with full gap (left) and full overlap (right) manufacturing strategy.

The previous imperfections affect such large areas because the course width is kept constant throughout the steering process. In order to reduce the defect area, the course width has to decrease or increase whenever a course intersects the successive one or it does not reach the precedent course's edge, respectively. The increase or decrease of the course width is achieved by cutting an individual tow and restarting its deposition. This comports the generation of small triangular defected regions, as evidenced in Figure 3.

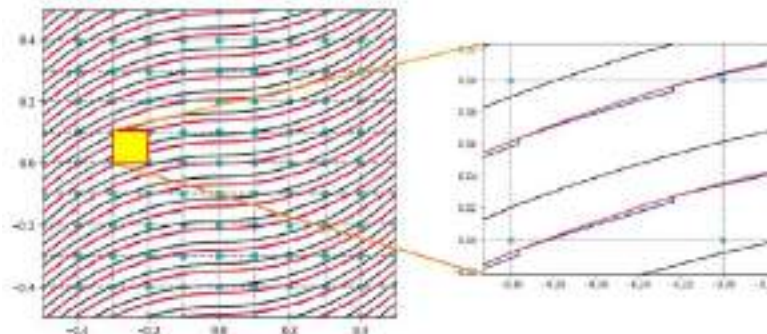


Figure 3. Gap defect correction over a $[(0, 45)]$ ply. The zoomed area shows the triangular gaps that are generated.

Effect of gap defects on fundamental frequency

In this section, the effect of manufacturing defects is addressed. As depicted in the previous section, two manufacturing strategies are considered: without and with defect correction. These two strategies are denoted as Type 1 and Type 2, respectively. For the following analyses, the tow paths are conformed by sixteen tows, each with a width of $t_w = 3.125$ mm. The FE mesh comprises 10×10 Q9 elements, based on a convergence analysis performed beforehand.

Table 1 presents the effect of gaps on the first five fundamental frequencies of the $[(0, 45), (-45, -60), (0, 45)]$ plate from [8]. An LW-1 LE2 model is employed since, when gaps are considered, the thickness of the laminate remains unaltered, and no additional computational effort is required when compared to the ideal plate. It is observed that gaps lead to a decrease in the fundamental frequency because resin-rich areas are present within the layers. Type 1 defects present a much lower frequency than the ideal case, whereas Type 2 limits the fundamental frequency reduction.

Table 1. Effect of manufacturing gaps on the $[(0, 45), (-45, -60), (0, 45)]$ plate.

Model	f_1 [Hz]	f_2 [Hz]	f_3 [Hz]	f_4 [Hz]	f_5 [Hz]
No defects	609.91	903.93	1216.18	1328.88	1469.58
Gap Type 1	547.82	797.10	1083.41	1159.71	1295.57
Gap Type 2	599.10	888.99	1193.21	1306.87	1442.75

Conclusions

This manuscript has discussed the effect of manufacture-induced gaps on the fundamental frequency of VSC laminates. The position where gaps and overlaps will appear during manufacturing has been predicted. These defects were incorporated into the FE model by means of the Defect Layer Method. As it was expected, the presence of gaps incurred a decrease in the fundamental frequency. Future works will be related to the optimization of VAT plates in which the aforementioned manufacturing imperfections are considered.

References

- [1] R. Olmedo, Z. Gürdal. Buckling response of laminates with spatially varying fiber orientations. In 34th Structures, Structural Dynamics and Materials Conferences (1993), 1567. <https://doi.org/10.2514/6.1993-1567>
- [2] A. W. Blom, C. S. Lopes, P. J. Kromwijk, Z. Gürdal, P. P. Camanho. A theoretical model to study the influence of tow-drop areas on the stiffness and strength of variable-stiffness laminates. *Journal of Composite Materials* 43(5) (2009), 403-425. <https://doi.org/10.1177/0021998308097675>
- [3] K. Fayazbakhsh, M. A. Nik, D. Pasini, L. Lessard. Defect layer method to capture effect of gaps and overlaps in variable stiffness laminates made by automated fiber placement. *Composite Structure* 97 (2013), 245-251. <https://doi.org/10.1016/j.compstruct.2012.10.031>
- [4] E. Carrera, M. Cinefra, M. Petrolo, E. Zappino. *Finite Element Analysis of Structures through Unified Formulation*. Wiley & Sons, Hoboken, New Jersey. 2014.
- [5] A. R. Sánchez-Majano, R. Azzara, A. Pagani, E. Carrera. Accurate stress analysis of variable angle tow shells by high-order equivalent-single-layer and layer-wise finite element models. *Materials* 14(21) (2021), 6486. <https://doi.org/10.3390/ma14216486>
- [6] A. Pagani, M. Petrolo, A.R. Sánchez-Majano. Stochastic characterization of multiscale material uncertainties on the fibre-matrix interface stress state composite variable stiffness plates. *International Journal of Engineering Science* 183 (2023), 103787. <https://doi.org/10.1016/j.ijengsci.2022.103787>
- [7] E. Carrera. Theories and finite elements for multi-layered, anisotropic, composite plates and shells. *Archives of Computational Methods in Engineering* 9(2) (2002), 87-140.
- [8] H. Akhavan, P. Ribeiro. Natural modes of vibration of variable stiffness composite laminates with curvilinear fibers. *Composite Structures* 93(11) (2011), 3040-3047. <https://doi.org/10.1016/j.compstruct.2011.04.027>

An analytical tool for studying the impact of process parameters on the mechanical response of composites

E. Zappino^{1,a*}, M. Petrolo^{1,b}, R. Masia^{1,c}, M. Santori^{1,d} and N. Zobeiry^{2,e}

¹MUL2 Lab, Department of Mechanical and Aerospace Engineering, Politecnico di Torino, 10129 Turin, Italy

²Department of Materials Science and Engineering, University of Washington, Seattle, WA, 98195, USA

^aenrico.zappino@polito.it, ^bmarco.petrolo@polito.it, ^crebecca.masia@polito.it,

^dmartina.santori@polito.it, ^enavidz@uw.edu

Keywords: Virtual Manufacturing, Carrera Unified Formulation, Process-Induced Deformations, Residual Stresses

Abstract. The present work presents a numerical framework able to predict the impact of the manufacturing process on the mechanical performance of the composite component. A simple one-dimensional thermochemical model has been used to predict the evolution of the degree of cure of the resin for a given thermal cycle. The homogenized properties at the lamina level have been obtained through a classical mixtures law and employed to predict the process-induced deformations. A refined one-dimensional model, derived in the framework of the Carrera Unified Formulation, has been used to provide accurate results with reduced computational costs. The virtual manufacturing framework has been used to investigate the impact of the process parameters on process-induced defects of a simple composite part. Different curing cycles have been considered and their outcomes discussed. The results demonstrate the capability of the present numerical tool to correlate the manufacturing process parameters with the mechanical performances of the final component.

Introduction

Composite materials are increasingly being used in various applications in industry due to their superior mechanical properties [1]. The manufacturing of composite structures for aerospace applications must meet strict requirements in terms of process-induced defects. The use of autoclave processes ensures higher mechanical performances of the final component by reducing the presence of voids but, on the other hand, involves the use of high temperature and pressure that can lead to residual deformations and stresses. [2]. The process-induced defects may lead to an early failure of the component or to geometrical inaccuracies that make the structural assembly complicated. Numerical tools based on the finite element method (FEM) can be used to predict process-induced defects but, the three-dimensional nature of the problem requires solid models to be used with a consequent high computational cost. In this work, a refined one-dimensional model, developed within the field of Carrera Unified Formulation (CUF) [3], is used to obtain residual deformations due to the curing process accurately with low computational cost [4]. A one-dimensional thermochemical model is used to predict the evolution of temperature and degree of cure during the process of the composite structure [5]. The mechanical properties of the composite laminate are obtained from a micromechanical model based on the law of mixtures [6].

Equations and model

The cure model is based on the heat transfer governing equation through thickness, i.e., the one-dimensional Fourier thermal conduction equation:



$$\dot{Q} + k \frac{\partial^2 T}{\partial z^2} = \rho H_r V_r \frac{d\alpha}{dt} + k \frac{\partial^2 T}{\partial z^2} = \rho c_p \frac{\partial T}{\partial t} \quad \text{for } T(z, t) \text{ in } (0 < z < l) \quad (1)$$

where k , ρ , and c_p are the thermal conductivity, density, and specific heat of the composite, respectively, and are assumed constant during the process. α is the degree of cure, H_r is the total heat released from the resin reaction, V_r is the volume fraction of the resin. The thickness of the laminate is equal to l . T and t are temperature and time. The normal to the inplane dimension of the composite is the z -direction. The term \dot{Q} represents the internal heat generated by the exothermic chemical reaction of the resin.

The cure rate for graphite/epoxy material follows this expression, where k_1 , k_2 and k_3 are defined by the Arrhenius equation [5]:

$$\begin{aligned} \frac{d\alpha}{dt} &= (k_1 + k_2\alpha)(1 - \alpha)(0.47 - \alpha) & \text{for } (\alpha \leq 0.3) \\ \frac{d\alpha}{dt} &= k_3(1 - \alpha) & \text{for } (\alpha > 0.3) \\ k_i &= A_i e^{\frac{-\Delta E_i}{RT}} & \text{for } i = 1, 2, 3 \end{aligned} \quad (2)$$

R is the universal gas constant, A_i are the pre-exponential coefficients, and ΔE_i are the activation energies.

The mechanical properties of the resin are strongly dependent on the curing process. The instantaneous modulus of the resin can be expressed as a function of the degree of cure according to the α mixing rule [6]:

$$\begin{aligned} E_m &= (1 - \alpha_{mod})E_m^\circ + \alpha_{mod}E_m^\circ + \gamma\alpha_{mod}(1 - \alpha_{mod})(E_m^\infty - E_m^\circ) \\ \alpha_{mod} &= \frac{\alpha - \alpha_{gel}^{mod}}{\alpha_{diff}^{mod} - \alpha_{gel}^{mod}} \end{aligned} \quad (3)$$

The parameters E_m° and E_m^∞ are the moduli of the fully uncured and fully cured resin, respectively. α_{gel}^{mod} and α_{diff}^{mod} are the extreme values of the degree of cure considered during the process and are assumed to be $\alpha_{gel}^{mod} = 0$ and $\alpha_{diff}^{mod} = 1$. The parameter γ allows quantification of the contrasting mechanisms of chemical hardening and stress relaxation. It is assumed null in this study. The instantaneous shear modulus of the resin is calculated by the relation of isotropic materials. During the process, the resin has a chemical shrinkage that induces a uniform strain for all principal directions. The mechanical properties of the fiber do not depend on the curing process and are assumed constant. The micromechanics model [6] evaluates homogeneous mechanical properties, chemical shrinkage, and thermal expansion coefficient from fiber and matrix properties.

Results

The considered laminate is 2.54 cm thick and is made of AS4/3501-6 material (graphite/epoxy). The thermophysical characteristics of the material are: $\rho = 1.52 \times 10^3 \text{ kg/m}^3$, $c_p = 942 \text{ J/(W}^\circ\text{C)}$, $k = 0.4457 \text{ W/(m}^\circ\text{C)}$, $A_1 = 3.502 \times 10^7 \text{ s}^{-1}$, $A_2 = -3.357 \times 10^7 \text{ s}^{-1}$, $A_3 = 3.267 \times 10^3 \text{ s}^{-1}$, $\Delta E_1 = 8.07 \times 10^4 \text{ J/mol}$, $\Delta E_2 = 7.78 \times 10^4 \text{ J/mol}$, $\Delta E_3 = 5.66 \times 10^4 \text{ J/mol}$, $H_r = 198.9 \text{ kJ/kg}$ [6]. The one-dimensional model consists of ten elements. Convection boundary conditions are applied to the top and bottom of the laminate. The first study allows the present thermochemical model to be verified by comparing the trends in the degree of polymerization and temperature at the centerline of the laminate with those predicted by Bogetti [7] for a cure cycle. The curing process consists of two hold-on periods at temperatures of 389.25 K and 450.55 K for

70 min and 127 min, respectively. As can be seen in Fig.1(a), there is a good match between the two models. The small initial discrepancy in the degree of cure may be due to a different choice of the initial degree of cure not being specified in the reference. The temperature spikes when the air temperature is kept constant are due to the exothermic nature of the resin reaction.

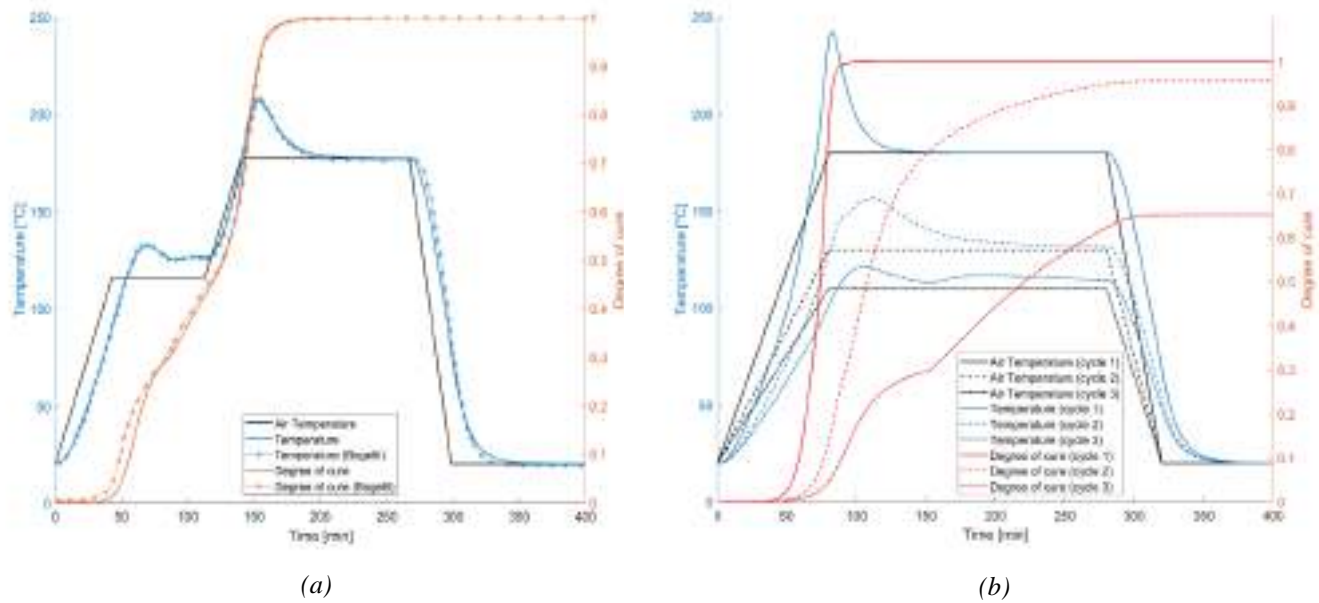


Figure 1: (a) Comparison of the prediction of degree of cure and temperature for a cure cycle with Bogetti's prediction at the centreline of the laminate, (b) Degree of cure and temperature for three different cure cycles

After evaluating the model's accuracy, three cure cycles are applied to the same laminate as in the previous case. The first cycle reaches the maximum temperature of $T_1 = 453.15$ K, the second one the temperature $T_2 = 403.15$ K, and the third $T_3 = 383.15$ K and they are kept constant for 200 min. Fig. 1(b) shows the time trends of temperature and cure degree at the center of the laminate for the three cure cycles. The resin characteristics vary with the degree of cure, except for the Poisson and thermal expansion coefficients, which are assumed constant. The instantaneous resin modulus is calculated using Eq. (3) for each time step, knowing that $E_m^0 = 3.447$ MPa and $E_m^\infty = 3.447 \times 10^3$ MPa. The fiber properties are kept constant. Through the micromechanical model, the homogeneous properties of the composite are obtained. These parameters are used as input to the analysis to calculate the deformation of an L-shaped component with an angle of 93° between the two flanges. Since the structure is symmetrical, only half is considered. The length of the single flange is 0.1 m. Refined one-dimensional kinematic model [4] can predict the structure's spring-in angle for the three cure cycles along the curvilinear coordinate x that follows the curvature of the flange. The greatest deviation of spring-in angle is obtained in the curved part of the L-shaped structure. For the three cycles the maximum values of spring-in angle are shown in Table 1.

Table 1: Maximum spring-in angle for the three cycles

	Cycle 1	Cycle 2	Cycle 3
Spring-in angle [deg]	1.02	0.965	0.939

Summary

A simple one-dimensional thermochemical model made it possible to accurately predict the trends in the degree of cure and temperature of the composite given a cure cycle. If the maximum temperature of the cure cycle is low, the resin is not fully cured at the end of the process. Through the micromechanical model, it was possible to obtain the homogeneous properties of the composite as the degree of cure changes and thus obtain the inputs to derive the deformations induced by the cure cycle. A refined one-dimensional kinematic model allowed the spring-in angle to be estimated. It was shown that the cure cycle influences the spring-in angle. The deformation decreases as the maximum temperature of the cycle decreases.

Further developments may include process optimization, the development of defect mitigation methodologies, or in the development of active process monitoring strategies.

Acknowledgments

This research work has been carried out within the project “Sviluppo di modelli per la manifattura virtuale basati sull'intelligenza artificiale per ridurre i difetti causati dal processo di cura di strutture in composito” funded by Ministero degli Affari Esteri e della Cooperazione Internazionale.

References

- [1] M. Hojjati, S.V. Hoa. Some Observations in Curing of Thick Thermosetting Laminated Composites. *Science and Engineering of Composite Materials*, vol. 4, no. 2, 1995, pp. 89-108. <https://doi.org/10.1515/SECM.1995.4.2.89>
- [2] G. Fernlund, C. Mobuchon, N. Zobeiry. 2.3 autoclave processing. *Comprehensive Composite Materials II*, Elsevier; 2018, pp. 42–62 [chapter 2]. <https://doi.org/10.1016/B978-0-12-803581-8.09899-4>
- [3] E. Carrera, M. Cinefra, M. Petrolo, E. Zappino. *Finite element analysis of structures through unified formulation*. John Wiley & Sons; 2014. <https://doi.org/10.1002/9781118536643>
- [4] E. Zappino, N. Zobeiry, M. Petrolo, R. Vaziri, E. Carrera, A. Poursartip. Analysis of process-induced deformations and residual stresses in curved composite parts considering transverse shear stress and thickness stretching. *Composite Structures*, Volume 241, 2020. <https://doi.org/10.1016/j.compstruct.2020.112057>
- [5] A. C. Loos, G. S. Springer. Curing of Graphite/epoxy Composites. Technical Report AFWAL-TR-83-4040, Air Force Wright Aeronautical Laboratories, Wright Patterson AFB, OH, 1983.
- [6] T.A. Bogetti, J.W. Gillespie Jr. Process-Induced Stress and Deformation in Thick-Section Thermoset Composite Laminates. *Journal of Composite Materials* 26. (5), 1992. <https://doi.org/10.1177/002199839202600502>
- [7] A. Johnston. An integrated model of the development of process-induced deformation in autoclave processing of composite structures. PhD thesis. University of British Columbia, 1997.

Acoustic characteristics evaluation of an innovative metamaterial obtained through 3D printing technique

L.M. Cardone^{1*a}, S. De Rosa^{1b}, G. Petrone^{1c}, G. Catapane^{1d}, A. Squillace^{2e},
L. Landolfi^{2f}, A.L.H.S. Detry^{2g}

¹ PASTA-Lab (Laboratory for Promoting experiences in Aeronautical Structures and Acoustics),
Department of Industrial Engineering - Aerospace Section, Università degli Studi di Napoli
"Federico II", Via Claudio 21, Napoli, 80125, Italy

² Department of Chemical, Materials and Industrial Production Engineering, University of Naples
Federico II, Naples, Italy

^aluigimaria.cardone@unina.it, ^bsergio.derosa@unina.it, ^cgiuseppe.petrone@unina.it,
^dgiuseppe.catapane@unina.it, ^eantonino.squillace@unina.it, ^fluca.landolfi@unibg.it,
^gandrealorenzohenrisergio.detry@unina.it

Keywords: Noise Reduction, Sustainability, 3D Printing, Metamaterial

Abstract. The reduction of interior noise level in the transportation sector is a big problem to cope with in view to increase the comfort of passengers. For this reason a great emphasis from the research community is devoted to develop new technology which are able to satisfy the mechanical requirements with concrete benefits from the acoustic point of view. Currently, it does not exist a solution for wideband range of frequency. Indeed, porous materials are characterized by outstanding dissipation in the high frequency range but they exhibit poor performance in the low and medium frequency range, where instead resonant cavities systems have the best performances but with narrow-band sound absorption. For this reason, the design and development of new materials which offers a good acoustic absorption over a wide range of frequencies is requested. In this paper, a hybrid metamaterial is designed, by coupling resonant cavities with micro-porous material and obtained through additive manufacturing technique which enables to model complex geometries that could not be feasible with classical manufacturing. Numerical and experimental studies have been conducted on the manufactured samples of PLA, with an interesting focus on the effect of each parameter which affects the absorption properties.

Introduction

Materials have been used to control wave propagation for centuries. The evolution of these are the metamaterials: artificial structures, typically periodic, composed of small meta-atoms that, in the bulk, behave like a continuous material with unconventional effective properties. Acoustics Metamaterial are classified by the mechanism of sound absorption, i.e. how they can manipulate and control sound waves in ways that are not possible in conventional materials. Metamaterials with zero, or even negative, refractive index for sound offer new possibilities for acoustic imaging and for the control of sound at subwavelength scales [1].

In literature it is possible to find three macro-classes: porous metamaterials, membrane resonators and cavity resonators. The first acoustic meta-atoms were spherical metal cores coated with a soft rubber shell packed to a simple-cubic lattice in a host material, which could exhibit a Mie-type resonance frequency far below the wavelength-scale Bragg resonance frequency of the lattice [2]. Other architectures for acoustic metamaterials involve segments of pipes and resonators in the form of open and closed cavities. In 2006, these configurations composed a metamaterial characterized by a waveguide loaded with an array of coupled Helmholtz resonators [3]. At their collective resonance frequency, a low-frequency stopband is formed. Several other metamaterial-



based approaches for realizing unusual acoustic refraction have been demonstrated, as example by coiling up space with labyrinthine structures [4], the sound propagation phase is delayed such that band folding with negative dispersion. Most of the acoustic metamaterial designs described above make use of periodic structures, but given that the concept of acoustic metamaterials is based on the local, internal mechanical response of the structure, there is no reason why metamaterials cannot be made from aperiodic architectures. This idea is beginning to be explored using metamaterials composed of a soft matrix containing an unstructured array of bubbles of a second material. This is the main idea of the concept that has been realized in the laboratory. The subject of this work is a hybrid metamaterial composed by resonant cavities and porous material obtained through 3D printing technique. The 3D printing technique has given to the researcher the possibility to invent different geometry that could be impossible to realize with classical manufacturing. The work will firstly illustrate the technical evolution that has led to the construction of the different type of metamaterials that nowadays are subject of study. In the middle it will be introduced the technique of 3D printing used to create the sample, and in the end the numerical simulation and the experimental results will be reported.

3D printing of porous materials

The samples in additive manufacturing used in this research have been obtained using a printer based on Fused Deposition Modeling (FDM) technology. FDM technology consists in depositing on a printing surface several layers of a material that, layer after layer, form a three-dimensional object. The raw material is usually a filament of a certain diameter, which is found on the market in the form of a coil. The filament is pushed by an extruder and passes into the heated nozzle at a temperature above the glass transition temperature of the material in use. The technology used during the realization phase consists in solubilizing the blowing agent in the print blanks, so that the material is expanded during printing. Unlike foaming the piece by solubilizing an expanding agent inside in a post-printing phase, this methodology, obtaining the desired morphology by controlling a rapid jump in pressure and temperature, allows you not to face problems related to the control of the geometry of the workpiece, because the high residual stresses due to printing deform the workpiece during foaming [5]. The production of polymer foams consists of several stages listed: (a) selection of granules and fibres; (b) extrusion of filament; (c) solubilization of the blowing agent in the filament; (d) AM foam printing. By controlling parameters such as the solubilization time, speed and temperature of the extrusion, it is possible to block filaments and then the foams at different densities (Fig. 1) [6]. In the case of study, in the realization of the specimens it was chosen to proceed with medium density foams. The versatility of this process has allowed the realization of the metamaterial of which it has been chosen to characterize the absorption.

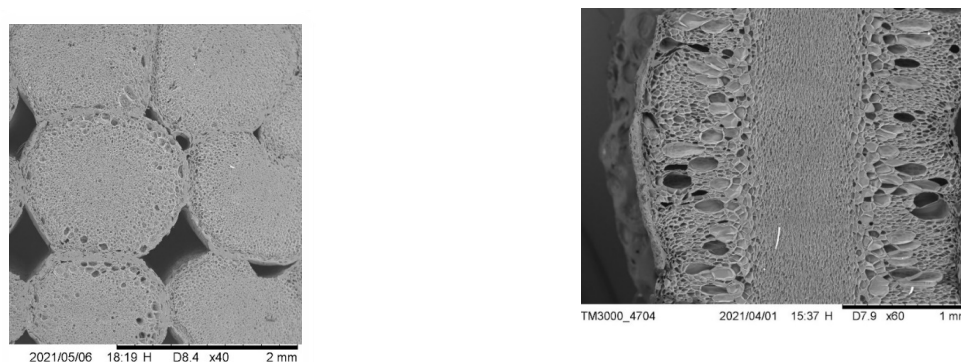


Figure 1 SEM Images of foamed filament (Tammaro et al., 2021)

Analyzed configuration

The tested specimens have the following geometrical data: height of 30mm and 19 holes with a diameter of 3mm, passed, arranged radially. A numerical analysis was immediately carried out using Comsol software to evaluate the acoustic performance of the identified geometry. Subsequently, the specimen were manufactured. In addition to the foaming parameter, it was also chosen to evaluate two possible printing logics: the first consists of printing the full cylinder and then drilling the holes using different techniques; the second, on the other hand, involves creating the holes during printing. This dual mode of realization showed how the production process clearly affects the behavior from the point of view of absorption.

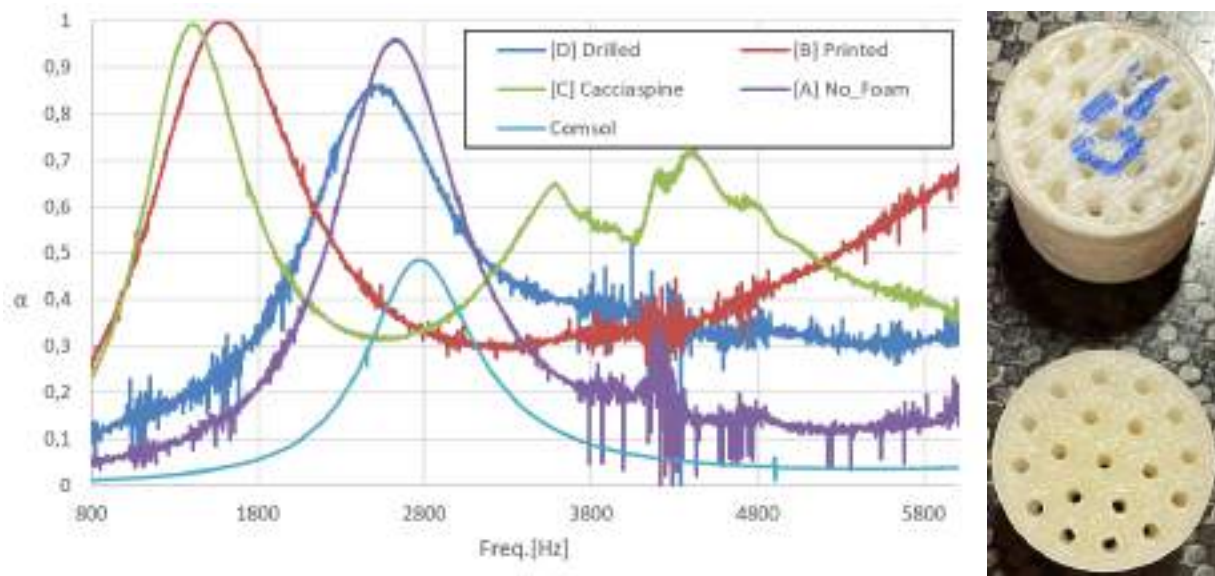


Figure 2: Absorption coefficient diagram

Several aspects are evident from the diagram in Fig. 2: 1) Validation of the numerical model: in order to obtain this comparison, the specimen was first printed using both modes mentioned above, then it was then tested in the impedance tube, complying with the regulations of test's standard, and finally after extracting the data, the curve of the numerical model (petrol) was compared with the experimental (violet). It is observed that the material (unfoamed PLA) is found to have a damping effect that amplifies the absorption curve at the frequency identified by the numerical model reaching almost unity. 2) Drilling method: it is interesting to note how the methodology used to make the holes alters the absorption behavior of the specimen. Three drilling methodologies were chosen to be analyzed. The first one is to drill the specimen in a cold running water bath by using a drill press. Despite the cold water immersion, the temperature reached between the drill bit and the material was such that the hole channel melted locally, thus occluding the internal porous structure of the filament, in fact obtaining the same absorption behavior as the specimen printed with unfoamed filament (blue curve). The second methodology consists of cold drilling using a drill bit and a hand vise to exert compression force. The effect of this second methodology is reported by the green curve. There is a copious shift present due to possible delaminating of the various layers of the specimen and imperfect flatness of the channels. Also from this curve, it is possible to see the presence of a new, higher bell, attributable to the behavior of the foams. Third and last methodology examined consists in directly printing the specimen with the hole locations. First fundamental difference from the previous methodologies lies in the definition of the channel of the hole. The mold in fact overlaps many circles thus obtaining the outer channel of the hole. This overlap is not always perfect and this kind of internal losses in the specimen, thus altering the path that the wave can follow. The result of this condition is the curve

in orange. Further tests are in progress to obtain a drilling method that allows full use of the porous structure inside the filament.

Conclusion

Metamaterials are the subject of interest in the world's leading research centers, and the spread of 3D printing has facilitated the creation of prototypes characterized by geometries that cannot be obtained by classical mechanical machining processes. The aim of this work was to create a metamaterial capable of encapsulating all the advantages of the various sound absorption systems. Numerical and experimental analysis were conducted on one of the simplest configurations that could be realized. The results shows that the main difficult aspect is the realization of the holes. Those holes are the inlet for the acoustics wave to the porous foam of the inner part of the filament. If the channel of the hole is melted the only advantage of this technology is the lightness of the sample respect of an unfoamed one. Further analysis would be conducted to determine the best way of perforation and to implement new geometry with an consistent airgap inside the sample.

Reference

- [1] L. Chang, A. Jiang, M. Rao, F. Ma, H. Huang, Z. Zhu, Y. Zhang, Y. Wu, B. Li, Y. Hu, Progress of low-frequency sound absorption research utilizing intelligent materials and acoustic metamaterials, *RSC Adv.* 11 (2021), 37784–37800. <https://doi.org/10.1039/D1RA06493B>
- [2] L. Z., Zhang, X., Mao, Y., Zhu, Y.Y., Yang, Z., Chan, C.T., Sheng, P., Locally Resonant Sonic Materials. *Science* 289 (2000), 1734–1736. <https://doi.org/10.1126/science.289.5485.1734>
- [3] N. Fang,, D. Xi, J. Xu, M. Ambati, W. Srituravanich, C. Sun, X. Zhang, Ultrasonic metamaterials with negative modulus, *Nat. Mater.* 5 (2006), 452–456. <https://doi.org/10.1038/nmat1644>
- [4] M. Yang, P. Sheng, Sound Absorption Structures: From Porous Media to Acoustic Metamaterials. *Annu. Rev. Mater. Res.* 47 (2017), 83–114. <https://doi.org/10.1146/annurev-matsci-070616-124032>
- [5] M.G.M. Marascio, J. Antons, D.P. Pioletti, P.E. Bourban, 3D Printing of Polymers with Hierarchical Continuous Porosity, *Adv. Mater. Technol.* 2 (2017), 1700145. <https://doi.org/10.1002/admt.201700145>
- [6] D. Tammaro, A.L. Henry Detry, L. Landonfi, F. Napolitano, M.M. Villone, P.L. Maffettone, A. Squillace , Bio-Lightweight Structures by 3D Foam Printing, in: 2021 IEEE 6th International Forum on Research and Technology for Society and Industry (RTSI), IEEE, (2021) Naples, Italy, pp. 47–51. <https://doi.org/10.1109/RTSI50628.2021.9597272>

Hygrothermal effects in aeronautical composite materials subjected to freeze-thaw cycling

Christian Bianchi¹, Pietro Aceti^{1*} and Giuseppe Sala¹

¹ Department of Aerospace Science and Technology, Politecnico di Milano, Milan, Italy

*pietro.aceti@polimi.it

Keywords: Fibre Reinforced Composite, Humidity Absorption, Freeze-Thaw Cycle, Hygrothermal Effects

Abstract. Fiber-reinforced composites (FRC) are becoming increasingly popular in aerospace, automotive and energy sectors. Despite the advantages owed to their strength and lightweight, understanding their behavior in different environments poses challenges. Particularly, humidity, temperature, and freeze-thaw cycles can significantly affect the durability of FRC components. This study investigates the impact of humidity, temperature, and freeze-thaw cycles on FRC inter-laminar areas and the matrix/fiber interface. Experimental methods, including heat analysis, X-Ray tomography and mechanical testing will assess the material's response to changing environmental conditions. This research enhances our understanding of FRC behavior, crucial for designing and maintaining FRC components.

Introduction

Fiber-reinforced composites (FRC) are increasingly utilized in various industries, including aerospace, automotive and energy. However, the extensive application of these advanced materials introduces new challenges in understanding their component behavior throughout their operational lifespan. Environmental factors, such as humidity and temperature, can adversely affect the properties of the matrix and weaken the fiber/matrix interface. Research indicates that the interlaminar regions and the matrix/fiber interface are particularly susceptible to the influence of humidity and temperature. Moreover, the mechanical properties of the composite are significantly impacted by the combined presence of moisture and the freeze-thaw cycle, surpassing the effects of individual environmental factors. Microcracks are induced by freeze-thaw cycles, which increases moisture penetration into composite structures [1,2].

Case studies

A/c structures, designed to withstand challenging conditions while prioritizing strength, weight and safety, are highly specialized and technologically advanced. Keeping this in mind, two case studies are conducted to establish accurate and meaningful thermal cycles. One of them considers the environmental conditions of commercial flights, typically cruising at altitudes between FL320 and FL400. At these altitudes, the International Standard Atmosphere (ISA) indicates temperatures ranging from -48°C to -55°C. The atmospheric pressure varies between 27450Pa and 18750Pa. Due to the compression of air by the aircraft's body, the skin temperature of the aircraft is higher than the static air temperature of -55°C as described in the following equation (1):

$$T_s = T_\infty - T_\infty \cdot \frac{(k-1) \cdot Ma^2}{2} \quad (1)$$

Where T_s is the stagnation point temperature of an ideal gas at temperature T_∞ impacting an object with a Mach number Ma . The temperature cycle is performed considering the ASTM-D7792 each one constituted of a 3-hour static phase at 30°C and 90% relative humidity, followed by a 3-hour thermal ramp to -22°C. General aviation planes typically cruise between 4500 and



9500 feet in altitude (data collected considering the data-sheet of a Cessna-172). For the ISA at this altitude, temperature values span between 6°C and -3°C, far less in respect of a commercial flight. Each cycle consists of 3-hour static phase at 30°C and 90% relative humidity, followed by 3-hour thermal ramp to -22°C.

Interlaminar shear strength

The relevant literature shows how composite materials behave when conditioned and frozen-thawed [3,4]. To understand the phenomena, one must investigate the adhesion between reinforcing fibre and epoxy matrix. Internal microcracks, voids and water inclusion can reduce the material's interlaminar characteristics, lowering its mechanical properties and operational life. The interlaminar shear strength is a matrix-dominated feature that plays a significant role in a variety of applications, as interlaminar shear is frequently the mechanism for load transmission across various composite components. The ASTM D2344 is adopted for manufacturing and test.

Test specimens

Two types of aeronautical composite materials are investigated using 0° ASTM specimens. One consists of carbon-reinforced fibre, while the other consists of glass-reinforced fibers. In both material a differential scanning calorimetry test is performed to assess the glass transitional glass temperature, T_g values span between 140°C and 145°C.

Conditioning process

Temperature and relative humidity influence composite materials degradation. Moisture affects resin and fiber-resin interface under humid conditions. Temperature affects moisture absorption as well, expanding it in freezing conditions and contracting it at room temperature. Moisture absorption is a diffusion process, where water molecules move from high to low concentration until equilibrium. In moisture uptake conditioning, ASTM D5229's "B" procedure is followed. Specimens are immersed in distilled water at 80°C and weighed at defined intervals until saturation. Another parameter variation was investigated to better define composite material humidity absorption. To study carbon fiber-reinforced composites' humidity absorption, two types of specimens were created. The first type, according to ASTM D5229, is made of 0° fibers, while the second is made of 90° fibers.

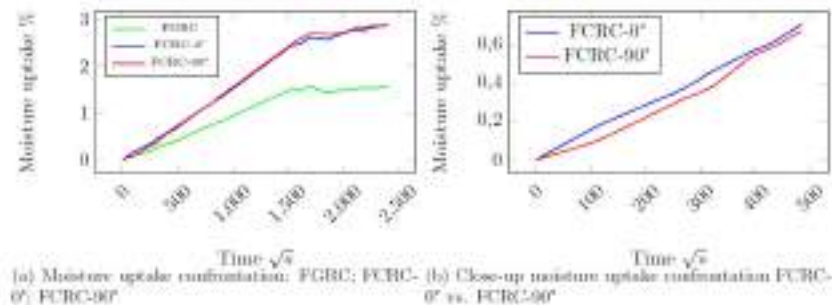


Figure 1: Conditioning results in different experimental conditions

Fig.1 data shows that both materials reached saturation in approximately 30 days. Fig.1.b demonstrates an opposite initial humidity absorption trend than expected, considering the higher concentration of fiber ends on the long side of the specimen. Specifically, FCRC-0° exhibits a higher absorption coefficient compared to FCRC-90°. However, after an initial transient, both specimen types (FCRC-0° and FCRC-90°) show similar behaviors regarding the rate and nature of moisture absorption. Ultimately, both reach saturation simultaneously, indicating that the fiber orientation in the plies has minimal impact on the absorption process.

Computed Tomography

A North Star Imaging X25 CT X-Ray Inspection is employed to inspect intralaminar damage due to conditioning and thermal cycling. The technique works well also if material to be analyzed is not radioopaque (as for example carbon fibers). In this case it previously moistened with a Zinc Iodide solution, which penetrates defects by capillarity, making them visible to X-rays. For non-radio-opaque composite materials an opaque enhanced dye penetrant was been used

Experimental results

Thermal and hygrothermal behavior is studied by separating the effects of water inclusion from those due to environmental temperature variation. The effects of thermal cycles are investigated as a final step.

Thermal effects. Temperature significantly affects the mechanical properties of composites, causing microstructural and property transformations including thermal expansion, degradation, and softening. To establish accurate testing conditions, dry specimens are referenced at a standard temperature of 23°C as a baseline. Shear strengths of carbon-reinforced and glass-reinforced composites are determined as $91.77 \pm 0.37 \text{ MPa}$ and $72.52 \pm 1.72 \text{ MPa}$, respectively, exhibiting a linear elastic phase followed by sudden load decrease until fracture, in accordance with ASTM D2344. Temperature-dependent behavior is assessed from tests conducted at 23°C, 60°C, 80°C, 110°C and 125°C; the results are presented in Fig.2. Samples undergo controlled heating in a convection oven aided by infrared lights to maintain desired temperatures. Interpolation curves generate mean shear stress summary graphs. Macroscopic examination and X-Ray Tomography confirm the expected fracture behavior of composites across different temperatures.

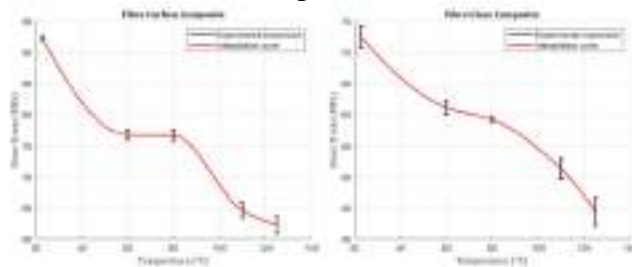


Figure 2: Interpolation ILSS results for FCRC and FGRC specimen at different temperatures.

Hygrothermal effects. Plasticization occurs when water molecules are absorbed into a material, transitioning it from a glassy to a rubbery state. This results in enhanced chain mobility and weaken intermolecular bonds. Consequently, there is a decrease in strength modulus and stiffness, while toughness and strain capacity increase. The ILSS test demonstrates that the carbon-reinforced composite exhibits plastic behavior with a less pronounced fracture compared to the dry material. Fracture occurs due to shear stress at mid-plane, confirmed by macroscopic examination, tomographic analysis (Fig. 3.a), and slow-motion videos. In contrast, the glass fiber reinforced composite initially shows an elasto-brittle behavior and the expected failure mode according to ASTM D2344. However, further investigation reveals an incorrect failure mode during the ILSS test. The wet glass-reinforced specimen collapses at the center until buckling occurs, as observed through tomography (Fig. 3.b).

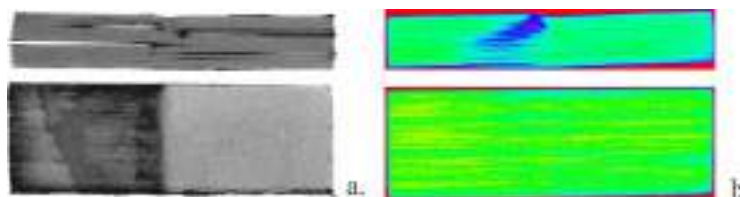


Figure 3: Tomography results on an FCRC and FGRC specimen tested in "wet" condition.

Thermal cycling effects. A drying cycle is included in both types of cycles to restore the material to a dry condition once the cycle is completed. By removing the internal water in the composite, the impacts of cycles can be separated from the plasticization effects of the matrix. Fig.4.a and Fig.4.b compare the "Freeze-Thaw" and "Hot-Hot" cycling outcomes. According to previous hypotheses, the results should demonstrate a distinction between the two curves indicating the severity of degradation caused by the "F-T", due to the nature of water expansion within the material. As a matter of fact, the results obtained cannot demonstrate this phenomenon.

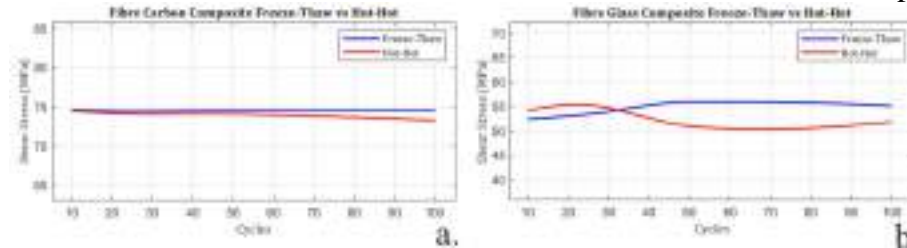


Figure 4: ILSS data confrontation for FCRC and FGRC "F-T" vs. "H-H" cycling.

Conclusions

The study is aimed to establish a representative coefficient indicating mechanical deterioration of materials under harsh environmental conditions, for timesaving in aeronautical industry destructive tests and standardized strength loss parameters in project planning. Two materials commonly used, carbon-reinforced and glass-reinforced composites, were selected. ILSS test investigated the phenomenon. Findings revealed significant shear strength reduction in both materials compared to the dry condition, with the "Hot-Wet" condition showing the most pronounced reduction. Further research is needed to understand failure mechanisms. Existing literature suggests a -25% shear strength reduction [1]. Research on multiple cycles and humidity absorption in composite materials coated with aeronautical paint is of interest, as it provides a more realistic understanding of aeronautical component behavior under hygrothermal effects.

References

- [1] Mohammad Abedi, S. Ebrahim Moussavi Torshizi, and Roohollah Sarfaraz. Damage mechanisms in glass/epoxy composites subjected to simultaneous humidity and freezethaw cycles. *Engineering Failure Analysis*, 120:105041, 2 2021. <https://doi.org/10.1016/j.engfailanal.2020.105041>
- [2] Laurent Cormier and Simon Joncas. Effects of cold temperature, moisture and freeze thaw cycles on the mechanical properties of unidirectional glass fiber-epoxy composites. *American Institute of Aeronautics and Astronautics*, 4 2010. <https://doi.org/10.2514/6.2010-2823>
- [3] Pietro Aceti, Luca Carminati, Paolo Bettini and Giuseppe Sala. Hygrothermal ageing of composite structures. Part 1: technical review. *Composite Structures*, 117076, 2023. <https://doi.org/10.1016/j.compstruct.2023.117076>
- [4] Pietro Aceti, Luca Carminati, Paolo Bettini and Giuseppe Sala. Hygrothermal ageing of composite structures. Part 2: mitigation technique, detection and removal. *Composite Structures*, 117076, 2023. <https://doi.org/10.1016/j.compstruct.2023.117076>

Polymer matrices for composite materials: monitoring of manufacturing process, mechanical properties and ageing using fiber-optic sensors

Davide Airoidi¹, Pietro Aceti^{1*} and Giuseppe Sala¹

¹ Department of Aerospace Science and Technology, Politecnico di Milano, Milan, Italy;

pietro.aceti@polimi.it

Keywords: Polymer Matrices, Humidity Absorption, Fiber Optic Sensors, Epoxy Resin, Hygrothermal Aging

Abstract. Composite materials have gained significant prominence in the field of aerospace engineering owing to their exceptional strength-to-weight ratio, making them well-suited for structural applications. However, these materials are susceptible to degradation due to exposure to environmental factors, such as humidity and temperature changes. Detecting and quantifying such damage presents considerable challenges, particularly in the case of cyclically loaded components. Fiber Bragg Grating (FBG) sensors provide a non-destructive means of monitoring composite material degradation by leveraging optical reflection to measure changes in strain and temperature. This research aims to assess and validate a methodology for employing FBG sensors to effectively monitor the degradation of composite material matrices. The investigation mainly consists in characterizing the correlation between FBG sensor wavelength shifts and the strains incurred due to the manufacturing process, moisture absorption, and thermal effects. The anticipated outcomes hold the potential to enhance the reliability and safety of composite structures employed within the aeronautical domain.

Introduction

The studies reported in this paper investigated the production process, conducted mechanical tests and evaluated the mechanical properties changes under different conditions in epoxy resin specimens. Understanding the behavior of epoxy resins is crucial due to their widespread usage in aircraft structures and their sensitivity to ageing caused by environmental conditions. Real-time monitoring is essential in aeronautic structures and two FBG sensors were used to monitor deformations and residual stresses during production and to monitor the strains developed during immersion in a hot-water environment. Tensile tests were performed to assess the mechanical properties, including the impact of moisture on resin performance and the recovery after drying. This work lays the foundation for further exploration of fiber optic sensors in moisture monitoring and highlights their potential for cost savings and enhanced aircraft safety [1].

FBG as humidity sensor

Several reference studies have demonstrated the feasibility of utilizing an FBG sensor as a humidity sensor by coating it with a moisture-sensitive coating. In this manner, when the sensor is exposed to a humid environment, the fiber detects a wavelength shift resulting from the strain induced by moisture absorption. The equation that relates the wavelength variations to the different contributions of relative humidity, mechanical deformations and temperature changes is reported here below:

$$\frac{\Delta\lambda_B}{\lambda_B} = (1 - p_e)\varepsilon_M + (1 - p_e)\frac{E_c A_c}{E_c A_c + E_f A_f}\beta_c \Delta RH + \left\{ (1 - p_e)\frac{E_c A_c \alpha_c + E_f A_f \alpha_f}{E_c A_c + E_f A_f} + \xi \right\} \Delta T$$

Where ε_M is the axial mechanical strain, ΔT is the temperature change, p_e is the photo-elastic constant, and ξ is the thermo-optical coefficient. Where E is the Young's modulus, A the cross-

sectional areas, α the coefficient of thermal expansion, and β_c the constant coefficient of hygroscopic expansion of the polymer. The subscript c stands for the coating, while f stands for the bare fiber. Once decoupled the mechanical, thermal and humidity effects it becomes possible to determine each contribution and monitor the manufacturing and conditioning processes [2], [3], [4], [5].

Production of test specimens

Before facing the testing phase, it was necessary to produce the specimens in compliance with ASTM D638 Standard. Epoxy resin was adopted, since it is a commonly used matrix material in composites due to its excellent adhesive properties, low viscosity, and exceptional mechanical properties. It finds applications in aerospace, automotive, sports, and marine industries. The production process consists of different phases:

- Heat the resin in the oven to make it liquid.
- Place the resin in the vacuum oven performing a degassing process.
- Heat the resin again to reduce its viscosity.
- Cast the resin in the mold using a syringe.
- Cure the resin in the oven.
- Allow the specimen to cool down.

During this process, the strains developed in the specimen were monitored by the FBG sensor, obtaining the plot in Figure 1:

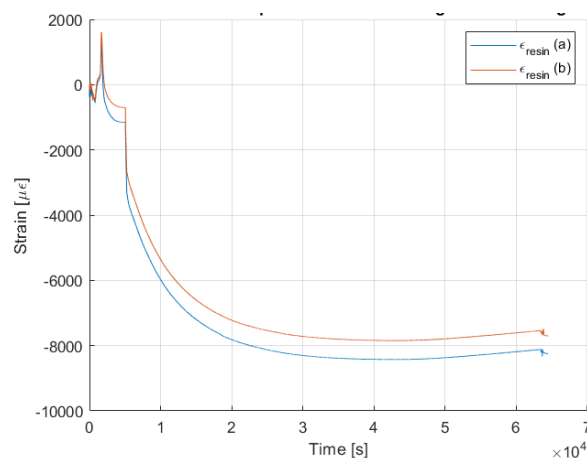


Figure 1: Total strain developed on the resin during manufacturing.

The entire production process caused a compression state-of-stress, leading to a total value of strain close to 8000 micro-strains and a residual internal stress of 25 MPa.

Conditioning process

To reproduce a hot-wet environment and accelerate the moisture absorption process, the test specimens were immersed in an 80°C water bath. The test lasted approximately 1500 hours, during which real-time monitoring of wavelength variations was carried out as shown in Figure 2. By extrapolating the collected data, it was possible to calculate the deformations of the specimens. The strains due to relative humidity shows a rapid increase in the first 100 hours, followed by a sharp decline until reaching a plateau. The non-monotonous behavior could be attributed to various factors, such as the slowdown of the hydrolysis process [6], [7]. The strains obtained in this phase are showed in the figure below:

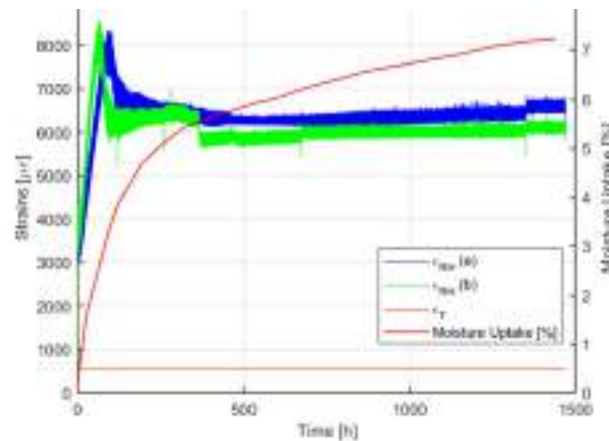


Figure 2: Strain comparison during conditioning.

Mechanical properties

Once having conditioned a series of specimens, their mechanical properties were compared to those characterizing unconditioned specimens and specimens dried after absorption. This was done to observe whether moisture absorption would degrade the material's performance and, if so, whether it could be recovered through a drying process. The figure 3 shows that the moisture absorption causes a degradation of the mechanical properties in terms of Young's modulus and resistance. After the drying process, the material is unable to regain its original properties. In fact, its performance worsens, exhibiting brittle behavior and being prone to premature failure. These tests were carried out using an electro-mechanical tensile machine in compliance with ASTM International Standards [8].

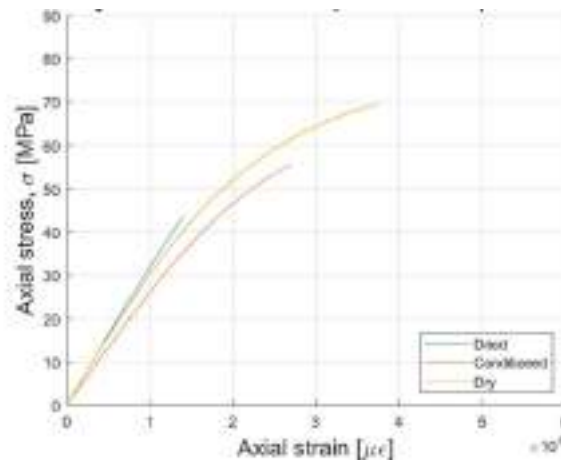


Figure 3: Comparison between dry, wet and dried specimens.

Conclusions

The research describes the technological challenges faced in studying the mechanical properties of epoxy resin. After developing production process to obtain defect-free specimens, tests were conducted to evaluate the material's mechanical properties under dry, conditioned, and dried conditions. The specimens immersed in hot water showed a reduction in mechanical properties: -14.3% in Young's modulus, -24% in breakage stress, -31.5% in strain at break. The dried specimens were unable to fully recover their initial characteristics, and they show a further reduction of resistance properties: -37.7% in stress at break, -64.5% in breakage strain. Fiber optic sensors were used to monitor the strains during production and conditioning, showing a good response in detecting the humidity variations. After being immersed for 1500 hours, the fibers were not able anymore to detect deformations during a tensile test because they were damaged.

Further research should investigate the causes of sensor malfunction and study the effect of humid environments and temperature variations on complete composite materials used in the aerospace industry.

References

- [1] V. Giurgiuntiu, *Structural Health Monitoring of Aerospace Composite*, Elsevier, 2016.
- [2] P. Giaccari, H. G. Limberger e P. Kronenberg, «*Influence of humidity and temperature on polyimide-coated*» in *Bragg Gratings, Photosensitivity, and Poling in Glass fibers and Waveguides: Applications and Fundamentals*, Optical Society of America, p. BFB2, (2001). <https://doi.org/10.1364/BGPP.2001.BFB2>
- [3] P. Aceti, «Sensing principles of FBG in humid environments,» Politecnico di Milano, 2023.
- [4] Teck L. Yeo, Tong Sun, Kenneth T. V. Grattan, David Parry, Rob Lade, and Brian D. Powell, «Polymer-Coated Fiber Bragg Grating for Relative Humidity Sensing,» *IEEE Sensor Journal*, 2005.
- [5] Pascal Kronenberg and Pramod K. Rastogi, Philippe Giaccari and Hans G. Limberger, «Relative humidity sensor with optical fiber Bragg gratings», *Optics Letters*, 2002. <https://doi.org/10.1364/OL.27.001385>
- [6] Pietro Aceti, Luca Carminati, Paolo Bettini and Giuseppe Sala. Hygrothermal ageing of composite structures. Part 1: technical review. *Composite Structures*, 117076, 2023. <https://doi.org/10.1016/j.compstruct.2023.117076>
- [7] Pietro Aceti, Luca Carminati, Paolo Bettini and Giuseppe Sala. Hygrothermal ageing of composite structures. Part 2: mitigation technique, detection and removal. *Composite Structures*, 117076, 2023. <https://doi.org/10.1016/j.compstruct.2023.117076>
- [8] ASTM International. Standard Test Method tensile properties of plastics. D638

An energy-based design approach in the aero-structural optimization of a morphing aileron

Alessandro De Gaspari^{1,a,*}, Vittorio Cavalieri^{1,b} and Nicola Fonzi^{1,c}

¹Department of Aerospace Science and Technology, Politecnico di Milano, Via La Masa 34, 20156 Milano, Italy

^aalessandro.degaspari@polimi.it, ^bvittorio.cavalieri@polimi.it, ^cnicola.fonzi@polimi.it

Keywords: Multi-Objective Optimization, Morphing, Aerodynamic Efficiency, Energy Efficiency

Abstract. This paper describes the application of an energy-based optimization procedure for the design of a morphing aileron as an alternative to replace a conventional hinged aileron. The design procedure starts with an aerodynamic shape optimization embedding skin structural constraints and energetic information. Different candidate morphing shapes able to provide reduced drag are obtained, and they differ for the required actuation level. The structural design is then performed through a dedicated multi-objective topology and sizing optimization, aimed at obtaining a structural configuration that achieves the target shape with minimum error and minimum actuation force. The energetic comparison between the designed solution and the hinged solution shows that morphing is convenient also from the energy viewpoint. Finally, a fluid-structure interaction simulation assesses the performances of the designed solution.

Introduction

Nowadays, there is a growing interest in mitigating the environmental impact of air transportation [1]. The morphing concept is one of the research topics that have the potential to improve aircraft efficiency and reduce pollutant emissions and noise [2].

The aim of this work is to design a morphing aileron and to compare its performances with a conventional hinged aileron. From the aerodynamic viewpoint, the smooth curvature change of morphing enables improved efficiency [3]. However, the morphing concept represents a valid alternative only if an overall benefit is achieved [4]. Therefore, the actuation requirement of the morphing solution is used as design objective and as performance index for validation.

The supercritical NASA SC(2)-0412 airfoil, modified to consider its shape change in the wing aileron region, is used as test case in a transonic flight condition (Reynolds=6000000, Mach=0.74). The design procedure is split in two levels. First, shape optimization is conducted, including aerodynamic analyses, skin structural constraints and energetic estimates. Second, structural optimization provides solutions according to the requirements of the previously defined target shapes. Finally, energetic and aero-structural assessments are performed.

Energy-based Shape Optimization

Parameterization technique. The Class-Shape Transformation (CST) method, specialized for morphing devices [5], is used for the airfoil identification and to introduce the morphing shape changes. The adopted approach allows the structural behavior of the morphing skin to be considered, with the analytical computation of the skin stresses from the geometrical description. The morphing shapes are parameterized using two design variables selected among the CST parameters, namely the trailing-edge equivalent rotation and the airfoil boat-tail angle variation.

Actuation energy estimate. The energy requirement for the morphing device is estimated as sum of strain energy and aerodynamic work [6]. The strain energy stored in the structure is due to the morphing deformation process and is computed analytically from the curvature variation of the



skin. The aerodynamic work corresponds to the energy required to counteract the application of the aerodynamic forces during the morphing process. It can be estimated from the pressure coefficient distribution and the morphing shape change. The actuation system is assumed to be a linear sliding actuator connected to the lower skin. Assuming a linear variation of the force with the stroke, the maximum actuation force is estimated from the actuation energy.

Problem statement. The shape optimization is formulated as a multi-objective problem. Drag coefficient and actuation force are objectives to minimize. The lift coefficient is constrained to be higher than 1.15. Other constraints prevent axial stresses in the upper skin and limit the maximum curvature variation. The uncertainty associated to the structural design, namely the thickness distribution of the skin, is also considered in the optimization by parametrically solving the optimization problem for different thickness values. Response surface models of the objective functions and constraints are built to perform the optimization.

Response surfaces. Lift and drag coefficients are computed with Reynolds-averaged Navier-Stokes (RANS) equations, solved in SU2 [7]. CST is used to compute strain energy, aerodynamic work, actuation energy and force. All these outputs are computed for a Latin hypercube sample in the space of the design variables. These simulated values are used to construct response surface models through Radial Basis Function (RBF) interpolation.

Shape optimization results. The multi-objective optimization based on response surfaces is performed for four thicknesses values, resulting in several Pareto fronts, which are reported in Fig. 1. Different morphing solutions can provide reduced drag, but they differ for the actuation level required to achieve the morphing shape. Three candidate shapes are selected for the subsequent steps of analysis and design.

Aerodynamic comparison with the hinged aileron. The aerodynamic performances of the selected optimal shapes are compared with the hinged aileron rotated of 9.7 deg, which corresponds to the target lift coefficient requirement. The rigid solution is characterized by higher drag, resulting in lower aerodynamic efficiency at each angle of attack.

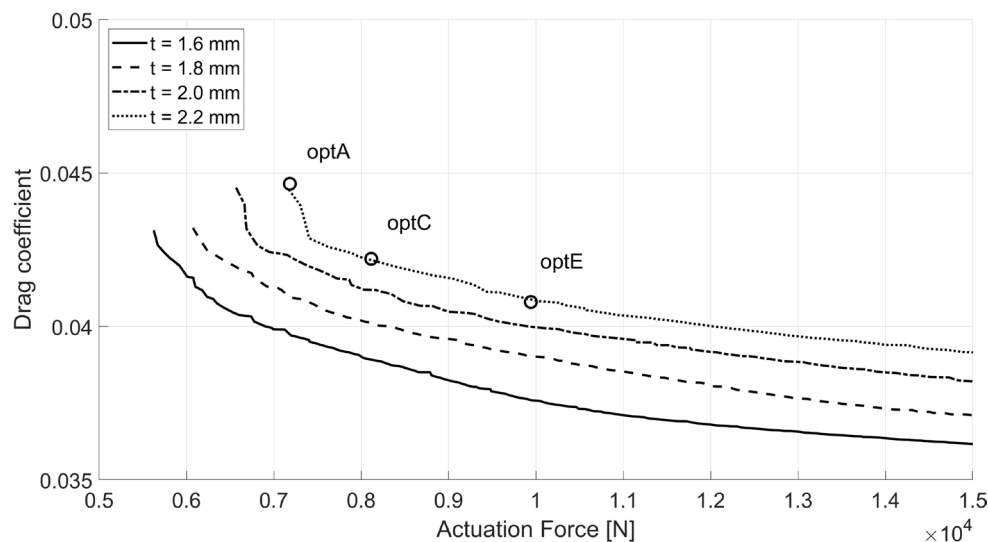


Figure 1: Pareto fronts from the shape optimization for different values of skin thickness t and equal value of target $C_L=1.15$.

Structural Topology and Sizing Optimization

The structural design of the morphing trailing-edge is based on a medium-fidelity FEM model consisting of a skin section and some internal beams connected to upper and lower skin.

Problem statement. A dedicated multi-objective genetic algorithm is used for the topology and sizing optimization. The design variables describe both the topology (beam attachment points,

beam existence) and the sizing (in-plane dimensions of skin and beams). Different objectives are minimized: i) the least-square error (LSE) between the target shape and the morphing shape of the actuated device subject to the aerodynamic loads of the target shape; ii) the actuation force to achieve the morphing shape; iii) the LSE between the undeformed configuration and the undeformed deformed shape under the baseline aerodynamic loads.

Structural design results. The adopted optimization enables to achieve the target shape with minimum error and minimum force. The process is repeated for the three candidate shapes.

Aerodynamic validation. Aerodynamic analyses of the achieved morphing shapes are performed to evaluate if the target lift coefficient is achieved. When this is not guaranteed (*optC*, *optE*), a slightly increase of the actuator stroke allows the target lift coefficient to be met. The three deformed morphing shapes are compared with the hinged shape in Fig. 2.

Structural validation. Strain in the structure is below 0.5%, as depicted in Fig. 3 in case of solution *optE*.



Figure 2: Morphing shapes and hinged shape corresponding to target $C_L=1.15$.

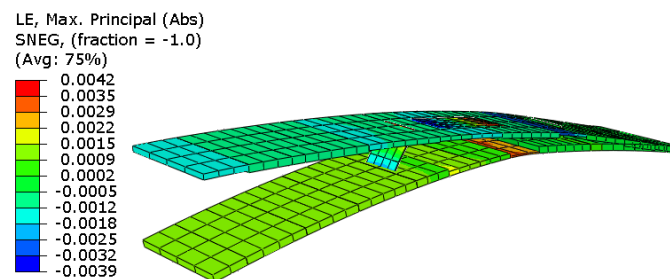


Figure 3: Strain distribution in the structure for solution *optE*.

Actuation Energy Evaluation

The designed structural solutions that guarantee the target lift coefficient are compared with the hinged solution from the actuation energy viewpoint. The actuation energy for the morphing solutions can be divided in a structural contribution (due to the strain energy) and an aerodynamic contribution (due to the aerodynamic loads), as reported in Fig. 4. The morphing results are compared with the hinged energy result, computed from hinge moment and aileron rotation, and totally due to aerodynamic loads. Although there is a strain energy contribution associated with the morphing process, the actuation energy for morphing solutions is lower than the energy required by hinged solution. This is possible because morphing solutions can achieve the target lift coefficient with smaller trailing-edge equivalent rotation with respect to the rigid rotation of the conventional aileron. Consequently, reduced drag is also achieved.

Performance Assessment

As final validation, a fluid-structure interaction (FSI) analysis, coupling RANS analyses and nonlinear structural analyses, is performed to evaluate how the aerodynamic performances are affected by the structural compliance. This FSI analysis shows that the morphing shape can be achieved as expected from FEM analyses, with negligible differences in the deployed

configuration, that do not compromise the requested lift coefficient increment. However, the structural compliance has a small impact on the baseline configuration of the airfoil.

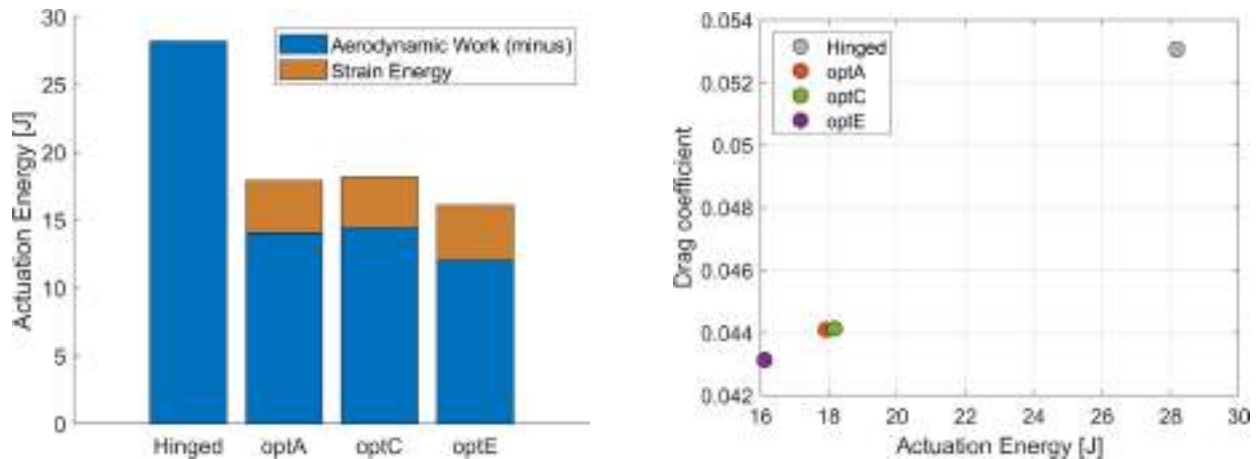


Figure 4: Actuation energy and drag coefficient comparison between morphing and hinged aileron.

Conclusions

This paper has presented the optimum design of a morphing aileron and the comparison of its performances with a corresponding hinged aileron. The proposed energy-based approach has proved successful in providing morphing solutions characterized by enhanced aerodynamic and energetic efficiency with respect to the conventional hinged solution.

References

- [1] European Commission, Flightpath. 2050-Europe's vision for aviation: maintaining global leadership and serving society's needs. Publications Office of the EU, 2012.
- [2] H. Monner, M. Kintscher, T. Lorkowski and S. Storm. Design of a smart droop nose as leading edge high lift system for transportation aircrafts. In 50th AIAA/ASME/ASCE/AHS/ASC Structures, Structural Dynamics, and Materials Conference, 2009.
<https://doi.org/10.2514/6.2009-2128>
- [3] B.K.S. Woods, O. Bilgen and M.I. Friswell. Wind tunnel testing of the fish bone active camber morphing concept. Journal of Intelligent Material Systems and Structures, 25(7):772–785, 2014. <https://doi.org/10.1177/1045389X14521700>
- [4] T.A. Weisshaar. Morphing aircraft technology - new shapes for aircraft design, 2006.
- [5] A. De Gaspari and S. Ricci. Knowledge-based shape optimization of morphing wing for more efficient aircraft. International Journal of Aerospace Engineering, 2015.
<https://doi.org/10.1155/2015/325724>
- [6] A. De Gaspari. Study on the actuation aspects for a morphing aileron using an energy-based design approach. In Actuators, volume 11, page 185. MDPI, 2022.
<https://doi.org/10.3390/act11070185>
- [7] R. Sanchez, R. Palacios, T.D. Economou, H.L. Kline, J.J. Alonso and F. Palacios. Towards a Fluid-Structure Interaction Solver for Problems with Large Deformations Within the Open-Source SU2 Suite. In 57th AIAA/ASCE/AHS/ASC Structures, Structural Dynamics, and Materials Conference, 2016. <https://doi.org/10.2514/6.2016-0205>

A boundary element method for thermo-elastic homogenization of polycrystals

Dario Campagna^{1,a}, Vincenzo Gulizzi^{1,b}, Alberto Milazzo^{1,c} and Ivano Benedetti^{1,d*}

¹Department of Engineering, University of Palermo, Viale delle Scienze, Edificio 8, 90128, Palermo, Italy

^a dario.campagna@unipa.it, ^b vincenzo.gulizzi@unipa.it, ^c alberto.milazzo@unipa.it,
^d ivano.benedetti@unipa.it

Keywords: Polycrystalline Materials, Steady-State Thermo-Elasticity, Computational Homogenization, Computational Micro-Mechanics, Multiscale Materials Modelling, Boundary Element Method

Abstract. A computational framework for thermo-elastic homogenization of polycrystalline materials is proposed. The formulation is developed at the crystal level and it is based on the explicit Voronoi representation of the micro-morphology. The crystal thermo-elastic equations are formulated in an integral form and numerically treated through the boundary element method. The presence of volume integrals, induced by the inherent physics of the thermo-elastic coupling, is addressed through a Dual Reciprocity Method (DRM), which allows recasting the formulation in terms of boundary integrals only. The developed methodology is applied for estimating the homogenized thermo-elastic constants of two widely employed ceramic materials. The method may find applications in multiscale analysis of polycrystalline structural component.

Introduction

Multiscale materials modelling, which focuses on understanding how mechanisms at different length/time scales interact and contribute to the emerging of materials properties at larger scales, is assuming increasing importance in engineering, thanks to developments in experimental materials nano/micro-characterization, which provide a wealth of detailed information about the materials constituents, and to the larger availability of high performance computing, which provides the means to process all the available information in complex modelling frameworks. This favours the understanding of existing materials and boosts the design of new ones, with desired properties at a given scale, consolidating the *materials-by-design* paradigm [1].

An essential item of multiscale modelling is materials homogenization, which generally focuses on inferring the materials aggregate properties at a given scale from the knowledge of the morphological and constitutive features of material constituents at lower scales. Examples are provided by the techniques focused on predicting the properties of composite materials at the laminate level from the characterization of the individual plies or even, at a lower scale, from the properties of fibers and matrices and their mutual arrangement. An important concept in materials homogenization is that of *representative volume element* that may be defined as a material sample small enough to be considered as a material point at the component scale, but large enough to contain a number of elementary micro-constituents sufficient to characterize the aggregate properties in an average sense, so that no meaningful fluctuations in average materials properties are induced by small variations of the specimen size [2].

In this work, an original framework for computational homogenization of polycrystalline materials, is discussed. Polycrystalline materials, which include metals, alloys, or ceramics, are widely employed in engineering and their properties at the component level emerge from the properties of individual crystals and their interactions. The framework is based on the employment of a multi-region boundary integral formulation for representing the thermo-mechanics of the



aggregate. Differently from finite element approaches, it allows examining the thermo-elastic problem considering as primary variables only crystal boundary displacements, temperature, tractions and thermal fluxes, promoting remarkable savings in terms of overall number of degrees of freedom and computational storage memory and resolution time, which is of paramount importance for effective multiscale analysis.

This work summarizes the main aspects of the developed framework and reports some homogenization results. The interested readers may access Refs.[3-13] for further details.

Formulation overview

The developed framework is based on: *i*) algorithms for the generation of sets of Voronoi polycrystalline specimens [3,6]; *ii*) robust meshing algorithms able to deal with the statistical features of polycrystalline aggregates [6]; *iii*) a boundary integral representation of the thermo-elastic problem obtained through the *dual reciprocity method* (DRM) [13]; *iv*) algorithms for the discretization and robust numerical integration of the thermo-mechanical boundary integral equations [13]; *v*) algorithms for the computation of volume averages of the micro-fields, needed for retrieving the *apparent* materials properties and estimating the *effective* ones [13].

Morphology generation/meshing. Voronoi-Laguerre tessellations are employed to represent polycrystalline morphologies retaining the main statistical features of real materials. Open-source packages, e.g. VORO++ (<https://math.lbl.gov/voro++/>) or NEPER (<https://neper.info>), are available to generate general 3D tessellations. Specialized algorithms for robust boundary elements meshing are presented in Ref.[6]. *Non-prismatic periodic realizations* are employed in this work, as they remove boundary walls distortions and enhance homogenization convergence.

Boundary integral formulation. Differently from finite elements, the starting point for the formulation is the single-crystal thermo-elastic boundary integral representation

$$c_{ij}(\mathbf{x}) U_j(\mathbf{x}) + \int_{\Gamma} \hat{T}_{ij}^*(\mathbf{x}, \mathbf{y}) U_j(\mathbf{y}) d\Gamma = \int_{\Gamma} U_{ij}^*(\mathbf{x}, \mathbf{y}) T_j(\mathbf{y}) d\Gamma + \int_{\Omega} U_{ij}^*(\mathbf{x}, \mathbf{y}) F_j(\mathbf{y}) d\Gamma \quad (1)$$

where: $i, j = 1, \dots, 4$; Γ and Ω denote the crystal boundary and domain; x and y are respectively the *collocation* and *integration* point; U_j and T_j are components of generalized thermo-elastic displacements and tractions respectively, which collect, respectively, components of displacements and the temperature jump and components of mechanical tractions and the thermal flux; U_{ij}^* and \hat{T}_{ij}^* are contain combinations of components of the elastic and thermal fundamental solutions, such as to introduce the thermo-elastic coupling in the integral representation, together with the volume terms F_j , which contains components of the thermal gradient. In Eq.(1) the first integral on the left-hand side must be intended as Cauchy principal value.

The presence of the volume integral in Eq.(1) requires special consideration: its presence would call for volume discretization, thus reducing the attractiveness of the integral formulation. To retrieve the benefits of a pure *boundary* representation, this integral can be transformed into a sum of boundary integrals employing the dual reciprocity technique described in Ref.[13] and references therein. Once this transformation is performed, the pure boundary integral equations can be employed for modelling the thermo-mechanics of the aggregate: for each grain, they are collocated at the nodes of the boundary mesh and are numerically integrated using the boundary element method. After such operations, discrete systems expressed in terms of generalized thermo-elastic boundary nodal displacements and tractions are associated with each grain; such equations are then coupled with suitable interface continuity/equilibrium equations and with consistent boundary conditions enforced on the overall aggregate producing a system of the form

$$\begin{bmatrix} \mathbf{A} \\ \mathbf{I} \end{bmatrix} \mathbf{X} = \begin{bmatrix} \mathbf{BY} \\ \mathbf{0} \end{bmatrix} \quad (2)$$

where the blocks \mathbf{A} and \mathbf{B} contain coefficients stemming from the boundary element integration, \mathbf{X} and \mathbf{Y} collect, respectively, unknown and known nodal components of displacements, temperature, tractions and thermal flux, and \mathbf{I} implements the intergranular continuity equations. Eq.(2) is to be solved with sparse-matrix specialized solvers, due to its numerical structure.

Once the numerical solution of the system in Eq.(2) is available, the micro-fields can be solved. The homogenization is performed enforcing periodic thermo-elastic boundary conditions and computing volume averages of stresses and thermal fluxes, which allows retrieving the apparent elastic, conductivity, and thermo-elastic apparent constants. In this work a *statistical computational homogenization* is implemented, which employs both ensemble and volume averages for estimating apparent and effective properties. Assuming ergodicity, ensemble averages of volume averages computed over sets of polycrystals containing a selected number of grains are computed to associate apparent properties with that number of grains; the operation is repeated at increasing number of grains until convergence of the apparent properties is recorded, thus providing an estimate of the material effective properties, see Ref.[13].

Some numerical results

Statistical computational homogenization results about polycrystalline silicon carbide and alumina are presented here. Single crystal properties at room temperature are taken as in Ref.[13] and Fig.(1) shows the convergence of the apparent thermo-elastic constants at increasing number of grains. Ensemble averages are computed over sets of ten realizations and up to 100 grains per realization are considered. The estimated properties always fall within Reuss and Voigt bounds.

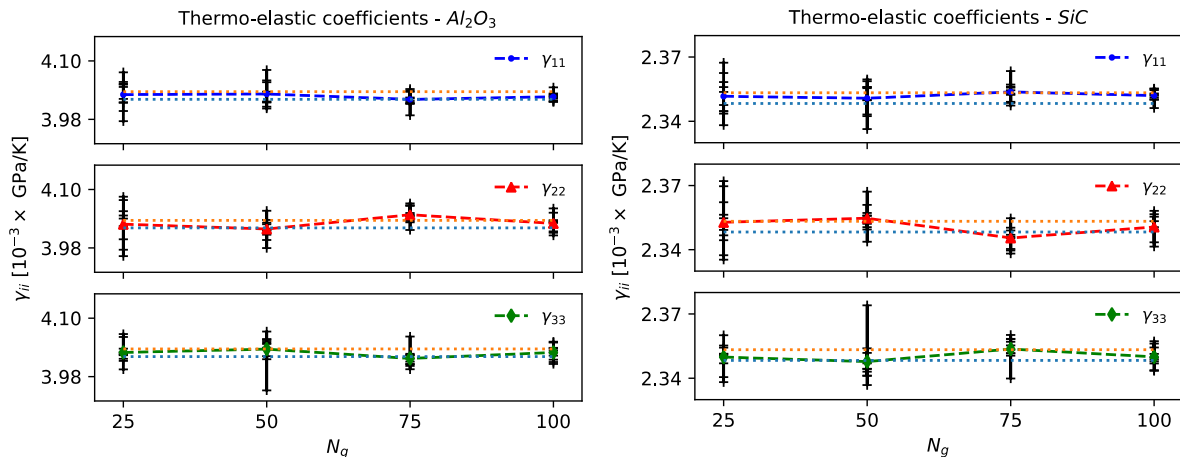


Fig.1: Computational homogenisation results for selected components of thermo-elastic coefficients for polycrystalline alumina and silicon carbide. The + markers identify volume averages over single realisations, the dashed curves correspond to ensemble averages, while the shaded area lies between the Reuss' and Voigt's bounds.

Summary

The development of an original multi-region dual reciprocity boundary elements framework for thermo-elastic homogenization of polycrystalline materials has been discussed, highlighting the benefits offered with respect to other popular approaches. The presented results highlight the effectiveness in estimating materials effective properties. The proposed tool may be employed as component of multiscale analysis tools.

References

- [1] M. J. Buehler, Materials by design? A perspective from atoms to structures, *MRS Bulletin* 38 (2) (2013) 169--176. doi:10.1557/mrs.2013.26. <https://doi.org/10.1557/mrs.2013.26>
- [2] S. Nemat-Nasser, M. Hori, Micromechanics: overall properties of heterogeneous materials, in: North-Holland Series in Applied Mathematics and Mechanics, Vol. 37, 1993.
- [3] I. Benedetti, M. Aliabadi, A three-dimensional grain boundary formulation for microstructural modeling of polycrystalline materials, *Comput. Mater. Sci.* 67 (2013) 249–260. <https://doi.org/10.1016/j.commatsci.2012.08.006>
- [4] I. Benedetti, M. Aliabadi, A three-dimensional cohesive-frictional grain-boundary micromechanical model for intergranular degradation and failure in polycrystalline materials, *Comput. Methods Appl. Mech. Engrg.* 265 (2013) 36–62. <https://doi.org/10.1016/j.cma.2013.05.023>
- [5] I. Benedetti, M. Aliabadi, Multiscale modeling of polycrystalline materials: A boundary element approach to material degradation and fracture, *Comput. Methods Appl. Mech. Engrg.* 289 (2015) 429–453. <https://doi.org/10.1016/j.cma.2015.02.018>
- [6] V. Gulizzi, A. Milazzo, I. Benedetti, An enhanced grain-boundary framework for computational homogenization and micro-cracking simulations of polycrystalline materials, *Comput. Mech.* 56 (4) (2015) 631–651. <https://doi.org/10.1007/s00466-015-1192-8>
- [7] I. Benedetti, V. Gulizzi, V. Mallardo, A grain boundary formulation for crystal plasticity, *Int. J. Plast.* 83 (2016) 202–224. <https://doi.org/10.1016/j.ijplas.2016.04.010>
- [8] V. Gulizzi, C. Rycroft, I. Benedetti, Modelling intergranular and transgranular micro-cracking in polycrystalline materials, *Comput. Methods Appl. Mech. Engrg.* 329 (2018) 168–194. <https://doi.org/10.1016/j.cma.2017.10.005>
- [9] I. Benedetti, V. Gulizzi, A. Milazzo, Grain-boundary modelling of hydrogen assisted intergranular stress corrosion cracking, *Mech. Mater.* 117 (2018) 137–151. <https://doi.org/10.1016/j.mechmat.2017.11.001>
- [10] I. Benedetti, V. Gulizzi, A grain-scale model for high-cycle fatigue degradation in polycrystalline materials, *Int. J. Fatigue* 116 (2018) 90–105. <https://doi.org/10.1016/j.ijfatigue.2018.06.010>
- [11] I. Benedetti, V. Gulizzi, A. Milazzo, A microstructural model for homogenisation and cracking of piezoelectric polycrystals, *Comput. Methods Appl. Mech. Engrg.* 357 (2019) 112595. <https://doi.org/10.1016/j.cma.2019.112595>
- [12] F. Parrinello, V. Gulizzi, I. Benedetti, A computational framework for low-cycle fatigue in polycrystalline materials, *Comput. Methods Appl. Mech. Engrg.* 383 (2021) 113898. <https://doi.org/10.1016/j.cma.2021.113898>
- [13] Benedetti, I. An integral framework for computational thermo-elastic homogenization of polycrystalline materials, *Comput. Methods in Appl. Mech. Engrg.* 407 (2023): 115927. <https://doi.org/10.1016/j.cma.2023.115927>

Flutter instability in elastic structures

Davide Bigoni^{1,a,*}, Francesco Dal Corso^{1,b}, Andrea Piccolroaz^{1,c},
Diego Misseroni^{1,d} and Giovanni Noselli^{2,e}

¹DICAM, University of Trento, Italy

²SISSA – International School for Advanced Studies, Trieste, Italy

^adavide.bigoni@unitn.it, ^bfrancesco.dalcorso@unitn.it, ^candrea.piccolroaz@unitn.it,
^ddiego.misseroni@unitn.it, ^egiovanni.noselli@sissa.it

Keywords: Flutter, Hopf Bifurcation, Non-Holonomic Systems

Abstract. Flutter instability caused by follower loads has become a reality after the invention of the "freely-rotating wheel device" by Bigoni and Noselli, of the "flutter machine", and of the device to generate Reut-type loads. Further research has proven that flutter instability, Hopf bifurcation, dissipation instabilities, and the Ziegler paradox are all possible in conservative systems, thus disproving an erroneous belief continuing since at least 50 years. Finally, a new type of flutter instability has been addressed, generated by the "fusion" of two structures which are separately stable, but become unstable when joined together. The analysis of instability involves here the treatment of a discontinuity in the curvature of a constraint.

Introduction

Flutter instability is a dynamic behaviour consisting in a blowing-up oscillatory motion, a phenomenon discovered in structural mechanics almost a century ago because of the application of non-conservative (follower forces) to structures. Beside aeroelastic flutter (which will not be considered here), research in this field embraces mechanobiology, growing of plant shoots, motility of cells through eukaryotic cilia, vertebral segmentation in embryos, control problems, the design of soft robotic actuators, graphene peeling, wire drawing, the deployment and retrieval of space tether systems, and solar sails. In the following, new findings are presented in this research topic, including experimental methodologies to follower forces [1-4], non-holonomic constraint [5], effects related to non-smoothness of the equations of motion [6].

The flutter machine

The concept of a follower force is controversial, because the application of these kind of forces to elastic structures leads to several unexpected and counter-intuitive effects: (i.) the lack of Eulerian instability; (ii.) the presence of a Hopf bifurcation; (iii.) the destabilizing effect of dissipation; (iv.) the so-called 'Ziegler paradox' [7]. In this context, Koiter [8] pointed out that follower forces should have been considered as mathematical abstractions, not reproducible in laboratories. As a consequence of that, several attempts to generate these forces have been criticized. A new approach was proposed by Bigoni and Noselli [1] and later perfected with the so-called 'flutter machine' by Bigoni et al. [2, 3], in which a tangentially follower force is generated through the sliding with friction of a freely rotating wheel against a moving support, Fig. 1.



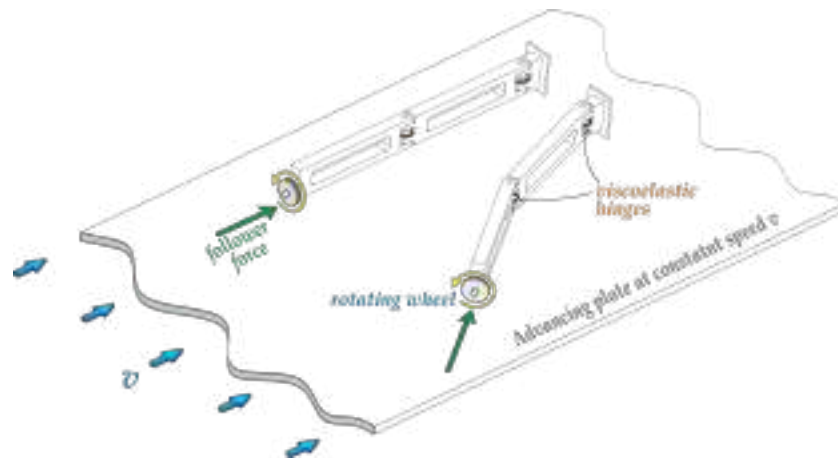


Fig. 1: The way to generate a follower force through the sliding of a freely-rotating wheel against a movable constraint. The wheel is mounted at the free end of a Ziegler double pendulum.

The new experimental set-up has permitted for the first time the systematic validation of the model of following forces and has led to a confirmation of the above listed features (i.)-(iv.). The concepts developed for follower forces also suggested the design of a device to produce forces of the Reut type [4].

Non-holonomic constraints

The concept of the sliding wheel has prompted the idea of substituting the wheel with a similar but purely non-holonomic constraint, Fig. 2. These constraints provide a prescription on the velocity of the end of structure, but not on its position.

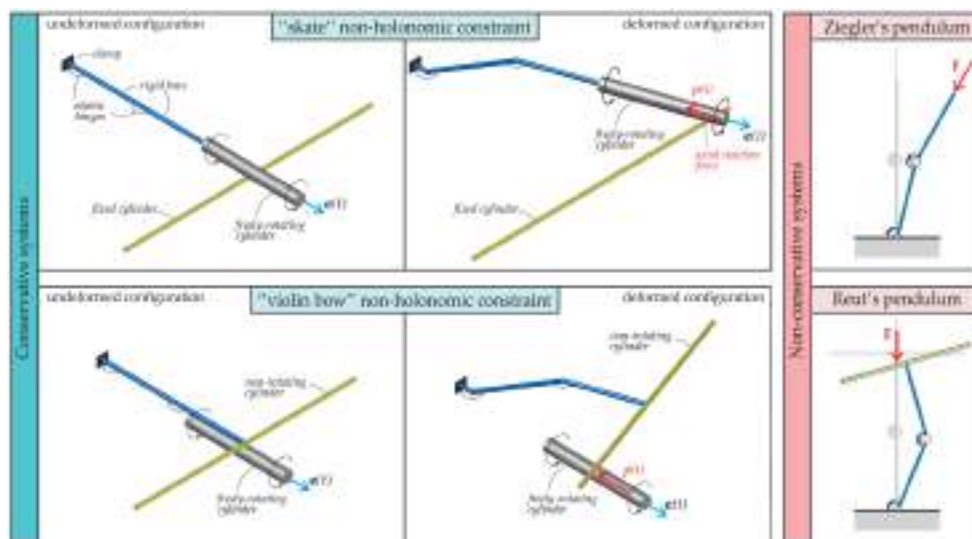


Fig. 2: Application of non-holonomic constraints to generate flutter instability in a double pendulum through the generation of forces similar to those pertinent to the Ziegler's and the Reut's structures.

The remarkable feature emerging from the analysis of non-holonomic constraint is that the latter preserves conservation of energy. Therefore, it is found that flutter instability, Hopf bifurcation, the destabilizing effects of viscosity, and the Ziegler paradox are all possible even within a conservative framework.

Non-smoothness of the equations of motion

As a continuation of the above-presented studies, an elastic structure subject to a follower force was considered in which one end can slide against a linear spring along a smooth constraint presenting a discontinuity in the curvature, as shown in Fig. 3.

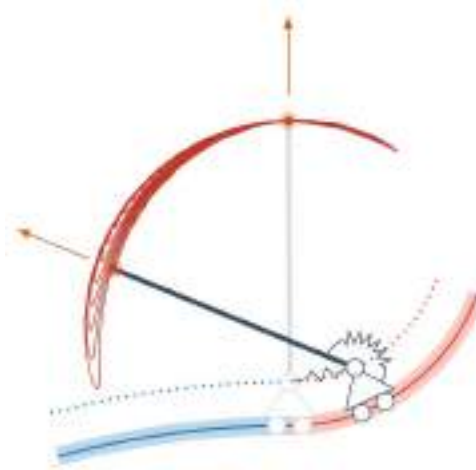


Fig. 3: A structure governed by a non-smooth system of differential equations showing flutter instability as a consequence of the application of a follower force together with a constraint with a jump in the curvature.

The dynamics of the structure is governed by a non-smooth system of differential equations leading to a flutter instability. The most relevant point is that such system can be viewed as the ‘fusion’ of two different structures, each with a circular sliding profile. Interestingly, the two separate structures are stable under the same load for which the compound structure is unstable. Therefore, the mechanical instability is the effect of both the follower nature of the load and of the discontinuity of the curvature of the sliding profile.

Acknowledgements

The authors gratefully acknowledge financial support from the European Research Council (ERC) under the European Union’s Horizon 2020 research and innovation programme (Grant agreement No. ERC-ADG-2021-101052956-BEYOND).

References

- [1] D. Bigoni and G. Noselli. Experimental evidence of flutter and divergence instabilities induced by dry friction. *J. Mech. Phys. Solids*, 59 (2011), 2208-2226. <https://doi.org/10.1016/j.jmps.2011.05.007>
- [2] M. Tommasini, O. Kirillov, D. Misseroni, D. Bigoni. The destabilizing effect of external damping: Singular flutter boundary for the Pfluger column with vanishing external dissipation, *J. Mech. Phys. Solids* 91 (2016), 204-215. <https://doi.org/10.1016/j.jmps.2016.03.011>
- [3] D. Bigoni, O. Kirillov, D. Misseroni, G. Noselli, M. Tommasini. Flutter and divergence instability in the Pfluger column: Experimental evidence of the Ziegler destabilization paradox, *J. Mech. Phys. Solids* 116 (2018), 99-116. <https://doi.org/10.1016/j.jmps.2018.03.024>
- [4] D. Bigoni, D. Misseroni. Structures loaded with a force acting along a fixed straight line, or the "Reut's column" problem, *J. Mech. Phys. Solids* 134 (2020), 103741. <https://doi.org/10.1016/j.jmps.2019.103741>

- [5] A. Cazzolli, F. Dal Corso, D. Bigoni. Non-holonomic constraints inducing flutter instability in structures under conservative loadings, *J. Mech. Phys. Solids* 138 (2020), 103919.
<https://doi.org/10.1016/j.jmps.2020.103919>
- [6] M. Rossi, A. Piccolroaz, D. Bigoni. Fusion of two stable elastic structures resulting in an unstable system, *J. Mech. Phys. Solids* 173 (2023), 105201.
<https://doi.org/10.1016/j.jmps.2023.105201>
- [7] H. Ziegler. Principles of structural stability, Birkhäuser, Basel und Stuttgart (1977).
<https://doi.org/10.1007/978-3-0348-5912-7>
- [8] W.T. Koiter. Unrealistic follower forces, *J. Sound Vib.* 194 (1996), 636–638.
<https://doi.org/10.1006/jsvi.1996.0383>

Can we use buckling to design adaptive composite wings?

Chiara Bisagni^{1,a *}

¹Politecnico di Milano, Department of Aerospace Science and Technology, via la Masa 34,
20156, Milano, Italy

^achiara.bisagni@polimi.it

Keywords: Buckling, Composite Structures, Adaptive Wing

Abstract. In aeronautics, buckling has long been considered as a structural phenomenon to be avoided, because characterized by large out-of-plane displacements and therefore by losing the ability to sustain the designed loads. Several recent studies show the possibility to allow composite stiffened panels of primary aeronautical components to work in the post-buckling field so to potentially reduce the structural weight. The present study aims to control buckling behavior of composite structural components for future adaptive wings using novel tailorable and effective mechanisms. Instead of the traditional design against buckling, the idea is to use the nonlinear post-buckling response to control stiffness changes which redistribute the load in the wing structure. Numerical studies are at first conducted on a composite plate and then implemented in a simplified thin-walled composite wing box, where stiffness changes is controlled using buckling.

Introduction

The development of aviation has always been characterized by the search for maximum efficiency in a holistic and multidisciplinary way, through optimal structural, aerodynamic and propulsive efficiency characteristics. Two contrasting challenges have recently become evident: on one side the growth of air traffic, which implies the need to increase transport capacity and reduce travel times while maintaining or improving the level of safety, and on the other the search for a reduction of the environmental impacts of air transport. The Advisory Council for Aviation Research and Innovation in Europe (ACARE) provided a Strategic Research and Innovation Agenda (SRIA), that contains the roadmap for aviation research, development and innovation for reaching the so-called “Clean Aviation” [1], that is part of the European Green Deal.

It is evident that a simple evolutionary improvement of aircraft technologies will not be sufficient to fulfil the challenging targets requested in terms of environmental impact reduction.

In the last years, a few papers appeared in literature showing how buckling could be used for innovative applications, but in aeronautics they are mainly devoted to use buckling for the design of energy harvesters or for bistable structures with limited morphing applications [2-3].

The project NABUCCO (New Adaptive and BUCKling-driven COMposite aerospace structures), funded by the European Union through an ERC Advanced Grant, is proposing to design new adaptive buckling-driven composite structural concepts for the next generation of aircraft configurations, that will impact on two of the biggest levels for reduction of fuel burn needed for future clean aviation: reduced weight and increased efficiency.

NABUCCO Project

The NABUCCO project aims to design new adaptive buckling-driven composite structures for next generation of aircraft configurations. The project is proposing a paradigm shift in aerospace design concepts, considering buckling no more as a phenomenon to be avoided, but as a favorable behavior to be actively exploited.

Let's suppose for a moment to change radically the traditional design approach, and to analyze what happens if from the beginning a structure is designed to exhibit buckling, and not to avoid it.



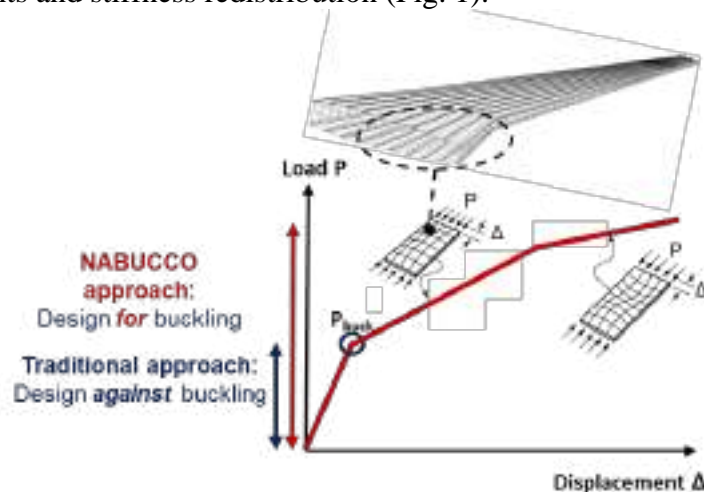
The main drawbacks that are commonly seen towards buckling in the design of composite aerospace structures are summarized in Table 1, together with the way they are seen positively in NABUCCO.

Table 1. From drawbacks to advantages of buckling.

Buckling must be avoided because...	Buckling can be exploited because...
Buckling produces stiffness reduction.	The stiffness reduction can be used for shape variation, load redistribution and dynamic response change.
Buckling generates large nonlinear deformations.	The large nonlinear deformations can be exploited to significantly change the structural shape with a minimum amount of provided energy.
The transition from pre- to post-buckling can be instantaneous (snap-through).	The fast structural response can be adopted for passive control of peak loads, such as those due to heavy gust excitation or maneuvers.
Buckling strongly depends on geometrical imperfections, material variability, external loads, boundary conditions.	The potential design space can become very large, allowing for many and unusual combinations of structural configurations to obtain pre-defined shapes.

The composite structures have the capability to work safely in the deep post-buckling field with large out-of-plane displacement, as shown for example in [4]. Besides, if appropriately designed, these structures can undergo repeated loading-unloading-loading cycles remaining in the elastic field for the different post-buckling configurations.

The idea of the NABUCCO project is to modify and adapt the aircraft wing shape during the flight mission by the direct use of the buckling phenomena, taking advantage of their typical large nonlinear displacements and stiffness redistribution (Fig. 1).



*Fig. 1. Approach of NABUCCO project:
Design for buckling of composite aeronautical components.*

Buckling-driven Mechanisms for Composite Adaptive Structures

All the potentialities offered by composite materials are used, thanks also to novel manufacturing processes, and the boundary conditions are modified to govern when buckling occurs so to tune multiple non-traditional post-buckling stable configurations.

Buckling-driven mechanisms are developed to obtain different stable configurations changing the boundary conditions, that require only small forces to be reconfigured. In this way it is possible

to induce controlled buckling, to obtain local stiffness increase or reduction, infinite number of shapes variation, and load redistribution.

The first steps of the buckling-driven methodology under development consisted in the numerical investigation of a composite plate and then of a simplified thin-walled composite wing box, where stiffness changes were controlled using three buckling-driven mechanisms by restraining the out-of-plane buckling deformation using point, area and maximum displacement constraints [5]. In particular, in the investigation of the composite wing box, the post-buckling behavior of the spar web was controlled by out-of-plane deflection constraints, so that the wing twisting performances were tailored by the relative stiffness of the spar web compared to the rest of the structure. In this way, the nonlinear post-buckling response is used to control stiffness changes, as shown in Fig. 2.

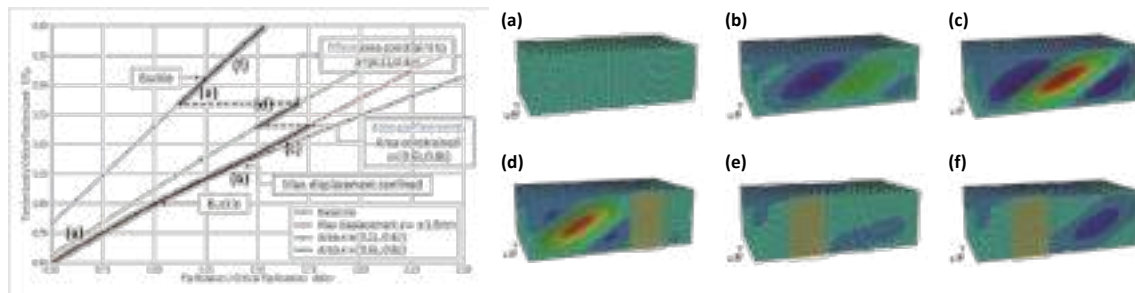


Fig. 2. Adaptive multi-stable composite wingbox: controlled torque-rotation load path and corresponding wingbox deformation.

In this way, the load in the wing structure is redistributed controlling the stiffness changes, and the methodology allows to gain the real-time controllability of the post-buckling behavior and to enhance the adaptivity of the wing structure to meet multi-stable tailorable situations, with a limited amount of load and actuation energy.

The investigated structures still requires an extensive research of feasibility as they need to be validated experimentally. For this reason NABUCCO is developing a strongly coupled computational-experimental framework, to demonstrate the feasibility of designing aircraft components with controllable buckling, starting from simple composite panel, and then increasing complexity considering a wingbox, and later an adaptive wing for morphing application, as shown in Fig. 3.

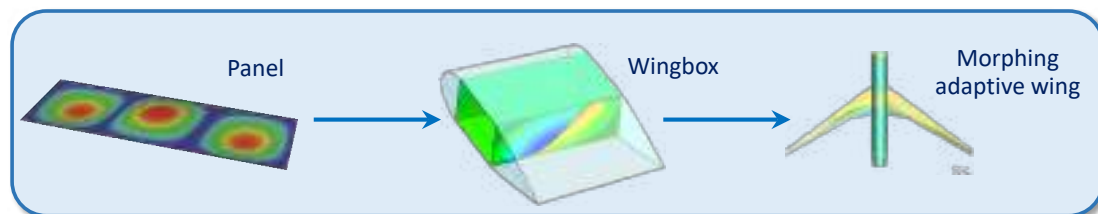


Fig. 3. Increasing complexity of the composite structures investigated in the NABUCCO project.

The first steps of the buckling-driven methodology under development for composite structures show that the design space is significantly enlarged and the designer can identify, manage and control the buckling phenomena.

Summary

The next generation aircraft will require to be lighter, more flexible and sustainable, with the same or increased level of safety. The relaxation of some of the established design constraints, together

with the use of new lightweight and recyclable materials, can contribute to the development of new breakthrough technologies and design philosophies.

Structures designed to work in the post-buckling field and able to adapt their shape during different flight conditions are under development. The first steps of the methodology consisted in the numerical investigation of a composite plate and then of a simplified thin-walled composite wing box, where the post-buckling behavior of the structural component is controlled by out-of-plane deflection constraints.

Even if the investigated configurations still require an extensive research of feasibility as they need to be validated experimentally, they show the capability of controlling the stiffness changes through the nonlinear post-buckling response and to enhance the adaptivity of the wing structure to meet multi-stable tailorable situations, with a limited amount of load and actuation energy. These new composite structures will act on two of the biggest levers for the future of clean aviation: reduced weight and increased efficiency.

Acknowledgment

Funded by the European Union (ERC Advanced Grant, NABUCCO, project number 101053309). Views and opinions expressed are however those of the author only and do not necessarily reflect those of the European Union or the European Research Council Executive Agency. Neither the European Union nor the granting authority can be held responsible for them.



References

- [1] Clean Aviation, Strategic Research and Innovation Agenda, December 2021. Information on https://clean-aviation.eu/sites/default/files/2022-01/CAJU-GB-2021-12-16-SRIA_en.pdf
- [2] A. F. Arrieta, I. K. Kuder, M. Rist, T. Waeber, P. Ermanni, Passive load alleviation aerofoil concept with variable stiffness multi-stable composites, *Composite Structures*. 116 (2014) 235-242. <https://doi.org/10.1016/j.compstruct.2014.05.016>
- [3] Y. Li, S. Pellegrino, A theory for the design of multi-stable morphing structures, *Journal of the Mechanics and Physics of Solids*. 136 (2020) 103772. <https://doi.org/10.1016/j.jmps.2019.103772>
- [4] K. S. van Dooren, B.H.A.H. Tijs, J.E.A. Waleson, C. Bisagni, Skin-stringer separation in post-buckling of butt-joint stiffened thermoplastic composite panels, *Composite Structures*, 304 (2023) 116294304. <https://doi.org/10.1016/j.compstruct.2022.116294>
- [5] J. Zhang, C. Bisagni, Buckling-driven mechanisms for twisting control in adaptive composite wings, *Aerospace Science and Technology*, 118 (2021) 107006. <https://doi.org/10.1016/j.ast.2021.107006>

Immersed boundary-conformal coupling of cylindrical IGA patches

Giuliano Guarino^{1,2,a*}, Pablo Antolin^{2,b}, Alberto Milazzo^{1,c} and Annalisa Buffa^{2,d}

¹Department of Engineering, Università degli Studi di Palermo, V.le delle Scienze, Bld. 8, 90128, Palermo, Italy

² Institute of Mathematics, École Polytechnique Fédérale de Lausanne, CH-1015, Lausanne, Switzerland

^agiuliano.guarino@unipa.it, ^bpablo.antolin@epfl.ch, ^calberto.milazzo@unipa.it,
^dannalisa.buffa@epfl.ch

Keywords: Kirchhoff-Love Shells, Isogeometric Analysis, Interior Penalty Coupling

Abstract. In this work an Immersed-Boundary-Conformal coupling method for coupling shells is presented. The linear elastic static analysis is carried out using the Kirchhoff-Love shell model. The variational statement is discretized with an Isogeometric Analysis approach. The method employs auxiliary shell patches conformal to the interfaces which are coupled to the main ones using an Interior Penalty formulation. Results showing the potential of such approach to study multi-component shell structures are provided.

Introduction

Cylindrical beams are extensively used in many engineering sectors due to their high stiffness-to-weight ratios, with typical examples that can be found in civil, marine, and automotive sectors. Truss structure relying on cylindrical beams are usually investigated using one-dimensional elements that allow to characterize the general mechanical response of the assembly but do not describe accurately the displacement and stress fields near the interfaces between elements. Here, a two or three-dimensional analysis is typically required.

The Isogeometric Analysis (IGA) method [1] employs spline basis for both the description of the geometry and the approximation of the solution, allowing for a straightforward incrementation of the polynomial order while at the same time limiting the increase in the number of degrees of freedom. However, describing the geometry obtained from the intersection of two cylinders with splines is not an easy task. A possible approach consists in using an Immersed-Boundary description for each cylindrical patch. In details, an additional curve is used to embed each of the two parametric domains to describe the boundary corresponding to the interface between the intersecting cylinders. This approach results in a subdivision of each parametric domain in an active and a non-active region, and in a trimming of the elements in between the two. However, such approach requires a weakly imposed continuity between the patches and an ad-hoc refinement strategies for the region near the interface if a higher resolution is required.

In this work, the proposed coupling strategy relies on an auxiliary patch for each cylinder. These are constructed conformal to the interface on one side. As such, while the coupling of the rotational degrees of freedom is still performed in a weak sense, the coupling of the displacements is obtained in a strong sense by merging corresponding degrees of freedom. The other side of each patch is used to define the boundary of the corresponding parametric domain, and to enforce the continuity using an Interior Penalty approach. The main advantage of such strategy is the arbitrariness of the auxiliary patches, that allows for a straightforward local refinement in the region close to the intersection.

To demonstrate the potential of the proposed approach, preliminary numerical results are provided regarding the creation of a boundary conformal patch for a Kirchhoff plate and the coupling of cylindrical shell through the Interior Penalty approach.



Kirchhoff-Love shells

The starting point of the proposed method is the Kirchhoff-Love shell equation. The weak form of the equation for a single patch shell is stated as finding the displacement field \mathbf{u} such as $a(\mathbf{v}, \mathbf{u}) = f(\mathbf{v}) \quad \forall \mathbf{v}$. Where the definition of the spaces for \mathbf{u} and \mathbf{v} depends on the essential boundary condition for the problem at hand (see [3]). The bilinear and the linear form are defined as:

$$a(\mathbf{v}, \mathbf{u}) = \int_{\Omega} \boldsymbol{\varepsilon}(\mathbf{v}) : \mathbf{N}(\mathbf{u}) d\Omega + \int_{\Omega} \boldsymbol{\kappa}(\mathbf{v}) : \mathbf{M}(\mathbf{u}) d\Omega \quad (1a)$$

$$f(\mathbf{v}) = \int_{\Omega} \mathbf{v} \cdot \tilde{\mathbf{F}} d\Omega + \int_{\Gamma_{N_1}} \mathbf{v} \cdot \tilde{\mathbf{T}} d\Gamma + \int_{\Gamma_{N_2}} \theta_n(\mathbf{v}) \tilde{M}_{nn} d\Gamma + \sum_{C \in \chi} (v_3 \tilde{S})|_C, \quad (1b)$$

where $\boldsymbol{\varepsilon}$ and $\boldsymbol{\kappa}$ are the membrane and bending strain respectively, \mathbf{N} and \mathbf{M} are the generalized force and moment, $\tilde{\mathbf{F}}$, $\tilde{\mathbf{T}}$, \tilde{M}_{nn} and \tilde{S} are the applied domain force, boundary force, bending moment and corner force, θ_n is the bending rotation, and Ω , Γ_{N_1} , Γ_{N_2} , and C are the surface, the boundary where force and moment boundary conditions are applied and the corners, respectively. The interested reader is referred to [2] for the details regarding the formulation.

Interior penalty coupling

When dealing with multiple patch shell structures, a coupling strategy is necessary. In some cases, when the patches are conformal to the interface, the coupling condition can be imposed strongly by appropriately selecting the spaces for \mathbf{u} and \mathbf{v} . However, in general, the coupling condition needs to be imposed weakly through integrals along the interface. This is particularly true when the patches are trimmed in an immersed boundary approach. In such cases, the problem becomes finding \mathbf{u}_h such as

$$\sum_{p=1}^{N_p} a_p(\mathbf{v}_h, \mathbf{u}_h) + \sum_{i=1}^{N_i} b_i(\mathbf{v}_h, \mathbf{u}_h) = \sum_{p=1}^{N_p} f_p(\mathbf{v}_h) \quad \forall \mathbf{v}_h \quad (2)$$

where \mathbf{u}_h and \mathbf{v}_h are the discretized displacements and test function, respectively. $a_p(\mathbf{v}_h, \mathbf{u}_h)$ and $f_p(\mathbf{v}_h)$ represent the discretized version of Eq. (1) for the p -th of the N_p patches. $b_i(\mathbf{v}_h, \mathbf{u}_h)$ is the bilinear form associated to the i -th of the N_i interfaces and is defined as

$$\begin{aligned} b_i(\mathbf{v}_h, \mathbf{u}_h) = & \int_{\Gamma_h^I} (\{\mathbf{T}(\mathbf{v}_h)\} \cdot \llbracket \mathbf{u}_h \rrbracket + \llbracket \mathbf{v}_h \rrbracket \cdot \{\mathbf{T}(\mathbf{u}_h)\}) d\Gamma + \\ & + \int_{\Gamma_h^I} (\{M_{nn}(\mathbf{v}_h)\} \llbracket \theta_n(\mathbf{u}_h) \rrbracket + \llbracket \theta_n(\mathbf{v}_h) \rrbracket \{M_{nn}(\mathbf{u}_h)\}) d\Gamma + \\ & + \mu_D \int_{\Gamma_h^I} \llbracket \mathbf{v}_h \rrbracket \cdot \llbracket \mathbf{u}_h \rrbracket d\Gamma + \mu_R \int_{\Gamma_h^I} \llbracket \theta_n(\mathbf{v}_h) \rrbracket \llbracket \theta_n(\mathbf{u}_h) \rrbracket d\Gamma \end{aligned} \quad (4)$$

where Γ_h^I is the i -th interface, \mathbf{T} and M_{nn} are the fluxes associated with the Ersatz force and bending moment (see [3]), and $\llbracket a \rrbracket$ and $\{a\}$ are the standard jump and average operator. μ_D and μ_R are the penalty parameters associated with the displacements and the rotation, that are chosen here as $\mu_d = \beta \frac{Et}{h}$ and $\mu_r = \beta \frac{Et^3}{h}$, where E , t , and h are the maximum young modulus of the material, the shell thickness, and mesh size, and β is a problem independent constant chosen here as 10^3 .

The Immersed Boundary-Conformal approach

In the immersed boundary paradigm, the shell surface is embedded within a trimming curve, resulting in the presence of entire, partial, and empty elements. On the partial elements boundary and coupling condition can only be imposed in a weak sense. In the proposed method, an auxiliary boundary conforming patch is generated along the trimming curve. Although coupling between the auxiliary patch and the internal domain becomes necessary, it occurs in a more internal region of the domain where local phenomena are less likely to occur. Furthermore, these auxiliary patches

can be refined as needed to capture these local phenomena more accurately. One of the difficulties associated with the proposed method lies in the integration in the trimmed elements. Here, the algorithm described in [4] is adopted, which is based on a high-order reparameterization of the trimmed elements.

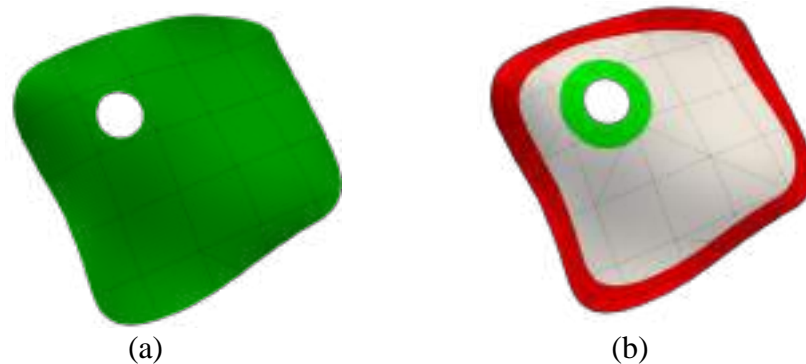


Figure 1 Same shell structure discretized using a trimmed single patch (a) and a combination of a main patch and two auxiliary boundary conformal ones (b).

In Fig. (1), it is shown an example of a shell structure with boundary conformal patches aligned with the trimmed domain. In a similar fashion, we believe that coupling two intersecting surfaces creating an interface conformal patch for each surface would be beneficial to the accuracy of the analysis and is currently under investigation.

Numerical Results

In this session some preliminary results leading to the immersed boundary conformal coupling are presented.

Kirchhoff plate with pseudo cut-outs: The plate shown in Fig. (2), characterized by edge size $L = 10$ m, Poisson ratio $\nu = 0.3$, thickness $t = 0.1$ m, Young modulus $E = 12(1 - \nu^2)/t^3$ Pa, and having simply supported boundary condition, is subjected to a constructed force that produces the displacement field described by $u_3 = \sin(2\pi x/L) \sin(2\pi y/L)$. In Fig. (2a) it is shown the parametric space with two pseudo cut-outs surrounded by boundary conformal patches. In this test the holes have been filled to easily retrieve the analytical solution. Fig(2b) shows the contour of the solution with superimposed mesh of the main and the auxiliary patches, it is pointed out the smoothness of the solution. Fig. (2c) shows the L_2 convergence for this test.

Intersecting cylindrical patches: Fig.(3a) shows a structure constituted of five intersecting cylindrical shells characterized by Young modulus $\nu = 0.3$, Poisson ratio $\nu = 0.3$, and thickness 10 mm. On the vertical cylinder, simply supported boundary conditions are applied at the opposite ends. A uniform domain force $f = [1,1,1]$ is applied on each patch. In Fig. (3b) it can be noted how the interior penalty method guarantees coupling conditions of the complex structure under investigation.

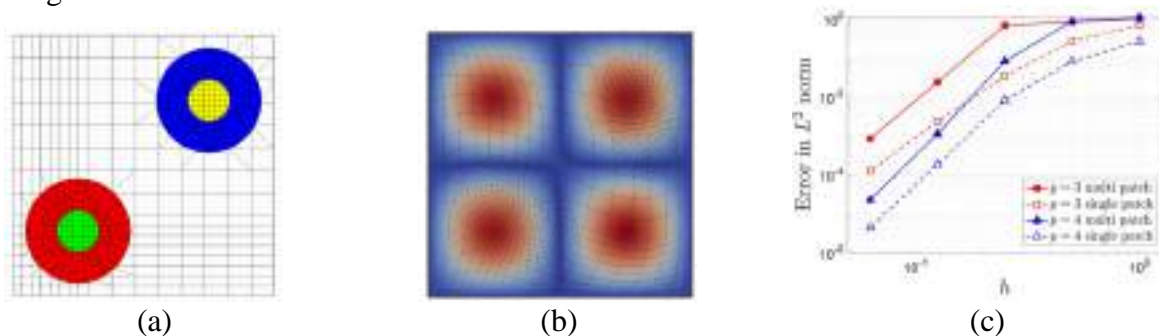


Figure 2 Kirchhoff plate with two pseudo cut-outs. (a) Parametric domain (b) physical domain with superimposed displacements contour (c) L^2 convergence of the displacements field.

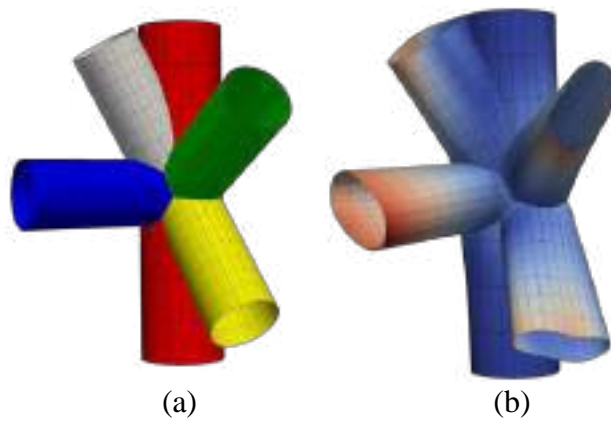


Figure 3 Shell structure with multiple cylindrical patch (a). Contour of the magnitude of the displacement (b).

Conclusions

This contribute introduces the boundary conformal method for the coupling of shell patches and provides initial results towards the implementation of a complete approach. The proposed formulation is based on the interior penalty method for coupling shell patches, the utilization of auxiliary interface conformal patches, and a high-order integration scheme for trimmed elements. The presented results suggest the potential of the method, which is currently being developed.

References

- [1] T.J.R. Hughes, J.A. Cottrell, Y. Bazilevs, Isogeometric analysis: CAD, finite elements, NURBS, exact geometry and mesh refinement, *Computer Methods in Applied Mechanics and Engineering*, 194 (2005), 4135-4195. <https://doi.org/10.1016/j.cma.2004.10.008>
- [2] J. Kiendl, K.-U. Bletzinger, J. Linhard, R. Wüchner, Isogeometric shell analysis with Kirchhoff–Love elements, *Computer Methods in Applied Mechanics and Engineering*, 198 (2009) 49-52. <https://doi.org/10.1016/j.cma.2009.08.013>
- [3] J. Benzaken, J. A. Evans, S. F. McCormick, R. Tamstorf, Nitsche’s method for linear Kirchhoff–Love shells: Formulation, error analysis, and verification, *Computer Methods in Applied Mechanics and Engineering*, 374 (2021), 113544. <https://doi.org/10.1016/j.cma.2020.113544>
- [4] Wei, X., Marussig, B., Antolin, P. et al, Immersed boundary-conformal isogeometric method for linear elliptic problems. *Computational Mechanics* 68 (2021), 1385–1405. <https://doi.org/10.1007/s00466-021-02074-6>

Folding simulation of TRAC longerons via unified one-dimensional finite elements

Riccardo Augello^{1,a*}, Erasmo Carrera^{2,b}, Alfonso Pagani^{2,c} and Sergio Pellegrino^{2,d}

¹California Institute of Technology, Pasadena, CA, 91125

²Department of Mechanical and Aerospace Engineering, Mul2 Lab, Politecnico di Torino, Torino, Italy

^araugello@caltech.edu, ^berasmo.carrera@polito.it, ^calfonso.pagani@polito.it,
^dsergiop@caltech.edu

Keywords: Deployable Booms, TRAC longerons, Carrera Unified Formulation, Contact Mechanics, Nonlinear Analysis

Abstract. This paper proposes a simulation of the folding phase of TRAC deployable booms using refined one-dimensional finite elements in the framework of the Carrera Unified Formulation. The mathematical model involves standard beam finite elements placed along the length of the longeron, and Lagrange polynomials as expansion functions for the cross-sectional domain. The nonlinear governing equations are written recalling the principle of virtual work, and they are linearized using the Newton-Raphson scheme. The contact between the two flanges is simulated with linear spring which activate when pre-defined node pairs approach under a fixed tolerance. Two simulations are carried out, including or not the contact behavior, respectively. The results highlight the capability of the proposed model to deal with large displacements and contact between the ultra-thin flanges of the structure.

Introduction

Over the years, deployable structures have become increasingly popular in space engineering, since they make it possible to obtain a consistent reduction of mass, volume, and consequently, the cost of a satellite. Deployable booms found a large number of applications such as for telescopes [1] and antennas [2].

The most common type of deployable booms is tape springs, which can be described as thin-walled elastic strips. A combination of those can be used to generate other types of booms, such as the Triangular Rollable And Collapsible (TRAC). Originally invented by Murphey and Banik [3] and developed by the Air Force Research Laboratory, it consists of two circular domains (flanges) made of tape-spring that are attached along the common edge (web). The resultant cross-section gives TRAC longerons larger bending stiffness than other popular options (such as the Collapsible Tubular Mast (CTM) [4], the Storable Tubular Extendable Member (STEM) [5] and bi-STEM [6]).

The present work deals with the simulation of the folding phase of TRAC booms. By employing the Carrera Unified Formulation [7], the ultra-thin boom can be modeled using refined one-dimensional beam finite elements. The nonlinear governing equations are solved using a Newton-Raphson linearization scheme along with a displacement control.

One dimensional model of the TRAC longeron

The deployable mechanism analyzed in this work is shown in Fig. 1, and it consists of a foldable TRAC longeron. The geometric properties are $L = 400$ mm, $h = 8$ mm, $r = 12.8$ mm, $\vartheta = 105^\circ$ and $t = 80$ μ m.



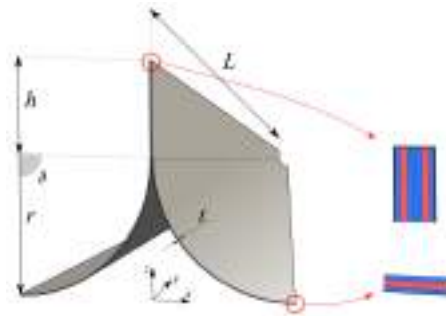


Figure 1 - Geometry of the considered TRAC longeron

As far as the material properties are concerned, the composite layup in the flanges of the longeron is $[\pm 45 \text{ GFPW} / 0 \text{ CF} / \pm 45 \text{ GFPW}]$, and that in the web region is $[\pm 45 \text{ GFPW} / 0 \text{ CF} / \pm 45 \text{ GFPW} / 0 \text{ CF} / \pm 45 \text{ GFPW}]$, where CF represents a thin ply with unidirectional carbon fibers. GFPW represents plain weave scrim glass. Both plies are impregnated with resin, as described in [8].

For the numerical model, a Cartesian reference system is used, so that the y direction is placed in the length direction, and the x, z identify the cross-sectional domain. According to the Carrera Unified Formulation (CUF), the three-dimensional displacement field can be written in the following unified manner:

$$\mathbf{u}(x, y, z) = F_\tau(x, z) N_i(y) \mathbf{u}_{\tau i} \quad \tau = 1, 2, \dots, M \quad i = 1, 2, \dots, N_n \quad (1)$$

where $\mathbf{u}(x, y, z)$ is the displacement vector, whose components are expressed in the general reference system (x, y, z) of Fig. 1, F_τ represent the cross-sectional functions depending on the x, z coordinate, τ is the sum index and M is the number of terms of the expansion in the cross-section plane assumed for the displacements. N_i stands for the i th one-dimensional shape function, $\mathbf{u}_{\tau i}$ is the vector of the FE nodal parameters, i indicates summation and N_n is the number of the FEs nodes per element. In this work, a cubic interpolation for the axis direction is assumed. Figure 2 shows the resultant one-dimensional model of the TRAC longeron.

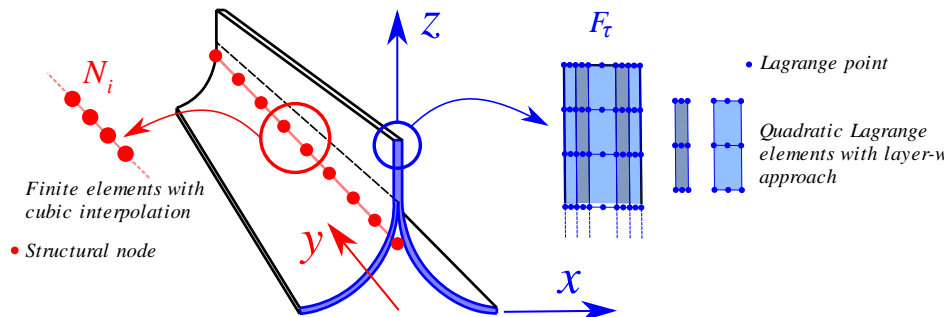


Figure 2 - Modeling of the TRAC longeron

Boundary conditions

The considered boundary conditions are reported in Fig. 3. Basically, one side of the TRAC can rotate around the z axis, whereas the other can rotate around the z axis and move along the y axis.

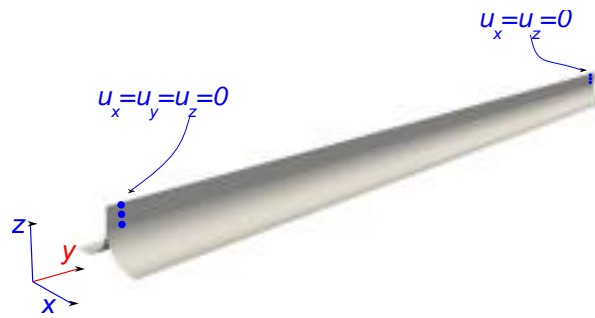


Figure 3 - Boundary conditions

Subsequently, the structure is subjected to a pinching in the middle, by imposed displacements, as depicted in Fig. 4(a). Figure 4(b) reports the folding process, where the rotations are ensured by pairs of displacements at the sides of the structure.

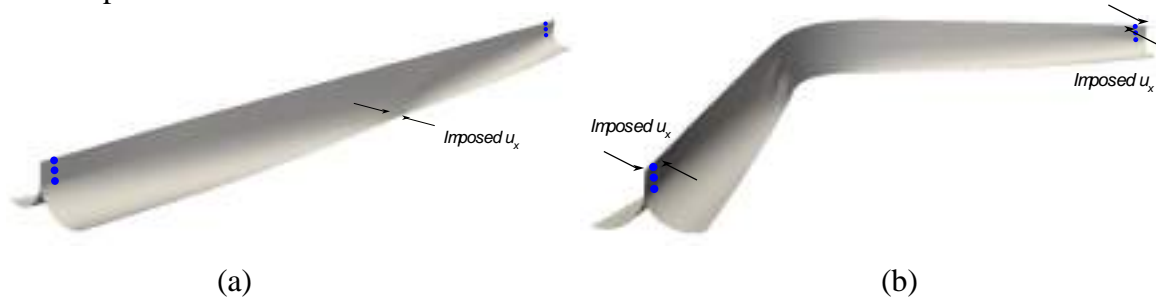


Figure 4 - Pinching and folding of the TRAC longeron

Nonlinear governing equations

The set of the nonlinear governing equations, which full derivation is described in [10], is expressed in the following:

$$K_S q - p = 0 \quad (2)$$

where K_S , q and p are the global, assembled FE stiffness, displacement and external force arrays of the final structure. Equation (2) represents a nonlinear algebraic system of equation for which an iterative method is needed. We employ here the same procedure detailed in [11], where a Newton–Raphson scheme is used by making use of a path following constraint. This procedure demands for the linearization of the nonlinear governing equations. As a result, we need to introduce the so-called tangent stiffness matrix $K_T = \frac{d(K_S q - p)}{dq}$: The explicit form of K_T is not given here, but it is derived in a unified form in [12]. Finally, in this work, a displacement control algorithm is introduced.

Contact mechanics

In the present work, contact between the flanges of the TRAC longeron is simulated. A node-to-node contact approach is employed, recalling the penalty technique. Basically, a linear spring is simulated between the nodes of the two flanges, as depicted in Fig. 5.

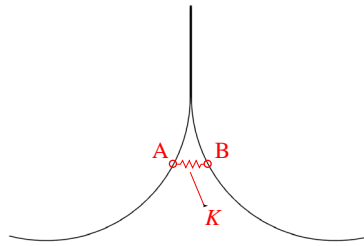


Figure 5 - Node-to-node contact simulation

The nodes are paired as input of the analysis, so the mesh coincidence between the inner surfaces of the two flanges must be ensured. The springs activate under a particular tolerance, which is set as $1\ \mu\text{m}$, and produces two opposite forces on the nodes. Thus, the force vector \mathbf{p} and the stiffness matrix K_T are updated at each iteration step of the previously described Newton-Raphson algorithm.

Numerical results

The numerical results regard two simulation, including or not the contact between the two flanges. The developed mathematical model involves 20 cubic FEs for the axis discretization and 64 quadratic Lagrange polynomials for the cross-sectional domain (30 for each flange and 4 for the web). The total number of degrees of freedom is 74871.

As far as the simulation without contact is concerned, the pinching phase is reported in Fig. 6.

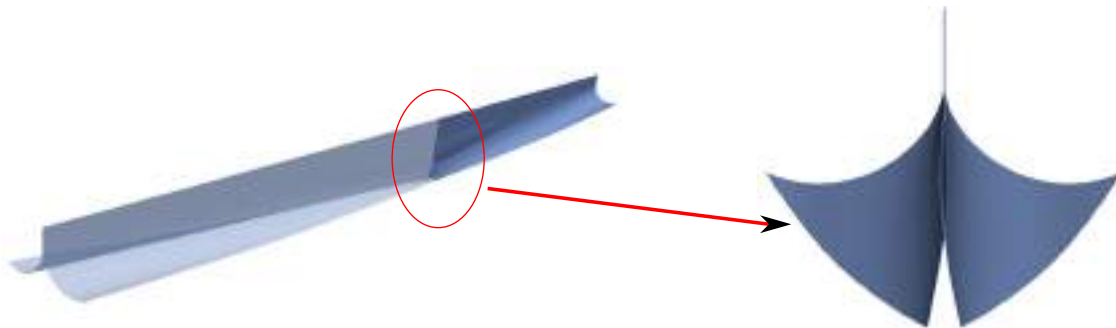


Figure 6 - Pinching simulation of the TRAC longeron without contact mechanics

As can be seen from Fig. 6, the penetration between the two flanges arises in a large domain of the boom. The complete folding simulation is reported in Fig. 7.



Figure 7 - Folding simulation of the TRAC longeron without contact mechanics

The folding of the TRAC boom can be simulated, although, the penetration between the two flanges persists during the overall simulation..

The same simulation is conducted including the contact between the two flanges. The results for the pinching simulation are reported in Fig. 8.

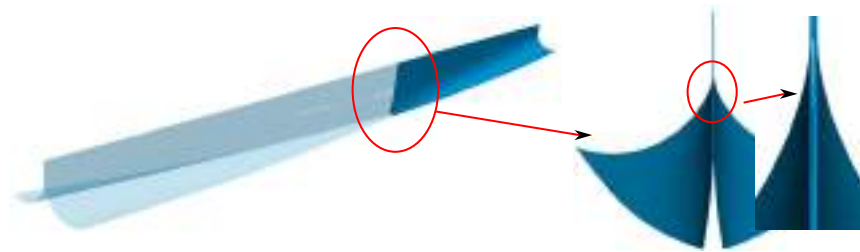


Figure 8 - Pinching simulation of the TRAC longeron including contact mechanics

In contrast to the case without contact, no penetration is observed between the two flanges. Moreover, since the web has one additional layer that the two flanges (see Fig. 1), the two flanges do not contact each other in the proximity of the web (see the enlargement in Fig. 8). The full folding simulation is reported in Fig. 10.



Figure 10 - Folding simulation of the TRAC longeron including contact mechanics

Finally, Fig. 10 reports the contact between the two flanges in one of the equilibrium state.

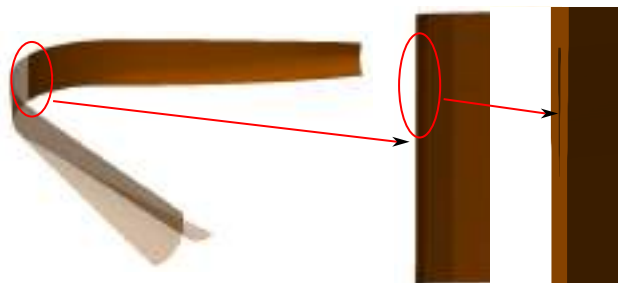


Figure 10 - Particular of the folding simulation of the TRAC longeron including contact mechanics

Conclusions

The present work focussed on the simulation of the folding phase of a deployable boom, namely the TRAC longeron. This composite ultra-thin structure was modelled with the Carrera unified formulation, thanks to which refined one-dimensional finite elements can be built, accounting for any cross-sectional deformation. The nonlinear governing equations were derived in terms of the fundamental nuclei, which represent the basic building block of the overall stiffness matrix. Then, a Newton-Raphson scheme was employed, and a consistent linearization of the governing equation was performed. The contact between the two flanges of the TRAC longeron is simulated with node-to-node linear springs, which are updated at every iteration of the nonlinear procedure. Two

simulations with and without the contact were carried out. The results show the robustness of the present approach to deal with far nonlinear regimes and contact nonlinearities. Future works will deal with the introduction of nonlinear springs to improve the convergence rate of the nonlinear solution and for the dynamic nonlinear simulation of the deployment of the TRAC longerons.

Acknowledgment

This work is part of the project NOVITAS, funded by the European Union's Horizon Europe research and innovation program under the Marie Skłodowska-Curie grant agreement No 101059825.

References

- [1] L. Blanchard. A tape-spring hexapod for deployable telescopes: Dynamics. In ESA Special Publication, pp. 1-5, 2006.
- [2] F. Royer and S. Pellegrino. Ultralight ladder-type coilable space structures. In 2018 AIAA Spacecraft Structures Conference, pp. 1-14, 2018. <https://doi.org/10.2514/6.2018-1200>
- [3] T.W. Murphey and J. Banik, Triangular rollable and collapsible boom, US Patent 7,895,795, 2011.
- [4] D.S. Crouch, Mars viking surface sampler subsystem, 25th Conference on Remote Systems Technology, pp. 142–151, 1977.
- [5] F. Roybal, J. Banik, and T.W. Murphey, Development of an elastically deployable boom for tensioned planar structures, 48th AIAA/ASME/ASCE/AHS/ASC Structures, Structural Dynamics, and Materials Conference, Honolulu, Hawaii, USA, pp. 1–14, 2007. <https://doi.org/10.2514/6.2007-1838>
- [6] M.W. Thomson, Deployable and retractable telescoping tubular structure development, The 28th Aerospace Mechanisms Symposium, Cleveland, Ohio, USA, 1994.
- [7] E. Carrera, M. Cinefra, M. Petrolo, and E. Zappino, Finite Element Analysis of Structures through Unified Formulation, Wiley, Chichester, West Sussex, UK, 2014. <https://doi.org/10.1002/9781118536643>
- [9] N.H. Reddy, and S. Pellegrino, 2023. Dynamics of the Caltech SSPP deployable structures: structure–mechanism interaction and deployment envelope. <https://doi.org/10.2514/6.2023-2065>
- [10] A. Pagani, and E. Carrera, 2018. Unified formulation of geometrically nonlinear refined beam theories. *Mechanics of Advanced Materials and Structures*, 25(1), pp.15-31. <https://doi.org/10.1080/15376494.2016.1232458>
- [11] E. Carrera, A. Pagani, and R. Augello, 2020. Evaluation of geometrically nonlinear effects due to large cross-sectional deformations of compact and shell-like structures. *Mechanics of Advanced Materials and Structures*, 27(14), pp.1269-1277. <https://doi.org/10.1080/15376494.2018.1507063>
- [12] A. Pagani, and E. Carrera, 2017. Large-deflection and post-buckling analyses of laminated composite beams by Carrera Unified Formulation. *Composite Structures*, 170, pp.40-52. <https://doi.org/10.1016/j.compstruct.2017.03.008>

Numerical-analytical evaluation about the impact in water of an elastic wedge using the SPH method

D. Guagliardo^{1,a}, E. Cestino^{1,b*} and G. Nicolosi^{1,c}

¹ Politecnico di Torino (DIMEAS), Corso Duca degli Abruzzi, 24 10129 Turin, Italy

^as272087@studenti.polito.it, ^benrico.cestino@polito.it, ^cgabriele.nicolosi93@gmail.com

Keywords: Fluid-Structure Interaction, LS-DYNA, Smoothed Particle Hydrodynamics, Elastic Wedge

Abstract. In a preliminary study about the structural behaviour of a body, the material can be supposed infinitely rigid. This choice is useful to simplify the problem and to obtain results that well approximate reality. In this specific case under study, it proves how the effect of the material elasticity has a fundamental role on the pressures developed when a wedge impacts water. The analysis is made using ANSYS LS-DYNA software modelling the wedge through the FEM method, characterized by the material defined by the MAT_001-ELASTIC keyword, and the water defined by the SPH (Smoothed-Particle Hydrodynamics) method. The elastic body behaviour will be evaluated through the presence of a displacement in the middle point, on the face impacting water, and the comparison between the obtained pressure and the one predicted by the analytical theories of von Karman¹ and Wagner², which study the impact of a rigid wedge.

Introduction

The student team "TEAM S55" of Polytechnic of Turin was born in 2017 to rebuild the SIAI-Marchetti S55 seaplane on a 1:8 scale [1-3]. The following paper is created by the FSI section which studies the interaction between the aircraft and the water at ditching.

In a preliminary study of the phenomena [4, 5], the rigid wedge approximation can be used to predict the maximum slamming pressure.

The purpose of this paper is to evaluate the pressure trend and the displacement of the wedge's impacting surface during the penetration of a wedge into the water. The numerical analysis was done using the software ANSYS LS-DYNA, in which due to the high computational requirements inherent in the SPH method, the influence of air is neglected to reduce the computational time since it doesn't influence the accuracy of stress prediction [6].

Starting from analytical theory developed by von Karman [7] and Wagner [8] based on a rigid wedge, subsequent studies [3, 9] have been considered that go beyond rigid wedge considerations and move towards different aspects of elasticity. The effect of the structure elasticity on the pressure peak and distribution will be considered. Furthermore, along the impacting surface, the results of displacements will be considered as the speed varies.

Von Karman and Wagner theories

Wagner [8, 10] and Von Karman [7] theories are the most indicated theories in literature to estimate the ditching of a wedge in the water.

Von Karman theory, Eq. 1, is based on the application of the momentum theorem on a body whose weight increases at the impact with the water. The increase is caused by the water contained in a cylinder of diameter equal to the wedge width. Von Karman [7] aimed to find out how the dihedral angle affected the result of the pressure on landing.

$$P_{VK}(x) = \frac{\rho V_0^2}{2} \frac{\pi}{\left(1 + \frac{y \pi x^2}{2W}\right)^3} \cot(\alpha) \quad (1)$$



$$P_{VK_{Max}} = \frac{\rho V_0^2}{2} \pi \cot(\alpha) \quad (2)$$

According to his study, the maximum pressure, Eq. 2, is found at the keel of the wedge and the pressure increases as the dihedral angle decreases.

Wagner [10] studied the impact to estimate the pressure considering the superposition principle. The first studied phenomenon is the wedge penetration in the water studied like a perfectly inelastic collision. The second one is the water molecules behavior. In fact, when the wedge penetrates the water, the stationary molecules start to move, reducing the internal pressure. This decrease is function of the wedge penetration: during the phenomena both the wedge and water molecules velocity have a decreasing trend that causes a minor reduction of pressure, Eq. 3 and Eq. 4.

$$P_W(x) = \frac{1}{2} \rho V^2 \left[\frac{\pi}{\tan(\alpha) \sqrt{1 - \frac{x^2}{L^2}}} - \frac{\frac{x^2}{L^2}}{1 - \frac{x^2}{L^2}} + 2 \frac{\ddot{y}}{V^2} \sqrt{L^2 - x^2} \right] \quad (3)$$

$$P_{W_{Max}} = \frac{1}{2} \rho V^2 \left[1 + \frac{\pi^2}{4 \tan^2(\alpha)} \right] \quad (4)$$

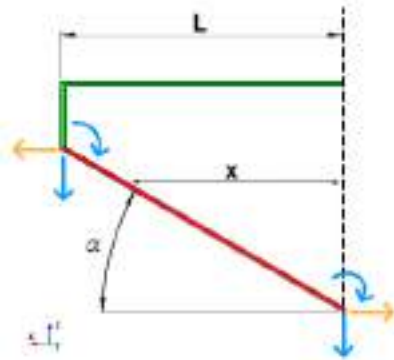


Figure 1: Model constraints

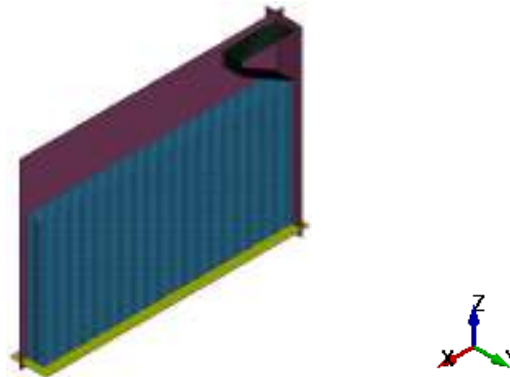


Figure 2: Half wedge model in ANSYS LS-DYNA

Model

The elastic model shown in Fig. 1 is a wedge modelled in ANSYS LS-DYNA PrePost. The wedge has a width of 127.4 mm, a height of 105 mm, a thickness of 2 mm and a dihedral angle α of 30° . It is 0.43 kg heavy, and the material is considered as isotropic. The surface impacting water, the oblique one, and the others are modelled respectively through 001 MAT_ELASTIC and 020 MAT_RIGID, both considering a steel with a Young's modulus of 190GPa. The decision to use MAT_RIGID in non-impact water surfaces is in according to reduce the computational cost and to model the boundary as desired.

The boundary conditions, shown in Fig. 1 and Fig. 2 are:

- displacements allow in x and z directions, and rotation allow along y direction for elastic surface;
- displacements constrain in x and y directions at the edge of elastic surface;
- displacements allowed just in z directions and all rotations blocked for the rigid surfaces;
- control volume is composed of a *RIGIDWALL_PLANAR, in the bottom (yellow plane), a *BOUNDARY_SPH_NON_REFLECTING, perpendicular to x-direction and on the side

opposite the wedge, and three **BOUNDARY_SPH_SYMMETRY-PLANE* (purple planes), two perpendicular to the y-direction and one perpendicular to the x direction and close to the wedge.

The material used for the water is 009 MAT_NULL and the Equation Of State is **EOS_GRUNEISEN*.

The total number of elements is 901200, which 1200 are shell elements and 900000 are SPH (Smoothed Particle Hydrodynamics). The computational cost for each simulation is about 15 h using 48 CPUs simultaneously.

Pressure and displacement results

The study results plotted in Fig. 3 and Fig. 4 show the pressure trend as function of the wedge surface and velocity respectively. The Fig. 3 represents the Von Karman and Wagner theories applied to our wedge and the results of the numerical analysis, when the impact velocity is 5.8 m/s. The Fig. 4 considers the pressure detection sensor, in all analyses, is positioned at 13.93 mm along the x direction. The maximum pressure expected is reached at the wedge's keel for Von Karman and Wagner theory both. It is interesting to notice that Von Karman predicts higher pressure value than Wagner along the surface. This Wagner trend is due to fluid dynamic effect that becomes increasingly negligible along the surface.

The numerical model results are included between the two theories values until they reach the middle of the impact surface. Over that position the numerical results estimate higher pressure values than the two theories.

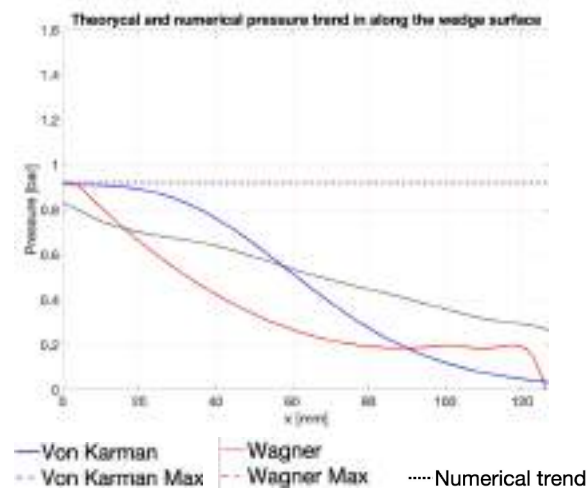


Figure 3: Pressure as function of the surface

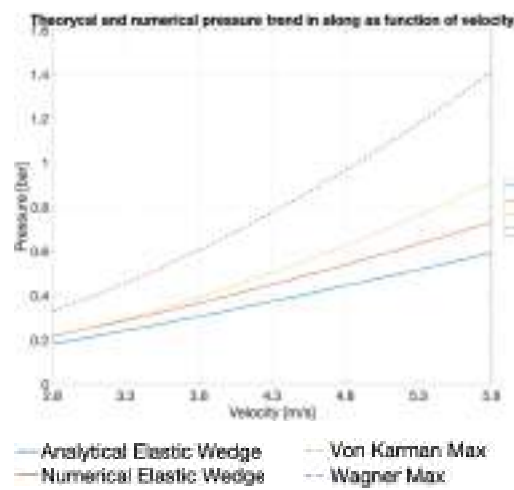


Figure 4: Pressure as function of the velocity

The phenomena studied correspond to a perfectly inelastic collision, so it is important to observe how the pressure changes as function of velocity. Fig. 4 compares the wedge behaviour assuming a rigid, as described by Von Karman and Wagner theories, and an elastic material, as reported in [3]. At the impact, the rigid material undergoes a higher-pressure magnitude than elastic material, because part of the impact energy is the source of the deformation of the impact surface and the remaining part is absorbed by the body. Moreover, the analytical and numerical results are different due to the boundary conditions considered; in [3] the panel is considered simply supported and greater freedom to deform have consequently a reduction of pressure.

In Fig. 5 is showed the maximum displacement for each node that makes up the mesh, not to be confused with the maximum deformation. As expected, the numerical results of maximum displacement depend on the vertical speed; as higher as speed, the higher the maximum displacement will be.

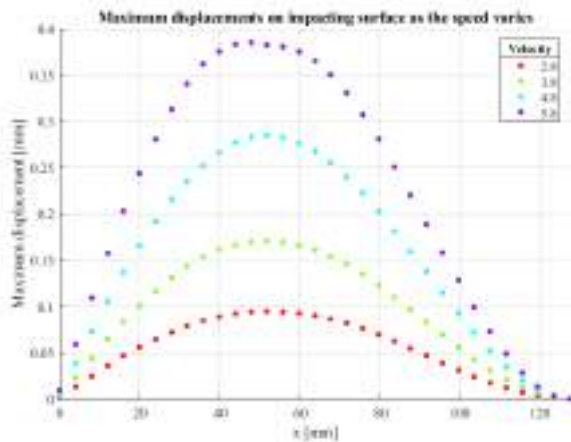


Figure 5: Displacement as function of the velocity

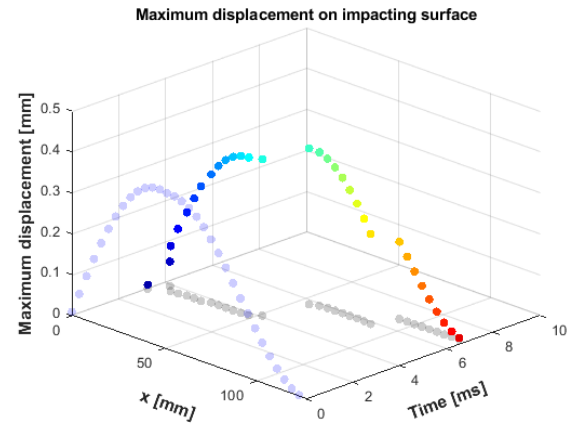


Figure 6: Displacement as function of the velocity

In Fig. 6 the vertical velocity considered is 5.8 m/s; being the maximum displacement in function of surface position, the blue shadow is the same curve plotted in Fig. 5. In Fig. 6, the added value is given by the providing of how the maximum displacement evolves over time. Being the keel to impact the water first, the maximum displacement moves with the increase of the wetted part.

Conclusions

A preliminary study on a rigid wedge impacting water be made neglecting the elasticity behaviour to predict the maximum slamming pressure. On the other hand, results of real impacting model can be conflicting and for pressure can be lower than expecting. An elastic model may be introduced trying to predict a better behaviour of the real nature of things.

The elastic model introduces the possibility of wedge deformation, this allows a local increase of dihedral angle with a decrease of pressure. In conclusion, the effect of flexibility on pressure distribution is more important as speed increases due to the higher displacement measured.

Acknowledgement

The authors thank the Politecnico di Torino and the DIMEAS department for the provision of resources and facilities. We thank DAUIN for computational resources provided through High Performance Computing Polito (HPC@POLITO), a project of Academic Computing within the Department of Control and Computer Engineering at the Politecnico di Torino (<http://www.hpc.polito.it>). Special thanks to ANSYS and EnginSoft SpA for the support and for providing us with the software licenses.

References

- [1] CESTINO, E.; FRULLA, G.; SAPIENZA, V.; PINTO, P.; RIZZI, F.; ZARAMELLA, F.; BANFI, D. (2018) Replica 55 Project: A Wood Seaplane In The Era Of Composite Materials, In: Proc of 31st ICAS 2018 Congress, 9-14 September 2018, Belo Horizonte (Brasil)
- [2] NICOLOSI G., VALPIANI F., GRILLI G., SAPONARO PIACENTE A., DI IANNI L., CESTINO E., SAPIENZA V., POLLA A., PIANA P. Design Of A Vertical Ditching Test. Proc. 32nd ICAS Congress 6-10 September 2021 - Shanghai, China
- [3] Cestino, E., Frulla, G., Polla, A., Nicolosi, G. (2023). Equivalent Material Identification in Composite Scaled Hulls Vertical Impact Tests. In: Lopresto, V., Papa, I., Langella, A. (eds) Dynamic Response and Failure of Composite Materials. DRAF 2022. Lecture Notes in Mechanical Engineering. Springer, Cham. https://doi.org/10.1007/978-3-031-28547-9_6

- [5] Valpiani F, Polla A, Cicolini P, Grilli G, Cestino E, Sapienza V. Early Numerical Evaluation of Fluid-Structure Interaction of a Simply Wedge Geometry with Different Deadrise Angle. AIDAA XXVI International Congress, Pisa, 2021.
- [6] Fragassa C, Topalovic M, Pavlovic A, Vulovic S. Dealing with the Effect of Air in Fluid Structure Interaction by Coupled SPH-FEM Methods. *Materials*. 2019; 12(7):1162.
<https://doi.org/10.3390/ma12071162>
- [7] von Kármán T. The impact on seaplane floats during landing. NACA Technical Notes N.321, 1929.
- [8] Wagner H. Über Stoß- und Gleitvorgänge an der Oberfläche von Flüssigkeiten. Zeitschrift Für Angewandte Mathematik Und Mechanik, Vol. 12, No. 4, 1932.
<https://doi.org/10.1002/zamm.19320120402>
- [9] I. Stenius, A. Rosén, and J. Kutteneuler, 'Explicit FE-modelling of hydroelasticity in panel-water impacts', International Shipbuilding Progress, vol. 54, no. 2–3, pp. 111–127, 2007.
- [10] Shah S.A. Water Impact Investigations for Aircraft Ditching Analysis thesis, School of Aerospace, RMIT University, 2010.

Data-driven deep neural network for structural damage detection in composite solar arrays on flexible spacecraft

Federica Angeletti^{1,a*}, Paolo Gasbarri^{1,b} and Marco Sabatini^{1,c}

¹Scuola di Ingegneria Aerospaziale, Sapienza University of Rome, Via Salaria 851, Rome, Italy

^afederica.angeletti@uniroma1.it, ^bpaolo.gasbarri@uniroma1.it, ^cmarco.sabatini@uniroma1.it

Keywords: Structural Health Monitoring, Deep Learning, Flexible Spacecraft

Abstract. A data-driven approach based on Deep Neural Network (DNN) techniques is here proposed for Structural Health Monitoring of large in-orbit flexible systems. Damage scenarios are generated via a Finite Element commercial code to train and test the machine learning model, by considering equivalent properties of the composite material of the solar panels. The fully coupled 3D equations for the flexible spacecraft are integrated to test typical profiles of attitude manoeuvres in case of different damages. The DNN model is trained using sensor-measured time series responses, with each response associated with the label of the corresponding damage scenario, and tested via k-folding approach. This methodology offers a promising approach to detect structural damage in solar arrays on spacecraft using machine learning techniques.

Introduction

With the increasing use of composite materials in solar arrays on modern spacecraft, structural damages during the operational life have become a significant concern. Such events often lead to modifications of the control/structure interaction dynamics, thus posing an issue for the implemented system controller. Detecting failures in flexible structures can however be challenging: local damages may not cause significant changes in the global dynamics of the satellites to be detected by on-board sensors. Therefore, a set of sensors at structural level is beneficial to identify promptly the location and the entity of the damages.

As far as current state-of-the-art solutions for damage identification are concerned, there are mostly two adopted philosophies: physics-based and data-driven methods [1-3]. The purpose of this study is to propose a Deep Learning methodology with multi-classification damage capabilities, with respect to the research proposed by the authors' previous work [4-5]. Indeed, the present study aims at proposing an architecture and guidelines for performing SHM of space structured based on LSTM-NNs. A challenging study case in terms of impact of failures on the global spacecraft dynamics is selected, and a more complex problem in terms of higher dimensionality of the multi-class identification problem is addressed, giving information not only about the presence, but also the location of the damage. The structure and damage entity is implemented taking into account the equivalent properties and effects on a traditional composite space structure, in particular, an aluminum honeycomb.

The approach is carried out as follows. Firstly, the 3D mathematical model of a flexible spacecraft is implemented in a simulator for carrying out a wide set of in-orbit attitude maneuvers. Then, the spacecraft test case model is described, including the network of distributed sensors for the SHM and the damage configurations addressed herein. The implemented deep neural architecture is described, based on an LSTM variant. Finally, the main results about the performance of the trained classification network are discussed.

Bidirectional Long-Short Term Memory Network

The efficacy of Long Short-Term Memory (LSTM) models has been validated in various domains, notably within the area of time series prediction [6][7], as well as for both single-variable and

multi-variable time sequence classification tasks [8]. LSTMs are purposefully crafted to exploit long-range dependencies, enabling them to effectively address scenarios where the present time step is distant from correspondent information. By incorporating the capability to effectively process historical data within a single cell, Deep Neural Network (DNN) architectures can benefit by establishing connections across multiple LSTM layers.

Details about the structure of a LSTM network can be found in [8]. In this study, we use a multivariate deep classification model composed of an input layer, two stacked Bi-LSTM layers, including a dropout layer to address overfitting issues, a Softmax layer, and a final classification layer.

Spacecraft Dynamics and Damages

This section briefly introduces a representative case of a spacecraft equipped with two solar panels of 3 x 1 m (composed of two sub-panels each), designed using MSC Nastran FEM tool based on information available in literature about dimensions, mass and shape of the panels. The first three modes of the assembled spacecraft are illustrated in Fig.1. Since the size and mass constraints at launch require solar panels to be lightweight, while strong and stiff, a composite material – an aluminium honeycomb here specifically - is selected for each sub-panel. Moreover, to reduce the complexity of FE model, an equivalent model of the multi-layer composite structure is here considered as a single-layer panel. The equivalent thickness t_{eq} , and stiffness moduli E_{eq} and G_{eq} , obtained by solving the equations in available literature [9], are

$$t_{eq} = \sqrt{3h_c^2 + 6h_c t_f + 4t_f^2} \quad E_{eq} = (2t_f E_f)/t_{eq} \quad G_{eq} = (2t_f G_f)/t_{eq} \quad (1)$$

where t_f is the skins thickness, h_c is the height of honeycomb core, E_f and G_f skins moduli. The equivalent data for a 10mm sandwich panel are $t_{eq} = 0.0156m$, $E_{eq} = 90GPa$, $G_{eq} = 3.31GPa$.

At the same time, the Modal Strain Energy (MSE) - defined as the amount of elastic energy stored in a finite element - associated to the flexible appendages was computed. The related MSE map (see Fig. 2) is used to identify the locations of the elements whose change in mechanical properties could be more problematic for the global dynamics of the system. The objective is to avoid building a heavy set of data including damages all over the structure (also damages associated with low risk, i.e. inducing a negligible change in the modal properties of the satellite), potentially leading to an excessively high dimension multivariate classification problem. Instead, the approach proposed here is to discriminate a set of potential critical damages, to be identified via the deep learning architecture, based on MSE concentration.

In this research, damages are considered as resulting from space debris hits, causing a perforation in the structure. The dimension of damage is assumed as not exceeding 5cm x 5cm, which is a representative size for high velocity impacts for aluminium honeycomb [10]. Damages are simulated only on one solar panel. Hence, a set of three-axis accelerometers sensors are installed on one side. In particular, the position of the sensors is depicted in Fig. 3.

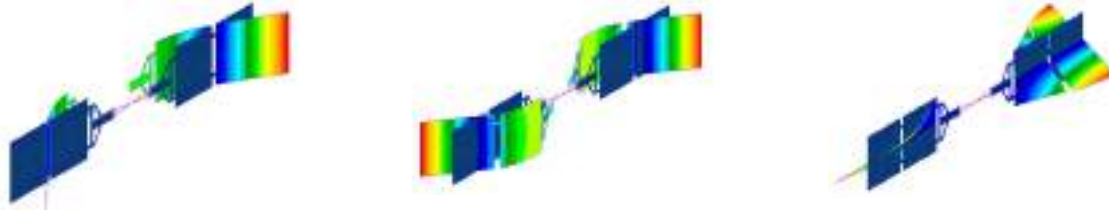


Fig. 1: Modal shapes. From left to right, 1st mode: 0.97 Hz, 2nd mode: 1.58 Hz, 3rd mode: 3.27 Hz



Fig. 2: Modal Strain Energy (MSE) map. From left to right, 1st mode, 2nd mode, 3rd mode

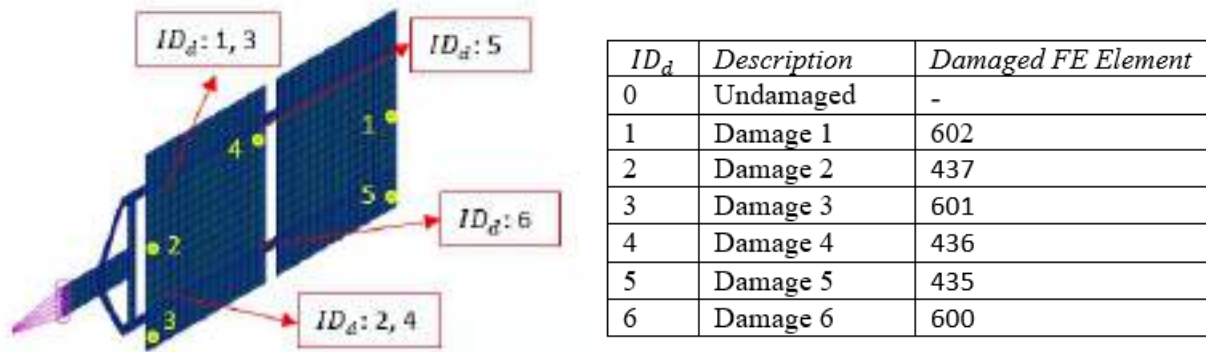


Fig. 3: Overview of damages (indicated as ID_d) and sensors (indicated with numbers from 1 to 5).

Training and Validation

To generate the training set, a 3D simulator of in-orbit flexible spacecraft dynamics – developed in house [11-12] – is used to reproduce satellite attitude maneuvers. A finite element model is created for each damage scenario. Once the damaged structural sub-models, deriving from the original undamaged one, and the network of sensors are defined, the dataset generation for the training of the DNN can be set up. In detail, the followed steps are:

- The finite element structural models are imported in Matlab to perform the non-linear simulation of attitude maneuvers for the flexible spacecraft.
- Several one-, two- and three-axis attitude maneuvers are simulated by varying not only the target orientations, but also the gains of the quaternion-based PD control law to further diversify the dataset.
- Time histories from installed accelerometers sensors are recorded and saved to create the training and testing data, not before being pre-processed and normalized according to their mean and standard deviation.

Results

Several parameters are considered and optimized to improve the performance of the network: the DNN hyperparameters, the data pre-processing and the number and location of sensors. Finally, Table 1 shows the results in terms of accuracy (mean value and standard deviation) of the adopted classification network. In detail, four damages in the area of the structure associated with both highest MSE (red areas in Fig. 2) and lower MSE (green areas in Fig. 2) are considered. Despite inducing a reduced change in the system frequencies and modal shape (about 1% relative difference), the DNN shows a good classification accuracy even in this challenging case. The confusion matrix is illustrated in Fig. 4.

Table 1: Classification accuracy

Case	Description	Rationale	Accuracy
1	ID_d : 0, 1, 2, 5, 6 Sensors: 1, 2, 3, 4, 5	Identify the location of different damages in different MSE concentration areas (highest and second highest)	85.09% \pm 4.87%

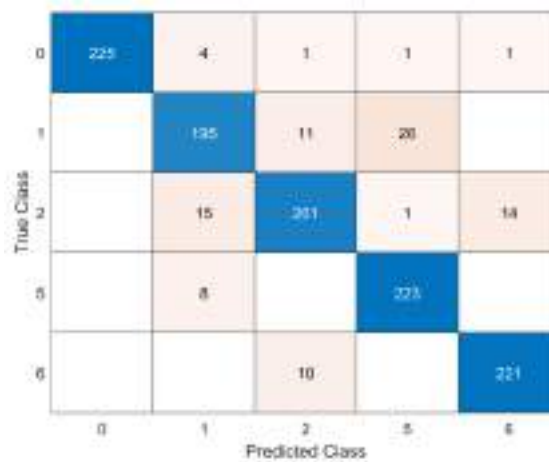


Fig. 4: Confusion matrix

Conclusions

This work has showcased the potential of LSTM networks in identifying damages in large space structures by analyzing time responses measured by sensors. The presented results are not only preparatory to carry out a laboratory experimental validation phase on a flexible spacecraft test-rig, but also propaedeutic to apply the system to several innovative composite materials. Indeed, future research endeavors could explore the possibility of training deep neural networks using real-world measured data, enabling them to operate in practical conditions and accurately predict actual damages.

Acknowledgments

We would like to thank Prof. Massimo Panella and Prof. Antonello Rosato for their expertise and insights, which were instrumental in shaping the direction and focus of this research.

Funding

The work was financed by the *European Union - NextGenerationEU* (National Sustainable Mobility Center CN00000023, Italian Ministry of University and Research Decree n. 1033 - 17/06/2022, Spoke 11 - Innovative Materials & Lightweighting). The opinions expressed are those of the authors only and should not be considered as representative of the European Union or the European Commission's official position. Neither the European Union nor the European Commission can be held responsible for them.

References

- [1] E. Figueiredo, et al., Machine learning algorithm for damage detection, computational and experimental methods in structure, *Vibration-Based Techniques for Damage Detection and Localization in Engineering Structures*, 10 (2018) 1-39.
https://doi.org/10.1142/9781786344977_0001
- [2] J. Vitola, et al., Data-Driven Methodologies for Structural Damage Detection Based on Machine Learning Applications, *Pattern Recognition - Analysis and Applications*, (2016).
<https://doi.org/10.5772/65867>

- [3] G. B. Palmerini, F. Angeletti, P. Iannelli, Multiple Model Filtering for Failure Identification in Large Space Structures, *Lecture Notes in Civil Engineering*, 128 (2021) 171-181.
https://doi.org/10.1007/978-3-030-64908-1_16
- [4] P. Iannelli, F. Angeletti, P. Gasbarri, M. Panella, A. Rosato, Deep learning-based Structural Health Monitoring for damage detection on a large space antenna, *Acta Astronautica*, 193 (2022) 635-643, <https://doi.org/10.1016/j.actaastro.2021.08.003>
- [5] F. Angeletti, P. Iannelli, P. Gasbarri, M. Panella, A. Rosato, A Study on Structural Health Monitoring of a Large Space Antenna via Distributed Sensors and Deep Learning, *Sensors*, 23(1) (2023) 368, <https://doi.org/10.3390/s23010368>
- [6] F. Succetti, A. Rosato, R. Araneo, M. Panella, Deep neural networks for multivariate prediction of photovoltaic power time series, *IEEE Access*, 8 (2020) 211490-211505.
<https://doi.org/10.1109/ACCESS.2020.3039733>
- [7] Z. Ma, M. Yao, T. Hong and B. Li, Aircraft Surface Trajectory Prediction Method Based on LSTM with Attenuated Memory Window, *Journal of Physics: Conference Series*, 1215 (2019).
<https://doi.org/10.1088/1742-6596/1215/1/012003>
- [8] F. Karim, S. Majumdar, H. Darabi, S. Harford, Multivariate LSTM-FCNs for Time Series Classification, *Neural network*, 116 (2019) 237-245.
<https://doi.org/10.1016/j.neunet.2019.04.014>
- [9] J. K. Paik, A. K. Thayamballi and G. S. Kim, The Strength Characteristics of Aluminum Honeycomb Sandwich Panels, *Thin-Walled Struct.*, 35 (1999) 205–31.
[https://doi.org/10.1016/S0263-8231\(99\)00026-9](https://doi.org/10.1016/S0263-8231(99)00026-9)
- [10] X. Kunbo, Z. Jiandong, G. Zizheng, C. Yan, Z. Pinliang et al., Investigation on solar array damage characteristic under millimetre size orbital debris hypervelocity impact, *Proc. 7th European Conference on Space Debris*, Darmstadt, Germany, 18–21 April 2017, published by the ESA Space Debris Office.
- [11] F. Angeletti, P. Iannelli, P. Gasbarri, M. Sabatini, End-to-end design of a robust attitude control and vibration suppression system for large space smart structures, *Acta Astronautica*, 187 (2021) 416–428. <https://doi.org/10.1016/j.actaastro.2021.04.007>
- [12] F. Angeletti, P. Iannelli, P. Gasbarri, Automated nested co-design framework for structural/control dynamics in flexible space systems, *Acta Astronautica*, 198 (2022) 445–453.
<https://doi.org/10.1016/j.actaastro.2022.05.016>

A numerical parametric study on delamination influence on the fatigue behaviour of stiffened composite components

Angela Russo^{1,a*}, Andrea Sellitto^{1,b}, Concetta Palumbo^{1,c}, Rossana Castaldo^{1,d}
and Aniello Riccio^{1,e}

¹University of Campania “Luigi Vanvitelli”, Department of Engineering, Via Roma 29, 81031
Aversa (CE), Italy

^aangela.russo@unicampania.it, ^bandrea.sellitto@unicampania.it,
^cconcetta.palumbo@unicampania.it, ^drossana.castaldo@unicampania.it,
^eaniello.riccio@unicampania.it

Keywords: CFRP, Fatigue, SMXB, Delamination Growth

Abstract. This paper investigates the fatigue phenomenon in Carbon Fibre Reinforced Plastic (CFRP) composite materials. Fatigue is a major problem in composite materials, due to their complex microstructures and inhomogeneous properties. In composite materials, fatigue is caused by cyclic loading, which leads to the accumulation of damage and eventually failure. This is related to several factors such as material properties, geometry, loading conditions, and environmental conditions. The fatigue life of composite materials is usually much lower than that of metals, and it is often catastrophic and unpredictable. Therefore, it is mandatory to understand behaviour of composite materials subjected to cyclic loading condition and to develop strategies to improve their fatigue performance. To this end, a Paris Law-based module has been implemented in the well-establish SMart-time XB (SMXB) procedure, being able to accurately numerically simulate the delamination growth caused by cyclic loads in complex composite structures. This process, which takes advantages of the mesh and load independency of the SMXB method in the evaluation of the delamination growth, has been implemented in the Ansys Parametric Design Language to create a highly versatile and parametric procedure. A numerical parametric study has been carried out to investigate the behaviour of a pre-existing circular delamination under cyclic loading, to assess the influence of delamination radius and thickness on the delamination growth. The results of this study will provide important insights into how delamination radius and thickness affect the delamination growth and the durability of composite structures. This study will help to inform the design of composite structures for various applications.

Introduction

Damage mechanisms in composite materials are the main reason behind the limited use of these materials for aircraft component construction. Delamination, in particular, is one of the most serious failure events that composites may experience, as it is undetectable and can therefore propagate, causing a rapid structural collapse. Fatigue phenomenon amplifies the weaknesses in terms of damage propagation in composite materials [1].

The study of interlaminar damage propagation has been extensively addressed in the literature, both experimentally and numerically. In particular, the Virtual Crack Closure Technique (VCCT) [2] and Cohesive Zone Models (CZM) are the most widely used computational methodologies for the investigation of delamination propagation in finite element (FE) environment. Among the others, the numerical procedure SMart time XB (SMXB) [2,3] is a FE tool based on the VCCT, which, however, has the unique feature to simulate delamination without dependence on the size of the elements used for the discretization of the model and independent from the load step size used in the numerical analyses. These characteristics are the basis for a further development of the SMXB, which is the possibility of simulating the evolution of delamination due to fatigue, i.e. a



load acting on the structure in a cyclic fashion. The fatigue delamination simulation method integrated in SMXB has been implemented using the Ansys Parametric Design Language and is based on the Paris law relation. In [4], the mesh independence of the results obtained with the FaTigue SMXB (FT-SMXB) tool has been demonstrated in the case of a Double Cantilever Beam specimen.

In this work, a parametric study has been performed to investigate the behaviour of a CFRP typical stiffened panel with a pre-existing circular delamination, which aims to simulate an impact damage. The panel has been subjected to cyclic loads in order to assess the influence of the delamination radius and depth on the global compressive behaviour of the structure. The principal added value of this work is the use of the FT-SMXB, due to its inherent characteristics. Standard VCCT and CZM probably would affect the results due to their dependence on the mesh and time step of the finite element analysis.

Methodology

The SMart Time XB procedure has been introduced for the first time in [2] by Pietropaoli and Riccio in 2010. The tool has been improved over the years with different capabilities, for example the introduction of double delamination front in the case of skin-stringer debonding [3] or also the possibility to consider the R-curve. It is still being studied and enhanced today, in particular, by introducing the capability to simulate the fatigue driven delamination [4].

Fatigue in composite materials can be simulated considering the Paris Law equation, which has been developed for metals and then extended for composite materials. Equation (1) reports the Paris Law equation for composites, where a is the crack length, N is the number of cycles, G is the Energy Release Rate and n , c are experimentally derived constant parameters. This equation expresses the crack growth rate as a function of the number of fatigue cycles.

$$\frac{da}{dN} = cf(G)^n \quad (1)$$

The function of ERR, $f(G)$, may assume different expressions. In the FT-SMXB, $f(G)$ can be selected among more than 4 expressions [], depending on the user needs.

The implemented tool considers the accumulation of damage on the crack front, so that the number of cycles at which the delamination propagates and the position of propagation on the crack front can be correctly assessed. Moreover, the procedure allows to take into account the load ratio and permits to evaluate the residual strength of the structure after a certain number of fatigue cycles.

Numerical application

The studied structure, shown in Figure 1, is a typical aeronautical component with two T-shaped stringers tied on a skin panel. It is characterized by a circular delamination, located in the middle of the bay, representing an example of typical impact damage. Two different configurations have been examined, both under cyclic loading conditions, which share all the geometrical properties except the radius of the delamination and its depth. Two radii have been considered, 30 mm and 40 mm, for each of them the delamination has been placed under 2 and 3 layers.

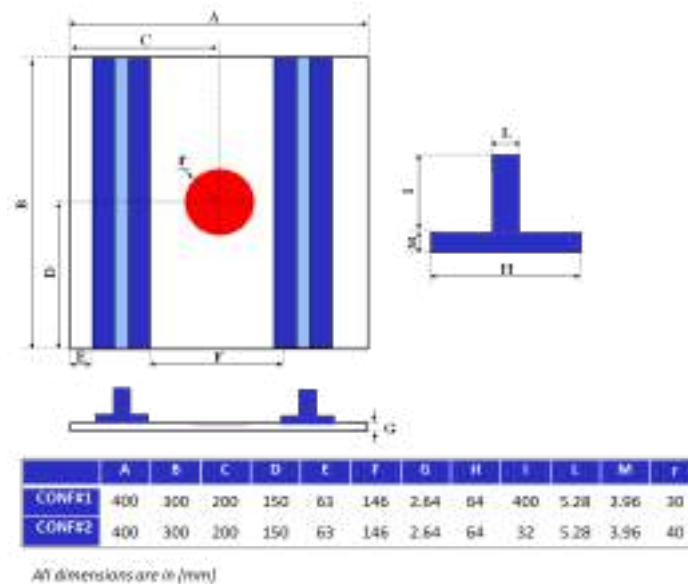


Figure 1. Geometry of the analysed panel

The stacking sequence of the skin panel contains 16 layers with a layup of $(45^\circ, 0^\circ, 90^\circ, -45^\circ)_{2s}$, the foot stringer has 24 layers with a sequence of $(45^\circ, 0^\circ, 90^\circ, -45^\circ)_{3s}$, finally the web stringer has 32 layers with a layup of $(45^\circ, 0^\circ, 90^\circ, -45^\circ)_{4s}$.

The finite element model has been built in the Ansys Mechanical environment and a global-local approach has been used, whereby the structure has been discretised with a sparse mesh in the area not involved in the crack propagation phenomenon and a local area, characterised by the initial circular delamination and the propagation region, discretised on the contrary with a fine mesh. Both solid and shell parts have been considered, in order to reduce the computational cost of the analyses. The panel has been clamped on one side, while compressive cyclic load has been applied on a pilot node, linked to the other side nodes of the structure by means of rigid link elements.

Results

The panel has been analysed under cyclic loading conditions: 90% and 80% of the static onset load has been considered for the analyses. For each configuration static analysis has been performed in order to obtain the onset load on which the applied fatigue load is based. However, for the sake of brevity, only the results of fatigue simulations are reported in this section.

The results in terms of delaminated area as a function of the number of cycles are shown in Figure 2 for the configuration with 30 mm delamination radius. For simplicity, the configurations have been named CONF#1 for radius of 30 mm and CONF#2 for radius of 40 mm, in particular CONF#1-2 is the configuration with delamination radius of 30 mm under 2 plies.

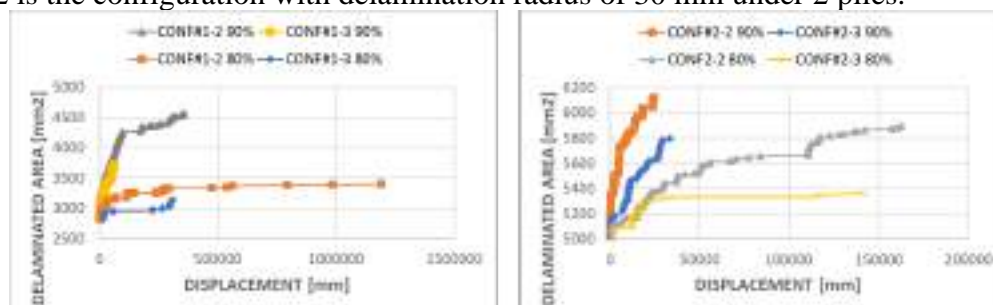


Figure 2. Delaminated area vs. Number of cycles

The analyses stop when propagation reaches the limit of propagation depending on the propagation region defined by the user (this is a numerical issue) or when the number of cycles

overcome 1E6. According to Figure 2, in the selected configurations, only CONF#1-2 at 80% load exceeds one million cycles. The behaviour of the two configurations is similar: increasing the delamination depth reduces the delaminated area at the same number of cycles. Moreover, as expected, for a higher load the delamination is considerably unstable. Table 1 summarize the results in terms of delamination onset, buckling load and number of cycles to failure.

Table 1. Result summary

Configuration	Delamination buckling	Global panel buckling	Delamination onset load (static)	Number of cycles onset – 90%	Number of cycles failure – 90%	Number of cycle onset – 80%	Number of cycles failure – 80%
CONF#1-2	8264 N	207590 N	146117 N	148	358469	3174	>1E6
CONF#1-3	27325 N	207241 N	140209 N	385	64597	18000	309403
CONF#2-2	4696 N	206758 N	145539 N	92	24443	1208	162791
CONF#2-3	15610 N	205516 N	135655 N	69	33433	1650	144271

The local buckling load of delamination is different for all the configurations, it decreases by increasing the radius, while, at the same radius, it increases by increasing the delamination depth. The global buckling remains almost the same, between 205 and 207 kN.

Conclusions

In this paper the fatigue driven delamination has been studied in a composite stiffened panel with circular delamination. It has been found that the fatigue response of the panel depends on the delamination depth. Increasing the depth reduce the number of cycle to failure of the panel. the propagation trend remains similar as the delamination radius changes.

References

- [1] C. B. Carlos G. Dávila, «Fatigue life and damage tolerance of postbuckled composite stiffened structures with initial delamination,» Composite Structures, pp. 73-84, 2017. <https://doi.org/10.1016/j.compstruct.2016.11.033>
- [2] E. Pietropaoli e A. Riccio, « On the robustness of finite element procedures based on Virtual Crack Closure Technique and fail release approach for delamination growth phenomena. Definition and assessment of a novel methodology.,» Compos. Sci. Technol, p. 1288–1300, 2010. <https://doi.org/10.1016/j.compscitech.2010.04.006>
- [3] A. Riccio, A. Raimondo e F. Scaramuzzino, « A robust numerical approach for the simulation of skin–stringer debonding growth in stiffened composite panels under compression.» Compos. Eng., pp. 131-142, 2015. <https://doi.org/10.1016/j.compositesb.2014.11.007>
- [4] Russo, A., Riccio, A., & Sellitto, A. (2022). A robust cumulative damage approach for the simulation of delamination under cyclic loading conditions. Composite Structures, 281. <https://doi.org/10.1016/j.compstruct.2021.114998>

On the use of double-double design philosophy in the redesign of composite fuselage barrel components

Antonio Garofano^{1,a,*}, Andrea Sellitto^{1,b} and Aniello Riccio^{1,c}

¹University of Campania "Luigi Vanvitelli", Department of Engineering, Via Roma 29, 81031, Caserta, Italy

^aantonio.garofano@unicampania.it, ^bandrea.sellitto@unicampania.it,
^caniello.riccio@unicampania.it

Keywords: Composite Structures, Double-Double, Laminates Optimization, Mass Saving

Abstract. Mass minimization and mechanical performance maximization constitute the basic aspects of the structural optimization processes. In particular, the laminate redesign in terms of thickness and lay-up grants the main approach for the optimization of composite components. The innovative Double-Double laminate concept provides an effective approach to design composite components for weight and strength requirements, overcoming the use of the conventional 0° , 90° and $\pm 45^\circ$ ply orientations. In Double-Double designed components, 4-ply building blocks are stacked one upon the other to constitute a laminate. Each building block is made up of four $[\pm\Phi, \pm\Psi]$ oriented plies. In the present work, the Double-Double approach has been adopted in the redesign of the composite lay-up and thickness profile of frames in a composite fuselage barrel. The DD optimized frames achieved a total mass reduction by up to 35% while ensuring mechanical performances comparable to the starting configuration.

Introduction

Laminate lay-up optimization represents the most feasible field in which structural engineers can work as compared to material changing and components redesign to design more efficient, lightweight and performing composite load-bearing structures in the aviation field. Lay-ups typically used in composite aviation components only involve 0° , 90° and $\pm 45^\circ$ plies orientations. Moreover, symmetry and balancing requirements must be accounted for manufacturing and performance needs, limiting the optimization processes for mass and mechanical performance requirements to sub-optimal solutions. One step forward is proposed by the newly Double-Double approach introduced by Professor S.W. Tsai [1]. Double-Double laminates are made up by stacking 4-ply building blocks without symmetry and balancing requirements. Each building block, or sub-laminate, consists of four plies based on double bi-axial angles $[\pm\Phi, \pm\Psi]$. Φ and Ψ angles can be tuned assuming each value between 0° and 90° to manage mechanical performances of laminates. DD angles and number of the required building blocks are directly optimized for the application and its load conditions. A new composite lay-up scheme able to optimize the components for weight and strength requirements is given, enabling to overcome the conventional 0° , 90° and $\pm 45^\circ$ plies orientations [2]. The Excel-based Lam-Search optimizer tool automatically determines the best $[\pm\Phi, \pm\Psi]$ angles among all allowed combinations of DD angles to minimize the safety margin by computing the strength ratio R with respect to a selected failure criterion. Laminate thickness is updated according to the computed strength ratio value [3]. In this framework, the present paper is aimed to perform an optimization process on the frames of a composite fuselage barrel subjected to static loads through the Double-Double design approach for mass reduction purposes.



FE model description

The FE model of a regional aircraft's fuselage barrel has been developed in the Abaqus environment, as showed in Fig. 1. Main structural sub-components have been modelled as solid extruded parts while frames as 3D shell parts allowing to run sequential analyses with variable thickness during the optimization process. The optimized $[\pm 37.5, \pm 45]$ Double-Double lay-up has been employed for the skin [4]. A uniform $[90, 45, 0, 45, -45, 90, 45, -45, 0, -45, 45, -45]_s$ stacking sequence characterized the frames in the starting configuration. The IMS/977-2 CFRP [4], a Woven Fabric [4] and the T700 CPLY64 [4] have been adopted for the composite components while Aluminum 2024-T42 for the metal parts. The FE model has been discretized by means of 8-node continuum shell elements (SC8R) and 8-node linear brick elements (C3D8R) for composite and aluminum components, respectively, while 4-node general-purpose shell elements (S4R) have been used for frames.

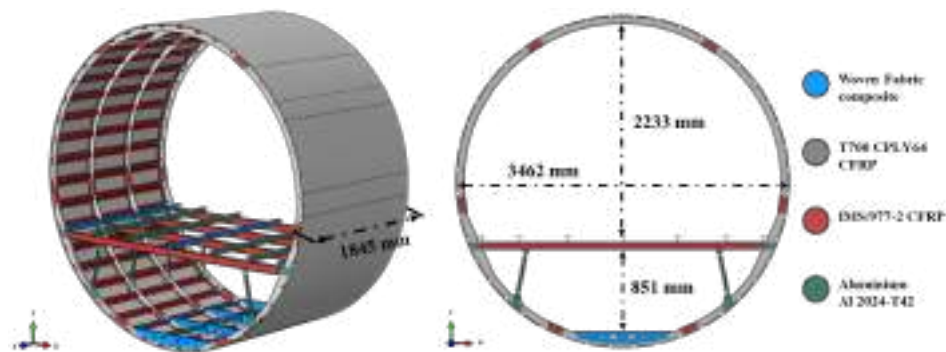


Figure 1. Fuselage barrel FE model and dimensions: a) isometric view; b) frontal view

According to the Lam-Search optimizer tool needs to perform the optimization process, frames have been subdivided in zones and cells. A zone has been defined for each frame, enabling one best $[\pm\Phi; \pm\Psi]$ DD lay-up for each frame. Seven cells have been defined in each zone by considering only the half of each frame being the structure symmetry, as showed in Fig. 2a. Thereafter, results have been extended to the other half. The thickness profile in cells is computed according to the strength ratio R value with respect to the controlling cell.

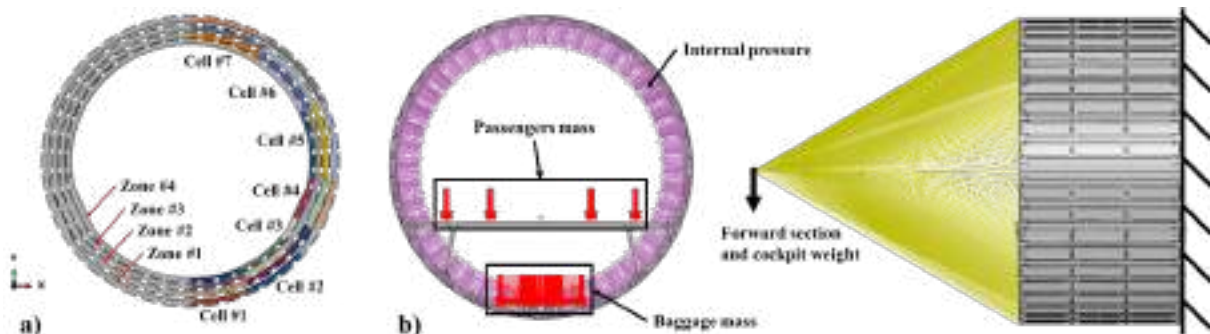


Figure 2. a) Zone and cells subdivision of the frames; b) applied loading and boundary conditions

An iterative process has been carried out to reach the strength optimized laminate design for frames through thickness and layup variation in cells of each zone. Linear static analyses considering the operating loads presented in Fig. 2b have been performed in each iteration. In detail, a pressure has been applied to the internal surfaces to simulate pressurization while a force representing the cockpit and forward section weight has been applied to a reference point and transferred to the structure. Mass loads of passengers and baggage have been considered.

Optimization process

A preliminary linear static FE analysis has been performed on the fuselage barrel in the starting configuration with quad laminates frames and assumed as Iteration 0. The average stress components in all cells of each zone have been used as input data to the Lam-Search optimizer tool, resulting in the best DD angles and cells thickness profiles for each zone as output. The same process has been individually applied to each zone. Results in Iteration 0 suggested the best DD angles and thickness profiles for cells in zones 1 to 4, respectively, leading to a total mass reduction of frames up to 85%. However, R values went above the unity. Consequently, the starting FE model has been updated according to Iteration 0 results and a new FE analysis has been carried out to update the stress components in the cells, generating new input data for the Lam-Search optimizer tool. This process has been repeated until identical DD angles in each zone between two iterations were achieved and any cell exhibited a strength ratio below unity.

At the end of Iteration 3, all cells in all zones achieved a strength ratio R greater than unity. Furthermore, the optimal DD angles in each zone resulted $[\pm 37.5; \pm 60]$, $[\pm 30; \pm 52.5]$, $[\pm 30; \pm 60]$, and $[\pm 45; \pm 45]$ for zones 1 to 4, respectively, and identical to those obtained in the previous iteration. The thickness optimization led to a total mass reduction of frames up to 71%. The time-history variation of the average value of strength ratio R for each zone across iterations is shown in Fig. 3. In Iteration 3, the thickness optimization led the R-values above and close the unity, offering an effective design solution in terms of mass saving.



Figure 3. Time-history variation of the strength Ratio R in cells in all zones across iterations
(Note: R-values below the unity in red, R-values above the unity in green)

The optimized design for frames provided by the optimization process is characterized by a continuously scaled thickness across cells, not applicable to composite materials, as laminates have a discrete thickness. Hence, digitization is required to conservatively convert the cells thickness to discrete values according to the building block thickness. In addition, cells thickness within the same frame sub-components have been equalized to the thickest one to promote an easy manufacturing and uniformity of the sub-component, performing a tapering operation. Digitizing and tapering operations, showed in Fig. 4, reduced the mass saving given by Double-Double designed frames to 65% while providing an increase in the easy of manufacturing.

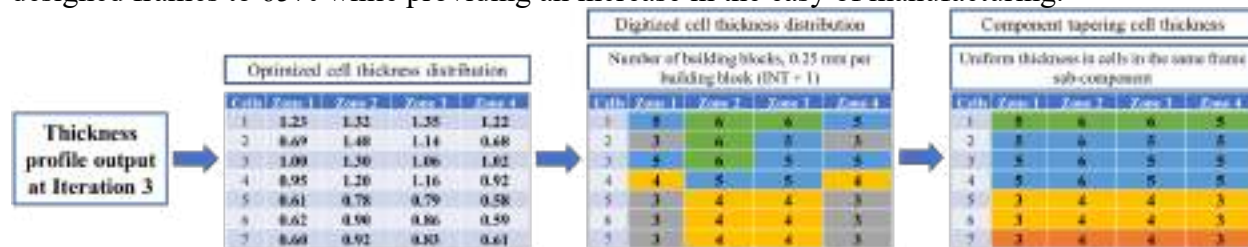


Figure 4. Thickness evolution in digitizing and tapering operations starting from the optimized design

Thickness variation led to a change in the frames total mass and consequently in the fuselage barrel total mass. The time history of the mass variation and mass saving in the frames and in the whole fuselage barrel, compared to the initial configuration is shown in Fig. 5. The frames optimization performed through the Lam-Search optimizer tool resulted in a frames design that

reduced their total mass to 35% of the initial mass after tapering. Consequently, the mass variation in frames resulted in the mass reduction of the overall fuselage barrel by up to 12%.

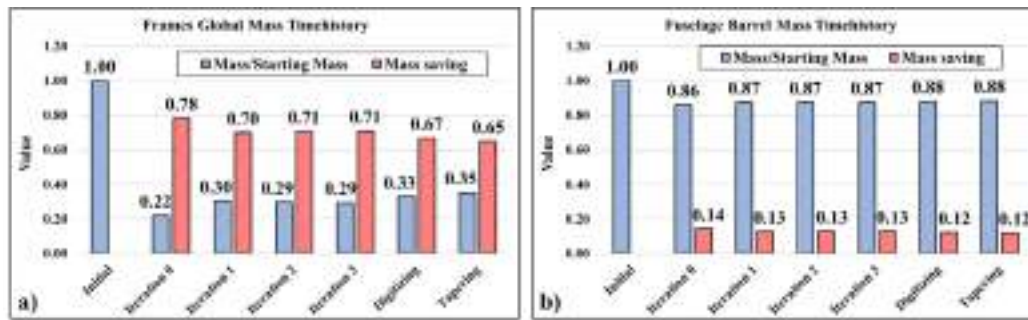


Figure 5. Mass and mass saving variation in frames and in the whole fuselage barrel through optimization

Conclusions

In the present work, the Double-Double lay-up concept has been applied to the frames of a composite fuselage barrel, considering the operating loads. Throughout iterations, the procedure identified the best DD composite lay-up and thickness profiles, providing mechanical performances comparable to the initial configuration while significantly reducing the components total mass. At the end of the optimization process, the initial configuration of frames with quad laminates has been replaced by an optimized configuration with the best DD lay-up for each of the frames, corresponding to $[\pm 37.5; \pm 60]$, $[\pm 30; \pm 52.5]$, $[\pm 30; \pm 60]$ and $[\pm 45; \pm 45]$ for zones 1 to 4, respectively. The thickness profile has been tailored to the acting loading condition ensuring a total mass reduction of frames by up to 35%. Thus, the use of the Double-Double laminates concept and the Lam-Search optimizer tool proved to be an effective method for optimizing the design of composite components for mass reduction purposes while ensuring a mechanical behavior comparable to the starting configuration.

References

- [1] Shrivastava, S., Sharma, N., Tsai, S. W., & Mohite, P. M. (2020). D and DD-drop layup optimization of aircraft wing panels under multi-load case design environment. *Composite Structures*, 248, 112518. <https://doi.org/10.1016/j.compstruct.2020.112518>
- [2] Tsai, S. W. (2021). Double-double: new family of composite laminates. *AIAA Journal*, 59(11), 4293-4305. <https://doi.org/10.2514/1.J060659>
- [3] Vermes, B., Tsai, S. W., Riccio, A., Di Caprio, F., & Roy, S. (2021). Application of the Tsai's modulus and double-double concepts to the definition of a new affordable design approach for composite laminates. *Composite Structures*, 259, 113246. <https://doi.org/10.1016/j.compstruct.2020.113246>
- [4] Garofano, A., Sellitto, A., Acanfora, V., Di Caprio, F., & Riccio, A. (2023). On the effectiveness of double-double design on crashworthiness of fuselage barrel. *Aerospace Science and Technology*, 108479. <https://doi.org/10.1016/j.ast.2023.108479>

Multifunctional composites as Solid-Polymer-Electrolytes (SPE) for Lithium Ion Battery (LIB)

Salvatore Mallardo^{1,a,*}, Gennaro di Mauro^{2,b}, Michele Guida^{2,c}, Pietro Russo^{1,d},
Gabriella Santagata^{1,e}, Rosa Turco^{3,f}

¹Institute for Polymers, Composites and Biomaterials, National Research Council, Pozzuoli, Italy

²Department of Industrial Engineering, University of Naples Federico II, Naples, Italy

³Department of Chemical Sciences, University of Naples Federico II, Naples, Italy

^asalvatore.mallardo@ipcb.cnr.it, ^bgennaro.dimauro@unina.it, ^cmichele.guida@unina.it,

^dpietro.russo@ipcb.cnr.it, ^egabriella.santagata@ipcb.cnr.it, ^frosa.turco@unina.it

Keywords: Multifunctional Materials, Polymer Composites, Solid Polymer Electrolyte (SPE), Energy Generation, Aircraft Structures

Abstract. Novel solid-polymer-electrolytes (SPE) have been formulated as key components of structural multifunctional materials to develop Lithium Ion Battery (LIB). To this aim, SPE blends based on polyethylene oxide (PEO), different molecular weights polyethylene glycole (PEG), PEG-modified sepiolite (SEP) and lithium triflate have been prepared by one pot melt mixing. The films were obtained by compression moulding following a method easily scalable to industrial level. The different films have been characterized by structural (FTIR-ATR), thermal (DSC, TGA), morphological (SEM) and mechanical (tensile tests) analysis. The different properties could be mainly addressed to the diverse PEG both amounts and molecular weight and to the specific physical interaction occurring between PEO, PEG sepiolite and lithium ions strongly influencing crystallinity, thermal stability and mechanical response. Thus, SPE2 sample evidenced the highest both crystallinity and mechanical stiffness and toughness, whereas SPE1 and SPE3 film showed the best compromise between molecular crystallinity and mechanical performances, mostly as strain at break are concerned. Finally, SPE4 film, including the highest amount of PEG showed a peculiar increasing of mechanical rigidity in opposition to molecular plasticization effect exploited by PEG. The many features of SPE systems requires special attention and further research when it comes time to design structural multifunctional materials for LIB based batteries of Type-III.

Introduction

The emerging technologies of structural batteries (SBs), i.e., multi-component-based systems able to combine the functions of energy storage and the load-bearing ability in the attempt to improve such performances, are gaining even more attention to solve the environmental sustainability at decarbonizing the transportation sector [1]. SBs are based on solid polymer electrolytes (SPEs), i.e., solid polymeric materials with ability to transport lithium ions. Usually, SPEs consist of polymer matrices and lithium ions obtained after dissolution of polymer with lithium salts and following drying process. The result is the formation of a thin, inflammable, and flexible film of a coordination complex between the polymer and the lithium ions [2]. When a potential difference is applied across the solid electrolyte, the lithium ions move from the anode to the cathode through the polymer matrix, they react with the cathode material to produce a flow of electrons. Among the polymers, polyethylene oxide (PEO) is the most attractive since it shows excellent solubility for lithium salts, is a low cost, non-toxic, biocompatible, water soluble, high conductive material [4] with high energy density, high electrochemical stability, and excellent compatibility with inorganic salts. It is widely accepted that lithium-ion transport occurs at the expense of the flexible amorphous phase [5, 6]. In this paper, PEO as organic electrolyte, lithium triflate (lithium



trifluoromethanesulfonate) LiCF_3SO_3 as electrolyte, sepiolite ($\text{Si}_{12}\text{O}_{30}\text{Mg}_8(\text{OH})_4(\text{H}_2\text{O})_{4 \times 8}\text{H}_2\text{O}$) (SEP) as a natural, low cost and abundant fibrous clay mineral enhancing the dissociation of lithium salts, have been used to develop SPEs [7, 8, 9]. To enhance SEP dispersion in PEO thus avoiding fiber aggregation, organic modification of SEP surface has been performed by blending it with water solutions of polyethylene glycol (PEG), a plasticizer able to reduce PEO crystallinity promoting the ion conductivity [10]. All components were melted, composed, and compressed into films in a "one pot solution" avoiding solvents, thus following an environmentally sustainable approach. The SPEs were characterized by thermal, mechanical, and morphological analysis to evaluate their chemical-physical performance.

Experimental: Materials and methods

PEG1000 and PEG1550 by Fluka, polyethylene oxide (PEO) Mw 5.000.000, Sepiolite and Lithium triflate by Sigma Aldrich. Mixtures of PEG and sepiolite (SEP) were prepared by SEP water dispersion and subsequently adding 5% and 10 % w/w of PEG1000 and PEG1550, as detailed in Table 1. The suspension was washed, centrifuged, and dried thus obtaining organo-modified sepiolite (SEPmod). The raw physical blends of SEPmod, Polyethylenoxide (PEO) and Lithium triflate (LiTfr), obtained by their physical mixing, were melt blended, using a Brabender Plasti-Corder mixer kept at 140°C and 80 rpm of screw rate. The resulting SPEs were recovered, cooled at room temperature, roughly powdered, dried and compression molded at 130°C by using a table hydraulic hot-press. FTIR-ATR, DSC, TGA, SEM and tensile tests have been performed on samples. DSC analysis were carried out using a Mettler DSC/822 calorimeter at a nitrogen gas flow of 50 ml/min. Samples were firstly heated from 25 to 150 °C at 10 °C min⁻¹, then cooled up to -80 °C at a rate of 50 °C min⁻¹ and newly heated up 250 °C at 10 °C min⁻¹.

TGA analysis were performed using a thermogravimetric analyzer TGA/DTG Perkin-Elmer Pyris Diamond. The samples were heated from 25°C to 600°C at 10°C min⁻¹, under nitrogen at 30 mL/min. SEM analysis were carried out using a Quanta 200 FEG, 338 FEI scanning electron device. Prior to the observation, surfaces were coated with a homogeneous layer (18 ± 0.2 nm) of Au and Pd alloy. The micrographs were performed at room temperature and in high vacuum mode. Tensile tests were carried out by using a dynamometer model 4301, Instron equipped with a load cell of 1 kN. The tests were performed on dumbbell-shaped films. Young's modulus, stress and strain at break values were determined and reported data are the average values of six determinations. All the tests were carried out at room temperature and at a crosshead rate of 2mm/min.

Table 1 Film percentage composition and identification codes.

IC	Percentage composition (wt%)				
Sample	PEO	LiCF ₃ SO ₃	SEP	PEG1000	PEG1550
SPE_Li	91.5	8.5	-	-	-
SPE_0	87.5	8.13	4.36	-	-
SPE_1	87.5	8.13	4.15	-	0.21
SPE_2	87.5	8.13	4.15	0.21	-
SPE_3	87.5	8.13	3.96	-	0.40
SPE_4	87.5	8.13	3.96	0.40	-

Results and Discussion

The thermal parameters of the SPEs samples are showed in Table 2.

Table 2 Thermal parameters of SPE based films and neat polymers measured by DSC and TGA analysis. The values of crystallization and melting enthalpy in parentheses (ΔH) and the crystallinity (χ) are normalized with respect to the weight fraction of the polymer in the blend.

	DSC					TGA		Crystallinity
	$\Delta H_c [J/g]$ $\pm 2\%$	$T_{c,onset} [^{\circ}C]$ $\pm 2\%$	$T_c [^{\circ}C]$ $\pm 2\%$	$\Delta H_m [J/g]$ $\pm 1\%$	$T_m [^{\circ}C]$ $\pm 1\%$	$T_{onset} [^{\circ}C]$ $\pm 2\%$	$T_{peak} [^{\circ}C]$ $\pm 2\%$	$\chi_c (\%)$
PEO	146.9	-31.7	-40.6	121.8	66.4	366.7	400.2	59.4
SPE_0	118.2	-51.7	-64.0	117.4	62.4	391.9	419.7	65.4
SPE_1	117.4	-21.7	-36.4	118.4	61.3	388.7	419.0	66.0
SPE_2	140.7	-18.3	-30.5	133.5	60.5	383.8	421.3	74.4
SPE_3	119.2	-22.5	-33.8	136.1	61.2	386.	419.8	75.9
SPE_4	134.3	-20.8	-34.4	123.8	60.9	376.1	409.0	69.0

It is worthy to highlight that all the samples began to crystallize at very low temperatures. This result is due to the fast-cooling rate ($50^{\circ}C/min$), which decreases the crystallization process as the polymer chains, entangled in the melt, do not have enough time to separate enough to form crystals, so the amorphous nature of the melt is "frozen into" the solid. In the investigated system, all the samples reported in table 1, started to crystallize before than neat PEO and before SPE0 composite and show higher crystallinity percentage (χ_c). SPE2 systems crystallize before the other systems due to the balanced effects of nucleating effect and plasticizing action of PEG1000. No substantial differences have been detected among SPE1, SPE3, SPE4 samples, except for a slight decrease in T_c compared to SPE2, overall ΔH_c and an increase crystallinity. Neat PEO starts to crystallize at lower temperatures, as expected. The absence of PEG in SPE0 sample drastically decreased onset and peak crystallization temperatures. During the second heating run, except for PEO showing the highest melting temperature, all the samples evidenced similar T_m likely associated with the melting of quite regular crystalline pattern developed during the cooling from the melt.

TGA results are reported in table 1 as the onset of temperature degradation, (T_{onset}), taken as the temperature at which 5% weight loss (WL) of sample occurred, and the peak of DTG thermograms, corresponding to the temperature of maximum degradation rate of the polymer (T_{peak}). From the analysis of these data, it emerged that all samples degrade around $419^{\circ}C$, while at higher temperatures, around $470^{\circ}C$, lithium triflate begins to degrade.

In addition, all SPE based systems showed higher thermal stability than the neat polymer. The neat PEO thermal degradation process is ranged in a shorter space of time than other SPE based samples, as expected, since no reinforcing and stabilizing agents were included inside the polymer matrix. This experimental outcome suggests the formation of tight intermolecular entanglements between the components likely due to their physical compatibility leading to mutual stabilization except for SPE4 sample, strongly influenced by the prevailing effect of high concentrations of PEG1000, significantly affecting PEO thermal stability.

In Figure 1, morphological analysis (SEM) of SPE based films are reported. As for brevity of discussion, only SPE0, SPE1 and SPE2 micrographs have been investigated and discussed. SPE0 sample (Figure 1a), evidenced a quite uneven and highly structured polymer surface with a fine and homogenous distribution of discrete microdomains of rod-like sepiolite filler, visible as white dots on the polymer surface. Moreover, the morphology changed in presence of PEG plasticizers. In SPE1 sample (Figure 1b), a homogeneous, quite smoothed and continuous polymer surface can be observed with the very fine distribution of sepiolite particles between the polymer macromolecular chains. Low concentrations of the higher Mw PEG allow suitable polymer plasticization, improving the physical interactions among the polar residues and the ionic charges of all the components of the biocomposite.

As concerning SPE2 sample, a very different surface topography is found (Figure 1c). A continuous but coarsened polymer surface can be observed characterized by a good interfacial

adhesion between the polymer matrix and the plasticizer, as expected since PEO and PEG show the same polymer network but very different molecular weights. Profuse well dispersed and well embedded sepiolite particles occur confirming that the very close-fitting polymer-based network can deeply entrap these particles to the point of being disguised and no longer visible.

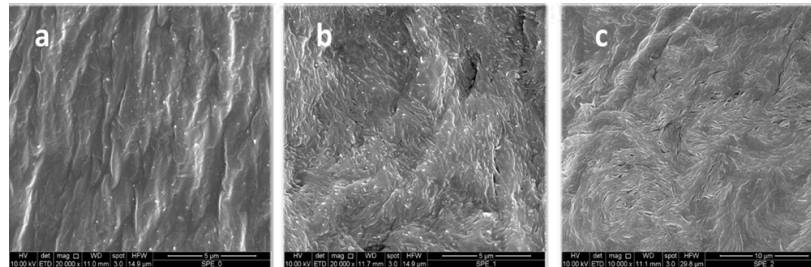


Figure 1 SEM micrographs of SPE0 (a), SPE1 (b) and SPE2 (c) surfaces.

The averaged values of elastic modulus (YM), stress at break (σ_b), strain at break (ϵ_b) are detailed in Table 3.

Table 3. Tensile test parameters for each adopted formulation

Sample	Thickness (mm)	Young Modulus (YM) [MPa]	Strain at Break (ϵ_b) [%]	Stress at Break (σ_b) [MPa]
SPE_Li	0.092	99.0±13.27	3.5±0.4	1.1±0.2
SPE_0	0.130	331.7 ± 30.0	4.5 ± 07	1.2 ± 0.1
SPE_1	0.145	305.6 ± 13.1	5.9 ± 2.6	1.1 ± 0.4
SPE_2	0.130	343.8 ± 10.8	4.8 ± 0.8	1.2 ± 0.2
SPE_3	0.148	397.9 ± 46.9	6.4 ± 1.5	0.8 ± 0.5
SPE_4	0.103	426.4 ± 65.3	3.8 ± 0.4	1.9 ± 0.1

The addition of lithium salt into the PEO matrix caused a general reduction of mechanical properties with respect to the other PEO based compositions including SEP. Indeed, from the analysis of the results, the system SPE0 evidenced the lowest YM. This finding is not surprising since the lack of inorganic filler is responsible for macromolecular chain mobility restriction and increasing stiffness and rigidity. In addition, also strain at the break of this system evidenced detrimental values. This last outcome could be due to the peculiar PEO Lithium salt interaction occurring between the polar ether groups of PEO and the positive charge of lithium hindering the regular flow of PEO macromolecular chains under tensile test. As concerning the other SPE based composites, the results indicate that usually, except for the SPE1 formulation, the addition of the plasticizer causes an increase in the tensile stiffness of the tested film. This effect is in line with the higher degree of crystallinity of the formulations found in DSC analysis. The crystallization behaviour of polymers the crystallinity, strongly influenced the macroscopic behaviour of polymers, such as the mechanical performances [11]. Both plasticizers induce an increase in this parameter with more marked effects in the case of PEG1000 compared to the PEG1550. This outcome is likely due to different behaviour induced by two PEG molecular weights. The most significant increase in stress for PEG 1000 samples is in line with the greater nucleating effect witnessed by Young's modulus values. Finally, about the strain undergone by the specimens, it seems that all the formulations are characterized by a value usually higher than that of the reference sample (SPE0) without plasticizers. In any case, for the system containing PEG1550, the strain at the peak of the curve seems to increase for a plasticizer content equal to 0.21% by weight and then decrease slightly for higher contents. The results indicate an exactly reversed trend for systems with PEG1000 as the content of this additive increases.

References

- [1] European Commission. Clean Sky Benefits.
- [2] Zhang, Y., Feng, W., Zhen, Y., Zhao, P., Wang, X, Effects of lithium salts on PEO-based solid polymer electrolytes and their all-solid-state lithium-ion batteries, *Ionics*, 28, (2022) 2751–2758. <https://doi.org/10.1007/s11581-022-04525-3>
- [3] Long, L., Wang, S., Xiao, M., Meng, Y. (2016). *J. Mater. Chem. A*, 4: 10038–10069. <https://doi.org/10.1039/C6TA02621D>
- [4] Christie, A.M., Lilley, S.J., Staunton, E. et al. *Nature* 433, (2005) 50. <https://doi.org/10.1038/nature03186>
- [5] Meyer, W.H. (1998). *Adv. Mater.* 10: 439–448. [https://doi.org/10.1002/\(SICI\)1521-4095\(199804\)10:6%3C439::AID-ADMA439%3E3.0.CO;2-I](https://doi.org/10.1002/(SICI)1521-4095(199804)10:6%3C439::AID-ADMA439%3E3.0.CO;2-I)
- [6] Zhu, Q., Ye, C., Mao, D. (2022). Solid-State Electrolytes for Lithium– Sulfur Batteries: Challenges, Progress, and Strategies, *Nanomaterials*, 12, 3612. <https://doi.org/10.3390/nano12203612>
- [7] Zhao, Q., Stalin, S., Zhao, C.Z., Archer, L. A. (2020). Designing solidstate electrolytes for safe, energy-dense batteries, *Nat. Rev. Mater.* 5, 229–252. <https://doi.org/10.1038/s41578-019-0165-5>
- [8] Han, L., Wang, J., Mu, X., Wu, T., Liao C., Wu, N., Xing, W., Song, L., Kan, Y., Hu, Y. (2021). Controllable magnetic field aligned sepiolite nanowires for high ionic conductivity and high safety PEO solid polymer electrolytes, *Journal of Colloid and Interface Science* 585, 596–604. <https://doi.org/10.1016/j.jcis.2020.10.039>
- [9] Wright, P.V. *Electrochim. Acta* 43: 1998 1137–1998 1143. [https://doi.org/10.1016/S0013-4686\(97\)10011-1](https://doi.org/10.1016/S0013-4686(97)10011-1)
- [10] Dhatarwal, P., Sengwa R. J. (2017). *Indian J. Pure Appl. Phys.*, 55, 7.
- [11] Kong, Y., Hay, J.N. (2002). The measurement of the crystallinity of polymer by DSC. *Polymer*, 43, 3873–3878. [https://doi.org/10.1016/S0032-3861\(02\)00235-5](https://doi.org/10.1016/S0032-3861(02)00235-5)

Virtual element method for damage modelling of two-dimensional metallic lattice materials

Marco Lo Cascio^{1,a,*}, Ivano Benedetti^{1,b} and Alberto Milazzo^{1,c}

¹Dipartimento di Ingegneria, Università degli Studi di Palermo, Viale delle Scienze, Ed. 8, Palermo, 90128, Italy

^amarco.locascio01@unipa.it, ^bivano.benedetti@unipa.it, ^calberto.milazzo@unipa.it

Keywords: Virtual Element Method, Metallic Lattice Materials, Damage

Abstract. Additively-manufactured metallic lattice materials are a class of architected solids that is becoming increasingly popular due to their unique cellular structure, which can be engineered to meet specific design requirements. Understanding and modelling the damage in these innovative materials is a significant challenge that must be addressed for their effective use in aerospace applications. The Virtual Element Method (VEM) is a numerical technique recently introduced as a generalisation of the FEM capable of handling meshes comprising an assemblage of generic polytopes. This advantage in creating domain discretisation has already been used to model the behaviour of materials with complex microstructures. This work employs a numerical framework based on a nonlinear VEM formulation combined with a continuum damage model to study the fracture behaviour of two-dimensional metallic lattice material under static loading. VEM's effectiveness in modelling lattice failure behaviour is assessed through several numerical tests. The influence of micro-architecture on the material's failure behaviour and macroscopic mechanical performance is discussed.

Introduction

The computational modelling of the behaviour of lattice materials is an active field of research aimed at complementing the experimental activity in the quest for a better understanding of the potential of these materials in engineering applications. The Virtual Element Method (VEM) [1] is a recent generalisation of the Finite Element Method (FEM) for the treatment of general polygonal/polyhedral mesh elements that has been already used for several problems in structural mechanics [2,3,4,5,6] applications.

Formulation

For the lowest-order VEM formulation herein adopted, for a general polygonal virtual element E , the element degrees of freedom are the values of the components of the displacement at each of its n vertex, collected into the vector \mathbf{u}_E . The displacements field is expressed as $\mathbf{u} = \mathbf{N}(x, y) \mathbf{u}_E$, where $\mathbf{N}(x, y)$ is the matrix containing the virtual shape functions $\mathbf{N}_v(x, y)$ associated with each vertex v . Shape functions are known only on the element edges of E , where they are globally continuous linear polynomials. An explicit expression for the strains is unavailable because the shape functions \mathbf{N}_v are not explicitly known within the polygonal element. An approximated constant strain field $\boldsymbol{\varepsilon}_\Pi$ is assumed within each element, which can be computed from the degrees of freedom \mathbf{u}_E as $\boldsymbol{\varepsilon}_\Pi = \boldsymbol{\Pi}_E \mathbf{u}_E$, where $\boldsymbol{\Pi}_E \in \mathbb{R}^{3 \times 2n}$ is the matrix representation of a projection operator defined as

$$\boldsymbol{\Pi}_E = \frac{1}{A_E} \sum_{v=1}^n \int_{e_v} \mathbf{N}_v^E \mathbf{N}(x, y) ds \quad (1)$$

where A_E is the area of the polygonal element E , bounded by its n edges e_v and \mathbf{N}_v^E is the matrix containing the components n_x and n_y of the outward unit normal vector over each edge. Since the

virtual shape functions \mathbf{N}_v on the element edges are known polynomials, the integrals appearing at the right-hand side of previous equation are exactly computable.

The tangent stiffness matrix \mathbf{K}_E for a general virtual element E is given by the sum of two terms. The first term, named the consistency term, is given by

$$\mathbf{K}_E^c = \mathbf{A}_E \mathbf{\Pi}_E^T \mathbf{C} \mathbf{\Pi}_E \quad (2)$$

where \mathbf{C} is the material tangent stiffness tensor in Voigt notation. \mathbf{K}_E^s is a stabilization term whose presence is motivated by the need to avoid zero-energy modes not associated with rigid body motions. The loss of material integrity is governed by the internal damage variable ω , $0 \leq \omega \leq 1$. The constitutive equations for an isotropic damage model is

$$\boldsymbol{\sigma} = (1 - \omega) \mathbf{C}^0 \boldsymbol{\varepsilon}_\Pi \quad (3)$$

where $\boldsymbol{\sigma}$ and $\boldsymbol{\varepsilon}_\Pi$ collect the Voigt components of the stress and strain respectively, and \mathbf{C}^0 is the elasticity matrix for the pristine elastic material. The evolution of damage is governed by the linear softening law

$$\omega(\kappa) = \frac{\kappa_f}{\kappa_f - \kappa_0} \left(-\frac{\kappa_0}{\kappa} \right) \quad (4)$$

and loading-unloading conditions

$$f(\boldsymbol{\varepsilon}, \kappa) = \varepsilon_{eq}(\boldsymbol{\varepsilon}) - \kappa \leq 0, \quad \dot{\kappa} \geq 0, \quad f(\boldsymbol{\varepsilon}, \kappa) \dot{\kappa} = 0 \quad (5)$$

in which f is the damage loading function, ε_{eq} is the modified Von Mises equivalent strain [8], and κ is an internal variable that corresponds to the maximum level of equivalent strain ever reached in the previous history of the material. The stress at a generic point \mathbf{x} and at a generic loading increment λ is given by $\boldsymbol{\sigma} = \boldsymbol{\sigma}(\lambda, \mathbf{x}, \boldsymbol{\varepsilon}_\Pi, \mathcal{H})$, where \mathcal{H} contains the history variables of the damage model. The tangent material stiffness matrix \mathbf{C} at a certain time t is consistently computed from the constitutive law as

$$\mathbf{C}(t, \mathbf{x}, \boldsymbol{\varepsilon}_\Pi, \mathcal{H}) = \frac{\partial \boldsymbol{\sigma}}{\partial \boldsymbol{\varepsilon}_\Pi} \quad (6)$$

To avoid damage localisation and mesh dependency of the solution, an integral-type nonlocal damage model has been employed. The adopted weight function is the truncated quadratic polynomial function [4].

Numerical Tests

The specimen design used for the following numerical tests is based on the Extended Compact Tension, EC(T), specimen, shown in Fig. 1(a). The EC(T) has been developed for fatigue and fracture testing of solid (dense) materials but has been adapted and used for characterizing lattice structures. The rectangular specimen consists of repeated unit cells of side length l . Each specimen is eleven unit cells wide (W), forty unit cells high (H), and two unit cells thick (t). Only half of the EC(T) specimens were modelled by applying appropriate symmetry boundary conditions as shown in Fig. 1(b). The unit cell of the lattice structure studied in this work is shown in Fig. 2(a) and is based on a two-dimensional representation of a body-centred cubic (GBCC) unit cell (Fig. 1(b)). Each unit cell has external dimensions of $l \times l$, with $l = 3.5$ mm. Each lattice unit cell is discretised with 176 polygonal virtual elements (Fig. 2(c)), and the numerical model has 157882 degrees of freedom. Simulations are carried out under displacement control and plane-strain

assumption. The material selected as the constituent material is an additive manufactured Ti-6Al-4V alloy whose mechanical and damage properties are [7]: Young's Modulus $E = 123$ GPa, Poisson's ratio $\nu = 0.3$, yield strength $\sigma_y = 932$ MPa and fracture strain $\kappa_f = 0.1105$. The interaction radius has been set to $R = 2$ mm. Two different unit cell configurations have been analysed, with truss diameter $d = 0.5$ mm and $d = 0.75$ mm. For each configuration, numerical tests have been performed with crack length $a = 2l$ and $a = 3l$.

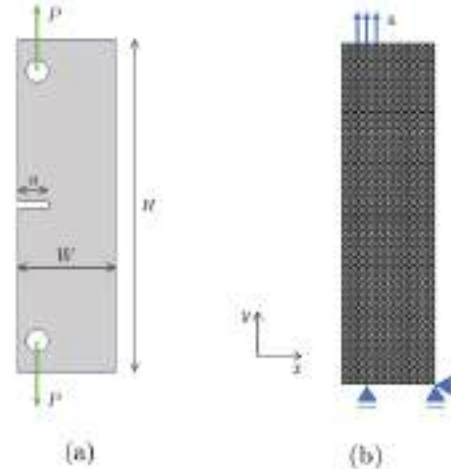


Figure 1: (a) Extended Compact Tension, EC(T), specimen; (b) computational model.

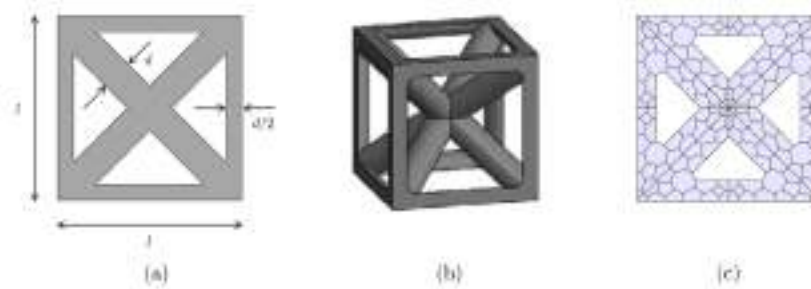


Figure 2: (a) 2D representation of the GBCC unit cell geometry; (b) actual 3D geometry.

Conclusions

A nonlinear VEM formulation combined with a continuum damage model has been employed to model the fracture behaviour of two-dimensional metallic lattice material under static loading. VEM's effectiveness in modelling complex morphologies such as lattice structures has been verified. The load as a function of the load-line displacement remains relatively linear for most specimens until close to reaching the critical load and a reduction of the critical load with initial crack extension can be observed for both unit cell configuration.

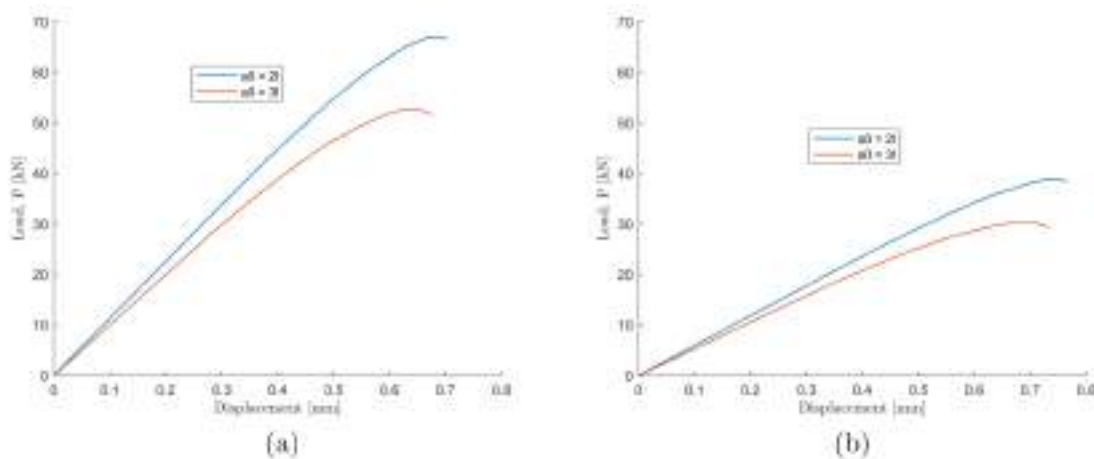


Figure 3: Load-displacement responses of the (a) 0.75 mm and (b) 0.50 mm uniform diameter EC(T) specimens showing the applied load as a function of load-line displacement for different initial crack lengths.

Acknowledgments

The authors would like to acknowledge the support from Azione 1.2.1.03 – Specializzazione tecnologica territori – Accordo di Programma tra MIUR e Regione Siciliana - Codice Progetto PONPE03_00206_1 – “Advanced framework for Manufacturing Engineering and product Lifecycle Enhancement ” - Acronimo “AMELIE” CUP G76I20000060007.

References

- [1] Beirão da Veiga, L., Brezzi, F., Cangiani, A., Manzini, G., Marini, L. D., Russo, A., Basic principles of virtual element methods, *Mathematical Models and Methods in Applied Sciences* 23(01) (2013) 199-214. <https://doi.org/10.1142/S0218202512500492>
- [2] Wriggers, P., Reddy, B. D., Rust, W., & Hudobivnik, B., Efficient virtual element formulations for compressible and incompressible finite deformations, *Computational Mechanics*, 60 (2017) 253-268. <https://doi.org/10.1007/s00466-017-1405-4>
- [3] M. Lo Cascio, Marco, A. Milazzo, I. Benedetti, Virtual element method for computational homogenization of composite and heterogeneous materials. *Composite Structures* 232 (2020) 111523. <https://doi.org/10.1016/j.compstruct.2019.111523>
- [4] M. Lo Cascio, Marco, A. Milazzo, I. Benedetti, A hybrid virtual-boundary element formulation for heterogeneous materials, *International Journal of Mechanical Sciences* 199 (2021) 106404. <https://doi.org/10.1016/j.ijmecsci.2021.106404>
- [5] M. Lo Cascio, I. Benedetti, Coupling BEM and VEM for the Analysis of Composite Materials with Damage, *Journal of Multiscale Modelling* 13.01 (2022) 2144001. <https://doi.org/10.1142/S1756973721440017>
- [6] M. Lo Cascio, Marco, A. Milazzo, I. Benedetti, Virtual element method: Micro-mechanics applications. In *Key Engineering Materials* 827 (2020) 128-133, Trans Tech Publications Ltd. <https://doi.org/10.4028/www.scientific.net/KEM.827.128>
- [7] L. Dong, V. Deshpande, H. Wadley, Mechanical response of Ti-6Al-4V octet-truss lattice structures, *International Journal of Solids and Structures* 60 (2015) 107-124.
- [8] J. H. P. De Vree, W.A.M. Brekelmans, M.A.J. van Gils, Comparison of nonlocal approaches in continuum damage mechanics, *Computers and Structures* 55.4 (1995) 581-588.

A meso-scale model of progressive damage and failure in LSI-produced ceramic matrix composites for aerospace applications

A. Airolidi^{1,a,*}, M. Riva^{1,b}, E. Novembre^{1,c}, A.M. Caporale^{1,d}, G. Sala^{1,e},
M. De Stefano Fumo^{2,f} and L. Cavalli^{3,g}

¹Dept. of Aerospace Science and Technology, Politecnico di Milano, Via La Masa 34, 20156, Milano, Italy

²CIRA, Italian Aerospace Research Centre, Via Maiorise, 81043 Capua (CE), Italy

³Petroceramics S.p.A., Viale Europa, 2, 24040 Stezzano (BG), Italy

^aalessandro.airolidi@polimi.it, ^bmarco.riva@polimi.it, ^cedoardo.novembre@polimi.it,

^dantoniomaria.caporale@polimi.it, ^egiuseppe.sala@polimi.it, ^fm.destefano@cira.it,

^gcavalli@petroceramics.com

Keywords: Ceramic Matrix Composites, Continuum Damage Mechanics, Binary Models, Stochastic Properties

Abstract. The paper is focused on the development of a modelling approach for Ceramic Matrix Composites (CMC) laminates, produced through a cost-affordable Liquid Silicon Infiltration (LSI) technique. The objective is the development of a tool capable of evaluating the design values for the material in the presence of technological defects and complex geometrical features, which could be used at the level of structural elements of details of reusable space vehicles. The model exploits a bi-phasic decomposition to capture four important aspect of the material: the non-linear behaviour occurring when load is not applied in the fibre direction, the significant bending to tensile strength ratio, the role of matrix fractures in the failure process and the role of delamination phenomena in the response. The correlation with tensile and bending tests performed with different lay-ups indicates that the developed approach can fulfil such objectives and may be used in the definition of structural details and of damage tolerance of innovative space vehicles.

Introduction

Ceramic Matrix Composites represent one of the most promising solutions for the development of structures capable of performing structural roles at temperatures beyond 1000 °C, such as the ones occurring in re-entry or single-stage-to-orbit vehicles in space missions, or in hypersonic vehicles and in propulsive systems in the aerospace field [1].

The increasing demand for truly reusable space and hypersonic transport systems introduces significant issues regarding the structural integrity and the damage tolerance of such hot structures. The material cost is another critical aspect for the development of the next generation of space vehicles. The LSI technique, can significantly reduce the cost of the CMC production, with respect to more traditional techniques, like chemical vapour infiltration or polymer infiltration and pyrolysis [2], but the porosity levels and the possible occurrence of technological defects can increase, thus emphasizing the need for controlling damage development in the material [4].

The activity presented in this paper was performed within the project AM³aC²A, funded by the Italian Space Agency (ASI), aimed at developing develop multi-scale approaches for the structural integrity of CMC in reusable aerospace components. The objective was the formulation of a non-linear numerical approach to be used in models of CMC laminates at the level of structural details or element, with a ply-wise (meso-scale) approach. The prediction of the structural response in the presence of geometrical features such as holes, cutouts, highly curved parts, and macro-porosity is one of the final goal of model, which in this paper is proved capable to idealize the most important



failure mechanisms and to capture the quantitative response of multi-directional CMC laminates in tension and bending, thus providing a proof of its potential.

Experimental characterization

A test campaign was conducted with the aim of obtaining the basic properties of the orthotropic C/SiC fabric plies produced through the LSI technique and, at the same time, of providing validation experiments for the model to be developed. Figure 1-A reports the stress vs. strain responses recorded in four types of quasi-static tensile tests on laminates with lamination sequence of $[0]_{20}$ ("T0"), $[45/-45]_{10s}$ ("T45"), $[30/-30]_{10s}$ ("T30"), and $[0/45/90/-45]_{5s}$ ("TQI").

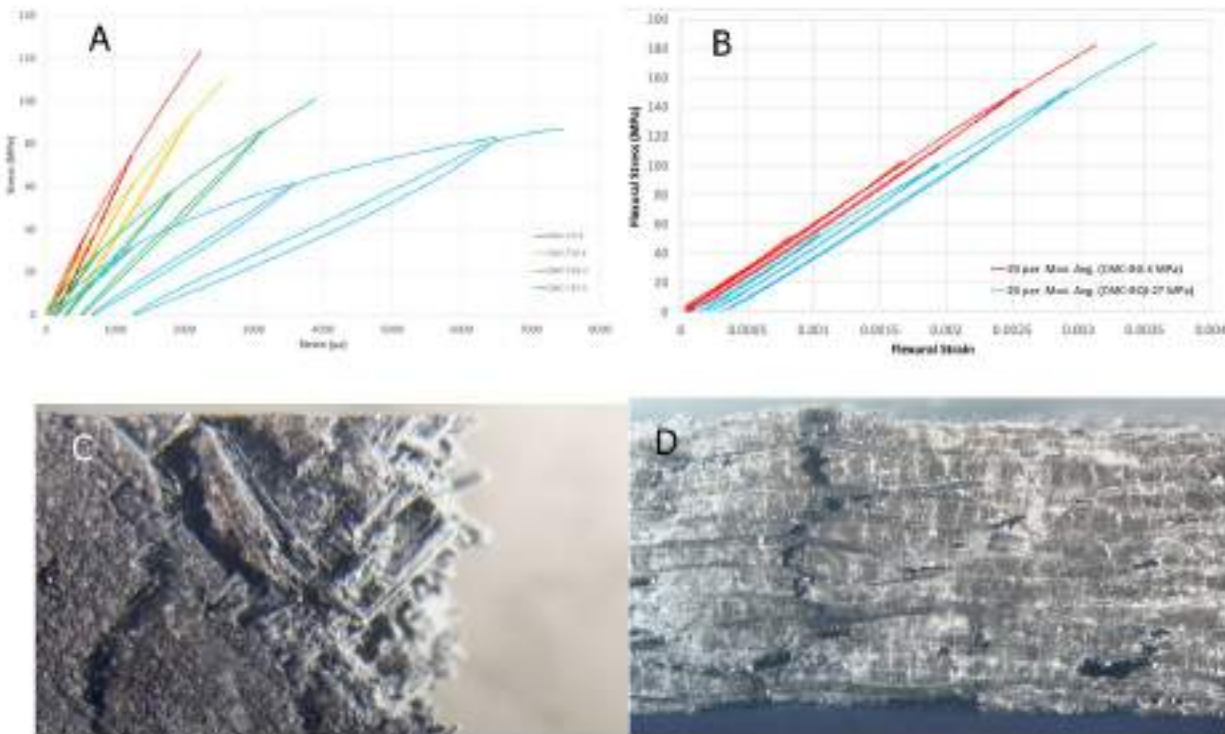


Fig. 1 – Response of tensile (A) and bending (B) test on CMC laminates, failure modes in "T45"(C) and "B0" tests (D)

The standard ASTM C1275-15 was taken as a guideline to design the specimens and perform the tests. All the specimens were dog-bone shaped, with (a total length of 200 mm, a gauge length of 45 mm, and an average thickness of 4.2 mm. All the tensile specimens were equipped with glass-fiber reinforced epoxy tabs to mitigate the risk of failures out of the grip. The stress vs. strain response reported in Fig. 1-B were obtained in two three-point bending tests performed on $[0]_{20}$ laminates ("B0") and $[0/45/90/-45]_{5s}$ laminates ("BQI").

The response in the tensile tests was characterized by increasing non-linear behavior and ultimate strain at failure, as the percentage of fibers not aligned with the load application direction is increased. The maximum stress carried by the external plies of the laminate B0 was significantly higher than the value recorded in the tensile "T0" stress. The failure mode in "T45" specimens indicated a diffused damage state in the matrix, as shown in Fig. 1-C, while the failure in "B0" test was characterized by a neat fracture in the 90°-oriented fiber yarns, while the 0°-oriented fibers do not show a clear fracture line (Fig. 1-D).

Overview of the numerical approach

The numerical approach adopted moved from the technique developed in [3,4] for polymer matrix composites. The CMC homogenized material model was decomposed into two idealized phases: fiber and matrix. The fiber were modelled through a layer of membrane element, which carried

stress only in the fabric reinforcement directions, while the matrix was represented by solid elements. In general, the technique makes possible the representation of delamination without the use of zero-thickness cohesive elements, the development of different constitutive laws for matrix- and fiber-dominated responses, the representation of the interactions between matrix damage inside the plies and the delamination phenomena. The in-plane damage in the matrix was modelled by using a single scalar damage variable, as represented in Eq. 1. Such variable evolved with the distance from a threshold damage function, shaped as a Tsai-Wu criterion, expressed in Eq. 2. For the sake of brevity, the aspects related to the integration of delamination damage in the modelling technique are not reported (see [3,4] for further details).

$$\begin{bmatrix} \varepsilon_{11}^m \\ \varepsilon_{22}^m \\ \gamma_{12}^m \end{bmatrix} = \begin{pmatrix} \frac{1}{(1-d_m)E_{11}^m} & \frac{\nu_{21}^m}{E_{22}^m} & 0 \\ \frac{\nu_{12}^m}{E_{11}^m} & \frac{1}{(1-d_m)E_{22}^m} & 0 \\ 0 & 0 & \frac{1}{(1-d_m)G_{12}^m} \end{pmatrix} \begin{bmatrix} \sigma_{11}^m \\ \sigma_{22}^m \\ \tau_{12}^m \end{bmatrix} \quad (1)$$

$$f(\tilde{\sigma}^m) = \sqrt{F_1 \tilde{\sigma}_{11}^m + F_2 \tilde{\sigma}_{22}^m + F_{11} (\tilde{\sigma}_{11}^m)^2 + F_{22} (\tilde{\sigma}_{22}^m)^2 + 2F_{12} \tilde{\sigma}_{11}^m \tilde{\sigma}_{22}^m + F_{66} (\tilde{\tau}_{12}^m)^2} \quad (2)$$

Results and Conclusions

A couple of iso-damage surfaces are shown in black and red colors in Fig. 3-A. Figures 3-B and C present the finite element models of the tensile and bending tests, respectively. The need of modelling the influence of matrix damage on the failure led to calibrate a new surface for the peak stress carried by the matrix phase (in green in Fig. 3-B), beyond which an exponentially decaying strain softening regime was modelled. Such second surface and the limit stress carried by the fiber phase were not fixed in the models, but were statistically distributed in the elements of the models. The parameters of such distribution have been identified through a Monte-Carlo approach, considering the correlation with the ultimate strength in all the tests as main performance index.

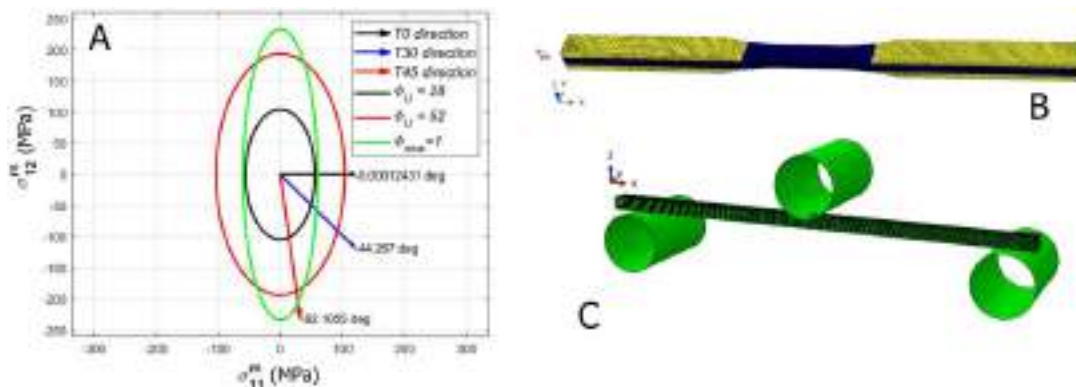


Fig. 3 – Tsai-Wu shaped surface for matrix damage evolution (A) and FE models of tensile (B) and bending (C) tests

The bi-phasic nature of the approach, the choice and the calibration of the damage evolution laws, the statistical distribution of the ultimate strength of the idealized phases led to obtain the results presented in Fig. 4, which indicate the all the quantitative and qualitative aspects of the responses are captured. In particular both the ultimate tensile strength in the “T0” test (Fig. 4-A) and the force vs. displacement response in the bending “B0” tests is obtained, thus indicating that the statistical distribution of properties can represent the bending/tensile strength ratio (Fig 4_D). Moreover, the localization of fracture can be represented, as shown in Fig. 4-E. For such localization, the integration of delamination damage in the analyses was found to play a fundamental role. Hence. the modelling approach was able of representing, without meshes at the

sub-ply or microscopic levels, the fundamental quantitative and qualitative aspects of non-linear response and failure of the CMC material.

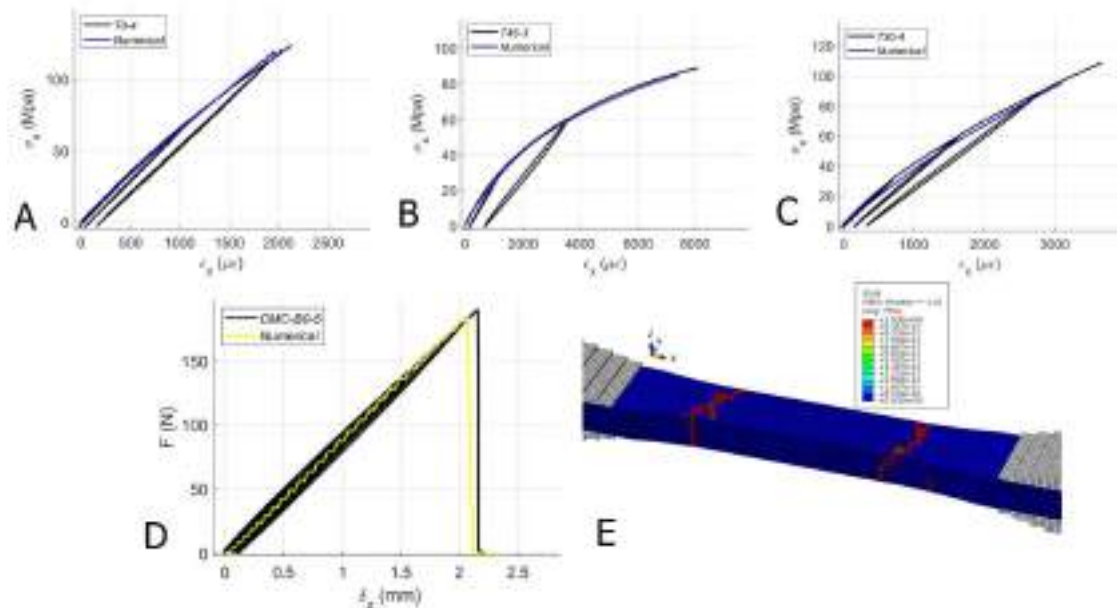


Fig. 4 – Numerical-experimental correlation in test “T0” (A), “T45” (B), “T30” (C), “B0” (D), and numerical failure mode (fiber damage) in “T30” analysis

Acknowledgements

The activities were funded by the Italian Space Agency (ASI), within the AM³aC²A project

References

- [1] H. Hald, Operational limits for reusable space transportation systems due to physical boundaries of C/SiC materials. *Aerospace Science and Technology* 7(2003) 551–9, [https://doi.org/10.1016/S1270-9638\(03\)00054-3](https://doi.org/10.1016/S1270-9638(03)00054-3)
- [2] W. Krenkel, F. Berndt, C/C–SiC composites for space applications and advanced friction systems, *Materials Science and Engineering: A* 412 (2005) 177–81. <https://doi.org/10.1016/j.msea.2005.08.204>
- [3] A. Airoidi, C. Mirani, L. Principito, A bi-phasic modelling approach for interlaminar and intralaminar damage in the matrix of composite laminates, *Composite Structures*, 234 (2020), 111747. <https://doi.org/10.1016/j.compstruct.2019.111747>
- [4] A. Airoidi, E. Novembre, C. Mirani, G. Gianotti, R. Passoni, C. Cantoni, A model for damage and failure of carbon-carbon composites: development and identification through Gaussian process regression, *Materials Today Communication*, 35 (2023) 106059. <https://doi.org/10.1016/j.mtcomm.2023.106059>

A peridynamics elastoplastic model with isotropic and kinematic hardening for static problems

Mirco Zaccariotto^{1,a,*}, Atefeh Pirzadeh^{1,b}, Federico Dalla Barba^{1,c},
Lorenzo Sanavia^{2,d}, Florin Bobaru^{3,e} and Ugo Galvanetto^{1,f}

¹ Dep. of Industrial Engineering, University of Padova, Padova, Italy

² Dep. of Civil, Environmental and Architectural Eng., University of Padova, Padova, Italy

³ Dep. of Mechanical and Materials Eng., University of Nebraska-Lincoln, Lincoln, USA

^amirco.zaccariotto@unipd.it, ^batefeh.pirzadeh@phd.unipd.it, ^cfederico.dallabarba@unipd.it,

^dlorenzo.sanavia@unipd.it, ^efbobaru2@unl.edu, ^fugo.galvanetto@unipd.it

Keywords: Ordinary State-Based Peridynamics, Elastoplastic Materials, Isotropic Hardening, Kinematic Hardening

Abstract. This study proposes a formulation equivalent to J2 plasticity with the associated flow rule to simulate the elastoplastic behavior of materials with isotropic or kinematic hardening in a peridynamic framework. The capabilities of the developed formulation are analysed through 2D and 3D case studies whose results (displacement and stress field) are compared with those obtained from the corresponding FEM models.

Introduction

The evaluation of the structural residual life of aerospace structures requires the ability to predict damage propagation. In recent years, Peridynamics (PD) [1], a new non-local continuum theory, attracted the attention of many researchers for its capability to simulate crack initiation, propagation and interaction. The theory has been widely used to model crack propagation in brittle materials, while the analysis of elastoplastic materials [2] has been mainly limited to the perfectly elastoplastic behavior [3,4]. Unfortunately, in the case of metals, experimental observations reveal a complex plastic behavior, which requires models with isotropic and kinematic hardening [2]. A PD constitutive model for 2D elastoplasticity with isotropic hardening is presented in [6] and extended to the 3D case in [7]. In this paper, an elastoplastic formulation equivalent to J2 plasticity is presented with which it is possible to simulate the elastoplastic behavior in the case of both isotropic and kinematic hardening.

Formulation

The PD equation of motion, for the static case, is [1]:

$$\int_{\mathcal{H}} (\underline{T}[\mathbf{x}](\mathbf{x}' - \mathbf{x}) - \underline{T}[\mathbf{x}'](\mathbf{x} - \mathbf{x}')) dV_{\mathbf{x}'} + \mathbf{b}(\mathbf{x}) = 0 \quad (1)$$

where $\mathbf{b}(\mathbf{x})$ is the body force on the material point \mathbf{x} , $\underline{T}[\mathbf{x}]$ is the force state on the material point \mathbf{x} corresponding to the bond vector $\mathbf{x}' - \mathbf{x}$ and \mathcal{H} represents the neighborhood of \mathbf{x} whose radius δ is the *horizon*, see Fig.1. The force vector state is a vector of modulus \underline{t} (the scalar force state) and direction coincident with the deformed configuration of the bond (ordinary state-based PD).



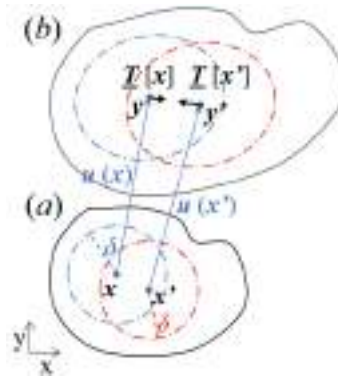


Figure 1: Positions of two interacting material points \mathbf{x} and \mathbf{x}' ; (a) initial and (b) deformed configuration.

The extension of a bond (a scalar quantity) is $\underline{e} = \underline{y} - \underline{x}$, where $\underline{y} = |\mathbf{y}' - \mathbf{y}|$ and $\underline{x} = |\mathbf{x}' - \mathbf{x}|$. \mathbf{x} is the position of the material point in the initial configuration while \mathbf{x}' denotes the generic point belonging to the neighborhood of \mathbf{x} . While \mathbf{y} and \mathbf{y}' are, respectively, the positions of \mathbf{x} and \mathbf{x}' in the deformed configuration.

In order to study problems involving elastoplastic behavior, it is necessary to distinguish between the isotropic and deviatoric component of the bond extension and of the scalar force state [1]. The extension of a bond is the sum of two components [1]: the isotropic and the deviatoric. Therefore, $\underline{e} = \underline{e}^{iso} + \underline{e}^d$, similarly for the scalar force state we have: $\underline{t} = \underline{t}^{iso} + \underline{t}^d$. In [3,4] it is emphasized that \underline{t}^{iso} does not depend on \underline{e}^d and the extension component \underline{e}^{iso} is only elastic. Whereas \underline{e}^d is itself the sum of two components, elastic and plastic respectively $\underline{e}^d = \underline{e}^{de} + \underline{e}^{dp}$. Finally, the deviatoric component of the scalar force state, in the case of materials with elastoplastic behavior, results in the 3D case, [4]:

$$\underline{t}^d = -5\mu\theta \frac{\omega \underline{x}}{m} + \frac{15\mu}{m} \underline{\omega}(\underline{e} - \underline{e}^{dp}) \quad (3)$$

Where μ is the shear modulus, θ is the dilatation, m is the weighted volume and $\underline{\omega}$ is the influence function (see [1,4] for further details).

Furthermore, on the basis of classical plasticity theory, the load-unload conditions in the Kuhn-Tucker form and the consistency condition [2] must be fulfilled when solving elastoplastic problems. In the case of the peridynamic formulation [3] these conditions become:

$$\begin{cases} \lambda \geq 0, f(\underline{t}^d) \leq 0, \lambda f(\underline{t}^d) = 0 \\ \lambda \dot{f}(\underline{t}^d) = 0 \end{cases} \quad (4)$$

where f is the yield function and λ is the continuum consistency parameter; while the plastic flow rule is [3]:

$$\dot{\underline{e}}^{dp} = \lambda \nabla^d \psi(\underline{t}^d) \quad (5)$$

in which $\nabla^d \psi(\underline{t}^d)$ is the constrained Fréchet derivative of $\psi(\underline{t}^d)$ defined hereafter.

In [3,4] based on the formulation introduced in [1] the following equation for the yield function for materials with perfectly plastic behavior is proposed:

$$f(\underline{t}^d) = \psi(\underline{t}^d) - \psi_0 = \frac{\|\underline{t}^d\|^2}{2} - \psi_0 \quad (6)$$

where $\|\underline{t}^d\|^2 = \int_{\mathcal{H}} (\underline{t}^d)^2 dV_{x'}$ and $\psi_0 = 25\sigma_Y^2/8\pi\delta^5$ in which σ_Y is the material's yield stress. Eq.6 is equivalent to the yield function $f = \sigma_{VM} - \sigma_Y$ used in classical mechanics [2] where σ_{VM} is the von Mises stress.

The proposed formulation to study the behavior of materials with isotropic and kinematic hardening, was inspired by the corresponding yield function used in classical mechanics [2]

$$f = |\sigma_{VM} - q| - (\sigma_Y + K\alpha) \quad (7)$$

In this equation, K is the isotropic hardening modulus, q is the back stress resulting from the kinematic hardening, and α is the internal hardening variable. q and α , initially zero, vary according to the following equations [2]:

$$\dot{q} = \dot{\varepsilon}_p H \quad \text{and} \quad \dot{\alpha} = \text{sign}(\sigma_{VM} - q) \dot{\varepsilon}_p \quad (8)$$

Where H is the kinematic hardening modulus and ε_p is the equivalent plastic strain. Rewriting Eq. 7 in the context of the peridynamic formulation (for details see [5]) one obtains an equation analogous to Eq.6 in which, however, ψ_0 is no longer a constant and depends on the load increment at the material point considered. Therefore ψ_0 becomes:

$$\psi_0(\mathbf{x}, t) = \frac{25[\sigma_Y + K\alpha + \text{sign}(\sigma_{VM} - q)q]^2}{8\pi\delta^5} \quad (9)$$

In Eq.9, q and α are found using Eq.8 in which the equivalent plastic strain should be replaced with the corresponding quantity expressed in the peridynamic formulation, which is a function of the deviatoric plastic extension [6,7]. It is worth noting that Eq.9 is obtained by considering small displacements.

The numerical implementation strategy of the proposed formulation involves discretizing the domain with a uniform grid of nodes. Then the non-linear static problem is solved using an incremental approach. Therefore, an iterative procedure using a return mapping algorithm was implemented for the determination of the deviatoric plastic extension and the various dependent quantities [5].

Numerical examples

In the following examples $E=200$ (GPa), $\nu=0.3$, $\rho=8000$ (kg/m³) and $\sigma_{Y0}=600$ (MPa). The isotropic hardening modulus is $K=20$ (GPa), and the kinematic hardening modulus is $H=20$ (GPa). All cases were studied using the proposed PD formulation and classical FE simulations.

The first case is a thin plate with a central hole (Fig.2a) in plane stress conditions, subjected to an imposed displacement (Fig.2b) applied in increments of 0.0125 (mm).

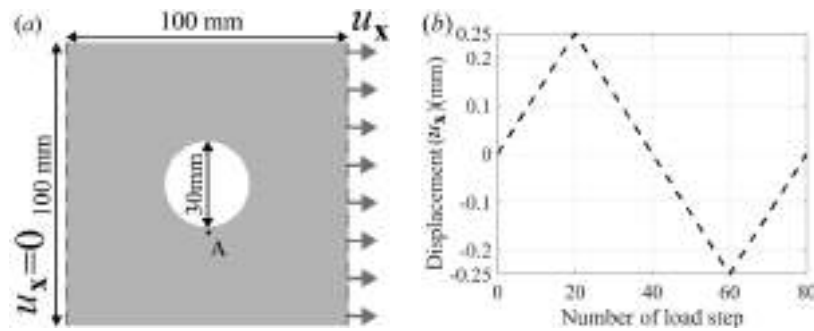


Figure 2: (a) Geometry and boundary conditions; (b) displacement loading in the x direction.

In Fig. 3, the displacements in the x -direction calculated by PD and FE at the 20th load step ($u_x = 0.25$ mm) are compared. Good agreement can be observed between the results obtained from the two models.

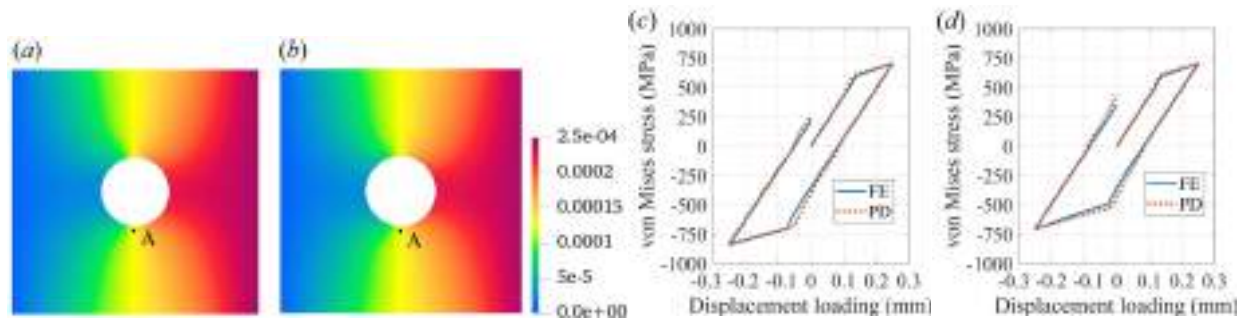


Figure 3: Displacement (m) in the x direction solved by: (a) FE, (b) PD. von Mises stress at point A vs loading displacement, (c) isotropic hardening case; (d) kinematic hardening case.

Fig.3c-d compares the von Mises stress at point A (Fig.2a) for the entire load history for both the isotropic (Fig.3c) and kinematic (Fig.3d) hardening cases. Point A is located in the region of the body where plastic deformation develops. The agreement between the PD and FE results is good: in particular, the PD model correctly estimates the maximum expected stress values obtained with the FE model. Note that in Fig.3c-d positive von Mises stresses are associated with a tensile load and negative von Mises stresses with a compressive load.

The second example studies a 3D structure whose dimensions, load and constraint conditions are shown in Fig.4. The material behavior is elastoplastic with isotropic hardening. The load cycle (imposed displacement) is similar to that shown in Fig.2b with a maximum displacement value of 0.35 (mm). Fig.4 compares the results obtained with the PD and FE models in terms of both displacement (u_y component) and von Mises stress in the xy plane containing the longitudinal axis of the specimen at the 20th load increment (at which the maximum displacement is applied). Good agreement is observed between the PD and FEM results despite the fact that no strategies were adopted to mitigate the surface effect in the PD model.

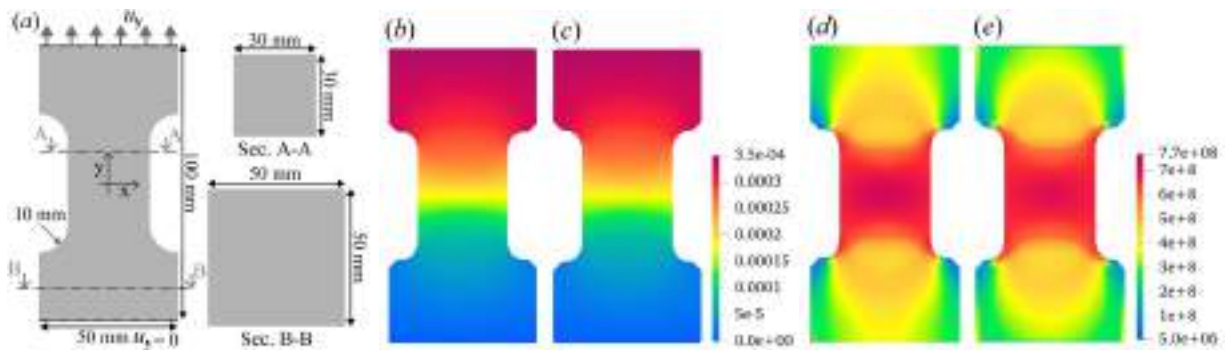


Figure 4: 3D example, (a) main dimensions. Displacement (m) in the y direction on plane xy computed by: (b) FE, (c) PD ($u_y = 3.5 \cdot 10^{-4}$ m). Distribution of von Mises stress (Pa) on plane xy obtained by: (d) FE, (e) PD ($u_y = 3.5 \cdot 10^{-4}$ m).

Conclusions

This study presents an extension of the elastoplastic model in Peridynamics capable of describing isotropic and kinematic hardening behavior. The proposed formulation is equivalent to J2 plasticity with associated flow rule. 2D and 3D cases were studied, and the comparison between the results of the PD models and the corresponding FE models highlighted the capabilities of the developed approach, which represents the necessary first step for the simulation of ductile fracture in a peridynamic framework.

Acknowledgements

U. Galvanetto and M. Zaccariotto would like to acknowledge the support they received from University of Padua under the research project BIRD2020 NR202824/20.

References

- [1] S.A. Silling, M. Epton, O. Weckner, J. Xu, E. Askari, Peridynamic states and constitutive modeling, *J. Elasticity* 88 (2007) 151-184. <https://doi.org/10.1007/s10659-007-9125-1>
- [2] Simo, J.C., Hughes, T.J.R., *Computational inelasticity*. volume 7. Springer-Verlag, New York, 1998. <https://doi.org/10.1007/b98904>
- [3] Mitchell, J.A., A nonlocal, ordinary, state-based plasticity model for peridynamics, Technical Report. Sandia National Laboratories, Albuquerque, NM, and Livermore, CA, (2011).
- [4] Mousavi, F., Jafarzadeh, S., Bobaru, F., An ordinary state-based peridynamic elastoplastic 2D model consistent with J2 plasticity. *Int. J. of Solids and Structures* 229 (2021). <https://doi.org/10.1016/j.ijsolstr.2021.111146>
- [5] A. Pirzadeh, F. Dalla Barba, F. Bobaru, L. Sanavia, M. Zaccariotto, U. Galvanetto, Elastoplastic Peridynamic formulation for materials with isotropic and kinematic hardening, submitted for publication (2023).
- [6] Madenci, E., Oterkus, S., Ordinary state-based peridynamics for plastic deformation according to von mises yield criteria with isotropic hardening. *J. of the Mech. and Ph. of Solids* 86 (2016) 192–219. <https://doi.org/10.1016/j.jmps.2015.09.016>
- [7] Liu, Z., Bie, Y., Cui, Z., Cui, X., Ordinary state-based peridynamics for nonlinear hardening plastic materials' deformation and its fracture process. *Eng. Fract. Mech.* 223 (2020). <https://doi.org/10.1016/j.engfracmech.2019.106782>

Structural batteries challenges for emerging technologies in aviation

Gennaro Di Mauro^{1,a}, Michele Guida^{1,b,*}, Gerardo Olivares^{2,c},
Luis Manuel Gomez^{2,d}

¹Department of Industrial Engineering, Università degli Studi di Napoli Federico II

²National Institute for Aviation Research (NIAR), Wichita State University, Kansas, USA

^agennaro.dimauro@unina.it, ^bmichele.guida@unina.it; ^cgerardo.olivares@wichita.edu,

^dluismanuel@niar.wichita.edu

Keywords: Structural Batteries, Multifunctional Materials, Airworthiness Requirements, Certification by Analysis

Abstract. In a global context where modern societies need to move towards greater environmental sustainability, ambitious targets to limit pollutant emissions and combat climate change have been set out. Concerning the aviation sector, research centers and industries are carrying out new aircraft designs with increased use of electrical energy onboard aircraft both for non-propulsive and propulsive purposes, leading to the concepts of More Electric Aircraft (MEA), Hybrid Electric Aircraft (HEA) and All-Electric Aircraft (AEA). Despite the expected flight emissions reduction, new potential air transportation missions, safer flights, and enhanced design flexibility, there are some drawbacks hindering the trend to HEA solutions, strictly bounded to the limited performance of traditional battery systems. The reference is to low energy and power densities, which impact on aircraft weight and flight performances. A new technology, namely structural battery, combining energy storage and load-bearing capacity in multifunctional material structures, is now under investigation since capable to mitigate or even eliminate barriers to the electrification of air transport sector. Although, the deployment of this technology raises relevant questions regarding airworthiness requirements, which need to be applied when considering such multifunctional materials. The purpose of the presented activity is to take a step towards the definition of aircraft certification requirements when dealing with structural batteries, considering them both as a structure and as a battery, to maintain unchanged or even improve the level of safety in all normal and emergency conditions.

Introduction

Aviation is a continuously growing sector that has seen an increase of 6% per year in passengers and goods transported since 1950 and it is estimated that this number will increase by a further 44% by 2050 [1]. The need for reduce the environmental impact of the sector with the help of eco-friendly initiatives, to achieve the objectives, set by the Paris agreements, which provide for the reduction of total CO₂ emissions. The importance of such a change is evident considering the eventuality of continuing to use fossil fuels as a source of power, there would be a 17% increase in CO₂ compared to the current situation. Instead, in a different scenario, in which the electric alternative was able to acquire a greater application space, a 45% reduction in CO₂ would be achieved compared to the levels present in 2005. Among the solutions identified aimed at reducing the environmental impact of aviation the hybrid electric, electric and solar energy aircraft are applied, [2], there are already certified aircraft projects and others are in the experimental stage, and it is interesting how these projects exclusively concern aircraft of categories glider, very light aircraft and unmanned.

The main reason for such a circumscription and, consequently, for the non-inclusion of larger and heavier aircraft, lies in two parameters: specific energy density and specific energy, [3]. The



first concerns the amount of energy available per unit mass; while the second is the amount of energy that can be contained in each volume. The batteries currently used are the lithium ones as they guarantee a reduced volume and mass compared to the competitors. By comparing the lithium batteries available on the market with the fossil fuels currently in use, such as kerosene and diesel, the parameters suggest that, with the same specific energy density, the batteries would weigh about 50 times more than their fossil alternatives. At the same time, for the same specific energy, batteries would occupy about 18 times the volume of their fossil alternatives. At this point, one wonders how to overcome these physical limitations. A potential solution, object of this thesis work, is represented by multifunctional materials, [6]. The latter are materials capable of fulfilling several functions simultaneously: in our case reference will be made to the structural batteries, which, as mentioned above, perform both a structural and energy storing function at the same time. This work deals with the most interesting points concerning the applications of Structural Batteries in the aeronautical field, [4]. The main environmental issues and the objectives that push aviation towards a 'green' perspective were discussed. Subsequently, a summary of the most relevant literature on the state of the art available regarding structural batteries was discussed. A focus on the mechanical point of view was made by discussing the main issues related to their manufacturing and certification requirements. The main current regulations issued by the FAA and EASA were discussed and a 'tailoring' between lithium-ion battery standards and composite material standards was discussed to find a certification process for this type of materials.

Material and Process Control

It is more important than ever to ensure that batteries are safe, strong, and dependable. However, the safety, performance, and longevity of a battery are only as excellent as the materials used to make them. *Electrodes, separators, current collectors, and electrolytes* must be extensively characterized and monitored from the moment they enter the production plant until they are incorporated into the finished product.

Solid electrode materials, it is well known that the parameters of the electrochemically active material have a substantial influence on the performance of battery electrodes. Following the formulation of the electrode, the components must be combined to produce a slurry or a dry blend. Relevant influencing variables include particle size, aggregate or agglomeration size, and particle size distributions of the different components. Furthermore, determining features such as powder rheological qualities or particle density and porosity can aid in tailoring the dry-mixing process. The characteristics of the powders are critical for functional and process-relevant factors. These include particle size distribution and mean particle size, particle shape, porosity, and specific surface area. They affect the flowability, dispersibility, and viscosity of the particles, as well as the sedimentation (stability) of the final slurry. The latter influences structural recovery after application, drying and calendaring behaviour of the produced electrode layer, mechanical characteristics, and, lastly, the electrochemical parameters of the battery cell.

Electrode slurries, proper design and development of the mixing and coating procedures of the anode and cathode slurry is critical to battery performance. Knowing a slurry's rheological behaviour can also aid in the dimensioning of slurry pumps and anticipating slurry storage behaviour. The uniform thickness and density of the slurry layer are critical to ensuring the battery's lifetime, charge-discharge performance, and ion transfer rate - regardless of battery size. Finally, the proportion of solid particles in a slurry determines the quality and uniformity of the final coating.

Separators: A lithium-ion battery's separator is a thin, porous membrane that plays an important role in battery performance by avoiding a short circuit between the anode and cathode while permitting ion movement between them. Separators must be mechanically strong, stable in active battery conditions, and inert to other cell components while remaining porous enough to allow ion passage. The separator's through-pore size is an important characteristic for guaranteeing optimal

battery performance since the holes must be tiny enough to prevent dendrites from growing across the separator while yet being large enough to allow ion movement between the cathode and anode. Larger pores or pin holes must also be searched for and avoided since they might contribute to short-circuit generation. Mechanical strength and structural qualities are another important criterion for separators. Measuring the amount of pre-tension necessary for the separator is critical for avoiding rupture or tearing during assembly as well as drooping after assembly.

Liquid electrolyte, lithium-ion electrolytes are essential in batteries because they allow charge transfer between the anode and cathode. Lithium-containing salts dissolved in an organic solvent are employed for this purpose. The salt lithium hexafluorophosphate (LiPF₆) is most often utilized. Because of the reactivity of lithium in water, organic solvents serve as matrix in which lithium salts are embedded.

Raw material quality, adequate salt dissolving, and ion mobility are all critical elements to consider.

Performance-based regulations

Performance-based regulation is commonly regarded as a preferable way to regulation [7]. Rather than outlining the actions that regulated companies must take, performance-based regulation mandates the achievement of results and provides flexibility in how to reach them. Thus, assuming this approach is valid, it is possible, e.g., to treat a composite laminate in which a structural battery is integrated as a laminate in which a delamination has occurred evolving the current regulatory activities, and which meets the structural and electrical requirements considering that:

- regarding the structural aspect, the concept of damage tolerance and fatigue assessment of the structure, a strength assessment, detail design and fabrication shall demonstrate that catastrophic failure due to fatigue, manufacturing defects, deterioration, Environmental (ED) or Accidental Damage (AD) will be avoided for the operational life of the aircraft systems [13].
- regarding the aspect of the interaction between systems and structure, for aircraft equipped with systems that affect structural performance, either directly or because of a failure or malfunction, the influence of these systems and their failure conditions shall be considered when demonstrating compliance with airworthiness requirements, to evaluate the structural performance of airplanes equipped with these systems [13].

In addition to FAA requirements [11] and [12], the AGATE [9] and NCAMP [10] programs are two databases that provide a list of composite materials certified according to FAR part 25 regulations, reporting, in addition, the entire material certification procedure.

Certification Requirements for Composite Materials

One of the problems associated with this new technology concerns the certification process. This research activity seeks to carry out a 'tailoring' between the existing certification regulations of composite materials and lithium batteries, since the structural batteries, simultaneously fulfilling the functions of structural element and energy storing, must simultaneously comply with the two regulations.

For the structural airworthiness requirements, reference is made to the Advisory Circular 20-107 of the Federal Aviation Administration, which refers to the Code of Federal Regulation 14 parts 23, 25, 27 and 29.

In particular, the latter impose that the structure, regardless of the material it is made of, must be subjected to static tests, performed at 150% of the Design Limit Load, fatigue tests where the structure is subjected to cyclic loads with frequencies between 5 and 10 Hz, and impact tests and Damage Tolerance with impactors of different sizes.

At the first level (coupon level) we are interested in defining the mechanical properties of foil and laminate, thus defining the admissible ones.

The second level of analysis is dedicated to establishing the eligibility for critical structural details present in the project. The elements are still relatively simple structures, such as: glued or bolted joints, skin-stringer combinations, panels or laminates which in the design are loaded more in tension, compression and shear.

These elements are tested both at room temperature and in extreme environmental conditions, depending on the fatigue loads that could be encountered in real service conditions of the structure. Then the sub-component level analysis takes place in which are tested for example: wing panels reinforced by currents, simplified mobile surfaces, spars, ribs.

It is a generally unnecessary test that is only required when new materials are used in the project.

The last level of analysis is the full scale, which concerns the entire structure, which must be tested both statically and for durability and damage tolerance in different environmental conditions.

Focusing on the coupon level test, the legislation imposes the test execution methods and the selection of the samples to be tested (number, type and size). A-Basis type samples are distinguished with mechanical properties higher than 99% of the population with a confidence interval of at least 95% (for their determination, at least 55 different specimens are tested, obtained starting from 5 banks of material); B-Basis which have mechanical properties greater than 90% of the population with a confidence interval of 95% (for their determination at least 18 specimens obtained from 3 banks of material are tested).

The samples are tested according to regulations in various conditions and the tests are performed in compliance with the standards imposed by the American Society for Testing and Materials, which set out the test conditions, the methods of execution, the dimensions of the sample, the number of tests necessary and the conditions of acceptability of the test results.

From an energy storing point of view, the structural batteries must be certified according to Advisory Circular 20-174 which establishes the rules relating to safety, health monitoring, continuing airworthiness and maintenance of these devices.

Conclusions

In this report general considerations about certification requirements on composite material structures and the current trend of certification agencies to move towards a performance-based regulations have been addressed.

We are still a long way from certifying an aircraft of this type, the solutions currently available do indeed allow for 'full-electric' travel but at the expense of the aircraft's distance and duration ranges. In the meantime, other solutions are also being evaluated, such as integrating the batteries into the floor or within other constituent elements of the aircraft. In other fields of application such as the automotive one, research seems to have obtained better results, think of Tesla which has managed to integrate the battery pack into the powertrain or other solutions that provide for the integration of structural batteries into the vehicle body, [5]; clearly this is possible because on the ground it is not necessary to submit to the weight limits physically imposed by the aeronautical field.

Although the application of this technology, to date, is easier to apply for a field such as the automotive one, not subject to the physical and certification limitations imposed, however, in the aeronautical field, it is always necessary to continue to look to the future by pushing the research towards new frontiers and solutions.

References

- [1] European Commission. Communication from the Commission—The European Green Deal.

- [2] Yildiz, M. (2022). Initial airworthiness requirements for aircraft electric propulsion. *Aircraft Engineering and Aerospace Technology*, 94(8), 1357-1365. <https://doi.org/10.1108/AEAT-08-2021-0238>
- [3] Sziroczak, D., Jankovics, I., Gal, I., Rohacs, D. (2020). Conceptual design of small aircraft with hybrid-electric propulsion systems. *Energy*, 204, 117937. <https://doi.org/10.1016/j.energy.2020.117937>
- [4] Adam, T.J., Liao, G., Petersen, J., Geier, S., Finke, B., Wierach, P., Kwade, A., Wiedemann, M. (2018). Multifunctional Composites for Future Energy Storage in Aerospace Structures. *Energies*, 11, 335. <https://doi.org/10.3390/en11020335>
- [5] Scholz, A.E., Hermanutz, A., Hornung, M. (2018). Feasibility Analysis and Comparative Assessment of Structural Power Technology in All-Electric Composite Aircraft. In *Proceedings of the Deutscher Luftund Raumfahrtkongress, Friedrichshafen, Germany*.
- [6] Nguyen, S.N., Millereux, A., Pouyat, A., Greenhalgh, E.S., Shaffer, M.S.P., Kucernak, A.R.J., Linde, P. (2021). Conceptual Multifunctional Design, Feasibility and Requirements for Structural Power in Aircraft Cabins. *Journal of Aircraft*, 58, 677–687. <https://doi.org/10.2514/1.C036205>
- [7] <https://www.easa.europa.eu/sites/default/files/dfu/Report%20A%20Harmonised%20European%20Approach%20to%20a%20Performance%20Based%20Environment.pdf>
- [8] <https://www.acquisition.gov/far/part-25>
- [9] <https://agate.niar.wichita.edu/>
- [10] https://www.wichita.edu/industry_and_defense/NIAR/Research/ncamp.php
- [11] FAA. AC20-107B: *Composite Aircraft Structure*. 2009.
- [12] FAA. AC20-184: *Guidance on Testing and Installation of Rechargeable Lithium Battery and Battery Systems on Aircraft*. 2015.
- [13] EASA. CS-25: *Certification Specifications for Large Aeroplanes*.

Dynamic buckling structural test of a CFRP passenger floor stanchion

Gennaro Di Mauro^{1,a}, Michele Guida^{1,b,*}, Fabrizio Ricci^{1,c}, Leandro Maio^{1,d}

¹Department of Industrial Engineering, University of Naples Federico II, Naples, Italy

^agennaro.dimauro@unina.it, ^bmichele.guida@unina.it, ^cfabrizio.ricci@unina.it

^dleandro.maio@unina.it

Keywords: Composite Material, Transient Analysis, Test Validation, Dynamic Buckling

Abstract. The work focuses on the study of the structural behavior of a composite floor beam in the cargo area of a commercial aircraft subjected to static and dynamic loads. Experimental tests have been performed in the laboratories of the Dept. of Industrial Engineering (UniNa) jointly with the development of numerical models suitable to correctly simulate the phenomenon through the LS-DYNA software. The definition of a robust numerical model allowed to evaluate the possibility of buckling triggering. The test article was equipped with potting supports on both ends of the tested beam, filling the pots with epoxy resin toughened with glass fiber nanoparticles. This allowed to uniformly load the beam ends in compression and to carry out the tests loading the specimen statically and dynamically, to observe the differences in the behavior of the beam in correspondence with the two different types of applied load. The result obtained through the comparison between the numerical model and the experimental test is that the dynamic buckling is triggered by a quantitatively smaller load than in the static case. Furthermore, it has been observed that the experimental compressive displacement to trigger the dynamic buckling instability is greater than the displacement observed in the static case.

Introduction

Buckling is an instability phenomenon that is common in "thin" structures. Buckling was formerly thought to be a totally static occurrence. The classic example is the Euler column buckling, in which a beam properly restrained and statically loaded in compression at the ends experiences the equilibrium instability usually in the linear elastic material behavior range.

Depending on the applied load, the beam can return to the initial equilibrium configuration (stable equilibrium), move to a new equilibrium condition different from the initial one (indifferent equilibrium), or move away from the initial equilibrium configuration indefinitely (unstable equilibrium). The buckling load is the smallest load for which equilibrium is indifferent.

Buckling can, however, be produced by varying loads over time. Many writers [1-3] have explored the application of a time-dependent axial stress to a beam, which causes lateral vibrations and can eventually lead to instability.

Dynamic buckling is a relatively new phenomenon. One of the first researchers to investigate dynamic buckling was [4], who proposed a theoretical solution for the situation of a simply supported rectangular plate exposed to variable floor loads over time. A criterion that connected dynamic buckling to load duration was developed in [5] and [6] where it was investigated the effects of a high intensity, short duration load. According to the findings, long-term critical dynamic buckling stresses may be less intense than matching static buckling loads.

According to the findings, long-lasting critical dynamic buckling stresses may be less intense than matching static buckling loads.

In this study, the structural behaviour of a composite floor beam subjected to low-frequency cyclic load conditions has been explored. Three distinct loads—below, near to, and over the static critical buckling load—have been taken into account to determine the structural response.



The aim is to conduct an experimental numerical investigation of the dynamic buckling phenomenology on a composite material beam. It was important to modify the test object to make sure the experimental test was carried out correctly. In specifically, two pottings were attached to the ends of the bar using epoxy resin castings toughened with glass fibre nanoparticles to guarantee that the compressive force was applied symmetrically.

The department laboratory's test equipment was used to conduct the experimental experiments. LS-DYNA software was used to mathematically recreate the treated phenomena. The Matlab working environment was used to process the results.

Case study description

The geometrical model and the numerical model, discretized in the Finite Element (FE) environment, are reported in Figure 1, while the mechanical properties of the composite lamina are reported in Table 1. The stacking sequence of the beam is [-45; 45; 90; 45; -45; 0; 0; 0; 0; 0; -45; 45; 90; 45; -45].

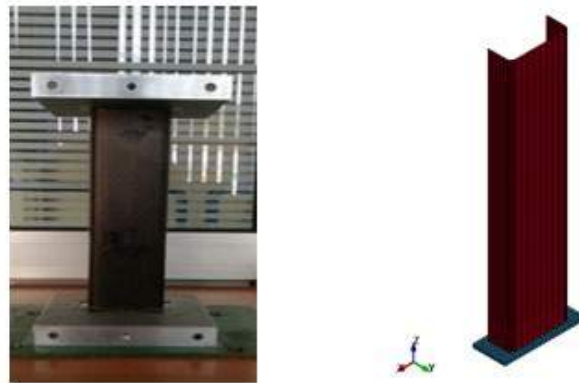


Figure 1. Left: geometrical model; right: numerical model.

Table 1. Mechanical properties of the lamina.

ρ [g/cm ³]	th [mm]	E_{11} [MPa]	E_{22} [MPa]	G_{12} [MPa]	G_{13} [MPa]	G_{23} [MPa]	ν_{12}	X_t [MPa]	X_c [MPa]	Y_t [MPa]	Y_c [MPa]	Sc [MPa]
1.6	0.186	135000	8430	4160	4160	3328	0.26	2257	800	75	171	85

To find the optimal balance between computational costs and the correctness of the findings in terms of expected stiffness, a preliminary mesh convergence study has been performed. As a result, several static linear studies with varied in-plane and through-the-thickness element sizes have been carried out. Particularly, three distinct mesh element sizes—coarser (8 mm), moderate (4 mm), and finer (2 mm) were taken into consideration. Nine mesh configurations have been examined, and analyzed, three through-the-thickness mesh configurations having been researched for each in-plane element size.

Results

The numerical model has been verified by comparison with the stiffness and failure findings of an experimental test programme, the compressive experimental test up to ultimate failure and reported in the last work [8] underlined the results:

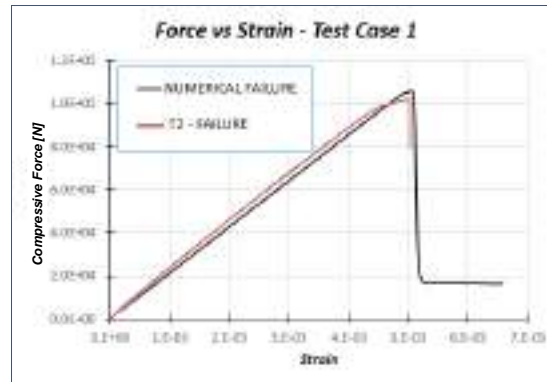


Figure 2. Numerical-experimental comparisons: Load vs. strain.

According to these experimental testing, the breaking load was 103kN, and up to the failure load, there are no buckling events, both experimentally.

The table 2 reports the failure displacements and loads, there is good agreement between the solutions of both formulations.

Table 2. Numerical-experimental comparisons: Failure displacement and failure load.

	Failure Displacement	Failure Load
Numerical	1.59 mm	107.3 kN
Experimental	1.60 mm	104.0 kN
Error	0.06%	3.1%

Then, a compressive experimental test designed to measure the structure's stiffness was repeated without taking the failure into account to confirm the linear deformation on the 315mm-long stanchion made of a composite material that combines carbon fibres with a highly toughened epoxy matrix and a 15-ply lamination sequence.

Figure 3 shows the good agreement in stiffness and failure load between the numerically predicted solutions and the outcomes of the experimental campaign testing. Additionally, the Hashin's failure criteria were used to compute the test article's failure mode, which was then predicted with a high degree of accuracy.

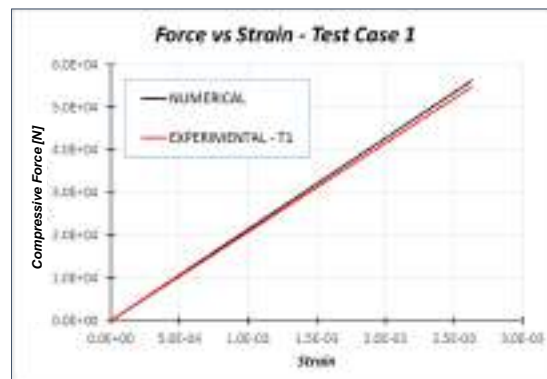


Figure 3. Numerical-experimental comparisons: Load vs. strain.

Once the numerical model is validated by static test, the dynamic experimental test is executed applying a load increase and constant speed of 100 mm/s. The explicit numerical investigations have been carried out to investigate how the dynamic buckling phenomena came to be. Every explicit analysis has been run with a structural dampening of 2%.

In figure 4 is plotted the $F(t)$, from the analysis of the following graphs, the phenomenon of dynamic buckling instability can be observed, which occurs after 0.18 ms. Close to this time value, a buckling load equal to 89 kN and a displacement value equal to 0.063 mm are noted.

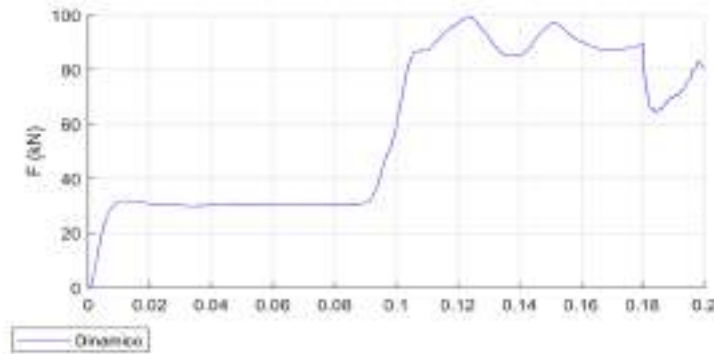


Figure 4. Time history of the force in the dynamic experimental test.

Conclusions

It is clear from an examination of the findings that: for composite materials, the buckling load in a dynamic compression test assumes a lower value than the buckling load in a quasi-static compression test. Additionally, in a dynamic compression test, a larger displacement than that required to cause buckling in a quasi-static compression test is required to cause the buckling phenomena. Finally, it can be shown that during the dynamic compression test, after buckling is attained, the structure does not collapse, but rather the bar tack may continue to operate in post buckling.

The figure 5 reports the differences between the numerical simulation about the post buckling static and dynamic, when the dynamic buckling value is exceeded in the left case, the post-buckling displacements are transmitted by the lower plate throughout the beam, whereas in the quasi-static compression test, the structure collapses and the displacements are not as effectively transmitted.

In the case of the dynamic compression test, it is observed that the curve $F(t)$ exhibits a plateau close to the buckling load. This is because some of the mechanical energy resulting from the application of the load is lost due to the deformation that took place after the beam protruded from its axis.

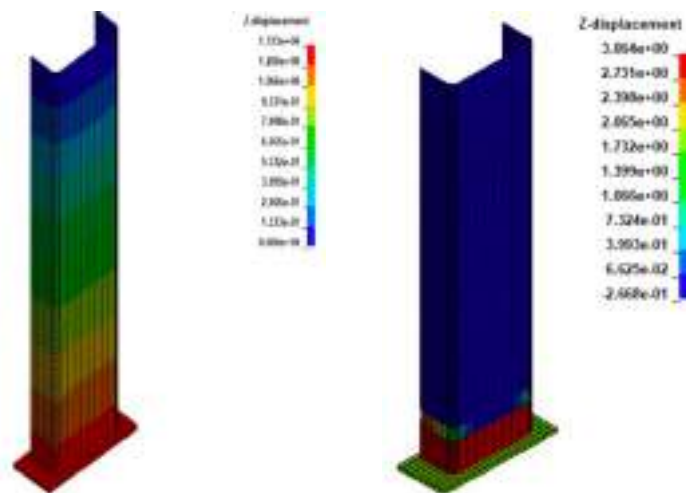


Figure 5. Post buckling in static and dynamic simulations.

References

- [1] M. Amabili, M.P. Païdoussis. Review of studies on geometrically nonlinear vibrations and dynamics of circular cylindrical shells and panels, with and without fluid-structure interaction. *Applied Mechanics Reviews*. 56(4):349-356, 2003. <https://doi.org/10.1115/1.1565084>
- [2] F. Alijani, M. Amabili. Non-linear vibrations of shells: A literature review from 2003 to 2013. *International Journal of Non-Linear Mechanics*. 58:233-257, 2014. <https://doi.org/10.1016/j.ijnonlinmec.2013.09.012>
- [3] T. Kubiak. Static and dynamic buckling of thin-walled plate structures. In. *Static and Dynamic Buckling of Thin-Walled Plate Structures*, 2013. <https://doi.org/10.1007/978-3-319-00654-3>
- [4] G.A. Zizicas. Dynamic buckling of thin elastic plates. *Transactions of the ASME*. 74(7):1257, 1952. <https://doi.org/10.1115/1.4016090>
- [5] B. Budiansky, R.S. Roth. Axisymmetric dynamic buckling of clamped shallow spherical shells. *NASA TN D-1510*: 597-606, 1962.
- [6] H.E. Lindberg, A.L. Florence. *Dynamic Pulse Buckling*, 1987. <https://doi.org/10.1007/978-94-009-3657-7>
- [7] A. Sellitto, F. Di Caprio, M. Guida, S. Saputo A. Riccio. “Dynamic pulse buckling of composite stanchions in the sub-cargo floor area of a civil regional aircraft”. *Materials*, 2020, vol. 13 issue 16, 3594. <https://doi.org/10.3390/ma13163594>

Deep learning algorithms for delamination identification on composites panels by wave propagation signals analysis

Ernesto Monaco^{1,a*}, Fabrizio Ricci^{1,b}

¹ Department of Industrial Engineering – Aerospace Section – Università degli Studi di Napoli “Federico II”, Italy

^aermonaco@unina.it, ^bfabricci@unina.it

Keywords: Structural Health Monitoring, Composites Structures, Deep Neural Networks

Abstract. Performances are a key concern in aerospace vehicles, requiring safer structures with as little consumption as possible. Composite materials replaced aluminum alloys even in primary structures to achieve higher performances with lighter components. However, random events such as low-velocity impacts may induce damages that are typically more dangerous and mostly not visible than in metals. Structural Health Monitoring deals mainly with sensorised structures providing signals related to their “health status” aiming at lower maintenance costs and weights of aircrafts. Much effort has been spent during last years on analysis techniques for evaluating metrics correlated to damages’ existence, location and extensions from signals provided by the sensors networks. Deep learning techniques can be a very powerful instrument for signals patterns reconstruction and selection but require the availability of consistent amount of both healthy and damaged structural configuration experimental data sets, with high materials and testing costs, or data reproduced by validated numerical simulations. Within this work will be presented a supervised deep neural networks trained by experimental measurements as well as numerically generated strain propagation signals. The final scope is the detection of delamination into composites plates for aerospace employ. The approach is based on the production of images trough signal processing techniques and on employ of an image recognition convolutional network. The network is trained and tested on combinations of experimental and numerical data.

Introduction

Last developments in the modern aerospace industry push towards an improvement in flight efficiency and autonomy leading to a great increment in the usage of composite materials. They allow to lower the weight and obtain easily more complex shapes, but, due to their peculiar composition and fabrication methods, they are affected by delamination and defects. So, every aircraft’s component is subject to time-scheduled maintenance sessions even when there is no clear evidence that it is required. This is a very expensive and time consuming process.

In this field, the Structural Health Monitoring technology (SHM system) [1,2,3], based on networks of distributed sensors embedded, or secondary bonded, throughout the whole structure under investigation, could be conveniently used for real-time health monitoring and/or as a data acquisition tool. Structural data, however, may constitute an enormous amount of information that in most cases is difficult to classify. Furthermore, since time is an important factor, the automation of the analysis process could be a significant advantage in this field. From this point of view, intelligent algorithms that can take decision in an autonomous manner reducing the human participation, like Deep Neural Networks (DNNs), may be useful to overcome this impasse.

Structural data may be adequately filtered with the aid of specific Deep Neural Networks designed and trained for the structural context and aimed to the classification and identification of significant parameters [4,5,6]. The DNNs, based on strategic engineering criteria, may represent an effective and efficient analysis tool to promote faster data analysis and classification. In the field of aircraft maintenance, this approach may lead, for example, to a faster awareness of a

component health situation or predict failures. Neural Networks typically requires a relevant amount of data in order to be trained and to acquire the necessary reliability in classifying and recognizing the occurrence of the selected event but, once trained, they can be extremely effective and low-time consuming in analysing each single scenario to be classified. In this study the potentialities of deep learning with high frequency Lamb waves propagation based SHM methodologies are investigated employing explicit finite element simulations to collect propagation signals due to impact damages on a composite plate; this approach will also be employed in the next future to populate experimental data sets necessary for deep learning algorithm. Previous experimental signals acquired on the real impacted carbon fiber panel have been used to validate a numerical equivalent to allow the expansion of the dataset available [5].

Numerical time history signals have been collected for both the healthy and un-healthy state of the structure and transformed into RGB images. A well-known convolutional algorithm trained on healthy and damaged signals is used to identify anomalies in the form of delamination in the structure. The paper presents the pre-liminary results achieved by the authors..

SHM algorithm implementation

The goal of the work is to develop a neural network capable of detecting damage and its position in a composite panel exploiting Lamb waves. For this purpose, a numerical model was used to simulate the propagation of Lamb waves in a flat composite panel. Then, a Matlab algorithm has been created to transform the detected signals into images that the adopted neural network classifies as damaged or intact.

Numerical model, experimental set-up and signal analysis

The composite panel considered consists of 12 plies of three different pre-preg types oriented according to multiple directions [7,8]. The PZT sensors, utilized for lamb waves generation and acquisition, are applied on the panel according to the geometry in Fig. 1b.

The "pitch-catch" technique has been adopted for signals acquisition and damage detection, that is, a transducer behaves as an actuator, while the remaining sensors detect the signal that has been released inside the panel. Four different positions were considered for impact damage simulation.

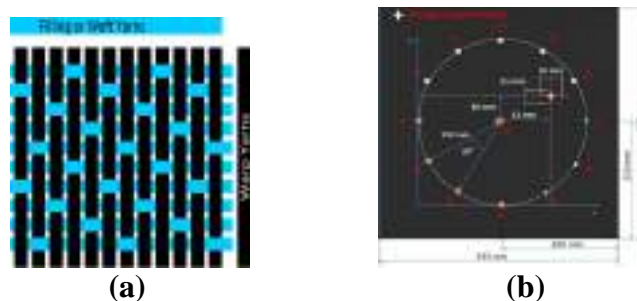


Fig. 1. a) 5-Harness Satin Weave Layer; b) composite panel sensors configuration

A key point is the data analysis from rough signals to get a proper identification system. Features (time of flight, group velocity, signal transmission factor, wave energy) are extracted with an appropriate signal processing technique obtaining a diagnosis that presents location and/or severity of the damage.

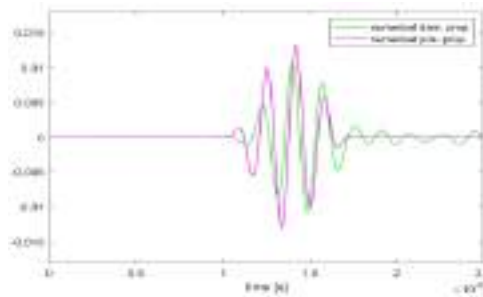


Fig. 2. Signals comparison between pristine and damaged model (path 20_46)

So, if “f” is the particular propagation feature considered, it is possible to define a damage index according to the following formulation:

$$DI = \frac{(f_d - f_b) \cdot (f_d - f_b)}{f_b \cdot f_b}$$

Where f_d is the value obtained by the signal of the panel as it is at the analysis time, while f_b is the one extracted by the baseline propagation. Then, a damage index (DI) close to zero suggests a healthy-like propagation, while a value over a certain threshold warns for a failure.

RGB images generation ,analysis and results

To implement the convolutional approach, the acquired signals are transformed into RGB images exploiting a MATLAB code. RGB (Red Green Blue) is an additive color model, that is, an abstract mathematical model that allows to represent colors in numerical form, using the red, green, and blue color components. Each image obtained concerns a specific actuator-sensor path and consists of the overlap between the signal detected in the intact panel and that detected in the damaged panel. Going from top to bottom, the signals overlap consists of 10 intact signals, 10 signals in which a damaged and an intact alternate, and finally 10 damaged signals. As shown in Fig. 3, it is clear that the damaged images are characterized by a series of horizontal knurls (that are missing in typical healthy images). The latter are induced by disturbances in signal reception, attributable to damage.

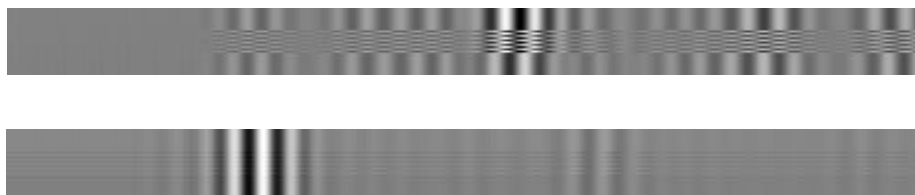


Fig. 3: Generic experimental image damaged (above) and intact (below) obtained by RGB conversion

For images analysis the Google Net neural network, already present in MATLAB, was used. It is a deep convolutional neural network architecture codenamed Inception that achieves the new state of the art for classification and detection in the ImageNet Large-Scale Visual Recognition Challenge 2014 (ILSVRC14); is a convolutional network consisting of 144 layers, which requires an image as input and returns its classification in output. The network training phase was carried out using MATLAB's Deep Network Designer, a tool that allows to graphically train a neural network, entering the appropriate training parameters such as learning speed, validation frequency and number of epochs. The network was trained in three different ways to evaluate the recognition efficiency of the experimental images and the relative reliability: numerical, experimental and